October 2018

THE BALANCE BETWEEN DIPOLE-DIPOLE INTERACTIONS AND STERIC EXCLUSION ON ORDERING IN CATIONIC POLYMERS

Chinomso Nwosu
University of Massachusetts Amherst

THE BALANCE BETWEEN DIPOLE-DIPOLE INTERACTIONS AND STERIC EXCLUSION ON ORDERING IN CATIONIC POLYMERS

A Dissertation Presented

By

CHINOMSO T. NWOSU

Submitted to the Graduate School of the University of Massachusetts Amherst in partial fulfillment of the requirements for the degree of

DOCTOR OF PHILOSOPHY

SEPTEMBER 2018

Polymer Science and Engineering

THE BALANCE BETWEEN DIPOLE-DIPOLE INTERACTIONS AND STERIC EXCLUSION ON ORDERING IN CATIONIC POLYMERS.

A Dissertation Presented

By

CHINOMSO T. NWOSU

Approved as to style and content by:

E. Bryan Coughlin

Greg Grason, Member

Sarah Perry, Outside Member

E. Bryan Coughlin, Department Chair

Polymer Science and Engineering

DEDICATION

To the Beautiful Journey and her Perfect Painting

ACKNOWLEDGEMENTS

I am thankful to my advisor, Prof. E. Bryan Coughlin, for his mentorship and support. Most importantly, he has always being available to talk to, not just about science, but student and career life in general. By extension, I will like to thank the whole Coughlin group members past and present: Dr. Hussain Tas, Dr. WenXu Zhang, and Dr. Patrick Homyak, Dr. Bryan Cromer, Jo, Rohit, Josh, Yifeng, Ria, Hyuen and Christian to mention just a few. I would not have asked for a better group.

I will also like to thank other members of my thesis committee, Prof. Grason and Prof. Perry for all their advice and availability through this program. I appreciate Prof. Hsu, Prof. Carter, and Prof. McCarthy for allowing me to make use of their group equipment and also for their encouraging quips on occasions that I have ran into them.

Special thanks to U.S. Army for providing the funding for this work. Also want to thank the Prof. Andrew Herring and his group for helping me with Electrochemical Impedance Spectroscopy characterization. Special thanks to Samuel Galito, Ye, and Tara, Himanshu and Ashley. In fact, I will like to thank the MURI team as a whole. Moreover, I am thankful to Soenke and the Argonne National Laboratory, Advanced Photon Source.

Many thanks to Prof. Muthukumar and Russell for their commitment to improving my understanding of polymer physics. Dr. Wieguo for introducing me to solid-state NMR. And also Emeritus Prof. Vim de Jeu for his precious suggestions.

I will also like to thank the Class of 2013, especially Ben, Di and Cristiam, for their friendship and support throughout this program.

Also, I am thankful to Lisa, Jessica, and Maria for their ardent commitment to graduate students.

I also want to thank my friends, Kachi, Kennedy, Damola, Niyi, Yetunde, Ziwen, and others who are not mentioned here for their support both socially and academically.

I am immensely thankful to my parents Festus and Ijeoma Nwosu for all their many love and sacrifice. My siblings Dimma, Eze, Uche, and Amara deserve honorable mention as well.

Finally, I am unreservedly grateful to my family: Ebru and Ijeoma II. You've been like a light that shines in a dark place - the morning stars that rise in my heart.

ABSTRACT

THE BALANCE BETWEEN DIPOLE-DIPOLE INTERACTIONS AND STERIC EXCLUSION ON ORDERING IN CATIONIC POLYMERS.

SEPTEMBER 2018

CHINOMSO NWOSU

B.Eng., FEDERAL UNIVERSITY OF TECHNOLOGY OWERRI

M.S., GRENOBLE INSTITUTE OF TECHNOLOGY

M.S., TECHNICAL UNIVERSITY OF DARMSTADT

M.S., UNIVERSITY OF MASSACHUSETTS AMHERST

Ph.D., UNIVERSITY OF MASSACHUSETTS AMHERST

Directed by: Prof. E. Bryan Coughlin

Structure-property correlations in charged polymers is an interesting facet of polymer science. Understanding the effects of intermolecular forces on the morphologies of polymers can lead to the design of membranes with desired structures to improve properties, for example ion conductivity. In random, comb-shaped polycations, competing intermolecular forces result in two different short-range orderings. Side-chain steric repulsion results in backbone-backbone morphology characterized by periodic spacing between polymer backbones. However, dipole - dipole attraction in these polycations can facilitate the formation of ionomer cluster morphology characterized by a spacing between clustered dipoles. Although both of these short-range orderings have disparate origins, their similar dimensions when characterized by X-ray scattering can lead to a misattribution of one morphology for the other. To investigate this interplay between side-chain sterics and dipole-dipole attraction in polycations, random copolymers, and terpolymer of

poly(4-vinylpyridine) (P4VP), polyisoprene (PI), and polystyrene (PS) were synthesized and fully quaternized with 1-alkylhalides. X-ray scattering show that in samples having 2 carbons on its pendant side-chain dipole-dipole attraction facilitates the formation of ionomer cluster morphology. Whereas samples with 4, or more carbons, on their pendant side-chains were dominated by side-chain sterics resulting in backbone-backbone morphology. Copolymers with polyisoprene, having flexible backbones, favored the formation of ionomer cluster morphology. An "In-Line" Dipole Model was developed to predict the separation between polymer backbones at which both ionomer cluster and backbone-backbone morphologies could coexist. The pendant polyisoprene units in the random copolymers of the fully quaternized P4VP and PI were crosslinked into robust anion exchange membranes (AEMs). Ionic conductivities for AEMs with coexistent morphologies were exceptionally high. To utilize these highly conducting AEM morphologies for fuel cell applications, stable quaternary ammonium monomers were designed, synthesized, and characterized. The monomers, norbonenepropoxy-6-azonia-spiro(5,5)undecane, and norbonenehexoxy-6-azonia-spiro(5,5)undecane, were readily polymerized into solvent processable AEMs. Random and block copolymerization of the stable quaternary ammonium monomers with norbornenemethylbenzylether were performed. The resultant copolymers were solvent processed into flexible anion conducting membranes. In the random copolymers, the competition between electrostatics and sterics facilitated the formation of coexistent morphologies resulting in high ionic conductivities in these membranes. In the block copolymers, electrostatics facilitated the formation of a continuous ionic phase even at low ionic volume fractions. This percolated phase in the block copolymers resulted in excellent bromide conductivity.

TABLE OF CONTENTS

Page

LIST OF TABLES

LIST OF FIGURES

Figure **Page**

LIST OF SCHEMES

Schemes **Page**

ABBREVIATIONS

AEMs	Anion Exchange Membranes
AEMFC	Anion Exchange Membrane Fuel Cells
AAEMs	Alkaline Anion Exchange Membranes
DCM	Dichloromethane
DMF	Dimethylformamide
DMSO	Dimethylsulfoxide
EIS	Electrochemical Impedance Spectroscopy
ESAXS	Extreme Small Angle X-ray Scattering
FTIR	Fourier Transform Infrared Spectroscopy
HEMs	Hydroxide Exchange Membranes
HEMFCs	Hydroxide Exchange Membrane Fuel Cells
MAXS	Medium Angle X-ray Scattering
NDMDC	Norbornenendimethyldichloride
NHS4	Norbornenehexoxy-6-azonai-spiro(5,4)decane
NHS5	Norbornenehexoxy-6-azonai-spiro(5,5)undecane
NHS6	Norbornenehexoxy-6-azonai-spiro(5,6)dodecane

NMP	Nitroxide Mediated Polymerization
NMR	Nuclear Magnetic Resonance
NPS4	Norbornenepropoxy-6-azonai-spiro(5,4)decane
NPS5	Norbornenepropoxy-6-azonai-spiro(5,5)undecane
NPS6	Norbornenepropoxy-6-azonai-spiro(5,6)dodecane
NOR	Norbornene
PEMs	Proton Exchange Membranes
P4VP	Poly(4-vinylpyridine)
P4VP_C2Br	Poly(4-vinylpyridine) fully quaternized by 1-ethylbromide
P4VP_C3Br	Poly(4-vinylpyridine) fully quaternized by 1-propylbromide
P4VP_C4Br	Poly(4-vinylpyridine) fully quaternized by 1-butylbromide
P4VP_C5Br	Poly(4-vinylpyridine) fully quaternized by 1-pentylbromide
P4VP_C6Br	Poly(4-vinylpyridine) fully quaternized by 1-hexylbromide
P4VP_C7Br	Poly(4-vinylpyridine) fully quaternized by 1-dodecylbromide
P4VP_C8Br	Poly(4-vinylpyridine) fully quaternized by 1-octylbromide
P4VP_C9Br	Poly(4-vinylpyridine) fully quaternized by 1-nonylbromide
P4VP_C10Br	Poly(4-vinylpyridine) fully quaternized by 1-decylbromide

P4VP_C11Br	Poly(4-vinylpyridine) fully quaternized by 1-undecylbromide
P4VP_C12Br	Poly(4-vinylpyridine) fully quaternized by 1-dodecylbromide
P4VP_C1I	Poly(4-vinylpyridine) fully quaternized by 1-methyliodide
P4VP_C2I	Poly(4-vinylpyridine) fully quaternized by 1-ethyliodide
P4VP_C12I	Poly(4-vinylpyridine) fully quaternized by 1-dodecyliodide
P4VP-*r*-P4VP_C9Br	Poly(4-vinylpyridine) randomly and partially quaternized 1-with nonylbromide
P4VP-*r*-PI	Random copolymer of poly(4-vinylpyridine) and polyisoprene
P4VP-*r*-PI_C2Br	Random copolymer of poly(4-vinylpyridine) and polyisoprene fully quaternized by 1-ethylbromide
P4VP-*r*-PI_C3Br	Random copolymer of poly(4-vinylpyridine) and polyisoprene fully quaternized by 1-propylbromide
P4VP-*r*-PI_C4Br	Random copolymer of poly(4-vinylpyridine) and polyisoprene fully quaternized by 1-butylbromide
P4VP-*r*-PI_C5Br	Random copolymer of poly(4-vinylpyridine) and polyisoprene fully quaternized by 1-pentylbromide
P4VP-*r*-PI_C6Br	Random copolymer of poly(4-vinylpyridine) and polyisoprene fully quaternized by 1-hexylbromide

P4VP-*r*-PI_C8Br	Random copolymer of poly(4-vinylpyridine) and polyisoprene fully quaternized by 1-octylbromide
P4VP-*r*-PI_C1I	Random copolymer of poly(4-vinylpyridine) and polyisoprene fully quaternized by 1-methyliodide
P4VP-*r*-PI_C2I	Random copolymer of poly(4-vinylpyridine) and polyisoprene fully quaternized by 1-ethyliodide
P4VP-*r*-PI_C3I	Random copolymer of poly(4-vinylpyridine) and polyisoprene fully quaternized by 1-propyliodide
P4VP-*r*-PI_C6I	Random copolymer of poly(4-vinylpyridine) and polyisoprene fully quaternized by 1-hexyliodide
P4VP-*r*-PI-*r*-PS	Random copolymer of poly(4-vinylpyridine), polyisoprene, and polystyrene
P4VP-*r*-PI-*r*-PS_C2Br	Random terpolymer of poly(4-vinylpyridine), polyisoprene, and polystyrene fully quaternized by 1-ethylbromide
P4VP-*r*-PI-*r*-PS_C3Br	Random terpolymer of poly(4-vinylpyridine), polyisoprene, and polystyrene fully quaternized by 1-propylbromide
P4VP-*r*-PI-*r*-PS_C4Br	Random terpolymer of poly(4-vinylpyridine), polyisoprene, and polystyrene fully quaternized by 1-butylbromide
P4VP-*r*-PI-*r*-PS_C5Br	Random terpolymer of poly(4-vinylpyridine), polyisoprene, and polystyrene fully quaternized by 1-pentylbromide

P4VP-*r*-PI-*r*-PS_C6Br	Random terpolymer of poly(4-vinylpyridine), polyisoprene, and polystyrene fully quaternized by 1-hexylbromide
P4VP-*r*-PI-*r*-PS_C8Br	Random terpolymer of poly(4-vinylpyridine), polyisoprene, and polystyrene fully quaternized by 1-octylbromide
P4VP-*r*-PI-*r*-PS_C1I	Random terpolymer of poly(4-vinylpyridine), polyisoprene, and polystyrene fully quaternized by 1-methyliodide
P4VP-*r*-PI-*r*-PS_C2I	Random terpolymer of poly(4-vinylpyridine), polyisoprene, and polystyrene fully quaternized by 1-ethyliodide
P4VP-*r*-PI-*r*-PS_C3I	Random terpolymer of poly(4-vinylpyridine), polyisoprene, and polystyrene fully quaternized by 1-propyliodide
P4VP-*r*-PI-*r*-PS_C6I	Random terpolymer of poly(4-vinylpyridine), polyisoprene, and polystyrene fully quaternized by 1-hexyliodide
P4VP-*r*-PI	Random copolymer of poly(4-vinylpyridine) and polystyrene
P4VP-*r*-PS_C2Br	Random copolymer of poly(4-vinylpyridine) and polystyrene fully quaternized by 1-ethylbromide
P4VP-*r*-PS_C3Br	Random copolymer of poly(4-vinylpyridine) and polystyrene fully quaternized by 1-propylbromide
P4VP-*r*-PS_C4Br	Random copolymer of poly(4-vinylpyridine) and polystyrene fully quaternized by 1-butylbromide

P4VP-*r*-PS_C5Br	Random copolymer of poly(4-vinylpyridine) and polystyrene fully quaternized by 1-pentylbromide
P4VP-*r*-PS_C6Br	Random copolymer of poly(4-vinylpyridine) and polystyrene fully quaternized by 1-hexylbromide
P4VP-*r*-PS_C8Br	Random copolymer of poly(4-vinylpyridine) and polystyrene fully quaternized by 1-octylbromide
P4VP-*r*-PS_C1I	Random copolymer of poly(4-vinylpyridine) and polystyrene fully quaternized by 1-methyliodide
P4VP-*r*-PS_C2I	Random copolymer of poly(4-vinylpyridine) and polystyrene fully quaternized by 1-ethyliodide
P4VP-*r*-PS_C3I	Random copolymer of poly(4-vinylpyridine) and polystyrene fully quaternized by 1-propyliodide
P4VP-*r*-PS_C6I	Random copolymer of poly(4-vinylpyridine) and polystyrene fully quaternized by 1-hexyliodide
P4VP-*b*-PS	Block copolymer of poly(4-vinylpyridine) and polystyrene
P4VP-*b*-PS_C2Br	Block copolymer of poly(4-vinylpyridine) and polystyrene fully quaternized by 1-ethylbromide
P4VP-*b*-PS_C3Br	Block copolymer of poly(4-vinylpyridine) and polystyrene fully quaternized by 1-propylbromide

P4VP-*b*-PS_C4Br	Block copolymer of poly(4-vinylpyridine) and polystyrene fully quaternized by 1-butylbromide
P4VP-*b*-PS_C5Br	Block copolymer of poly(4-vinylpyridine) and polystyrene fully quaternized by 1-pentylbromide
P4VP-*b*-PS_C6Br	Block copolymer of poly(4-vinylpyridine) and polystyrene fully quaternized by 1-hexylbromide
P4VP-*b*-PS_C8Br	Block copolymer of poly(4-vinylpyridine) and polystyrene fully quaternized by 1-octylbromide
PNDMDC-*b*-PNHS5	Block copolymer of polynorbornenedimethyldichloride and poly(norbornenehexoxy-6-azonia-spiro(5,5)undecane)
PNDMDC-*b*-PNPS5	Block copolymer of polynorbornenedimethyldichloride and poly(norbornenepropoxy-6-azonia-spiro(5,5)undecane)
PNDMDC	Polynorbornenedimethyldichloride
PNHS5-*r*-PNMBzE	Random copolymer of poly(norbornenehexoxy-6-azonia-spiro(5,5)undecane) and polynorbornenemethybenzylether
PNHS5-*b*-PNMBzE	Block copolymer of poly(norbornenehexoxy-6-azonia-spiro(5,5)undecane) and polynorbornenemethybenzylether
PI	Polyisoprene
PS	Polystyrene

PNHS5	Poly(norbornenehexoxy-6-azonia-spiro(5,5)undecane)
PNPS5	Poly(norbornenepropoxy-6-azonia-spiro(5,5)undecane)
PNPS5-*r*-PNMBzE	Random copolymer of poly(norbornenepropoxy-6-azonia-spiro(5,5)undecane) and polynorbornenemethybenzylether
PNPS5-*b*-PNMBzE	Block copolymer of poly(norbornenehexoxy-6-azonia-spiro(5,5)undecane) and polynorbornenemethybenzylether
PNOR	Polynorbornene
PNOR-*r*-PNHS5	Random copolymer of polynorbornene and poly(norbornenehexoxy-6-azonia-spiro(5,5)undecane)
PNOR-*r*-PNPS5	Random copolymer of polynorbornene and poly(norbornenepropoxy-6-azonia-spiro(5,5)undecane)
Q	Scattering vector
T	Temperature
THF	Tetrahydrofuran
SAXS	Small Angle X-ray Scattering
WAXS	Wide Angle X-ray Scattering
XP4VP-*r*-PI	Crosslinked random copolymer of poly(4-vinylpyridine) and polyisoprene

XP4VP-*r*-PI_C2Br	Crosslinked random copolymer of poly(4-vinylpyridine) and polyisoprene fully quaternized by 1-ethylbromide
XP4VP-*r*-PI_C3Br	Crosslinked random copolymer of poly(4-vinylpyridine) and polyisoprene fully quaternized by 1-propylbromide
XP4VP-*r*-PI_C4Br	Crosslinked random copolymer of poly(4-vinylpyridine) and polyisoprene fully quaternized by 1-butylbromide
XP4VP-*r*-PI_C5Br	Crosslinked random copolymer of poly(4-vinylpyridine) and polyisoprene fully quaternized by 1-pentylbromide
XP4VP-*r*-PI_C6Br	Crosslinked random copolymer of poly(4-vinylpyridine) and polyisoprene fully quaternized by 1-hexylbromide
XP4VP-*r*-PI_C8Br	Crosslinked random copolymer of poly(4-vinylpyridine) and polyisoprene fully quaternized by 1-octyllbromide
TEM	Transmission Electron Microscopy
Å	Angstrom
°C	Degrees Celsius
Đ	Dispersity
d_B	Backbone-backbone spacing
d_L	Limiting length
d_I	Cluster-cluster spacing

d_K	Keesom Length
F_{DA}	Dipole-dipole attraction potential
K	Kelvin
K_B	Boltzmann constant
λ	Degree of humidification
$\lambda_{f^{[N]+}}$	Backbone-backbone spacing per methylene group
n	number of carbons on the pendant side-chain
l_B	Bjerrum length
ρ	Dipole moment
σ	Conductivity
4VP	4-Vinylpyridine

CHAPTER 1

INTRODUCTION

1.1 Introduction

The global energy crisis has led to the increased interest in alternative forms of energy. A thriving part of these investigations is the use of fuel cell technology. Fuel cells have higher efficiency and lower adverse environmental impact in comparison to the use of fossil fuels.[1–3] They have been successfully commercialized as a source of alternative energy and are being used in a range of applications.[4–8] A leading candidate for portable applications is the Proton Exchange Membrane Fuel Cells (PEMFCs). They rely on noble metal catalysts to function, and given the scarcity of noble metals, the cost of PEMFCs is understandably high. There are also longevity and fueling issues which has prevented wider adoption.[9] An alternative to proton transport is hydroxide transport in Hydroxide Exchange Membrane Fuel Cells (HEMFCs). Liquid electrolytes are used in these hydroxide-based fuel cells.[9] Hydroxide Exchange Membrane Fuel Cells (HEMFCs) have the advantage of a more facile oxygen reduction reaction since the operating medium is alkaline rather than the acidic environment for PEMFCs. Thus, HEMFCs can function without the use of noble metal catalysts. The absence of noble metals as an integral part of their operation makes them more affordable in comparison to PEMFCs. Another advantage of the alkaline medium is the efficient electro-oxidation of non-conventional fuels like sodium borohydride.[9] Furthermore, the electro-osmotic drag in HEMFCs opposes fuel crossover since the hydroxide ions travel in opposite direction to the direction in which the fuel is injected. Consequently, fuels with higher energy density than hydrogen or methanol can be used.

A major challenge of HEMFCs, however, is the high purity of oxygen gas required to prevent the formation of carbonate salts from CO_2 that is present in air when air is used as an oxygen source.[9–11] To prevent these complications, polymers are generally preferred for use as separator membranes. In these membrane systems, the cation moiety is fixed to the polymer structure as this then prevents the formation of carbonate precipitates. These systems are generally known as Anion Exchange Membranes (AEMs). However, they suffer from low ion conduction, poor chemical stability in alkaline medium, and insufficient mechanical properties. As in most polymers in which structure is invariably tied to properties, mechanical and conductivity properties have been reported to be dependent on the morphology of anion exchange membranes.[4,12–15] Consequently, it is of importance to perform fundamental studies on the structure-property relationships in AEMs. It is also imperative to study the intermolecular forces that govern the formation of these morphologies.

Polyelectrolytes, like other polymers, have a tendency to form interesting microstructures and some of these structures have been fully assessed in the literature.[16–19] One of the signature morphologies of polyelectrolytes is the clustering of dipoles, especially, in random copolymer systems of an ionic and non-ionic polymer.[19–24] These randomly charged polycations or polyanions form what is known as an ionomer cluster morphology. According to Hsu and Gierke, this morphology consists of clustered ions randomly distributed in a hydrophobic matrix.[19–21,25,26]

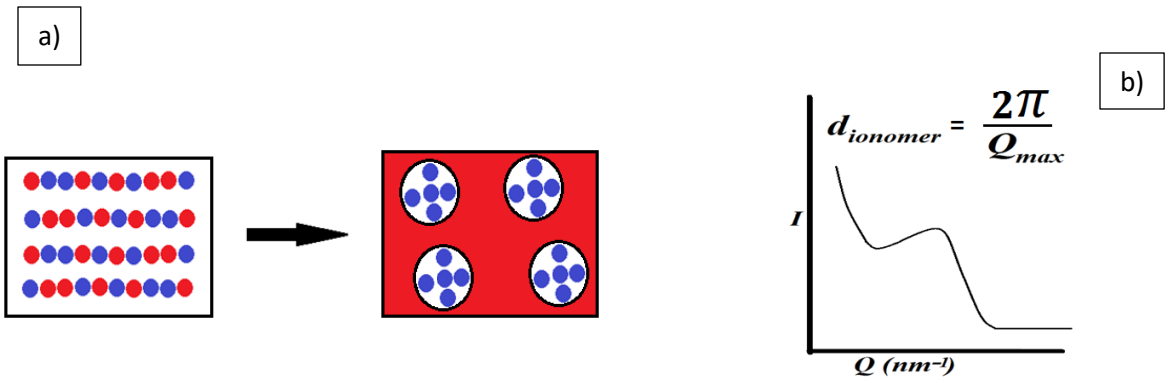

Figure 1.1. Schematic representation of a) dipole-dipole interaction resulting in ionomer cluster morphology, and b) X-ray scattering spectrum of an ionomer cluster morphology.

The average separation between these clusters can be directly measured using small angle X-ray scattering. The typical spacing within clusters in this microstructure is on the order of a few nanometers, however, this is also the length scale of the separation between alkylated polymer chains.[27–30] When pendant side-chains are introduced to polymer backbones (as in a comb-shaped polymer), a characteristic feature, the spacing between adjacent polymer backbones, can be measured by X-ray scattering. This periodic spacing in the polymer is due to the backbone-backbone morphology of these comb-shaped polymers. The spacing between backbones in these polymers increases with increasing length of side-chains.

The formation of ionomer cluster morphology results from the clustering of dipoles and the aggregation of the clustered dipoles into a larger collection of dipoles (multipoles). The spacing between the polymer backbones forms by an opposite principle, steric exclusion preventing polymer backbones from aggregating. Hence, in a polyelectrolyte system with the possibility of forming ionomer cluster and backbone-backbone morphology, some fundamental questions arise. Which of these two kinds of morphology will be the most favorable to be formed by a charged, random, comb-shaped polymer? Will the formation of the backbone-backbone morphology be

more favorable for a randomly charged comb-shaped polymer, or will the comb-shaped polymer preferentially form an ionomer cluster morphology? Can both morphologies (ionomers and backbone-backbone) coexist in a random, charged, comb-shaped polymer, or will the "driving forces" for the formation of both morphologies perfectly counterbalance each other; thereby, leading to the disappearance of any type of short-range ordering in the random, charged, comb-shaped polymer? Can we introduce a theoretical model that can explain the preference of a morphology in a model system?

A study of these competing morphologies (ionomers cluster and backbone-backbone morphology) which have similar length scales, arising from different physical origins, have not received much attention in the literature. As a matter of fact, there have been mischaracterizations of the scattering peak for backbone-backbone morphology that were erroneously attributed to the ionomer cluster morphology.[15,31,32] This dissertation offers a model that can explain the intermolecular origins of these two morphologies to further the understanding of both short and long-range ordering in anion exchange membranes. This dissertation also offers a study of the effect of dipole interactions beyond short and long-range ordering and how these interactions can lead to the formation of semi-crystalline morphology in comb-shaped homopolymers and block copolymers.

Anion exchange membranes are usually comprised of quaternary ammoniums (QAs). Quaternary ammoniums are notoriously unstable in alkaline medium.[9,33–51] Improving the chemical stability of the AEMs is of paramount importance to the furtherance of fuel cell science, especially, if AEMs are to compete as viable alternatives to proton exchange membranes. The motivation to synthesize stable QAs has led to an array of alkaline exchange membrane designs. However, until recently, only few studies on the design and synthesis of chemically stable QAs for anion exchange membranes have been reported. This is in part because studies comparing the chemical stability of

various monomer analogues of AEMs has been few in the literature.[11] Recently, Kreuer and Marino showed that Azo Spirocyclic Undecane-type (ASU-type) molecules show remarkable stability in very harsh alkaline environments.[11] Synthesizing these ASU-type monomers and then incorporating them into polymers have been a challenge for fuel cell scientists. Most ASU-type membranes have been prepared from the post modifications of polymers in which a precise control of the morphology and the corresponding property relationships are rarely studied.[52–60] A component of this dissertation will focus on designing ASU-type monomers that can be readily polymerized. The resultant polymers should be solvent processable into anion exchange membranes. These monomers will be designed to harness the effect of balancing dipole-dipole interactions and sterics on their morphologies. The morphology-conductivity relationships of these ASU-type AEMs will then be evaluated.

In Chapter 2, a model polymer, poly(4-vinylpyridine) was synthesized and quaternized. Poly(4-vinylpyridine) can be readily quaternized, transforming it into a charged, comb-shaped polymer. The transformation in the morphology of the polymer with extent of conversion (quaternization） was studied by both fourier transform infra-red spectroscopy and wide-angle X-ray scattering. The effect of hydration on the morphology of fully quaternized P4VP was evaluated. Morphology-ionic conductivity relations in fully quaternized P4VP were also evaluated.

In Chapter 3, block copolymers of poly(4-vinylpyridine) (P4VP) and polystyrene, PS, were synthesized and quaternized. The morphological changes associated with the block copolymer after quaternization was evaluated by X-ray scattering. The formation of a backbone-backbone substructure within a microphase separation between the ionic and the non-ionic block superstructure was investigated.

In Chapter 4, random copolymers of poly(4-vinylpyridine) (P4VP), and polyisoprene (PI), were synthesized and quaternized with 1-alkylhalides. A terpolymer of poly(4-vinylpyridine) and polyisoprene, with polystyrene (to introduce some stiffness into the P4VP-*r*-PI random copolymer) was synthesized and quaternized by 1-alkylhalides. Finally, a random copolymer of poly(4-vinylpyridine), P4VP, and polystyrene, PS, (a relatively stiffer polymer than both P4VP-*r*-PI and P4VP-*r*-PI-*r*-PS) was synthesized and quaternized with 1-alkylhalides. The In-Line Dipole Model, and its consequence on polymer morphology will also be introduced. Competition between dipole-dipole interaction and backbone-backbone sterics in P4VP-*r*-PI, P4VP-*r*-PI-*r*-PS, and P4VP-*r*-PS, and their resulting effect on the polymer morphology was analyzed in the light of the In-Line Dipole model.

In Chapter 5, the random copolymers of P4VP-*r*-PI quaternized by 1-alkylbromides were crosslinked by dithiol in the presence of UV-A light. The morphology-water uptake relationships were evaluated as well as the morphology-conductivity relationships.

In Chapter 6, the serendipitous discovery of semi-crystallinity in the atactic polymers of poly(4-vinylpyridine) quaternized by methyliodide, ethyliodide and ethylbromide were investigated by X-ray scattering, Differential Scanning Calorimetry (DSC) and Polarized Optical Microscopy (POM). This semi-crystallinity phenomenon was further evaluated in a block copolymer of poly(4-vinylpyridine) and polystyrene.

In Chapter 7, the design, synthesis and characterization of various ASU-type monomers was performed. Chemical stability tests were performed on two ASU-type monomers: norbornenepropoxy-6-azonia-spiro(5,5)undecane (NPS5) and norbornenehexoxy-6-azonia-spiro(5,5)undecane (NHS5). Homopolymerization of these ASU-monomers (NPS5 and NHS5)

was performed. The resultant homopolymers of poly(norbornenepropoxy-6-azonia-spiro(5,5)undecane), PNPS5, and poly(norbornenehexoxy-6-azonia-spiro(5,5)undecane), PNHS5, were characterized by X-ray scattering. Other ASU-type norbornene based monomers were synthesized and characterized as well.

In Chapter 8, random copolymers of poly(norbornenepropoxy-6-azonia-spiro(5,5)undecane), PNPS5, with polynorbornene, PNOR, were synthesized. Random copolymers of poly(norbornenehexoxy-6-azonia-spiro(5,5)undecane), PNHS5, with polynorbornene, PNOR, were also synthesized. The morphology of these random copolymers was characterized by X-ray scattering. Block copolymers of poly(norbornenepropoxy-6-azonia-spiro(5,5)undecane), PNPS5, with polynorbornenedimethyldichloride, PNDMDC, were synthesized. Block copolymers of poly(norbornenehexoxy-6-azonia-spiro(5,5)undecane), PNHS5, with polynorbornenedimethyldichloride, PNDMDC, were also synthesized. Morphologies of these block copolymers were evaluated by X-ray scattering and Transmission Electron Microscopy (TEM).

In Chapter 9, random copolymers of poly(norbornenepropoxy-6-azonia-spiro(5,5)undecane), PNPS5, with poly(norbornenemethylbenzylether), PNMBzE, (PNPS5-*r*-PNMBzE) were synthesized. Random copolymers of poly(norbornenehexoxy-6-azonia-spiro(5,5)undecane), PNHS5, with poly(norbornenemethylbenzylether), PNMBzE, (PNHS5-*r*-PNMBzE), were also synthesized. The morphologies of these random copolymers were characterized by X-ray scattering and TEM. Ionic conductivity of these membranes was evaluated by Electrochemical Impedance Spectroscopy (EIS). Morphology-conductivity relationships of these random copolymers were discussed. Block copolymers of PNPS5 with PNMBzE (PNPS5-*b*-PNMBzE) were synthesized. Block copolymers of PNHS5 with PNMBzE (PNHS5-*b*-PNMBzE) were also

be synthesized. Morphologies of these block copolymers were evaluated by X-ray scattering and TEM. Ionic conductivity measurements of these block copolymers were performed by EIS measurements. Morphology-conductivity relationships were discussed.

This dissertation investigates the morphology of randomly, charged, comb-like polymers. Findings in this dissertation show that highly conducting ionic membranes can be prepared by understanding the forces driving the clustering of ions in random copolymers and the sterics that can mitigate against this clustering, thereby, increasing ionic conductivity. This blueprint for decreasing clustering is important if anion exchange membranes are to be an attractive alternative to proton exchange membranes for fuel cell applications. The In-Line Dipole model also presents a pathway to understanding the electrostatic interactions in polymer systems. More importantly, the dipole-dipole interaction presented in this model can be incorporated into other self-consistent liquid state theories to further expand on the understanding of the roles of electrostatics and sterics in dictating the morphologies of charged polymer systems. Experimental results obtained in this work can be further analyzed and compared with simulation results of ionomer cluster models in which the driving forces in these simulations are consistent with the driving forces for ionic clustering presented in the In-Line Dipole model. This can shed more light on the kinetics of ionic cluster formation which was not considered in the development of the In-Line Dipole model.

This dissertation also builds on the work by Marino and Kreuer by synthesizing novel alkaline stable monomers. Membranes synthesized from the copolymerization of these alkaline stable monomers with other norbornene-based monomers were flexible and solvent processable. These membranes had exceptionally high bromide conductivities at relatively low ion exchange capacity. Fuel cell tests on these membranes and how their performance compares to other anion exchange membranes and proton exchange membranes is clearly warranted. The Azo Spirocyclic Undecane-

type salts also described in this dissertation can be affixed to other polymer backbones, not just norbornene-based polymers, with functional halide groups that can undergo Williamson ether synthesis.

1.2 References

(1) Nguyen, N.-T.; Chan, S. H. Micromachined Polymer Electrolyte Membrane and Direct Methanol Fuel Cells—a Review. *J. Micromechanics Microengineering* **2006**, *16* (4), R1–R12.

(2) Aricò, A. S. A. S.; Sebastian, D.; Schuster, M.; Bauer, B.; D'Urso, C.; Lufrano, F.; Baglio, V.; D'Urso, C.; Lufrano, F.; Baglio, V. Selectivity of Direct Methanol Fuel Cell Membranes. *Membranes (Basel).* **2015**, *5* (4), 793–809.

(3) Moon, G. Y.; Rhim, J. W. Self-Assembly Modification of Perfluorosulfonic Acid Membranes for the Application to Direct Methanol Fuel Cells. *Macromol. Res.* **2008**, *16* (6), 524–531.

(4) Pan, J.; Lu, S.; Li, Y.; Huang, A.; Zhuang, L.; Lu, J. High-Performance Alkaline Polymer Electrolyte for Fuel Cell Applications. *Adv. Funct. Mater.* **2010**, *20* (2), 312–319.

(5) Smith, M. B.; March, J. March's Advanced Organic Chemistry: Reactions, Mechanisms, and Structure, 5th Edition. *Molecules* **2001**, *6* (12), 1064–1065.

(6) Diat, O.; Gebel, G. Fuel Cells: Proton Channels. *Nat. Mater.* **2008**, *7* (1), 13–14.

(7) Lee, W.-H.; Kim, Y. S.; Bae, C. Robust Hydroxide Ion Conducting Poly(biphenyl

Alkylene)s for Alkaline Fuel Cell Membranes. *ACS Macro Lett.* **2015**, *4* (8), 814–818.

(8) Steele, B. C.; Heinzel, A. Materials for Fuel-Cell Technologies. *Nature* **2001**, *414*, 345–352.

(9) Arges, C. G.; Ramani, V.; Pintauro, P. N. Anion Exchange Membrane Fuel Cells. *Elctrochemical Soc. Interface* **2010**, 31–35.

(10) Marino, M. G.; Melchior, J. P.; Wohlfarth, A.; Kreuer, K. D. Hydroxide, Halide and Water Transport in a Model Anion Exchange Membrane. *J. Memb. Sci.* **2014**, *464*, 61–71.

(11) Marino, M. G.; Kreuer, K. D. Alkaline Stability of Quaternary Ammonium Cations for Alkaline Fuel Cell Membranes and Ionic Liquids. *ChemSusChem* **2015**, *8* (3), 513–523.

(12) Tsai, T. Ionic Copolymers for Alkaline Anion Exchange Membrane Fuel Cells (AAEMFCs), University of Massachusetts, 2014.

(13) Zhang, W.; Liu, Y.; Jackson, A. C.; Savage, A. M.; Ertem, S. P.; Tsai, T. H.; Seifert, S.; Beyer, F. L.; Liberatore, M. W.; Herring, A. M.; et al. Achieving Continuous Anion Transport Domains Using Block Copolymers Containing Phosphonium Cations. *Macromolecules* **2016**, *49* (13), 4714–4722.

(14) Tsai, T. H.; Ertem, S. P.; Maes, A. M.; Seifert, S.; Herring, A. M.; Coughlin, E. B. Thermally Cross-Linked Anion Exchange Membranes from Solvent Processable Isoprene Containing Ionomers. *Macromolecules* **2015**, *48* (3), 655–662.

(15) Pan, J.; Chen, C.; Li, Y.; Wang, L.; Tan, L.; Li, G.; Tang, X.; Xiao, L.; Lu, J.; Zhuang, L. Constructing Ionic Highway in Alkaline Polymer Electrolytes. *Energy Environ. Sci.* **2014**, *7* (1), 354.

(16) Wanakule, N. S.; Virgili, J. M.; Teran, A. A.; Wang, Z. G.; Balsara, N. P. Thermodynamic Properties of Block Copolymer Electrolytes Containing Imidazolium and Lithium Salts. *Macromolecules* **2010**, *43* (19), 8282–8289.

(17) Ding, J.; Chuy, C.; Holdcroft, S. A Self-Organized Network of Nanochannels Enhances Ion Conductivity through Polymer Films. *Chem. Mater.* **2001**, *13* (7), 2231–2233.

(18) Hallinan, D. T.; Balsara, N. P. Polymer Electrolytes. *Annu. Rev. Mater Res* **2013**, *43*, 503–525.

(19) Beers, K. M.; Balsara, N. P. Design of Cluster-Free Polymer Electrolyte Membranes and Implications on Proton Conductivity. *ACS Macro Lett.* **2012**, *1* (10), 1155–1160.

(20) Eisenberg, A. Clustering of Ions in Organic Polymers. A Theoretical Approach. *Macromolecules* **1970**, *3* (2), 147–154.

(21) Eisenberg, A.; Hird, B.; Moore, R. B. A New Multiplet-Cluster Model for the Morphology of Random Ionomers. *Macromolecules* **1990**, *23* (18), 4098–4107.

(22) Kim, J. S.; Yeon Hwa Nah; Jarng, S. S. Comparison of Clustering in Various Acrylate Ionomers. *Polymer (Guildf).* **2001**, *42* (13), 5567–5571.

(23) Iojoiu, C.; Genova-Dimitrova, P.; Maréchal, M.; Sanchez, J. Y. Chemical and Physicochemical Characterizations of Ionomers. *Electrochim. Acta* **2006**, *51* (23), 4789–4801.

(24) Capek, I. Nature and Properties of Ionomer Assemblies. II. *Adv. Colloid Interface Sci.* **2005**, *118* (1–3), 73–112.

(25) Hsu, W. Y.; Gierke, T. D. Elastic Theory for Ionic Clustering in Perfluorinated Ionomers. *Macromolecules* **1982**, *15*, 101–105.

(26) Kusoglu, A.; Weber, A. Z. New Insights into Per Fluorinated Sulfonic-Acid Ionomers. *Chem. Rev.* **2017**, *117*, 987–1104.

(27) Platé, N. A.; Shibaev, V. P. Comb-like Polymers. Structure and Properties. *J. Polym. Sci. Macromol. Rev.* **1974**, *8* (1), 117–253.

(28) Salas-De La Cruz, D.; Green, M. D.; Ye, Y.; Elabd, Y. A.; Long, T. E.; Winey, K. I. Correlating Backbone-to-Backbone Distance to Ionic Conductivity in Amorphous Polymerized Ionic Liquids. *J. Polym. Sci. Part B Polym. Phys.* **2012**, *50* (5), 338–346.

(29) Miller, R. L.; Boyer, R. F.; Heijboer, J. X-Ray Scattering from Amorphous Acrylate and Methacrylate Polymers: Evidence of Local Order. *J. Polym. Sci. Polym. Phys. Ed.* **1984**, *22* (12), 2021–2041.

(30) Triolo, A.; Russina, O.; Hans-Jurgen Bleif, A.; Cola, E. Di. Nanoscale Segregation in Room Temperature Ionic Liquids†. *J. Phys. Chem. B* **2007**, No. 111, 4641–4644.

(31) Li, N.; Leng, Y.; Hickner, M. A.; Wang, C. Y. Highly Stable, Anion Conductive, Comb-Shaped Copolymers for Alkaline Fuel Cells. *J. Am. Chem. Soc.* **2013**, *135* (27), 10124–10133.

(32) Dang, H.-S.; Jannasch, P. Exploring Different Cationic Alkyl Side Chain Designs for Enhanced Alkaline Stability and Hydroxide Ion Conductivity of Anion-Exchange Membranes. *Macromolecules* **2015**, *48* (16), 5742–5751.

(33) Gottesfeld, S.; Dekel, D. R.; Page, M.; Bae, C.; Yan, Y.; Zelenay, P.; Seung, Y. Anion

Exchange Membrane Fuel Cells : Current Status and Remaining Challenges. *J. Power Sources* **2018**, *375*, 170–184.

(34) Long, H.; Pivovar, B. Hydroxide Degradation Pathways for Imidazolium Cations : A DFT Study. *J. Phys. Chem.* **2014**, *118* (19), 9880–9888.

(35) Heard, G. L.; Yates, B. F. Competing Rearrangements of Ammonium Ylides: A Quantum Theoretical Study. *J. Org. Chem.* **1996**, *61* (21), 7276–7284.

(36) Ghigo, G.; Cagnina, S.; Maranzana, A.; Tonachini, G.; Generale, C.; Azeglio, C. M.; Torino, I.-. The Mechanism of the Stevens and Sommelet - Hauser Rearrangements . A Theoretical Study. *J. Org. Chem.* **2010**, *75* (11), 3608–3617.

(37) Hugar, K. M.; Kostalik, H. A.; Coates, W. Imidazolium Cations with Exceptional Alkaline Stability: A Systematic Study of Structure − Stability Relationships. *J. Am. Chem. Soc.* **2015**, *137* (27), 8730–8737.

(38) Clark, T. J.; Robertson, N. J.; Iv, H. A. K.; Lobkovsky, E. B.; Mutolo, P. F. A Ring-Opening Metathesis Polymerization Route to Alkaline Anion Exchange Membranes : Development of Hydroxide-Conducting Thin Films from an Ammonium-Functionalized Monomer. *J. Am. Chem. Soc.* **2009**, *131* (36), 12888–12889.

(39) Hill, R. K.; Chan, T.-H. Transfer of Assymetry from Nitrogen to Carbon in Stevens's Rearrangement. *J. Am. Chem. Soc. Commun. to Ed.* **1966**, *88* (4), 866–867.

(40) Mohanty, A. D.; Bae, C. Mechanistic Analysis of Ammonium Cation Stability for Alkaline Exchange Membrane Fuel Cells. *J. Mater. Chem. A Mater. energy Sustain.* **2014**, *2* (41), 17314–17320.

(41) Zhu, T.; Xu, S.; Rahman, A.; Dogdibegovic, E.; Yang, P.; Pageni, P.; Kabir, M. P.; Zhou, X.; Tang, C. Cationic Metallo-Polyelectrolytes for Robust Alkaline Anion- Exchange Membranes. *Angew. Chemie Funct. Met.* **2018**, *57*, 1–6.

(42) Si, Z.; Qiu, L.; Dong, H.; Gu, F.; Li, Y.; Yan, F. Effects of Substituents and Substitution Positions on Alkaline Stability of Imidazolium Cations and Their Corresponding Anion-Exchange Membranes. *Appl. Mater. Interfaces* **2014**, *6*, 4346−4355.

(43) Chen, D.; Hickner, M. A. Degradation of Imidazolium- and Quaternary Ammonium-Functionalized Poly (Fl Uorenyl Ether Ketone Sulfone) Anion Exchange Membranes. *Appl. Mater. Interfaces* **2012**, *4* (11), 5776–5781.

(44) Lee, W.; Kim, Y. S.; Bae, C. Robust Hydroxide Ion Conducting Poly(biphenyl Alkylene)s for Alkaline Fuel Cell Membranes. *ACS Macro Lett.* **2015**, *4*, 814–818.

(45) Lee, W.; Mohanty, A. D.; Bae, C. Fluorene-Based Hydroxide Ion Conducting Polymers for Chemically Stable Anion Exchange Membrane Fuel Cells. *ACS Macro Lett.* **2015**, *4* (4), 453–457.

(46) Julia Ponce-Gonzalez, John R. Varcoe, and D. K. W. Commercial Monomer Availability Leading to Missed Opportunities? Anion-Exchange Membranes Made from Meta - Vinylbenzyl Chloride Exhibit an Alkali Stability Enhancement. *Appl. Energy Mater.* **2018**, *In print*.

(47) Dong, X.; Xue, B.; Qian, H.; Zheng, J.; Li, S. Novel Quaternary Ammonium Microblock Poly (P -Phenylene- Co -Aryl Ether Ketone) S as Anion Exchange Membranes for Alkaline Fuel Cells. *J. Power Sources* **2017**, *342*, 605–615.

(48) Fujimoto, C.; Kim, D.; Hibbs, M.; Wrobleski, D.; Seung, Y. Backbone Stability of Quaternized Polyaromatics for Alkaline Membrane Fuel Cells. *J. Memb. Sci.* **2012**, *423–424*, 438–449.

(49) Dekel, D. R. Review of Cell Performance in Anion Exchange Membrane Fuel Cells. *J. Power Sources* **2017**.

(50) Ye, Y.; Elabd, Y. A. Relative Chemical Stability of Imidazolium-Based Alkaline Anion Exchange Polymerized Ionic Liquids. *Macromolecules* **2011**, *44* (21), 8494–8503.

(51) Elabd, Y. A.; Hickner, M. A. Block Copolymers for Fuel Cells. *Macromolecules* **2011**, *44*, 1–11.

(52) Yang, Y.; Xu, Y.; Ye, N.; Zhang, D.; Yang, J. Alkali Resistant Anion Exchange Membranes Based on Saturated Heterocyclic Quaternary Ammonium Cations Functionalized Poly (2 , 6-Dimethyl-1 , 4-Phenylene Oxide) S. *J. Electrochem. Soc.* **2018**, *165* (5), 350–356.

(53) Strasser, D. J.; Graziano, B. J.; Knauss, D. M. Base Stable Poly(diallylpiperidinium Hydroxide) Multiblock Copolymers for Anion Exchange Membranes. *J. Mater. Chem. A Mater. energy Sustain.* **2017**, *5*, 9627–9640.

(54) Pham, T. H.; Olsson, J. S.; Jannasch, P. N‐Spirocyclic Quaternary Ammonium Ionenes for Anion-Exchange Membranes. *J. Am. Chem. Soc.* **2017**, 13–16.

(55) Pham, T. H.; Jannasch, P. Aromatic Polymers Incorporating Bis‐N‐Spirocyclic Quaternary Ammonium Moieties for Anion-Exchange Membranes. *ACS Macro Lett.* **2015**, 1370–1375.

(56) Olsson, J. S.; Pham, T. H.; Jannasch, P. Poly (N , N -Diallylazacycloalkane) S for Anion-Exchange Membranes Functionalized with N‑Spirocyclic Quaternary Ammonium Cations. *Macromolecules* **2017**.

(57) Olsson, J. S.; Pham, T. H.; Jannasch, P. Poly (Arylene Piperidinium) Hydroxide Ion Exchange Membranes : Synthesis , Alkaline Stability , and Conductivity. *Adv. Funct. Mater.* **2018**, *1702758*, 1–10.

(58) Gu, L.; Dong, H.; Sun, Z.; Li, Y.; Yan, F. RSC Advances Spirocyclic Quaternary Ammonium Cations for Alkaline Anion Exchange Membrane Applications : An Experimental and Theoretical Study †. *RSC Adv.* **2016**, *6*, 94387–94398.

(59) Dang, H.; Jannasch, P. Membranes Tethered with Di Ff Erent Hetero-. *J. Mater. Chem. A Mater. energy Sustain.* **2017**, *5*, 21965–21978.

(60) Chen, N.; Long, C.; Li, Y.; Lu, C.; Zhu, H. Ultrastable and High Ion-Conducting Polyelectrolyte Based on Six- Membered N‑Spirocyclic Ammonium for Hydroxide Exchange Membrane Fuel Cell Applications. *ACS Appl. Mater. Interfaces* **2018**, *10*, 15720–15732.

PART I:

BACKBONE-BACKBONE MORPHOLOGY IN QUATERNIZED P4VP HOMOPOLYMERS AND BLOCK COPOLYMERS

CHAPTER 2

EFFECT OF SIDE-CHAIN LENGTH AND EXTENT OF QUATERNIZATION ON MORPHOLOGY-PROPERTY RELATIONSHIPS IN QUARTERNIZED P4VP

2.1 Introduction

In the middle of the 20th century, Rehberg and Fisher successfully synthesized polymers with attached side-chains by polymerizing *n*-alkyl acrylates.[1] Spurred by a desire to study the crystallization of these side-chains on atactic backbones, and their crystallization process as an analogue to liquid crystals, these comb-like polymers became an interesting field of polymer physics.[2-4] As a consequence, different polymer backbones with varying number of carbons on the pendant side-chains were synthesized; poly (vinyl *n*-alkyl ethers and esters),[5] poly (*n*-acyl styrenes),[6] poly (α-olefins),[7,8] polymaloamides,[9] poly (*n*-alkyl methacrylates),[10] and recently poly (*n*-alkyl imidazolium)[11] ionic liquids and poly (3 *n*-alkyl thiophenes)[12] semiconductors. The literature is replete with reports of alkylated polymer backbones with interesting physical properties especially the characteristic feature size observed in their X-ray scattering spectra. It took another 20 years after Fisher's revolutionary work for Corradini to explain the significant change in microstructure when side-chains are attached to polymer backbones.[7]

In amorphous linear polymers, short-range ordering of polymer segments is determined by the intermolecular interaction between adjacent polymer segments. However, an amorphous comb-shaped polymer segment is comprised of the polymer backbone and pendant side-chains. The interaction between pendant side-chains on adjacent polymer segments in addition to the intermolecular interactions between the polymer backbones dictate the short-range ordering of amorphous comb-shaped polymer segments.[13] The sterics stemming from the pendant side-chains

leads to increased separation between the polymer backbones with increasing length of the pendant side-chains.[13] Owing to the electron density contrast between the polymer backbone and the pendant side-chains, the spacing between adjacent polymer backbones in comb-shaped polymers (backbone-backbone correlations) can be evaluated by X-ray scattering.

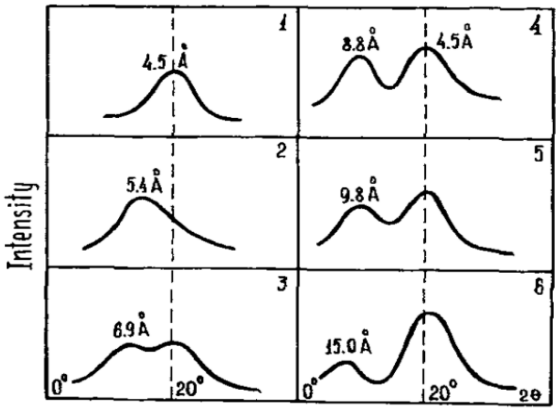

Figure 2.1. X-ray scattering data of poly (α-olefins) with attached side-chains (1) polyethylene; (2) polypropylene; (3) poly (1-butene); (4) poly (1-pentene); (5) poly (1-hexene); (6) poly(1-decene).[7,8,19]

From Figure 2.1, two peaks can be observed in all of the scattering spectra except for polyethylene and polypropylene where only one peak is observed. The same peak, the peak at higher angles, is actually present in longer side-chain polyolefins. The peak corresponds to a distance between non-bonded atoms in the first coordination sphere of the polymer chain.[13] This peak has been suggested to be characteristic of organic compounds and can be observed in polymers as well as *n*-paraffins.[14] Plate and Shibav, performed electron diffraction experiments, and observed periodic spacings of 1.5 and 2.5 Å. [3,15,16] The 1.5 Å – spacing is the bond length between two carbon atoms while 2.5 Å is the distance between three carbon atoms in a trans configuration. The observed peak in the WAXS spectra, being larger than 1.5 and 2.5 Å was suggested to be the closest distance between

non-covalently bonded carbon atoms. These non-covalently bonded carbon atoms are held in this periodic position (~4.5 - 5 Å) by van der Waals interactions. In their studies, they concluded that the van der Waal's (VDW) distance does not depend on the number of carbons on the polymer side chains ranging from butyl to octadecyl side-chains for poly (*n* – alkyl methacrylates). However, other researchers observed a slight increase in VDW spacing with increasing number of carbons in the side-chains for poly (*n* – cycloalkyl methacrylates) and poly (*n* – alkyl acrylates).[10]

In Figure 2.1, a second peak at lower angles which has a larger spacing in comparison to the van der Waal's peak, the LVDW peak, can be observed for poly (1-butene) to poly (1-decene). This peak has been shown to increase linearly with an increase in the number of carbons on the side-chains.[18-24]

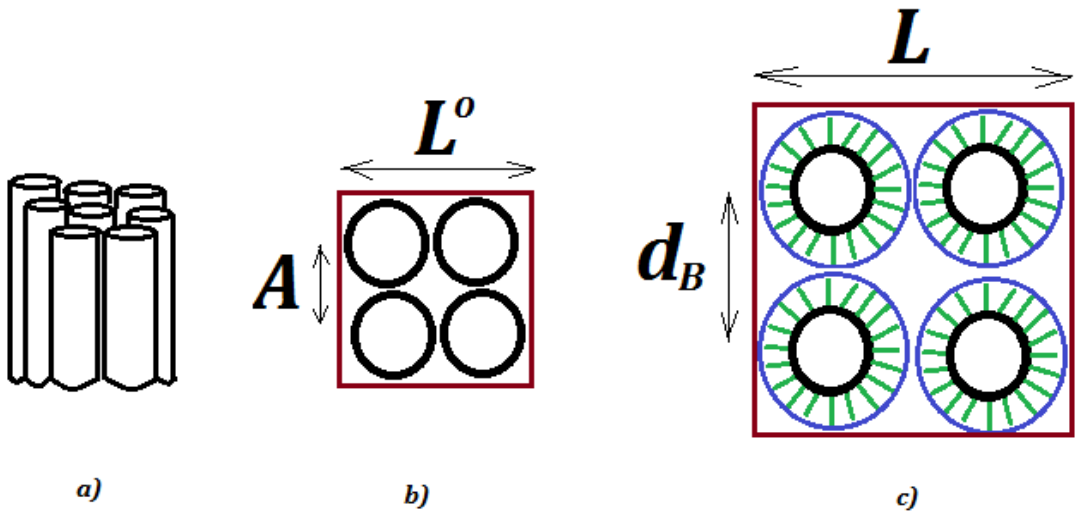

Figure 2.2. a) Parallel bundles of polymer chains b) cross-section of polymer chains in a square lattice, d) cross-section of a comb-shaped polymer in a square lattice.

If we assume that comb-shaped polymers are arranged as rigid rods in a square lattice. With increasing length of the pendant side-chains, the backbone-backbone spacing of these comb-shaped polymers increases. The density of the polymer rods without side-chains is given by

$$\rho_B \propto \frac{m}{{L_O}^2} \qquad 2.1$$

Where *m* is the molar mass of the polymer repeat unit and *Lo* is the area of the square lattice. L_O is twice the polymer backbone diameter, *A.* Upon the attachment of side-chains, the new density of the comb polymer is given by

$$\rho_A \propto \frac{m + nb}{L^2} \qquad 2.2$$

Where *n* is the number of carbons on the pendant side-chains, *b* is molar mass of the methylene group, and *L* is the new length of the square lattice. *L* is twice the backbone-backbone spacing d_B. If there are negligible differences between the polymer densities of the polymer main chains with or without pendant side-chains, then

$$\rho_A = \rho_B \qquad 2.3$$

Hence

$$\frac{m + nb}{{d_B}^2} = \frac{m}{A^2} \qquad 2.4$$

$$d_B = A(1 + \frac{b}{m}n)^{\frac{1}{2}} \qquad 2.5$$

Since the molar mass of the methylene group is generally less than the molar mass of the polymer repeat unit, for the case in which $\frac{b}{m}n < 1$,

$$d_B \sim A\left(1 + \frac{b}{m}n - \frac{1}{8}\left(\frac{b}{m}n\right)^2 + \frac{1}{16}\left(\frac{b}{m}n\right)^3 \ldots\ldots\right) \quad 2.6$$

Ignoring higher powers of $\frac{b}{m}n$,

$$d_B = A + \lambda n \quad 2.7$$

Where *A* is the diameter of the polymer main chain, and λ is the increase in the backbone-backbone spacing with increasing pendant side-chain and will depend on the rigidity, the diameter and the repeat unit molecular weight of the polymer backbone. This relationship is consistent with experimental observations in all comb-shaped polymer series.[5-19]

However, for cases in which $\frac{b}{m}n > 1$, at higher values of *n*, from this model, we expect

$$d_B{}^2 = A^2 + \lambda' n \quad 2.8$$

Plate and Shibaev has reported a deviation from linearity between d_B and *n* at high values of *n*, which is consistent with the prediction of this model.[13] Experimental data showed that the pendant side-chains will most likely assume an all trans configuration,[10-11, 19]although it has been suggested they may exhibit Gaussian character.[25-26]

This model is not absolute but has inherent limitations because these are not crystalline rather amorphous polymers with short-range ordering. This model assumes that these rigid rods are arranged with high orientational and positional ordering relative to each other. However, we are considering amorphous comb-shaped polymers and such orientational ordering of polymers segments is not characteristic of amorphous polymers. Moreover, comb-shaped polymer chains are not hard cylinders, thus, some degree of interdigitation between extended pendant side-chains on adjacent comb polymers is expected. Notwithstanding, this model presents an opportunity to

describe the conformational state of the polymer backbone and its pendant side-chains in an amorphous comb-shaped polymer.

Another interesting aspect of the SAXS spectra is the intensity of the LVDW peak relative to the VDW. This short-range backbone-backbone periodic spacing arises from parallel bundles of the polymer backbone segments, both intra and inter polymer chains.[28-30] In the SAXS spectra, intensity of the backbone-backbone spacing peak relative to the VDW may suggest the concentration of these parallel bundles in the polymer melt. Miller and Boyer affirmed this school of thought,[10] though Hiller *et al*. suggested that this is may be due to density fluctuations within the polymer melt and might not necessarily correlate with the fraction of spacing between backbones in the melt.[25]

The effect of the mole fraction of the side-chain repeat unit on the backbone-backbone spacing has not received much attention in the literature. Possibly because the comb-shaped polymers are formed directly from their corresponding monomers, and often times, not copolymerized with their un-functionalized counterparts.[10,3] Poly(4-vinylpyridine) can be alkylated by quaternization. The process of quaternization converts pyridine units to alkylated pyridinium units (*i.e.* pyridine groups with side-chains and charges, See Scheme 2.1). Thus, the extent of conversion of quaternized P4VP is the mole fraction of alkylated/comb-shaped P4VP. Consequently, by monitoring the conversion during quaternization, the effect of conversion (which is the mole fraction of alkylated pyridinium units) on the backbone-backbone spacing can be probed. The backbone-backbone spacing at a given alkylated pyridinium conversion is the backbone-backbone spacing of the mole fraction of alkylated pyridinium units in the polymer. Furthermore, ionomer formation has been observed for other solid polyelectrolytes like polystyrene sulfonate-*ran*-polystyrene (PSS-*r*-PS).[26-30] The process of quaternization also yields poly(4-vinylpyridine)-*ran*-(*n*-

alkyl4vinylpyridiniumbromide) (P4VP-*r*-P4VP_CnBr) at various extent of conversion which may exhibit ionomer morphology.

Hence research questions for which answers are sought are the following:

- What role does conversion play in chain spacing?
- Does it have any effect on the spacing between non-bonded atoms?
- Do ionomers form the same way they do in PSS-*r*-PS?
- Is there a possible model to explain the reason this chain spacing forms?
- Is there a relationship between intensity and number of carbons on the pendant side-chains as Miller *et al.* have suggested?

2.2 Materials and Methods

The monomer, 4VP (96%) was obtained from Alfar Aesar and was passed through a column of basic alumina. N-tert-butyl-N-[1-diethylphosphono-(2,2-dimethylpropyl)] nitroxide (SG1) was obtained from Arkema and used as obtained. The following quaternizing agents were used as obtained: bromoethane (99%) and 1-bromopropane (98%) (purchased from T.C.I), 1-bromopentane (purchased from Sigma-Aldrich), 1-bromobutane (98%), 1-bromohexane (99%), 1-bromoheptane (98%), 1-bromooctane (98%), 1-bromononane (99%), 1-bromodecane (98%), 1-bromoundecane (98%), and 1-bromododecane (98%) were all purchased from Alfa Aesar.

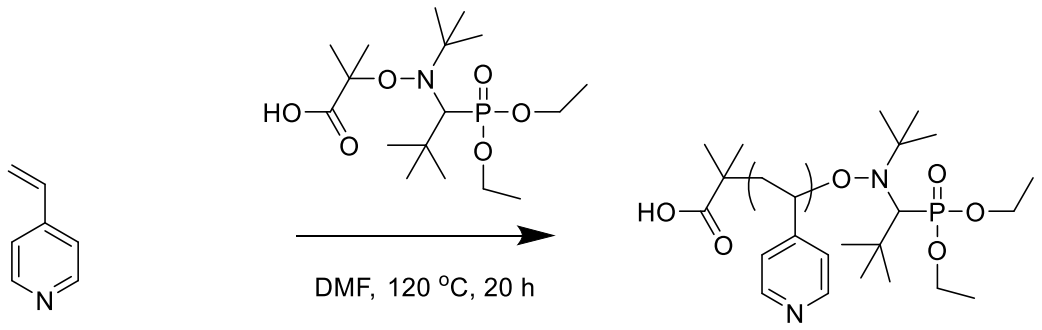

Scheme 2.1. Synthesis of poly(4-vinylpyridine) by nitroxide mediated polymerization.

2.2.1 Synthesis of Poly(4-vinylpyridine)

Poly(4-vinylpyridine) (P4VP) was synthesized by Nitroxide Mediated Polymerization (NMP). For the polymerization, 1.3 g (3.39 mmoles) of SG1 was mixed with 50 g (0.476 moles) of vinyl pyridine, in 60 wt% of dimethyl formamide (DMF). Polymerization was performed at 120 ˚C for 20 h. The resulting viscous liquid after polymerization was quenched in ice and precipitated twice from dichloromethane into diethyl ether to give a pink precipitate. Poly(4-vinylpyridine) (P4VP) was then dried for 48 h at room temperature in vacuum.

2.2.2 Characterization of P4VP

Number average molecular weight, M_n, was determined using a Gel Permeation Chromatography (GPC) in DMF at a flow rate of 1.0 mL/min using a refractive index detector on an Agilent Technologies 1260 Infinity system. The chemical composition of P4VP was determined using a Bruker 500 Fourier-Transform Nuclear Magnetic Resonance (FT-NMR). Results from DMF GPC show a number average molecular weight, M_n, of 26 Kg/mol and Đ of 1.21 relative to narrow

PMMA standards. NMR data showed the expected spectra for P4VP without any residual monomer.

2.2.3 Quaternization and Quaternization Conditions

A solution of 1.0 M quaternizing agent (1-ethylbromide – 1-dodecylbromide) was prepared in DMF. A fivefold excess of the prepared solution was used for quaternization of P4VP at 60 ˚C. Aliquots of butyl – decyl alkylated P4VP were precipitated into diethyl ether after 1, 6, 12, 24, 48, 75, 100, 150, 175, and 210 h. The sample was then dried at 60 ˚C in an oven for 48 h.

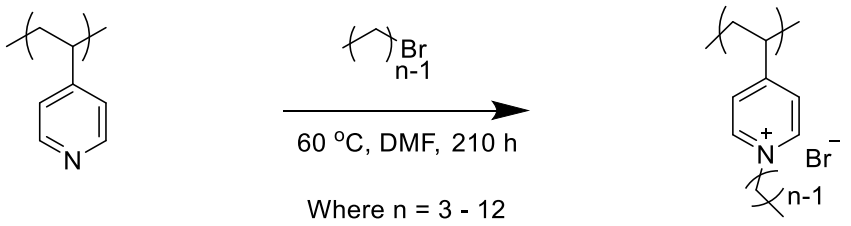

Scheme 2.2 Quaternization of P4VP with 1-alkylbromide.

2.2.4 Sample Preparation

Quaternized samples were drop cast from methanol for P4VP_C2Br to P4VP_C5Br and chloroform for P4VP_C6Br to P4VP_C12Br on a Teflon® sheet.

2.2.5 Characterization of P4VP by FTIR

PerkinElmer Spectrum 100 FTIR with a universal ATR was used to characterize the extent of quaternization. Film samples were mounted on the ATR crystal and secured by the sample holder.

2.2.6 Characterization of Samples by WAXS/MAXS

Ganesha SAXS Measurement: Wide-angle X-ray scattering (WAXS) and Medium-angle X-ray scattering (MAXS) measurements were performed in transmission geometry on Molmex Scientific Ganesha SAXS Lab. A double aperture for the Cu-Kα radiation (λ = 1.54 Å), which was the X-ray source, was used. Silver behenate was used as the standard for the momentum transfer calibration. Data collection was performed with a typical exposure time of two minutes. Depending on the signal-to-noise ratio, data collection could be longer. Azimuthal averaging of the obtained isotropic 2-D pattern was performed to obtain the intensity against wave vector plot.

Synchrotron SAXS Measurement: SAXS measurements were performed at the Advanced Photon Source Argonne National Laboratory on beamline 12 ID-B.[31] Data was collected from the X-ray beam at a wavelength of 1 Å and an energy of 12 KeV of the incident radiation. A *Q* range of 0.005 to 0.5 Å was possible from the resulting apparatus. During the course of the experiment, a 2-dimensional image was obtained which was converted into *I(Q)* against *Q* by circular averaging. The intensity obtained was in absolute scale. For each experiment sequence data was collected for a set of three samples and a Kapton background. The background would be subtracted from the obtained data. A typical exposure time of 5 seconds was used. Heating and humidification of the system was performed in a custom-made oven.[31] The humidity was controlled by heated streams of water-saturated nitrogen and dry nitrogen gas. SAXS data was collected first at room temperature and then dried for 40 mins at 60°C before collecting the first data set. The sample was then gradually humidified from 0 - 25% RH and the humidity was maintained for 20 minutes, after which SAXS measurements were performed. Then the RH was increased to 50, 75, and 95% and was maintained for 20 minutes before collection of scattering data. A dynamic analysis was also

performed on some of the samples. In the dynamic humidification a sequence of scattering data was collected as the RH was changed from 0 – 95% during SAXS measurements.

2.2.7 Characterization of Samples by Electrochemical Impedance Spectroscopy

Impedance data was collected over the frequency range, 10 – 10 KHz by a four-electrode test cell connected to a BioLogic VMP3 multichannel potentiostat. The TestEquity chamber in which experiments were made ensured a proper control of temperature and relative humidity. Measurements were performed through a temperature range of 40 – 90 °C by 10 °C step and 95% RH. The membrane resistance was obtained from the frequency intercept of the Nyquist plot. Ionic conductivity was obtained by measuring the in-plane resistance of the sample. The resistance is then converted to conductivity using the equation

$$\sigma = \frac{d}{Rwt} \qquad (2.9)$$

Where *d* is the distance between the electrodes, *t* is the thickness of the sample and *w* is the width of the membrane defined by the four-electrodes of the test cell.[1,2]

2.3 Results and Discussion

2.3.1 Extent of Quaternization and Morphological Transformation

Figure 2.3a show the changes in the FTIR spectra with quaternization. As reported in the literature, the disappearance of the peak characteristic of the C=N aromatic vibration of P4VP can be used to monitor the progress of quaternization.[32-35] The aromatic peaks in the range of 3021 – 3099 cm^{-1} were used for normalization of the intensities of the quaternized samples. The reduction in the

intensity of the 1414 cm^{-1} peak as shown was used to quantify the amount of pyridine groups converted to pyridinium during the reaction.

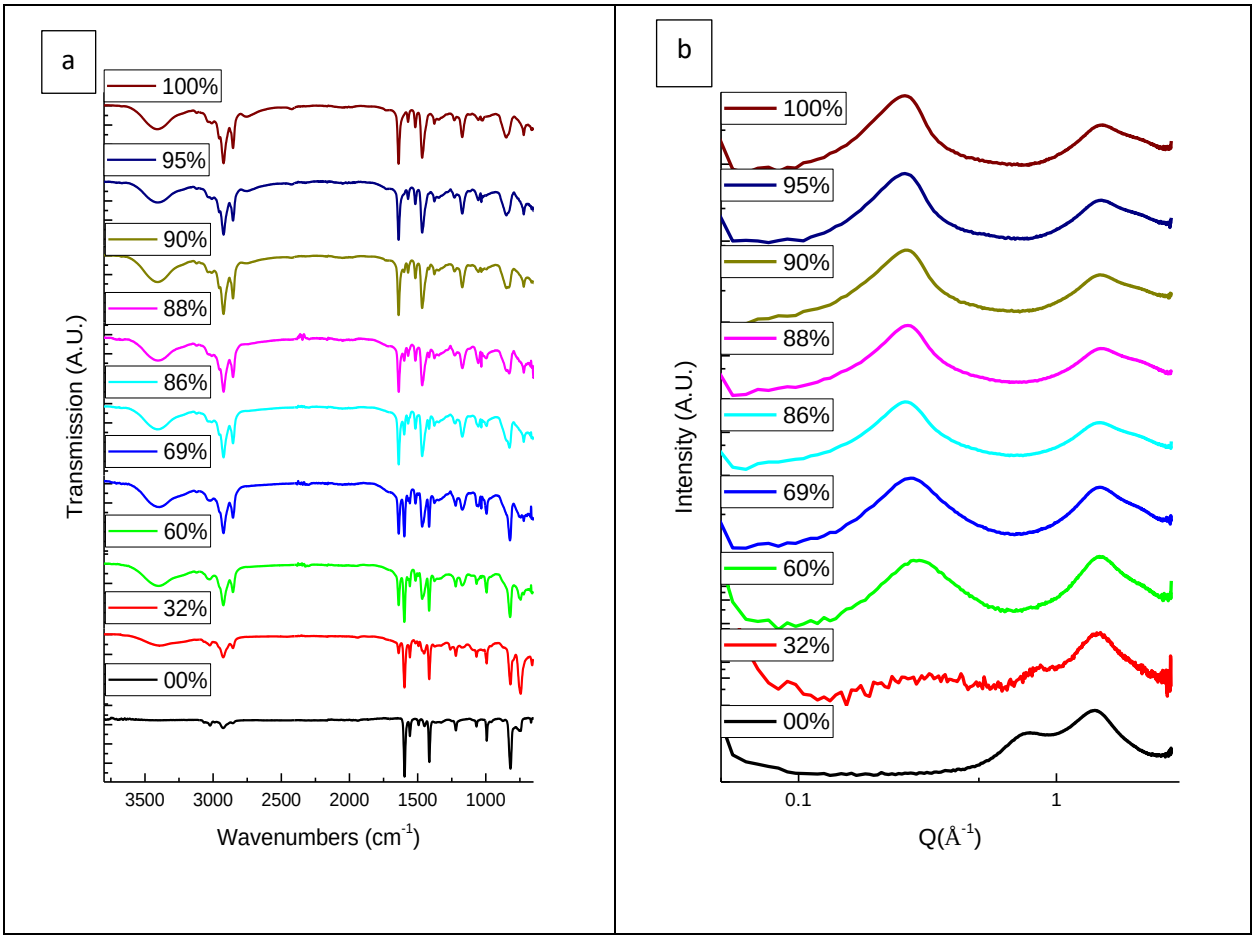

Figure 2.3. (a) The FTIR spectra of P4VP quaternization by 1-nonylbromide, (b) the SAXS spectra at different extent of conversion for P4VP-*r*-P4VP_C9Br.

The conversion of the pyridine to pyridinium follows a complicated second order reaction scheme heavily dependent on the electrostatic interactions present in the polymer chain as the reaction approach higher conversion. [36,37] From the graph (Figure 2.4) we see that there is first an abrupt increase in the conversion of pyridine to pyridinium initially followed by a more moderate

conversion with time. This exponential-like kinetics has been observed in the quaternization of P4VP with alkyl halides.[37]

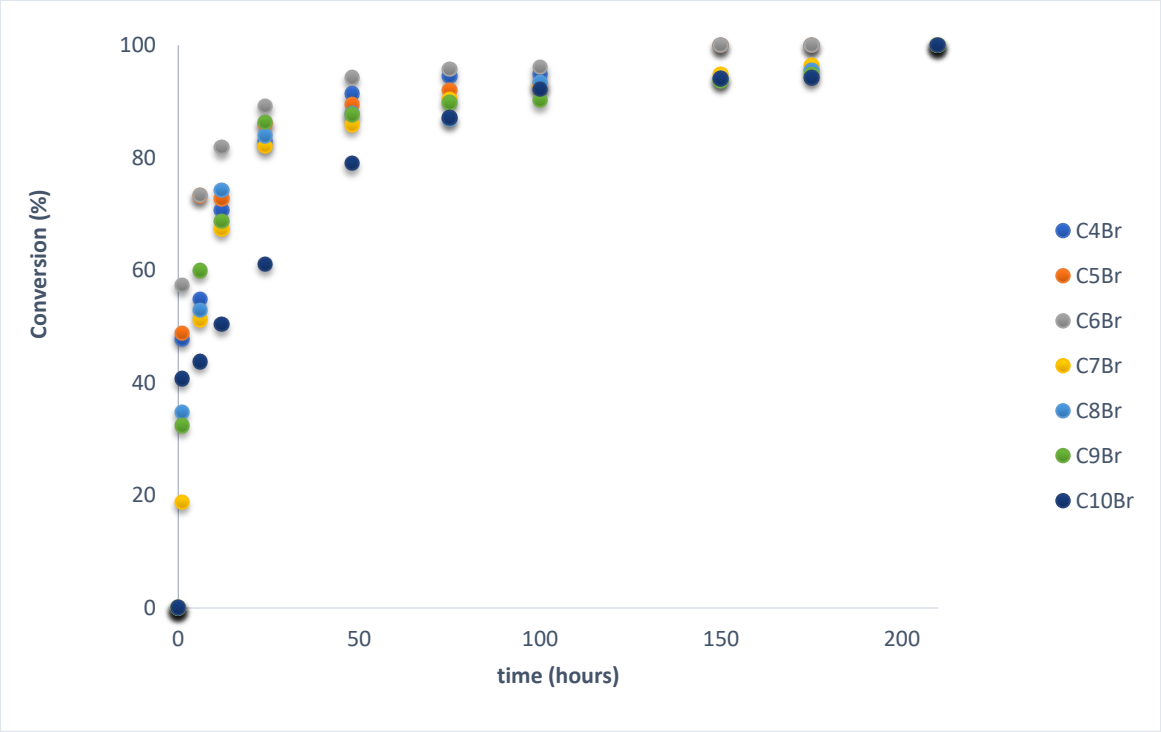

Figure 2.4. Extent of conversion against time for P4VP-*r*-P4VP_CnBr for *n = 4 – 10.*

Accompanying the chemical change is a physical transformation of P4VP-*r*-P4VP_C9Br evident by the appearance of some changes in the WAXS spectra. As can be observed in Figure 2.3b, the WAXS data reveals two peaks for all samples. The first peak at very low *Q* is due to the van der Waal's (VDW) spacing of non-bonded atoms which is a characteristic feature of organic compounds.[13] Upon the onset of quaternization, at approximately 30% conversion, this peak shift to lower *Q* values. This suggest tighter packing in the randomly quaternized polymer. The position of the peak remained constant through the course of quaternization. For the 100% quaternized

samples, the VDW spacing increased with increasing number of carbons on the side-chains from 3 – 12 after an initial decrease from the pristine sample (see Figure 2.5).

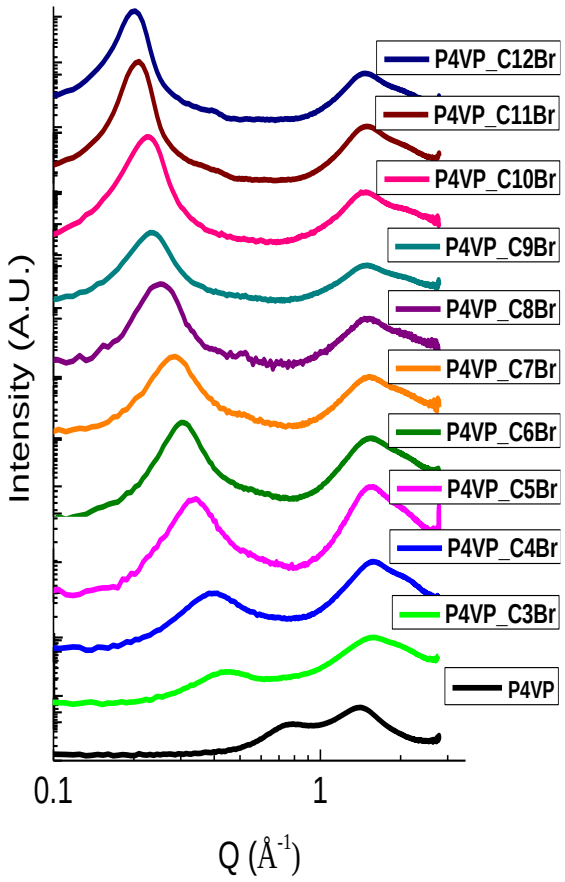

Figure 2.5. The WAXS spectra of P4VP_CnBr series.

Although an increase in VDW peak with number of carbons on the side-chains has been noted in different alkylated polymers,[10] the abrupt drop in the value of the spacing corresponding to the VDW peak; 4.50 Å for P4VP to 4.00 Å for P4VP_C3Br (see Figure 2.6a) might be due to dipolar interactions.

A second peak at slightly lower *Q*, the LVDW peak, corresponds to the spacing between two adjacent polyelectrolyte backbones. The same peak has been reported in other polymers with side-chains.[6-8]

The backbone-backbone spacing increases linearly increasing number of carbons on the pendant side-chain for the fully quaternized P4VP. See Figure 2.6a. Extrapolating the linear relationship between the backbone-backbone spacing and number of carbons to zero the number of carbons on the backbone gives the size of the P4VP chain diameter. This size which is about ~9 Å is equivalent to the backbone-backbone spacing of the pristine, unquaternized P4VP backbone-backbone spacing of about 8.7 Å. The extrapolated backbone-backbone spacing being equivalent to the pristine backbone-backbone spacing/diameter of the unquaternized P4VP, suggests an alternating repeat unit arrangement of the pendant side-chains on the polymer chain. Corroborating this alternating arrangement is the addition of a 2 Å spacing per added methylene group on the side-chains of P4VP_CnBr. Assuming an all trans configuration, the chain spacing should theoretically increase by 2.56 Å per methylene group on the side-chains in an alternating arrangement of pendant side-chains. However, in these systems, the pendant side-chains are rarely arranged in all trans configuration.[13,15] A slope of ~2.00 Å per methylene at full quaternization has also been reported in the literature for other comb-shaped polymer series.[10-11]

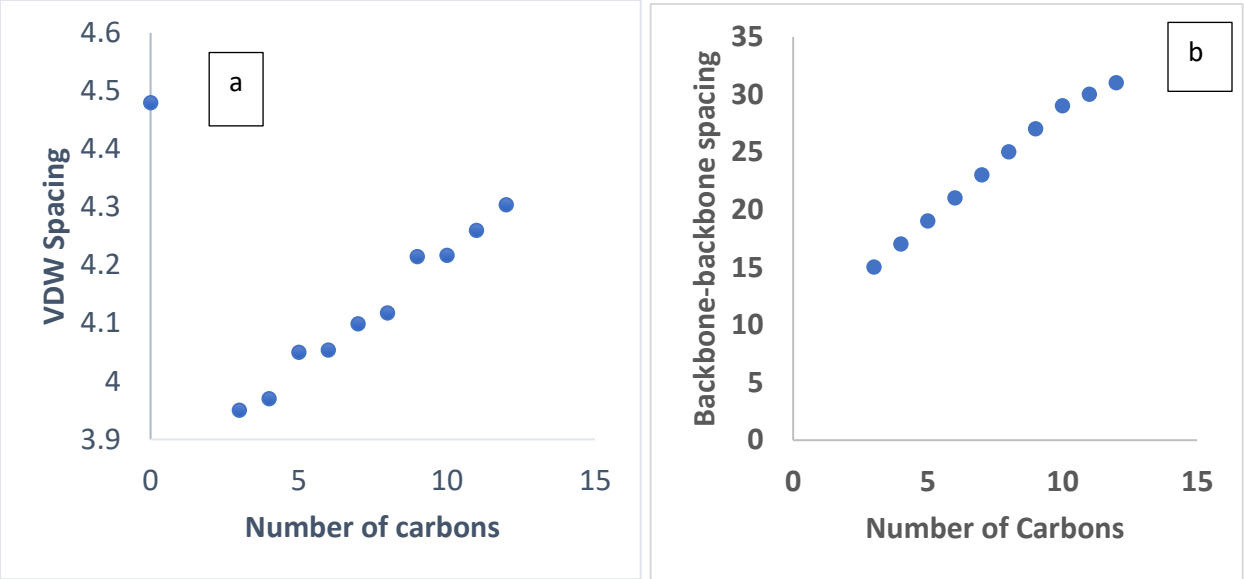

Figure 2.6. a) Relationship between VDW spacing and number of carbons, b) linear behavior of backbone spacing as a function of the number of carbons at 100% quaternization

2.3.2 Effect of Conversion on Backbone-Backbone Spacing

There appears to be a relationship between the disappearance of the C=N stretching (based on reaction kinetics) as seen by FTIR and the continuous morphological transformation as quaternization progresses as can be seen by WAXS. Figure 2.3b shows P4VP being quaternized by bromononane as a function of the extent of conversion. After 30% conversion, there are three peaks that can be observed from the WAXS spectra: The VDW (which has decreased in comparison to P4VP), the pristine LVDW, and a new LVDW due to the quaternization with bromononane. As more pyridine groups are converted to nonyl pyridinium bromide, the intrinsic polymer chain spacing (pristine LVDW) disappears and the new chain spacing becomes prominent. Interestingly, this 'new' backbone/chain spacing begins to move to lower *Q* values (higher chain spacing) with increasing conversion. Since the backbone-backbone spacing is an average of the total distance between the polymer chains, as the longer nonyl side-chain replaces

other P4VP having the intrinsic backbone-backbone spacing, the resultant chain spacing of the random copolymer, P4VP-*r*-P4VP_C9Br increases. Thus, a fundamental relationship could be proposed to exist between pyridine conversion and chain spacing.

Experimentally, the spacing between adjacent polymer chains is dependent on the extent of quaternization $\lambda_{f^{[N]^+}}$, the number of carbon on the side-chains n, and the backbone diameter (A) according to the expression,

$$\boldsymbol{d_B = A + \lambda_{f^{[N]^+}} \times n} \qquad (2.10)$$

Surprisingly, at conversions from ~50 – 100% (obtained from FTIR), the intrinsic backbone diameter (the intercept of the plot of backbone spacing against the number of carbons) decreased from ~11 to 9 Å at 100% conversion. This phenomenon is intriguing because the chain diameter (backbone-backbone spacing of the pristine P4VP) is expected to be the same irrespective of the length of the side-chains and should most likely be constant even if the concentration of the pendant side-chains is not the same. Nevertheless, it has been reported that the diameter of the backbone varies for the same comb-shaped polymer system depending on the number of data points used to extrapolate the graph to the intercept of the backbone spacing.[5,8]

There was also a deviation from a linear relationship between backbone-backbone spacing and number of carbons at high number of carbons (n = 11 and 12) as predicted by the square lattice model presented above.

Table 2.1. The changes in both the slope and the P4VP diameter with the number of carbons on the pendant side-chain for a given extent of conversion.

Conversion (%)	$\lambda_{f^{[N]+}}$ **(Å/Carbon)**	***A*(Å)**
53±6	1.16	11.3
70±3.5	1.47	9.89
90±2.5	1.60	10.1
95±2	1.92	8.99
100	2.00	8.96

The slope from equation (1) is proportional to the extent of quaternization $f^{[N]^+}$ obtained by FTIR. From FTIR values obtained,

$$\boldsymbol{\lambda_{f^{[N]+}} \sim 2f^{[N]^+}} \qquad (2.11)$$

$$\boldsymbol{d_B = A_{f^{[N]+},n_c} + 2f^{[N]^+} n} \qquad (2.12)$$

From equation (2.5), the chain spacing/backbone-backbone spacing is both linear with respect to the conversion at a fixed carbon length (see Figure 2.7b) and linear in with respect to the number of carbons at a given extent of conversion (see Figure 2.7a). An obvious corollary of this expression is that one can estimate the backbone spacing of polymers with side chains in a random copolymer provided that the molar fraction of the side-chain unit is known. Thus, this could be a characterization tool for comb-shaped polymer.

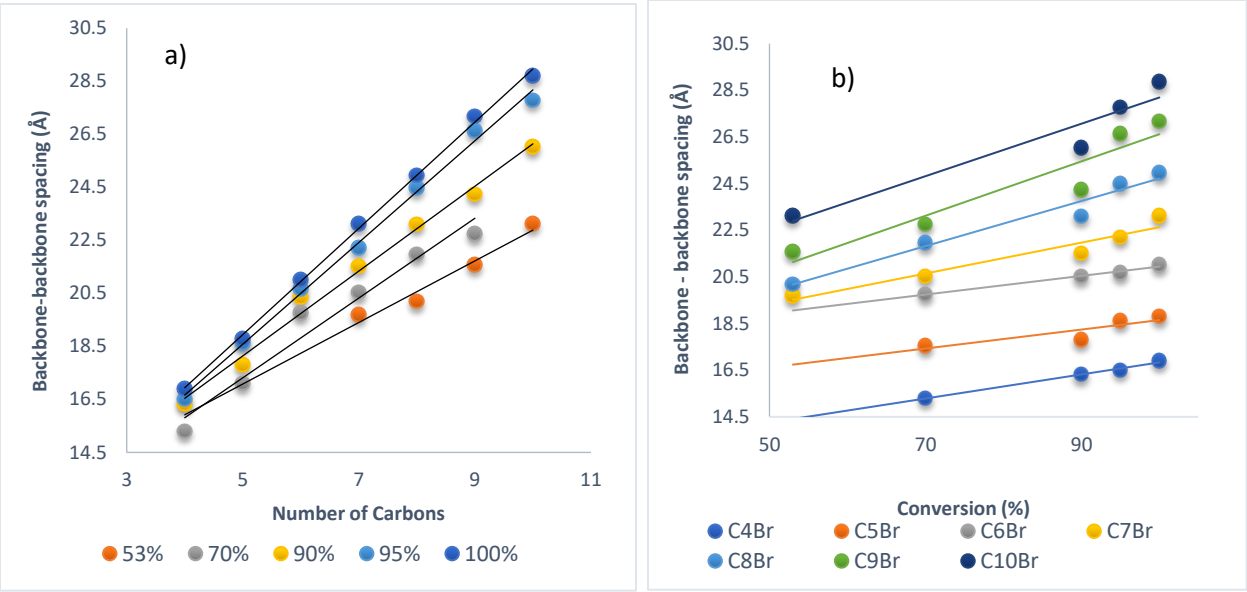

Figure 2.7. Backbone spacing as a function of a) the number of carbons at different conversions, b) extent of conversion at different number of carbons.

We can also simplify the relationship between backbone-backbone spacing and conversion for a given quaternizing agent. For a certain quaternizing agent, with increasing conversion, the backbone-backbone spacing increased for all the studied samples.

Table 2.2. The changes in both the slope and the P4VP diameter with the extent of conversion at a given number of carbon on pendant side-chain.

Number of Carbons (n)	Q_{n_c}(Å/%)	A'(Å)
4	5.2	11.7
5	4.1	14.6
6	4.0	16.8
7	6.6	16.0
8	9.7	15.1
9	11.7	15.0
10	11.3	17.0

A simplified linear relationship between the backbone-backbone spacing and conversion can be inferred from the experimental data.

$$d_B = A' + Q_{n_c} \times f^{[N]^+} \qquad (2.13)$$

Increase in backbone-backbone spacing per conversion, Q_{n_c}, increases with the number of carbons on the quaternizing agent. However, this linearization of the extent of conversion with backbone-backbone spacing at a given number of carbon is a simplification of the changes in backbone-backbone spacing with increasing conversion of 4-vinyl pyridine units to n-alkyl 4-vinylpyridinium bromide. This is evident in the large variance in the values of A' at 0% conversion of 4-vinyl pyridine units to n-alkyl 4-vinylpyridinium bromide for quaternization with different 1-alkylbromides. Ideally, at 0% quaternization, the value of A' should be constant and approach ~ 9 Å which is the backbone-backbone spacing of the unquaternized polymer.

2.3.3 Relative Intensity of Scattering

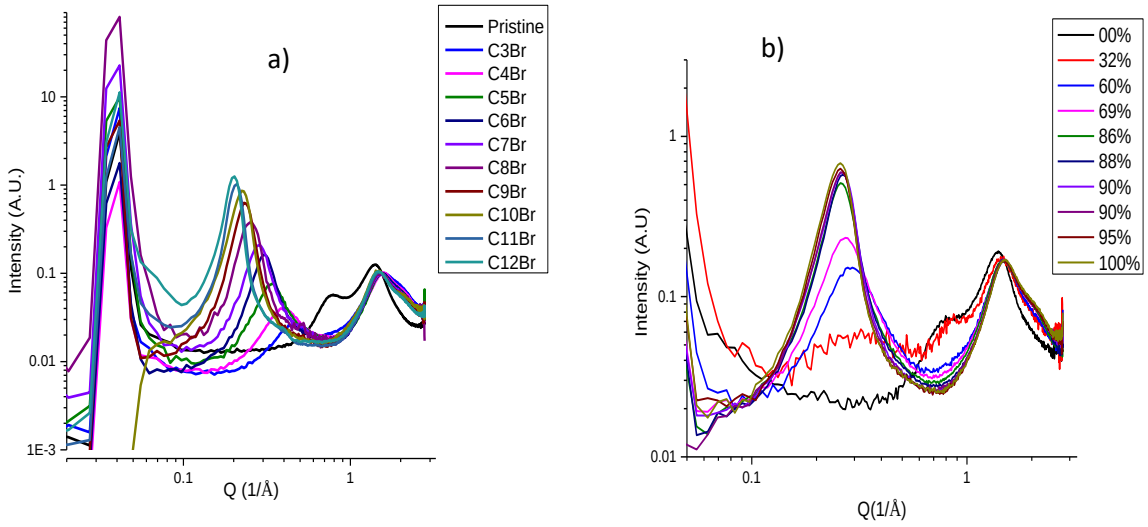

Figure 2.8. a) Intensity of LVDW peak relative to VDW peak for P4VP fully quaternized with 1-alkylbromide, b) intensity of LVDW peak relative to VDW peak at different extent of quaternization for P4VP-*r*-P4VP_C9Br.

In Figure 2.8a, it is evident that the intensity of scattering for quaternized samples increases with increasing number of carbons on the side-chains relative to the VDW peak. This increase in intensity with increasing side-chain length has been also been reported in the literature for some comb-shaped polymers.[38] Also, Figure 2.8b shows the increase in intensity of the LVDW peak with extent of quaternization relative to the VDW peak. The ratio of the intensity of LVDW relative to VDW can be used to infer the degree of ordering in the system.[10,25] Figure 2.8a and Figure 2.8b, suggests that both an increase in the number of carbons on the side-chains and extent of conversion during quaternization increases the quantity of backbone-backbone correlations in the polyelectrolyte. Thus, the concentration of backbone-backbone correlations increases with the

backbone-backbone spacing which is the one common variable in both Figure 2.8a and Figure 2.8b.

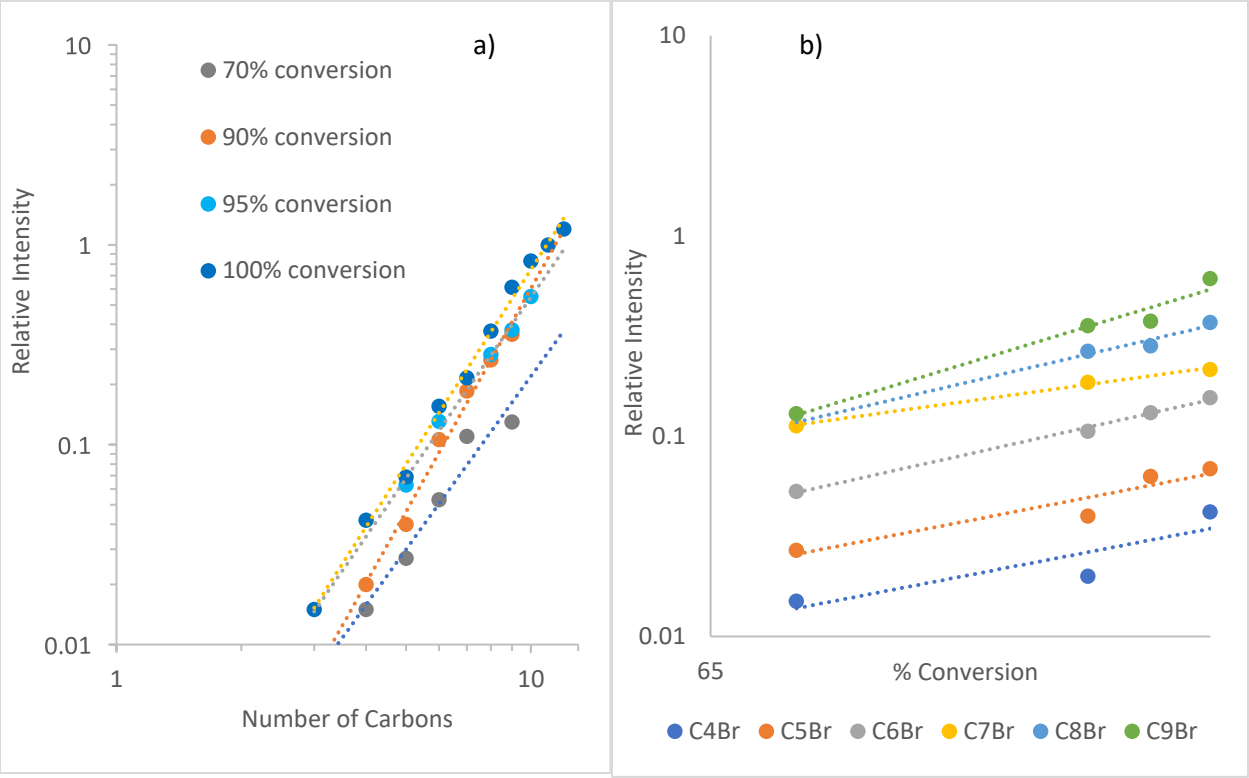

Figure 2.9. a) Relative intensity against number of carbons at different extent of conversions, b) relative intensity against conversion at different number of carbons on the pendant side-chain.

The relative intensity (R.I) obtained from the ratio of the LVDW to the VDW peak is a measure of the quantity of backbone-backbone correlations in the P4VP_CnBr series. At a fixed number of carbons on the pendant side-chain, the R.I has a power law relationship with the extent of conversion. Power law exponent is approximately 3 (see Figure 2.9a). At a fixed conversion, the R.I has a power law relationship with the extent of conversion. The power law exponent in this case is also approximately 3 (see Figure 2.9b). Both an increasing extent of conversion at a fixed number of carbons and an increasing number of carbons at a fixed extent of conversion increases

the length of the pendant side chain (see equations (2.12) and (2.13)). Increase in the length of pendant side-chains have been known to increase the rigidity of comb-shaped polymer chains. With increasing rigidity of the polymer chains the polymer chains behave essentially as rigid rods. These rods have higher persistence length along the polymer chains and this increases the likelihood of a polymer segment to have backbone-backbone correlations with nearby polymer segments thereby increasing the concentration of backbone-backbone correlations in P4VP_CnBr.

Although it is expected that with increasing length of the pendant side-chains, the free volume of the polymer increases thereby increasing the flexibility of the main chain, however, the interactions of interdigitated side-chains on adjacent polymer chains will increase the orientational ordering of the pendant side-chains. Thus, increasing the segmental anisotropy of the comb-shaped polymer backbones owing to the rigidity imposed on these polymer segments by the interacting pendant side-chains. Consequently, aligning the polymer backbones since the orientational ordering of the pendant side-chains exceeds the conformational ordering of the gaussian polymer chains.[13] Increasing the length of the pendant side-chains leads to a decrease in the flexibility of the polymer backbones in comb-shaped polymers. Some comb-shaped polymers have been known to exhibit "crystal-like" rigidity and anisotropy with increasing length of their pendant side-chains.[13] Tsevtkov *et al.* have also shown that the persistence length and the segmental anisotropy for comb-shaped poly(*n*-alkyl acrylates) increases with increasing number of carbons on their pendant side-chains.[13]

2.3.4 Humidification of Quaternized Polymer

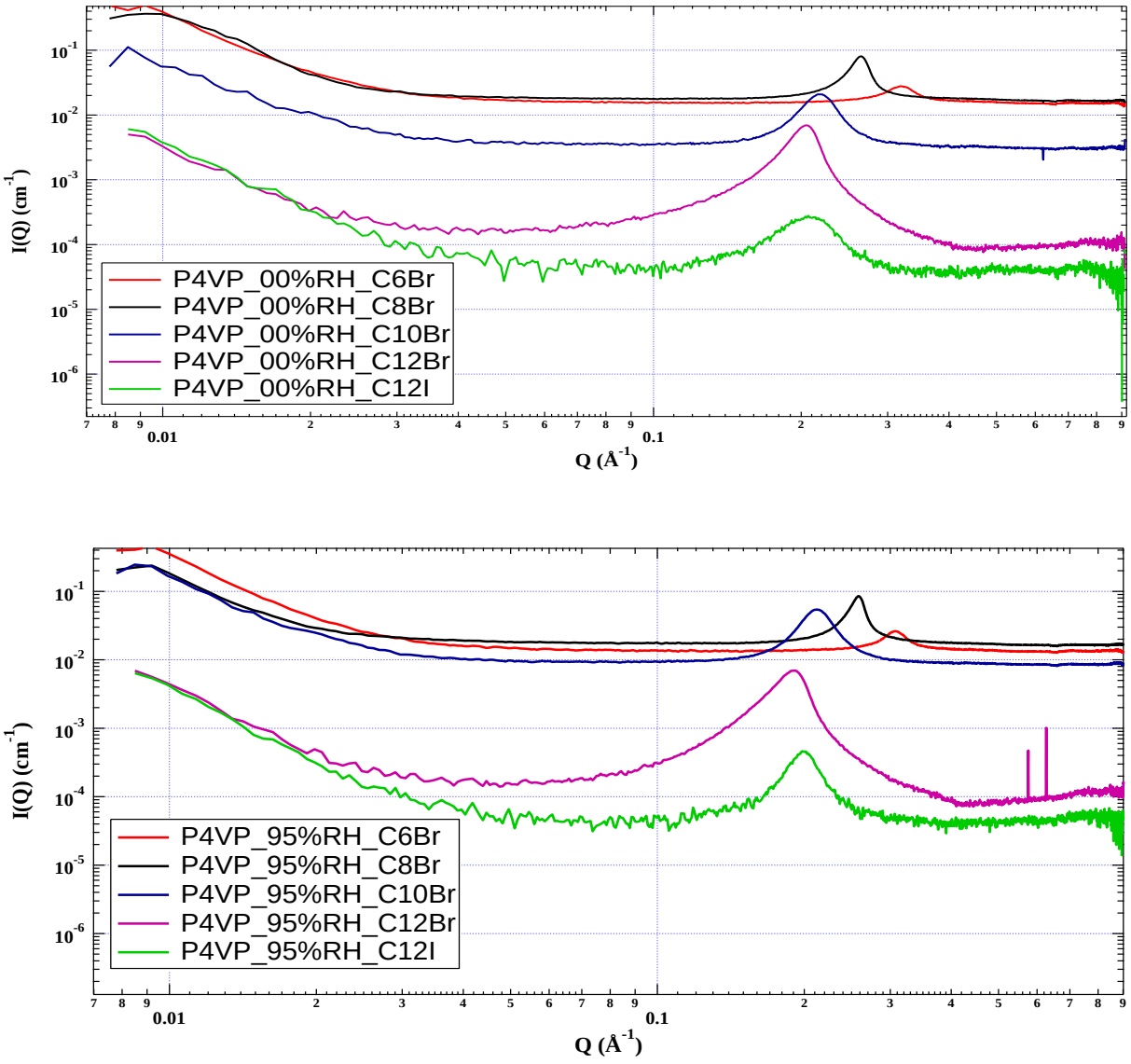

Figure 2.10. Quaternized P4VP samples before humidification (top) after humidification (bottom).

The SAXS spectra of quaternized samples under humidification shows that there is an increase in the backbone spacing due to swelling. Results are summarized in the Table 2.3 below.

Table 2.3. Change in backbone-backbone spacing with humidity.

Samples	$d_{B\_RH\_00\%}$(Å)	$d_{B\_RH\_95\%}$(Å)	% Increase
P4VP_C6Br	**19.7**	**20.4**	**3.6**
P4VP_C8Br	**23.7**	**24.5**	**3.4**
P4VP_C10Br	**28.8**	**29.8**	**3.8**
P4VP_C12Br	**30.9**	**33.1**	**7.8**
P4VP_C12I	**30.2**	**31.8**	**5.6**

With increasing number of carbons on the side-chain, the charge concentration in the system reduces. This can be quantified by the number of charges in mmoles per gram of sample as the ion exchange capacity.

$$IEC = \frac{number\ of\ counterions\ (mmoles)}{1\ gram\ of\ sample\ (g)} \qquad (2.14)$$

Generally, more charges in the sample is supposed to lead to higher moisture absorption, however, the trend observed was in the opposite direction. An increase in backbone spacing can be observed to increase with increasing number of carbons on the side-chains.

Also, of interest is the response of the counterion to swelling. Iodide and bromide counterions did have different swelling responses to the humidification of the system at the same side-chain length. This is not surprising since bromide is more kosmotropic than iodide in the Hofmeister series.[38] Bromide salts can take up more water in comparison to iodide salts. Bromide salts can also more

readily dissociate in the presence of water in comparison to iodide salts.[39] Hence, at high humidification, bromide counterions can dissociate from the polycation, thereby exposing the pyridinium cation on one polymer backbone to another pyridinium cation on an adjacent backbone. This can result in cation-cation repulsion thereby increasing the backbone-backbone spacing of the polymer. Alternatively, the difference in the swelling between P4VP_C12I and P4VP_C12Br may arise from the difference in backbone-backbone spacing, P4VP_C12I (30 Å) and P4VP_C12Br (31 Å). The shorter backbone-backbone spacing of P4VP_C12I in comparison to P4VP_C12Br may have resulted from the stronger dipole moment of the dipoles in the former in comparison to the dipole moment in the latter. Larger ions have larger dipole moment. The larger the dipole moment, the stronger the dipole-dipole interaction between dipoles on adjacent backbones. This could lead to more compact backbones in P4VP_C12I in comparison to P4VP_C12Br. The larger the backbone-backbone spacing, the more water molecules the chain spacing could accommodate, thus, causing more local hydration in these polymers than in those samples with smaller backbone-backbone spacing. This could lead to more swelling in polymers with larger spacing. As can be seen from Table 2.3, the larger the chain spacing, the higher the percent increase in the chain spacing at 95% RH for all samples irrespective of counterion type.

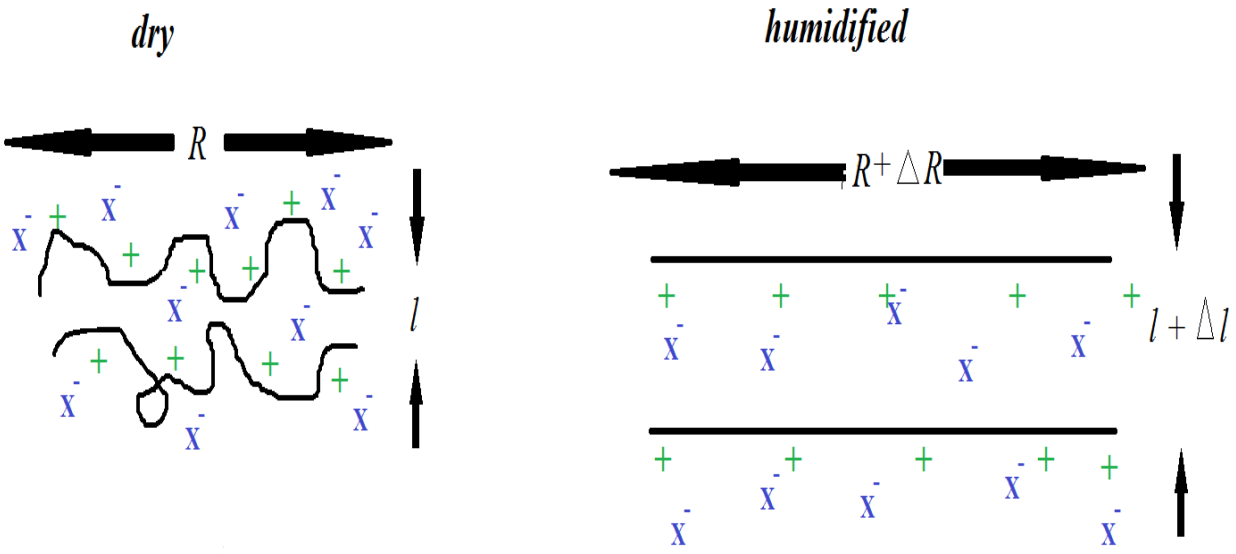

Figure 2.11. Depiction of the effect of humidification on backbone spacing. With increasing humidification, the backbone-backbone spacing between adjacent polymer chains increases.

The swelling of the sample does not just lead to chain extension as expected for polyelectrolytes in polar solvent, however, swelling also increases the backbone-backbone spacing between adjacent polyelectrolyte chains (see Figure 2.11). It is imperative to note that these feature peaks due to backbone-backbone spacing are not ionomer cluster peaks even though they like ionomer cluster peaks shift to lower Q values on humidification. Although ionomer domain sizes have been observed to increase with increasing humidification, this characteristic feature size (backbone-backbone spacing) are not the so-called ionomer spacing. However, their response during humidification is similar to that of ionomers.[30]

2.3.5 Conducting Properties of Quaternized Polymers

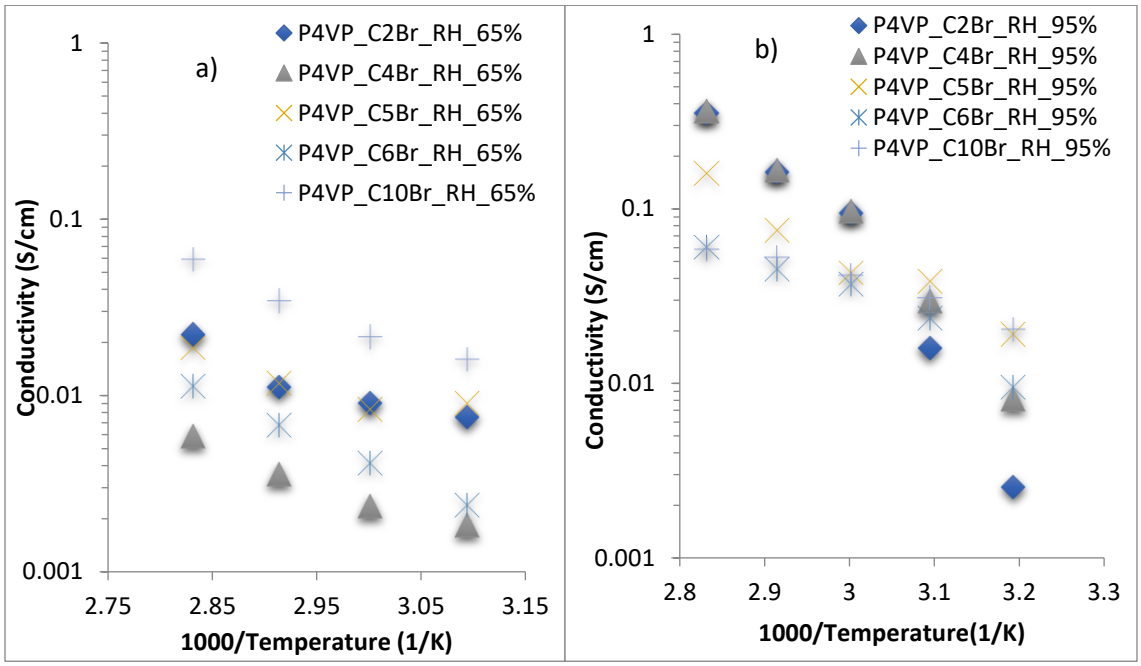

Figure 2.12. Plot of conductivity against inverse temperature at a) An RH of 65% b) An RH of 95%.

At 65% RH, conductivity decreased with increasing spacer (*i.e* lower IEC). This is evident from the drop in the conductivity plot from P4VP_C2Br to P4VP_C4Br. However, on increasing the number of carbons on the alkyl spacer there is an increase in the degree of order and consequently the conductivity. Strangely, P4VP_C5Br appears to have better conducting properties in comparison to P4VP_C6Br. In summary, the mobility of counterions at 65% RH is largely order-driven, though there is an appreciable dependence on the IEC.

However, at 95% RH., conductivity is dependent on IEC especially for systems with high moisture absorption. Since P4VP_C2Br, P4VP_C3Br and P4VP_C4Br are soluble in water, at high humidification, they become solvated leading to very high bromide conductivity; an order of magnitude higher than at 65% RH. At 95%, the conducting properties of all samples increased in

comparison to the bromide conductivities of the same samples at 65% RH at lower temperatures. Although humidification at 95% RH should decrease order in P4VP_C2Br and P4VP_C4B since both become solvated at high humidity, high counterion mobility in the presence of very humid conditions overcompensated for the decrease in order by a corresponding increase in the conductivity of ions. Furthermore, from the SAXS data, Figure 2.10, P4VP_C6Br and P4VP_C10Br maintained their backbone-backbone ordering at high humidification. However, at 95% RH, their conductive properties increased at lower temperatures in comparison to their conductive properties at 65% RH. Consequently, the conductive properties of P4VP_C6Br and P4VP_C10Br increased with increasing humidification at low temperatures. For P4VP_C5Br, there was an appreciable increase in the conductivity values at 95% RH in comparison to 65% RH. Thus, for all the studied sample series, conductivity at 95% RH is largely humidity-driven.

Table 2.4. Summary of theoretical and titrated IEC values, and activation energy values of bromide conductivity in P4VP_CnBr series at 65% and 95% RH.

Sample	**Theoretical IEC (mmoles/g)**	**Experimental IEC (mmoles/g)**	**Activation energy (RH 65%) kJ/mol**	**Activation energy (RH. 95%) kJ/mol**
P4VP_C2Br	4.67	-	**43.8**	**64.2**
P4VP_C3Br	4.39	-	-	-
P4VP_C4Br	4.13	-	**44.8**	**64.1**
P4VP_C5Br	3.91	3.85±0.09	**39.1**	**64.3**
P4VP_C6Br	3.70	3.70±0.06	**48.6**	**23.2**
P4VP_C7Br	3.52	3.51±0.06	-	-
P4VP_C8Br	3.36	3.28±0.04	-	-
P4VP_C9Br	3.21	3.12±0.01	-	-
P4VP_C10Br	3.07	3.02±0.04	**41.9**	**20.5**
P4VP_C12Br	2.83	2.65±0.01	-	-

This difference in the mode of ion transport at 65 and 95% RH is evident in the different slopes of the graph (*i.e* the activation energy) at these conditions. All samples measured had almost the same activation energy at 65% RH (as can be seen by the parallel nature of the data points), indicating possibly that the transport of Br^- follow the same dynamics. At an RH of 95%, it can be observed

that there are two classes of activation energy values. Materials with poor moisture absorbing properties (samples with low IEC) have lower activation energy compared to their activation energy at 65% RH while those with higher moisture absorbing properties (samples with high IEC) have higher activation energy in comparison to their values at 65% RH. These differences in the activation energies at different RH for low and high IEC samples suggest that there are different mechanisms for bromide conductivity in these samples.

2.4 Conclusion

The extent of quaternization of P4VP could be studied with FTIR as well as WAXS. The backbone spacing obtained does increase linearly with increasing side-chains of the quaternization agent. Backbone-backbone spacing and the relative intensity of the LVDW peak to VDW peak can be used to monitor the extent of quaternization. Relative intensity increases with increasing backbone spacing. Backbone-backbone spacing increases the rigidity of the comb-shaped polymer. With increasing rigidity of the polymer, the persistence length of the polymer increases, thereby, increasing the quantity of short-range ordering resulting from correlations between backbones of polymer segments and their nearest neighbors. Furthermore, we see that the mode of conductivity depends on the backbone morphology. At 65% RH, the conductivity seems to be dependent on the degree of backbone order, with high ordering, evidenced from the relative intensities of those polycations, increasing the mobility of dipoles. However, at 95% RH, the conductivity is heavily dependent on the moisture absorption of the polyelectrolyte.

Another interesting finding is that the spacing between the backbones changes on increasing humidification. Traditionally, it has been well-known that polymers when swelling may have an increase in the radius of gyration, however for P4VP_CnBr/I, swelling also increases the

separation between the chains almost by a factor of approximately 1 – 2 Å. Surprisingly, the longer the side-chains, the more increase in the chain spacing. This increase occurs though the P4VP_CnBr/I with larger *n* should be more hydrophobic. This phenomenon should be further investigated. Furthermore, like ionomer peaks, the characteristic feature size observed in SAXS spectra increases with humidification little wonder it may be confused for ionomers in the literature. However, unlike ionomers these feature sizes increase with increasing concentration of the ionic fraction.

No ionomer cluster morphology was observed in the random copolymer of P4VP and quaternized P4VP. This is possibly because typical ionomer cluster morphology formation in PS-*r*-PSS were formed at low mol% of PSS, typically about 7 – 10 mol%.[40] In the case of random copolymer of P4VP and quaternized P4VP, after 1 hour of quatenization, the mol% of the quaternized P4VP in P4VP-r-P4VP_CnBr was above 30% for all the 1-alkylbromide except for 1-Heptylbromide which had an extent of conversion of about 25%.

2.5 References

1. Rehberg C. E., and Fisher, C. H., *J. Amer. Chem. Soc.,* **1944,** 66, 1203.
2. Amerik Y. B., and Krentzel, B. A., **1973**, *Progress in the Chemistry and Physics of Polymers*, Chemistry, Publishing House, Moscow, p. 97.
3. Plate, N. A., V. P. V. P., and Petrukhin, B. S., *Vysokomol. Soedin*. B, 13, 757 (1971).
4. Plate, N. A., Shibaev, V. P., Petrukhin, B. S., Zubov, Y A., and Kargin, V. A., *J. Polym. Sci. A*-**1971**,1,9, 229.
5. Port, W., Jordan, E., Hansen, J., Swern, D., *J. Polym. Sci.,* **1952**, 9, 453,

6. Overberger, C. G., Fraizier, G., Mandelman, J., and Smith, H. F., *J. Amer. Chem. Soc.*, **1953,** 75, 3326.
7. Corradini, P., *Stereochernisty of Macromolecules*, A. D. Ketley, Ed., Dekker, New York, 1968, 3, 1
8. Turner-Jones, *Makromol. Chem.*, **1964,** 71, 1
9. Corradini, P., Lanzetta, R., Maglio, G., Palumbo, R., and Riva, F., *J. Polym. Sci. Polym. Chem. Ed.*, **1975,** 13, 1107.
10. Miller, L. R., and Boyer, R., Heijboer, J., *J Poly Sci: Polym. Phys. Ed*. **1984,** 22, 2021-2041
11. Salas-de la Cruz D., Green M.D, Ye. Y., Elabd, Y. A., Long, E. T., Winey, K. I., *J Polym Sci Part B: Polym Phys* **2012,** 50, 338–346
12. Pankaj S., and Beiner M., *Soft Matter*, **2010**, 6, 3506–3516
13. Plate, N. A., and Shibaev, V. P., *Macromol. Rev.*, **1974,** 8, 117-206
14. Corradini, P., *J. Polym. Sci. Polym. Symp*, **1975,** 50, 327-344.
15. Warren, B. E., *Phys. Rev.*, **1933,** 44,969.
16. Shibaev, V. P., Petrukhin, B. S., Zubov, Y. A., Plate, N. A., and Kargin, V. A., *Vysokomol. Soedin.* **1968,** A, 10, 216.
17. Beiner, M., Huth, H., *Nat. Mater*. **2003**, 2, 595–599.
18. Triolo, A., Russina, O., Bleif, H. J., Cola, E. D., *J. Phys. Chem. B* **2007**, 111, 4641–4644.
19. Semegen S. T., and Wakelin, J. H., *Rubber Age*, **1952,** 71, 57**.**
20. Triolo, A.; Russina, O.; Fazio, B.; Triolo, R.; Di Cola, *Chem. Phys. Lett.* **2008,** 457, 362–365.

21. Balta-Calleja, F. J., Ramos, J. G., and Barrales-Rienda, J. M., *Kolloid 2. 2. Polym.,* **1972** 250, 474**.**

22. Inomata K., Sakamaki Y., Nose T., and Sasaki S., *Polym J* **1996,** 28**,** 11.

23. Wunderlich, B., *Thermochim. Acta*, **2009**, 492, 2–15.

24. Russina, O.; Triolo, A.; Gontrani, L.; Caminiti, R.; Xiao, D.; Hines, L. G.; Bartsch, R. A.; Quitevis, E. L.; Pleckhova, N.; Seddon, K. R. *J. Phys. Condens. Matter* **2009**, 21, 1–9.

25. S, Hiller; O, Pascui; H, Budde; O, Kabisch; D., Reichert; M, Beiner. *New J. Phys*. **2004**, 6, 10.

26. Eisenberg A.; Kim, J.S. Introduction to Ionomers; Wiley-Interscience: NewYork, **1998**. [1b]Tant, M.R.; Mauritz, K. A.; Wilkes, G.L. Ionomers: synthesis, structure, properties and applications; Blackie Academic and Professional: London, 1991.

27. Essafi, W.; Lafuma, F. ; Baigl, D.; Williams, C. E. Europhys. Lett., **2005**, 71, 938-944.

28. Fitzgerald, J. J.; Weiss, R. A. *J. Macromol. Sci., Rev. Macromol. Chem. Phys.* **1988**, C28,99.

29. Ding, Y. S.; Hubbard, S. R.; Hodgson, K. O.; Register, R. A.; Cooper, S. L. *Macromolecules* **1988**, 21, 1698−1703.

30. Tsai T-H, Ertem S. P, Maes A. M, Seirfet S, Herring A. M, Coughlin E B, *Macromolecules* **2015,** 48, 655 – 662

31. Eisenberg. A., *Macromolecules* **1970**, 3, 147-154

32. Hu, F.X., Neoh, K.G., Cen, L. and Kang, E.T., *Biotech. Bioeng* **2005,** 89, 474

33. Yao, C., Li, X., Neoh, K.G., Shi, Z. and Kang, E.T., *J. Membr. Sci.,* **2008,** 320(1-2), 259-267

34. Caruso, U.; Maria, D.A.; Panunzi, B.; Roviello, A. *J. Polym. Sci. Part A: Polym. Chem.* **2002,** 40, 2987-2993

35. Patel M., Patel R., Chi W S., Kim J H., Sung J., *Chinese J of Polym Sci*, **2015,** 33, No. 2, 265–274

36. Coleman, B. D and R. M. Fuoss, *J. Am. Chem Soc.*, **1955,** 77, 5472

37. Fuoss B. M, Watanabe M, Coleman B, *J Polym Sci*, **1960,** 58, 5 – 15

38. X. Tadeo, M. Pons and O. Millet, *Biochemistry*, **2007,** 46, 917-923.

39. Marino, M. G.; Melchior, J. P.; Wohlfarth, A.; Kreuer, K. D. *J. Memb. Sci.* **2014**, *464*, 61–71

40. Grady, B. P. *Polym. Eng. Sci.* **2008**, 1029–1051.

CHAPTER 3

STRUCTURE-*WITHIN*-STRUCTURE: MORPHOLOGICAL PROPERTIES OF PS-*b*-P4VP_CnBr

3.1 Introduction

Block copolymers will always play a role in the morphological features of polymers and polyelectrolytes are no exemption. It has been posited that due to the ability to have different blocks with unique properties, the overall feature of these block-co-polyelectrolytes will be more mechanically robust than their random counterparts.[1–4] Besides their good structure and mechanical robustness, block copolymers also have been known to control the moisture content, and in some cases, conductivity in anionic exchange membranes.[5,6]

Due to the additional presence of electrostatic interactions, the χ parameter of block copolymers can skew the traditional block copolymer phase diagrams giving rise to unique morphological features that may improve conductivity and mechanical properties.[7] While most block copolymer polyelectrolytes focus on the interesting morphologies that can be obtained from the different blocks, the study of backbone-backbone spacing within a block is scarce in the literature.[1-6]

A common model system, PS-*b*-P4VP, which has been well studied is the template for investigating this phenomenon of intra block ordering. It is well known in the literature that complexing P4VP with pentadecylphenol (PDP), can provide structure-*within*-structure morphologies.[8–10] The block copolymer forms all the traditional phase separation morphologies consistent with their varying volume fraction while substructures within superstructures are formed in the P4VP domain. Ruokolainen *et al*. were one of the first to investigate these systems using hydrogen bonding to bind PDP to the pyridine group. They noticed an ODT of 60 °C for 1:1

ratio of PS-*b*-P4VP and PDP when the substructure arising from PDP was analyzed by an X-ray scattering equipment coupled with a heating device. They also found that thermal treatment of these polymers changes the morphologies of these systems and the obtained morphological structures depend on the weight fraction of the PDP in the sample.[8]

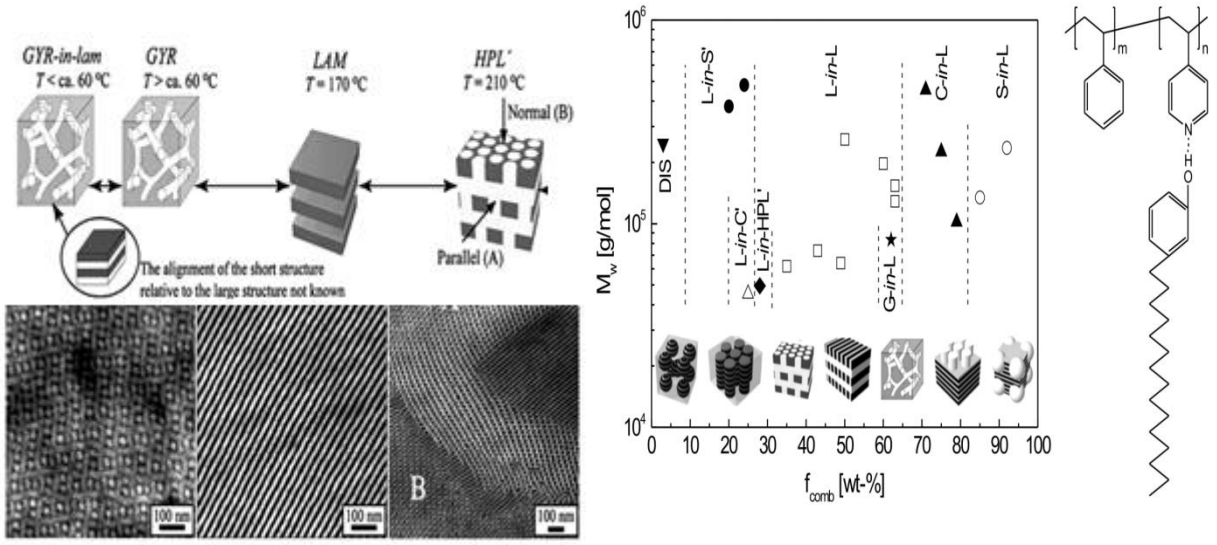

Figure 3.1. Morphologies obtained from PS-*b*-P4VP(PDP) indicating interesting morphological features difficult to obtain using the classic phase diagram.[8] b) Accessible morphology as a function of the weight fraction of PDP.[Images taken from Ref 8,9]

As can be seen from Figure 3.1, interesting structures have been obtained by hydrogen bonding. Furthermore, ionic bonding by treating the 4VP with a strong acid to give a quasi-proton conducting membrane gave rise to interesting morphologies as well.[7] However, studies on quaternized P4VP block copolymer and their structure-*within*-structure in a block copolymer have not received a lot of attention in the literature. The morphology of these quaternized P4VP block copolymers will be studied by both small-angle X-ray scattering (SAXS) and anomalous small-angle X-ray scattering (ASAXS).

3.1.1 ASAXS and the Degree of Ordering in Quaternized P4VP

To study concentration of counterions of polyelectrolytes, a technique that is sensitive to that counterion must be employed. Condensing counterions in dilute polyelectrolyte solutions has been studied using techniques like osmotic pressure and conductivity to contrast between free and uncondensed counterions. In solid state, the concentration of counterions in polyelectrolytes can be studied by scattering techniques that are sensitive to the counterions. Small angle X-ray Scattering (SAXS) has been extensively used to study phase separation in block copolymers by taking advantage of scattering contrasts provided by the microphase separated blocks. X-ray scattering depends on the number of electrons in a scattering entity. In block copolymers in which one block has atoms with large atomic number, this large atomic number atom can provide contrast to probe the morphology of the block copolymer. The concentration of this atom in the polymer can be estimated by directly probing the atom with the large atomic number. By changing the energy of the incident photons, it is possible to study the distribution of a specific atom or counterion in space. Small-angle X-ray scattering performed at incident energy close to the K-edge of the species of interest (like counterions) is known as anomalous small-angle X-ray scattering (ASAXS). At resonance between the incident photon and an electron in the K-shell, the electron can be ejected from inner shell of the species of interest. An electron at higher energy level drops into the empty inner K-shell orbital (see Figure 3.2). During this transition from higher energy to lower energy levels, energy is given out in form of photons. These photons are known as dispersion X-rays, and on detection gives information about the spatial orientation, arrangement, and quantity of the species of interest/counterions in the systems.

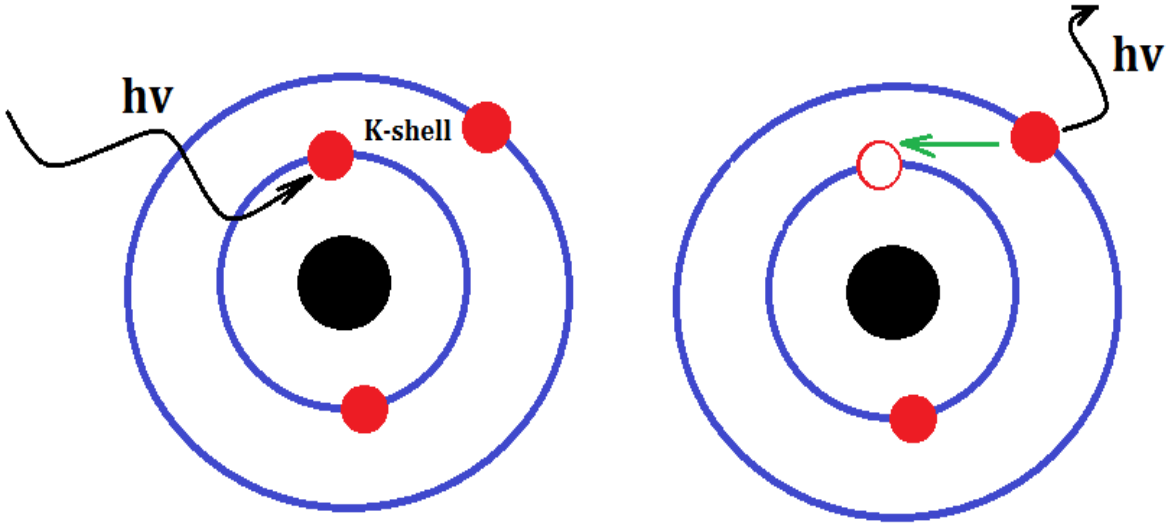

Figure 3.2. Schematic representation of the origin of ASAXS.

The scattering intensities of the macroion and counterion can be distinguished and separated. This is not possible in SAXS because the scattering intensities of all species present in the system are superimposed and cannot be easily isolated. Sturmann in 1985 had predicted that this can be useful in the field of polymer science.[11] However, in the decade following his prediction, ASAXS remained sparingly used for structural characterization of polymers. Most recently, there is a resurgence in its use as an important polymer characterization tool.[12–18]

In the literature, ASAXS has been used to study not just the spatial distribution of counterions but also their concentration in polyelectrolyte solutions.[14] There has also been reports of its use to study condensed counterions.[14,18,19] However, the application of this technique to study the distribution of counterions in solid polyelectrolytes remains relatively sparse. In this project we report the ordering and distribution of counterions in solid polyelectrolytes using SAXS. We corroborate our findings by studying directly the anomalous dispersion counterion X-rays using ASAXS. We use ASAXS to probe the relative quantity of periodically arranged backbones by probing the bromide counterions at the base of the pendant side-chains. We also compare this

parallelly arranged backbones obtained in the block copolymer with the relative quantity obtained by using the ratio of the backbone-backbone (LVDW) peak to the amorphous halo (VDW peak). See Chapter 2.

This project aims to answer the following questions:

- Can there be formation of structure-*within*-structure when a pendant side-chain is covalently bound to the 4VP in PS-*b*-P4VP and not just by hydrogen bonding?
- What types of structures are formed?
- Do these structures depend on the number of carbons on the pendant side-chain?
- How does the concentration of periodically spaced backbones obtained from ASAXS compare to those obtained by the ratio of LVDW to VDW in the homopolymer?

3.2 Materials and Methods

Styrene (98%) and 4VP (96%) were obtained from Alfar Aesar and was passed through a basic alumina column. N-tert-butyl-N-[1-diethylphosphono-(2,2-dimethylpropyl)] nitroxide (SG1) was obtained from Arkema and used as obtained. 1-bromopentane (purchased from Sigma-Aldrich), 1-bromobutane (98%), 1-bromohexane (99%), were all purchased from Alfa Aesar

3.2.1 Synthesis of PS-*b*-P4VP

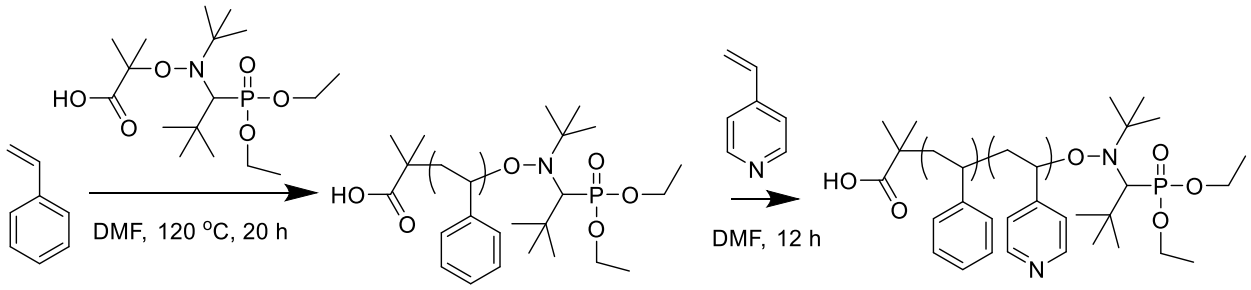

Scheme 3.1. Synthesis of PS-*b*-P4VP by nitroxide mediated polymerization.

In a round bottom flask, 17.5 g of styrene was polymerized with 160 mg of SG1 initiator; a molar equivalence of 400:1, [styrene]:[SG1]. Polymerization was performed in 70 wt% dimethyl formamide (DMF) at 120°C for 13 h. The resulting polystyrene (PS) sample was quenched in ice and precipitated thrice in hexanes from dichloromethane. Using PS-SG1 as microinitiator, 6 g and 7.5 g was used to polymerize 7.1 g (360:1, [4VP]:[PS]I) and 2.4 g of 4VP (96:1, [4VP:PS]II) respectively for 12 hours. The mixture was quenched in ice and precipitated twice from dichloromethane; first in methanol and then diethyl ether.

3.2.2 Quaternization of P4VP-*b*-PS by 1-Alkylbromides

A solution of 1.0 M quaternizing agent (1-butylbromide, 1-pentylbromide, and 1-hexylbromide) was prepared in DMF. An excess amount of the prepared solution was added to a solution of 100 mg of P4VP-*b*-PS in 1.5 ml of DMF. After 240 h, the solution was precipitated into diethyl ether to give an off-white colored powder. After filtration, the powder was dried in vacuum at room temperature.

3.2.3 Characterization of PS-*b*-P4VP by ^{1}H NMR and GPC

Number average molecular weight, M_n, was determined using a Gel Permeation Chromatography (GPC) in DMF at a flow rate of 1.0 mL/min using a refractive index detector on an Agilent Technologies 1260 Infinity system. The chemical composition of PS-*b*-P4VP was determined using a Bruker 500 Fourier-Transform Nuclear Magnetic Resonance (FT-NMR). Results are summarized in Table 3.1.

3.2.4 Characterization of PS-*b*-P4VP by FTIR

PerkinElmer Spectrum 100 FTIR with a universal ATR was used to characterize the extent of quaternization. Film samples were mounted on the ATR crystal and secured by the sample holder.

3.2.5 Characterization of PS-*b*-P4VP by WAXS/SAXS

Synchrotron SAXS and ASAXS Measurement: SAXS measurements were performed at the Advanced Photon Source Argonne National Laboratory on beamline 12 ID-B. Data was collected from the X-ray beam at a wavelength of 1 Å and an energy of 12 KeV of the incident radiation. A *Q* range of 0.005 to 0.5 Å was possible from the resulting apparatus. During the course of the experiment, a 2-dimensional image was obtained which was converted into *I(Q)* against *Q* by circular averaging. The intensity obtained was in absolute scale. For each experiment sequence data was collected for a set of three samples and a Kapton background. The background would be subtracted from the obtained membrane data. A typical exposure time of 5 seconds was used. Heating and humidification of the system was performed in a custom-made oven.[3,6,20,21] The humidity was controlled by heated streams of water-saturated nitrogen and dry nitrogen gas. SAXS data was collected first at room temperature and then dried for 40 mins at 60°C before collecting the first data set. The sample was then gradually humidified from 0 - 25% RH and the humidity

was maintained for 20 minutes, after which SAXS measurements were performed at 25% RH. Then the RH was increased to 50, 75, and 95% and was maintained for 20 minutes before collection of scattering data. A dynamic analysis was also performed on some of the samples. In the dynamic humidification a sequence of scattering data was collected as the RH was changed from 75-95%.

3.3 Results and Discussion

Characterization of the block copolymerization products by ^{1}H NMR (see Figure 3.3) showed that the ratio of PS to P4VP in the block copolymers were approximately equal to the monomer feed ratio of styrene to 4VP. The ratio of the PS to the P4VP blocks were determined by the integration of the two protons (2H) aromatic peaks of P4VP and the three protons (3H) aromatic peaks of PS. This confirms that the block copolymers, PS-*b*-P4VP(1:1) and PS-*b*-P4VP(3:1), were successfully synthesized by nitroxide mediated polymerization (NMP).

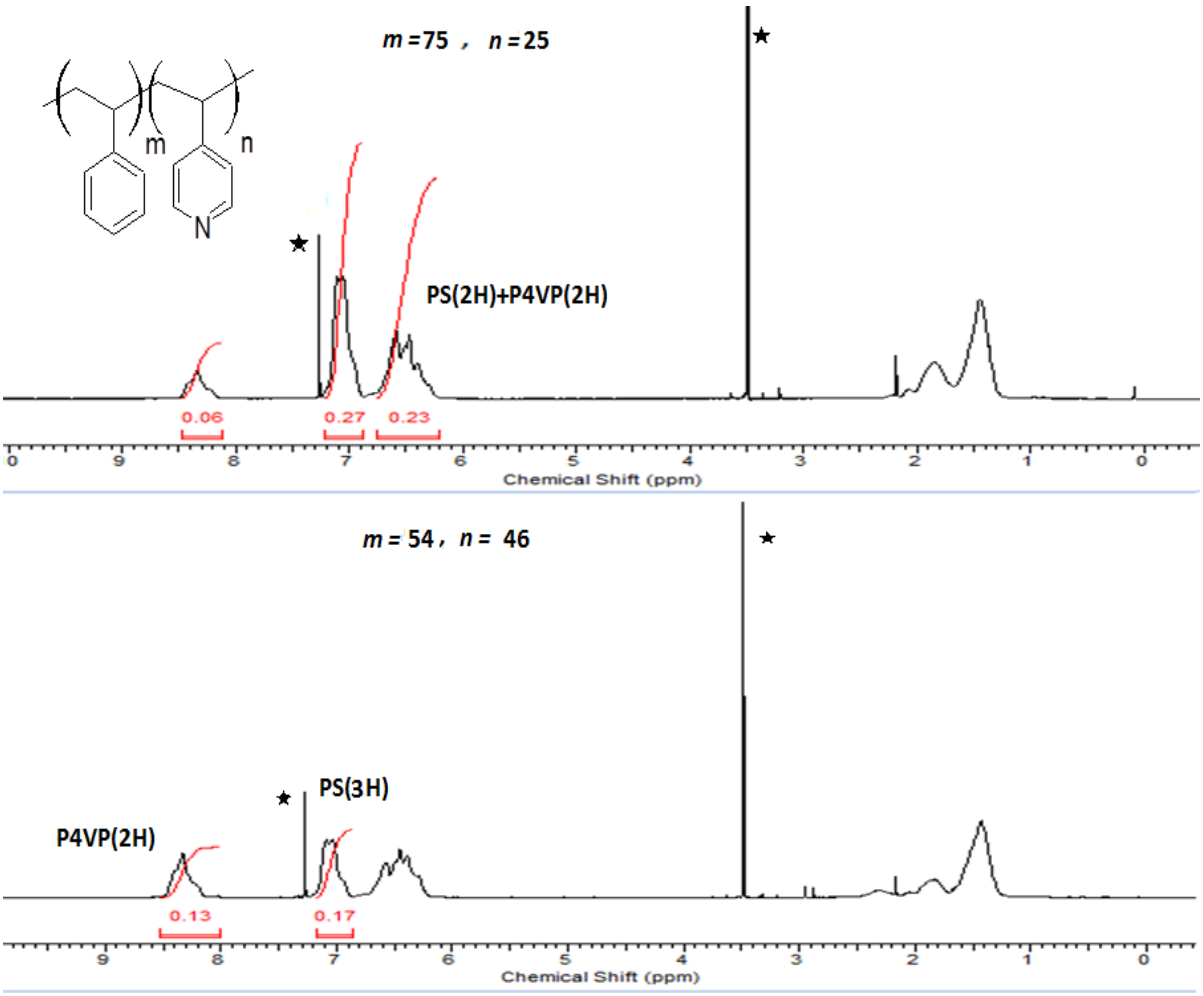

Figure 3.3. The ^{1}H NMR spectra of PS-*b*-P4VP(3:1) top and PS-*b*-P4VP(1:1) bottom.

The GPC chromatogram of the PS homopolymer, and block copolymers are presented in Figure 3.4. The determined values of the dispersity from the chromatogram show relatively narrow dispersities of the block copolymers. Summary of the results are presented in the table below.

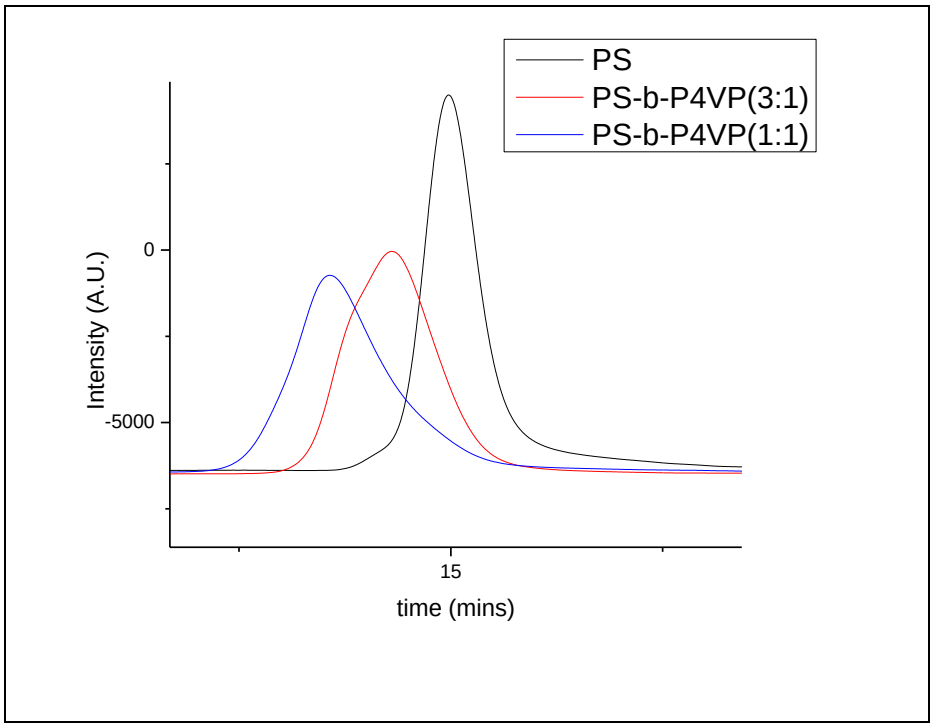

Figure 3.4. The GPC profile of PS-*b*-P4VP(1:1) and PS-*b*-P4VP(3:1) block copolymers.

Table 3.1. Summary of molecular weight properties of PS-*b*-P4VP block copolymers.

Sample	Feed ratio Styrene:4VP	NMR ratio	Target M_w (Kg/mol)	GPC M_w (Kg/mol)	Đ
PS-*b*-P4VP (1:1)	1:1	0.46:0.54	80	98	1.25
PS-*b*-P4VP (3:1)	3:1	0.75:0.25	53	68	1.17

3.3.1 FTIR Characterization of Complete Quaternization

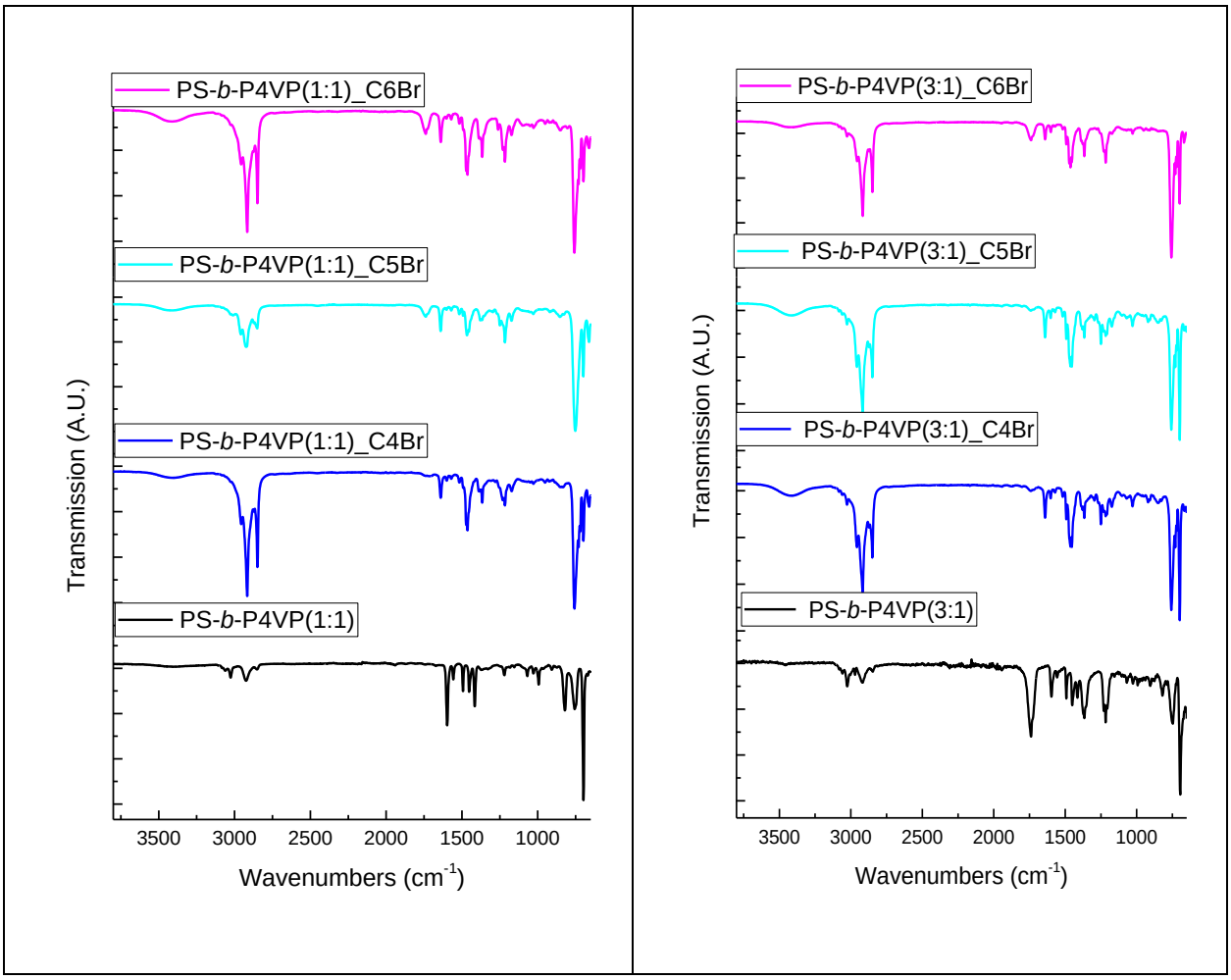

Figure 3.5. The FTIR spectra confirming the complete quaternization of PS-*b*-P4VP(1:1) and PS-*b*-P4VP(3:1).

Using FTIR, see Figure 3.5, the complete quaternization of the samples was confirmed with the disappearance of the pyridine peak at the 1414 cm^{-1} wavenumbers and the simultaneous appearance of the 1640 cm^{-1} pyridinium peak, as described for P4VP homopolymers in Chapter 2.

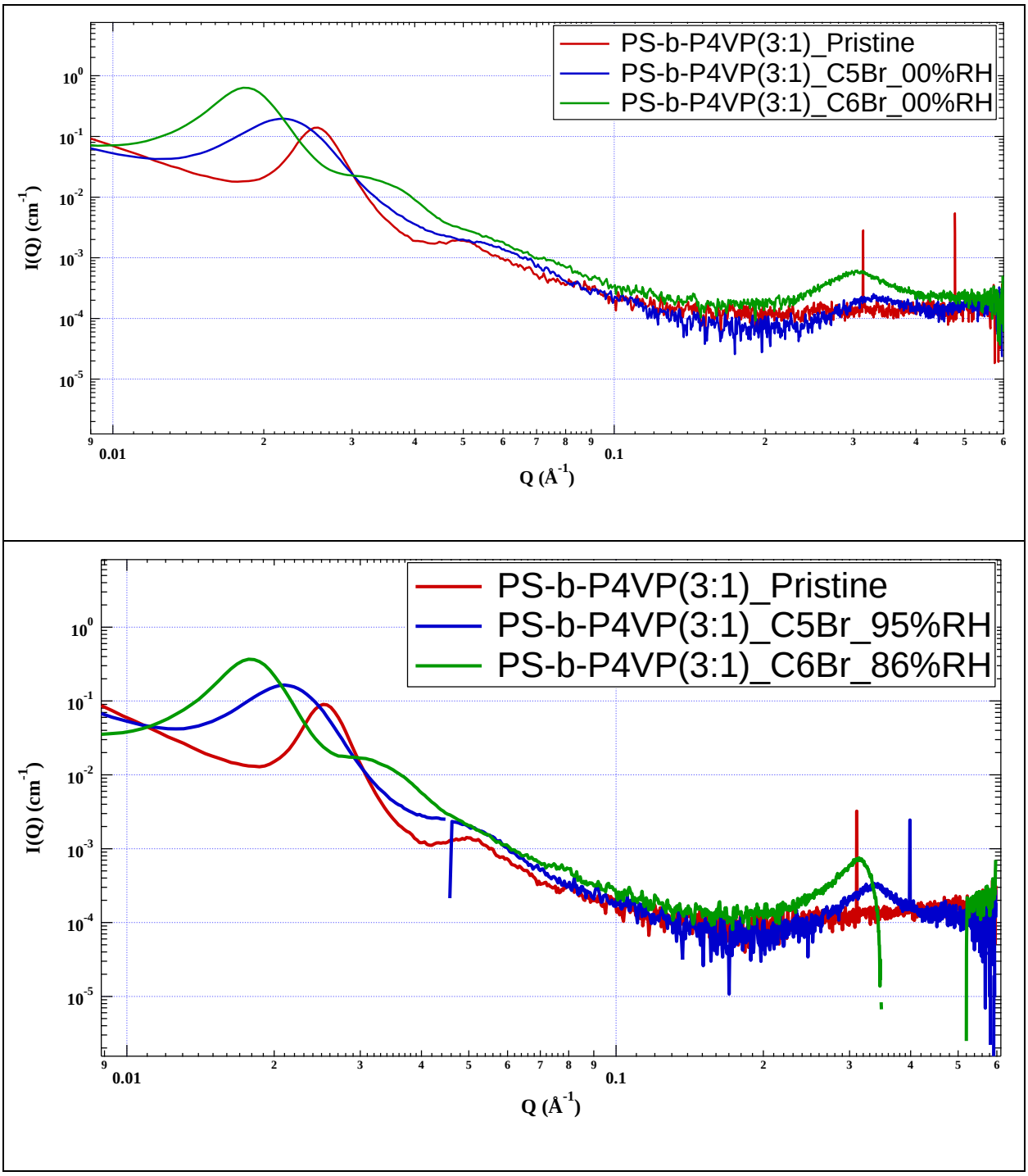

Figure 3.6. The SAXS profile of quaternized PS-*b*-P4VP(3:1) an RH of 00% (top), and an RH of 86 or 95% (bottom) .

From the above figure, a lamellar morphology was obtained for all samples. This is unexpected because the volume fraction of P4VP increased from approximately 0.25 in PS-*b*-P4VP(3:1) to approximately 0.5 in PS-*b*-P4VP(1:1). Furthermore, by quaternizing the P4VP, counterion and pendant side-chains are introduced into the P4VP domain, consequently decreasing the volume fraction of the PS-block in the block copolymer. The morphology of the block copolymer is therefore expected to change from PS-*b*-P4VP(3:1) to PS-*b*-P4VP(1:1) after quaternization. By observing similar morphology for all the studied samples, the X-ray scattering data suggest that these membranes may be kinetically trapped in a lamellar morphology since the samples were not thermally annealed. For PS-*b*-P4VP(3:1), the effect of quaternization gradually increased the size of the domain when compared to the pristine polymer. See Figure 3.6. This may be due to increasing molar volume of the quaternized P4VP chain in the block copolymer since quaternization increases the molecular weight of the quaternized repeat unit. However in the case of PS-*b*-P4VP(1:1), see Figure 3.7, the domain size decreased from the pristine sample, 47 nm to 39 nm for PS-*b*-P4VP(1:1)_C5Br, and then increased again to 45 nm for PS-*b*-P4VP(1:1)_C6Br. This trend was unexpected. However, since the quaternized block copolymers were not thermally annealed, the obtained domain spacing may not be the thermally equilibrated domain spacing.

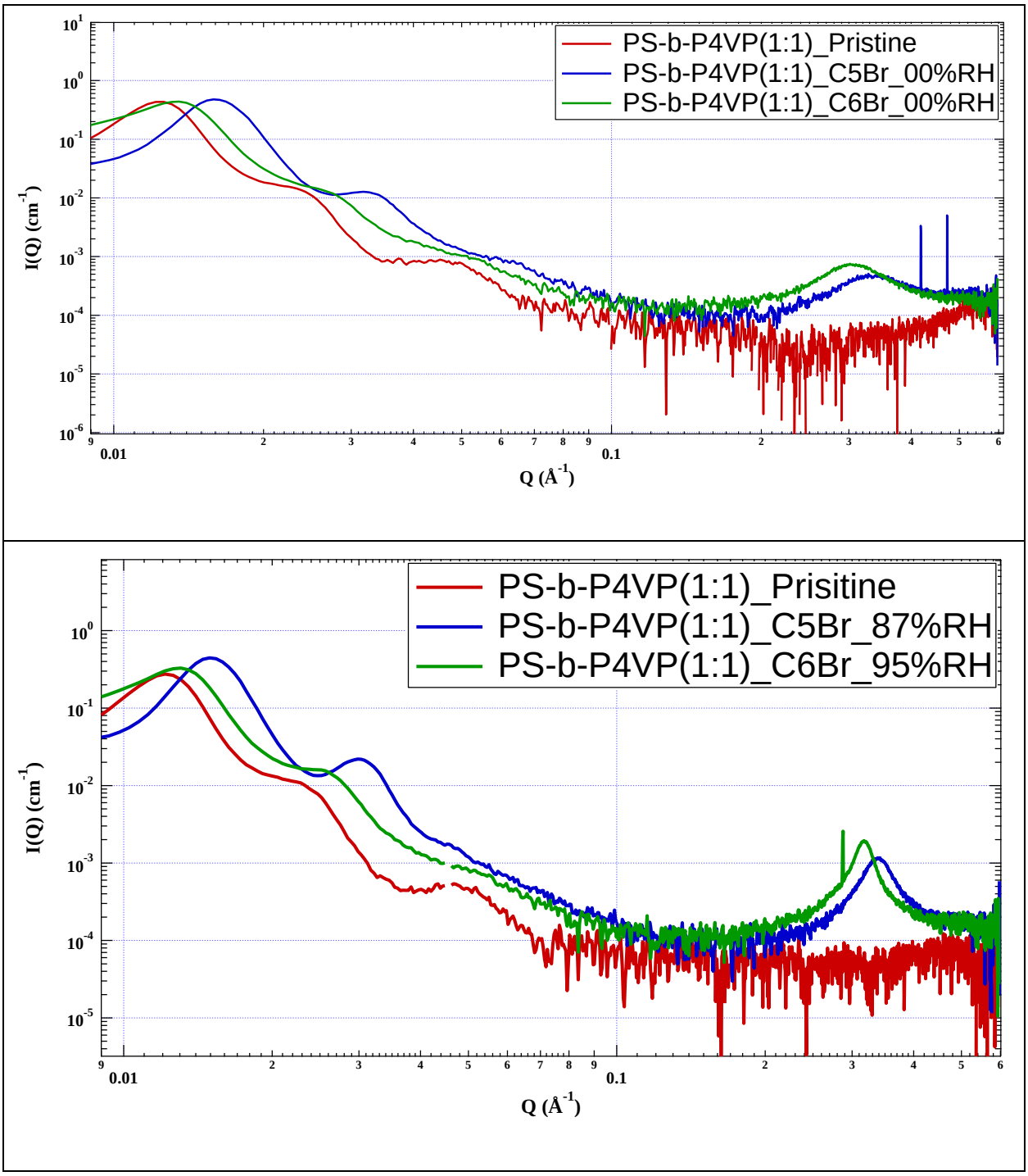

Figure 3.7. The SAXS profile of quaternized PS-*b*-P4VP(1:1) RH of 00% (top) RH of 95% (bottom).

Furthermore, as can be seen from Figure 3.6 and Figure 3.7, although there is observed swelling in all quaternized systems (PS-*b*-P4VP(1:1)_CnBr and PS-*b*-P4VP(3:1)_CnBr), they nevertheless maintained the same lamellar structure even after humidification to 95% RH. Coughlin *et al.* have reported that they noticed no swelling when polystyrene-*b*-poly(vinyl benzyl trimethylammonium tetrafluoroborate) were humidified under the same conditions.[3] This domain size swelling may be because of the density profile across the boundary of adjacent blocks. This boundary is comprised of quaternized P4VP and PS chains. The breadth of this region may get narrow as we humidify the system as predicted by Helfand.[22] This is because the χ parameter of the humidified PS-*b*-P4VP(1:1)_CnBr will change with increasing moisture content. However, Halfand had predicted that the breadth of this interface should not depend on molecular weight, which was not the case in the studied block copolymers.

Swelling increased with increasing hydrophilic content and increasing number of carbons on the pendant side-chain. In the case of PS-*b*-P4VP(1:1) quaternized by 1-alkylbromides, we do see higher swelling of the P4VP domains in comparison to that of the PS-*b*-P4VP(3:1). The observed swelling may be due to the higher volume fraction of the pyridinium block which increases the IEC. of PS-*b*-P4VP(1:1) in comparison to PS-*b*-P4VP(3:1). Quantitative results are summarized in Table 3.2.

Table 3.2. Changes in both domain size and backbone-backbone spacing upon humidification.

Samples	**Domain Spacing**			**Backbone-backbone spacing**		
	(nm) 00%RH	(nm) 90%RH	% Inc.	(Å) 00%RH	(Å) 90%RH	% Dec.
PS-*b*-P4VP(3:1)_C4Br	**28.5**	**29.8**	**4.5**	**17.0**	**16.6**	**2.3**
PS-*b*-P4VP(3:1)_C5Br	**29.1**	**30.1**	**3.5**	**19.2**	**18.8**	**2.1**
PS-*b*-P4VP(3:1)_C6Br	**33.9**	**34.7**	**2.3**	**21.1**	**19.7**	**6.6**
PS-*b*-P4VP(1:1)_C4Br	**78.1**	**85.6**	**9.6**	**16.5**	**17.0**	**-3.0**
PS-*b*-P4VP(1:1)_C5Br	**39.3**	**41.9**	**6.6**	**19.0**	**18.6**	**2.1**
PS-*b*-P4VP(1:1)_C6Br	**44.9**	**49.0**	**9.2**	**21.1**	**19.7**	**6.6**

Interestingly, from the SAXS measurement we also see a marked peak in the region of higher *Q* value. Since block copolymers do not usually form ionomers, this feature does not indicate the presence of ionic clusters in the P4VP domains. This feature, however, is the backbone spacing observed in the homopolymer. This peak therefore suggests that there is order within the microphase order of the PS and P4VP blocks. Since only one peak appears like in the case of the P4VP_C6Br and P4VP_C5Br homopolymers, it is difficult to conclude whether we have a cylinder-in-lamellar morphology or a lamellar-in-lamellar morphology. However, it is obvious that a structure-*within*-structure was formed in these polymer systems by quaternizing the P4VP block of a P4VP-*b*-PS block copolymer.

As already noted, humidification did increase the size of the parent domains. It also affected the arrangement of the backbone-backbone spacing, albeit in the opposite direction to that observed in their homopolymer counterpart. The peak moved to lower *Q* values and became narrower. This suggests that humidification compresses the backbones, thereby, decreasing the spacing between the backbones. This is possibly due to the confinement of the polyelectrolyte domains between incompressible blocks of PS. Consequently, any increase in the water concentration within the quaternized P4VP block compress the polymer chains within this block sandwiched between hard PS blocks. See Figure 3.8.

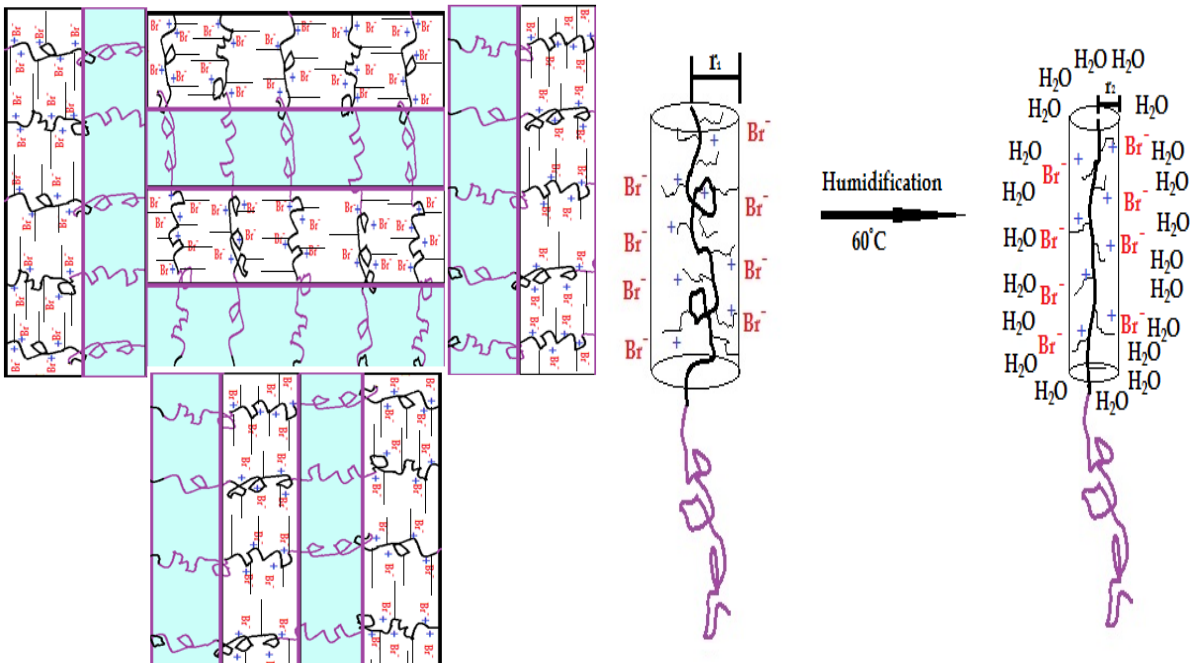

Figure 3.8. Schematic of humidification effect on the cylindrical diameter of the polymer chain.

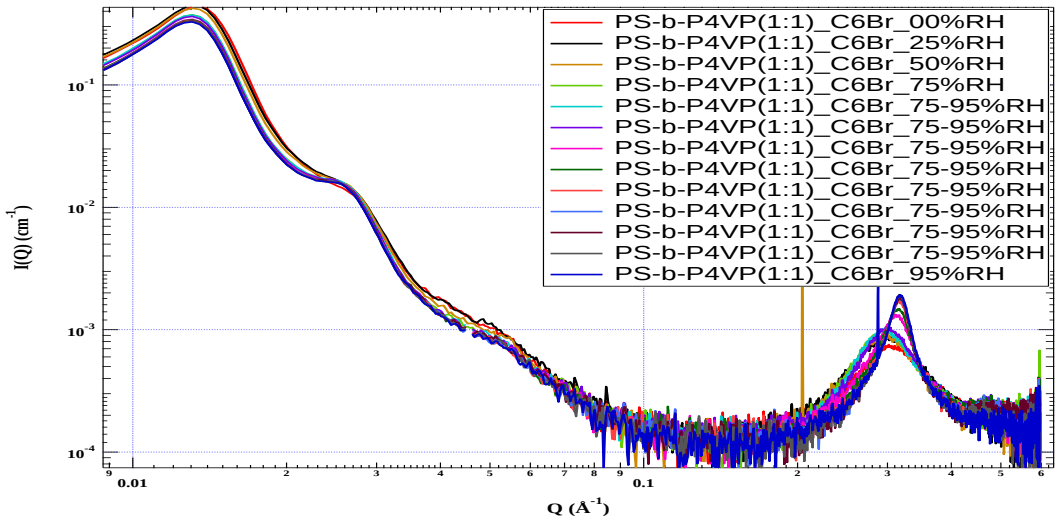

Figure 3.9. The SAXS profile of quaternized PS-*b*-P4VP(1:1)_C6Br showing the effect of humidification on the intra chain spacing.

From Figure 3.9, the decrease in the backbone-backbone spacing only appears at high RH. This is of importance because a noticeable change in the backbone-backbone spacing can be seen. It has been observed that at higher temperatures the structure within the parent structure might disappear due to the ODT.[8,9] By analogy, humidification is supposed to solvate the polymer thereby causing some degree of local disorder transition within the quaternized P4VP backbone. This RH in which there is a shift in backbone-backbone ordering can be seen as a kind of order to disorder relative humidity or *'ODRH'*. However, in these polyelectrolytes, with increasing humidification, the backbone-backbone spacing becomes more distinct as is evident from the above figure. The backbone-backbone peak actually moved to higher order. Since scattering experiments were not performed on the soaked samples (which are technically 100% RH) it is difficult to ascertain whether there can be an *ODRH* for a soaked PS-*b*-P4VP_CnBr. However, the dynamic humidification experiments did show that there was a move from order to higher order at about 75 - 95% RH.

Furthermore, a second order peak seems to have appeared at the onset of the 75 – 95% humidification and disappeared at the end of the process (Figure 3.10). Is there a morphological transition associated with this change or is this second peak due to increased scattering intensity? The ratio Q_2 to Q_1 is 1.46 approximately $\sqrt{2}$ for the observed peaks suggesting a cylindrical arrangement of the backbones in the 1-butylbromide quaternized P4VP block.

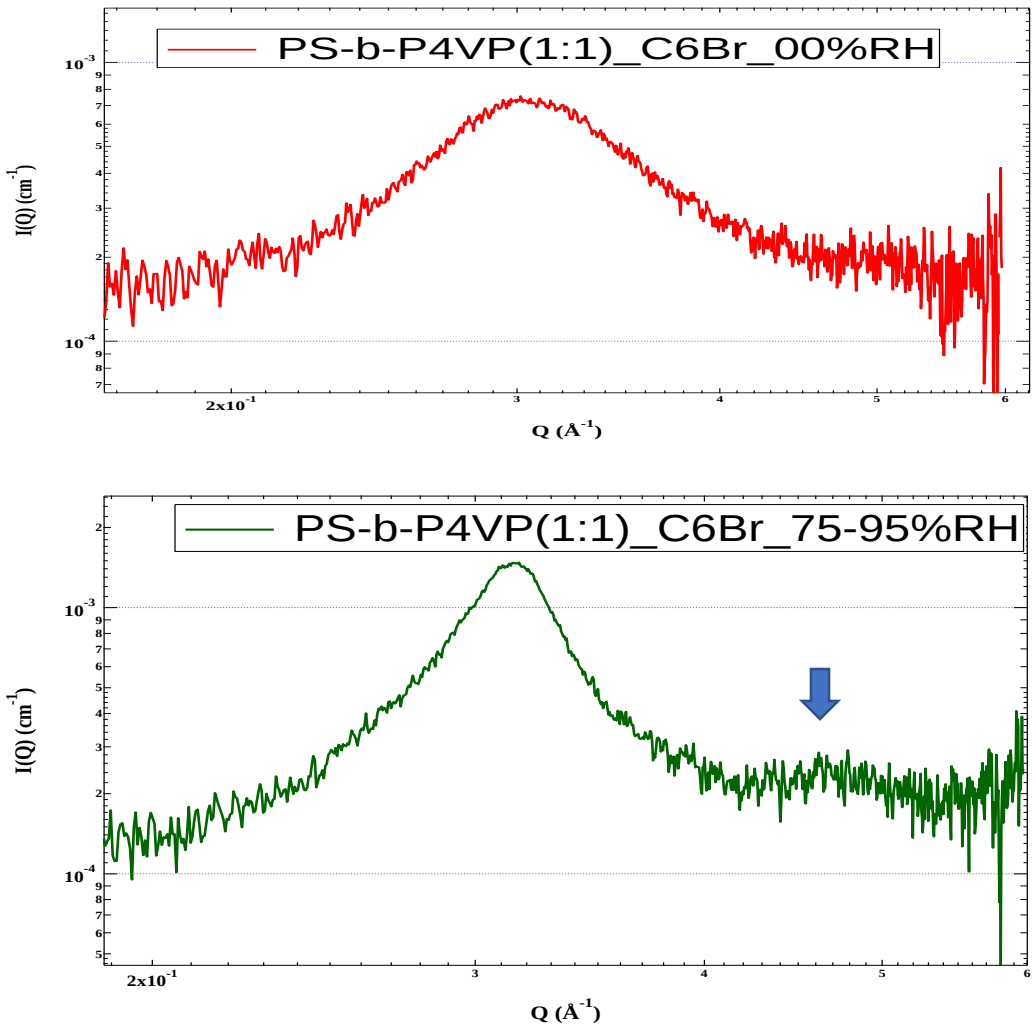

Figure 3.10. The SAXS profile of PS-*b*-P4VP(1:1)_C6Br at 0% RH (top), the SAXS profile of PS-*b*-P4VP(1:1)_C6Br at 95% RH (bottom). With the blue arrow showing the second order peak.

If the block is not well structured (i.e. relatively amorphous), then the block copolymer behaves like its homopolymer counterpart during humidification. The backbone-backbone spacing increases with humidification. PS-*b*-P4VP(4:1)_C4Br is a case in point. Although it can form a well-structured morphology as can be seen in PS-*b*-P4VP(4:1)_C5Br and PS-*b*-P4VP(4:1)_C6Br, however, when cast from a micellar solution the sample does not show highly ordered phase separation (see Figure 3.11). The hydrophilic regions are not clearly defined in the matrix. Thus, the chain spacing will tend to become larger without confinement regions that will inhibit them. Given that the backbones will always want to go far apart so as to increase their entropy. The SAXS profile in Figure 3.11 show that the changes in backbone spacing begin at 25% RH unlike in the well-structured blocks with changes starting at 75% RH albeit in the opposite direction. From the same figure, an increase in intensity can also be observed which suggest that more of the backbones become ordered in this process. In all the systems studied with increasing humidification, the intensity of the superstructures decreased.

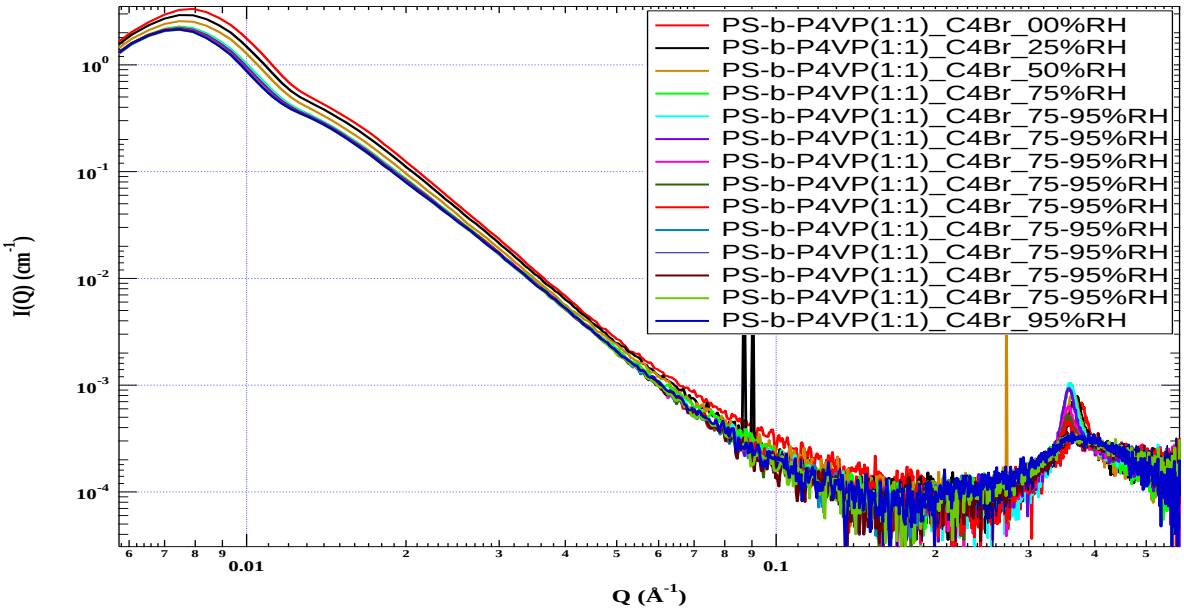

Figure 3.11. The SAXS profile of quaternized PS-*b*-P4VP(1:1)_C4Br showing that the effect of humidification becomes apparent for the chain spacing only at very high RH.

3.3.2 ASAXS and Relative Intensity in Quaternized P4VP

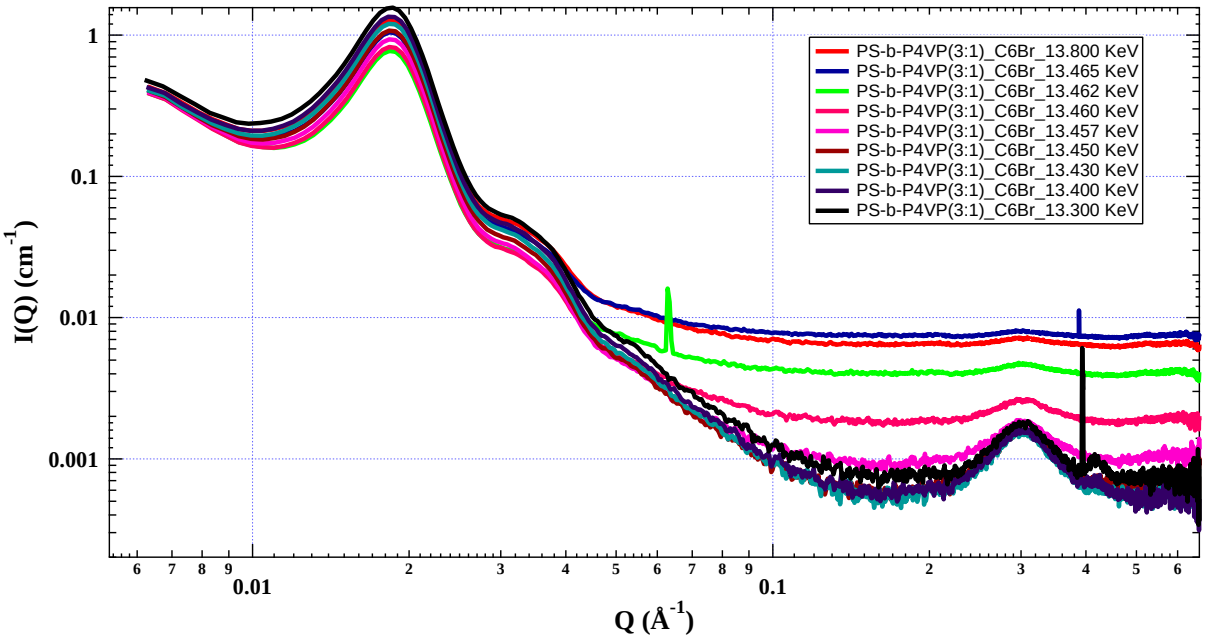

Figure 3.12. The ASAXS profile for PS-*b*-P4VP(3:1)_C6Br at different photon energies.

Photon energies ranging from 13.3 – 13.8 KeV were incident on the PS-*b*-P4VP(3:1)_C6Br to determine the photon energy that could produce the highest signal to noise ratio. This range of energies were also chosen to determine the photon energy that can provide the most information on the nature of ordering in the quaternized block copolymer for the *Q* values ranging from 1 – 0.06 $Å^{-1}$. The ASAXS spectra is presented in Figure 3.12. It is evident from the spectra that with increasing photon energy, the information of the membrane that can be obtained at higher *Q* values is lost. The absolute intensity of the backbone-backbone spacing peak decreases with increasing energy of the photons. Also, the intensity of the scattering resulting from microphase separation of the PS and P4VP_C6Br blocks decreased with increasing energy of the incident photons. With increasing energy of the incident photons, higher order reflections of the block copolymer structure are lost. Surprisingly, at a photon energy of 13.462 KeV, the third order peak arising from the block copolymer structure is lost. This photon energy is closer to the theoretical binding energy of bromine, 13.474 KeV, and thus expected to give the most information on the spatial distribution of bromide ions in the membrane. However, it does not provide adequate information of the membrane at higher *Q* values in which backbone-backbone spacing ordering is present. Thus, scattering intensity of the backbone-backbone spacing peak which correlates to the concentration of bromide counterions on periodically spaced polymer backbones at higher photon energy may be underestimated. For the analysis of the relative quantity of bromide counterions that are ordered between adjacent polymer backbones in these membranes, ASAXS was performed by photons having 13.800 and 13.300 KeV energy.

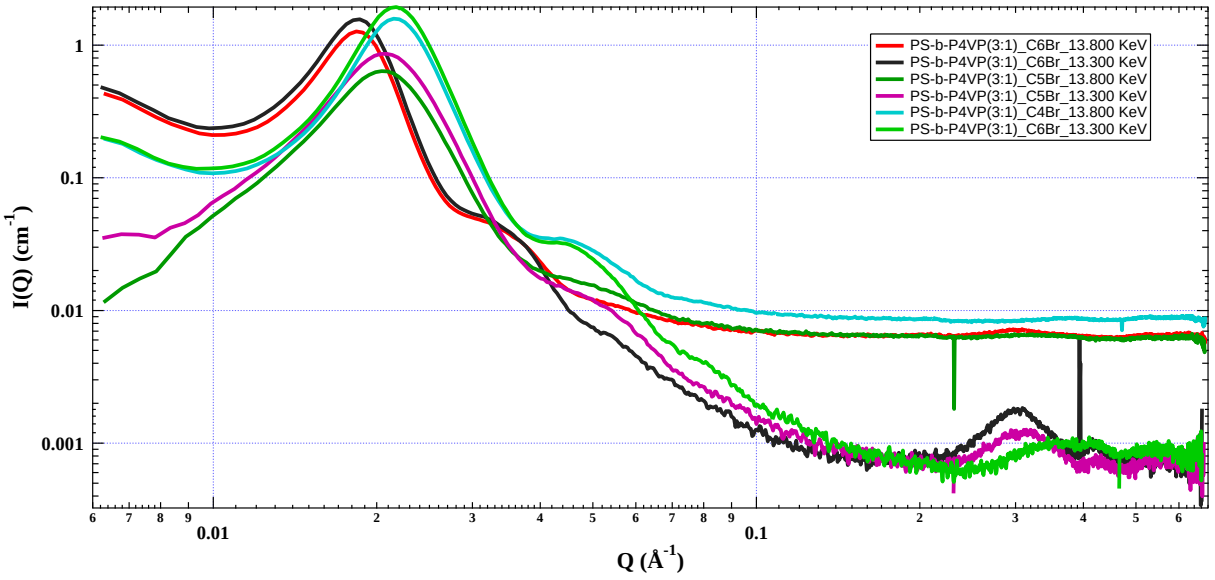

Figure 3.13. The ASAXS profile for PS-*b*-P4VP(3:1)_C4Br, PS-*b*-P4VP(3:1)_C5Br, and PS-*b*-P4VP(3:1)_C6Br at 13.3 and 13.8 KeV.

As expected, the intensities of the backbone-backbone peak increased with increasing number of carbons on the pendant side-chain. This is consistent with what have been observed in the quaternized P4VP homopolymer. This suggests that with increasing backbone-backbone spacing, more backbones in the polymer assumes a parallel arrangement. A ratio of the absolute intensities of the backbone-backbone spacing peak for PS-*b*-P4VP(1:1)_C4Br, PS-*b*-P4VP(1:1)_C5Br, and PS-*b*-P4VP(1:1)_C6Br can be determined form the ASAXS spectra presented in Figure 3.13. To make a comparison of the intensities of the backbone-backbone spacing peak in the block copolymers and the backbone-backbone spacing peak in the homopolymer, the intensity of the block copolymers relative to PS-*b*-P4VP(3:1)_C4Br and the intensity of the quaternized homopolymers relative to P4VP_C4Br were calculated. A tabular summary of the relative intensities by ASAXS and that determined by the backbone-backbone spacing peak (LVDW peak) to the amorphous halo (VDW peak) is presented in Table 3.3.

Table 3.3. Comparison of the relative peak intensities of the LVDW peak obtained from ASAXS and the ratio of LVDW to VDW

	ASAXS		LVDW/VDW
PS-*b*-P4VP(3:1)_C4Br	1	P4VP_C4Br	1
PS-*b*-P4VP(3:1)_C5Br	1.3	P4VP_C5B	1.6
PS-*b*-P4VP(3:1)_C6Br	2.0	P4VP_C6Br	3.7

It is evident from the relative intensities derived from ASAXS and LVDW/VDW that the LVDW/VDW overestimates the quantity of backbone-backbone spacing in the homopolymer or that the ASAXS relative intensity underestimates the backbone-backbone spacing in the block copolymer. The lower relative intensity values obtained for ASAXS may have resulted from the variation of the intensity of the backbone-backbone peak intensity with photon energy of the incident radiation.

3.4 Conclusion

The domain sizes changed with different quaternizing agent for PS-*b*-P4VP(1:1)_CnBr and PS-*b*-P4VP(3:1)_CnBr. While in the former, a decrease in the domain size from the pristine to PS-*b*-P4VP(3:1)_C5Br was observed, the latter increased. However, in both quaternized systems (PS-*b*-P4VP(1:1)_CnBr and PS-*b*-P4VP(3:1)_CnBr), the longer the side-chain the larger the domains size. Structure-*within*-structure can be found for PS-*b*-P4VP_ CnBr in which *n=4-6*. The specific morphology (cylinderical or lamellar) is difficult to ascertain from SAXS because only one peak

was observed. This structure-*within*-structure has a different response than the parent morphology during humidification. While the parent morphology shows an expansion in size, the chain spacing decreases. However, when the parent morphology is not well-structured, the behavior of the chain spacing during humidification is similar to the amorphous quaternized homopolymer. It increases in size. Anomalous small-angle X-ray scattering show that the quantity of the backbone-backbone spacing in PS-*b*-P4VP(3:1)_C6Br increased with increasing number of carbons on the pendant side-chains.

3.5 References

(1) Singh, M.; Odusanya, O.; Wilmes, G. M.; Eitouni, H. B.; Gomez, E. D.; Patel, A. J.; Chen, V. L.; Park, M. J.; Fragouli, P.; Iatrou, H.; et al. Effect of Molecular Weight on the Mechanical and Electrical Properties of Block Copolymer Electrolytes. *Macromolecules* **2007**, *40* (13), 4578–4585.

(2) Soo, P. P.; Huang, B.; Jang, Y.-I.; Chiang, Y.-M.; Sadoway, D. R.; Mayes, A. M. Rubbery Block Copolymer Electrolytes for Solid-State Rechargeable Lithium Batteries. *J. Electrochem. Soc.* **1999**, *146* (1), 32.

(3) Tsai, T. Ionic Copolymers for Alkaline Anion Exchange Membrane Fuel Cells (AAEMFCs), University of Massachusetts, 2014.

(4) Bouchet, R.; Maria, S.; Meziane, R.; Aboulaich, A.; Lienafa, L.; Bonnet, J.-P.; Phan, T. N. T.; Bertin, D.; Gigmes, D.; Devaux, D.; et al. Single-Ion BAB Triblock Copolymers as Highly Efficient Electrolytes for Lithium-Metal Batteries. *Nat. Mater.* **2013**, *12* (5), 452–

457.

(5) Tsang, E. M.; Zhang, Z.; Shi, Z.; Soboleva, T.; Holdcroft, S. Considerations of Macromolecular Structure in the Design of Proton Conducting Polymer Membranes: Graft versus Diblock Polyelectrolytes. *J Am Chem Soc* **2007**, *129* (49), 15106–15107.

(6) Zhang, W.; Liu, Y.; Jackson, A. C.; Savage, A. M.; Ertem, S. P.; Tsai, T. H.; Seifert, S.; Beyer, F. L.; Liberatore, M. W.; Herring, A. M.; et al. Achieving Continuous Anion Transport Domains Using Block Copolymers Containing Phosphonium Cations. *Macromolecules* **2016**, *49* (13), 4714–4722.

(7) Sing, C.; Zwanikken, J.; Cruz, M. D. La. Electrostatic Control of Block Copolymer Morphology. *Nat. Mater.* **2014**, *13* (7), 694–698.

(8) Valkama, S.; Ruotsalainen, T.; Nykänen, A.; Laiho, A.; Kosonen, H.; Ten Brinke, G.; Ikkala, O.; Ruokolainen, J. Self-Assembled Structures in Diblock Copolymers with Hydrogen-Bonded Amphiphilic Plasticizing Compounds. *Macromolecules* **2006**, *39* (26), 9327–9336.

(9) Zoelen, W. Van. PS-B-P4VP (PDP) Comb-Shaped Supramolecules : Nanorods and Thin Films for Nanotemplating, University of Groningen, 2009.

(10) Zoelen, W. Van; Polushkin, E.; Brinke, G. Hierarchical Terrace Formation in PS-b-P4VP (PDP) Supramolecular Thin Films Hierarchical Terrace Formation in PS-b-P4VP (PDP) Supramolecular Thin Films. *Macromolecules* **2008**, 8807–8814.

(11) Sturhmann, H. B. Resonance Scattering in Macromolecular Structure Research. *Adv. Polym. Sci.* **1885**, *67*, 123–163.

(12) Sztucki, M.; Cola, E. Di; Narayanan, T. Anomalous Small-Angle X-Ray Scattering from Charged Soft Matter. *Eur. Phys. J. Spec. Top.* **2012**, *208*, 319–331.

(13) Patel, M.; Rosenfeldt, S.; Ballauff, M.; Dingenouts, N.; Pontoni, D.; Narayanan, T. Analysis of the Correlation of Counterions to Rod-like Macroions by Anomalous Small-Angle X-Ray Scattering. *Phys. Chem. Chem. Phys* **2004**, *6*, 2962–2967.

(14) Pabit, S. A.; Meisburger, S. P.; Li, L.; Blose, J. M.; Jones, C. D.; Pollack, L. Counting Ions around DNA with Anomalous Small-Angle X-Ray Scattering. *J. Chem. Soc.* **2010**, *132*, 16334–16336.

(15) Goerigk, G.; Huber, K.; Schweins, R. Probing the Extent of the Ion Condensation to Anionic Polyacrylate Coils : A Quantitative Anomalous Small-Angle X-Ray Scattering Study Probing the Extent of the Sr 2 + Ion Condensation to Anionic Polyacrylate Coils : A Quantitative Anomalous Small-Angle X. *J. Chem. Phys.* **2007**, *127* (154908), 1–8.

(16) de Robillard Q., Guo X., Dingenouts N., and Ballauff M., G. G. Application of Anomalous Small-Angle X-Ray Scattering to Spherical Polyelectrolyte Brushes. *Macromol. Symp.* **2001**, *164*, 81–90.

(17) Ballauff, M.; Jusufi, A. The Distribution of Sr 2 + Counterions around Polyacrylate Chains Analyzed by Anomalous Small- Angle X-Ray Scattering The Distribution of Sr 2 + Counterions around Small-Angle X -Ray Scattering. *Europhys. Lett.* **2004**, *66*, 331–337.

(18) Akiba, I.; Takechi, A.; Sakou, M.; Handa, M.; Shinohara, Y.; Amemiya, Y.; Yagi, N.; Sakurai, K. Anomalous Small-Angle X‐Ray Scattering Study of Structure of Polymer Micelles Having Bromines in Hydrophobic Core. *Macromolecules* **2012**, No. 45, 6150–

6157.

(19) Huber, K.; Scheler, U. New Experiments for the Quanti Fi Cation of Counterion Condensation. *Curr. Opin. Colloid Interface Sci.* **2012**, *17*, 64–73.

(20) Tsai, T. H.; Ertem, S. P.; Maes, A. M.; Seifert, S.; Herring, A. M.; Coughlin, E. B. Thermally Cross-Linked Anion Exchange Membranes from Solvent Processable Isoprene Containing Ionomers. *Macromolecules* **2015**, *48* (3), 655–662.

(21) Yuan, H. Synthesis and Structure-Property Relationships of Polymeric Membranes for Small Molecule Transport, University of Massachusetts, Amherst, 2017.

(22) Helfand, E.; Wasserman, Z. R. Block Copolymer Theory. 4. Narrow Interphase Approximation. *Macromolecules* **1976**, *9* (6), 879–888.

PART II:

ELECTROSTATIC INTERACTIONS AND STERICS IN P4VP-BASED POLYMERS.

CHAPTER 4

THE MISNOMER OF THE IONOMER: EFFECT OF PENDANT SIDE-CHAIN STERICS ON SHORT RANGE ORDERING IN P4VP RANDOM COPOLYMERS

4.1 Introduction

Due to the ubiquitous application of charged polymers in polymer science, the study of their structure-property relationships has received considerable attention in the literature.[1–7] Understanding the correlation between structure and polyelectrolyte properties could be used to design better ion conducting and mechanically robust polyelectrolyte membranes.[7] However, studies that focus on the role of intermolecular forces in the formation of a particular structure are scarce in the literature.

Random polyelectrolytes form interesting short-range, ordered morphologies. A characteristic short-range ordering in random polyelectrolyte, is the ordering of ionic clusters in a hydrophobic matrix.[3,4,8–11] These ionic clusters have characteristic spacing between 2 – 10 nm that can be observed by wide-angle X-ray scattering (WAXS) and medium-angle X-ray scattering (MAXS).[4] Polymers that form this type of morphology are known as ionomers generally having 10 mol% or less ionic content.[12,13] Nevertheless, ionomer cluster morphology have been observed in random copolymers with 30 – 50 mol% ion content.[10,13,14] The ionomer cluster morphology is a consequence of dipole-dipole attraction. As a result, dipoles can attract other dipoles to form an aggregation of dipoles (dipole clusters). These aggregates can attract other dipoles to form larger clusters. [9,10]

Another short-range ordering that can be observed in WAXS for random polyelectrolytes is the periodic spacing between adjacent polymer backbones. Polyelectrolytes with pendant side-chains,

for example, poly (1-*n*-alkyl-3-vinylimidazoliumbromide), show this kind of morphology.[15] The characteristic spacing obtained from the backbone–backbone morphology has similar dimensions to the cluster–cluster spacing present in the ionomer cluster morphology. However, this short-range order is a consequence of the separation between adjacent polymer backbones. The length of the pendant side-chains dictate the spacing between adjacent backbones by sterically repelling other pendant side-chains on adjacent polymer backbones.[16] The spacing between adjacent backbones, the so-called backbone-backbone spacing, increases with increasing length of the pendant side-chains and was first observed in non-polyelectrolyte comb-shaped polymers.[17–19]

While ionomer cluster morphology, formed by the clustering of dipoles, is driven by dipole-dipole attraction; backbone-backbone morphology, formed by the separation of adjacent polymer backbones, is driven by sterics between pendant side-chains. The ionomer cluster and the backbone-backbone morphologies result from fundamentally different origins. However, the morphologies associated with the dominance of electrostatic attraction, or sterics, could be mischaracterized one for the other because of their similar spacing dimension. This misnomer of the ionomer cluster morphology attribution can be found in recent literature where groups working on anion exchange membranes have misattributed an X-ray scattering peak resulting from backbone-backbone morphology to ionomer cluster morphology.[20–22]

Polymers with pendant side-chains[16,18,19,23] and ionomers[4,10,12–14,24] have been studied independently and extensively in the literature. However, a study on these morphologies competing, or coexisting, in a copolyelectrolyte system has received little attention in the literature.

Quaternization of poly(4-vinylpyridine) (P4VP)-based copolymers with 1-alkylbromides provides an avenue to investigate the direct interplay between dipole attraction, due to charges, and

adjustable pendant side-chain sterics, The length of the pendant side-chain can be controlled by varying the number of carbons on the alkyl group of the quaternizing agent (1-alkylbromide). [25,26] Consequently, the competition between the morphologies due to dipole-dipole attraction (ionomer cluster morphology) and pendant side-chain sterics (backbone-backbone morphology), and the possibility that both morphologies can coexist could be studied. Ionomer cluster morphology has been predicted and observed in random copolymers with 50 mol% charge content.[10,27,28] Backbone-backbone morphology has also been observed in random copolymers with about 40 mol% of repeat units with pendant side-chains.[29,30] In this study, poly(4-vinylpyridine), P4VP, random copolymers and terpolymer of 4-vinyl pyridine were prepared with isoprene (P4VP-*r*-PI), styrene (P4VP-*r*-PS), and a mixture of isoprene and styrene (P4VP-*r*-PI-*r*-PS), each with 40 mol% 4VP content. The homopolymer, random copolymers, and terpolymer were fully quaternized with various 1-alkylbromides, and the relationships between ionomer cluster and backbone-backbone morphologies were evaluated by WAXS. To study the effect of counter ions on the short-range ordering of the P4VP-*r*-PI, P4VP-*r*-PI-*r*-PS, and P4VP-*r*-PS, the random copolymers and terpolymer were also quaternized by 1-alkyliodides. The number of carbons on the quaternizing agent, *n*, ranges from 1 – 12. The morphology of the resultant polymers, P4VP-*r*-PI_CnI, P4VP-*r*-PI-*r*-PS_CnI, and P4VP-*r*-PS_CnI was evaluated by WAXS.

4.1.1 Theoretical Background: The "In-line" Dipole Model

Building on the phenomenological argument put forth by Colby,[13,14] on the formation of ionomer morphology, a characteristic spacing below which dipole-dipole attraction energy is dominant can be estimated. The thermal energy, K_BT, where K_B is the Boltzmann's constant, and T is temperature, is a measure of the reach of dipole-dipole attraction energy. Since dipole-dipole interactions are distance dependent, on equating the dipole-dipole interaction energy to K_BT, a

limiting length below which dipolar attractions are dominant and beyond which K_BT is dominant can be defined. The limiting length is analogous to the Bjerrum length of free ions. See Figure 4.1.

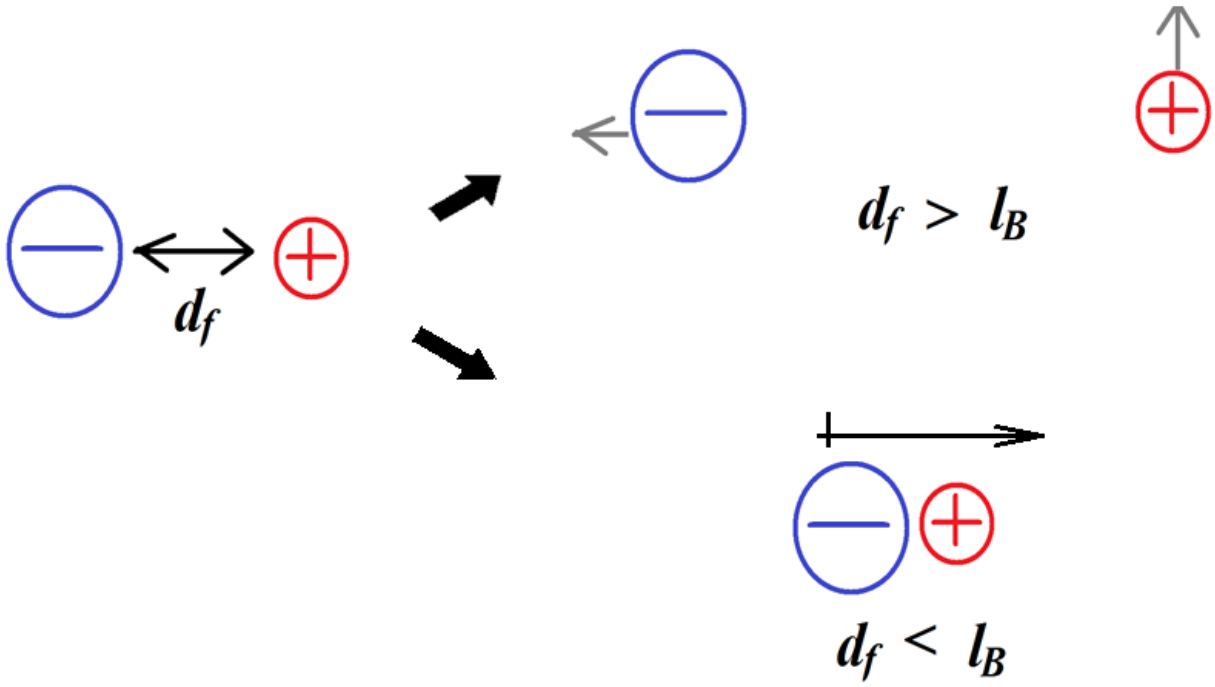

Figure 4.1. Schematic representation of the Bjerrum length.

Colby defined the reach of dipole-dipole interaction energy by equating the rotational dipole-dipole interaction (Keesom Energy) to K_BT.[13] The derivation of Keesom energy assumes that the interaction of rotating dipoles is less than K_BT. Thus, as acknowledged by Colby, the Keesom length obtained from equating the Keesom energy to K_BT should be used to show the "trend" of the dipole-dipole interactions in their system.[13] This Keesom length does not strictly define a circumference, respective to a reference dipole, within which another dipole is attracted and forms a cluster or beyond which there is no clustering.[13] A schematic representation of this model is shown in Figure 4.2.

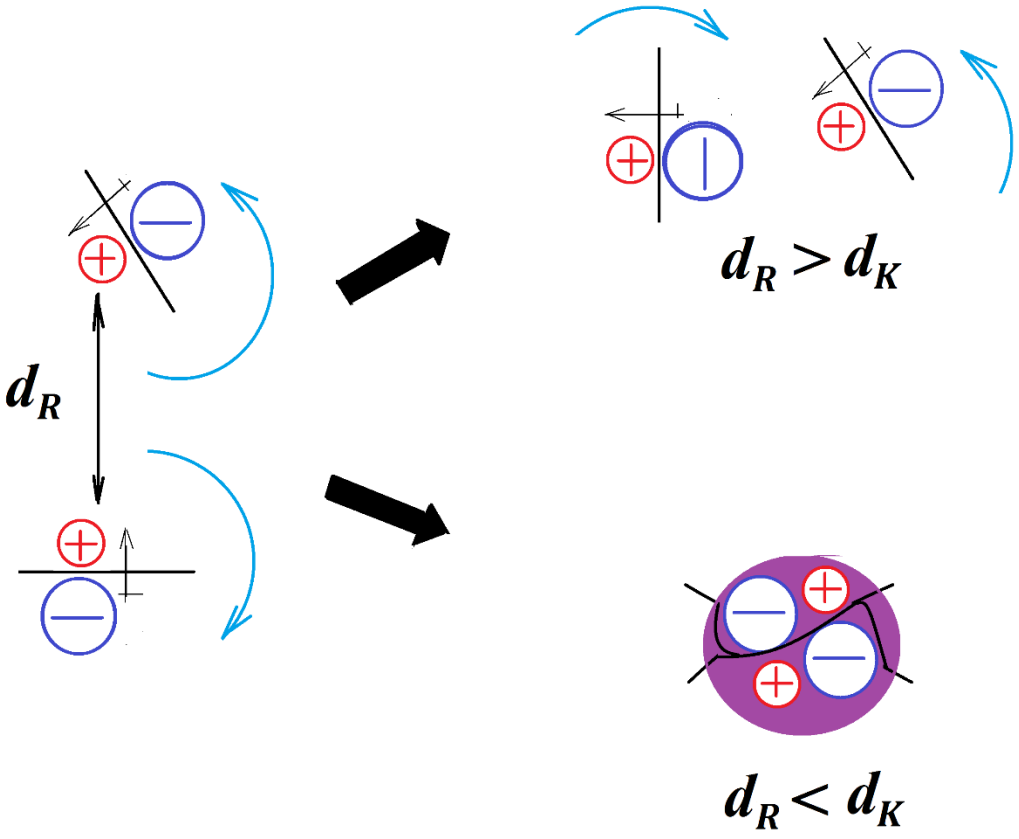

Figure 4.2. Schematic representation of the Colby rotational dipole model.

In our model, we define the reach of dipole-dipole interaction energy by equating the fixed dipole-dipole interaction energy to K_BT. This interaction energy, at length scale of molecular separation, is equal to, or greater than, K_BT. Thus, the fixed dipole-dipole interaction energy can facilitate the binding of dipoles in liquids and solids at ambient temperature.[31] Since the dipole moment is orientation dependent, to quantify the interaction energy of fixed dipoles, we assume that the prevalent orientation of interacting dipoles on adjacent polymer backbones is the "in-line" orientation. This orientation maximizes the dipole-dipole interaction energy, thus, resulting in the lowest energy state of the system.[31] The dipole-dipole interaction energy, F_{DA}, for fixed dipoles in this orientation is given by:

$$F_{DA} = -2\frac{\rho_1\rho_2}{4\pi\varepsilon_o\varepsilon_p d^3} \qquad (4.1)$$

Where ρ_1 and ρ_2 are dipole moments of the two dipoles on adjacent backbones, ε_o is the permittivity of free space, ε_p is the dielectric constant of the polymer matrix, d is the distance between the two dipoles on adjacent polymer backbones. On equating the dipole-dipole attraction energy with the thermal energy, K_BT, we can determine the distance, d_L. Below d_L the dipole-dipole attraction dominates. Beyond d_L, the fixed dipole-dipole attraction is weak relative to K_BT, and the dipoles interact by Keesom energy. Here we term d_L the limiting length.

$$-2\frac{\rho_1\rho_2}{4\pi\varepsilon_o\varepsilon_p d_L^3} + K_BT = 0 \qquad (4.2)$$

Hence, d_L can be calculated as follows:

$$d_L = \left(2\frac{\rho_1\rho_2}{4\pi\varepsilon_o\varepsilon_p K_BT}\right)^{\frac{1}{3}} \qquad (4.3)$$

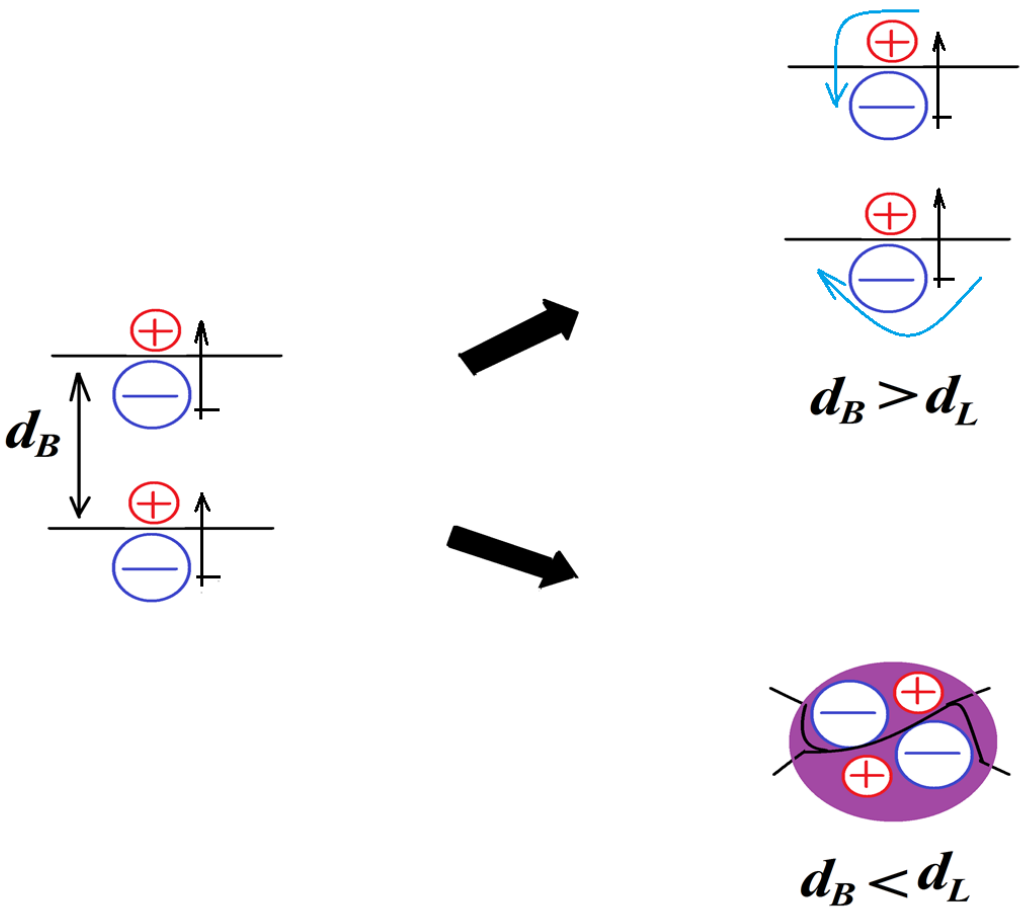

Figure 4.3. Schematic representation of the In-Line Dipole Model.

A schematic representation of the In-Line dipole model is represented in Figure 4.3. Since the dipoles in quaternized P4VP-based polymers are situated on the backbones at the base of the pendant side-chains, then the reach of the dipole-dipole attraction of dipoles on adjacent backbones can be directly estimated by varying the dimension of the backbone-backbone spacing. Consequently, three morphological regimes with respect to the relationship between backbone-backbone spacing and d_L can be expected:

First Regime: The backbone-backbone spacing is less than d_L. A dipole on the backbone can feel the attraction from another dipole on an adjacent backbone. These dipoles are likely to aggregate to form dipole clusters. Consequently, the polymer system will be dominated by ionomer cluster morphology.

Second Regime: The backbone-backbone spacing is approximately equal to d_L. The dipole-dipole interaction between dipoles on adjacent backbones are partially weak relative to the thermal energy. The polymer can form both ionomer cluster and backbone-backbone morphologies leading to a coexistence of both morphologies.

Third Regime: The backbone-backbone spacing is greater than d_L. The dipole-dipole attraction between dipoles on adjacent backbones is very weak relative to the thermal energy because these dipoles are far enough from each other. In this regime, the morphology is dominated by backbone-backbone morphology.

4.2 Materials and Methods

Styrene (98%) and 4-vinylpyridine (96%) were both obtained from Alfar Aesar and passed through a basic alumina column. Isoprene (97%) was procured from Acros Organics and was distilled. The initiator, N-tert-butyl-N-[1-diethylphosphono-(2,2-dimethylpropyl)]nitroxide (SG1), was kindly provided by Arkema and used as obtained. N,N-dimethylformamide (99%) was purchased from Fisher Scientific. Pyridine (99%) purchased from Acros Organics was used as received. The following quaternizing agents were used as obtained: bromoethane (99%) and 1-bromopropane (98%) (purchased from T.C.I), 1-bromopentane (purchased from Sigma-Aldrich), 1-bromobutane (98%), 1-bromohexane (99%), 1-bromoheptane (98%), 1-bromooctane (98%), 1-bromononane

(99%), 1-bromodecane (98%), 1-bromoundecane (98%), and 1-bromododecane (98%) were all purchased from Alfa Aesar.

4.2.1 Synthesis and Quaternization of P4VP, P4VP-*r*-PI, P4VP-*r*-PI-*r*-PS, and P4VP-*r*-PS

4.2.1.1 Synthesis of P4VP: Poly(4-vinylpyridine) homopolymer, P4VP, was prepared as follows: 120 mg (0.31 mmoles) of SG1 was added to a solution of 10.5 g (0.1 moles) 4-vinylpyridine (4VP) in 10 ml of N,N-Dimethylformamide (DMF). After degassing by three freeze-pump-thaw cycles, polymerization was performed at 110 ˚C for 18 hours. The resulting viscous liquid was quenched in ice and precipitated twice from dichloromethane into diethyl ether. The product was dried in vacuum at room temperature for 24 h.

4.2.1.2 Synthesis of P4VP-*r*-PI: Random copolymer, P4VP-*r*-PI, was prepared as follows: 42 mg (0.105 mmoles) of SG1 was added to 10.5 g (0.1 moles) of 4VP and 10.2 (0.15 moles) of isoprene in a Schlenk flask. To the mixture was added 10 ml of pyridine as solvent. After degassing by three freeze-pump-thaw cycles, polymerization was performed at 120 ˚C for 48 hours. The resulting viscous liquid was quenched in ice and precipitated thrice from dichloromethane in a mixture of hexanes and diethyl ether (1:1). The product was dried in vacuum at room temperature for 48 h.

4.2.1.3 Synthesis of P4VP-*r*-PI-*r*-PS: Random terpolymer, P4VP-*r*-PI-*r*-PS, was prepared as follows: 40 mg (0.104 mmoles) of SG1 was added to 7.8 g (0.074 moles) of 4VP, 5 g (0.074 moles) of isoprene and 3.9 g (0.037 moles) of styrene in a Schlenk flask. To the mixture was added 10.5 ml of pyridine as solvent. After degassing by three freeze-pump-thaw cycles, polymerization was performed at 120 ˚C for 48 hours. The resulting viscous liquid was quenched in ice and precipitated thrice from dichloromethane in a mixture of hexanes and diethyl ether (1:1). The product was dried in vacuum at room temperature for 48 h.

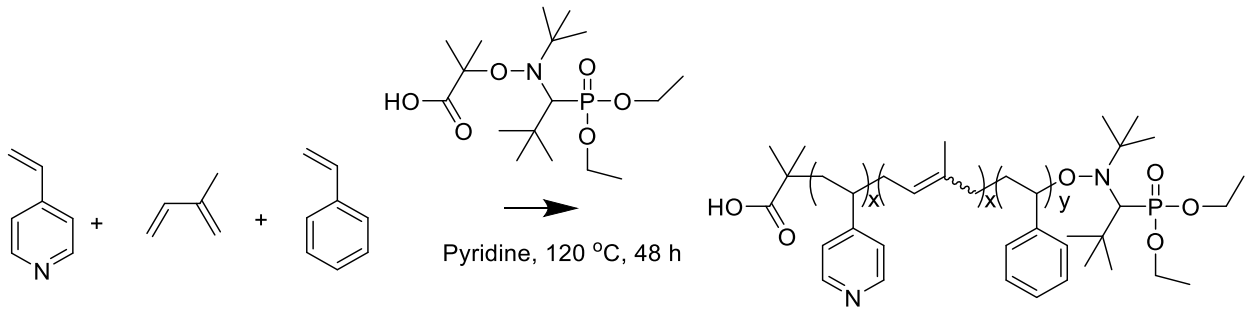

Scheme 4.1. Synthesis of P4VP-*r*-PI-*r*-PS by nitroxide mediated polymerization.

4.2.1.4 Synthesis of P4VP-*r*-PS: Random copolymer P4VP-*r*-PS was prepared as follows: 46 mg (0.12 mmoles) of SG1 was added to 6 g (0.057 moles) of 4VP and 9 g (0.086 moles) of styrene in a Schlenk flask. To the mixture was added 16 ml of DMF as solvent. After degassing by three freeze-pump-thaw cycles, polymerization was performed at 110 ˚C for 6 h. The resulting viscous liquid was quenched in ice and precipitated thrice from dichloromethane in a mixture of hexanes and diethyl ether (1:1). The product was dried in vacuum at room temperature for 48 h.

4.2.1.5 Quaternization of P4VP: A solution of 1.0 M quaternizing agent (propyl to dodecylbromide) was prepared in DMF. 20 ml of the solution was added to a solution of 200 mg of P4VP in DMF at 60 °C. After 10 d, the solution was precipitated into diethyl ether to give an off-white powder. After filtration, the product, P4VP_CnBr, was dried in vacuum at room temperature for 24 h.

4.2.1.6 Quaternization of P4VP-*r*-PI by 1-Alkylbromide: The random copolymer, P4VP-*r*-PI, was quaternized by ethylbromide, 1-propylbromide, 1-butylbromide, 1-pentylbromide, 1-hexylbromide, and 1-octylbromide. In a typical quaternization protocol, 20 ml of a 1.0 M solution of the quaternizing agent in DMF was added to a solution of 300 mg of polymer in DMF at 60 °C

for 10 d. At the end of the reaction, the solution was precipitated into diethyl ether to give a brown solid. The product, P4VP-*r*-PI_CnBr, was dried in vacuum at room temperature for 1 d.

4.2.1.7 Quaternization of P4VP-*r*-PI-*r*-PS by 1-Alkylbromide: The random terpolymer, P4VP-*r*-PI-*r*-PS, was quaternized by ethylbromide, 1-propylbromide, 1-butylbromide, 1-pentylbromide, 1-hexylbromide, and 1-octylbromide. In a typical quaternization protocol, 20 ml of a 1.0 M solution of the quaternizing agent in DMF was added to a solution of 300 mg of polymer in DMF at 60 °C for 10 d. At the end of the reaction, the solution was precipitated into diethyl ether to give a brown solid. The product, P4VP-*r*-PI-*r*-PS_CnBr, was dried in vacuum at room temperature for 24 h.

4.2.1.8 Quaternization of P4VP-*r*-PS by 1-Alkylbromide: The random copolymer, P4VP-*r*-PS, was quaternized by by ethylbromide, 1-propylbromide, 1-butylbromide, 1-pentylbromide, 1-hexylbromide, and 1-octylbromide. In a typical quaternization protocol, 20 ml of a 1.0 M solution of the quaternizing agent in DMF was added to a solution of 300 mg of polymer in DMF at 60 °C for 10 d. At the end of the reaction, the solution was precipitated into diethyl ether to give a light brown powder. The product, P4VP-*r*-PS_CnBr, was dried in vacuum at room temperature for 1 d.

4.2.1.9 Quaternization of P4VP-*r*-PI by 1-Alkyliodide: The random copolymer, P4VP-*r*-PI, was quaternized by methyliodide, ethyliodide, 1-propyliodide, 1-hexyliodide, and 1-dodecyliodide. In a typical quaternization protocol, 20 ml of a 1.0 M solution of the quaternizing agent in DMF was added to a solution of 300 mg of polymer in DMF at 60 °C for 10 d. At the end of the reaction, the solution was precipitated into diethyl ether to give a brown solid. The product, P4VP-*r*-PI_CnI, was dried in vacuum at room temperature for 1 d.

4.2.1.10 Quaternization of P4VP-*r*-PI-*r*-PS by 1-Alkyliodide: The random terpolymer, P4VP-*r*-PI-*r*-PS, was quaternized by methyliodide, ethyliodide, 1-propyliodide, and 1-hexyliodide. In a typical quaternization protocol, 20 ml of a 1.0 M solution of the quaternizing agent in DMF was added to a solution of 300 mg of polymer in DMF at 60 °C for 10 d. At the end of the reaction, the solution was precipitated into diethyl ether to give a brown solid. The product, P4VP-*r*-PI-*r*-PS_CnI, was dried in vacuum at room temperature for 24 h.

4.2.1.11 Quaternization of P4VP-*r*-PS by 1-Alkyliodide: The random copolymer, P4VP-*r*-PS, was quaternized by methyliodide, ethyliodide, 1-propyliodide, and 1-hexyliodide. In a typical quaternization protocol, 20 ml of a 1.0 M solution of the quaternizing agent in DMF was added to a solution of 300 mg of polymer in DMF at 60 °C for 10 d. At the end of the reaction, the solution was precipitated into diethyl ether to give a light brown powder. The product, P4VP-*r*-PS_CnI, was dried in vacuum at room temperature for 1 d.

4.2.2 Characterization of P4VP-based Polymers

Number average molecular weights, M_n, was determined using Gel Permeation Chromatography (GPC) in DMF at a flow rate of 1.0 mL/min using a refractive index detector on an Agilent Technologies 1260 Infinity system. The chemical compositions of (P4VP-*r*-PI), (P4VP-*r*-PI-*r*-PS), and (P4VP-*r*-PS) were determined using a Bruker 500 Fourier-Transform Nuclear Magnetic Resonance (FT-NMR). Quaternized samples of (P4VP-*r*-PI), (P4VP-*r*-PI-*r*-PS), and (P4VP-*r*-PS) were drop cast from methanol on a Teflon® sheet. Characterization was performed on the resulting films. PerkinElmer Spectrum 100 FTIR with a universal ATR was used to confirm the complete quaternization of the 4-Vinylpyridine units in the homopolymer, copolymers, and terpolymer.

Wide-angle X-ray scattering (WAXS) measurements were performed in transmission geometry on Molmex Scientific Ganesha SAXS Lab. A double aperture for the Cu-Kα radiation (λ = 1.54 Å), which was the X-ray source, was used. Silver behenate was used as the standard for the momentum transfer calibration. Data was collected for 180 seconds. Depending on the signal-to-noise ratio, data collection could be longer. Azimuthal averaging of the obtained isotropic 2-D pattern was performed to obtain the intensity versus wave vector plot.

4.3 Results and Discussion

The homopolymer of 4-vinylpyridine, poly(4-vinylpyridine) (P4VP) was synthesized by nitroxide mediated polymerization (NMP). Characterization of P4VP by ^{1}H NMR confirms the successful synthesis of the homopolymer (see Figure 4.4).

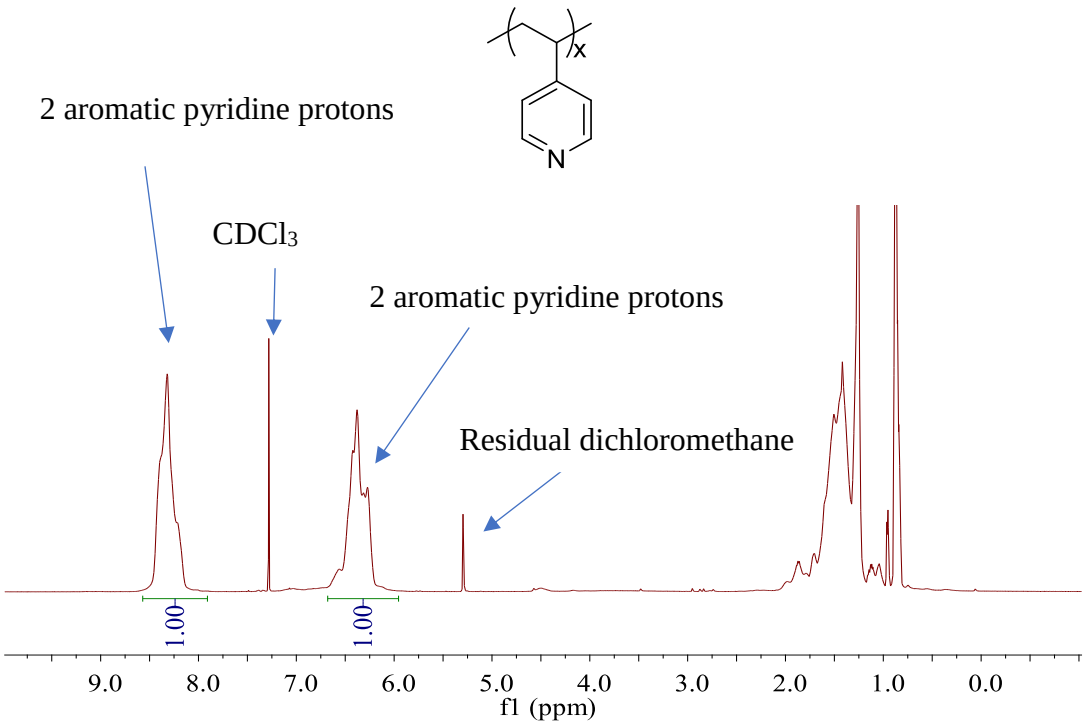

Figure 4.4. The ^{1}H NMR spectrum of P4VP.

The molecular weight and dispersity of P4VP was determined by DMF-GPC. See Figure 4.5. The GPC chromatogram confirm the successful synthesis of P4VP. The target molecular weight of the homopolymer was approximately equal to the molecular weight determined by GPC.

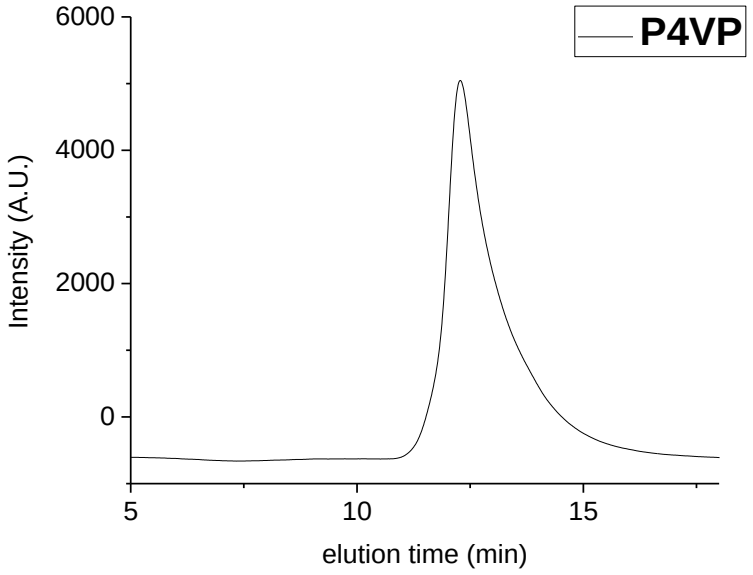

Figure 4.5. The GPC chromatogram of P4VP.

A summary of the molecular weights, and dispersity for P4VP is presented in Table 4.1.

Table 4.1. Summary of molecular weight, dispersity, and composition of P4VP.

	Feed ratio (**4VP:isoprene:styrene)**	**NMR ratio** (**4VP:isoprene:styrene)**	**Target M_n(Kg/mol)**	**GPC M_n (Kg/mol)**	**Đ**
P4VP	2:0:0	2:0:0	30	35	1.5

4.3.1 Characterization of Quaternized P4VP, P4VP-*r*-PI, P4VP-*r*-PI-*r*-PS, and P4VP-*r*-PS

The 4VP units in all prepared samples were fully quaternized by 1-alkylbromides (CnBr) with varying number of carbons, *n*. The homopolymer, P4VP, was quaternized by a solution of 1.0 M, propyl – dodecyl bromides (*n = 3 – 12*) in DMF at 60 °C. The copolymers (P4VP-*r*-PI, and P4VP-*r*-PS) and terpolymer (P4VP-*r*-PI-*r*-PS) were quaternized by reaction with a solution of 1.0 M ethyl, propyl, butyl, pentyl, hexyl, and octyl bromide (*n = 2-6, and 8*) in DMF at 60 °C.

The complete quaternization of the 4VP units in the homopolymer, P4VP, and its subsequent transformation to poly (1-*n*-alkyl-4vinyllpyridiniumbromide) (P4VP_CnBr) can be confirmed by ATR-FTIR. Figure 4.6 shows the disappearance of the 1414 cm^{-1} stretch which is the stretching vibration of the C=N aromatic ring and the subsequent emergence of the pyridinium vibration at 1640 cm^{-1}.[32] These changes in the FTIR spectra (see Figure 4.6) have been used previously to confirm the complete quaternization of poly(4-vinylpyridine). [25,26,33–38]

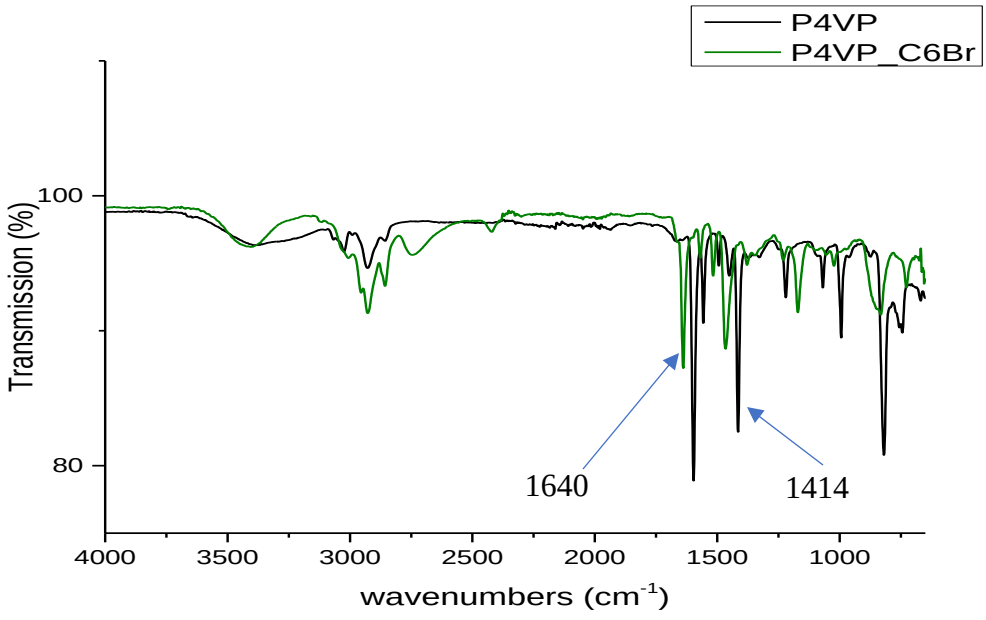

Figure 4.6. FTIR spectra showing the complete quaternization of P4VP by 1-hexylbromide.

In a similar fashion, after the quaternization of the copolymers P4VP-*r*-PI, P4VP-*r*-PS, and the terpolymer P4VP-*r*-PI-*r*-PS by 1-alkylbromides with varying number of carbons in the alkyl group, *n*, ranging from *2 – 8*, the complete quaternization of their respective products P4VP-*r*-PI_CnBr, P4VP-*r*-PI-*r*-PS_CnBr, and P4VP-*r*-PS_CnBr was confirmed by ATR-FTIR.

4.3.2 Short-Range Ordering in P4VP_CnBr Series

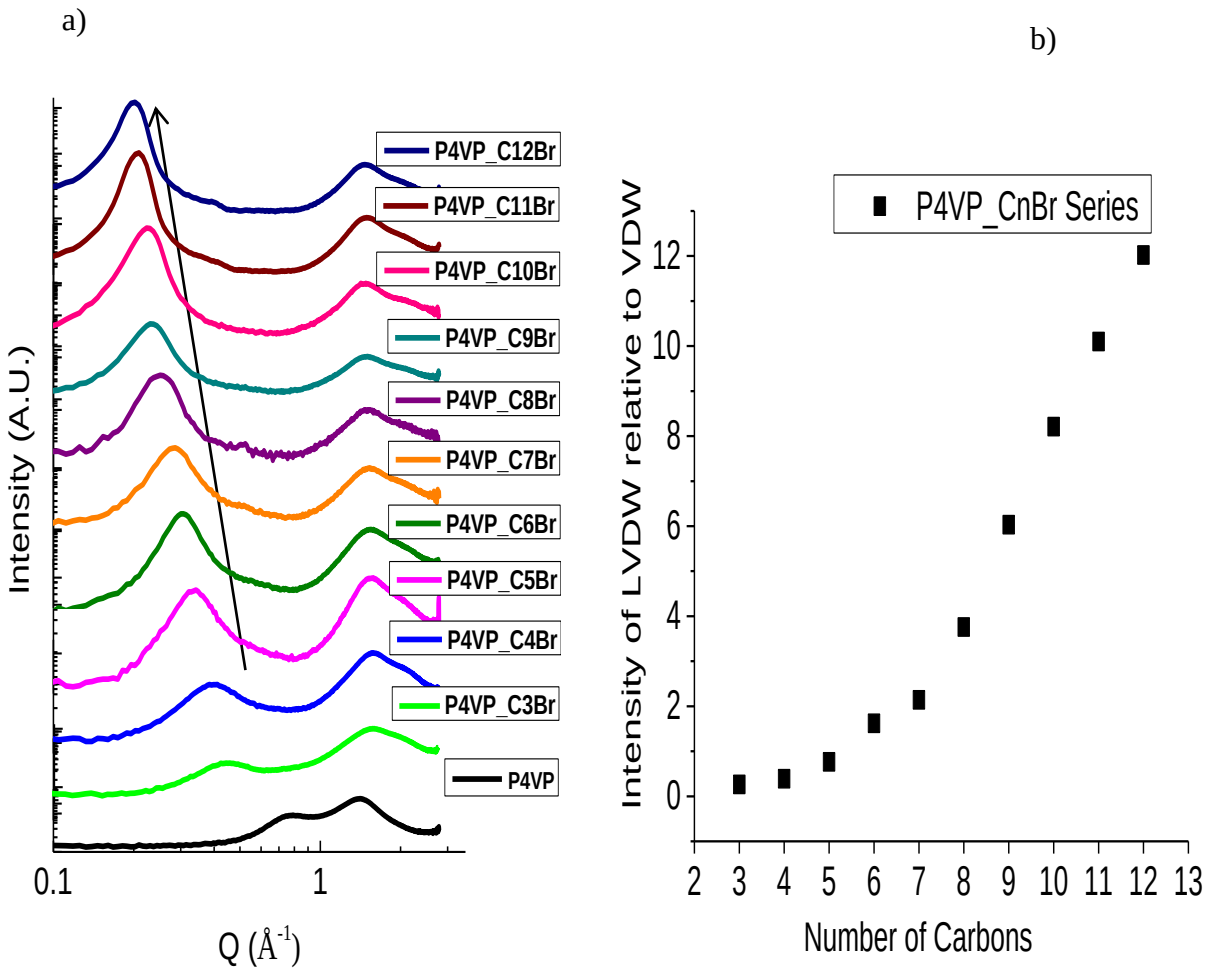

Figure 4.7. a) The WAXS spectra of the P4VP_CnBr series, b) relative intensities of feature peaks in the P4VP_CnBr series.

X-ray scattering experiments were performed on the completely quaternized homopolymer (P4VP_CnBr). The obtained WAXS spectra (see Figure 4.7a) show two distinct peaks for all quaternized polymers. The spacing correlated to the peak at high *Q* is the so-called van der Waal's distance (VDW) between non-bonded atoms in the polymer. This VDW peak, also known as the amorphous halo, is ubiquitous in amorphous polymers.[18,19] Upon quaternization, the VDW spacing decreased from its value in the pristine polymer. This indicates tighter packing of polymer chains.[39] Given that a decrease in VDW spacing have not been observed in non-charged, comb-shaped polymers,[18,19] this decrease in VDW spacing from the unquaternized (P4VP) to the quaternized polymer series (P4VP_CnBr) may have resulted from the introduction of bromide counter ions. For the quaternized sample series, P4VP_CnBr, the VDW spacing increased with increasing number of carbons on the pendant side-chains from 4.00 Å for P4VP_C3Br to 4.34 Å for P4VP_C12Br. An increase in the VDW spacing with increasing number of carbons on the pendant side-chains has also been reported in poly(*n* – cycloalkylmethacrylates) and poly(*n* – alkylacrylates).[19] The intensity of the VDW peak has been used to correlate the fraction of other observed features in WAXS. For instance, the intensities of crystalline or ionomer peaks relative to the VDW peak intensity has been used to estimate the fraction of these morphological features in a polymer.[14,19,40]

A second peak with *Q* values lower than the VDW peak, the LVDW peak, can also be observed in the WAXS spectra of the quaternized samples (see Figure 4.7a). The characteristic spacing derived from the LVDW peak is the backbone-backbone spacing, d_B, between adjacent polymer segments. There was a linear increase in d_B with increasing number of carbons on the pendant the side-chains. This linear relationship has also been observed in comb-shaped polymers; poly(*n*-alkylvinylesters),[16] poly(α-olefins),[16] poly(*n*-fluorofumarates),[41] poly(*n*-alkylfluoroacrylate),[41]

poly(*n*-alkylfluoromethacrylate),[41] poly(*n*-alkylmethacrylates),[17,19] poly(*n*-cycloalkylmethacrylates),[19] poly(*n*-alkylacrylates),[17,19] poly(1-*n*-alkyl-3-vinylimidazolium bromide)[15] and poly(3-*n*-alkylthiophenes).[42] Pendant side-chains in comb-shaped polymers have been posited to be in an all trans configuration with some degree of interdigitation.[16] The linear increase of d_B with number of carbons on the side-chain show a slope of 2.0 Å/methylene unit. The same slope has been observed in other comb-shaped polyelectrolytes,[15] and non-polyelectrolytes.[16–18]

The intensity of the LVDW peak increases with increasing number of carbons on the pendant side-chain. The intensity of the LVDW peak relative to VDW has been used to correlate the fraction of backbone-backbone spacing in the polymer.[19] The increase in the intensity of the LVDW peak with increasing number of carbons on the pendant side-chains relative to the VDW peak (see Figure 4.7b) suggests that the fraction of periodically spaced polymer segments also increases with increasing number of carbons on the side-chain.

4.3.3 Short-Range Ordering in P4VP-*r*-PI_CnBr and P4VP-*r*-PI_CnI Series

The copolymer of 4-vinylpyridine and isoprene, P4VP-*r*-PI, was synthesized by Nitroxide Mediated Polymerization (NMP). Characterization of P4VP-*r*-PI by ^{1}H NMR confirms the successful synthesis of the copolymer (see Figure 4.8). The compositions of 4-vinylpyridine and isoprene in the copolymer were determined by comparing the integrals of the aromatic protons of poly(4-vinylpyridine) and the vinyl protons of polyisoprene.

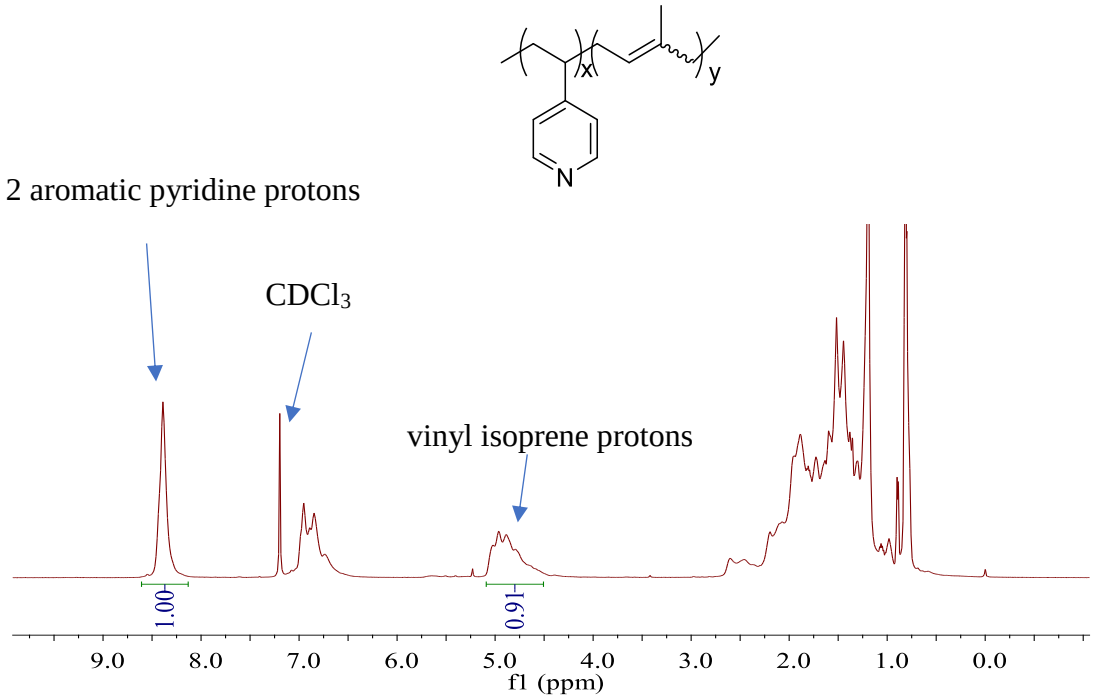

Figure 4.8. The ^{1}H NMR spectrum of P4VP-*r*-PI.

The integral value of the vinyl peak has contributions from the isomers of polyisoprene, 1H from the 1,4 isomer (-C=C**H**-), 2H from the 1,2 isomer (-C=C**H**$_2$), and 1H from the 3,4 isomer (-C=C**H**-). A random copolymer synthesized using SG1 by Nitroxide Mediated Polymerization (NMP) is generally comprised of 93 %, 1 %, and 6 %, of 1,4 isomer, 1,2 isomer, and 3,4 isomer respectively.

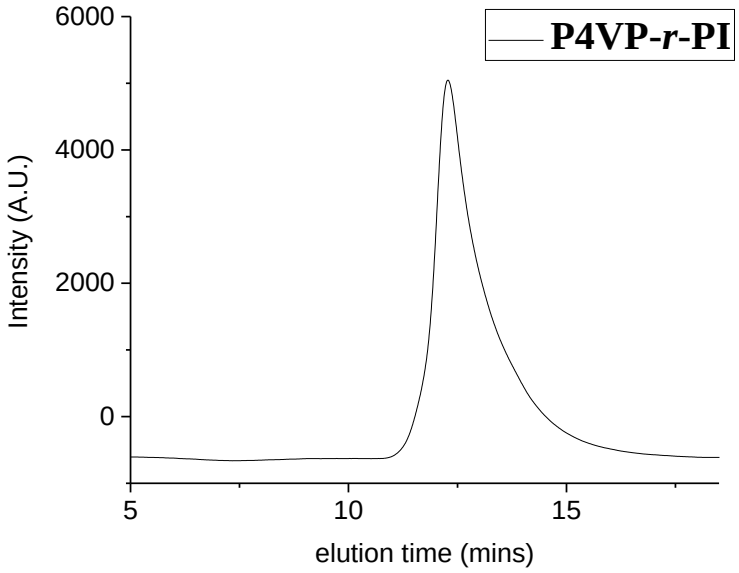

Figure 4.9. The GPC chromatogram of P4VP-*r*-PI.

The molecular weight and dispersity of the copolymer, P4VP-*r*-PI, was determined by DMF-GPC (see Figure 4.9). The GPC chromatogram confirm the successful synthesis of P4VP-*r*-PI. The target molecular weight was lower than the molecular weight determined by GPC. This difference in the target and determined molecular weights could have arisen from the solubility of the copolymer in the eluent. Polyisoprene homopolymer is insoluble in DMF.

A summary of the molecular weights, copolymer feed and target compositions, and dispersity for P4VP-*r*-PI is presented in Table 4.2.

Table 4.2. Summary of molecular weight, dispersity, and composition of P4VP-*r*-PI.

	Feed ratio (**4VP:isoprene:styrene)**	**NMR ratio** (**4VP:isoprene:styrene)**	**Target M_n(Kg/mol)**	**GPC M_n (Kg/mol)**	**Đ**
P4VP-*r*-PI	2:3:0	2:3:0	191	30	1.8

Since the comonomer ratios in the feed and the synthesized copolymer determined by NMR are the same, the copolymer P4VP-*r*-PI can be said to show random character. Furthermore, the reactivity ratios of 4VP (0.39) and isoprene (1.06) in P4VP-*r*-PI confirm the random character of the copolymer.[43]

The 4VP units in P4VP-*r*-PI, were completely quaternized by 1-alkylbromides with varying number of carbons in the alkyl group, ranging from *2 - 8*. Characterization of the resultant sample series, P4VP-*r*-PI_CnBr, by FTIR-ATR confirmed the complete disappearance of the C=N aromatic ring stretching vibration at 1414 cm^{-1} and the appearance of the pyridinium vibration at 1640 cm^{-1}.[36–38] The FTIR spectra of P4VP-*r*-PI quaternized by 1-alkylbromides is presented in Figure 4.10a.

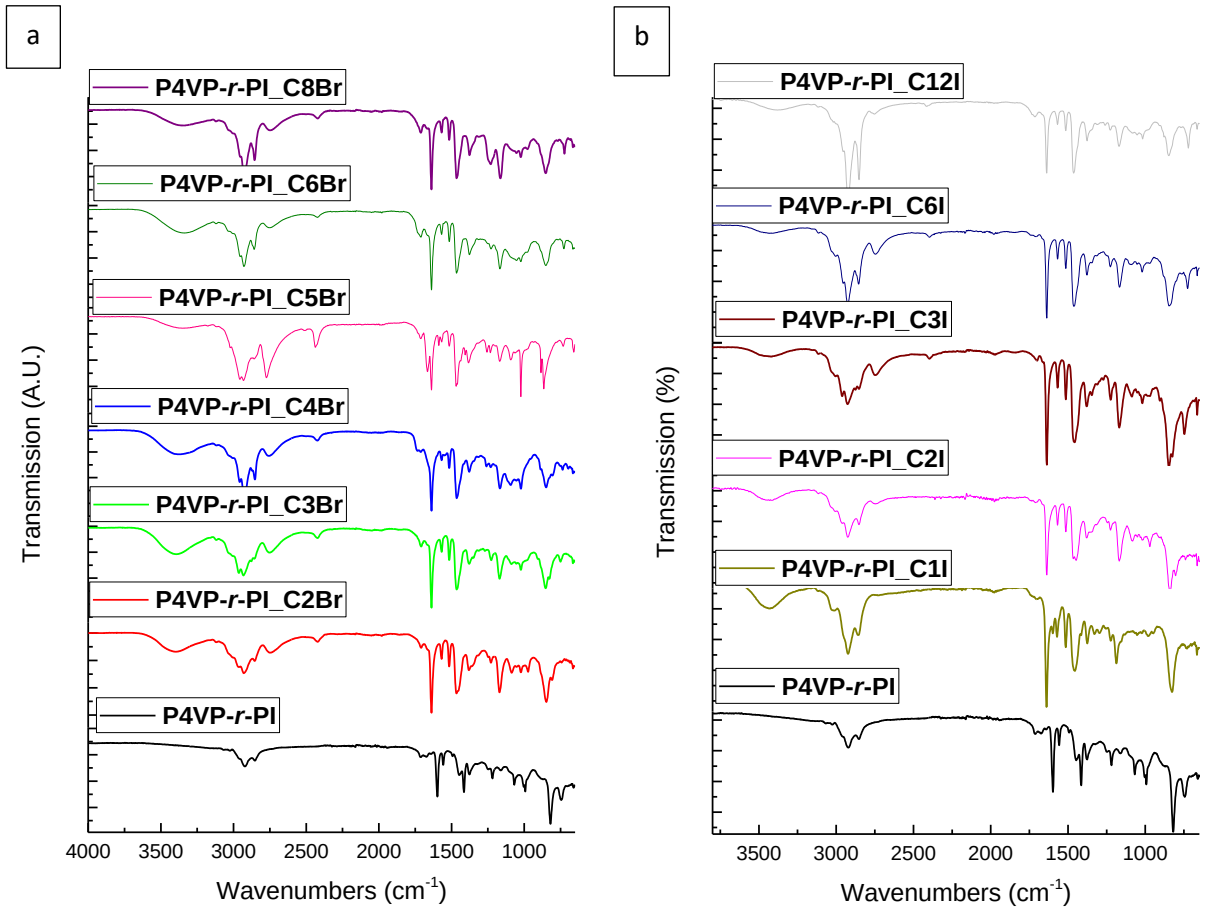

Figure 4.10. The FTIR spectra for the a) P4VP-*r*-PI_CnBr and b) P4VP-*r*-PI_CnI series.

To evaluate the effect of counter ions on the short-range ordering, the 4VP units in P4VP-*r*-PI, were also completely quaternized by 1-alkyliodides with varying number of carbons in the alkyl group, ranging from *1 - 12*. Characterization of the resultant sample series, P4VP-*r*-PI_CnBr, by FTIR-ATR confirmed the complete disappearance of the C=N aromatic ring stretching vibration at 1414 cm^{-1} and the appearance of the pyridinium vibration at 1640 cm^{-1}.[36–38] The FTIR spectra confirming the complete quaternization of P4VP-*r*-PI by 1-alkyliodides is presented in Figure 4.10b.

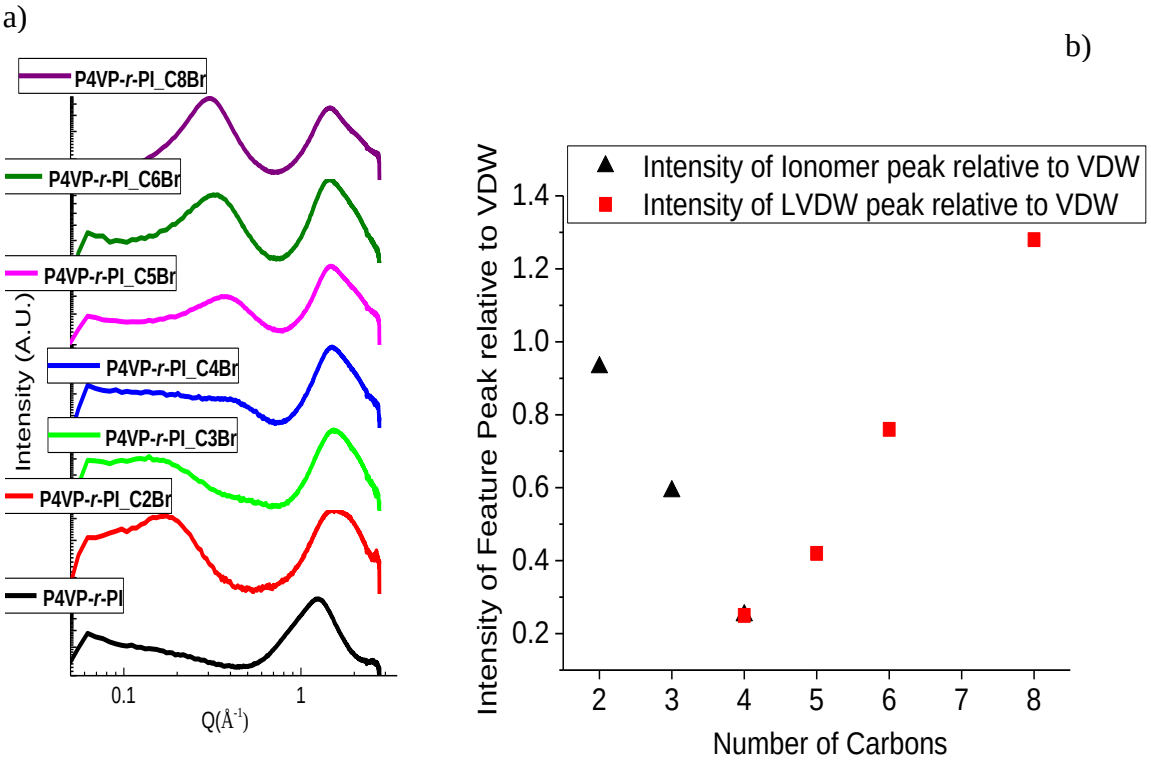

Figure 4.11. a) The WAXS spectra of the P4VP-*r*-PI_CnBr series, b) relative intensities of feature peaks in the P4VP-*r*-PI_CnBr series.

In the P4VP-*r*-PI_CnBr series, the WAXS spectra (See Figure 4.11a) show the VDW peak at higher *Q* values as in the P4VP_CnBr series. As in the homopolymers series, upon quaternization, the VDW peak moves to higher *Q* values (VDW spacing decreases) suggesting a more compact arrangement of polymer chains. For the quaternized P4VP-*r*-PI series, P4VP-*r*-PI_C2Br to P4VP-*r*-PI_C8Br, the VDW spacing increased with increasing number of carbons. Also noticeable in the WAXS spectra of the P4VP-*r*-PI_CnBr series is the emergence of a LVDW peak next to the VDW from P4VP-*r*-PI_C4Br to P4VP-*r*-PI_C8Br. The LVDW peak correlates to the backbone-backbone spacing, d_B, that have been observed in the P4VP_CnBr series. However, the values of d_B in the P4VP-*r*-PI_CnBr series was smaller than the d_B values at a given number of carbons in

the quaternized homopolymer. Changes in the values of d_B in P4VP_CnBr and P4VP-*r*-PI_CnBr series, for a given number of carbons on the pendant side-chain, is due to the difference in the mole fractions of the pendant side-chain monomer units in the quaternized homopolymer and random copolymer. The larger the fraction of the pendant side-chain unit, the greater the d_B.[17,23,39,44] A characteristic feature of d_B is its linear correlation with number of carbons as can be observed in the P4VP_CnBr series. Accordingly, from P4VP-*r*-PI_C4Br to P4VP-*r*-PI_C8Br, d_B increased linearly with increasing number of carbons on the pendant side-chain with a slope of 1.8 Å/methylene unit. The spacing between ionic clusters in random copolymers does not show such linearity with increasing hydrophobic content.[8–10]

The introduction of isoprene as a comonomer into the poly(4-vinylpyridine) backbone facilitates the formation of dipole clusters. The WAXS spectra for P4VP-*r*-PI_C2Br and P4VP-*r*-PI_C3Br (see Figure 4.11a) show an "ionomer peak" at lower Q values which correlates to the average cluster-cluster spacing.[40,45,46] The spacing between clusters in these systems was larger than their equivalent backbone-backbone spacing in the homopolymer. Furthermore, the cluster-cluster distance increased with increasing number of side-chain carbons. The increase in cluster-cluster spacing with decreasing ion content have been observed in other ionomer-based systems.[47,48]

The formation of dipole clusters in P4VP-*r*-PI_CnBr series requires that the separation between dipoles on the polymer backbone is less than d_L, thus, shorter pendant side-chains. However, with longer pendant side-chains due to sterics the spacing between dipoles on the polymer backbone becomes greater than d_L, thus, decreasing the likelihood for ion clustering. As predicted by the "In-Line" Dipole Model, three regimes could be observed from the WAXS spectra of P4VP-*r*-PI_CnBr. In the first regime, P4VP-*r*-PI_C2Br to P4VP-*r*-PI_C3Br, an ionomer cluster morphology can be observed. The absence of backbone-backbone spacing suggests that the

backbone-backbone spacing is less than the characteristic spacing ($d_B < d_L$). Consequently, an ionomer cluster morphology is dominant in this regime. From P4VP-*r*-PI_C2Br to P4VP-*r*-PI_C3Br, the intensity of the ionomer peaks relative to the VDW peak decreased. The difference in the relative ionomer peak intensities suggest that even below d_L side-chain sterics still have an effect on the population of ionomer clusters in the system. Given that d_B spacing of P4VP-*r*-PI_C3Br should be greater than d_B of P4VP-*r*-PI_C2Br, it follows that dipoles are more likely to cluster and form ionomer cluster morphology in P4VP-*r*-PI_C2Br than P4VP-*r*-PI_C3Br. A second regime, the coexistence regime, can be observed in P4VP-*r*-PI_C4Br ($d_B = 14.5$ Å). The WAXS spectra of P4VP-*r*-PI_C4Br show neither a distinct ionomer or LVDW peak, but a broad feature, which suggests a co-existence or overlap of these two morphologies in the copolymer. In this regime, the value of $d_B \sim d_L$. A coexistence of the backbone-backbone spacing and cluster-cluster spacing features have also been reported recently by Zhang *et al*.[14] A third regime can be observed from P4VP-*r*-PI_C5Br to P4VP-*r*-PI_C8Br, ($d_B = 17 – 21$ Å). In this regime $d_B > d_L$. The dipoles near the polymer backbones are "shielded" from each other due to the long pendant side-chains, and backbone-backbone morphology is dominant. As with the homopolymer, the peak intensity of the LVDW relative to the VDW, also increased with increasing number of carbons on the pendant side-chain. As the relative intensity of the LVDW peak increases, that of the ionomer peak relative to VDW decreases and gradually disappears. See Figure 4.11b.

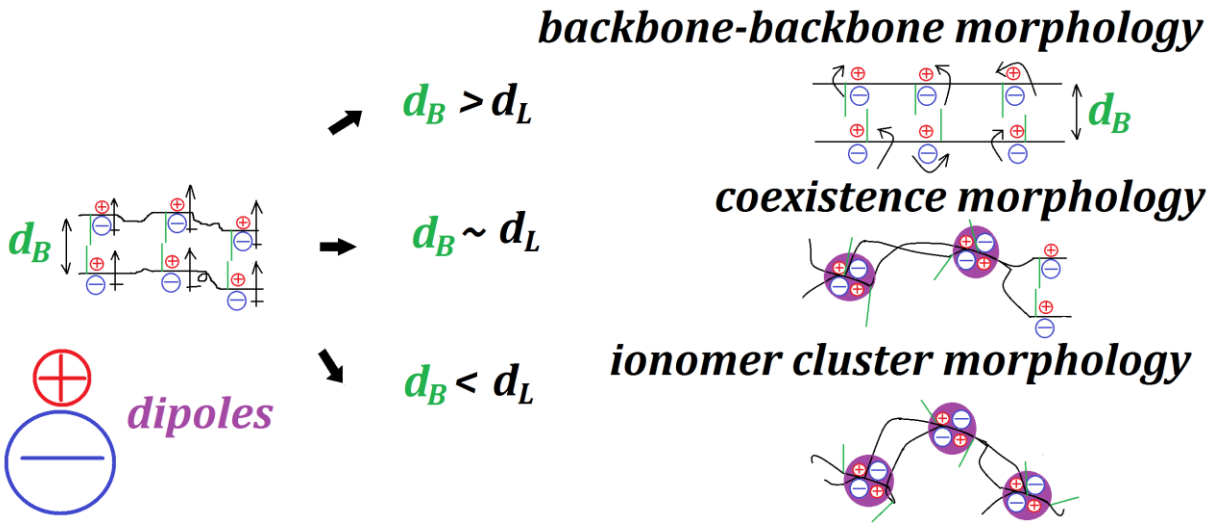

Figure 4.12. Schematics of the three regimes in random, charged, comb-shaped copolymers.

Using equation (4.3), we can estimate the approximate equilibrium spacing between backbones for which these regimes may be found. Since the dipole moments of two interacting dipoles in this medium is the same and is approximately 9.1 D for methylpyrdiniumalkylbromide,[49] and assuming that the matrix, polyisoprene, acts as a continuum with a dielectric constant of about 2.4-2.6,[50,51] then at room temperature (T = 298 K) the characteristic spacing at which dipole-dipole attraction equals the thermal energy, d_C, is approximately 12 Å. For $d_B < 12$ Å, dipole-dipole interactions are dominant and facilitate the formation of dipole clusters. When $d_B > 12$ Å the side-chain sterics "shields" the dipole-dipole attraction from dipoles on adjacent backbones, consequently, backbone-backbone morphology is dominant. For $d_B \sim 12$ Å, a coexistence of both morphologies is possible. In the case of P4VP-*r*-PI_CnBr, the coexistence morphology was observed for $d_B = 14.5$ Å, which is slightly higher than the equilibrium distance predicted by this model. However, the diminished ionomer peak intensity of P4VP-*r*-PI_C3Br in comparison to P4VP-*r*-PI_C2Br suggests that some degree of coexistence may yet be present even though it was not obvious in

WAXS. The morphological regimes predicted by the model are consistent with experimental results.

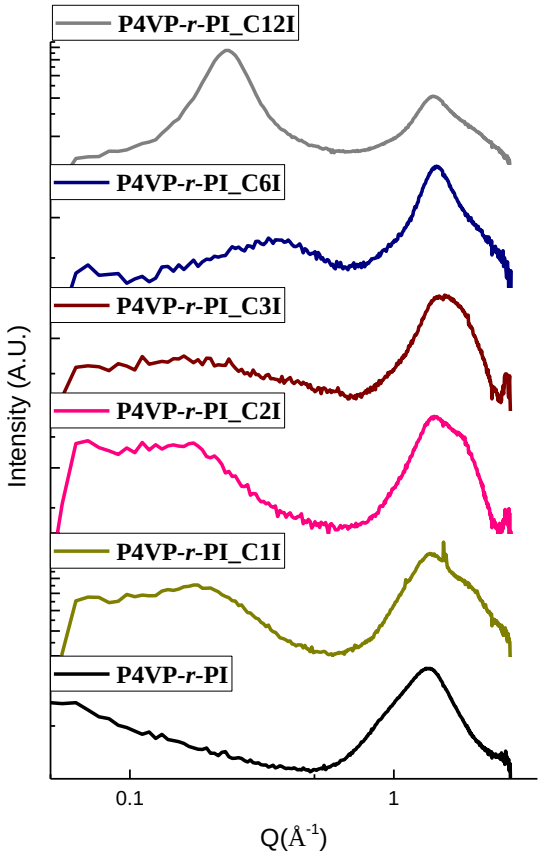

Figure 4.13. The WAXS spectra of the P4VP-*r*-PI_CnI series.

Characterization of the P4VP-*r*-PI_CnI series by X-ray scattering is presented in Figure 4.13. The spectra show the ubiquitous VDW peak at high values of *Q* for all samples. Unlike the P4VP-*r*-PI_CnBr series, upon quaternization of P4VP-*r*-PI by 1-alkyliodides, the VDW peak remained constant for all the quaternized samples. A constant VDW spacing with increasing number of carbons on the pendant side-chain have also been observed in other comb-shaped polymers.

The X-ray scattering profiles of P4VP-*r*-PI_C6I and P4VP-*r*-PI_C12I show an LVDW peak at smaller *Q* values. This peak correlate to the backbone-backbone spacing between polymer chains. Like in the P4VP-*r*-PI_CnBr series, the backbone-backbone spacing increased with increasing number of carbons on the pendant side-chains. The backbone-backbone spacing in P4VP-*r*-PI_C6I was slightly less than the backbone-backbone spacing in P4VP-*r*-PI_C6Br. This decrease in backbone-backbone spacing with increasing counter ion size may have resulted from the differences in the dipole moment of the respective dipoles. The dipole moment is the product of the elementary charge, *q*, and the distance between the center of the ions in the dipole. Consequently, larger ions will have larger dipole moment. Iodide counter ions are larger than bromide counter ions, thus the dipole moment of the alkylpyridiniumiodide would be larger than the dipole moment of the alkylpyridiniumbromide. The dipole-dipole attraction between adjacent backbones with iodide counter ions will be stronger than those with bromide counter ions with similar number of carbons on the pendant side-chains. This will lead to a shorter backbone-backbone spacing, more compact backbones, in charged comb-shaped polymers having iodide counter ions in comparison to charged comb-shaped polymers with bromide counter ions.

The X-ray scattering profiles of P4VP-*r*-PI_C1I and P4VP-*r*-PI_C2I show an ionomer peak. This is consistent with the tendency of P4VP-*r*-PI quaternized by 1-alkylhalides with low number of carbons in the alkyl groups to form ionomer cluster morphology as was observed in P4VP-*r*-PI_C2Br and P4VP-*r*-PI_C3Br. The domain spacing of the clusters in P4VP-*r*-PI_C1I and P4VP-*r*-PI_C2I increased with increasing number of carbons. The same trend was observed in the ionomer cluster morphology of the P4VP-*r*-PI_CnBr series. The cluster-cluster spacing dimension for P4VP-*r*-PI_C2I was equivalent with the cluster-cluster spacing dimension of P4VP-*r*-PI_C2Br. This suggests that counter ion had minimal effect on the dimension of the cluster-cluster spacing.

The WAXS spectrum of P4VP-*r*-PI_C3Br, although shows an ionomer peak, also show an inflexion feature between the VDW and the ionomer peak. However, the WAXS spectrum of P4VP-*r*-PI_C3I show a broad ionomer-like peak with no such inflexion between the ionomer and the VDW peak. The ionomer peak intensities of the P4VP-*r*-PI_CnI series relative to the VDW peak decreases with increasing number of carbons on the pendant side-chain similar to the trend observed in P4VP-*r*-PI_CnBr series.

Given that the dipole moment of the dipoles in P4VP-*r*-PI_CnI series would be higher than the dipoles in P4VP-*r*-PI_CnBr series, the limiting length obtained from equation (4.3) would be higher in P4VP-*r*-PI_CnI series in comparison to P4VP-*r*-PI_CnBr series. The difference in the dipole moment in P4VP-*r*-PI_CnI series and P4VP-*r*-PI_CnBr series will also result in shorter backbone-backbone spacing in the P4VP-*r*-PI_CnI series in comparison to the backbone-backbone spacing in P4VP-*r*-PI_CnBr series. Thus, the transition to a backbone-backbone dominant morphology was observed at a higher number of carbons on the pendant side-chain in P4VP-*r*-PI_CnI series compared to P4VP-*r*-PI_CnBr series.

4.3.4 Short-Range Ordering in P4VP-*r*-PI-*r*-PS_CnBr and P4VP-*r*-PI-*r*-PS_CnI Series

The terpolymer of 4-vinylpyridine, isoprene, and styrene (P4VP-*r*-PI-*r*-PS) was synthesized by Nitroxide Mediated Polymerization (NMP). Characterization of P4VP-*r*-PI-*r*-PS by ^{1}H NMR confirms the successful synthesis of the copolymer (see Figure 4.14). The compositions of 4-vinylpyridine, isoprene, and styrene in the copolymer were determined by comparing the integrals of the aromatic protons of poly(4-vinylpyridine), the vinyl protons of polyisoprene, and the aromatic protons of the polyisoprene.

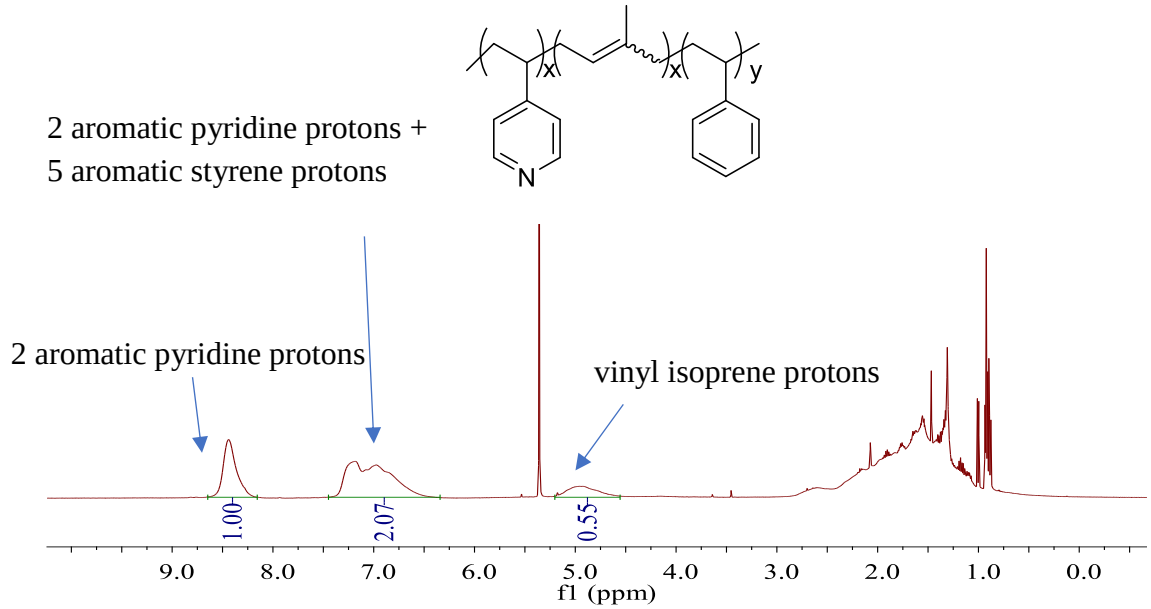

Figure 4.14. ^{1}H NMR spectrum of P4VP-*r*-PI-*r*-PS.

The integral value of the vinyl peak has contributions from the isomers of polyisoprene, 1H from the 1,4 isomer (-C=C**H**-), 2H from the 1,2 isomer (-C=C**H**$_2$), and 1H from the 3,4 isomer (-C=C**H**-). A random copolymer synthesized using SG1 by Nitroxide Mediated Polymerization (NMP) is generally comprised of 93 %, 1 %, and 6 %, of 1,4 isomer, 1,2 isomer, and 3,4 isomer respectively.

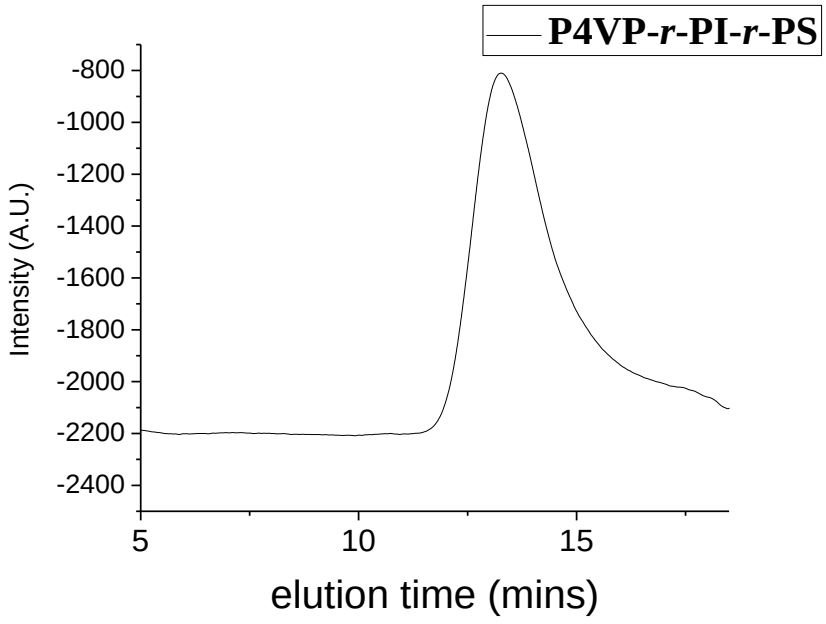

Figure 4.15. The GPC chromatogram for P4VP-*r*-PI-*r*-PS.

The molecular weight and dispersity of the copolymer, P4VP-*r*-PI-*r*-PS, was determined by DMF-GPC (see Figure 4.15). The GPC chromatogram confirm the successful synthesis of P4VP-*r*-PI-*r*-PS. The target molecular weight was lower than the molecular weight determined by GPC. This difference between the target and determined molecular weights could have arisen from the solubility of the copolymer in the eluent. Polyisoprene homopolymer is insoluble in DMF. Polystyrene does not have an extended chain conformation in DMF.

A summary of the molecular weights, copolymer feed and target compositions, and dispersity for P4VP-*r*-PI-*r*-PS is presented in Table 4.3.

Table 4.3. Summary of molecular weight, dispersity, and composition of P4VP-*r*-PI-*r*-PS.

	Feed ratio (**4VP:isoprene:styrene)**	**NMR ratio** (**4VP:isoprene:styrene)**	**Target M_n(Kg/mol)**	**GPC M_n (Kg/mol)**	**Đ**
P4VP-*r*-PI-*r*-PS	2:2:1	2:2:1	150	40	1.6

Since the commoner ratios in the feed and the synthesized polymer determined by NMR are the same, the terpolymers P4VP-*r*-PI-*r*-PS can be said to show random character.

The 4VP units in the terpolymer, P4VP-*r*-PI-*r*-PS, were completely quaternized with various 1-alkylbromides with varying number of carbons in the alkyl group, ranging from *2 – 8*. Characterization of the resultant sample series, P4VP-*r*-PI-*r*-PS_CnBr, by FTIR-ATR again confirmed the complete disappearance of the C=N aromatic ring stretching vibration at 1414 cm^{-1} and the appearance of the pyridinium vibration at 1640 cm^{-1}.[36–38] The FTIR spectra of P4VP-*r*-PI-*r*-PS quaternized by 1-alkylbromides is presented in Figure 4.15a.

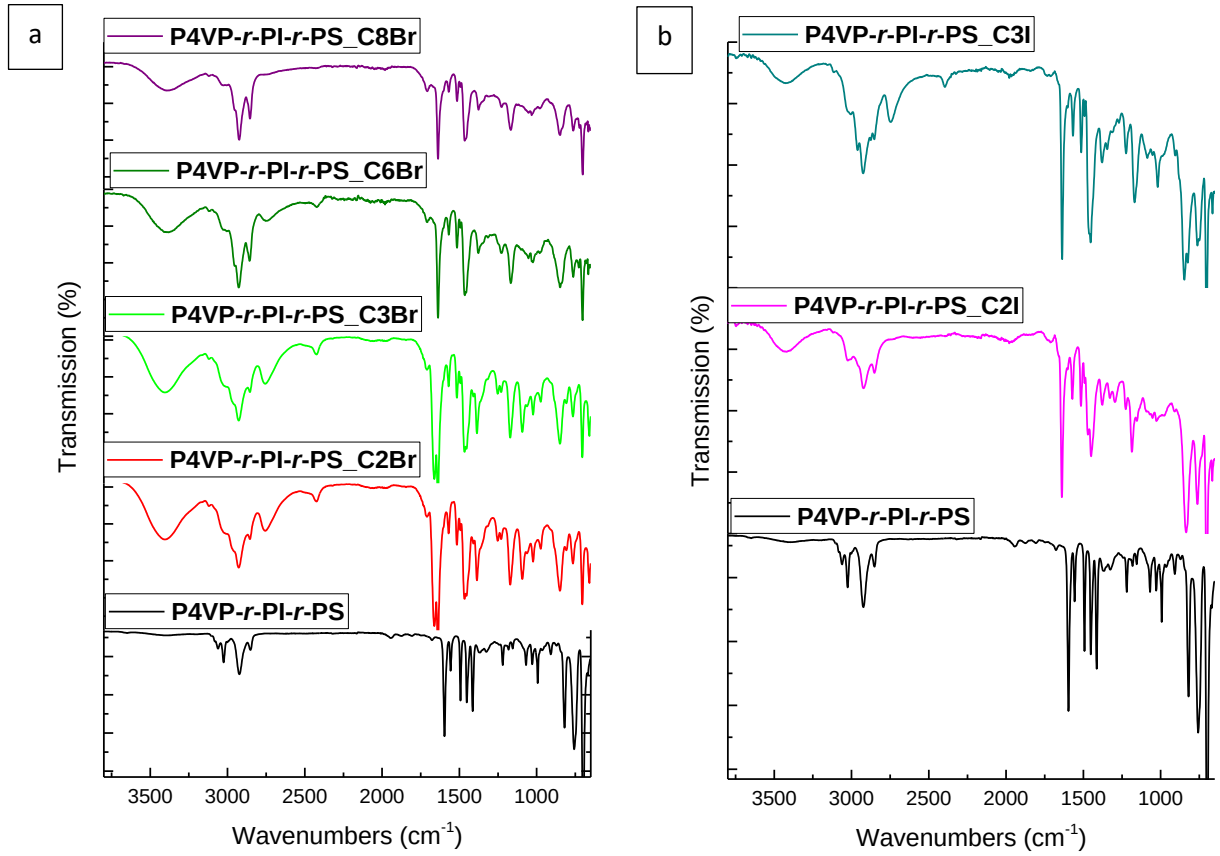

Figure 4.16. The FTIR spectra for the a) P4VP-*r*-PI-*r*-PS_CnBr and b) P4VP-*r*-PI-*r*-PS_CnI series.

To evaluate the effect of counter ions on the short-range ordering, the 4VP units in P4VP-*r*-PI-*r*-PS, were also completely quaternized by 1-alkylIodides with varying number of carbons in the alkyl group, ranging from *1* - *6*. Characterization of the resultant sample series, P4VP-*r*-PI-*r*-PS _CnBr, by FTIR-ATR confirmed the complete disappearance of the C=N aromatic ring stretching vibration at 1414 cm^{-1} and the appearance of the pyridinium vibration at 1640 cm^{-1}.[36–38] The FTIR spectra confirming the complete quaternization of P4VP-*r*-PI-*r*-PS by 1-alkyIodides is presented in Figure 4.16b.

a) b)

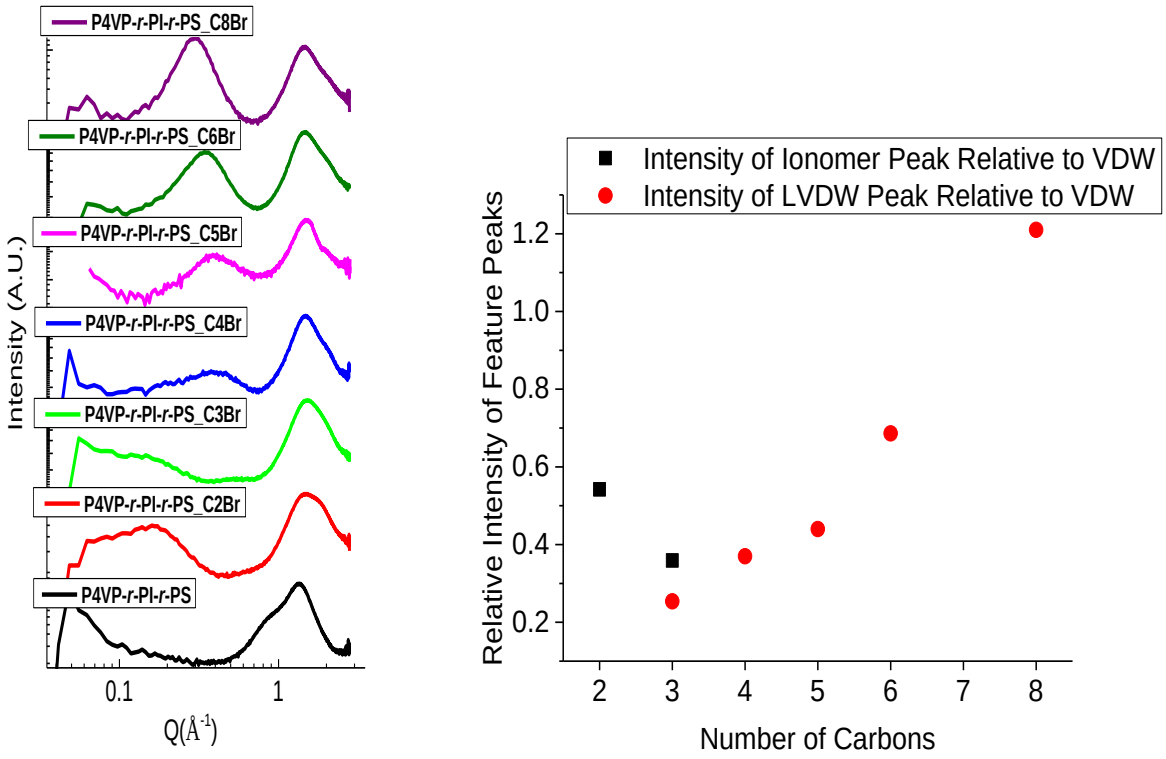

Figure 4.17. a) The WAXS spectra of the P4VP-*r*-PI-*r*-PS_CnBr series, b) relative intensities of feature peaks in the P4VP-*r*-PI-*r*-PS_CnBr series.

The effect of quaternization on the short-range ordering of P4VP-*r*-PI-*r*-PS_CnBr series can be observed from the WAXS spectra (see Figure 4.17a). The VDW peak, present in both P4VP_CnBr and P4VP-*r*-PI_CnBr series, can be observed at large *Q* values in the terpolymer. The value of the VDW spacing in the quaternized polymer series, P4VP-*r*-PI-*r*-PS _CnBr decreased in comparison to the value of the VDW spacing of the pristine terpolymer P4VP-*r*-PI-*r*-PS. For the quaternized series, P4VP-*r*-PI-*r*-PS_CnBr, the VDW spacing increased with increasing number of carbons on the pendant side-chains. A similar trend was observed in the P4VP_CnBr and P4VP-*r*-PI_CnBr series. The LVDW peak, arising from backbone-backbone spacing, can also be observed at lower *Q* values next to the VDW peak from P4VP-*r*-PI-*r*-PS_C3Br to P4VP-*r*-PI-*r*-PS_C8Br while

ionomer peaks can be observed at even lower Q values next to VDW peak in P4VP-*r*-PI-*r*-PS_C2Br and P4VP-*r*-PI-*r*-PS_C3Br. Three morphological regimes can also be observed for this series. The first regime is observed in P4VP-*r*-PI-*r*-PS_C2Br, where $d_B < d_L$, dipole-dipole attraction is dominant. This dipole-dipole attraction facilitates dipole cluster formation. A second regime can be observed in P4VP-*r*-PI-*r*-PS_C3Br, ($d_B = 12.5$ Å). Next to the VDW peak, two feature peaks are evident, an ionomer peak and an emerging LVDW peak. Thus, a backbone-backbone morphology and ionomer cluster morphology coexist. In this regime, the dipole-dipole attractive potential is balanced by the thermal energy. Hence, $d_B \sim d_L$. The calculated value of d_B for which coexistence should occur, 12 Å, fits well with the data obtained from scattering 12.5 Å. The third regime ranges from P4VP-*r*-PI-*r*-PS_C4Br to P4VP-*r*-PI-*r*-PS_C8Br ($d_B = 14.7 – 21$ Å). In this regime $d_B > d_L$. Dipole-dipole interaction between dipoles on adjacent polymer backbones are "shielded" and the backbone-backbone morphology is dominant. The value of d_B in P4VP-*r*-PI-*r*-PS_CnBr series increased linearly with increasing number of carbons as in the cases of P4VP_CnBr and P4VP-*r*-PI_CnBr series. The value of d_B for a given number of carbons on the pendant side-chain was similar to the corresponding d_B value in the P4VP-*r*-PI_CnBr series. Accordingly, the slope of the linear increase in d_B with number of carbons on the pendant side-chains in P4VP-*r*-PI-*r*-PS_CnBr and P4VP-*r*-PI_CnBr were similar. Like the P4VP-*r*-PI_CnBr series, the intensity of ionomer peaks relative to its corresponding VDW peak decreased with increasing number of carbons on the pendant side-chains in the P4VP-*r*-PI-*r*-PS_CnBr series (see Figure 4.17b). This suggests a decrease in dominance of ionomer morphology. Conversely, the intensity of the LVDW peak increased with increasing number of carbons on the pendant side-chain.

Unlike the P4VP-*r*-PI_CnBr series, the LVDW peak of P4VP-*r*-PI-*r*-PS_CnBr series became distinct at P4VP-*r*-PI-*r*-PS_C4Br. Given that the dielectric constants of polyisoprene and polystyrene have similar values, this change in the onset of backbone-backbone morphology may be attributed to the rigidity of the styrene comonomer. This suggests that the onset of the third regime has a dependence on the styrene comonomer content.

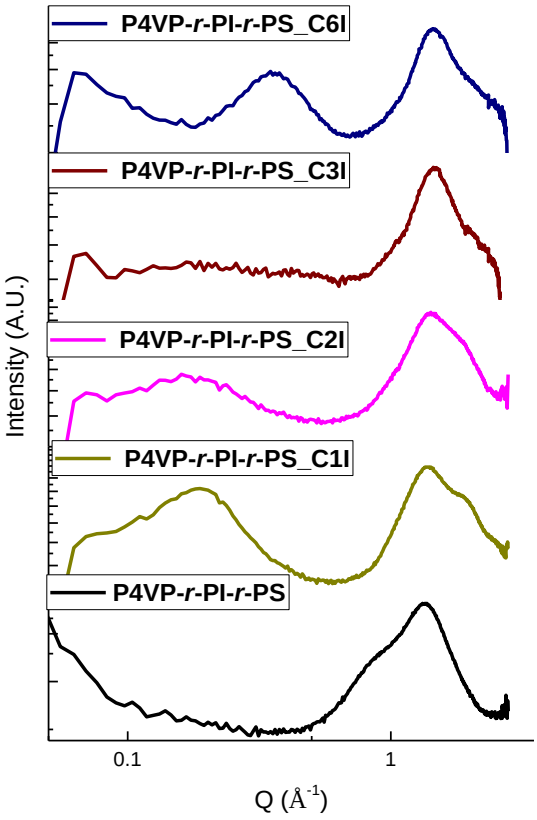

Figure 4.18. The WAXS spectra of the P4VP-*r*-PI-*r*-PS_CnI series.

The X-ray scattering data for the P4VP-*r*-PI-*r*-PS_CnI series is shown in Figure 4.18. The scattering profiles show the VDW peak at large *Q* values for all the studied samples. Similar to the P4VP-*r*-PI_CnI series, the VDW spacing did not change on quaternization. At smaller *Q* values,

an LVDW peak could be observed in P4VP-*r*-PI-*r*-PS_C6I. This peak correlates to the backbone-backbone spacing in comb-shaped polymers. The value of the backbone-backbone spacing in P4VP-*r*-PI-*r*-PS_C6I was slightly lower than the value of the backbone-backbone spacing in P4VP-*r*-PI-*r*-PS_C6Br. This may have resulted from the stronger dipole-dipole attraction between adjacent backbones in P4VP-*r*-PI-*r*-PS_CnI series in comparison to P4VP-*r*-PI-*r*-PS_CnBr series. The strong dipole-dipole attraction in the P4VP-*r*-PI-*r*-PS_CnI series stems from the high dipole moment of alkylpyridiniumiodide. The same trend was observed in P4VP-*r*-PI_C6I and P4VP-*r*-PI_C6Br. However, the backbone-backbone spacing dimension in P4VP-*r*-PI-*r*-PS_C6I was similar to the backbone-backbone spacing in P4VP-*r*-PI_C6I. The same trend was observed for the backbone-backbone spacing dimension in the P4VP-*r*-PI_CnBr series and P4VP-*r*-PI-*r*-PS_CnBr series at a certain number of carbons on the pendant side-chains.

The X-ray scattering profiles of P4VP-*r*-PI-*r*-PS_C1I and P4VP-*r*-PI-*r*-PS_C2I show ionomer peaks at lower *Q* values. This ionomer peak correlates to the cluster-cluster spacing between dipole clusters in an ionomer cluster morphology. The dimensions of the cluster-cluster spacing for P4VP-*r*-PI-*r*-PS_C1I and P4VP-*r*-PI-*r*-PS_C2I were equivalent to the dimensions of the cluster-cluster spacing for P4VP-*r*-PI_C1I and P4VP-*r*-PI_C2I respectively. Like the backbone-backbone spacing, the cluster-cluster dimension is independent of the component of the copolymer. Furthermore, the cluster-cluster dimension in P4VP-*r*-PI-*r*-PS_C2I was equivalent to the cluster-cluster dimension in P4VP-*r*-PI-*r*-PS_C2Br. The cluster-cluster spacing is the distance between nearest clusters that are randomly distributed in a hydrophobic matrix. Thus, this distance will depend on the concentration of clusters which in turn depends on the concentration of dipoles. Consequently, the size of the ions in the dipoles or the strength of the dipole interaction will have minimal effect on the distribution of these clusters. The cluster-cluster spacing is unlike the

backbone-backbone spacing that is affected by the counter ion size. The relative intensity of the ionomer peaks decreases with increasing number of carbons on the pendant side-chains in the P4VP-*r*-PI-*r*-PS_CnI series and then disappears. The same trend has been observed in P4VP-*r*-PI_CnBr, P4VP-*r*-PI_CI, and P4VP-*r*-PI-*r*-PS_CnBr series.

The WAXS spectra for P4VP-*r*-PI-*r*-PS_C3I show no distinct ionomer or LVDW peak. This might be have resulted from a perfect balance between the driving forces for ionomer cluster morphology and backbone-backbone morphology resulting in the elimination of short-range ordering.

The larger limiting length and the shorter backbone-backbone spacing in P4VP-*r*-PI-*r*-PS_CnI series suggests a delayed onset of the backbone-backbone morphology in comparison to the P4VP-*r*-PI-*r*-PS_CnBr series. The delay in the onset of the backbone-backbone spacing can be observed when the WAXS spectra of P4VP-*r*-PI-*r*-PS_C3I and P4VP-*r*-PI-*r*-PS_C3Br are compared (see Figure 4.17a and Figure 4.18). In P4VP-*r*-PI-*r*-PS_C3Br, a backbone-backbone spacing could be observed between the ionomer peak and the VDW peak. However, in the X-ray scattering profile of P4VP-*r*-PI-*r*-PS_C3I, only a plateau could be observed without any backbone-backbone spacing. This confirms that the size of the counter ion can delay the onset of the backbone-backbone morphology.

Unlike the P4VP-*r*-PI_CnI series, the ionomer peak of P4VP-*r*-PI-*r*-PS_CnI series completely disappeared at P4VP-*r*-PI-*r*-PS_C3I. The total disappearance of the ionomer peak is dependent on the copolymer type. Rigid copolymers like polystyrene facilitate the disappearance of the ionomer cluster morphology.

4.3.5 Short-Range Ordering in P4VP-*r*-PS_CnBr and P4VP-*r*-PS_CnI Series

The copolymer of 4-vinylpyridine and styrene, P4VP-*r*-PS, was synthesized by Nitroxide Mediated Polymerization (NMP). Characterization of P4VP-*r*-PS by ^{1}H NMR confirms the successful synthesis of the copolymer (see Figure 4.19). The compositions of poly(4-inylpyridine) and polystyrene in the copolymer were determined by comparing the integrals of the aromatic protons of poly(4-vinylpyridine) and the aromatic protons of polystyrene.

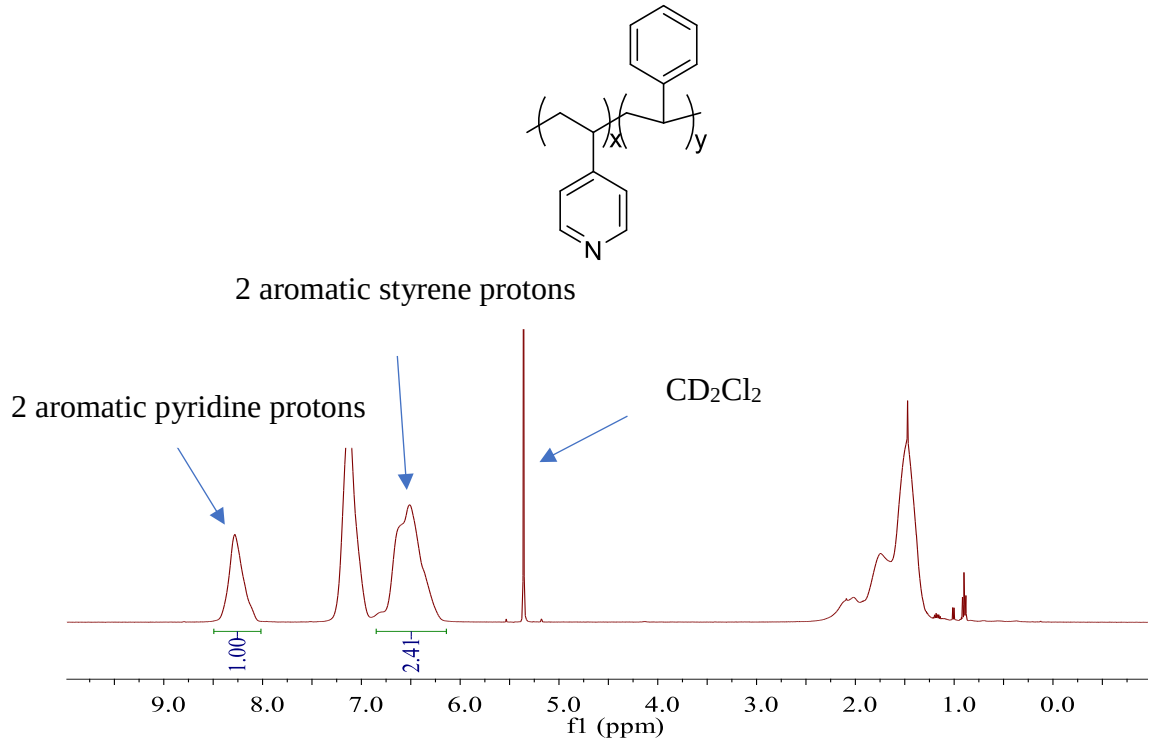

Figure 4.19. The ^{1}H NMR spectrum of P4VP-*r*-PS.

Since the commoner ratios in the feed and the synthesized polymer determined by NMR are the same, the copolymers P4VP-*r*-PS can be said to show random character. Furthermore, the reactivity ratios of 4VP (0.86) and styrene (0.66) in P4VP-*r*-PS, confirm the random character of these polymers.[43]

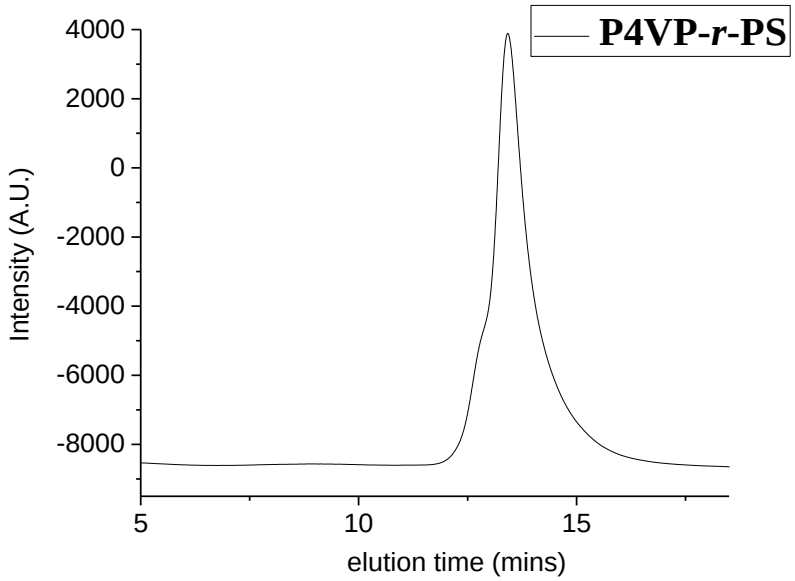

Figure 4.20. The GPC chromatogram of P4VP-*r*-PS.

The molecular weight and dispersity of the copolymer, P4VP-*r*-PS, was determined by DMF-GPC (see Figure 4.20). The GPC chromatogram confirm the successful synthesis of P4VP-*r*-PS. The target molecular weight was lower than the molecular weight determined by GPC. This difference in the target and the GPC determined molecular weights could have arisen from the solubility of the copolymer in the eluent. Polystyrene does not show extended chain conformation in DMF.

A summary of the molecular weights, copolymer feed and target compositions, and dispersity for P4VP-*r*-PS is presented in Table 4.4.

Table 4.4. Summary of molecular weight, dispersity, and composition of P4VP-*r*-PS

	Feed ratio (**4VP:isoprene:styrene)**	**NMR ratio** (**4VP:isoprene:styrene)**	**Target M_n(Kg/mol)**	**GPC M_n (Kg/mol)**	**Đ**
P4VP-*r*-PS	2:0:3	2:0:3	190	100	1.2

The 4VP units in the copolymer, P4VP-*r*-PS, were completely quaternized with 1-alkylbromides having varying number of carbons on the alkyl group, ranging from *2 - 8*. Characterization of the resulting P4VP-*r*-PS_CnBr by FTIR-ATR confirm the complete disappearance of the C=N aromatic ring stretching vibration at 1414 cm^{-1} and the appearance of the pyridinium vibration at 1640 cm^{-1}.[36–38] The FTIR spectra confirming the complete quaternization of P4VP-*r*-PS by 1-alkybromides is presented in Figure 4.21a.

The 4VP units in P4VP-*r*-PS, were completely quaternized by 1-alkylIodides with varying number of carbons in the alkyl group, ranging from *1 - 6*. Characterization of the resultant sample series, P4VP-*r*-PI_CnBr, by FTIR-ATR confirmed the complete disappearance of the C=N aromatic ring stretching vibration at 1414 cm^{-1} and the appearance of the pyridinium vibration at 1640 cm^{-1}.[36–38] The FTIR spectra confirming the complete quaternization of P4VP-*r*-PS by 1-alkyIodides is presented in Figure 4.21b.

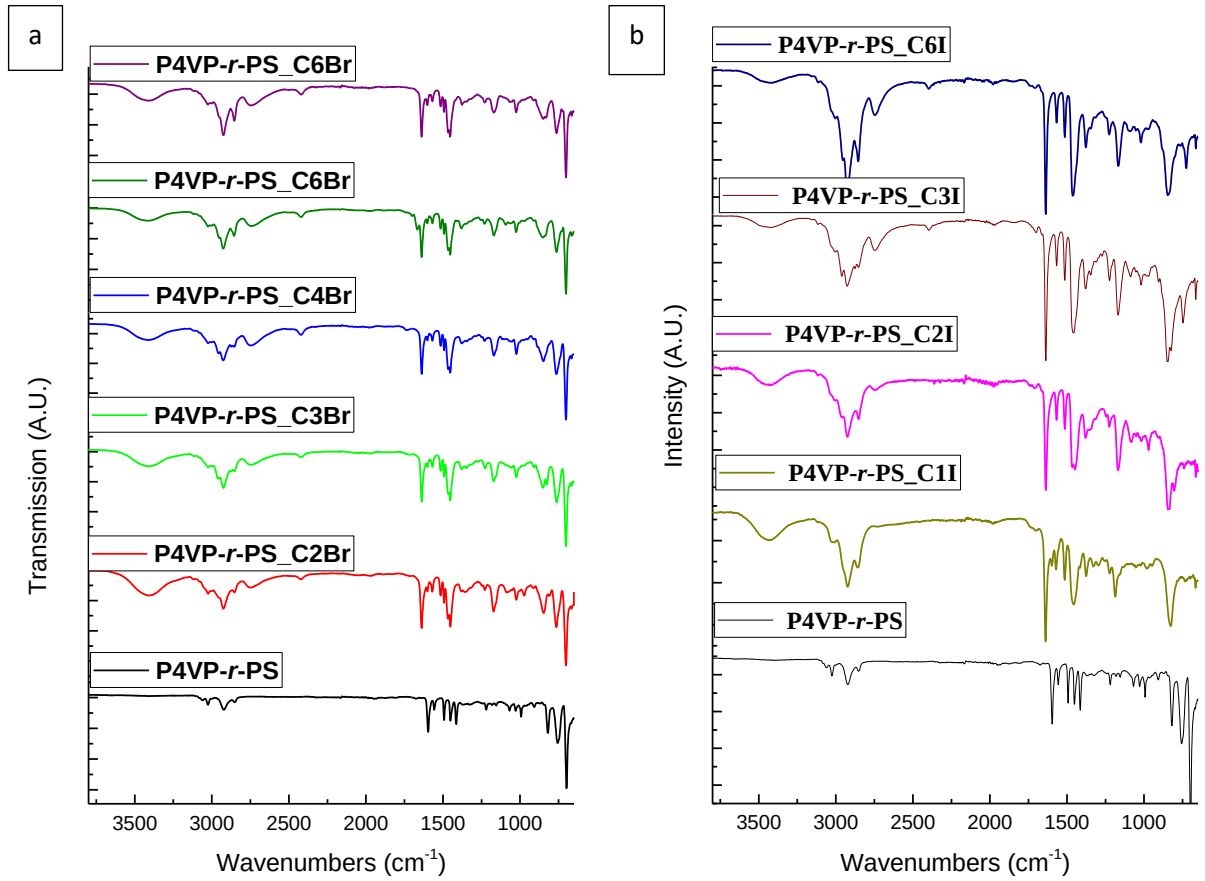

Figure 4.21. The FTIR spectra for a) P4VP-*r*-PS_CnBr and b) P4VP-*r*-PS_CnI series.

On completely replacing the isoprene content by styrene, P4VP-*r*-PS, the interplay between the backbone-backbone morphology and ionomer morphologies were probed by WAXS (see Figure 4.22). The WAXS spectra of the P4VP-*r*-PS_CnBr series show the VDW peak at high Q values. Upon quaternization, the VDW peak shifts to higher *Q* values (smaller dimensions) in comparison to the pristine P4VP-*r*-PS. Similar trends have been observed in P4VP_CnBr, P4VP-*r*-PI_CnBr, P4VP-*r*-PI-*r*-PS_CnBr. Next to the VDW peak, for samples P4VP-*r*-PS_C3Br to P4VP-*r*-PS_C8Br is the LVDW peak that correlates to d_B of P4VP-*r*-PS_CnBr ($n = 2 - 8$) and an ionomer peak for P4VP-*r*-PS_C2Br.

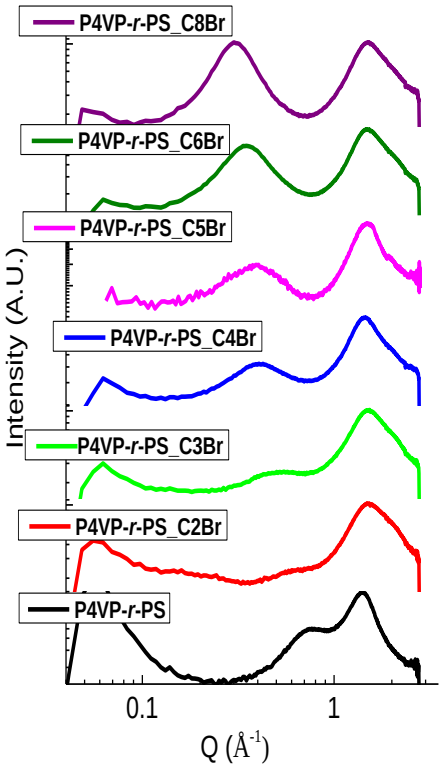

Figure 4.22. WAXS spectra of P4VP-*r*-PS_CnBr series.

Unlike the P4VP-*r*-PI_CnBr and P4VP-*r*-PS-*r*-PS_CnBr series, the P4VP-*r*-PS_CnBr series has two morphology regimes. The first regime, a coexistence regime, can be observed in P4VP-*r*-PS. In this regime, a broad ionomer peak and an emerging LDVW peak can be observed on the WAXS spectra. The measured value of d_B, for coexistence, 11.0 Å, is slightly lower than that predicted by the model, 12.0 Å. In the second regime, P4VP-*r*-PS_C3Br to P4VP-*r*-PS_C8Br (d_B = 12.7 – 21 Å), $d_B > d_L$. Consequently, backbone-backbone spacing morphology is dominant. By completely replacing the isoprene comonomer (P4VP-*r*-PI-*r*-PS_CnBr series) with styrene (P4VP-*r*-PS_CnBr series), backbone-backbone spacing morphology can be observed even at P4VP-*r*-PS_C2Br next to the VDW peak. This further confirms that the onset of a morphology regime depends not just on the side-chain sterics but the comonomer type (see Figure 4.23). By increasing

the concentration of styrene across the series, the polymer becomes dominated by backbone-backbone morphology. This finding shows that changing the comonomer type or side-chain length can be used to transition from one morphology regime to another.

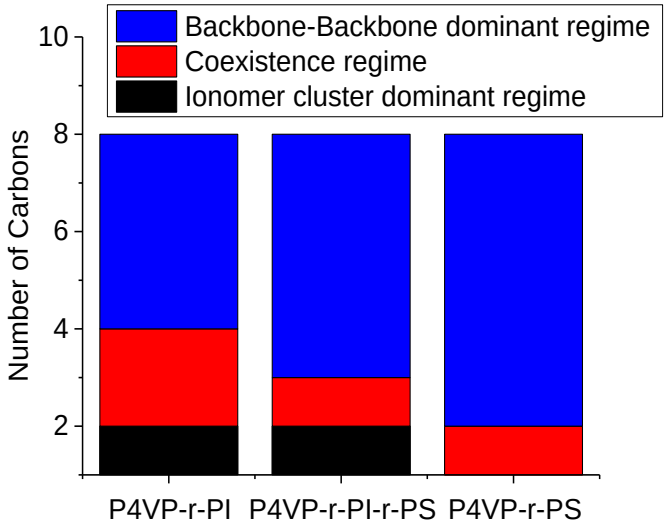

Figure 4.23. Summary of the different morphological regimes across the studied series with increasing styrene content.

While according to equation (4.3), the coexistence regime for P4VP-*r*-PI_CnBr, P4VP-*r*-PI-*r*-PS_CnBr, and P4VP-*r*-PS_CnBr (since the matrix in all these series have similar dielectric constants) is predicted to exist when d_B ~ 12 Å. However, coexistence regimes were observed at 11 Å for P4VP-*r*-PS_CnBr series, 12.5 Å for P4VP-*r*-PI-*r*-PS_CnBr_CnBr series, and 14.5 Å P4VP-*r*-PI_CnBr. Although the "In-Line" Dipole Model is a simplification of the interplay between dipoles and pendant side-chain sterics, nevertheless, the d_L predicted by this model can be used to estimate the approximate onset/end of a morphology regime. This model can also be used to predict the effect of the concentration of 4VP comonomer on the random copolymer morphology. Random copolymers, for example P4VP-*r*-PI, with high 4VP mole fraction have longer backbone-backbone spacing for a given number of carbon on the pendant side-chain in

comparison to random copolymers with low 4VP content. Consequently, in P4VP-*r*-PI_CnBr with higher 4VP mole fraction, the dominance of the backbone-backbone over ionomer cluster morphology will commence at a relatively shorter pendant side-chain in comparison to a P4VP-*r*-PI_CnBr with low 4VP mole fraction.

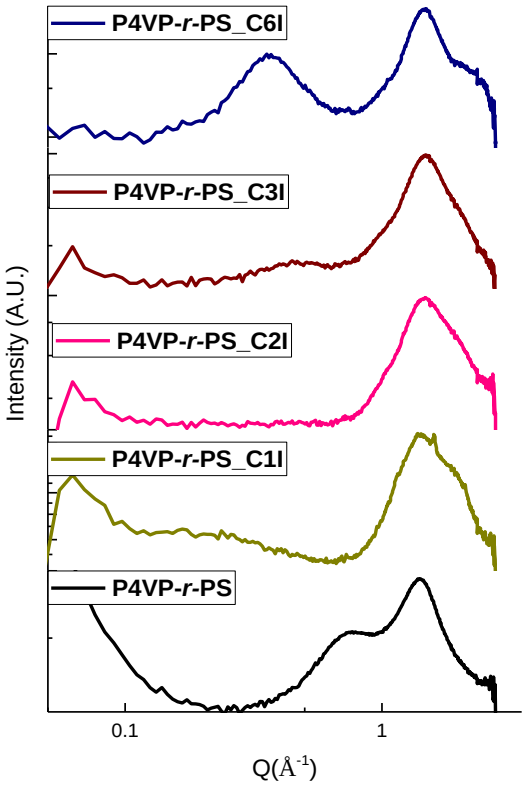

Figure 4.24. The WAXS spectra of the P4VP-*r*-PS_CnI series.

The scattering profiles of the P4VP-*r*-PS_CnI series are presented in Figure 4.23. The ubiquitous VDW peak can be observed in all polymer samples at *Q* values. The VDW spacing remained unchanged for both quaternized and unquaternized P4VP-*r*-PS. The same trend was observed in P4VP-*r*-PI and P4VP-*r*-PI-*r*-PS upon quaternization with 1-alkyliodides. This is unlike P4VP-*r*-

PS_CnBr that show a change in the VDW spacing between the quaternized and unquaternized samples.

The scattering profiles of P4VP-*r*-PS_C3I and P4VP-*r*-PS_C6I show an LVDW peak at lower *Q* values. This peak correlate to the backbone-backbone spacing in comb-shaped polymers. The backbone-backbone spacing dimension of P4VP-*r*-PS_C3I was similar to the dimension of P4VP-*r*-PS_C3Br. However, the dimension of P4VP-*r*-PS_C6I was slightly smaller than the dimension of P4VP-*r*-PS_C6Br. The same trend has been observed when comparing the backbone-backbone spacing between P4VP-*r*-PI_C6I and P4VP-*r*-PI_C6Br. This change in backbone-backbone spacing dimension at equivalent number of carbons on the pendant side-chains results from the stronger dipole-dipole interaction in charged comb-shaped polymers with iodide counter ions in comparison to the dipole-dipole interaction in charged comb-shaped polymers with bromide counter ions.

An ionomer peak can be observed in the WAXS spectra of P4VP-*r*-PI_C1I at larger *Q* values. This peak correlate to the spacing between clusters in an ionomer cluster morphology. However, unlike the P4VP-*r*-PI_C2I and P4VP-*r*-PI-*r*-PS_C2I that show ionomer peak, P4VP-*r*-PS_C2I show no ionomer peak but a plateau. This suggests that there is no short-range ordering in P4VP-*r*-PS_C2I. The same featureless peak was observed in P4VP-*r*-PI-*r*-PS_C3I. Where a coexistence of both morphologies is observed in P4VP-*r*-PI-*r*-PS_CnBr and P4VP-*r*-PS_CnBr series a complete elimination of both morphologies is observed in their iodide counterpart.

The In-Line Dipole Model predicts a larger limiting length for the P4VP-*r*-PS_CnI series due to the large dipole-dipole moment of alkylpyridinium iodide. Thus, according to this model, the onset of the backbone-backbone morphology will be delayed to a longer pendant side-chain in P4VP-*r*-

PS_CnI series in comparison to P4VP-*r*-PS_CnBr series. An evaluation of the X-ray scattering spectra of P4VP-*r*-PS_C2I and P4VP-*r*-PS_C2Br seem to confirm this prediction. The WAXS spectra of P4VP-*r*-PS_C2Br show an LVDW peak suggesting the onset of backbone-backbone morphology while the WAXS P4VP-*r*-PS_C2I show no LVDW peak. Although the large size of the iodide counter ion suggests the corresponding large dipole moment will facilitate the formation of ionomer cluster morphology, however, scattering data show that iodide counter ion tend to suppress the formation of backbone-backbone morphology and not necessarily facilitate the formation of ionomer morphology.

Interestingly though, the comonomer type had little to do with the dimension between backbones or dipole clusters. A tabular summary of observed characteristic spacing (cluster-cluster and backbone-backbone spacing) against number of carbons on pendant side-chains for all the studied series is presented in Table 4.4. As discussed already, there is a variation of both cluster-cluster and backbone-backbone spacing dimensions with number of carbons on the pendant side-chain in all the series studied. However, there was minimal variation in any characteristic spacing (cluster-cluster and backbone-backbone spacing) across different series for a given number of carbons on the pendant side-chain. While the comonomer type may favor dipole clustering to backbone-backbone spacing for a certain number of carbon and vice-versa, it does not necessarily dictate the characteristic dimensions associated with each type of short-range order.

Table 4.5. Summary of the characteristic dimensions of the morphologies determined from WAXS in the studied series.

CnBr	P4VP	P4VP-*r*-PI		P4VP-*r*-PI-*r*-PS		P4VP-*r*-PS	
	d_B(Å)	d_I(Å)	d_B(Å)	d_I(Å)	d_B(Å)	d_I(Å)	d_B(Å)
C2Br	-	36.1		36.5		37	11.0
C3Br	15	42.5	-	43.1	12.5	-	12.7
C4Br	17	-	14.5	-	14.5	-	15.0
C5Br	19	-	16.6	-	17	-	16.5
C6Br	21	-	18.8	-	18.4	-	18.4
C7Br	23	-	-	-	-	-	-
C8Br	24	-	21.0	-	21.5	-	20.9
C9Br	27	-		-		-	
C10Br	29	-		-		-	
C11Br	30	-		-		-	
C12Br	31	-		-		-	
C1I	-	33.9	-	32.9	-	31.3	-
C2I	-	36.9	-	36.8	-	-	

C3I	-	41.9	-	-		-	13.2
C6I	-	-	17.6	-	17.8	-	17.6
C12I	-	-	26.7	-		-	

4.4 Conclusion

In charged, random, comb-shaped copolymers and terpolymers, both ionomer and backbone-backbone morphologies can be observed. The backbone-backbone spacing dimension increases with increasing number of carbons on the pendant side-chain. The dimensions corresponding to the backbone-backbone or cluster-cluster spacing are similar. However, the backbone-backbone spacing and cluster-cluster spacing are characteristic of two distinct morphologies. In principle, the short-range ordering in backbone-backbone morphology and ionomer cluster morphology have different origins. While the former is fostered by sterics between pendant side-chains on the polymer backbones, the latter is facilitated by electrostatic attraction between dipoles on the backbone of the polymer. Caution is advised when evaluating X-ray scattering data to avoid attributing one feature for the other. The "In-Line" Dipole Model predicts a stratification of morphology regimes by defining a limiting length, d_L, which balances the attractive dipole-dipole energy with the thermal energy. Since the dipoles are situated on the polymer backbones, the backbone-backbone spacing d_B is the spacing between dipoles. When $d_B < d_L$, ionomer cluster morphology is dominant. When $d_B > d_L$, backbone-backbone morphology is dominant, and when $d_B \sim d_L$, a coexistence of both morphologies can be observed. Furthermore, the non-polar component of the random copolyelectrolytes also determines the onset of the dominance of backbone-backbone morphology or the end of the dominance of ionomer cluster morphology.

Copolymers with isoprene, having flexible backbones, for example P4VP-*r*-PI_CnBr series, facilitate the formation of ionomer cluster morphology and delay the onset of the transition to backbone-backbone morphology. Backbone-backbone morphology becomes dominant at P4VP-*r*-PI_C5Br. Upon the introduction of styrene, for the terpolymer (P4VP-*r*-PI-*r*-PS_CnBr series), the backbones become relatively rigid in comparison to P4VP-*r*-PI_CnBr series. Backbone-backbone morphology becomes dominant at P4VP-*r*-PI-*r*-PS_C4Br. When isoprene comonomer content is completely replaced with styrene, (P4VP-*r*-PS_CnBr series), the copolymer, having rigid backbones, disfavors the formation of ionomer cluster morphology. Backbone-backbone morphology becomes dominant at P4VP-*r*-PS_C3Br.

Iodide counter ion, though not affecting the cluster-cluster dimension, affects the dimensions of the backbone-backbone spacing. No coexistence of ionomer and LVDW peak was observed in all the series with iodide counter ion. Featureless spectra were observed in the transition from ionomer cluster morphology to backbone-backbone morphology for P4VP-*r*-PI-*r*-PS_C3I and P4VP-*r*-PS_C2I.

4.5 References

(1) Allen, F. I.; Comolli, L. R.; Kusoglu, A.; Modestino, M. A.; Minor, A. M.; Weber, A. Z. Morphology of Hydrated as-Cast Nafion Revealed through Cryo Electron Tomography. *ACS Macro Lett.* **2015**, *4* (1), 1–5.

(2) Wanakule, N. S.; Virgili, J. M.; Teran, A. A.; Wang, Z. G.; Balsara, N. P. Thermodynamic Properties of Block Copolymer Electrolytes Containing Imidazolium and Lithium Salts. *Macromolecules* **2010**, *43* (19), 8282–8289.

(3) Bae, B.; Yoda, T.; Miyatake, K.; Uchida, H.; Watanabe, M. Proton-Conductive Aromatic

Ionomers Containing Highly Sulfonated Blocks for High-Temperature-Operable Fuel Cells. *Angew. Chemie - Fuel Cell Membr.* **2010**, *49* (2), 317–320.

(4) Beers, K. M.; Balsara, N. P. Design of Cluster-Free Polymer Electrolyte Membranes and Implications on Proton Conductivity. *ACS Macro Lett.* **2012**, *1* (10), 1155–1160.

(5) Zhang, Z.; Yang, M.; Zhang, X.; Zhang, L.; Liu, B.; Zheng, P.; Wang, W. Enhancing Gelation Ability of a Dendritic Gelator through Complexation with a Polyelectrolyte. *Chem. - A Eur. J.* **2009**, *15* (10), 2352–2361.

(6) Zhang, W.; Liu, Y.; Jackson, A. C.; Savage, A. M.; Ertem, S. P.; Tsai, T. H.; Seifert, S.; Beyer, F. L.; Liberatore, M. W.; Herring, A. M.; et al. Achieving Continuous Anion Transport Domains Using Block Copolymers Containing Phosphonium Cations. *Macromolecules* **2016**, *49* (13), 4714–4722.

(7) Sing, C.; Zwanikken, J.; Cruz, M. D. La. Electrostatic Control of Block Copolymer Morphology. *Nat. Mater.* **2014**, *13* (7), 694–698.

(8) Eisenberg, A.; Hird, B.; Moore, R. B. A New Multiplet-Cluster Model for the Morphology of Random Ionomers. *Macromolecules* **1990**, *23* (18), 4098–4107.

(9) Moore, R. B.; Gauthier, M.; Williams, C. E.; Eisenberg, A. Heterogeneities in Random Ionomers - a Small-Angle X-Ray-Scattering Investigation of Alkylated Polystyrene-Based Materials. *Macromolecules* **1992**, *25* (21), 5769–5773.

(10) Eisenberg, A. Clustering of Ions in Organic Polymers. A Theoretical Approach. *Macromolecules* **1970**, *3* (2), 147–154.

(11) Kim, J. -S; Eisenberg, A. Effect of Sample Preparation Conditions and Degree of

Neutralization on the Dynamic Mechanical Properties of Poly(styrene-co-sodium Methacrylate) Ionomers. *J. Polym. Sci. Part B Polym. Phys.* **1995**, *33* (2), 197–209.

(12) Grady, B. P. Review and Critical Analysis of the Morphology of Random Ionomers Across Many Length Scales. *Polym. Eng. Sci.* **2008**, 1029–1051.

(13) Chen, Q.; Bao, N.; Wang, J. H.; Tunic, T.; Liang, S.; Colby, R. H. Linear Viscoelasticity and Dielectric Spectroscopy of Ionomer / Plasticizer Mixtures : A Transition from Ionomer to Polyelectrolyte. *Macromolecules* **2015**, *48*, 8240–8252.

(14) Zhang, Z.; Liu, C.; Cao, X.; Wang, J.-H. H.; Chen, Q.; Colby, R. H. Morphological Evolution of Ionomer/Plasticizer Mixtures during a Transition from Ionomer to Polyelectrolyte. *Macromolecules* **2017**, *50* (3), 963–971.

(15) Salas-De La Cruz, D.; Green, M. D.; Ye, Y.; Elabd, Y. A.; Long, T. E.; Winey, K. I. Correlating Backbone-to-Backbone Distance to Ionic Conductivity in Amorphous Polymerized Ionic Liquids. *J. Polym. Sci. Part B Polym. Phys.* **2012**, *50* (5), 338–346.

(16) Platé, N. A.; Shibaev, V. P. Comb-like Polymers. Structure and Properties. *J. Polym. Sci. Macromol. Rev.* **1974**, *8* (1), 117–253.

(17) Beiner, M.; Huth, H. Nanophase Separation and Hindered Glass Transition in Side-Chain Polymers. *Nat. Mater.* **2003**, *2*, 595–599.

(18) Hiller, S.; Pascui, O.; Budde, H.; Kabisch, O.; Reichert, D.; Beiner, M. Nanophase Separation in Side Chain Polymers: New Evidence from Structure and Dynamics. *New J. Phys.* **2004**, *6*.

(19) Miller, R. L.; Boyer, R. F.; Heijboer, J. X-Ray Scattering from Amorphous Acrylate and

Methacrylate Polymers: Evidence of Local Order. *J. Polym. Sci. Polym. Phys. Ed.* **1984**, *22* (12), 2021–2041.

(20) Pan, J.; Chen, C.; Li, Y.; Wang, L.; Tan, L.; Li, G.; Tang, X.; Xiao, L.; Lu, J.; Zhuang, L. Constructing Ionic Highway in Alkaline Polymer Electrolytes. *Energy Environ. Sci.* **2014**, *7* (1), 354.

(21) Li, N.; Leng, Y.; Hickner, M. A.; Wang, C. Y. Highly Stable, Anion Conductive, Comb-Shaped Copolymers for Alkaline Fuel Cells. *J. Am. Chem. Soc.* **2013**, *135* (27), 10124–10133.

(22) Dang, H.-S.; Jannasch, P. Exploring Different Cationic Alkyl Side Chain Designs for Enhanced Alkaline Stability and Hydroxide Ion Conductivity of Anion-Exchange Membranes. *Macromolecules* **2015**, *48* (16), 5742–5751.

(23) Haifeng Shi, Ying Zhao, Xia Dong, Y. Z. and D. W. Frustrated Crystallisation and Hierarchical Self-Assembly Behaviour of Comb-like Polymers. *Chem. Soc. Rev.* **2012**, *42*, 2075–2099.

(24) Yarusso, D. J.; Cooper, S. L. Microstructure of Ionomers : Interpretation of Small-Angle X-Ray Scattering Data. *Macromolecules* **1983**, *16* (12), 1871–1880.

(25) Yao, C.; Li, X.; Neoh, K. G.; Shi, Z.; Kang, E. T. Surface Modification and Antibacterial Activity of Electrospun Polyurethane Fibrous Membranes with Quaternary Ammonium Moieties. *J. Memb. Sci.* **2008**, *320* (1–2), 259–267.

(26) Hu, F. X.; Neoh, K. G.; Cen, L.; Kang, E. T. Antibacterial and Antifungal Efficacy of Surface Functionalized Polymeric Beads in Repeated Applications. *Biotechnol. Bioeng.*

2005, *89* (4), 474–484.

(27) Tsai, T. Ionic Copolymers for Alkaline Anion Exchange Membrane Fuel Cells (AAEMFCs), University of Massachusetts, 2014.

(28) Kim, S. Y.; Park, M. J.; Jackson, A. Confinement Effects on Watery Domains in Hydrated Block Copolymer Electrolyte Membranes. *Macromolecules* **2010**, 8128–8135.

(29) Li, N.; Yan, T.; Li, Z.; Thurn-Albrecht, T.; Binder, W. H. Comb-Shaped Polymers to Enhance Hydroxide Transport in Anion Exchange Membranes. *Energy Environ. Sci.* **2012**, *5*, 7888–7892.

(30) Katsuhiro Inomata, Yoshiaki Sakamaki, T. N. & S. S. Solid-State Structure of Comb-Like Polymers Having N-Octadecyl Side Chains II. Cocrystallization of Side Chain with N-Octadecanoic Acid. *Polym. J.* **1996**, No. 28, 986–991.

(31) Israelachvili, J. N. *Intermolecular and Surface Forces*; 2011; Vol. 53.

(32) Sahiner, N.; Yasar, A. O. Journal of Colloid and Interface Science The Generation of Desired Functional Groups on Poly (4-Vinyl Pyridine) Particles by Post-Modification Technique for Antimicrobial and Environmental Applications. *J. Colloid Interface Sci.* **2013**, *402*, 327–333.

(33) Jin, H.; An, Q.; Zhao, Q.; Qian, J.; Zhu, M. Pervaporation Dehydration of Ethanol by Using Polyelectrolyte Complex Membranes Based on Poly (N-Ethyl-4-Vinylpyridinium Bromide) and Sodium Carboxymethyl Cellulose. *J. Memb. Sci.* **2010**, *347* (1–2), 183–192.

(34) Caruso, U.; De Maria, A.; Panunzi, B.; Roviello, A. Poly(4-Vinylpyridine) as the Host Ligand of Metal-Containing Chromophores for Second-Order Nonlinear Optical Active

Materials. *J. Polym. Sci. Part A Polym. Chem.* **2002**, *40* (17), 2987–2993.

(35) Patel, M.; Patel, R.; Chi, W. S.; Kim, J. H.; Sung, J. S. Antibacterial Behaviour of Quaternized Poly(vinyl Chloride)-G-poly(4-Vinyl Pyridine) Graft Copolymers. *Chinese J. Polym. Sci. (English Ed.* **2015**, *33* (2), 265–274.

(36) Li, Y.; Yang, M. J.; She, Y. Humidity Sensitive Properties of Crosslinked and Quaternized Poly (4-Vinylpyridine-Co-Butyl Methacrylate). *Sensors Actuators B* **2005**, *107*, 252–257.

(37) Li, D.; He, Q.; Cui, Y.; Li, J.; Potsdam, G. Fabrication of pH-Responsive Nanocomposites of Gold Nanoparticles / Poly (4-Vinylpyridine). *Chem. Mater.* **2007**, *19*, 412–417.

(38) Hao, E.; Lian, T. Layer-by-Layer Assembly of CdSe Nanoparticles Based on Hydrogen Bonding. *Langmuir* **2000**, *16* (21), 7879–7881.

(39) Andruzzi, F.; Lupinacci, D.; Magagnini, P. L. Comb-like Polymers. 2. Poly(octadecylethy1ene Oxide). *Macromolecules* **1980**, *13* (1), 15–18.

(40) Gierke, T. D.; Munn, G. E.; Wilson, F. C. The Morphology in Nafion Perfluorinated Membrane Products, as Determined by Wide- and Small- Angle X-Ray Studies. *J. Polym. Sci. Polym. Phys. Ed.* **1981**, *19* (11), 1687–1704.

(41) Volkov, V. V; Plat, N. A. Aggregation State and Mesophase Structure of Comb-Shaped Polymers with Fluorocarbon Side Groups. *Polymer (Guildf).* **1992**, *33* (6), 1316–1320.

(42) Pankaj, S.; Beiner, M. Long-Term Behavior and Side Chain Crystallization of poly(3-Alkyl Thiophenes). *Soft Matter* **2010**, *6* (15), 3506–3516.

(43) Greenley. R. Z. Q. *Q and E Values for Free Radical Copolymerizations of Vinyl Monomers and Telogens*, In Polymer.; Brandrup, J., Imermergut, E. H., Grulke, E. A., Ed.; John Wiley & Sons, Inc.: New York, 1999.

(44) Pankaj, S.; Hempel, E.; Beiner, M. Side-Chain Dynamics and Crystallization in a Series of Regiorandom Poly (3-Alkylthiophenes). *Macromolecules* **2009**, *42*, 716–724.

(45) Kreuer, K. D.; Portale, G. A Critical Revision of the Nano-Morphology of Proton Conducting Ionomers and Polyelectrolytes for Fuel Cell Applications. *Adv. Funct. Mater.* **2013**, *23* (43), 5390–5397.

(46) Cornet, N.; Diat, O.; Gebel, G.; Jousse, F.; Marsacq, D.; Mercier, R.; Pineri, M. Sulfonated Polyimide Membranes: A New Type of Ion-Conducting Membrane for Electrochemical Applications. *J. New Mater. Electrochem. Syst.* **2000**, *3* (1), 33–42.

(47) Chen, D.; Hickner, M. A. Ion Clustering in Quaternary Ammonium Functionalized Benzylmethyl Containing Poly(arylene Ether Ketone)s. *Macromolecules* **2013**.

(48) Tsai, T. H.; Ertem, S. P.; Maes, A. M.; Seifert, S.; Herring, A. M.; Coughlin, E. B. Thermally Cross-Linked Anion Exchange Membranes from Solvent Processable Isoprene Containing Ionomers. *Macromolecules* **2015**, *48* (3), 655–662.

(49) Verma, P. L.; Rao, S. S.; Gejji, S. P. Probing Molecular Interactions Underlying Imidazolium and Pyridinium Based Ionic Liquids. *J. Mol. Liq.* **2015**, *212*, 885–899.

(50) Ahmad, Z. Polymer Dielectric Materials, Dielectric Material; Silaghi, M. A., Ed.; IntechOpen, 2012; pp 3–26.

CHAPTER 5

OPTIMIZATION OF IONIC CONDUCTIVITY THROUGH THE COEXISTENCE OF IONOMER CLUSTER AND BACKBONE-BACKBONE MORPHOLOGIES IN AEMs

5.1 Introduction

The use of fuel cells as alternative means of harvesting energy has rightfully attracted much research interest.[1–11] Besides having higher efficiency in comparison to traditional sources of energy utilization like the combustion of fossil fuel, the by-product from the fuel cell redox reaction, when hydrogen gas is used as a fuel, is water unlike the CO_2 released by the combustion of fossil fuel. Fuel cells show great promise for use in portable, mobile, and stationary applications.[12,13] Polymer based fuel cells are particularly attractive because they are solid and flexible, and thus, can be readily made into the shape of the appliance for which they are to be used.

Proton exchange membranes (PEMs), based on perfluoro sulfonic acid polymer membranes, like Nafion®, has been used for commercial and industrial fuel cell applications.[7,14–17] However, proton exchange membrane fuel cells (PEMFCs) require noble metals as catalysts in their membrane electrode assembly for the oxidation of hydrogen gas at the anode. This increases the cost of PEMFCs devices and discourages their use as an alternative source of energy. To make fuel cells competitive with more established energy sources the cost-factor must be considered. Fuel cells based on Anion exchange membranes (AEMs), are noble metal-free, cost-effective alternative to PEMFCs. Like PEMs, they are polymer-based. But unlike PEMs, the anion is the principal conducting species not a proton. The diffusion rate of protons is at least twice larger than that for anions.[3] Therefore, AEMs generally have lower conductivities in comparison to PEMs. To design

high ion conducting AEMs, it is generally required that anion exchange membrane have high concentration of charge (high ion exchange capacities (IEC.)).[11] The ion exchange capacity is defined as the amount in moles of ions in one gram of dry membrane. Anion exchange membranes with high IEC generally have poor mechanical properties. This is because high IEC membranes swell excessively in humidified environment, which compromises their mechanical integrity.[18]

To improve mechanical properties of AEMs are generally copolymerized with a hydrophobic monomer. Coughlin *et al.* copolymerized 4-vinylbenzylchloride with isoprene.[4,19] The resulting random copolymer was quaternized with trimethylamine and crosslinked to obtain mechanically robust, ion conducting, anion exchange membranes. However, an inevitable consequence of this type of randomly copolymerized AEMs is the formation of ionomer cluster morphology.[6,20] Ionomer cluster morphology has also been observed in PEMs of random copolymers of a proton/cation monomer and a hydrophobic comonomer.[21–24] Ionomer cluster morphology results from strong dipole-dipole attraction between dipoles in these random membranes. This attraction leads to the clustering of dipoles. Clustered dipoles in turn attract other dipoles or dipole clusters to form larger-sized clusters. These clusters will continue to grow until they are stabilized by the overall entropy of the system. The random distribution of these clusters in a hydrophobic matrix results in a characteristic cluster – cluster separation between 2 – 10 nm.[25] This separation between clusters can be probed by wide-angle X-ray scattering (WAXS). To facilitate the transport of ions from cluster to cluster across a membrane with ionomer cluster morphology, the clusters must form a network of interconnected water channels. A percolated network of these water channels results in better conductive performance. However, the clustering of ions decreases ionic conductivity of ion exchange membranes. Because, the ions are clustered, their mobility from one cluster to another, which constitutes ion conductivity, is dependent on the separation between the

clusters. Smaller separation of conducting ions (counter ions) results in better conductive performance because the activation barrier of ions hoping from one cluster to another is decreased. This can be achieved by eradicating clusters. Thus, conductivity of AEMs can be improved if cluster free-membranes with percolated water channels.[25]

From the preceding chapter, we have shown that the strength of dipole-dipole interaction in random anion exchange membranes can be mitigated by pendant side-chains sterics. The sterics between pendant side-chains on adjacent polymer backbones results in a characteristic separation between polymer backbones.[26–28] As a result, backbone-backbone spacing morphology is formed. Because dipoles are situated near polymer backbones, a direct competition between the attractive dipole-dipole interactions and the pendant side-chain sterics results in the transition from ionomer cluster morphology to backbone-backbone spacing morphology with increasing number of carbons on the pendant side-chains. Consequently, the ionomer cluster morphology of the membrane can be replaced by a backbone-backbone spacing morphology with unclustered dipoles by controlling the number of carbons on the pendant side-chains. To obtain high conductivity, constructing a morphology that retains some ionomer cluster morphology with its network of water channels and a high proportion of unclustered dipoles is necessary. This morphology can be obtained by a combination of the sterics between pendant side-chains, and electrostatic attraction between dipoles.

In the previous chapter, Chapter 4, we have designed and synthesized pol(4-vinylpyridine)-*r*-polyisoprene polymer (P4VP-*r*-PI). The random copolymer was then quaternized with 1-alkylbromides (CnBr) having varying number of carbons n = 2,3,4,5,6, and 8. In this work, we crosslink the pendant dienes of the polyisoprene units in P4VP-*r*-PI_CnBr by thiolene chemistry to obtain mechanically robust, water-insoluble ionic conducting membranes. The effect of

crosslinking on the membrane morphology was characterized by wide-angle X-ray scattering (WAXS) and medium-angle X-ray scattering (MAXS). The bromide conductivity determined by electrochemical impedance spectroscopy was correlated to the morphology of the anion exchange membranes. We also studied the water uptake behavior of the membranes with dynamic vapor sorption (DVS) and the relationships between the water uptake behavior and the morphology of the anion exchange membranes.

5.2 Materials and Methods

The monomer, 4-vinylpyridine (96%), was obtained from Alfar Aesar and passed through a basic alumina column. Isoprene (97%) was procured from Acros Organics and was distilled. The initiator, N-tert-butyl-N-[1-diethylphosphono-(2,2-dimethylpropyl)]nitroxide (SG1), was kindly provided by Arkema and used as obtained. N,N-dimethylformamide (99%) was purchased from Fisher Scientific. Pyridine (99%) purchased from Acros Organics was used as received. The following quaternizing agents were used as obtained: bromoethane (99%) and 1-bromopropane (98%) (purchased from T.C.I), 1-bromopentane (purchased from Sigma-Aldrich), 1-bromobutane (98%), 1-bromohexane (99%), 1-bromoheptane (98%), 1-bromooctane (98%), 1-bromononane (99%), 1-bromodecane (98%), 1-bromoundecane (98%), and 1-bromododecane (98%) were all purchased from Alfa Aesar.

5.2.1 Synthesis of P4VP-*r*-PI: Random copolymer, P4VP-*r*-PI, was prepared as follows: 42 mg (0.105 mmoles) of SG1 was added to 10.5 g (0.1 moles) of 4VP and 10.2 (0.15 moles) of isoprene in a Schlenk flask. To the mixture was added 10 ml of pyridine as solvent. After degassing by three freeze-pump-thaw cycles, polymerization was performed at 120 ˚C for 48 hours. The resulting

viscous liquid was quenched in ice and precipitated thrice from dichloromethane in a mixture of hexanes and diethyl ether (1:1). The product was dried in vacuum at room temperature for 48 h.

5.2.2 Quaternization of P4VP-*r*-PI: The random copolymer, P4VP-*r*-PI, was quaternized by ethylbromide, 1-propylbromide, 1-butylbromide, 1-pentylbromide, 1-hexylbromide, and 1-octylbromide. In a typical quaternization protocol, 20 ml of a 1.0 M solution of the quaternizing agent in DMF was added to a solution of 300 mg of polymer in DMF at 60 °C for 10 d. At the end of the reaction, the solution was precipitated into diethyl ether to give a brown solid. The product, P4VP-*r*-PI_CnBr, was dried in vacuum at room temperature for 24 h.

5.2.3 Crosslinking of P4VP-*r*-PI_CnBr: Based on ^{1}H NMR data obtained for P4VP-*r*-PI_CnBr, the pendant vinyl group is assumed to be approximately 10 mol % of the isoprene component. In a typical crosslinking protocol, 100 mg (0.054 mmoles of vinyl group) of P4VP-*r*-PI_C3Br is dissolved in methanol. About 3.03 mg (0.0135 mmoles) of photoinitiator and 23 µL (0.11 mmoles) of 1,10 decanedithiol is added to the solution. The solution is stirred and then cast in the dark on Teflon® sheet. The dried film was then crosslinked by exposure to UV radiation. After treatment with UV, the resulting crosslinked anion exchange membranes, XP4VP-*r*-PI_CnBr, was insoluble in both methanol and water.

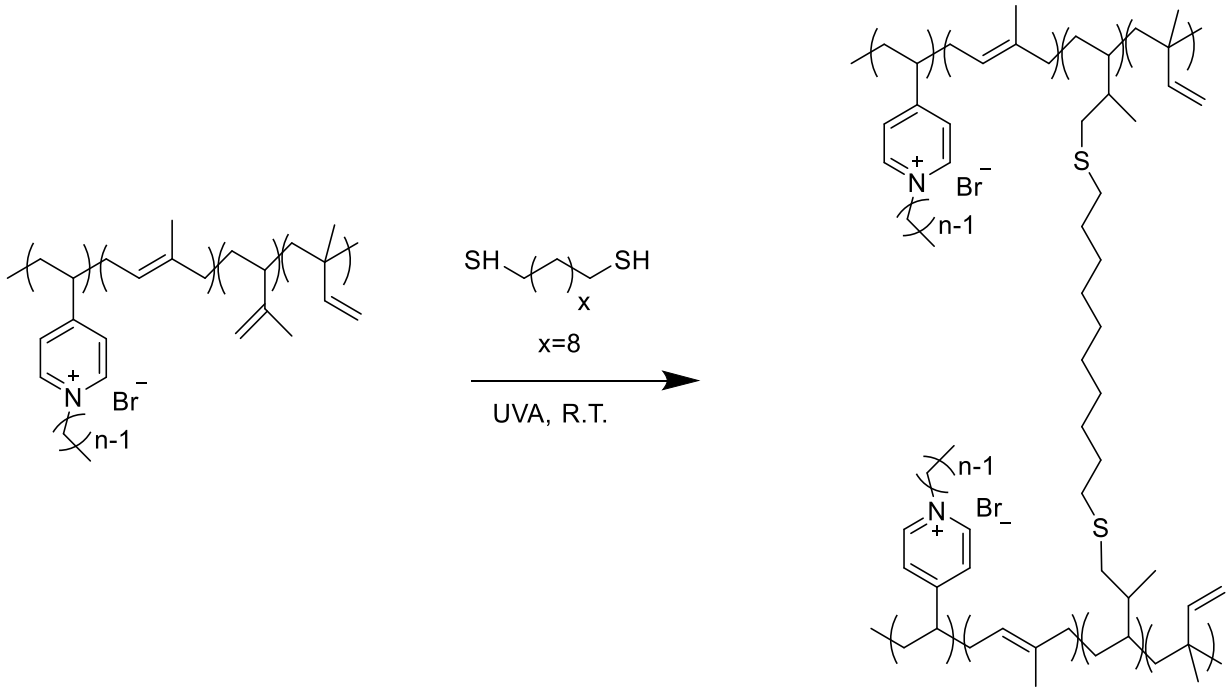

Scheme 5.1. Crosslinking of Quaternized P4VP-*r*-PI (P4VP-*r*-PI_CnBr).

5.2.4 Titration of XP4VP-*r*-PI_CnBr: The change in IEC of the crosslinked polymers was characterized by Mohr's titration. In a typical titration protocol, 70 mg of crosslinked membrane was dried overnight in vacuum. The membrane was then immersed in 20 ml of 0.2 M aqueous solution of $NaNO_3$. After 24 hours, the solution was removed and a second 20 ml of the same $NaNO_3$ with the same molarity was added to the membrane to ensure the complete exchange of anions. The 40 ml solution was then titrated against 0.1 M aqueous solution of $AgNO_3$. Approximately 2 ml of 0.25 M aqueous solution of K_2CrO_4 as indicator was added to the $NaNO_3$/ NaBr before titration. The IEC of XP4VP-*r*-PI_CnBr was calculated from the quantity of $AgNO_3$ that reacted during the titration.

5.2.5 Characterization of XP4VP-*r*-PI_CnBr Series

Number average molecular weight, M_n, was determined using a gel permeation chromatography (GPC) in DMF at a flow rate of 1.0 mL/min using a refractive index detector on an Agilent Technologies 1260 Infinity system. The chemical composition P4VP-*r*-PI was determined using a Bruker 500 fourier-transform nuclear magnetic resonance (FT-NMR). Quaternized samples, P4VP-*r*-PI_CnBr, were drop cast from methanol on Teflon® sheet. Characterization was performed on the resulting films. PerkinElmer Spectrum 100 FTIR with a universal ATR was used to characterize the extent of quaternization. Film samples were mounted on the ATR crystal and secured by the sample holder. Crosslinking of the film was performed via ultraviolet (UV) radiation sourced from an Oriel Flood Exposure System Model. The instrument had a power of 500 W and an irradiation wavelength of 365 nm. Samples were exposed to UV for 20 minutes. Impedance data was collected over the frequency range, 1Hz – 10 KHz by a four-electrode test cell connected to a BioLogic VMP3 multichannel potentiostat. The TestEquity chamber in which experiments were made ensured a proper control of temperature and relative humidity. Measurements were performed through a temperature range of 40 – 90 °C by 10 °C step and 95% RH. The membrane resistance was obtained from the frequency intercept of the Nyquist plot. Ionic conductivity was obtained by measuring the in-plane resistance of the sample. The resistance is then converted to conductivity using the equation

$$\sigma = \frac{d}{Rwt} \qquad (5.1)$$

Where *d* is the distance between the electrodes, *t* is the thickness of the sample and *w* is the width of the membrane defined by the four-electrodes of the test cell.[4,29]

Wide-angle X-ray scattering (WAXS) and medium-angle X-ray scattering (MAXS) measurements were performed in transmission geometry on Molmex Scientific Ganesha SAXS Lab. A double aperture for the Cu-Kα radiation (λ = 1.54 Å), which was the X-ray source, was used. Silver behenate was used as the standard for the momentum transfer calibration. Data was collected for 180 seconds. Depending on the signal-to-noise ratio, data collection could be longer. Azimuthal averaging of the obtained isotropic 2-D pattern was performed to obtain the intensity against wave vector plot.

Scattering results are reported in Figure 5.1. The WAXS spectra show two peaks for XP4VP-*r*-PI_CnBr series. The peak at lower *Q* values is the amorphous halo also known as the van der Waal's peak. It is the van der Waal's distance between non-bonded atoms. The

5.3 Results and Discussion

5.3.1 Characterization of XP4VP-*r*-PI_CnBr by WAXS

Figure 5.1 show the superimposition of X-ray scattering data collected over both the WAXS regime (*Q* ranging from 0.1 – 2 $Å^{-1}$) and the MAXS regime (*Q* ranging from 0.01 – 0.7 $Å^{-1}$). While the WAXS spectra capture the short-range ordering and their corresponding spacing, the MAXS regime probes relatively longer-range ordering and their corresponding spacing. The WAXS spectra show a peak at higher *Q* values, the van der Waal's (VDW) peak. This peak can be observed for all the studied samples of XP4VP-*r*-PI_CnBr series. The VDW peak correlates to the closest distance (VDW spacing) between non-bonded atoms.[27] It is also referred to as the amorphous halo, and it is ubiquitous in amorphous polymers. The intensity of the VDW peak has been used to estimate the relative quantity of backbone-backbone correlations (parallelly arranged backbones) in a polymer.[30] There was no change in the VDW spacing before, and after crosslinking

for a membrane with a given number of carbon on its pendant side-chain. This suggests that crosslinking had no effect on the VDW spacing.

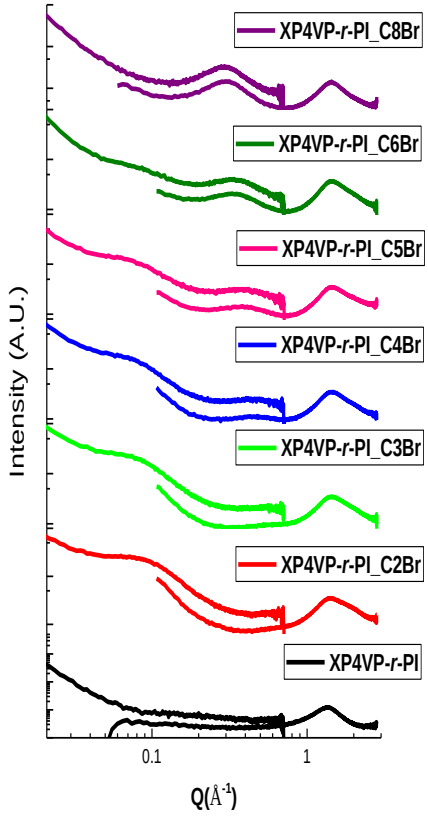

Figure 5.1. Combined MAXS and WAXS scattering profiles for the XP4VP-*r*-PI_CnBr series.

The WAXS spectra also show, to the left of the VDW peak (at lower *Q* values), a peak corresponding to larger spacing, the LVDW peak. This peak was observed for the crosslinked membranes: XP4VP-*r*-PI_C3Br to XP4VP-*r*-PI_C8Br. This peak corresponds to the backbone-backbone spacing between two adjacent polymer backbones.[26,27,31–33] The backbone-backbone spacing increases with increasing number of carbons on the pendant side-chains. The LVDW peak has been observed in the X-ray scattering spectra of other comb-shaped polymers. There were no

differences between the backbone-backbone spacing before and after crosslinking of P4VP-*r*-PI_CnBr. This suggest that crosslinking between the pendant side-chains of adjacent backbones had minimal effect on the value of the backbone-backbone spacing. Although crosslinking did not change the backbone-backbone spacing, it however influenced the LVDW feature in the WAXS spectra of the membranes.

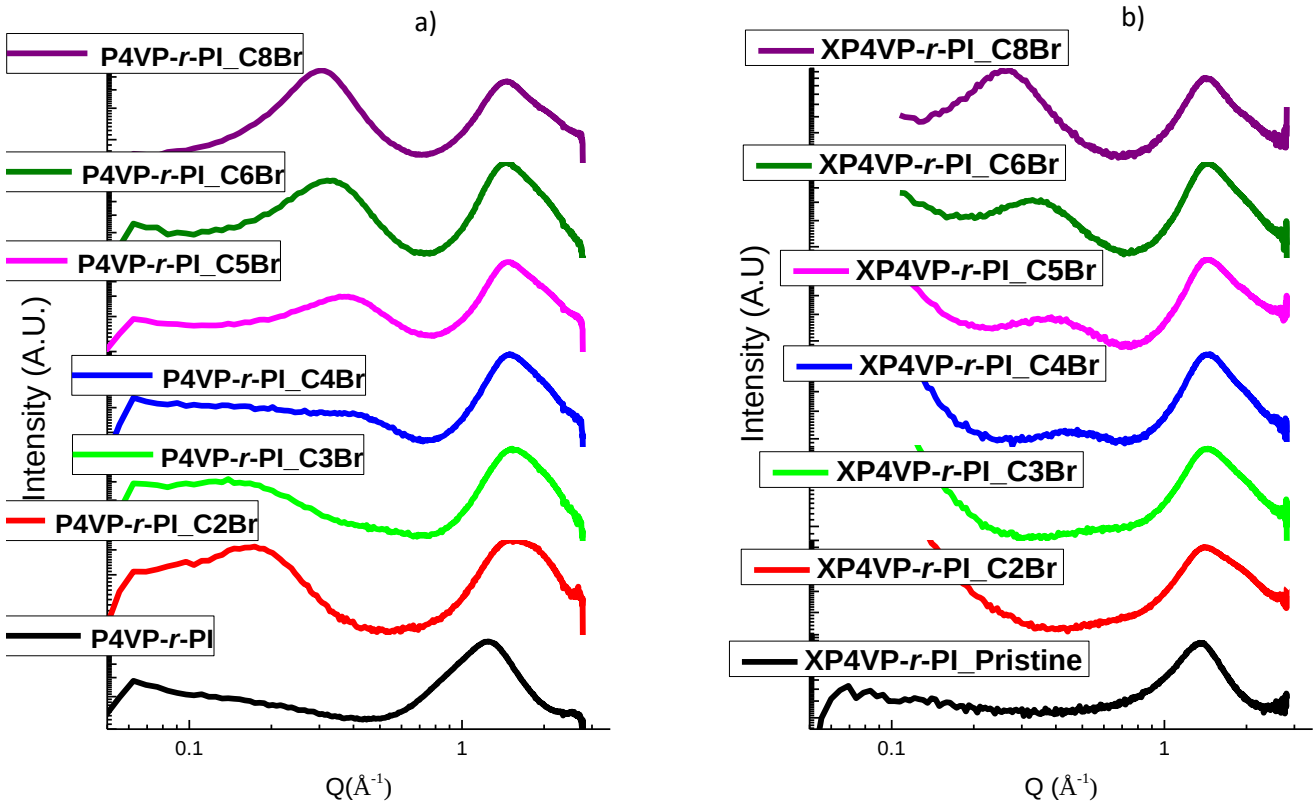

Figure 5.2. Wide-angle X-ray scattering (WAXS) a) spectra before crosslinking, b) after crosslinking.

This effect can be observed in the WAXS spectra of XP4VP-*r*-PI_C4Br (see Figure 5.2). Before crosslinking, P4VP-*r*-PI_C4Br WAXS spectra show a broad peak (which suggests an overlap

between backbone-backbone spacing and cluster-cluster spacing peaks). After crosslinking, XP4VP-*r*-PI_C4Br WAXS spectra show a distinct, LVDW peak, with a distinct backbone-backbone spacing. This deconvolution of an overlapping ionomer and LVDW peak may have been due to the introduction of hydrophobic crosslinkers which decreases the concentration of the overall charges in the crosslinked polymer. Consequently, increasing the spacing between ionic clusters. Thus, shifting the ionomer peak to lower *Q* values. The ratio of the LVDW to VDW, which correlates the quantity of parallel arranged adjacent backbones in the polymer, show that as the number of carbons on the pendant side-chain increases, the fraction of backbone-backbone correlation in the polymer increases. And like in the P4VP-*r*-PI_CnBr series, as the ratio of the LVDW to VDW increases, the ionomer cluster peak intensity decreases and then disappears.

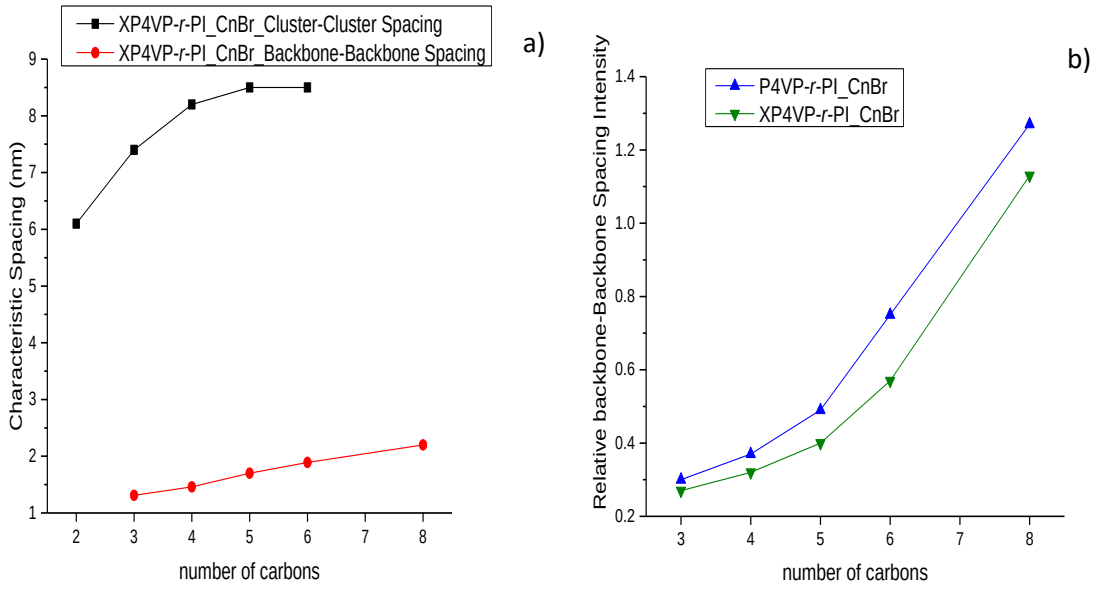

Figure 5.3. a) Characteristic spacing in XP4VP-*r*-PI_CnBr versus number of carbons, b) effect of crosslinking on relative of intensity of backbone – backbone spacing.

The WAXS spectra of the crosslinked membranes show an upturn at lower *Q* values (see Figure 5.2). This upturn suggests a structure beyond the WAXS region. Medium Angle X-ray scattering was performed on XP4VP-*r*-PI_CnBr series to evaluate any morphological features beyond WAXS region. As can be seen from the MAXS spectra (see Figure 5.1), the addition of hydrophobic crosslinkers increases the spacing between ionic clusters due to an increase in the hydrophobic content of the polymer. Unlike the backbone-backbone spacing which increased with increasing number of carbons on the pendant side-chains; the cluster-cluster spacing increased with increasing number of carbons before plateauing at higher number of carbons on the pendant side-chains. Also, with increasing number of carbons on the pendant side-chain the cluster-cluster spacing of the membranes also increases.

An excess of dithiol crosslinker (1,10 decanedithiol) was used for crosslinking of the membranes. The crosslinker has a high boiling point (172 °C at 0.5 mm of Hg), therefore, a substantial quantity of these dithiol crosslinkers remained in the quaternized polymer after the solvent (methanol) from which these membranes were cast has vaporized. These crosslinkers act as plasticizers. The plasticizing effect of these crosslinkers was evident in the tackiness of the polymer membranes after drying the cast membranes for three days at room temperature. This tackiness suggests that the polymer backbones are less rigid, and increase the propensity of the polymer membranes to form an ionomer cluster morphology. Thus, resulting in the formation of ionomer cluster morphology even when there are 6 carbons in the pendant side-chain (an expanded coexistence window). In Chapter 4, a comparison of the P4VP-*r*-PI_CnBr and P4VP-*r*-PI-*r*-PS_CnBr series, also showed that the coexistence window expanded with increasing flexibility of the copolymer. In P4VP-*r*-PI_CnBr, an expanded coexistence window can be observed at 3 – 4 carbons on the

pendant side-chain. However, the more rigid P4VP-*r*-PI-*r*-PS_CnBr series showed a coexistence at 3 carbons on the pendant side-chain.

In the previous chapter, we have shown that with increasing backbone stiffness of the copolymer, backbone-backbone morphology becomes dominant. Even though crosslinking has been known to increase the T_g of crosslinked polymers, however, the plasticization by excess crosslinkers had the opposite effect, thereby, increasing the likelihood for the formation of ionomer cluster morphology. Upon irradiation by UV-A light, the membrane becomes crosslinked, thus, "setting" the membrane morphology. Although these crosslinkers increase the tendency for the membrane to form an ionomer morphology, they do not inhibit the ability of XP4VP-*r*-PI_CnBr to form backbone-backbone morphology. The coexistence regime can be observed using a combination of MAXS and WAXS from XP4VP-*r*-PI_C3Br to XP4VP-*r*-PI_C6Br. Thus, by chemically modifying the copolymer, coexistence between ionomer cluster morphology and backbone-backbone morphology can be expanded in a random, charged, comb-shaped polymer.

The In-Line Dipole Model defines a definite backbone-backbone spacing at which coexistence of ionomer cluster morphology and backbone-backbone morphology should occur. However, this model assumes that the backbones are stiff, thus, it more accurately predicts the coexistence point for polymers with stiffer backbones as observed in Chapter 4. For polymers with more flexible backbones or plasticized matrices, the In-Line Dipole Model can be modified to include a dimensionless flexibility parameter, f, that expands the coexistence regime (see equation (5.2)). For rigid backbones, f is unity.

$$d_L = \left(2\frac{\rho_1\rho_2}{4\pi\varepsilon_o\varepsilon_p K_B T f}\right)^{\frac{1}{3}} \qquad (5.2)$$

5.3.2 Water-Uptake Measurements of the Crosslinked and Uncrosslinked Membranes

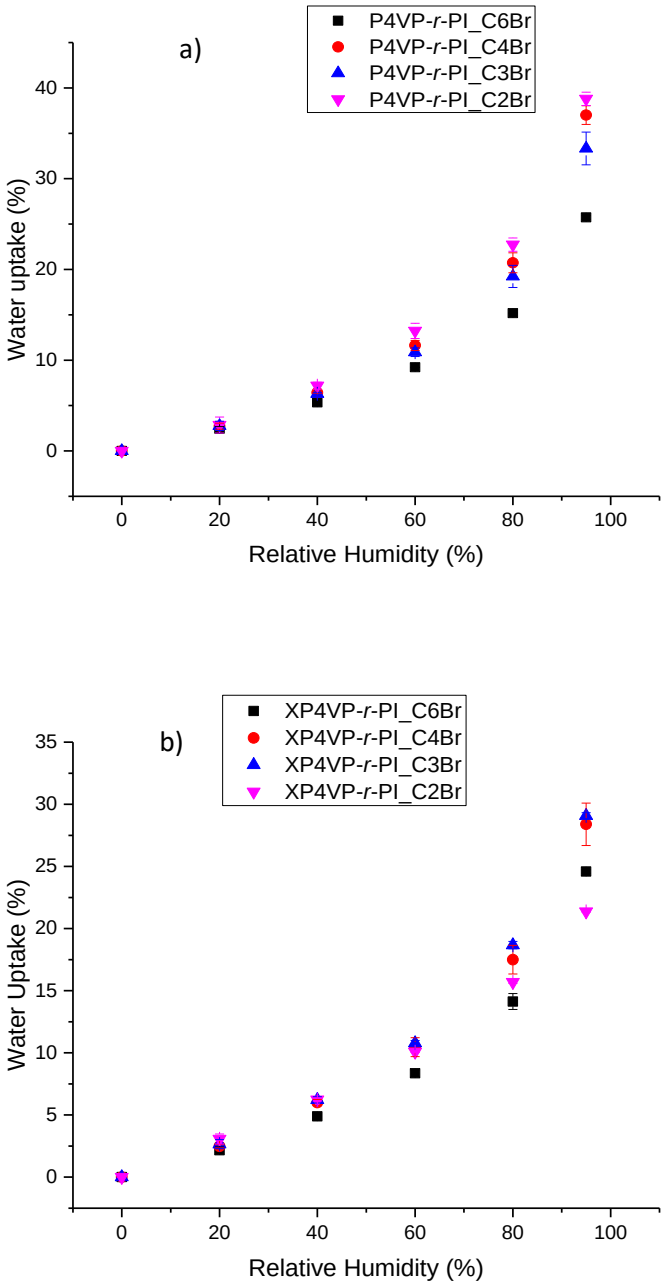

Figure 5.4. Water uptake data for a) P4VP-*r*-PI_CnBr series and b) XP4VP-*r*-PI_CnBr series.

Water uptake results are presented in Figure 5.4. In all cases, after crosslinking the water uptake decreased. However, crosslinking did not significantly affect the number of water molecules per

ion (λ ~7 - 10, at 95 % RH) since crosslinking decreases the concentration of charges in the membranes. A range of λ = 7 – 10, at ~ 95 % RH, for IECs 2.1 – 2.6 mmol/g have also been reported for anion exchange membranes (AEMs) with ionomer cluster morphology.[6]

As can be seen in Figure 5.5, λ, also known as the degree of humidification, increased with increasing number of carbons on the side-chain before decreasing. In ionic membranes, λ have been observed to be dependent on the membrane morphology.[34,35] It has been reported by Weiber and Jannasch that ionic clustering decreased the λ of AEMs in comparison to membranes with randomly distributed unclustered ions.[6] Unlike isolated, clustered dipoles, which form a *quasi-phase* separated morphology with the hydrophobic matrix, unclustered dipoles form a one-phase/continuous/percolated, hydrophilic phase in the membrane. This morphological difference results in higher degree of humidification for the unclustered dipoles in comparison to the clustered dipoles. Kim *et al*. also reported that membranes with clusters have lower λ in comparison to membranes with unclustered dipoles.[36]

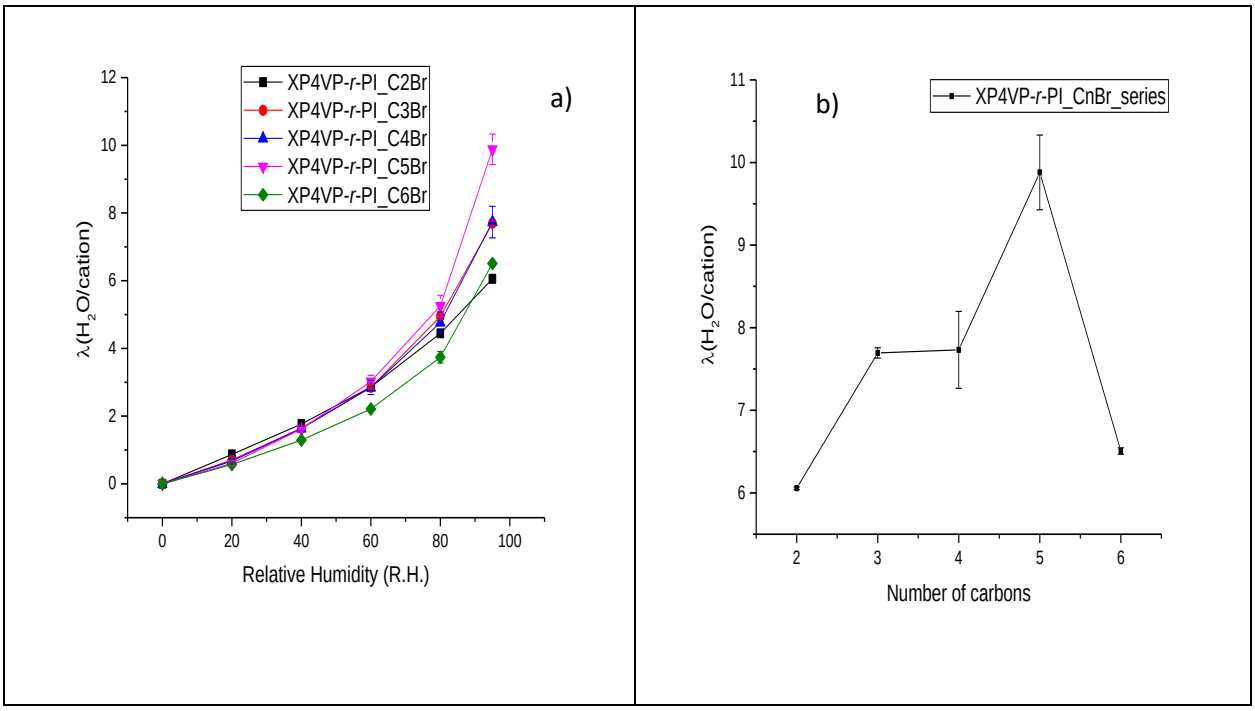

Figure 5.5. a) Water uptake per cation versus relative humidity, b) water uptake per cation versus number of carbons at 95 % relative humidity.

On the other hand, Li *et al.* have reported that increasing the backbone-backbone spacing decreases λ of anion exchange membranes. [34,35] For membranes to take up more water molecules, the dipoles must be within some distance of each other. This can enable water molecules between dipoles to overlap and thus increase the tendency of the overlapping water molecules to take up more water molecules. Dipoles on the polymer backbone take up water molecules on humidification, however, with increasing spacing between the backbones, these dipoles become further away from each other. The dipoles become isolated. Thus, decreasing the λ of the dipoles. See Figure 5.5.

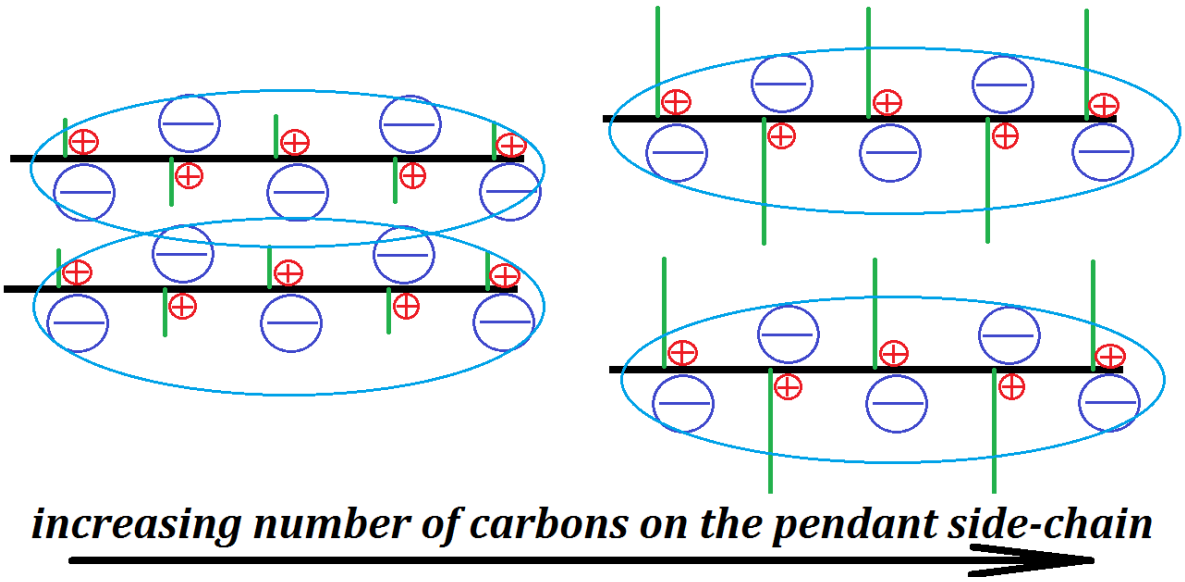

Figure 5.6. Schematic showing overlapping water molecules of dipoles on polymer backbones at shorter pendant side-chains.

Since clustering of ions decreases with increasing length of pendant side-chains, the degree of ionic clustering decreases from XP4VP-*r*-PI_C2Br (which shows no backbone-backbone morphology) to XP4VP-*r*-PI_C6Br (which show a coexistence of ionomer cluster and backbone-backbone morphology). Consequently, λ increased from XP4VP-*r*-PI_C2Br to XP4VP-*r*-PI_C5Br. However, the introduction of longer pendant side-chains (XP4VP-*r*-PI_C6Br), although decreasing the tendency for ions to cluster, increases the spacing between dipoles. This increase in backbone-backbone spacing, according to Li *et al.* would decrease the λ of the membrane. This can be seen in the decrease in λ from XP4VP-*r*-PI_C5Br to XP4VP-*r*-PI_C6Br. See Figure 5.5b.

Overall, λ increases with decreasing quantity of ionomer clusters in ionomer cluster morphology, but also decreases with increasing backbone-backbone spacing. Given that ionomer cluster morphology decreases with increasing backbone-backbone spacing, it follows that for XP4VP-*r*-

PI_CnBr series, an increase in λ with decreasing ionomer cluster morphology will peak followed by a decrease in λ with increasing backbone-backbone spacing.

5.3.2 Electrochemical Impedance Spectroscopy Measurements of XP4VP-*r*-PI_CnBr

Conductivity measurements of the XP4VP-*r*-PI_CnBr series were performed in the Br^- form rather than the OH^- form to decrease the effect of degradation on the structure-conductivity correlation of the series. [37,38]

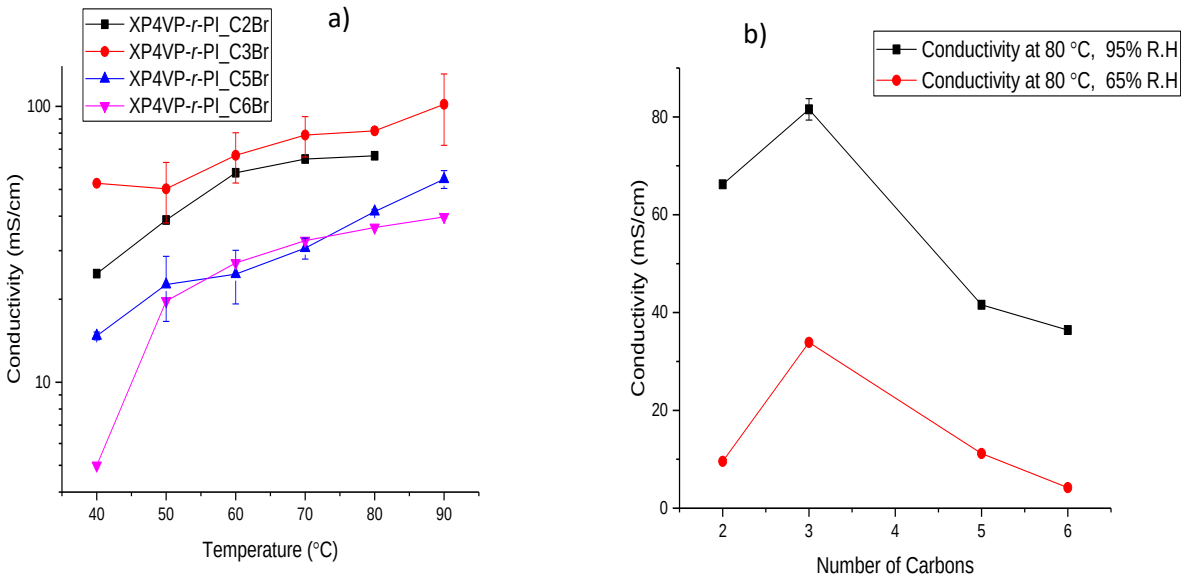

Figure 5.7. a) Conductivity of XP4VP-*r*-PI_CnBr series, b) conductivity data for XP4VP-*r*-PI_CnBr series at 80 °C at 65% and 95% RH.

The titrated IEC. of XP4VP-*r*-PI_CnBr series is approximately 2.0 mmol/g. Thus, significant changes in the conductivity of the XP4VP-*r*-PI_CnBr series is posited to arise from subtle differences in morphology due to the variation in the length of the pendant side-chain. From the

conductivity results (see Figure 5.7), samples with 2 – 3 carbons on the pendant side-chains had better conductivity than those with 5 – 6 carbons. Membranes with ionic clusters have water channels connecting these isolated clusters (dumbbell structure of clusters and water channel). These water channels act as conduits for ion transport, and facilitate the mobility of counter ions in ion exchange membranes.[6,20,25] However, the clustering of ions decreases the ionic conductivity of the counter ions. Firstly, geometric constraints limit the quantity of charges that can pass through the water channels from one cluster to another cluster. Secondly, clustering separates counter ions. The spacing between randomly distributed unclustered ions in a membrane is less than the spacing between randomly distributed ionic clusters in a membrane at the same ionic concentration. Conductivity of counter ions depends on the hopping of counter ions from one cluster to another or from one unclustered dipole to another.[25,39,40] The higher the cluster-cluster distance the more the energy barrier to the movement of counter ions from one cluster to another cluster.[25] Unclustered dipoles having smaller spacing result in a low energy barrier. This leads to higher ionic conductivity. Finally, conductivity is dependent on the concentration of mobile counter ions and not just concentration of counter ions. The clustering of ions decreases the concentration of mobile counter ions in the media. Clustered ions are arranged in a lattice-like substructure within a randomly distributed cluster-matrix superstructure. The ions in the clusters are bound together by Coulomb forces. The lattice energy of a cluster, which is approximately the Bonne – Lande lattice energy, is proportional to the coordination number of the ions (Madulung constant) and the number of ions in the cluster. Consequently, it will take a high degree of humidification and an elevated temperature to dissociate the ions in a cluster in comparison to unclustered dipoles. This is corroborated by SANS, and SAXS experiments which show the presence of ionic clusters even in highly humidified membranes.[25,36] Besides, from the water uptake measurement for XP4VP-*r*-

PI_CnBr series, the λ for ionic clusters is less than that for unclustered dipoles. This further suggests that the concentration of free counter ions in unclustered dipoles randomly distributed in a membrane would be higher than that in ionic clusters.

While ionic clusters provide water channels that improve conductivity, the clusters themselves are a barrier to improved conductivity. Elimination of clusters would therefore decrease the energy barrier impeding transport of counter ions from one point to another across the polymer membrane. Cluster-free membranes would have increased ionic conductivity.

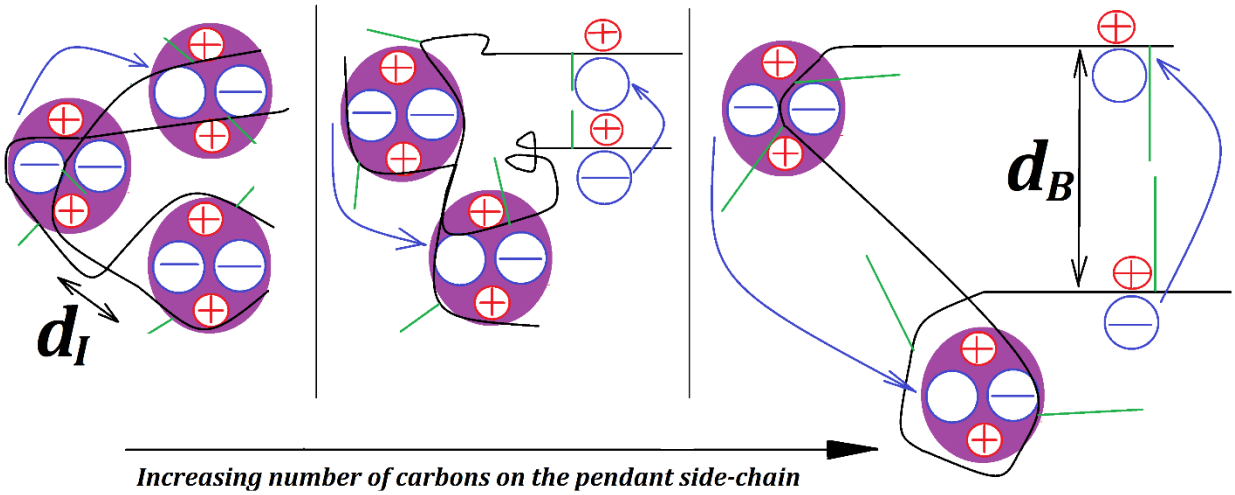

Figure 5.8. A scheme showing the different transport modes in the XP4VP-*r*-PI_CnBr series.

According to Balsara and Beers, conductivity in polyelectrolytes can be improved by eradicating ionic clusters.[25] Jannasch and Weiber have reported that the elimination of clusters increased the conductivity in anion exchange membranes with high IECs.[6] Hickner and Chen also reported that decreasing the degree of order in random quaternary ammonium functionalized poly- (arylene ether ketone)s increased conductivity.[20]

Table 5.1. Summary of theoretical and titrated IEC of the polymer membranes

	IEC_{TH} (mmol/g)	**IEC_{TIT} (mmol/g)**	λ_U	λ_X
XP4VP-*r*-PI_C8Br	**1.95**	**1.96±0.03**	-	-
XP4VP-*r*-PI _C6Br	**2.07**	**2.03±0.03**	**5.7±0.05**	**6.7±0.04**
XP4VP-*r*-PI_C5Br	**2.13**	**2.10±0.03**	-	-
XP4VP-*r*-PI_C4Br	**2.15**	**2.04±0.02**	**7.6±0.20**	**7.7±0.50**
XP4VP-*r*-PI_C3Br	**2.25**	**2.10±0.04**	**6.6±0.40**	**7.7±0.06**
XP4VP-*r*-PI_C2Br	**2.34**	**1.96±0.01**	**7.3±0.10**	**6.1±0.02**
XP4VP-*r*-PI	-	-	-	-
IEC_{TH} the IEC from the NMR, IEC_{TIT} is the titrated IEC, λ_U and λ_X are λ for the uncrosslinked and crosslinked respectively measured at 60 °C.				

The competition between backbone-backbone morphology and ionic clustering results in the decrease in the concentration of ionic clusters when pendant side-chains with higher number of carbons is introduced. This decrease in the degree of clustering may have resulted in the higher conductivity of XP4VP-*r*-PI_C3Br in comparison to XP4VP-*r*-PI_C2Br. However, while side-chains tend to disfavor ionic cluster formation, the longer pendant side-chains introduces another kind of counter ion separation. Replacing one form of Br^- - Br^- separation (cluster-cluster separation) by another (backbone-backbone spacing) could explain the decrease in conductivity from XP4VP-*r*-PI_C3Br to XP4VP-*r*-PI_C6Br. Cruz *et al.* have shown that the conductivity of ionic membranes decreases with increasing backbone-backbone spacing of poly (1-*n*-alkyl-3-vinylimidazoliumbromide).[28] Furthermore, the large cluster-cluster spacing in XP4VP-*r*-PI_C5Br and XP4VP-*r*-PI_C6Br may have further contributed to the decrease in its conductivity in

comparison to XP4VP-*r*-PI_C3Br. Larger cluster-cluster spacing in ionomer clusters have been known to hamper conductivity.[4]

In comparison to other Br^- conductivity measurements found in the literature, XP4VP-*r*-PI_CnBr series had high Br^- conductivity.[6,19,20] Conductivity of XP4VP-*r*-PI_C3Br from 40 – 80 °C (60 – 85 mS/cm) was about twice the conductivity values reported by both the Jannasch (20 – 44 mS/cm) and Hickner (20 – 59 mS/cm) groups even though those membranes had IECs > 2.5 mmol/g with similar λ values.[6,20] The improved conductivity of XP4VP-*r*-PI_CnBr series as a whole might be due to the synergistic effect of ionic clustering and backbone-backbone spacing. While the former preserves water channels, the later ensures that more unclustered dipoles are more homogeneously distributed in the matrix and readily available for conductivity. The exceptionally high conductivity of XP4VP-*r*-PI_C3Br may be due to this phenomenon.

5.4 Conclusion

Mechanically robust, water insoluble anion exchange membranes were prepared. Morphological characterizations of these membranes show ionomer cluster morphology for XP4VP-*r*-PI_C2Br, and coexistence of ionomer cluster and backbone-backbone morphologies for XP4VP-*r*-PI_C3Br to XP4VP-*r*-PI_C6Br and a backbone-backbone morphology for XP4VP-*r*-PI_C8Br. The X-ray scattering spectra for the XP4VP-*r*-PI_CnBr series show that the concentration of backbone-backbone correlations increases with increasing number of carbons on the pendant side-chain. The larger window of coexistence may have resulted from the plasticizing effect the 1,10 decanedithiol had on the polyisoprene matrix. Dynamic vapor sorption measurements show that with increasing quantity of parallel arranged backbones the degree of humidification, λ, increases (XP4VP-*r*-PI_C3Br to XP4VP-*r*-PI_C5Br). However, for membranes with high number of carbons on the

pendant side-chains (XP4VP-*r*-PI_C6Br), although they had comparatively higher concentration of periodically ordered backbones, the large backbone-backbone spacing between these parallel arranged backbones decrease the water uptake of the membrane. The bromide conductivity of the XP4VP-*r*-PI_CnBr series were exceptionally high. Conductivity increased with increasing number of carbons on the pendant side-chain. This is because with increasing number of carbons on the pendant side-chains, the concentration of unclustered dipoles increases. However, for membranes with high number of carbons on the pendant side-chain (XP4VP-*r*-PI_C6Br), the cluster-cluster spacing between the bromide counter ions is replaced with backbone-backbone spacing. Resulting in lower ionic conductivity.

5.5 References

(1) Yuan, H. Synthesis and Structure-Property Relationships of Polymeric Membranes for Small Molecule Transport, University of Massachusetts, Amherst, 2017.

(2) Marino, M. G.; Kreuer, K. D. Alkaline Stability of Quaternary Ammonium Cations for Alkaline Fuel Cell Membranes and Ionic Liquids. *ChemSusChem* **2015**, *8* (3), 513–523.

(3) Marino, M. G.; Melchior, J. P.; Wohlfarth, A.; Kreuer, K. D. Hydroxide, Halide and Water Transport in a Model Anion Exchange Membrane. *J. Memb. Sci.* **2014**, *464*, 61–71.

(4) Tsai, T. H.; Ertem, S. P.; Maes, A. M.; Seifert, S.; Herring, A. M.; Coughlin, E. B. Thermally Cross-Linked Anion Exchange Membranes from Solvent Processable Isoprene Containing Ionomers. *Macromolecules* **2015**, *48* (3), 655–662.

(5) Dang, H.-S.; Jannasch, P. Exploring Different Cationic Alkyl Side Chain Designs for

Enhanced Alkaline Stability and Hydroxide Ion Conductivity of Anion-Exchange Membranes. *Macromolecules* **2015**, *48* (16), 5742–5751.

(6) Weiber, E. A.; Jannasch, P. Ion Distribution in Quaternary-Ammonium-Functionalized Aromatic Polymers : Effects on the Ionic Clustering and Conductivity of Anion-Exchange Membranes. *ChemSusChem* **2014**, *7*, 2621–2630.

(7) Smitha, B.; Sridhar, S.; Khan, A. A. Solid Polymer Electrolyte Membranes for Fuel Cell Applications - A Review. *J. Memb. Sci.* **2005**, *259* (1–2), 10–26.

(8) Reshetenko, T.; Odgaard, M.; Schlueter, D.; Serov, A. Analysis of Alkaline Exchange Membrane Fuel Cells Performance at Di Ff Erent Operating Conditions Using DC and AC Methods. *J. Power Sources* **2018**, *375* (September 2017), 185–190.

(9) Zhang, X.; Chen, P.; Shi, Q.; Li, S.; Gong, F.; Chen, X.; An, Z. ScienceDirect Block Poly (Arylene Ether Sulfone) Copolymers Bearing Quaterinized Aromatic Pendants : Synthesis , Property and Stability. *Int. J. Hydrogen Energy* **2017**, *42* (42), 26320–26332.

(10) Dekel, D. R. Review of Cell Performance in Anion Exchange Membrane Fuel Cells. *J. Power Sources* **2018**, *375*, 158–169.

(11) Gottesfeld, S.; Dekel, D. R.; Page, M.; Bae, C.; Yan, Y.; Zelenay, P.; Seung, Y. Anion Exchange Membrane Fuel Cells : Current Status and Remaining Challenges. *J. Power Sources* **2018**, *375*, 170–184.

(12) Arges, C. G.; Ramani, V.; Pintauro, P. N. Anion Exchange Membrane Fuel Cells. *Elctrochemical Soc. Interface* **2010**, 31–35.

(13) Pan, J.; Chen, C.; Li, Y.; Wang, L.; Tan, L.; Li, G.; Tang, X.; Xiao, L.; Lu, J.; Zhuang, L.

Constructing Ionic Highway in Alkaline Polymer Electrolytes. *Energy Environ. Sci.* **2014**, *7* (1), 354.

(14) Gierke, T. D.; Munn, G. E.; Wilson, F. C. The Morphology in Nafion Perfluorinated Membrane Products, as Determined by Wide- and Small- Angle X-Ray Studies. *J. Polym. Sci. Polym. Phys. Ed.* **1981**, *19* (11), 1687–1704.

(15) Orfino, F. P.; Holdcroft, S. The Morphology of Nafion: Are Ion Clusters Bridged by Channels or Single Ionic Sites? *J. New Mater. Electrochem. Syst.* **2000**, *3* (4), 285–290.

(16) Michel, G.; Divoux, M.; Moore, R. B.; Baird, D. G.; Ellis, M. W.; Mcgrath, J. E.; Mauritz, K. A.; Michel, G.; Divoux, M. No Title, Virginia Polytechnic Institute and State, 2012.

(17) Bae, B.; Yoda, T.; Miyatake, K.; Uchida, H.; Watanabe, M. Proton-Conductive Aromatic Ionomers Containing Highly Sulfonated Blocks for High-Temperature-Operable Fuel Cells. *Angew. Chemie - Fuel Cell Membr.* **2010**, *49* (2), 317–320.

(18) Couture, G.; Alaaeddine, A.; Boschet, F.; Ameduri, B. Polymeric Materials as Anion-Exchange Membranes for Alkaline Fuel Cells. *Prog. Polym. Sci.* **2011**, *36* (11), 1521–1557.

(19) Tsai, T. Ionic Copolymers for Alkaline Anion Exchange Membrane Fuel Cells (AAEMFCs), University of Massachusetts, 2014.

(20) Chen, D.; Hickner, M. A. Ion Clustering in Quaternary Ammonium Functionalized Benzylmethyl Containing Poly(arylene Ether Ketone)s. *Macromolecules* **2013**.

(21) Eisenberg, A.; Hird, B.; Moore, R. B. A New Multiplet-Cluster Model for the Morphology of Random Ionomers. *Macromolecules* **1990**, *23* (18), 4098–4107.

(22) Eisenberg, A. Clustering of Ions in Organic Polymers. A Theoretical Approach. *Macromolecules* **1970**, *3* (2), 147–154.

(23) Middleton, L. R.; Winey, K. I. Nanoscale Aggregation in Acid- and Ion-Containing Polymers. *Annu. Chem. Biomol. Eng* **2017**, *8*, 499–523.

(24) Moore, R. B.; Gauthier, M.; Williams, C. E.; Eisenberg, A. Heterogeneities in Random Ionomers - a Small-Angle X-Ray-Scattering Investigation of Alkylated Polystyrene-Based Materials. *Macromolecules* **1992**, *25* (21), 5769–5773.

(25) Beers, K. M.; Balsara, N. P. Design of Cluster-Free Polymer Electrolyte Membranes and Implications on Proton Conductivity. *ACS Macro Lett.* **2012**, *1* (10), 1155–1160.

(26) Platé, N. A.; Shibaev, V. P. Comb-like Polymers. Structure and Properties. *J. Polym. Sci. Macromol. Rev.* **1974**, *8* (1), 117–253.

(27) Miller, R. L.; Boyer, R. F.; Heijboer, J. X-Ray Scattering from Amorphous Acrylate and Methacrylate Polymers: Evidence of Local Order. *J. Polym. Sci. Polym. Phys. Ed.* **1984**, *22* (12), 2021–2041.

(28) Salas-De La Cruz, D.; Green, M. D.; Ye, Y.; Elabd, Y. A.; Long, T. E.; Winey, K. I. Correlating Backbone-to-Backbone Distance to Ionic Conductivity in Amorphous Polymerized Ionic Liquids. *J. Polym. Sci. Part B Polym. Phys.* **2012**, *50* (5), 338–346.

(29) Zhang, W.; Liu, Y.; Jackson, A. C.; Savage, A. M.; Ertem, S. P.; Tsai, T. H.; Seifert, S.; Beyer, F. L.; Liberatore, M. W.; Herring, A. M.; et al. Achieving Continuous Anion Transport Domains Using Block Copolymers Containing Phosphonium Cations. *Macromolecules* **2016**, *49* (13), 4714–4722.

(30) Zhang, Z.; Liu, C.; Cao, X.; Wang, J.-H. H.; Chen, Q.; Colby, R. H. Morphological Evolution of Ionomer/Plasticizer Mixtures during a Transition from Ionomer to Polyelectrolyte. *Macromolecules* **2017**, *50* (3), 963–971.

(31) Beiner, M.; Huth, H. Nanophase Separation and Hindered Glass Transition in Side-Chain Polymers. *Nat. Mater.* **2003**, *2*, 595–599.

(32) Hiller, S.; Pascui, O.; Budde, H.; Kabisch, O.; Reichert, D.; Beiner, M. Nanophase Separation in Side Chain Polymers: New Evidence from Structure and Dynamics. *New J. Phys.* **2004**, *6*.

(33) Pankaj, S.; Hempel, E.; Beiner, M. Side-Chain Dynamics and Crystallization in a Series of Regiorandom Poly (3-Alkylthiophenes). *Macromolecules* **2009**, *42*, 716–724.

(34) Li, N.; Leng, Y.; Hickner, M. A.; Wang, C. Y. Highly Stable, Anion Conductive, Comb-Shaped Copolymers for Alkaline Fuel Cells. *J. Am. Chem. Soc.* **2013**, *135* (27), 10124–10133.

(35) Li, N.; Yan, T.; Li, Z.; Thurn-Albrecht, T.; Binder, W. H. Comb-Shaped Polymers to Enhance Hydroxide Transport in Anion Exchange Membranes. *Energy Environ. Sci.* **2012**, *5*, 7888–7892.

(36) Kim, S. Y.; Park, M. J.; Jackson, A. Confinement Effects on Watery Domains in Hydrated Block Copolymer Electrolyte Membranes. *Macromolecules* **2010**, 8128–8135.

(37) Arges, C. G.; Parrondo, J.; Johnson, G.; Nadhan, A.; Ramani, V. Assessing the Influence of Different Cation Chemistries on Ionic Conductivity and Alkaline Stability of Anion Exchange Membranes. *J. Mater. Chem.* **2012**, 3733–3744.

(38) Nun, S. A.; Hickner, M. A. Quantitative 1 H NMR Analysis of Chemical Stabilities in Anion- Exchange Membranes. *ACS Macro Lett.* **2013**, *2* (1), 49–52.

(39) Kusoglu, A.; Weber, A. Z. New Insights into Per Fluorinated Sulfonic-Acid Ionomers. *Chem. Rev.* **2017**, *117*, 987–1104.

(40) Wohlfarth, A.; Smiatek, J.; Kreuer, K.; Takamuku, S.; Jannasch, P.; Maier, J. Proton Dissociation of Sulfonated Polysulfones: In Fl Uence of Molecular Structure and Conformation. *Macromolecules* **2015**, *48*, 1134–1143.

CHAPTER 6

ELECTROSTATIC FORCES-INDUCED SEMI-CRYSTALLINITY IN QUATERNIZED HOMOPOLYMERS AND BLOCK COPOLYMERS OF P4VP

6.1 Introduction

The obvious correlation between the structure of polymer membranes and their properties have been an attractive part of polymer science.[1–14] The inter-play of intermolecular forces can be used to design new polymer structures with interesting property correlations.[15] However, understanding intermolecular forces that produce such structures in polymers has been scarce in the literature. In this work, utilizing electrostatic attractive and steric forces at the intermolecular level, we were able to design a new class of atactic semi-crystalline polyelectrolytes whose structure can be precisely controlled by the chemistry of post-polymerization modification of the polymer.

The formation of crystalline features in polymers is dependent on the ease of chain packing. Accordingly, vinyl polymers with stereo-regular pendant groups (isotactic and syndiotactic) are semi-crystalline. Atactic polymers do not form crystalline domains because of the stereo-irregularity of the pendant group arrangement on the polymer backbone. Nevertheless, atactic polyvinylalcohol (PVOH) is an exception. Synthesized from the hydrolysis of polyvinylacetate (PVA), the semi-crystalline nature of PVOH stems from the hydrogen bonding between the pendant hydroxyl groups.[16–18] However, similar semi-crystalline features has not been reported in other atactic polymers, not even those with hydroxyl groups.[19–27]

Hydrogen bonding is a type of dipole-dipole interaction.[1,28,29] Thus, in theory, strong dipole-dipole interaction between pendant groups in an atactic vinyl polymer backbone could give rise to a semi-crystalline structure. Charged species in random vinyl polyelectrolytes interact by dipole-dipole

interactions. Dipole-dipole interactions in these materials facilitates the clustering of dipoles. This results in a distribution of dipole clusters in the polymer matrix. [12,30–34] However, to the best of our knowledge, there has been no report suggesting that dipole-dipole interactions have produced a semi-crystalline feature in solid polyelectrolytes. As a result, most solid polyelectrolytes are amorphous. The lack of semi-crystalline character in solid polyelectrolytes may be because the dipole-dipole attraction needed to produce semi-crystalline features can be decreased by steric repulsion of pendant groups between polymer backbones. This effect can be observed in random polyelectrolytes with pendant side-chains. Longer side-chains will increase the spacing between polymer backbones, thus, diametrically reducing the strength of the interaction of dipoles situated on the backbones. This can prevent the formation of ionomer morphology.

To study the direct effect of side-chain length on dipole-dipole interaction, poly(4-vinylpyridine), due to its availability and ease of quaternization, was chosen as the platform polymer. Upon quaternization, both pendant side-chain and dipoles can be introduced into the polymer.

In Chapter 4, poly(4-vinylpyridine), P4VP, was prepared by the polymerization of 4-vinylpyridine, 4VP, by Nitroxide Mediated Polymerization, at 110 ˚C, for 3 hours. Characterization of the resultant polymer, P4VP, by ^{1}H NMR and DMF GPC showed that the polymer had a molecular weight of 33000 g/mol and a Đ of 1.5. The subsequent product, poly(4-vinylpyridine), P4VP, was successfully quaternized in DMF by *n*-alkylbromides (CnBr) (where *n* is the number of carbons on the alkylbromides). The quaternizing agents ethylbromide, 1-propylbromide, 1-butylbromide, 1-pentylbromide, 1-hexylbromide, 1-heptylbromide, 1-octylbromide, 1-nonylbromide, 1-decylbromide, 1-undecylbromide, and 1-dodecylbromide (that is *n* values ranging from 2 – 12). Characterization of the quaternized P4VP by X-ray scattering (WAXS) show backbone-backbone spacing for all quaternized polymers except the ethylbromide quaternized sample which

surprisingly showed semi-crystalline peaks. The long-range ordering in this polymer was attributed to the short side-chain which exposes the adjacent backbones to strong dipole-dipole interaction. It is more particularly interesting because the pristine homopolymer is atactic, therefore, this polymer P4VP_C2Br is also atactic. This is analogous to the semi-crystallinity in PVOH. This interesting result spurred us to quaternize P4VP homopolymer with methyl and ethyl iodides. We hypothesized that P4VP quaternized by these alkyl iodides would show similar semi-crystallinity to P4VP_C2Br due to the short pendant side-chains of the 1-alkyliodide quaternized samples.

6.1.1 Quaternization of P4VP by MethylIodide and EthylIodide

In a typical quaternization protocol, in a 50 ml centrifuge vial equipped with a stirrer, 300 mg of P4VP was dissolved in 15 ml of DMF. To the solution was added 4 molar equivalent amount of 1.0 M ethyliodide in DMF at 60 ˚C. There was an initial precipitation of the polymer in the vial after 2 hours. About 3 ml of methanol was then added to the mixture to give a clear solution. After 10 days, the solution was then precipitated in diethylether. The product, P4VP_C2Br, was dried in vacuum at room temperature for 2 days.

6.2 Results and Discussion

6.2.1 Characterization of Quaternized Samples by FTIR

The quaternized polymers, P4VP_C2Br to P4VP_C12Br was characterized by ATR-FTIR by monitoring the disappearance of the C=N aromatic pyridine vibration at 1414 cm^{-1} and the appearance of 1640 cm^{-1} associated with the pyridinium vibration.[35–41]See Figure 6.1.

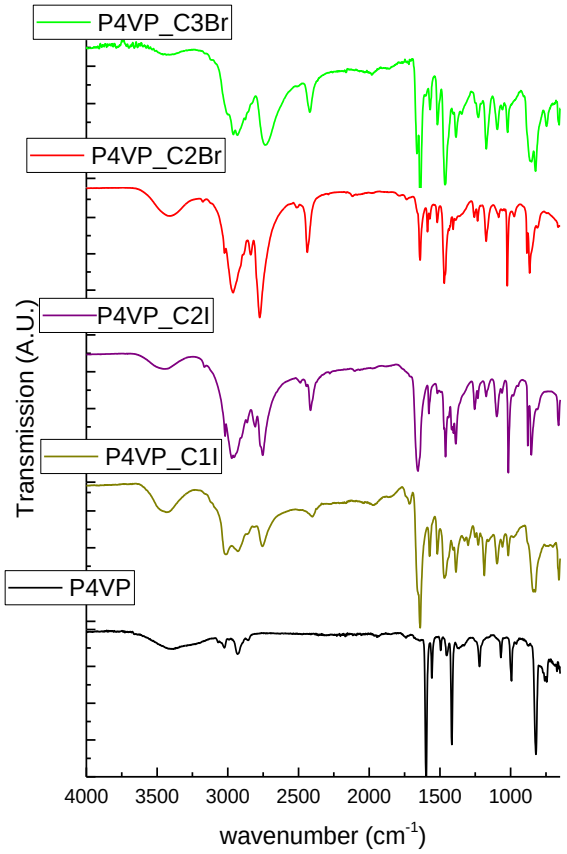

Figure 6.1. Characterization of P4VP, P4VP_C1I, P4VP_C2I, P4VP_C2Br, and P4VP_C3Br by FTIR confirming complete quaternization.

The WAXS spectra show two peaks for P4VP_C3Br (see Figure 6.2). The peak at larger *Q* values is the van der Waal's (VDW) distance between non-bonded atoms. This feature size, also known

as the amorphous halo, is characteristic of all amorphous polymers.[9,34] On quaternization the VDW shifts to lower *Q* values suggesting compact packing of the polymer chains.[42] The VDW distance increased with increasing number of carbons on the pendant side-chains. This suggests less compact packing with increasing length of the side-chain. Another peak larger than VDW peak, the LVDW peak, can be observed at lower *Q* values. This peak represents the backbone-backbone spacing between adjacent polymer chains. The backbone-backbone spacing increases linearly with increasing number of carbons on the pendant side-chains and has been observed in different comb-shaped polymer series.[12,33,43–46]Also see Chapter 4. This backbone-backbone morphology suggests that for P4VP_C3Br to P4VP_C12Br regime the sterics between pendant side-chain is dominant. The dipoles in the quaternized samples are situated near the backbone of the polymers. The dipole attractive potential, F_{D-A}, is dependent on the separation between adjacent dipoles. With increasing number of carbons on the pendant side-chain, the sterics between side-chains results in increasing spacing between dipoles on adjacent backbones. The strength of F_{D-A} between dipoles on adjacent polymer backbones decreases. Thus, the dominance of the backbone-backbone morphology is dependent on the sterics of the pendant side-chains.

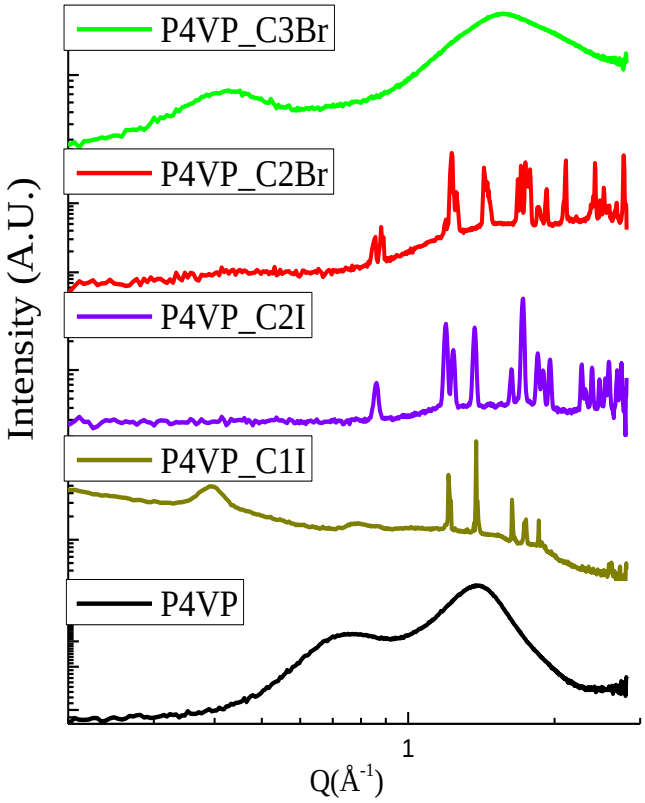

Figure 6.2. The WAXS spectra of P4VP, P4VP_C1I, P4VP_C2I, P4VP_C2Br, and P4VP_C3Br.

Also evident in Figure 6.2 is the semi-crystalline peaks in P4VP_C1I, P4VP_C2I and P4VP_C2Br. For samples with 2 or less carbons on the pendant side-chain (P4VP_C1I, P4VP_C2I and P4VP_C2Br), there is strong dipole-dipole attraction between the dipoles on adjacent polymer backbones. This interaction between polymer backbones facilitates the alignment of polymer chains, thereby, resulting in a semi-crystalline structure thus confirming our hypothesis. Furthermore, the ubiquitous amorphous halo peak disappears corroborating the semi-crystalline morphology of these samples.

The peaks in the WAXS spectra for the ethyl quaternized samples appear to be similar. These peaks are however different from the methyl quaternized P4VP. This suggests that the type of unit

structure is strongly dependent on the number of carbons on the pendant side-chains and less on the type of counterions. Some of the peaks in the WAXS spectra of P4VP_C2Br appear to be split. This suggests that there might be two or more unit cells in the polymer crystal structure. The semi-crystalline polymer may be polymorphic; being of similar structure but having different lattice parameters. The full indexing of the WAXS reflections of P4VP_C1I, P4VP_C2I, and P4VP_C2Br remains an open question for future investigators.

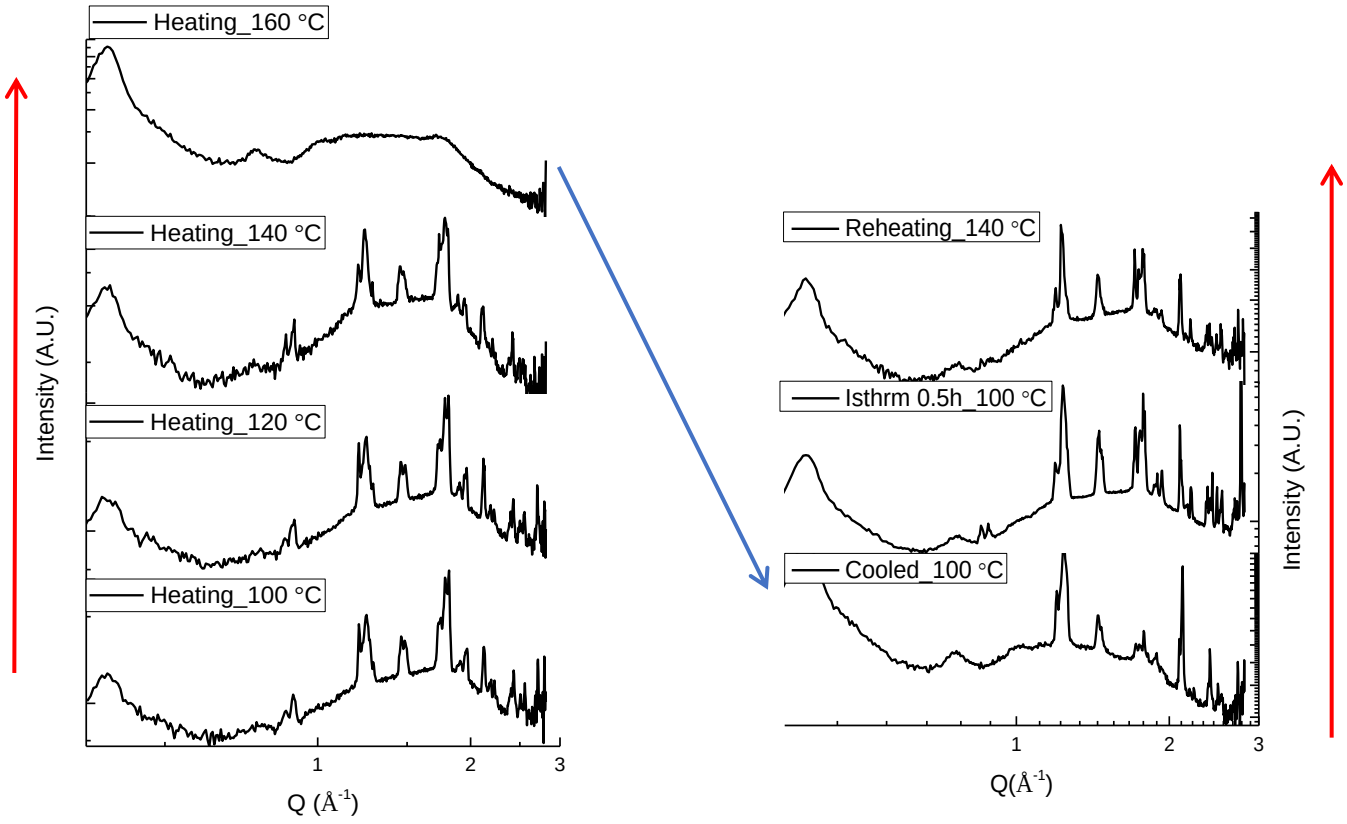

Figure 6.3. WAXS spectra of P4VP_C2Br on heating (left) and WAXS spectra of P4VP_C2Br on reheating (right).

The response of the semi-crystalline structure of P4VP_C2Br to heating was investigated. The heating, cooling, and reheating scattering data are presented in Figure 6.3. On heating from 25 –

75 °C, the WAXS spectra showed no noticeable changes in the relative peak intensities. However, from 100 – 140 °C, there were some changes in peak intensities. Peaks at 1.474 and 1.507 $Å^{-1}$, at 100 °C, merged into a single peak at 140 °C. There was also a decrease in the intensity of the peak at 1.955 $Å^{-1}$and a corresponding increase in 1.206 $Å^{-1}$ relative to 1.804 $Å^{-1}$. Furthermore, the intensity of the broad amorphous halo background relative to the Kapton peak increased with increasing temperature. At 160 °C, all traces of semi-crystallinity disappear, and the scattering result shows an amorphous halo. The sample, P4VP_C2Br, has melted.

On cooling rapidly to 100 °C, the crystalline peaks reappear. In comparison to the peaks at 100 °C before melting, the peaks at 0.871 and 0.899 $Å^{-1}$ were conspicuously absent. The intensity of peaks 1.210, 1.719, and 1.785 $Å^{-1}$ decreased while that of 2.120 $Å^{-1}$ increased relative to 1.253 $Å^{-1}$. The sample was then heated isothermally for 30 minutes at 100 °C. The structure of the sample after this treatment was similar to its pre-melt structure. This behavior of polymers having different diffraction peaks with respect to different recrystallization conditions, like temperature, is typical for polymorphous polymers.[47] The WAXS spectrum at 140 °C before and after melting have the same peak positions on the Q-axis but different intensities relative to one another. The heating and reheating experiments show that the melting-solidification transitions of P4VP_C2Br, like other semi-crystalline polymers, is reversible.

A characteristic feature of semi-crystalline polymers is their melting and recrystallization temperatures. The results obtained by DSC, (see Figure 6.4) show that P4VP_C1I, P4VP _C2Br and P4VP _C2I all have melting and recrystallization temperatures while P4VP, P4VP_C3Br show no such thermal profile. This confirms that with increasing number of carbons on the pendant side-chain of the polymer, the semi-crystalline character of the series disappears and the quaternized polymers revert to the amorphous structure typical of atactic backbones.

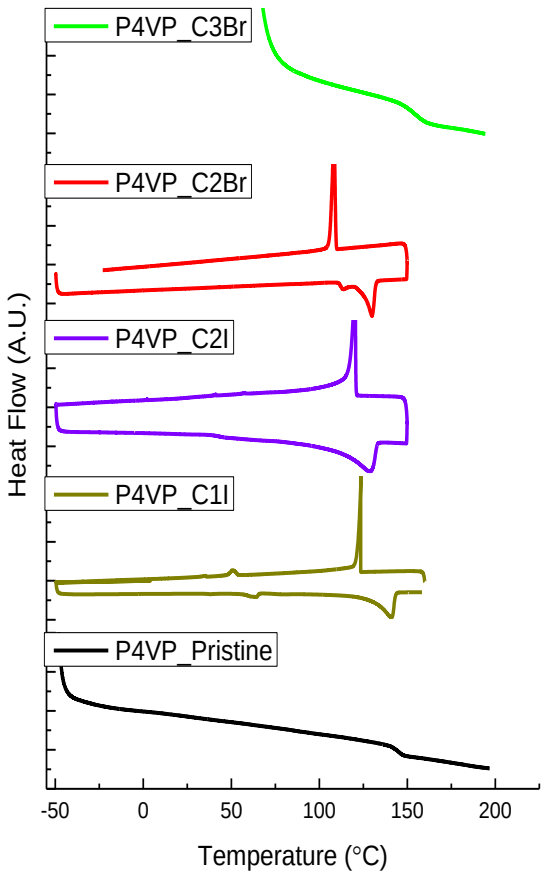

Figure 6.4. The DSC spectra of P4VP, P4VP_C1I, P4VP_C2I, P4VP_C2Br, and P4VP_C3Br

A tabular summary of the thermal characterization of P4VP, P4VP_C1I, P4VP_C2I, P4VP_C2Br, and P4VP_C3Br by differential scanning calorimetry (DSC) is presented in Table 6.1. The samples, P4VP_C1I and P4VP_C2Br, show evidence of polymorphism. Both samples had two melting endotherms, while only P4VP_C1I show two recrystallization exotherms. The melting endotherm of P4VP_C2I was about the same as P4VP_C2Br, 130 °C. This may be due to the similarity in their microstructure as observed by WAXS. The higher melting point of the methyl quaternized P4VP in comparison to the ethyl quaternized P4VP may be due to the effect of side-

chain length on the strength of the dipole – dipole attraction. Longer pendant side-chains results in weaker dipole-dipole interaction and possibly lower melting temperature.

Table 6.1. Summary of the thermal properties of P4VP, P4VP_C1I, P4VP_C2I, P4VP_C2Br and P4VP_C3Br.

	T_g(°C)	T_{m1}(°C)	T_{m2}(°C)	T_{c2}(°C)	T_{c1}(°C)
P4VP_C3Br	153	-	-	-	-
P4VP_C2Br	-	114	130	108	-
P4VP_C2I	43	-	130	120	-
P4VP_CI	-	142	57	120	51
P4VP	145	-	-	-	-

These atactic semi-crystalline polymers, however, had lower melting temperature in comparison to atactic semi-crystalline PVOH (~200 °C).[16,48]

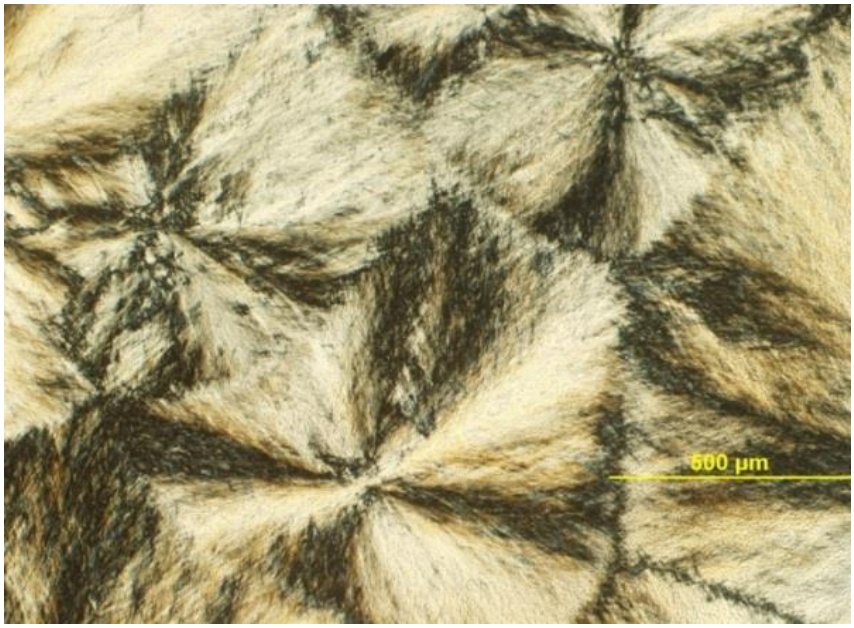

Figure 6.5. Polarized optical microscopy image of P4VP_C2Br.

Optical microscopy analysis was performed on sample to observe the effect of crystallinity on the microstructure of these semi-crystalline polyelectrolytes. The samples, P4VP_C1I, P4VP_C2I, and P4VP_C2Br, were heated to temperatures just above their melting points and allowed to solidify at room temperature. The results for the optical microscopy imaging of P4VP_C1I, P4VP_C2I, and P4VP_C2Br are presented in Figure 6.5, Figure 6.6 and Figure 6.7 respectively. Optical images show that like PVOH and other semi-crystalline polymers, P4VP_C2Br and P4VP_C2I formed spherulites on recrystallization.[49–51] The spherulite image obtained for P4VP_C2Br appeared blurry. However, that of P4VP_C2I show crisp microstructural features. The samples, P4VP_C2Br and P4VP_C2I have spherulites of similar orders of magnitude with an average size of 700 ± 200 µm.

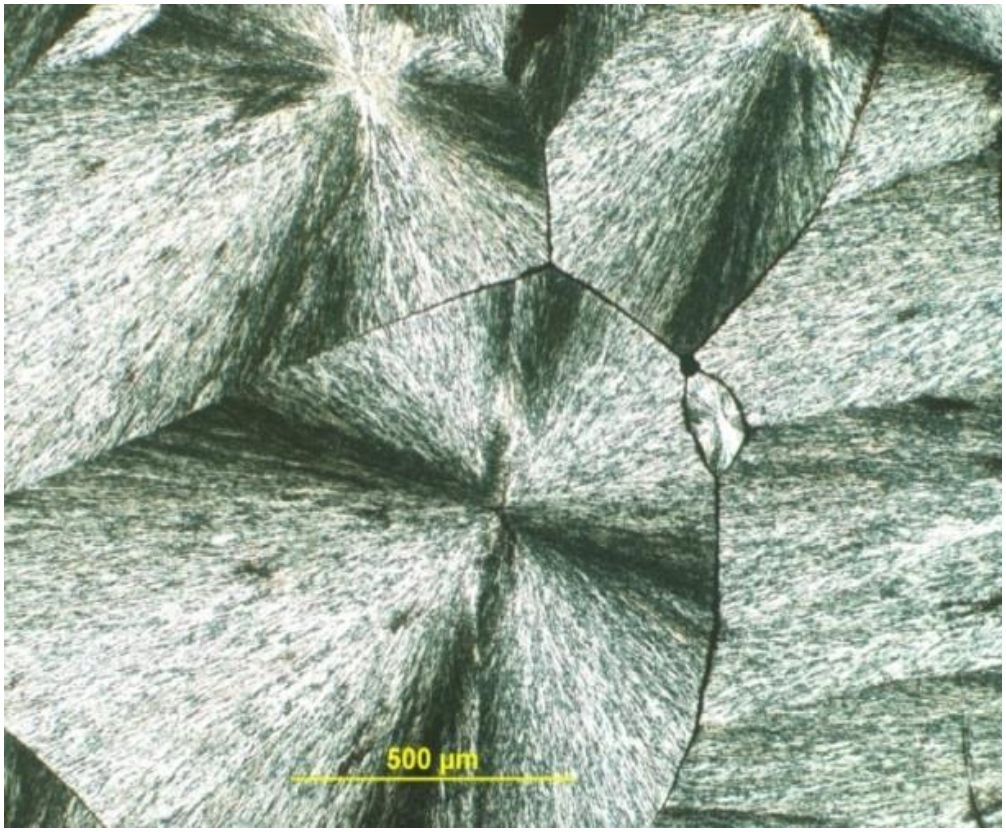

Figure 6.6. Polarized optical microscopy image of P4VP_C2I

The POM image of the methyl quaternized sample, P4VP_C1I, shows a long threadlike core feature (shish) with numerous short threadlike features branching out of the core (kebab). This morphology, the so-called shish-kebab structure, has been observed in semi-crystalline polymers.[52–54] However, shish-kebab feature, are commonly obtained by shearing molten polymers, and have rarely been observed in quiescent melts.[55–59] Given that shish-kebab morphology occurs only after coil-stretch transition in semi-crystalline polymers,[60–64] the shish-kebab structure of P4VP_C1I suggests that the polymer chains were in a stretched rather than coiled configuration in the melt. This is rather interesting, because charged polymers are rod-like (stretched) in dilute – semi-dilute regions but follow Gaussian statistics in the bulk.[65–67] The shish-

kebab structure of P4VP_C1I suggests that it has a rod-like/stretched chain conformation even in the bulk.

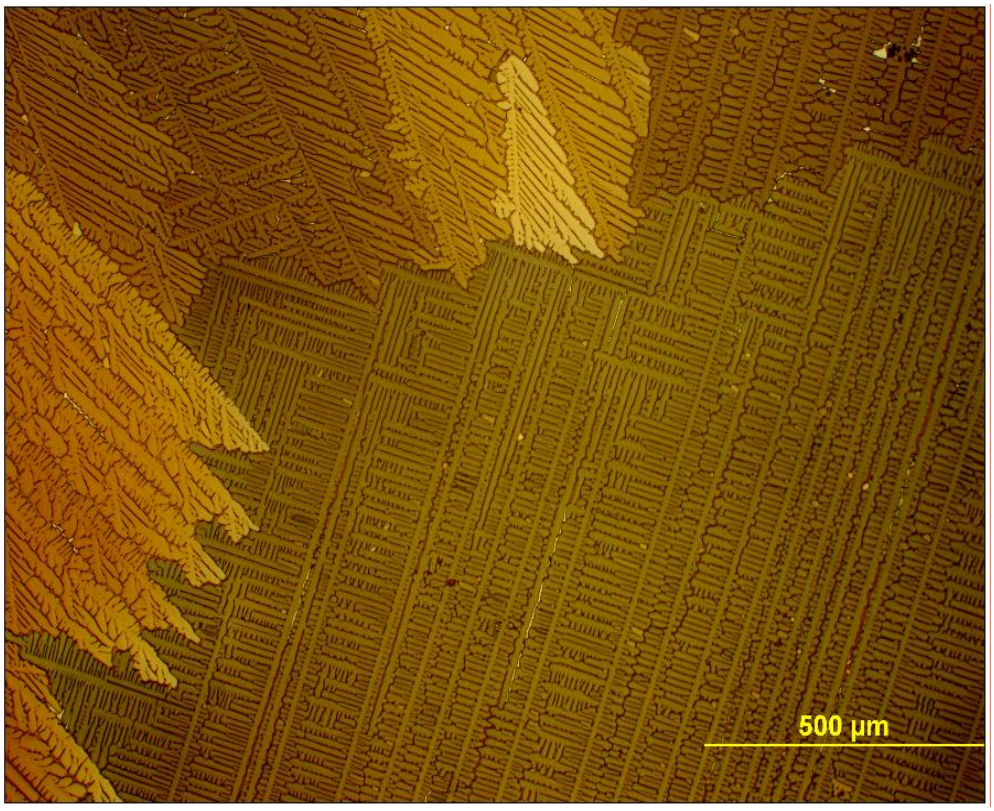

Figure 6.7. Polarized optical microscopy image of P4VP_C1I

The shish–kebab structure of P4VP_C1I show a shish–shish spacing of about 50 – 150 µm. There were first (parent) and second (daughter)-generation kebab structures with different periodicities. The first generation kebabs grow out of the shish structure, while the second generation kebab structures grow out of the first generation kebab.[54] The first generation kebab structures, aligned at about 90° from the shish, have periodicities of about 10 – 20 µm. The second-generation kebab structures, aligned at about 90° from the first-generation kebab, have periodicities of about 2 – 5 µm. However in some cases, the kebabs were aligned at steeper angles from their shish or parent

kebab. Finally, the microstructure of P4VP_C1I also shows the formation of some dendritic features.

6.3 Semi-Crystallinity in P4VP_C2Br Block Copolymer

In Chapter 3, block copolymers of poly(4-vinylpyridine), P4VP, and polystyrene, PS, were synthesized and quaternized by 1-alkylhalides. Characterization of the quaternized block copolymer by X-ray scattering show evidence of phase separation of the ionic and non-ionic block into ordered structures. Scattering measurements of the same block copolymers at high *Q* values also show that the backbone-backbone morphology, a consequence of the pendant side-chain sterics, is present within the microphase-separated ionic domain. We can therefore hypothesize that if a block copolymer of P4VP and PS were to be quaternized by ethylbromide, the P4VP_C2Br block will show evidence of long-range ordering (semi-crystallinity), like the P4VP_C2Br homopolymer, when evaluated by WAXS. To verify this hypothesis, a block copolymer of PS and P4VP was synthesized. The block copolymer was then quaternized with 1-alkylbromide with the number of carbons on the alkyl group ranging from 2 – 8. The ratio of the PS block to the P4VP block in the synthesized copolymer was 60:40. The same ratio of PS to P4VP was synthesized for the study of the PS-*r*-P4VP random copolymer in Chapter 4.

6.3.1 Synthesis of PS-*b*-P4VP

In a round bottom flask equipped with a magnetic stirrer, 17.5 g (0.166 moles) of styrene was polymerized with 160 mg (0.417 mmoles) of SG1 initiator; a molar equivalence of 400:1, [styrene]:[SG1]. Polymerization was performed in 70 wt% dimethyl formamide (DMF) at110 °C for 13 h. The resulting polystyrene (PS) sample was quenched in ice and precipitated thrice in hexanes from dichloromethane. In a round bottom flask equipped with a magnetic stirrer, 10 g of

PS-SG1, which is a microinitiator, was used to polymerize 6.8 g (0.0647 moles) of 4VP in 30 ml of DMF at 115 °C for 20 h. The mixture was quenched in ice and precipitated twice from dichloromethane; first in methanol and then diethyl ether.

6.3.2 Quaternization by 1-Alkylbromides

A solution of 1.0 M quaternizing agent (ethylbromide, propylbromide, butylbromide, pentylbromide, hexylbromide, and octylbromide) was prepared in DMF. An excess amount of the prepared solution was added to a solution of 100 mg of P4VP-*b*-PS in 3.5 ml of DMF. After 240 h, the solution was precipitated into diethyl ether to give an off-white colored powder. After filtration, the powder was dried in vacuum at room temperature.

From Figure 6.8, it obvious that the block copolymer PS-*b*-P4VP(3:2) was successfully synthesized by nitroxide mediated polymerization (NMP). The integral of the 2 aromatic protons of P4VP and the integral of 2 aromatic protons of PS and the other 2 aromatic protons of P4VP were used to calculate the ratio of both blocks in the polymer. The ratio of PS and P4VP in determined from the ^{1}H NMR of the block copolymer was the same with the ratio of both blocks in the target block copolymer. This further confirms the successful synthesis of our choice block copolymer.

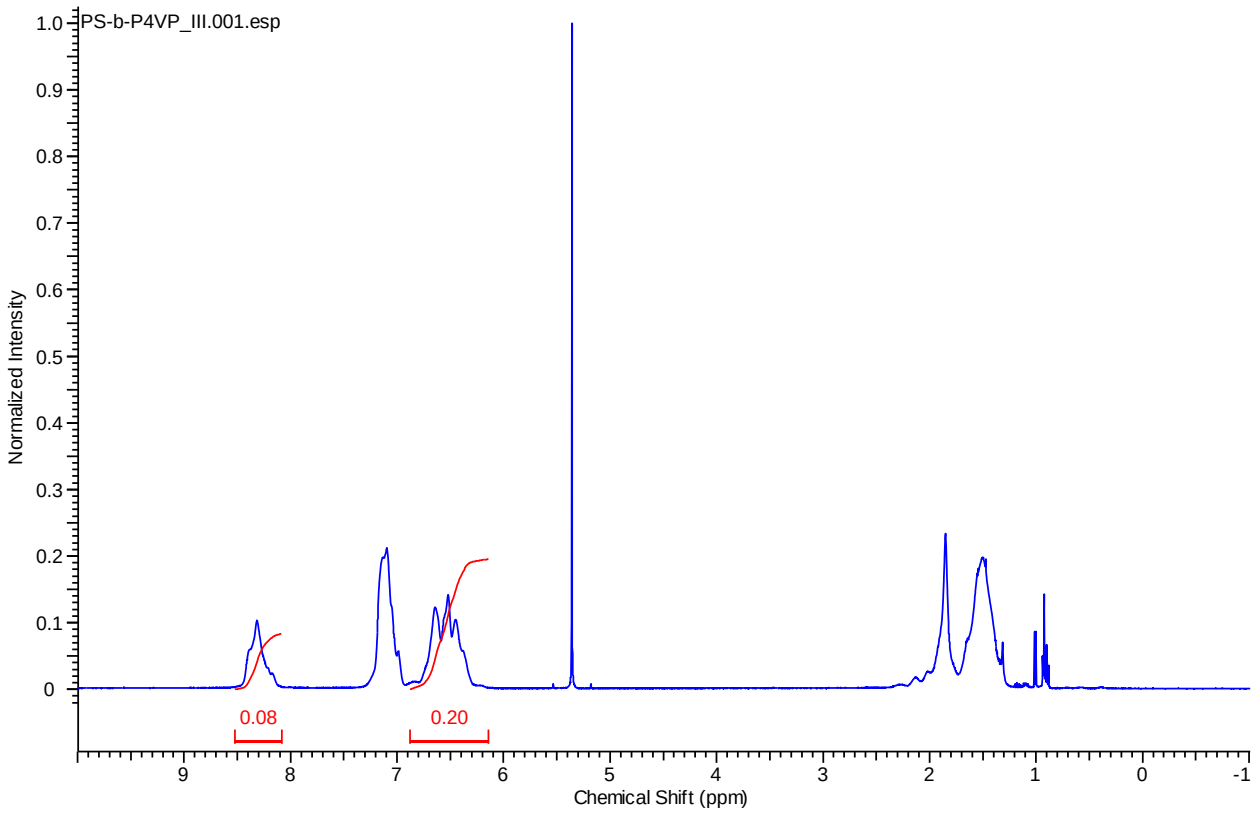

Figure 6.8. The ^{1}H NMR spectrum for PS-*b*-P4VP.

The GPC chromatograms of the PS homopolymer and block copolymer are presented in Figure 6.9. The determined values of the dispersity from the chromatograms show relatively narrow dispersity for the homopolymer and block copolymer.

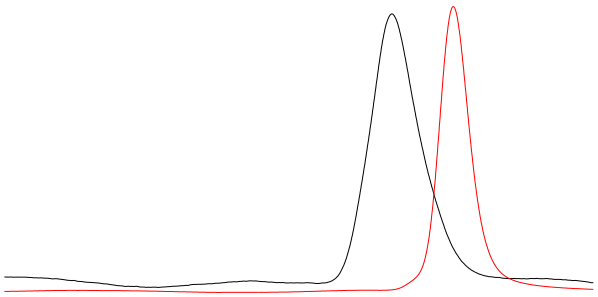

Figure 6.9. The GPC chromatograms for the homopolymer (red trace) and block copolymer (black trace).

A tabular summary of the ^{1}H NMR and GPC characterizations are presented in Table 6.2.

Table 6.2. Summary of the ^{1}H NMR and GPC characterizations of PS-*b*-P4VP.

Sample	Target ratio (%) (Styrene:4VP)	^{1}H NMR ratio (%) (Styrene:4VP)	Mn (Kg/mol)	Đ
PS	100:0	100:0	22	1.17
PS-*b*-P4VP	60:40	60:40	43	1.20

Using FTIR, complete quaternization of the PS-*b*-P4VP quaternized by 1-alkylbromide was confirmed like in the homopolymer with the disappearance of the pyridinium peak at the 1414 cm^{-}

[1] wavenumbers and the simultaneous appearance of the 1640 cm^{-1} peak as described for P4VP homopolymers.

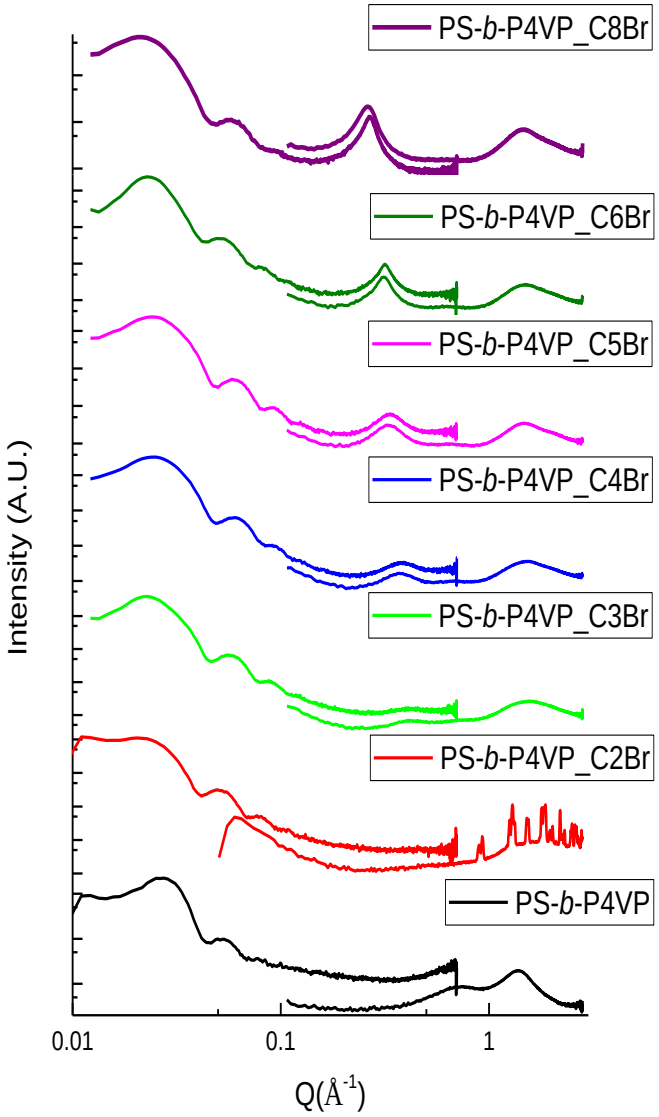

Figure 6.10. The MAXS and WAXS spectra for PS-*b*-P4VP_CnBr series.

X-ray scattering of the block copolymer show that upon quaternization, the polymer transitioned from lamellar to cylindrical morphology. See Figure 6.10. The quaternized block copolymer series maintained this morphology with increasing number of carbons on the pendant side-chain. The domain spacing of the block copolymer also increased with increasing number of carbons.

Figure 6.10 also show that, at high *Q* values, the morphology of the chain arrangement varied with increasing number of carbons on the pendant side-chain. From these scattering data (see the WAXS spectrum), the appearance of a semi-crystalline structure for PS-*b*-P4VP_C2Br in between the amorphous structures of PS-*b*-P4VP and PS-*b*-P4VP_C3Br is evident. For samples PS-*b*-P4VP_C3Br to PS-*b*-P4VP_C8Br, the substructure morphology of the chains within the phase separated ionic domain is characterized by the backbone-backbone short-range order. The periodic spacing of this short-range order, as expected, increased with increasing number of carbons on the pendant side-chain. Thus, there are three morphology regimes for the PS-*b*-P4VP_CnBr series with increasing number of carbons on the pendant side-chains. First, is the amorphous regime of the unquarternized polymer, PS-*b*-P4VP. Secondly, there is a window of semi-crystallinity observed for PS-*b*-P4VP_C2Br. Finally, a third regime, the backbone-backbone morphology amorphous regime. The same variation of morphology regimes with increasing number of carbons on the pendant side-chain has been observed in the quaternized and unquaternized P4VP homopolymer.

Although PS-*b*-P4VP_C2Br show a cylindrical morphology at lower *Q* values, the continuous and non-continuous phase of this morphology cannot be determined from the MAXS spectra. If the P4VP_C2Br block is the non-continuous phase, the formation of semi-crystallinity in the block copolymer suggests that confinement of the ionic block within a rigid non-ionic matrix did not affect the semi-crystallinity of the P4VP_C2Br block in the PS-*b*-P4VP_C2Br block copolymer.

However, if the ionic block is the continuous phase, which is most likely due to theoretical and experimental results on ionic block copolymers (see Chapter 8 and Chapter 9), the formation of semi-crystallinity in the PS-*b*-P4VP_C2Br suggests that cylinders of PS blocks hexagonally arranged in the ionic matrix did not impede the crystallization of the P4VP_C2Br block in the PS-*b*-P4VP_C2Br block copolymer.

Characterization of the block copolymer, PS-*b*-P4VP_C2Br by optical microscopy shows birefringence in the melt crystallized polymer film which suggests evidence of semi-crystallinity in one of the blocks. See Figure 6.11. The spherulite or shish-kebab patterns that were observed in the quaternized homopolymers were absent in the block copolymer image. Instead, the polarized optical microscopy image of show bundles of thin fiber-like structures propagating and intertwining through the film.

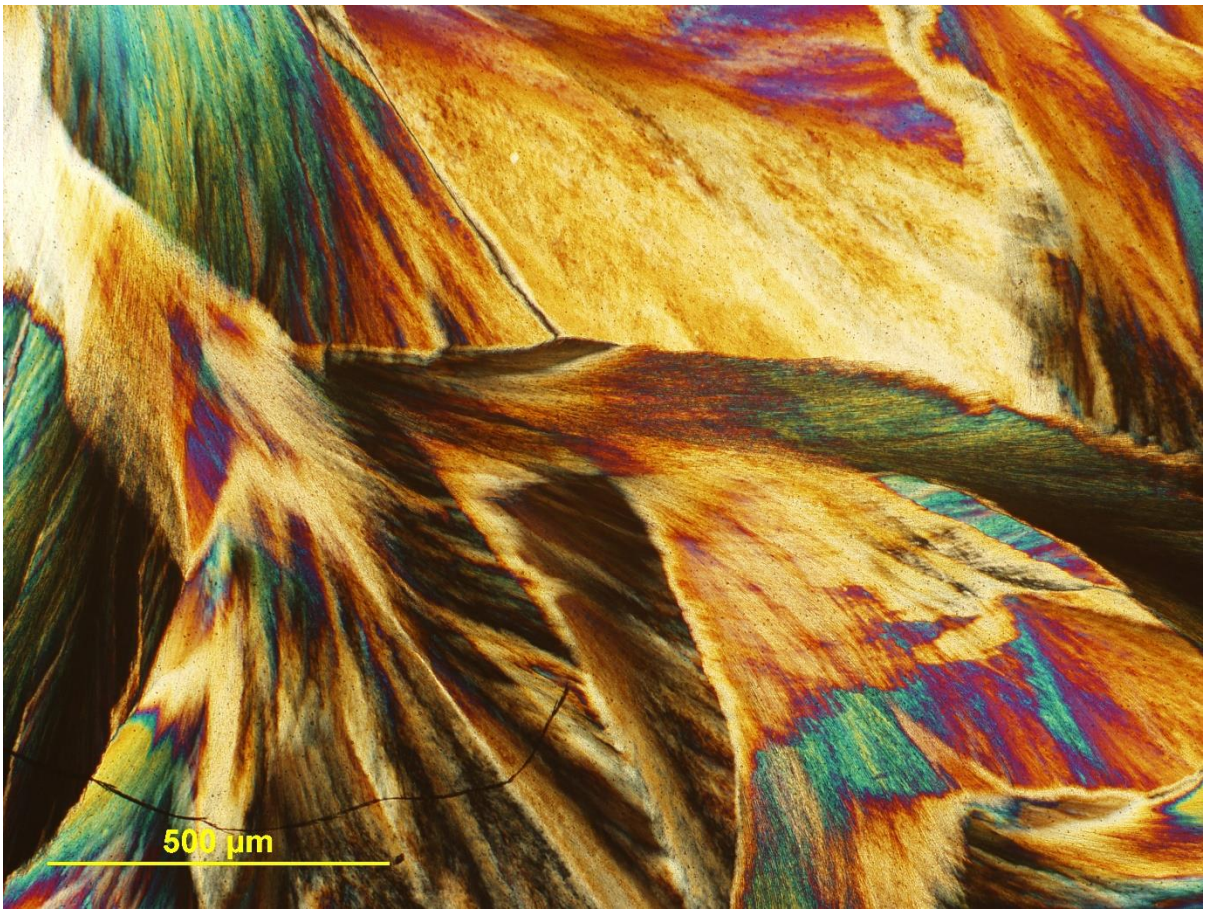

Figure 6.11. Polarized optical microscopy image of PS-*b*-P4VP_C2Br.

6.4 Conclusion

In summary, dipole-dipole interaction between dipoles on the backbone of quaternized P4VP transformed the atactic amorphous polymer to a semi-crystalline polymer. With increasing separation between polymer backbones, the polymer reverts to an amorphous microstructure. For shorter pendant side-chains, methyl and ethyl, the dipole-dipole interaction between adjacent backbones is stronger than the side-chain steric repulsion between them, thus, the quaternized polymers are semi-crystalline. For longer pendant side-chains, propyl – dodecyl, the steric-repulsion is stronger than the dipole-dipole interaction, the quaternized polymers are amorphous. Scattering experiments confirm that methyl and ethyl quaternized P4VP show Bragg diffraction

peaks, while propyl quaternized P4VP show scattering spectra reminiscent of the pristine P4VP. Furthermore, DSC spectra show both melting endotherms and recrystallization exotherms for P4VP_C1I, P4VP_C2I, and P4VP_C2Br. Thus, confirming their semi-crystallinity. Finally, images obtain from polarized optical microscopy also confirm the semi-crystallinity of the methyl and ethyl quaternized P4VP. Polarized optical microscopy images show that P4VP_C1I nucleate and grow into shish-kebab microstructure on recrystallization from a quiescent melt, while P4VP_C2I and P4VP_C2Br nucleate and grow into spherulitic microstructures. Block copolymer of PS-*b*-P4VP also show the same evidence of semi-crystallinity in the ethylbromide quaternized sample when characterized by WAXS.

6.5 References

(1) Israelachvili, J. N. *Intermolecular and Surface Forces*; 2011; Vol. 53.

(2) Kamperman, M.; Fierke, M. A.; Garcia, C. B. W.; Wiesner, U. Morphology Control in Block Copolymer/polymer Derived Ceramic Precursor Nanocomposites. *Macromolecules* **2008**, *41* (22), 8745–8752.

(3) Russina, O.; Triolo, A.; Gontrani, L.; Caminiti, R.; Xiao, D.; Hines Jr, L. G.; Bartsch, R. A.; Quitevis, E. L.; Pleckhova, N.; Seddon, K. R. Morphology and Intermolecular Dynamics of 1-Alkyl-3-Methylimidazolium Bis{(trifluoromethane)sulfonyl}amide Ionic Liquids: Structural and Dynamic Evidence of Nanoscale Segregation. *J. Phys. Condens. Matter* **2009**, *21* (42), 424121.

(4) Ding, J.; Chuy, C.; Holdcroft, S. Enhanced Conductivity in Morphologically Controlled

Proton Exchange Membranes: Synthesis of Macromonomers by SFRP and Their Incorporation into Graft Polymers. *Macromolecules* **2002**, *35* (4), 1348–1355.

(5) Kreuer, K. D.; Portale, G. A Critical Revision of the Nano-Morphology of Proton Conducting Ionomers and Polyelectrolytes for Fuel Cell Applications. *Adv. Funct. Mater.* **2013**, *23* (43), 5390–5397.

(6) Hird, B. Structure-Morphology Property Relations in Random Styrene Ionomers by, McGill University, 1991.

(7) Eisenberg, A.; Hird, B.; Moore, R. B. A New Multiplet-Cluster Model for the Morphology of Random Ionomers. *Macromolecules* **1990**, *23* (18), 4098–4107.

(8) Orfino, F. P.; Holdcroft, S. The Morphology of Nafion: Are Ion Clusters Bridged by Channels or Single Ionic Sites? *J. New Mater. Electrochem. Syst.* **2000**, *3* (4), 285–290.

(9) Zhang, Z.; Liu, C.; Cao, X.; Wang, J.-H. H.; Chen, Q.; Colby, R. H. Morphological Evolution of Ionomer/Plasticizer Mixtures during a Transition from Ionomer to Polyelectrolyte. *Macromolecules* **2017**, *50* (3), 963–971.

(10) Sing, C.; Zwanikken, J.; Cruz, M. D. La. Electrostatic Control of Block Copolymer Morphology. *Nat. Mater.* **2014**, *13* (7), 694–698.

(11) Grady, B. P. Review and Critical Analysis of the Morphology of Random Ionomers Across Many Length Scales. *Polym. Eng. Sci.* **2008**, 1029–1051.

(12) Salas-De La Cruz, D.; Green, M. D.; Ye, Y.; Elabd, Y. A.; Long, T. E.; Winey, K. I. Correlating Backbone-to-Backbone Distance to Ionic Conductivity in Amorphous Polymerized Ionic Liquids. *J. Polym. Sci. Part B Polym. Phys.* **2012**, *50* (5), 338–346.

(13) Zhang, W.; Liu, Y.; Jackson, A. C.; Savage, A. M.; Ertem, S. P.; Tsai, T. H.; Seifert, S.; Beyer, F. L.; Liberatore, M. W.; Herring, A. M.; et al. Achieving Continuous Anion Transport Domains Using Block Copolymers Containing Phosphonium Cations. *Macromolecules* **2016**, *49* (13), 4714–4722.

(14) Kusoglu, A.; Savagatrup, S.; Clark, K. T.; Weber, A. Z. Role of Mechanical Factors in Controlling the Structure − Function Relationship of PFSA Ionomers. *Macromolecules* **2012**, *45* (18), 7467–7476.

(15) Middleton, L. R.; Winey, K. I. Nanoscale Aggregation in Acid- and Ion-Containing Polymers. *Annu. Chem. Biomol. Eng* **2017**, *8*, 499–523.

(16) Guirguis, O. W.; Moselhey, M. T. H. Thermal and Structural Studies of Poly (Vinyl Alcohol) and Hydroxypropyl Cellulose Blends. *Nat. Sci.* **2012**, *4* (1), 57–67.

(17) Bunn, C. W. ©1948 Nature Publishing Group. *Nature* **1948**, *161*, 929–930.

(18) Mooney, R. C. L. An X-Ray Study of the Structure of Polyvinyl Alcohol. In *American Physical Society*, *1941*; Washington, 1941; Vol. 63, pp 2828–2832.

(19) Tuncer Caykara, Cengiz Ozyurek, Omer Kantoglu. Investigation of Thermal Behavior of Poly (2-Hydroxyethyl Methacrylate- Co -Itaconic Acid) Networks. *J. Appl. Polym. Sci* **2005**, *103*, 1602–1607.

(20) Olgun, C. T. and G. The Effect of Filler Type on the Thermal Degradation of Inorganic Filled Poly (2-Hydroxyethyl Methacrylate) Composites. *Polym. Degredation Stab.* **1998**, *62*, 267–270.

(21) Elbarbary, A. M.; Ghobashy, M. Thermal Behavior of Poly (2-Hydroxyethyl Thermal

Behavior of Poly (2-Hydroxyethyl Methacrylate-Bis-[Trimethoxysilylpropyl] Amine) Networks. In *IOP Conference Series: Material Science and Engineering*; 2013; pp 1–5.

(22) Li, D. and J. B. DMTA and FTIR Investigation of the Phase Behavior of Poly (Methyl Methacrylate) - Poly (4-Vinylphenol) Blends. *Macromolecules* **1996**, *29*, 868–874.

(23) Kuo, S. W.; Chang, F. C. Studies of Miscibility Behavior and Hydrogen Bonding in Blends of Poly (Vinylphenol) and Poly (Vinylpyrrolidone). *Macromolecules* **2001**, *34*, 5224–5228.

(24) H., C. Y. F. and G. S. Miscibility of Some Hydroxyl-Containing Polymers with Poly(Acetonyl Methacry Late), Poly(Tetrahydropyranyl-2- Methacrylate), and Poly(Cyclohexyl Methacrylate). *J. Appl. Polym. Sci.* **1992**, *44*, 633–637.

(25) Xing, P.; Dong, L.; An, Y.; Feng, Z. Miscibility and Crystallization of Poly (-Hydroxybutyrate) and Poly (P -Vinylphenol) Blends. *Macromolecules* **1997**, *30*, 2726–2733.

(26) Poly, S.; Russell, G. A.; K, P. A. H.; Donald, E.; C, A.; Andrade, J. D.; Al, R. E. T. Thermal and Dynamic Mechanical Relaxation. *J. Polym. Sci. Polym. Phys. Ed.* **1980**, *18*, 1271–1283.

(27) Rault, J.; Lucas, A.; Neffati, R.; Monleo, M. Thermal Transitions in Hydrogels of Poly (Ethyl Acrylate)/ Poly (Hydroxyethyl Acrylate) Interpenetrating Networks. *Macromolecules* **1997**, *30*, 7866–7873.

(28) Arunan, E.; Desiraju, G. R.; Klein, R. A.; Sadlej, J.; Scheiner, S.; Alkorta, I.; Clary, D. C.; Crabtree, R. H.; Dannenberg, J. J.; Hobza, P.; et al. Definition of the Hydrogen Bond (

IUPAC Recommendations 2011)*. *Pure Appl. Chem.* **2011**, *83* (8), 1637–1641.

(29) Umeyama, H.; Morokuma, K. The Origin of Hydrogen Bonding. An Energy Decomposition Study. *J. Am. Chem. Soc.* **1977**, *99* (5), 1316–1332.

(30) Hsu, W. Y.; Gierke, T. D. Elastic Theory for Ionic Clustering in Perfluorinated Ionomers. *Macromolecules* **1982**, *15*, 101–105.

(31) Eisenberg, A. Clustering of Ions in Organic Polymers. A Theoretical Approach. *Mucromolecules* **1970**, *3* (2), 147–154.

(32) Kim, J. S.; Yeon Hwa Nah; Jarng, S. S. Comparison of Clustering in Various Acrylate Ionomers. *Polymer (Guildf).* **2001**, *42* (13), 5567–5571.

(33) Platé, N. A.; Shibaev, V. P. Comb-like Polymers. Structure and Properties. *J. Polym. Sci. Macromol. Rev.* **1974**, *8* (1), 117–253.

(34) Miller, R. L.; Boyer, R. F.; Heijboer, J. X-Ray Scattering from Amorphous Acrylate and Methacrylate Polymers: Evidence of Local Order. *J. Polym. Sci. Polym. Phys. Ed.* **1984**, *22* (12), 2021–2041.

(35) Jin, H.; An, Q.; Zhao, Q.; Qian, J.; Zhu, M. Pervaporation Dehydration of Ethanol by Using Polyelectrolyte Complex Membranes Based on Poly (N-Ethyl-4-Vinylpyridinium Bromide) and Sodium Carboxymethyl Cellulose. *J. Memb. Sci.* **2010**, *347* (1–2), 183–192.

(36) Caruso, U.; De Maria, A.; Panunzi, B.; Roviello, A. Poly(4-Vinylpyridine) as the Host Ligand of Metal-Containing Chromophores for Second-Order Nonlinear Optical Active Materials. *J. Polym. Sci. Part A Polym. Chem.* **2002**, *40* (17), 2987–2993.

(37) Yao, C.; Li, X.; Neoh, K. G.; Shi, Z.; Kang, E. T. Surface Modification and Antibacterial Activity of Electrospun Polyurethane Fibrous Membranes with Quaternary Ammonium Moieties. *J. Memb. Sci.* **2008**, *320* (1–2), 259–267.

(38) Patel, M.; Patel, R.; Chi, W. S.; Kim, J. H.; Sung, J. S. Antibacterial Behaviour of Quaternized Poly(vinyl Chloride)-G-poly(4-Vinyl Pyridine) Graft Copolymers. *Chinese J. Polym. Sci. (English Ed.* **2015**, *33* (2), 265–274.

(39) Li, Y.; Yang, M. J.; She, Y. Humidity Sensitive Properties of Crosslinked and Quaternized Poly (4-Vinylpyridine-Co-Butyl Methacrylate). *Sensors Actuators B* **2005**, *107*, 252–257.

(40) Li, D.; He, Q.; Cui, Y.; Li, J.; Potsdam, G. Fabrication of pH-Responsive Nanocomposites of Gold Nanoparticles / Poly (4-Vinylpyridine). *Chem. Mater.* **2007**, *19*, 412–417.

(41) Hao, E.; Lian, T. Layer-by-Layer Assembly of CdSe Nanoparticles Based on Hydrogen Bonding. *Langmuir* **2000**, *16* (21), 7879–7881.

(42) Andruzzi, F.; Lupinacci, D.; Magagnini, P. L. Comb-like Polymers. 2. Poly(octadecylethy1ene Oxide). *Macromolecules* **1980**, *13* (1), 15–18.

(43) Volkov, V. V; Plat, N. A. Aggregation State and Mesophase Structure of Comb-Shaped Polymers with Fluorocarbon Side Groups. *Polymer (Guildf).* **1992**, *33* (6), 1316–1320.

(44) Beiner, M.; Huth, H. Nanophase Separation and Hindered Glass Transition in Side-Chain Polymers. *Nat. Mater.* **2003**, *2*, 595–599.

(45) Pankaj, S.; Beiner, M. Long-Term Behavior and Side Chain Crystallization of poly(3-Alkyl Thiophenes). *Soft Matter* **2010**, *6* (15), 3506–3516.

(46) Hiller, S.; Pascui, O.; Budde, H.; Kabisch, O.; Reichert, D.; Beiner, M. Nanophase Separation in Side Chain Polymers: New Evidence from Structure and Dynamics. *New J. Phys.* **2004**, *6*.

(47) Seguela, R. On the Strain - Induced Crystalline Phase Changes in Semi - Crystalline Polymers : Mechanisms and Incidence on the Mechanical Properties On the Strain-Induced Crystalline Phase Changes in Semi-Crystalline Polymers : Mechanisms and Incidence on the. *J. Macromol. Sci. Part C Polym. Rev.* **2005**, *45* (263–287).

(48) Jose, J.; Shehzad, F.; Al-harthi, M. A. Preparation Method and Physical, Mechanical, Thermal Characterization of Poly(vinyl Alcohol)/poly(acrylic Acid) Blends. *Polym Bull. Bull.* **2014**, *71*, 2787–2802.

(49) Shtukenberg, A. G.; Punin, Y. O.; Gunn, E.; Kahr, B. Spherulites. *Chem. Rev.* **2012**, *112*, 1805–1838.

(50) Crist, B.; Schultz, J. M. Progress in Polymer Science Polymer Spherulites : A Critical Review. *Prog. Polym. Sci.* **2016**, *56*, 1–63.

(51) Keller, A.; Chemical, I.; Division, D. The Spherulitic Structure of Crystalline Polymers. Part II. The Problem of Molecular Orientation in Polymer Spherulites. *J. Polym. Sci.* **1955**, *43* (19), 8128–8135.

(52) Cellino, A.; Paolicchi, P.; Binzel, R. P. Molecular Basis of the Shish-Kebab Morphology in Polymer Crystallization. *Science (80-.).* **2007**, *316* (May), 1014–1017.

(53) Chen, Y.; Fang, D.; Hsiao, B. S.; Li, Z. Insight into Unique Deformation Behavior of Oriented Isotactic Polypropylene with Branched Shish-Kebabs. *Polymer (Guildf).* **2015**,

60, 274–283.

(54) Roozemond, P. C.; Cui, K.; Li, L.; Peters, G. W. M. Multimorphological Crystallization of Shish-Kebab Structures in Isotactic Polypropylene: Quantitative Modeling of Parent − Daughter Crystallization Kinetics. *Macromolecules* **2014**, *47*, 5152–5162.

(55) Hobbs, J. K.; Miles, M. J. Direct Observation of Polyethylene Shish-Kebab Crystallization Using in-Situ Atomic Force Microscopy. *Macromolecules* **2001**, *34* (3), 353–355.

(56) Zuo, F.; Keum, J. K.; Yang, L.; Somani, R. H.; Hsiao, B. S. Thermal Stability of Shear-Induced Shish-Kebab Precursor Structure from High Molecular Weight Polyethylene Chains. **2006**, 2209–2218.

(57) Boutaous, M.; Bourgin, P.; Zinet, M. Journal of Non-Newtonian Fluid Mechanics Thermally and Flow Induced Crystallization of Polymers at Low Shear Rate. *J. Nonnewton. Fluid Mech.* **2010**, *165* (5–6), 227–237.

(58) Zhou, Q.; Liu, F.; Guo, C.; Fu, Q.; Shen, K.; Zhang, J. Shish E Kebab-like Cylindrulite Structures Resulted from Periodical Shear-Induced Crystallization of Isotactic Polypropylene. *Polymer (Guildf).* **2011**, *52* (13), 2970–2978.

(59) Wang, K.; Chen, F.; Zhang, Q.; Fu, Q. Shish – Kebab of Polyolefin by "' Melt Manipulation '" Strategy in Injection-Molding : A Convenience Pathway from Fundament to Application. *Polymer (Guildf).* **2008**, *49* (22), 4745–4755.

(60) Kumaraswamy, G. Crystallization of Polymers from Stressed Melts Crystallization of Polymers from Stressed Melts. *J. Macromol. Sci. Part C Polym. Rev.* **2005**, *1797* (45), 375–397.

(61) Hsiao, B. S.; Yang, L.; Somani, R. H.; Avila-orta, C. A.; Zhu, L. Unexpected Shish-Kebab Structure in a Sheared Polyethylene Melt. *Phys. Rev. Lett.* **2005**, *94* (March), 1–4.

(62) Nie, Y.; Zhao, Y.; Matsuba, G.; Hu, W. Shish-Kebab Crystallites Initiated by Shear Fracture in Bulk Polymers. *Macromolecules* **2018**, *51*, 480–487.

(63) Dukovski, I.; Muthukumar, M. Langevin Dynamics Simulations of Early Stage Shish-Kebab Crystallization of Polymers in Extensional Flow Langevin Dynamics Simulations of Early Stage Shish-Kebab Crystallization of Polymers in Extensional Flow. *J. Chem. Phys.* **2003**, *6648* (14), 6648–6655.

(64) Kimata, S.; Sakurai, T.; Nozue, Y.; Kasahara, T.; Karino, T.; Shibayama, M.; Kornfield, J. A. Molecular Basis of the Shish-Kebab Morphology in Polymer Crystallization. *Science (80-.).* **2018**, *316* (5827), 1014–1017.

(65) Weill, G. Conformation and Order in Polyelectrolyte Solutions. *J. Phys.* **1988**, *49* (6), 1049–1054.

(66) Solutions, P.; Odijk, T. Possible Scaling Relations for Semidilute. **1979**, 688–693.

(67) Dobrynin, A. V.; Rubinstein, M. Theory of Polyelectrolytes in Solutions and at Surfaces. *Prog. Polym. Sci.* **2005**, *30* (11), 1049–1118.

PART III:

SYNTHESIS AND CHARACTERIZATION OF ALKALINE-STABLE AZO-SPIROCYCLIC UNDECANE-TYPE POLYMERS FOR ANION EXCHANGE MEMBRANES

CHAPTER 7

SYNTHESIS AND CHARACTERIZATION OF CHEMICALLY STABLE ASU-TYPE MONOMERS AND HOMOPOLYMERS

7.1 Introduction

From the previous projects (see Chapter 2, Chapter 3, Chapter 4, Chapter 5, and Chapter 6), fundamental studies on poly(*n*-alkyl 4-vinylpyridinium halides) show the importance of intermolecular forces in the physics of polyelectrolyte morphologies, and the consequence on the conducting properties of AEMs. However, one of the fundamental challenges with AEMs is their chemical instability. In alkaline media, cationic centers of anionic exchange membranes, especially quaternary ammoniums, are susceptible to chemical degradation.[1–4] These degradation reactions reduce the quantity of ions in the system. Thus, adversely affect conducting performance in AEMs. Two facile degradation pathways for quaternary ammoniums are β–hydrogen elimination (Hofmann Elimination) and neuclophilic substitution (see Scheme 7.1) However, other mechanisms for quaternary ammonium (QA) degradation like ortho substitution and Stevens rearrangement, can also occur.[4–7]

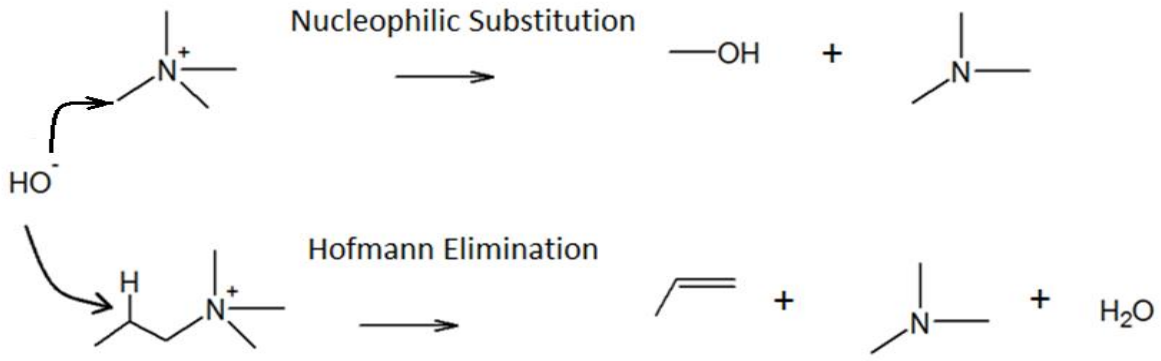

Scheme 7.1. Schematic of nucleophilic substitution and Hofmann elimination of quaternary ammoniums.

Degradation by means of nucleophilic substitution can occur in *all* quaternary ammonium molecules provided the cationic center is readily accessible by the nucleophile. On the other hand, an elimination reaction with a faster rate constant can only occur in molecules with a β-hydrogen. Most research in the literature has therefore rightly focused on quaternary ammonium compounds that do not undergo Hofmann elimination. Benzyl trimethyl ammonium (BMA) has been the prime candidate for use in AEMs.[8–10] However, the use of benzylic cations has its own challenges. The electron-withdrawing benzyl group increases the susceptibility of the cation to nucleophilic substitution. Furthermore, the aromatic group can stabilize degradation intermediates by resonance, thereby furthering their instability in aggressive alkaline medium.[4,11] This is well evidenced by results that show tetramethyl ammonium, $N^+(CH_3)_4$, with a half-life sixteen times that of BMA.[4]

Since deterring elimination reactions from occurring does not increase the chemical stability of QAs, an alternative approach might be to reduce the rate of degradation altogether instead of eliminating possible degradation pathways. Hofmann elimination reaction being an E2 elimination

reaction is stereospecific. It can occur when the β-proton and the cation are in a *syn-periplanar* or *anti-periplanar* orientation.

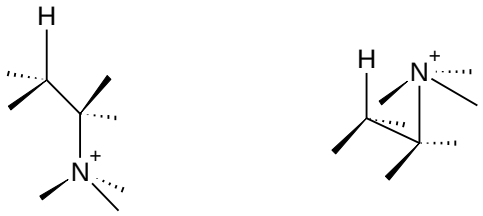

Scheme 7.2. Depiction of anti-periplanar (left), syn-periplanar (right) orientations.

Although there is a possibility of a *syn-elimination*, which occurs when the β-proton is in a *cis* position with the cation, the preferred elimination route occurs in molecules with a 180° dihedral angle between the β-hydrogen and the cation (*i.e.* an *anti-periplanar* position). It has been suggested that the staggered configuration of the *anti-periplanar* orientation may be responsible for their increased susceptibility to elimination.[11] The staggered conformation, is the more energetically favorable conformation. Thus, the transition states of a *staggered* conformation may have lower energy than other *non-staggered* conformations. This increases the propensity of *anti-periplanar* molecules to undergo an elimination reaction. Consequently, fuel cell membrane researchers have attempted to increase the resistance of QAs to nucleophilic attack by designing molecules in which the β-hydrogen is in a *non-anti-periplanar* position to the cation. Nevertheless, only a few QAs with these structures has been synthesized and studied. A study of 1,4 diazabicyclo [2,2,2] octane (DABCO) show poor stability even though there are β-protons locked in a *non-anti-periplanar* position. The possible reasons for its poor stability may be due to its high ring strain and the proximity of the second nitrogen to the QA.[4]

Marino and Kreuer, in their seminal work, examined other QAs with β-protons locked in both a *non-anti-periplanar* and *anti-periplanar* position.[4] They found that dimethyl pyrrolidinium

performed better than benzyl trimethly ammonium (BMA) salt in a 6 M sodium hydroxide aqueous solution at 160 °C. The pipyridinium counterpart with lower ring strain, albeit with two β-protons in an *anti-periplanar* position, showed better stability results under the same testing conditions. Reducing susceptibility to nucleophilic substitution by replacing the methylene groups by another 6 membered ring (*i.e*. 6-azonia-spiro[5,5] undecane 'ASU') showed increased stability even though the number of *anti-periplanar* β-protons is now increased to 4. This suggests that ring strain was as much an important a factor as the orientation of the β-proton in space.[4,11,12] They predicted that polymer molecules based on this structure will be stable for use as anion exchange membranes.

Although some studies have appeared in the literature most recently on ASU-type molecules (*i.e.* double cyclic structure with ammonium bridging the two rings), most of this work focuses on post polymer modification. Morphology and composition of the hydrophilic content is difficult to control in these cases.[13–21] In addition to not easily been solvent processable due to post-polymerization modifications, these studies rarely perform chemical stability tests on their membranes. Furthermore, few studies in the literature have focused on the competition between ring strain in these ASU – type molecules and their β-protons.

In this project, synthesis of novel ASU-type monomers and their corresponding polymers will be investigated. Stability tests on these monomers will be performed to assay the chemical stability. Other ASU-style monomers with varying number of carbons from the backbones will also be synthesized and polymerized. The morphology of ASU-type monomers will be probed by X-ray scattering.

7.2 Materials, Methods, Results, and Discussion

Dicyclopentadiene (97%), dibromohexane (95%), dibromopentane (98%), dibromobutane (98%), were procured from TCI Chemicals. 4-hydroxypiperidine (98%), 3-bromopyridine (98%) were purchased from Matrix Scientific. Cis 1,4 dichlorobutene (95%) was purchased from Alfa Aesar. Norbornene (99%), 4-vinylbenzylchloride (96%), piperidine (99%), sodium hydride (60 wt% in mineral oil) and Grubbs' II catalysts were purchased from Sigma Aldrich. The monomer 4-vinylbenzylchloride was passed through basic alumina. All other chemicals were used as obtained.

7.2.1 Design and Synthesis of 6-Azonia-spiro[5,4]decene chloride

The designed monomer, 6-Azonia-spiro[5,4]decene chloride, has two features of interest. A chemically stable azo-type cation and a cyclic double bond that can be polymerized by ring-opening metathesis polymerization to give anion exchange membranes.

Scheme 7.3. Synthesis of 6-Azonia-spiro[5,4]decene chloride.

7.2.2 Synthesis of 6-Azonia-spiro[5,4]decene chloride

A mixture of 0.625 g (5 mmoles) of Cis-1,4 dichlorobut-2-ene and 0.84 g (6 mmoles) of K_2CO_3 and 10 ml of anhydrous acetonitrile was charged into a two-neck round bottom flask equipped with a stirrer. The mixture was heated to reflux. A solution of 0.425 g (5 mmoles) of piperidine in 2 ml of anhydrous acetonitrile was added by syringe and needle into the reflux mixture. The mixture was refluxed for 18 h. The reaction was then rotovapped to give a brown solid. This solid

was then dissolved in 10 ml of ethanol to filter off the excess K_2CO_3. The solvent was then concentrated on a roto-evaporator. The concentrated solution was precipitated into diethyl ether to give a light brown solid. The solid was washed thrice in diethyl ether and then dried overnight in vacuum at room temperature for 24 h to give 0.63 g (72 % yield) of the product.

A similar method was used to synthesize 6-azonia-spiro[5,5]undecane.[4]

Characterization of the product by ^{1}H NMR confirm the successful synthesis of 6-azonia-spiro[5,4]decene. The protons of 6-azonia-spiro[5,4]decene and their corresponding peaks on the ^{1}H NMR spectrum are shown in Figure 7.1.

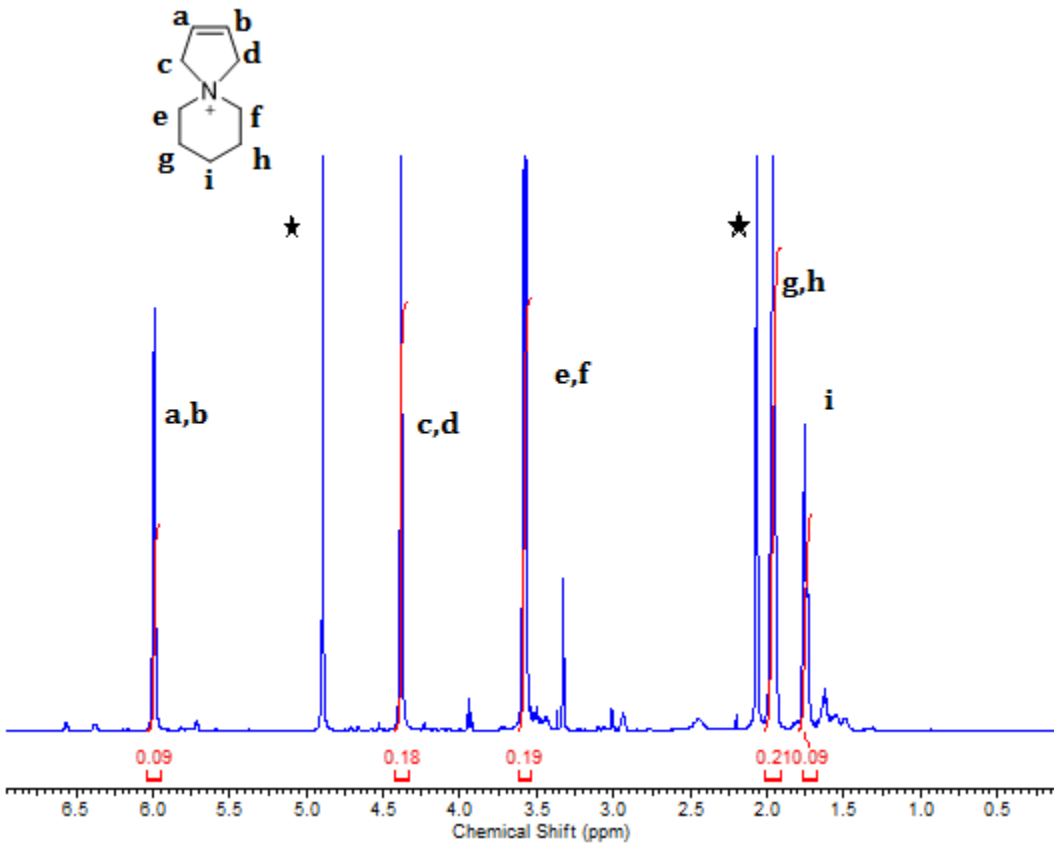

Figure 7.1. The ^{1}H NMR spectrum for 6-azonia-spiro[5,4]decene chloride.

7.2.3 Homopolymerization of 6-azonia-spiro[5,4]decene chloride

A solution of 200 mg of azospirocyclic[5,4]decene chloride in 1 ml methanol was charged into a 20 ml scintillation vial equipped with a stirrer. To the solution was added a solution of 2 mg of Grubb's 1st generation catalyst. After 30 mins the reaction was quenched with 1 ml of divinyl ether. The reaction mixture was then precipitated into diethyl ether. Characterization of the precipitate by ^{1}H NMR show that azospirocyclic[5,4]decene chloride did not homopolymerize. This line of research was not further explored.

7.2.4 Design and Synthesis of 4-Vinylbenzoxy-6-azonia-spiro[5,5]undecane bromide

The design of the monomer 4-vinylbenzoxy-6-azonia-spiro[5,5]undecane bromide was then pursued. Two features in the monomer are of interest. A chemically stable azo-type cation attached to a radical, cationic, or anionic polymerizable vinyl benzylic head. See Scheme 7.4 and Scheme 7.5.

7.2.5 Synthesis of 4-Hydroxy-6-azonia-spiro[5,5]undecane

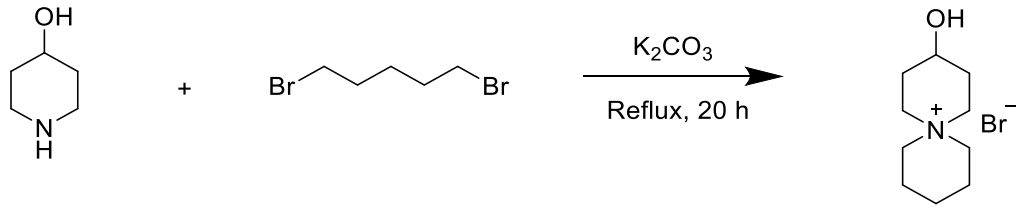

Scheme 7.4. Synthesis of 4-hydroxy-6-azonia-spiro[5,5]undecane.

In a two-neck round bottom flask, 21 g (0.152 moles) of potassium carbonate was charged into a solution of 27.6 g (0.124 moles) of 1,5 dibromopentane in 300 ml of acetonitrile equipped with a magnetic stirrer. The mixture was heated to reflux. After 10 minutes, a solution of 10.1 g (0.1 moles) of 4-hydroxypiperidine in 50 ml of acetonitrile was added to the mixture. After 20 h the

reaction bath was gradually cooled to room temperature. The reaction mixture was then rotovapped to remove the solvent leaving a yellow like solid which was dissolved in 300 ml of ethanol and the excess potassium carbonate was removed by filtration. The solution was then partially evaporated to obtain a concentrated solution that was precipitated into diethyl ether. Afterwards, the yellowish solid was filtered and washed in DCM thrice. The solid was then dried in vacuo at room temperature to afford 18.3 g (73% yield) of an off-white solid. A similar method was used to synthesize 6-azonia-spiro[5,5]undecane.[4]

Characterization of the product by ^{1}H NMR confirm the successful synthesis of 4-hydroxy-6-azonia-spiro[5,5]undecane. The protons of 4-hydroxy-6-azonia-spiro[5,5]undecane and their corresponding peaks on the ^{1}H NMR spectrum are shown in Figure 7.2.

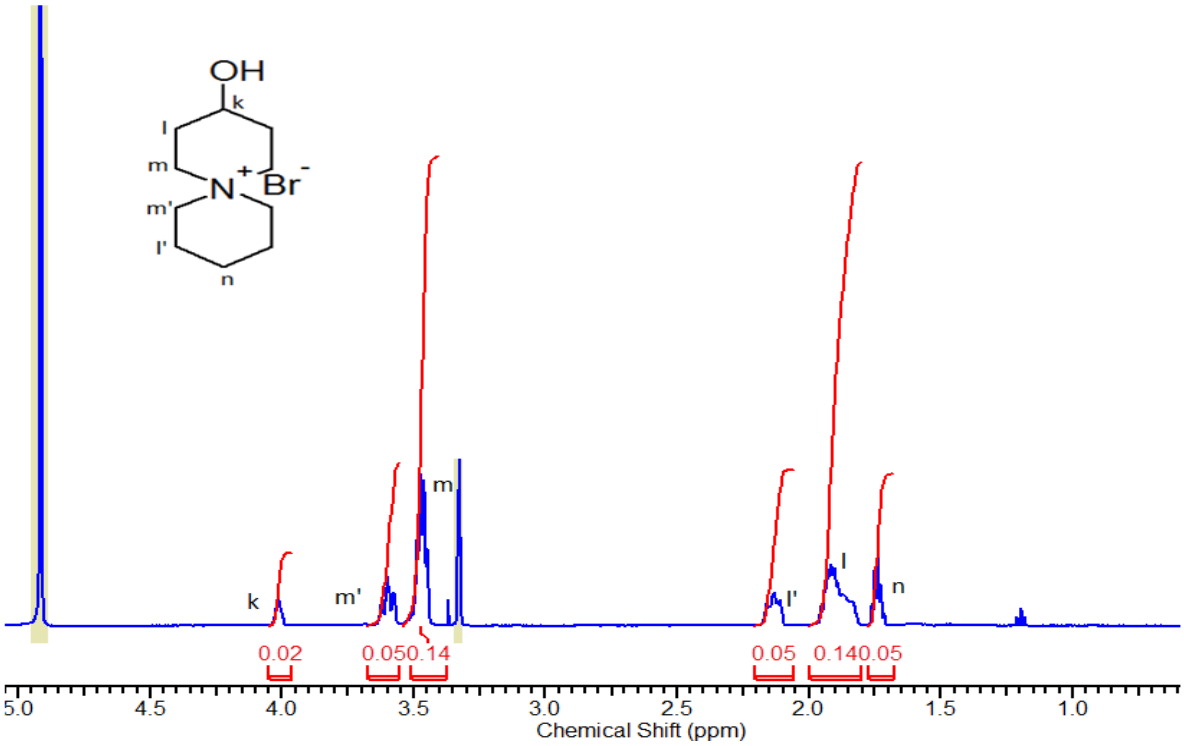

Figure 7.2. The ^{1}HNMR spectrum of 4-hydroxy-6-azonia-spiro[5,5]undecane.

The product, 4-hydroxy-6-azonia-spiro[5,5]undecane, was further characterized by TOF-Mass Spectrometer. From the chromatogram of 4-hydroxy-6-azonia-spiro[5,5]undecane, shown in Figure 7.3, a spectral line on the molecular weight to charge ratio of 170 g/mol.C corresponds to the molecular weight of 4-hydroxy-6-azonia-spiro[5,5]undecane without the bromide counterion. Two spectral lines on 419 and 421 g/mol.C resulting from the two isotopes of bromine (79 and 81 g/mol) are visible on the spectra at higher m/z ratios. These spectral lines corresponds to two 4-hydroxy-6-azonia-spiro[5,5]undecane and one bromide (with its two isotopes) counterion. These results confirm that 4-hydroxy-6-azonia-spiro[5,5]undecane was successfully synthesized.

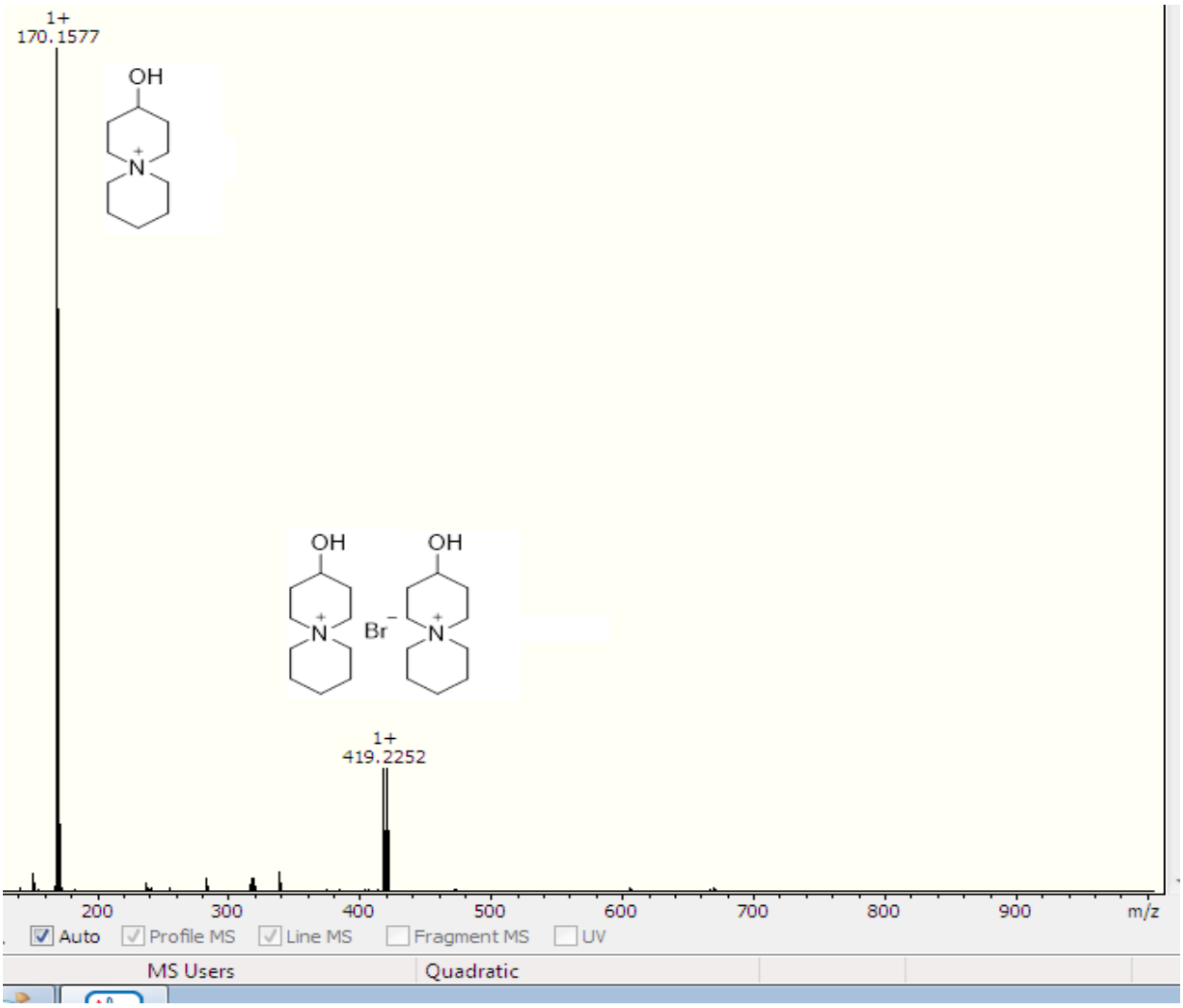

Figure 7.3. The TOF-Mass spectrometer chromatogram of 4-hydroxy-6-azonia-spiro[5,5]undecane.

7.2.6 Synthesis of 4-Vinylbenzoxy-6-azonia-spiro[5,5]undecane chloride

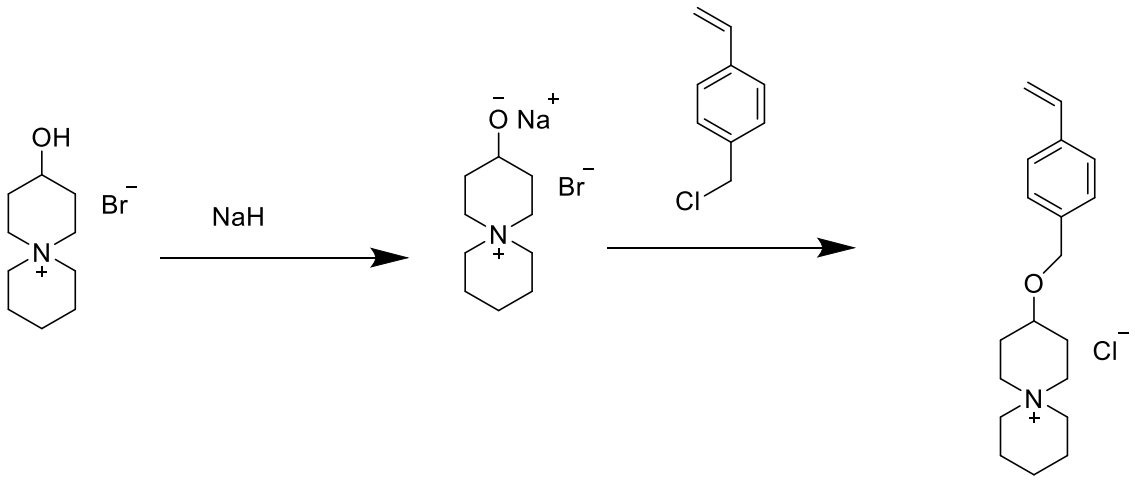

Scheme 7.5. Synthesis of 4-vinylbenzoxy-6-azonia-spiro[5,5]undecane chloride.

In a round bottom flask, 5.6 g (22.4 mmoles) of 4-hydroxy-6-azonia-spiro[5,5]undecane was dissolved in 60 ml of anhydrous DMSO. The solution was gradually added to another round bottom flask containing 1.79 g (44.8 mmoles) of sodium hydride equipped with a magnetic stirrer. The reaction proceeded at room temperature for 1 h. Afterwards, 17 g (112 mmoles) of 4-vinylbenzylchloride was gradually added into the reaction mixture. The color of the mixture changed from white to light brown. The reaction was allowed to proceed for 20 h. Thereafter, the mixture was vacuum filtered to remove unreacted sodium hydride. The filtrate was a viscous clear yellow liquid. The filtrate was then precipitated into diethyl ether to give an off-white solid. The off-white solid was then washed with diethyl ether and dried in vacuum to afford 4.39 g (61% yield) of desired product.

Characterization of the product by ^{1}H NMR confirm the successful synthesis of 4-vinylbenzoxy-6-azonia-spiro[5,5]undecane chloride. The protons of 4-vinylbenzoxy-6-azonia-

spiro[5,5]undecane chloride and their corresponding peaks on the ^{1}H NMR spectrum are shown in Figure 7.4.

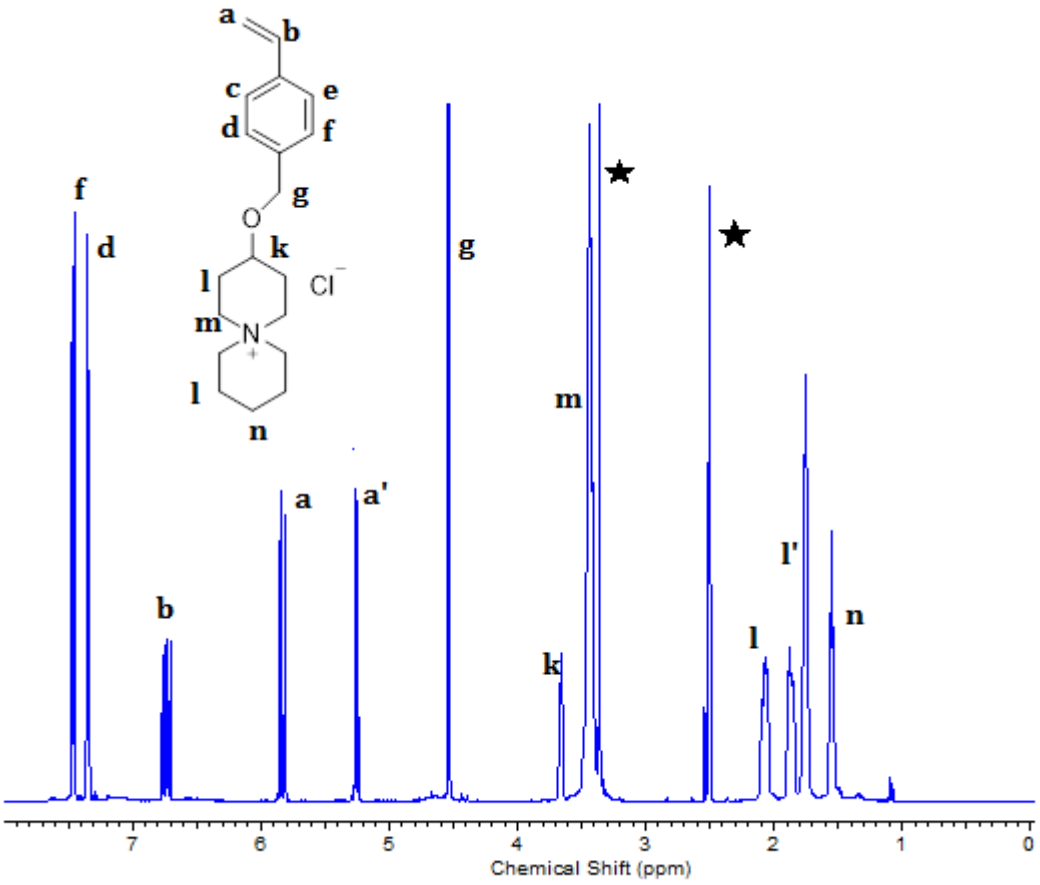

Figure 7.4. The ^{1}H NMR spectrum of 4-vinylbenzoxy-6-azonia-spiro[5,5]undecane chloride.

7.2.7 Homopolymerization of 4-Vinylbenzoxy-6-azonia-spiro[5,5]undecane chloride

1.075 g (3.35 mmoles) of 4-vinylbenzoxy6-azonia-spiro[5,5]undecane chloride was dissolved in 15 ml of pyridine in a Schlenk tube equipped with a stirrer. 5 mg (0.0130 mmoles) of SG1 was added to the solution mixture at 125 °C. After 24 h, the reaction was quenched in ice and then precipitated into diethyl ether. Characterization by ^{1}H NMR show that 4-vinylbenzoxy-6-azonia-spiro[5,5]undecane bromide did not homopolymerize.

Although the attempt to radically polymerize 4-vinylbenzoxy-6-azonia-spiro[5,5]undecane chloride was discontinued, an attempt to affix the salt, 4-hydroxy-6-azonia-spiro[5,5]undecane, by Williamson's ether synthesis unto a polymerizable backbone was continued.

7.2.8 Design and Synthesis of Norobornenedimethyl-6-azonia-spiro[5,4] bromide

Norbornene-based monomers can be polymerized via Ring-Opening Metathesis Polymerization (ROMP). Ring-opening metathesis polymerization chemistry has been shown to be very efficient in polymerizing norbornene based monomers giving a high monomer conversion.[22–28] This is important in these systems because separation of monomers, which are solids at room temperature, from polymers might be difficult. Additionally, ring-opening metathesis polymerization of norbornene-based monomers can be performed at room temperature and also at relatively shorter time periods.[29–34]

The monomer norobornenedimethyl-6-azonia-spiro[5,4] bromide was designed and synthetic procedures are shown in in Scheme 7.6 and Scheme 7.7 to synthesize the norbornene-based monomer.

7.2.9 Synthesis of Norbornenedimethyldichloride

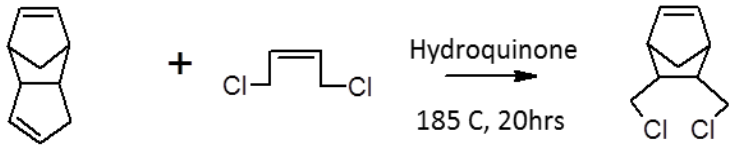

Scheme 7.6. Synthesis of norbornenedimethyldichloride (NDMDC).

In a round bottom flask, 7 g (0.053 moles) of dicyclopentadiene was dissolved in 20 g (0.16 moles) of cis1,4dichlorobutene. The solution was charged into a Schlenk tube equipped with a magnetic stirrer and trace amount of hydroquinone, 50 mg (0.45 mmoles). The mixture was placed in an oil bath with a temperature of 185°C and allowed to proceed for 18 h. Fractional distillation was performed on the mixture to remove excess cis 1,4 dichlorobutene (40°C, 200 mTorr) and 10.9 g (54% yield) of desired product, norbornenediemethyldichloride (70 °C, 150 mTorr).

Characterization of the product by ^{1}H NMR confirm the successful synthesis of norbornenedimethyldichloride. The protons of norbornenedimethyldichloride and their corresponding peaks on the ^{1}H NMR spectrum are shown in Figure 7.5.

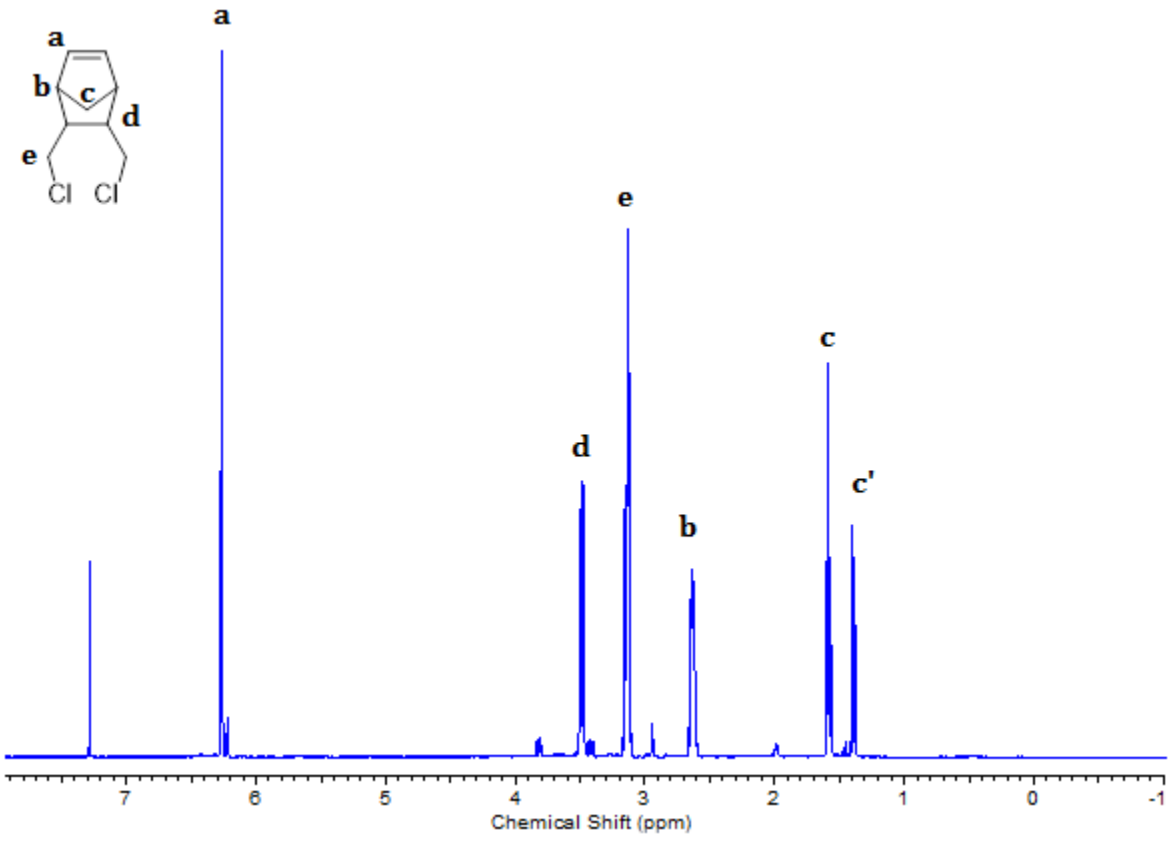

Figure 7.5. The ^{1}H NMR of norbornenedimethyldichloride.

7.2.10 Synthesis of Norobornenedimethyl-6-azonia-spiro[5,4]decane chloride

A mixture of 4.8 g (0.025 moles) of norobornenedimethyldichloride and 4.2 g (0.3 moles) of potassium carbonate and 0.44 g (0.0026 moles) of potassium iodide, and 80 ml of anhydrous acetonitrile was charged into a two-neck flask equipped with a stirrer. The mixture was heated to reflux. A solution of 2.14 g (0.025 moles) of piperidine in 15 ml of anhydrous acetonitrile was added by syringe into the reflux mixture. The mixture was refluxed for 18 h. The reaction was then rotovapped to give a light brown solid. This solid was then dissolved in 100 ml of ethanol to filter off the unreacted potassium carbonate. The solvent was then concentrated by rotovapping. The concentrated solution could not be precipitated into diethyl ether. Characterization of the resultant reaction mixture show that there was no reaction between norobornenedimethyldichloride and pyridine. Norobornenedimethyl-6-Azonia-spiro[5,4] chloride could not be synthesized.

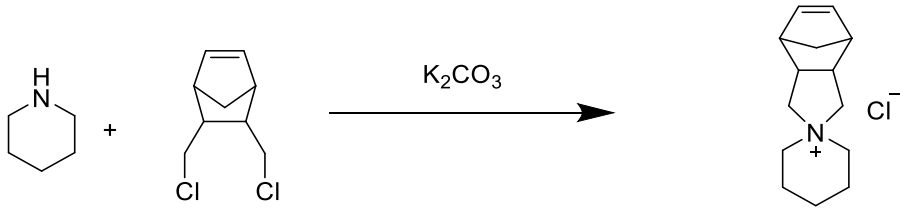

Scheme 7.7. Synthesis of norobornenedimethyl-6-azonia-spiro[5,4]decane chloride.

Alternatively, an attempt was made to synthesize norbornenedimethoxydi-6-azonia-spiro[5,5]undecane chloride from the reaction of norbornenedimethyldichloride and hydroxyl group in 4-hydroxy-6-azonia-spiro[5,5]undecane.

7.2.11 Synthesis of Norbornenedimethoxydi-6-azonia-spiro[5,5]undecane chloride.

A solution of 1.6 g (0.0064 moles) of 6-azonia-spiro[5,5]undecane in 60 ml of DMSO was charged into a round bottom flask equipped with a stirrer. To the solution, 0.31 g (0.0128 moles) of sodium hydride was gradually added at room temperature. After 1 h, 2.45 g (0.0128 moles) of norbornenedimethyldichloride was added to the reaction mixture. The reaction proceeded for 20 h. Afterwards, the reaction mixture was filtered. The filtrate was precipitated into diethyl. Characterization of the resultant solid show that there was no reaction between norbornenedimethyldichloride and 4-hydroxy-6-azonia-spiro[5,5]undecane bromide. Norbornenedimethoxydi-6-azonia-spiro[5,5]undecane chloride could not be synthesized.

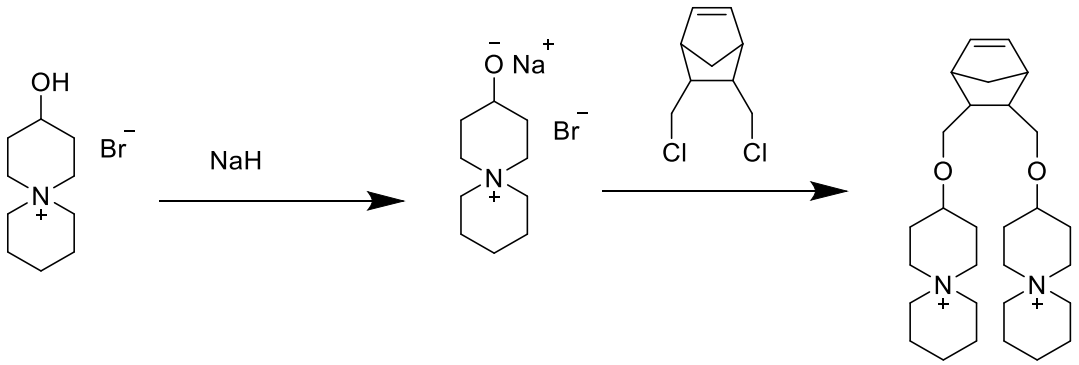

Scheme 7.8. Synthesis of norbornenedimethoxydi-6-azonia-spiro[5,5]undecane chloride.

7.2.12 Inertness of Norbornenedimethyldichloride to Halogen Exchange and Nucleophilic Substitution

Norbornenedimethyl dichloride is inert to ether synthesis and the Finkelstein reaction. The inertness of the chloride to reaction seem to have resulted from the steric hinderance of the exo bridge that makes it impossible for a nucleophile to attack from the backside of the chlorides in a conventional S_N2 reaction.

7.2.13 Synthesis of Norbornene Propoxy Spirocyclic Salt

A new design was adopted for the preparation of the monomer norbornenepropoxy-6-azonia-spiro[5,5]undecane. Two features in the monomer are of interest. A chemically stable azo-type cation attached to a norbornene head. The norbornene head can be polymerized by ring-opening metathesis polymerization to give anion exchange membranes. See Scheme 7.9 and Scheme 7.10 for the synthetic outline of norbornenepropoxy-6-azonia-spiro[5,5]undecane.

7.2.14 Synthesis of Norbornenepropylbromide

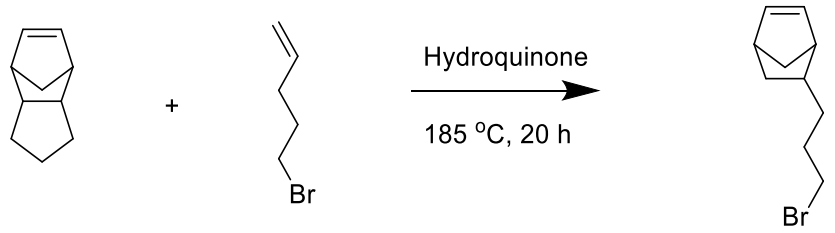

Scheme 7.9. Synthesis of norbornenepropylbromide.

In a round bottom flask, 20 g (0.134 moles) of 5-bromo-1-pentene was mixed with 5.9 g of dicyclopentadiene (0.045 moles). The mixture was charged into a Schlenk tube equipped with a magnetic stirrer. Catalytic amount, 16 mg (0.15 mmoles), of Hydroquinone was added to the reaction mixture. The tube was then placed in an oil bath at a temperature of 185 °C. After 20 h, the reaction was gradually cooled to room temperature. There was a change in color of the reaction mixture from a colorless solution to dark brown. Fractional vacuum distillation was performed at 27 – 40 °C, 300 mTorr to remove the excess reactant (5-bromo-1-pentene), and then distilled at 58 – 60 °C, 50 mTorr to obtain 11.6 g (61% yield) of norbornenepropylbromide colorless oil.

Characterization of the product by ^{1}H NMR confirm the successful synthesis of norbornenepropylbromide. The protons of norbornenepropylbromide and their corresponding peaks on the ^{1}H NMR spectrum are shown in Figure 7.6.

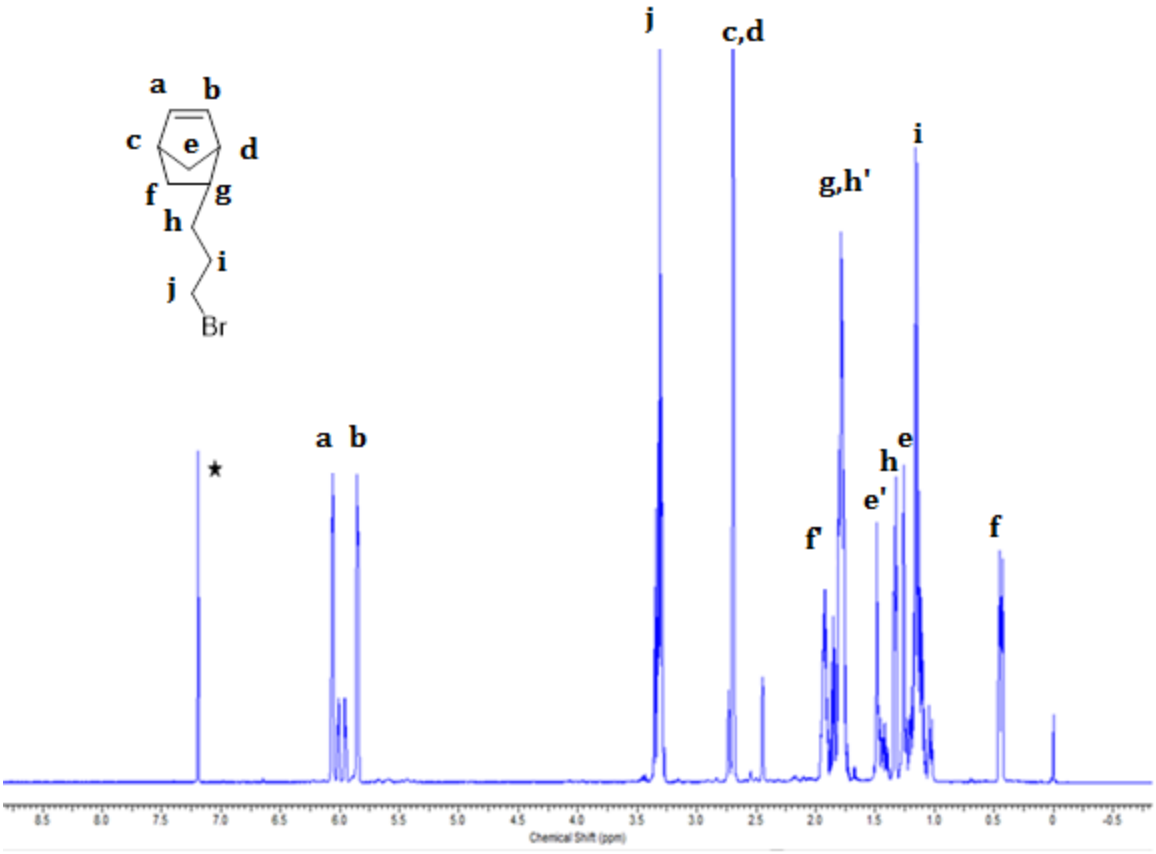

Figure 7.6. The ^{1}H NMR spectrum of norbornenepropylbromide.

7.2.15 Synthesis of Norbornenepropoxy-6-azonia-spiro[5,5]undecane (NPS5)

In a round bottom flask, 3.1 g (12.4 mmoles) of 4-hydroxy-6-azonia-spiro[5,5]undecane was dissolved in 50 ml of anhydrous DMSO. The solution was gradually added to another round bottom flask containing 1 g (24 mmoles) of sodium hydride equipped with a magnetic stirrer. The reaction proceeded at room temperature for 1 h. Afterwards, 5.1 g (23.7 mmoles) of norbornene

propyl bromide dispersed in 5 ml anhydrous DMSO was gradually added into the reaction mixture. The color of the mixture changes from white to light brown. The reaction was allowed to proceed for 20 h. Thereafter, the mixture was vacuum filtered to remove unreacted sodium hydride. The filtrate was a viscous clear brown liquid. The filtrate was then precipitated into diethyl ether to give a white solid. After filtration, the white solid was then washed with diethyl ether again and dried. The white solid was then dissolved in 200 ml of hot acetone to filter-off unreacted 4-hydroxy-6-azonia-spiro[5,5]undecane and sodium bromide. The product was then recrystallized from acetone by cooling the solution to 4 ºC. After filtration, the crystals were then washed with diethyl ether and dried in vacuum to afford 4.4 g (92% yield) of desired product.

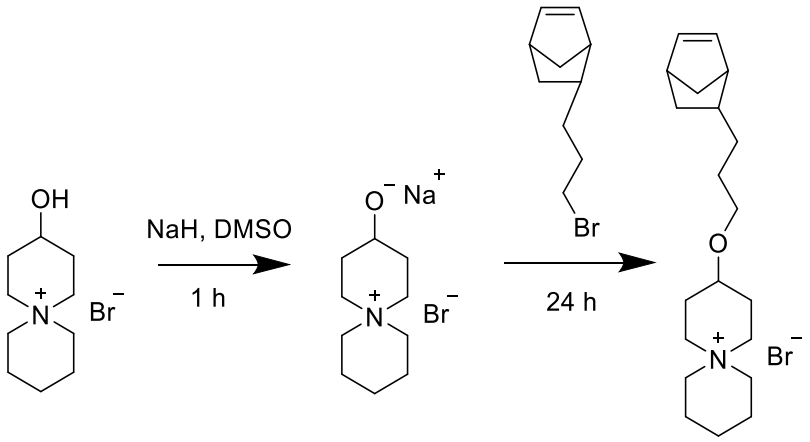

Scheme 7.10. Synthesis of norbornenepropoxy-6-azonia-spiro[5,5]undecane (NPS5).

Characterization of the product by ^{1}H NMR confirm the successful synthesis of norbornenepropoxy-6-azonia-spiro[5,5]undecane. The protons of norbornenepropoxy-6-azonia-spiro[5,5]undecane and their corresponding peaks on the ^{1}H NMR spectrum are shown in Figure 7.7.

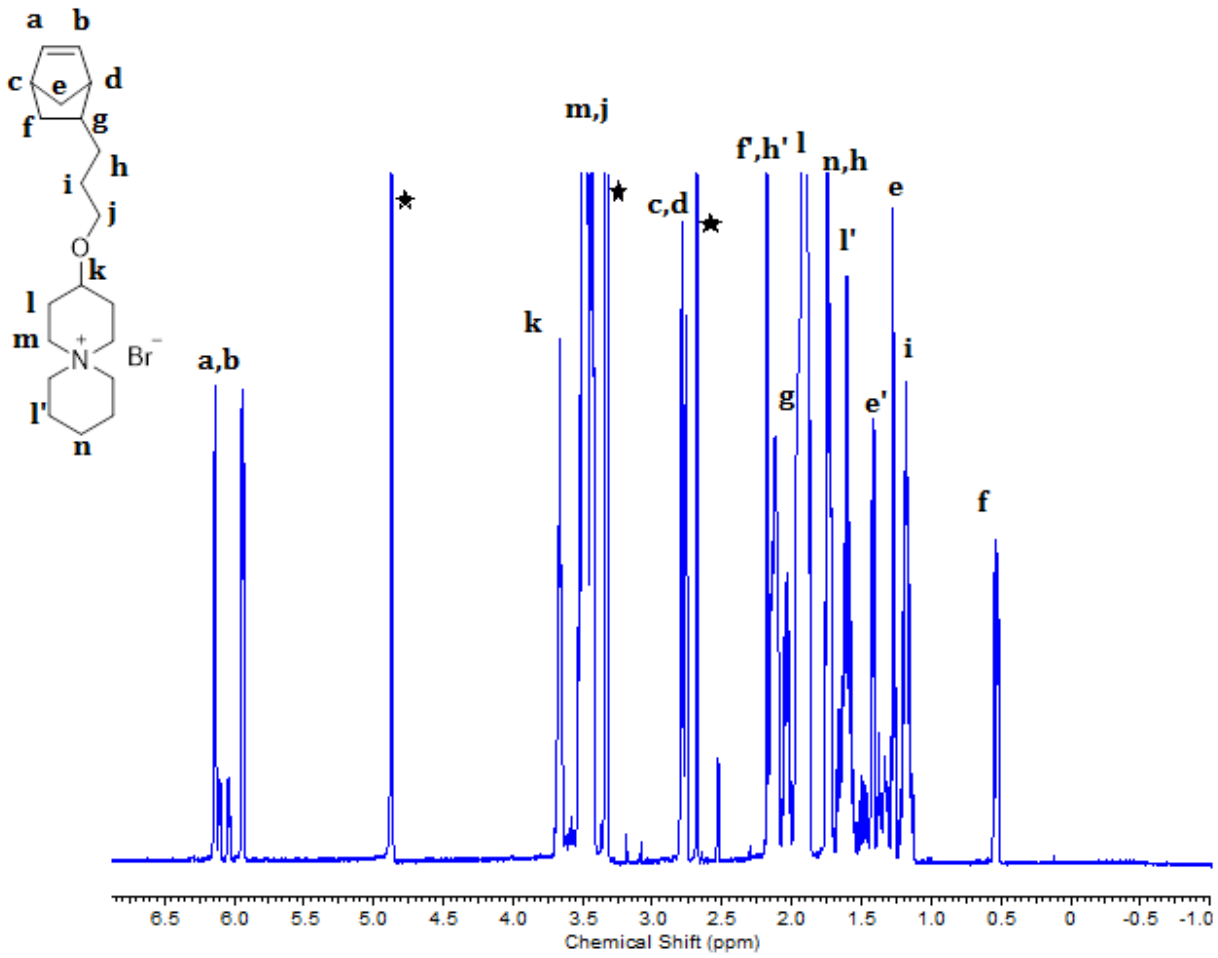

Figure 7.7. The ^{1}H NMR spectrum of norbornenepropoxy-6-azonia-spiro[5,5]undecane (NPS5).

The product, norbornenepropoxy-6-azonia-spiro[5,5]undecane, was further characterized by TOF-Mass Spectrometer. The product, norbornenepproproxy-6-azonia-spiro[5,5]decane, was further characterized by TOF-Mass spectrometer. From the chromatogram of norbornenepropoxy-6-azonia-spiro[5,5]decane, shown in Figure 7.8, a spectral line on the molecular weight to charge ratio of 304 g/mol.C corresponds to the molecular weight of norbornenepropoxy-6-azonia-spiro[5,5]decane without the bromide counterion. Two spectral lines on 687 and 689 g/mol.C resulting from the two isotopes of bromine (79 and 81 g/mol) are visible on the spectra at higher m/z ratios. These spectral lines corresponds to two norbornenepropoxy-6-azonia-spiro[5,5]decane

and one bromide (with its two isotopes) counterion. These results confirm that norbornenepropoxy-6-azonia-spiro[5,5]decane was successfully synthesized.

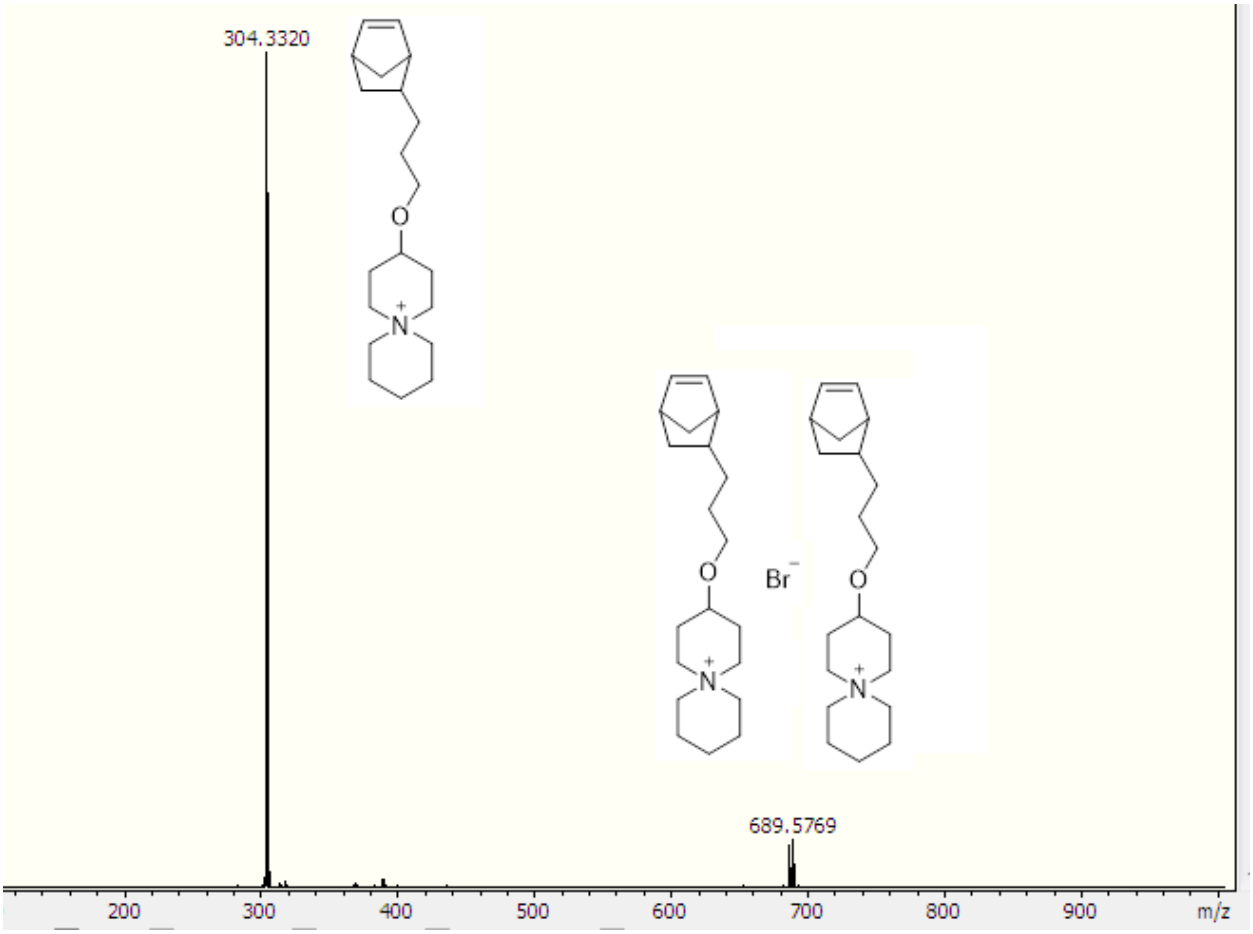

Figure 7.8. The TOF-Mass spectrometer chromatogram of norbornenepropoxy-6-azonia-spiro[5,5]undecane (NPS5).

7.2.16 Homopolymerization of NPS5

In a 20 ml scintillating vial, 300 mg (0.78 mmoles) of NPS5 in 5 ml of DMF was charged into a solution of 3 mg (0.0035 mmoles) of Grubbs' II catalyst in 0.5 ml of DCM equipped with a

magnetic stirrer. The reaction proceeded for 24 h and afterwards precipitated in diethyl ether to afford 261 mg (87% yield) of polymer.

Characterization of the product by ^{1}H NMR confirm the successful synthesis of polynorbornenepropoxy-6-azonia-spiro[5,5]undecane. The protons of polynorbornenepropoxy-6-azonia-spiro[5,5]undecane and their corresponding peaks on the ^{1}H NMR spectrum are shown in Figure 7.9.

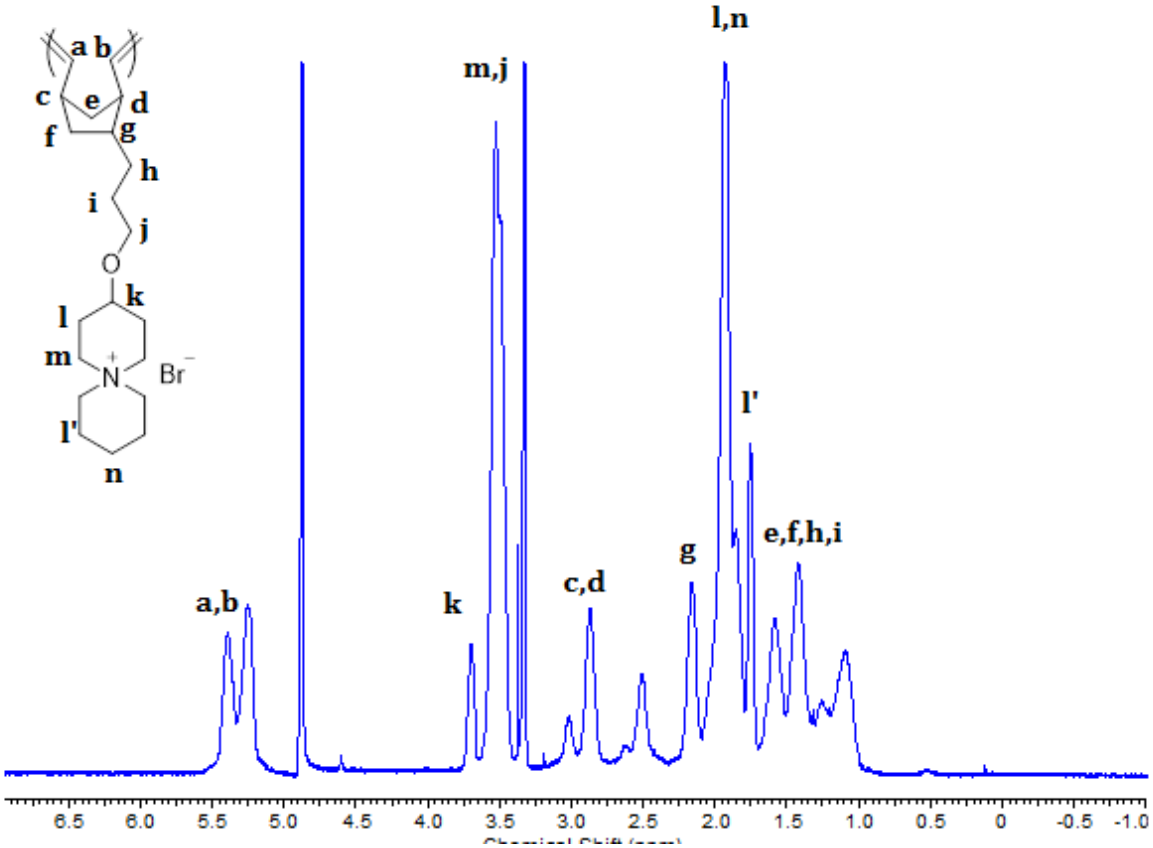

Figure 7.9. The ^{1}H NMR spectrum of polynorbornenepropoxy-6-azonia-spiro[5,5]undecane (PNPS5).

7.2.17 Design and Synthesis of Norbornenehexoxy-6-azonia-spiro[5,5]undecane

In the previous chapter, we have explored the effect of pendant side-chain sterics on the clustering of dipoles. The longer the pendant side-chain, the less likely is it for ionic clusters to form in randomly charged comb-shaped polymers. The elimination, or reduction, in the quantity of clusters increases the conductivity of anion exchange membranes. To increase the number of carbons on the pendant side-chain, a new monomer was designed, norbornenehexoxy-6-azonia-spiro[5,5]undecane. Instead of norbornenepropylbromide, norbornenehexylbromide was synthesized as a precursor. While the polymer synthesized from norbornenepropylbromide precursor has 3 carbons on the pendant side-chain between the norbornene backbone and the 6-azonia-spiro[5,5]undecane; the polymer that will be synthesized from norbornenehexylbromide will have 6 carbons on the pendant side-chain between the norbornene backbone and the 6-azonia-spiro[5,5]undecane. The same spirocyclic salt, 4-hydroxy-6-azonia-spiro[5,5]undecane, used in the synthesis of norbornenepropoxy-6-azonia-spiro[5,5]undecane will be used in the synthesis of norbornenehexoxy-6-azonia-spiro[5,5]undecane. See Scheme 7.11 and Scheme 7.12 for the synthetic outlines of norbornenehexoxy-6-azonia-spiro[5,5]undecane.

7.2.18 Synthesis of Norbornenehexylbromide

In a scintillation vial, 10 g (0.052 moles) of 8-bromo-1-octene was mixed with 2.34 g of dicyclopentadiene (0.018 moles). The mixture was charged into a Schlenk tube equipped with a magnetic stirrer. Trace amount, 21 mg (0.19 mmoles), of hydroquinone was added to the reaction mixture. The tube was then placed in an oil bath at a temperature of 185 °C. After 20 h, the reaction was gradually cooled to room temperature. There was a change in color of the reaction mixture from a colorless solution to light brown. Vacuum distillation was performed at 60 °C, 300 mTorr

to remove the excess reactant. Flash chromatography of the residue was performed in hexanes to afford 5.2 g (57% yield) of a colorless oil of norbornenehexylbromide.

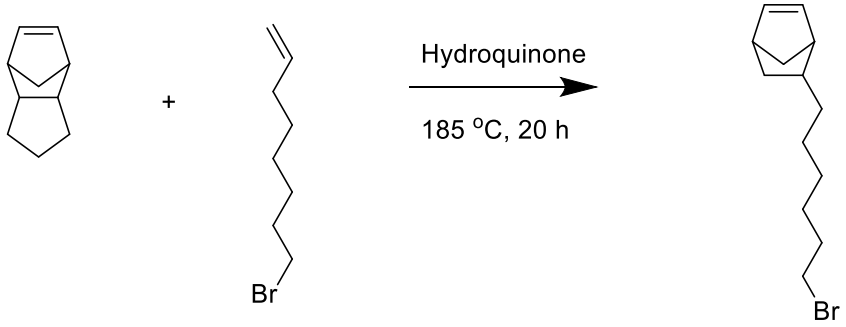

Scheme 7.11. Synthesis of norbornenehexylbromide

Characterization of the product by ^{1}H NMR confirm the successful synthesis of norbornenehexylbromide. The protons of norbornenehexylbromide and their corresponding peaks on the ^{1}H NMR spectrum are shown in Figure 7.10.

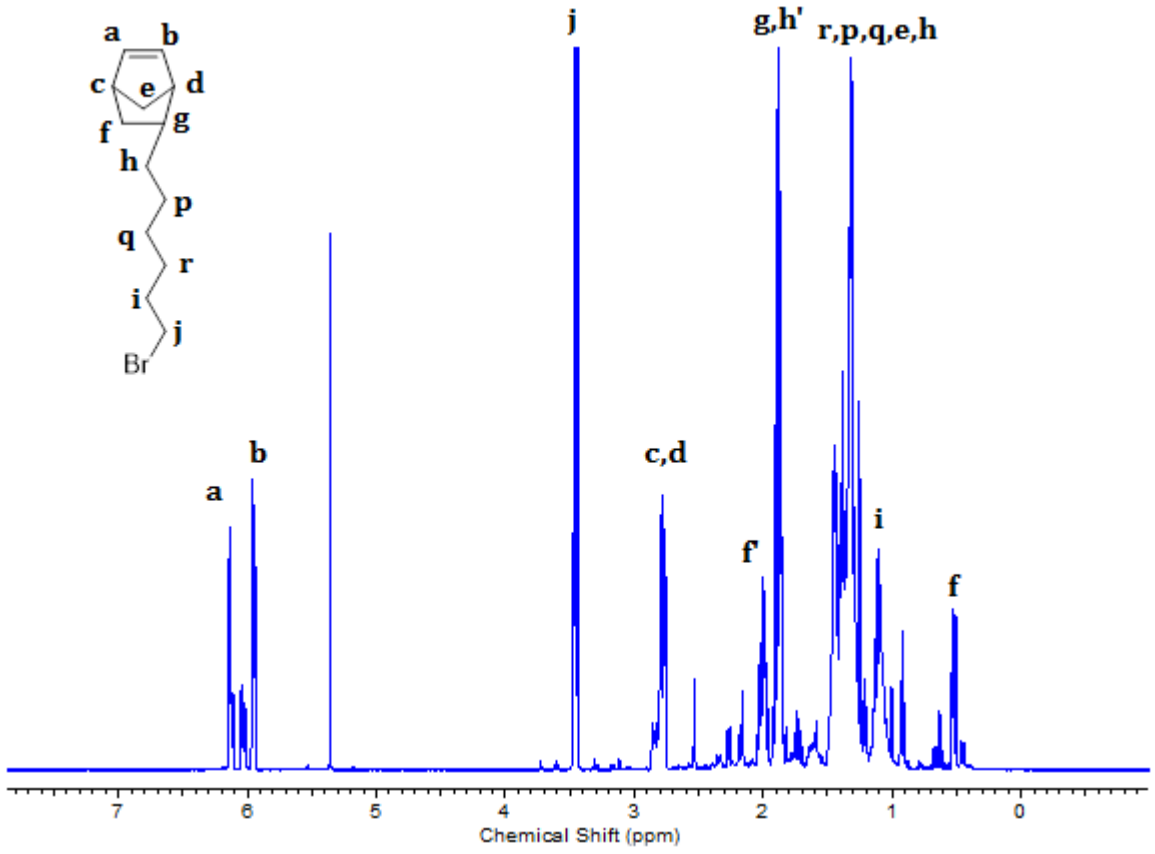

Figure 7.10. The ^{1}H NMR spectra for norbornenehexylbromide.

7.2.19 Synthesis of Norbornenehexoxy-6-azonia-spiro[5,5]undecane (NHS5)

In a round bottom flask, 1.15 g (4.6 mmoles) of 4-hydroxy-6-azonia-spiro[5,5]undecane was dissolved in 50 ml of anhydrous DMSO. The solution was gradually added to 0.35 g (9 mmoles) of sodium hydride in another round bottom flask equipped with a magnetic stirrer. The reaction proceeded at room temperature for 1 h. Afterwards, 1.96 g (9 mmoles) of norbornenehexylbromide dispersed in 5 ml anhydrous DMSO was gradually added into the reaction mixture. The color of the mixture changes from white to light brown. The reaction was allowed to proceed for 20 h. Thereafter, the mixture was vacuum filtered to remove unreacted sodium hydride. The filtrate was a viscous clear brown liquid. The filtrate was then precipitated into diethyl ether to give a white

solid. After filtration, the white solid was then washed in diethyl ether again and dried. The white solid was then dissolved in 100 ml of hot acetone to filter-off unreacted 4-hydroxy-6-azonia-spiro[5,5]undecane and sodium bromide. The product was then recrystallized from acetone by cooling the solution to 4 ºC. After filtration, the crystals were then washed in diethyl ether and dried in vacuum to afford 1.86 g (95% yield) of desired product.

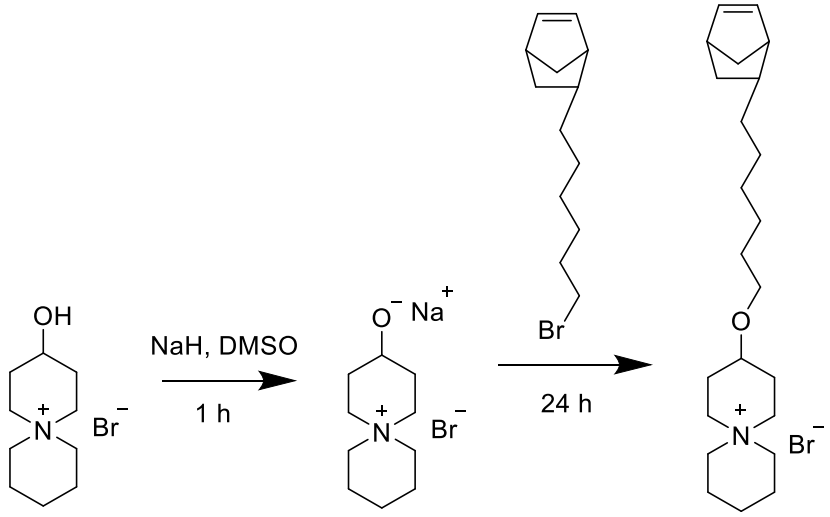

Scheme 7.12. Synthesis of norbornenehexoxy-6-azonia-spiro[5,5]undecane (NHS5).

Characterization of the product by ^{1}H NMR confirm the successful synthesis of norbornenehexoxy-6-azonia-spiro[5,5]undecane. The protons of norbornenehexoxy-6-azonia-spiro[5,5]undecane and their corresponding peaks on the ^{1}H NMR spectrum are shown in Figure 7.11.

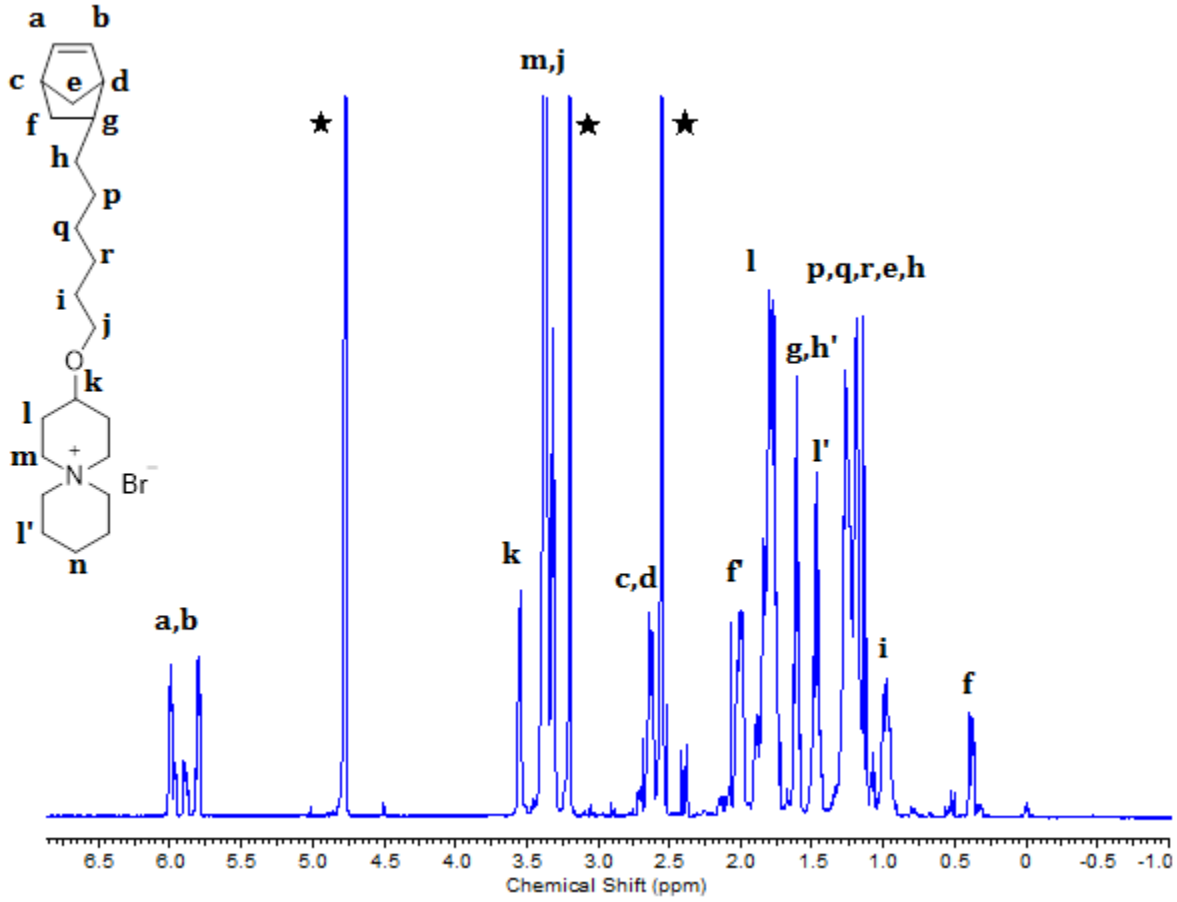

Figure 7.11. The ^{1}H NMR spectrum of norbornenehexoxy-6-azonia-spiro[5,5]undecane (NPS5).

The product, norbornenehexoxy-6-azonia-spiro[5,5]undecane, was further characterized by TOF-Mass Spectrometer. The product, norbornenehexoxy-6-azonia-spiro[5,5]decane, was further characterized by TOF-Mass Spectrometer. From the chromatogram of norbornenehexoxy-6-azonia-spiro[5,5]decane, shown in Figure 7.12, a spectral line on the molecular weight to charge ratio of 346 g/mol.C corresponds to the molecular weight of norbornenehexoxy-6-azonia-spiro[5,5]decane without the bromide counterion. These results confirm that norbornenehexoxy-6-azonia-spiro[5,5]decane was successfully synthesized.

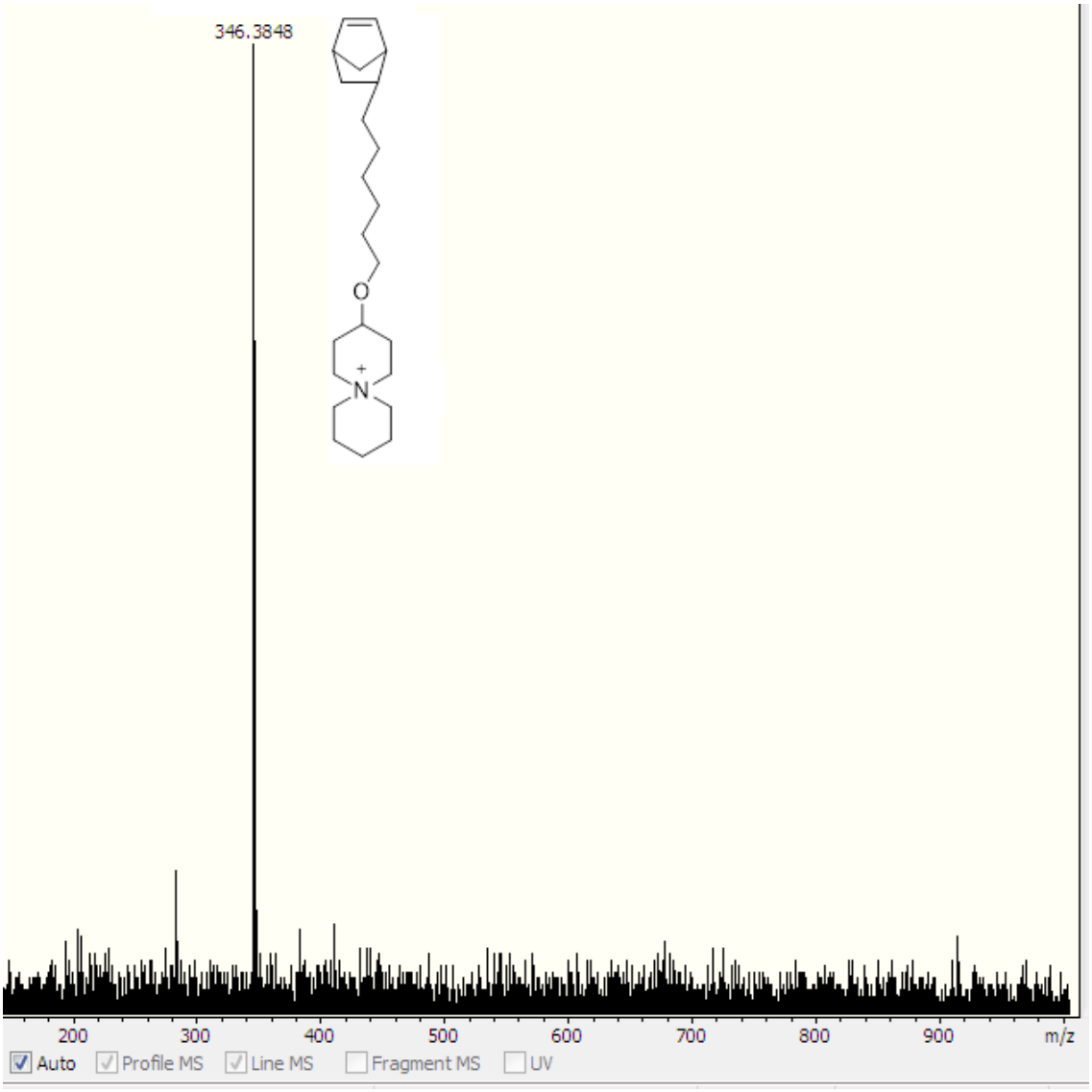

Figure 7.12. The TOF-Mass spectrometer chromatogram of norbornenehexoxy-6-azonia-spiro[5,5]undecane (NHS5).

7.2.20 Homopolymerization of Norbornenehexoxy-6-azonia-spiro[5,5]undecane (NHS5)

In a 20 ml scintillation vial, 200 mg (0.45 mmoles) of NHS5 in 5 ml of DMF was charged into a solution of 3 mg (0.0035 mmoles) of Grubbs' II catalyst in 0.5 ml of DCM equipped with a magnetic stirrer. The reaction proceeded for 24 h and afterwards precipitated in diethyl ether to afford 168 mg (84% yield) of polymer.

Characterization of the product by ^{1}H NMR confirm the successful synthesis of polynorbornenehexoxy-6-azonia-spiro[5,5]undecane. The protons of polynorbornenehexoxy-6-azonia-spiro[5,5]undecane and their corresponding peaks on the ^{1}H NMR spectrum are shown in Figure 7.13.

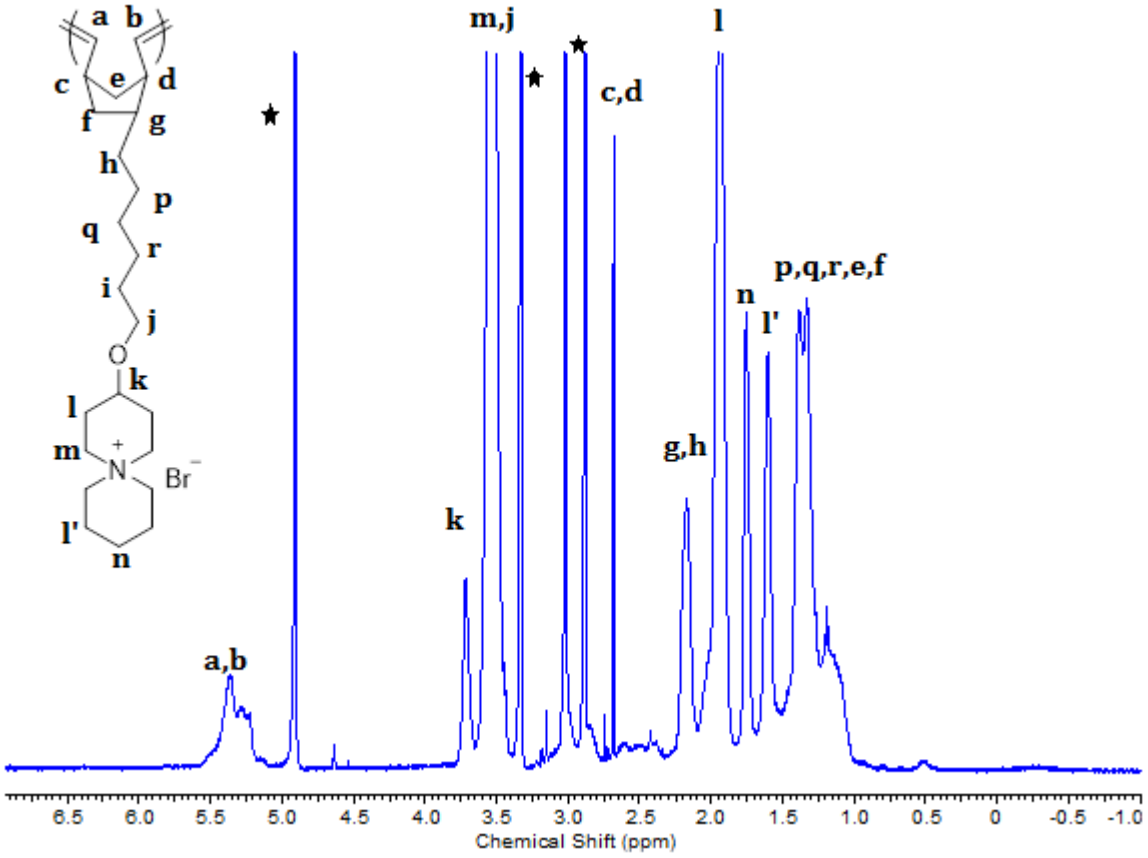

Figure 7.13. The ^{1}H NMR spectrum of polynorbornenehexoxy-6-azonia-spiro[5,5]undecane (PNHS5).

7.2.21 Characterization of PNPS5 and PNHS5 by MAXS and WAXS

Medium-angle X-ray scattering (MAXS) and Wide-angle X-ray scattering (WAXS) measurements were performed in transmission geometry on Molmex Scientific Ganesha SAXS Lab. A double aperture for the Cu-Kα radiation (λ = 1.54 Å), which was the X-ray source, was used. Silver behenate was used as the standard for the momentum transfer calibration. Data collection was performed with a typical exposure time of two minutes. Depending on the signal-to-noise ratio, data collection could be longer. Azimuthal averaging of the obtained isotropic 2-D pattern was performed to obtain the intensity against wave vector plot.

7.2.22 Results and Discussion for Homopolymer Characterization

From the MAXS spectra, see Figure 7.14, a peak at higher *Q* values is evident for both homopolymers. With increasing number of carbons on the pendant side-chain connecting the polymer backbone to the spirocyclic salt, the scattering peak moves to lower *Q* values. This peak is the backbone-backbone spacing in both PNPS5 and PNHS5 homopolymers. This spacing result from the comb-like shape of the homopolymers. The effect of backbone-backbone spacing has been discussed in the study of quaternized P4VP and the same effect can be observed in these homopolymers.

The scattering data also show a slope of 3 at lower *Q* values for both PNPS5 and PNHS5. A scattering slope of 3 for colloids suggests a lamellar arrangement pattern. A similar X-ray scattering slope in these homopolymers suggest that the backbone-backbone arrangement in PNPS5 and PNHS5 are arranged in a lamellar pattern.

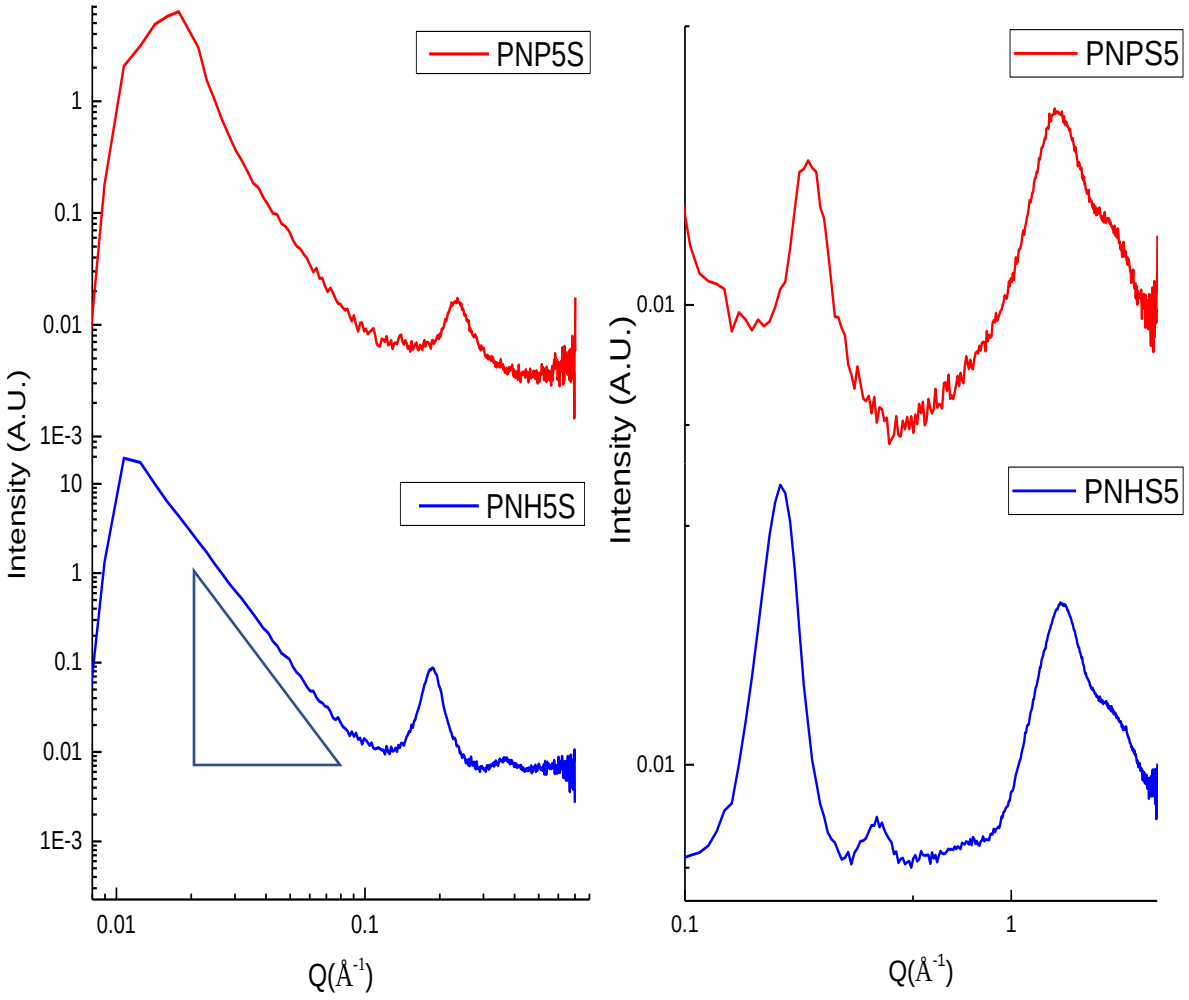

Figure 7.14. The Scattering profiles of PNPS5 and PNHS5 MAXS (right) and WAXS (left).

A cursory count of the number of carbons away from the norbornene backbones show that these chain spacing increases with increasing number of backbone carbons. polynorbornenepropoxy-6-azonia-spiro[5,5]undecane is approximately 9 carbons away from the backbone with a spacing of 2.7 nm while PNPS5 is approximately 12 carbons away with a backbone spacing of 3.2 nm. The increase in the backbone-backbone spacing with increasing number of carbons on the pendant side-chains is common in comb-shaped polymers.[35] However, most comb-shaped polymers

studied in the literature do not have cyclic pendant groups. The MAXS spectra for PNPS5 and PNHS5 show that the relationship between the backbone-backbone spacing and number of carbons on the pendant group in comb-shaped polymers with cyclic side-groups is comparable to the relationship between backbone-backbone spacing and number of carbons on the pendant group in comb-shaped polymers with linear side-chains.

The scattering data show two peaks for PNHS5. This suggests that the degree of ordering in PNHS5 is higher than that in PNPS5. The increase in the degree of ordering with increasing number of carbons on the pendant side-chain was observed in P4VP_CnBr. The ratio of the peak at higher reflection to the primary peak in PNHS5 is approximately 2. This confirms a layered arrangement of the backbones in PNHS5. Given that the only difference between PNPS5 and PNHS5 is the addition of 3 carbons on the pendant side-chain connecting the backbone to the spirocyclic salt, the arrangement of backbones in PNSP5 should be similar to the arrangement of backbones in PNHS5. The backbones in PNPS5 would have a lamellar arrangement.

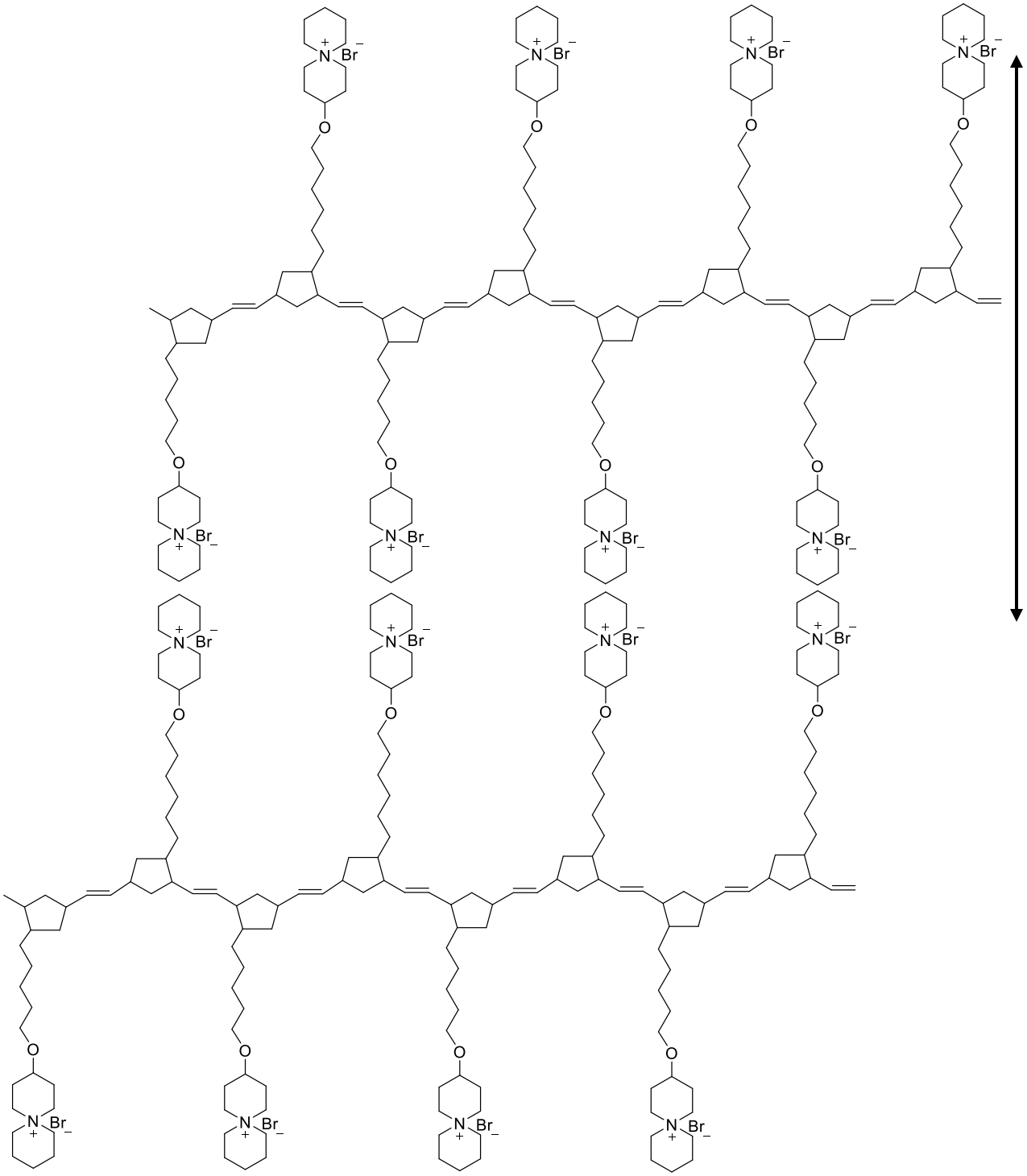

Figure 7.15. Depiction of backbone-backbone arrangement in PNHS5.

It is important to note that these are not ionomer peaks as ionomer peaks are generally found in the X-ray scattering of random copolymers in which the mole fraction of the ionic component does not exceed 0.5.[8] Ionomers generally have two regions, multiplet/cluster and matrix regions. In this case we have a one component system. A single component system like PNPS5 and PNHS5 does not have ionic and non-ionic copolymers that can facilitate an ionomer type phase separation. Thus, there are no clusters of ions in a hydrophobic matrix. The observed scattering peak is not due to 'two regions' but a consequence of the periodic spacing between the backbones of the polymers.

The effect of the backbone length on the morphology of PNPS5 and PNHS5 copolymers and the subsequent effect on conductivity will be investigated in the next chapter. Since conductivity is dependent on water uptake, the interaction of PNPS5 and PNHS5 and water is interesting. Both homopolymers are soluble in water. By comparing these ASU-type homopolymers with poly(*n*-alkyl4vinylpyridiniumbromide) homopolymers, P4VP_CnBr, it is evident that the structure of these homopolymers and not just their charge concentration affect their solubility. In the P4VP_CnBr series, samples having 5 or more carbons on the pendant side-chain are insoluble in water even though these samples have higher IECs than PNPS5 (2.6 mmoles/g) and PNHS5 (2.3 mmoles/g). The difference in the resistance of the pyridiniumbromide-based homopolymers and ASU-type homopolymers to solvation in water may be influenced by their short-range ordering. The backbone-backbone spacing in PNPS5 and PNHS5 is larger than the backbone-backbone spacing in P4VP_C5Br. However, the spacing between the dipoles in PNPS5 and PNHS5, although the same, is different from the spacing between the dipoles in P4VP_C5Br. The spacing between the dipoles in P4VP_C5Br is equivalent to the spacing between the backbones, however, the spacing between the dipoles in PNPS5 and PNHS5 is the spacing between the centers of two

spirocyclic groups on adjacent backbones. The smaller the spacing between dipoles, the more likely is it for dipoles to accrue water molecules, thereby, solvating the polymer membrane. The more isolated the dipoles are, the more likely is it for the membrane to be insoluble in water even if the membrane has a higher IEC. The same trend was observed in the water uptake of XP4VP-*r*-PS_CnBr series studied in Chapter 5. Due to the solubility of PNPS5 and PNHS5 in water, PNPS5 and PNHS5 will be copolymerized with a hydrophobic copolymer that can provide mechanical integrity in a humidified environment.

7.2.23 Chemical Stability Norbornenepropoxy-6-azonia-spiro[5,5]undecane (NPS5)

To assay the chemical stability of norbornenepropoxy-6-azonia-spiro[5,5]undecane in an alkaline environment, 200 mg of the monomer was dissolved in a 2 M solution of KOH in a mixture of methanol and water (9:1) was charged into a 20 ml plastic bottle equipped with a stirrer. The plastic bottle was sealed and placed in an oil bath at 80 °C. Aliquots were taken at 2, 4, 9, and 15 days and characterized by ^{1}H NMR to monitor the degradation of the monomer.

The ^{1}H NMR spectra show that the peak of the alpha proton of the secondary carbon in the ether linkage degraded slightly over the course of two weeks. The results obtained by Marino and Kreuer show that the salt, 6-azonia-**s**piro[5,5]undecane, was very stable in alkaline conditions. Concerns about the ability of the monomer, norbornenepropoxy-6-azonia-spiro[5,5]undecane, to withstand degradation in aggressive alkaline medium has centered around the alpha proton of the secondary carbon in the ether linkage in NPS5. The intensity of the peak arising from the alpha proton of the secondary carbon in the ether linkage show that the ether in norbornenepropoxy-6-azonia-spiro[5,5]undecane degraded by 1.5 % over the course of the experiment. Further analysis of the alpha protons in proximity to the ammonium cation show no degradation for the 15 days the

monomer was studied. These results suggest that polymers obtained from the ring-opening metathesis polymerization of norbornenepropoxy-6-azonia-spiro[5,5]undecane would be chemically stable in aggressive alkaline media.

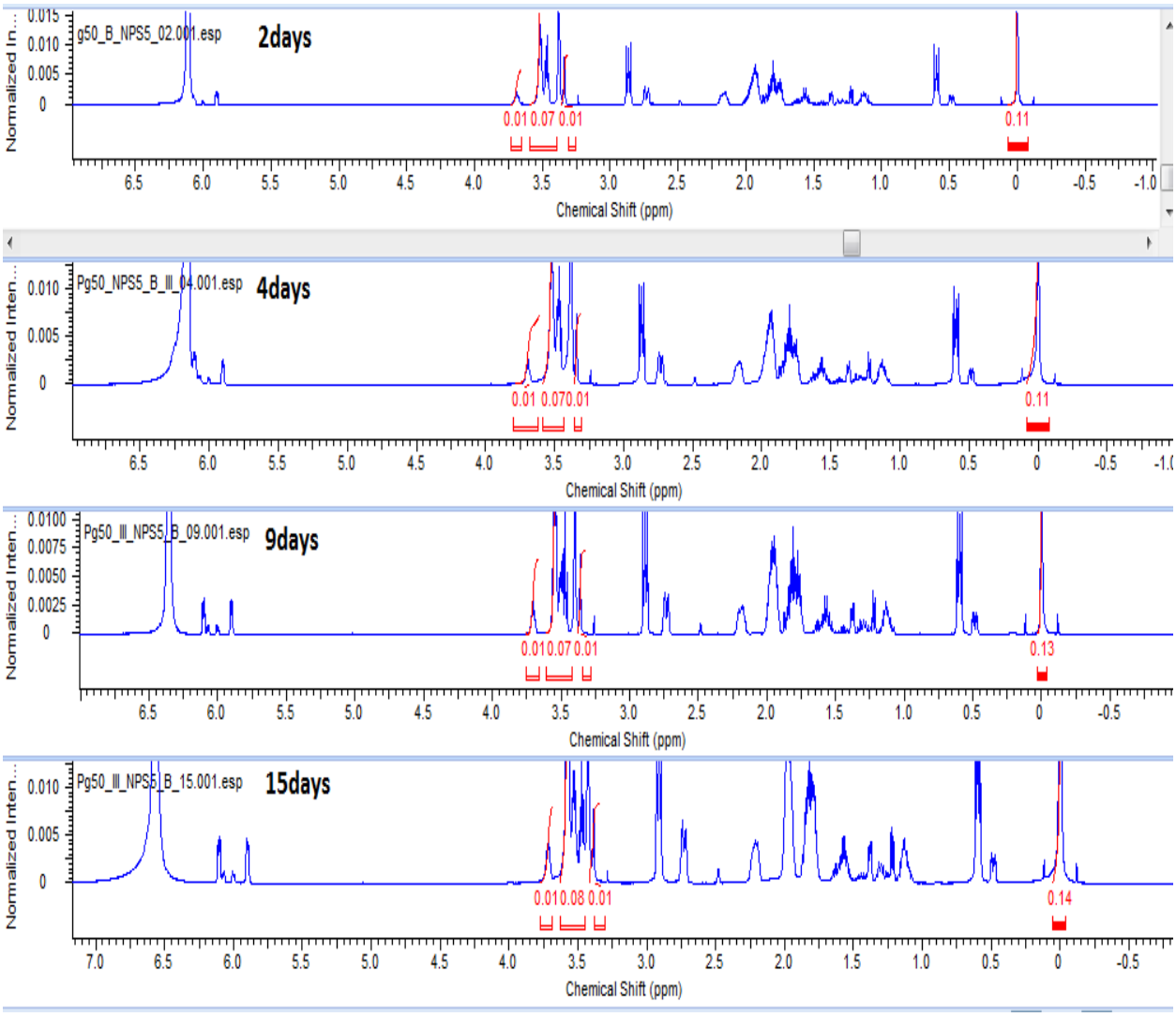

Figure 7.16. The ^{1}H NMR spectra showing the degradation of NPS5 in alkaline medium.

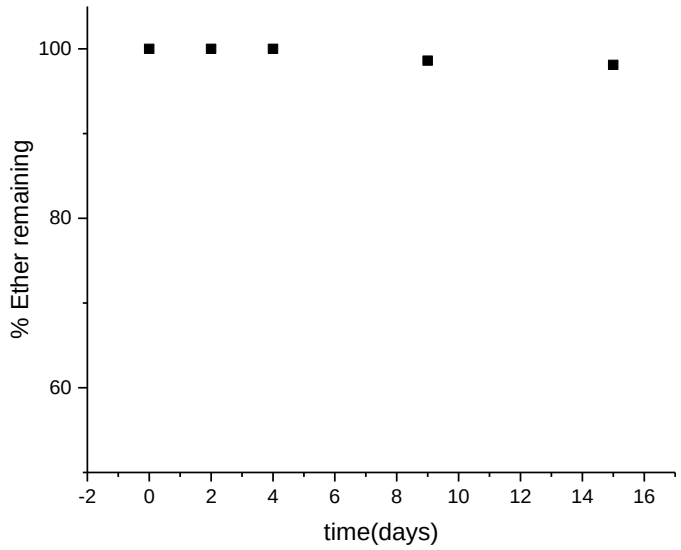

Figure 7.17. Degradation of the alpha proton of the secondary carbon in the ether linkage of NPS5 in alkaline medium.

Similar degradation rate for the alpha proton of the secondary carbon in the ether linkage in NPS5 monomer was observed in norbornenehexoxy-6-azonia-spiro[5,5]undecane. See Figure 7.18.

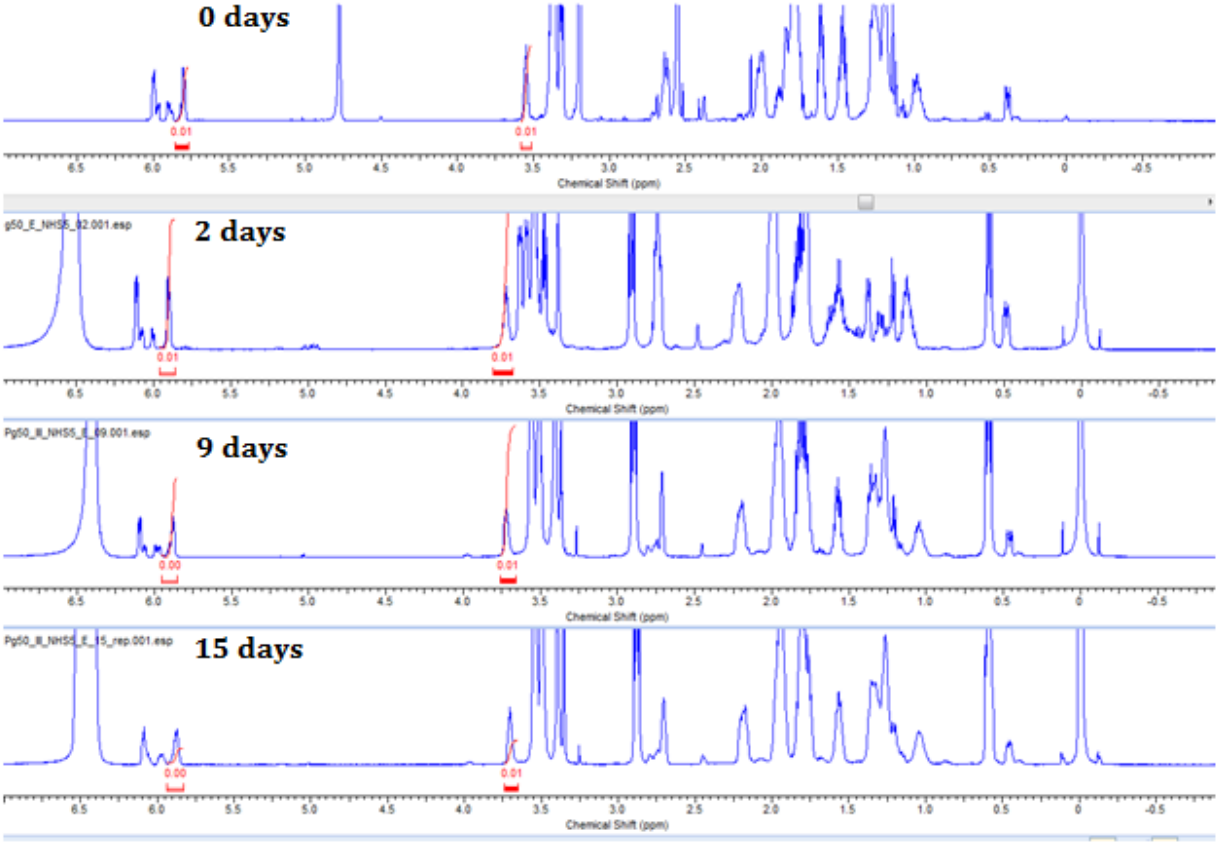

Figure 7.18. The ^{1}H NMR spectra showing the degradation of NHS5 in alkaline medium.

Having this robust synthetic platform motivated us to synthesize other azo-type norbornene monomers based on (6-azonia-spiro[5,4]decane and 6-azonia-spiro[5,6]dodecane) were designed and synthesized.

7.2.24 Synthesis of 4-Hydroxy-6-azonia-spiro[5,4]decane

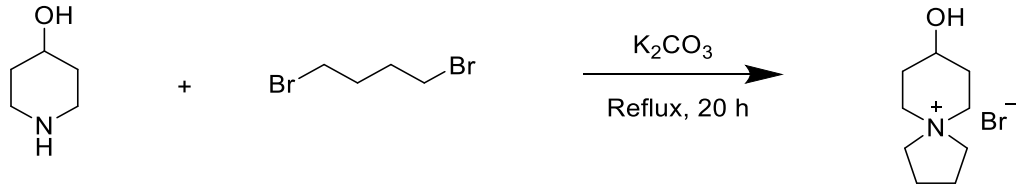

Scheme 7.14. Synthesis of 4-hydroxy-6-azonia-spiro[5,4]decane.

In a two-neck round bottom flask, 21 g (0.152 moles) of potassium carbonate was charged into a solution of 26 g (0.124 moles) of 1,4 dibromobutane in 300 ml of acetonitrile. The mixture was heated to reflux. After 10 minutes, a solution of 10.1 g (0.1 moles) of 4-hydroxypiperidine in 50 ml of acetonitrile was added to the mixture. After 20 h the reaction bath was gradually cooled to room temperature. The reaction mixture was then rotovapped to remove the solvent leaving an off-white solid which was re-dissolved in 300 ml of ethanol to filter-off the unreacted potassium carbonate. The solution was then partially evaporated to obtain a concentrated solution that was precipitated into diethyl ether. Afterwards, the yellowish was filtered and washed thrice in DCM. The solid was then dried in vacuo at room temperature to afford 16.9 g (72% yield) of an off-white solid.

Characterization of the product by ^{1}H NMR confirm the successful synthesis of 4-hydroxy-6-azonia-spiro[5,4]decane. The protons of 4-hydroxy-6-azonia-spiro[5,4]decane and their corresponding peaks on the ^{1}H NMR spectrum are shown in Figure 7.19.

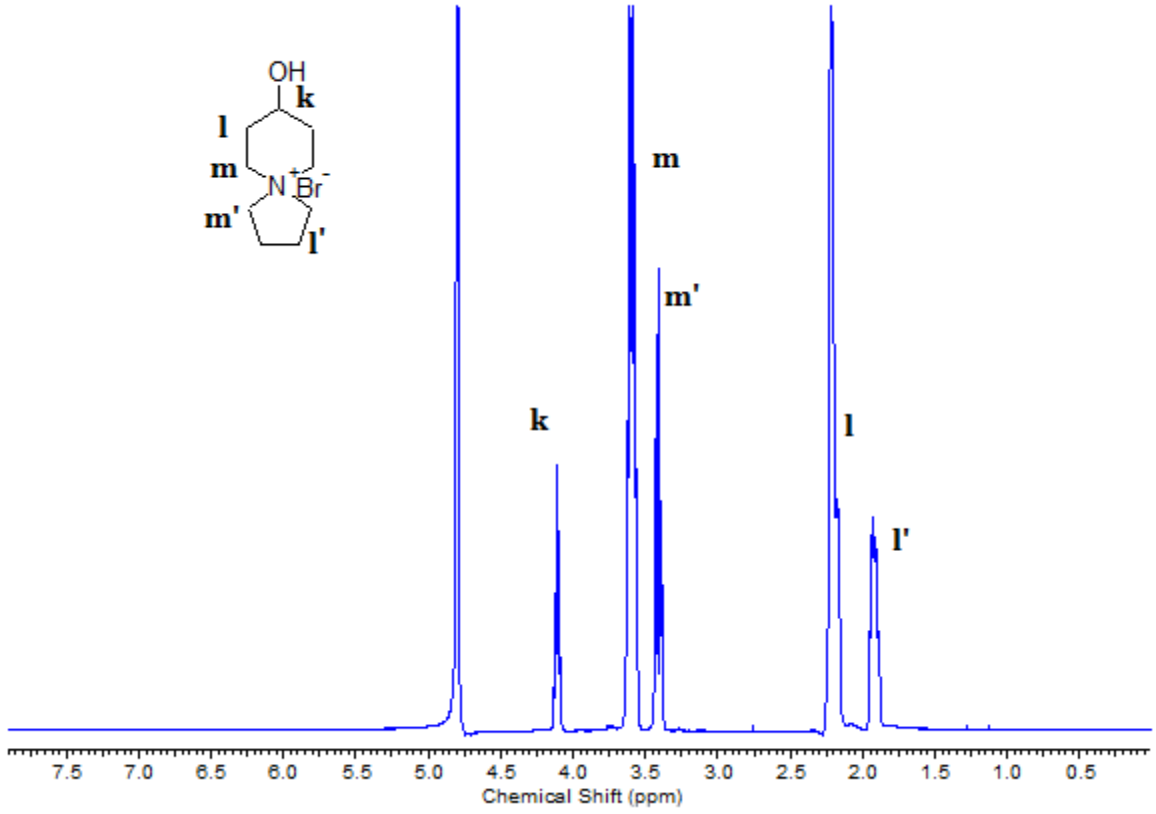

Figure 7.19. The ^{1}H NMR spectrum 4-hydroxy-6-azonia-spiro[5,4]decane.

The product, 4-hydroxy-6-azonia-spiro[5,4]decane, was further characterized by TOF-mass spectrometer. From the chromatogram of 4-hydroxy-6-azonia-spiro[5,4]decane, shown in Figure 7.20, a spectral line on the molecular weight to charge ratio of 156 g/mol.C corresponds to the molecular weight of 4-hydroxy-6-azonia-spiro[5,4]decane without the bromide counterion. Two spectral lines on 393 and 391 g/mol.C resulting from the two isotopes of bromine (79 and 81 g/mol) are visible on the spectra at higher m/z ratios. These spectral lines corresponds to two 4-hydroxy-6-azonia-spiro[5,4]decane and one bromide counterion. These results confirm that 4-hydroxy-6-azonia-spiro[5,4]decane was successfully synthesized.

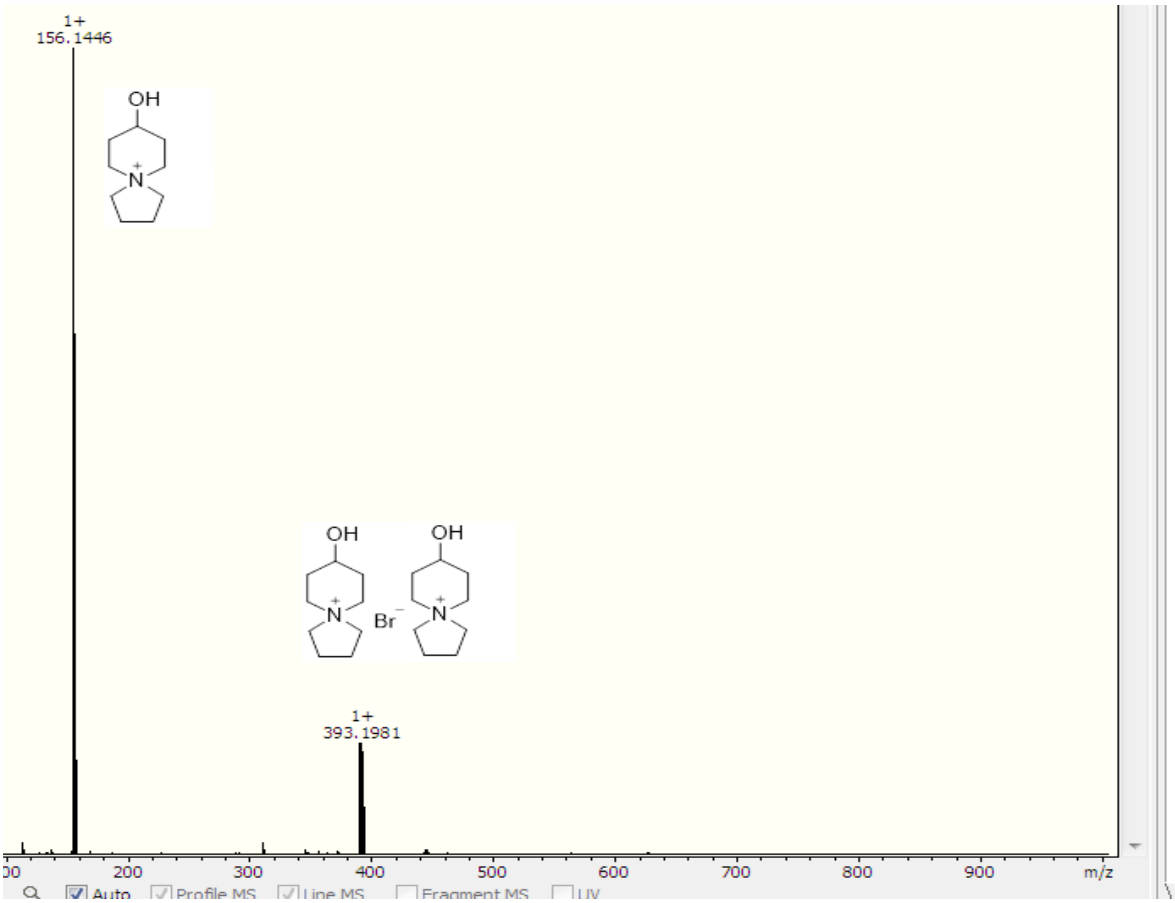

Figure 7.20. The TOF-mass spectrometer chromatogram of 6-azonia-spiro[5,4]decane

7.2.25 Synthesis of Norbornenepropoxy-6-azonia-spiro[5,4]decane (NPS4)

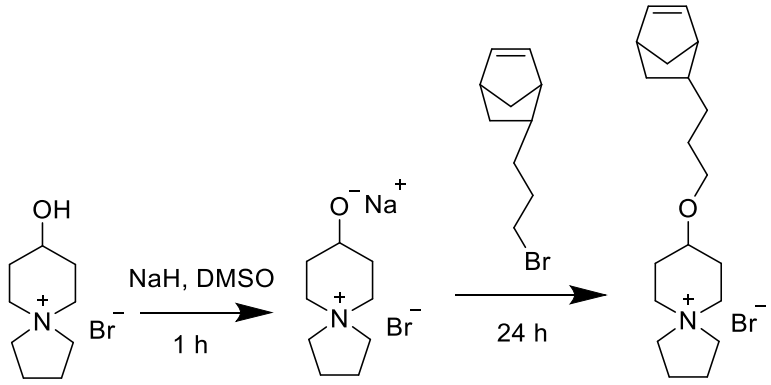

Scheme 7.15. Synthesis of norbornenepropoxy-6-azonia-spiro[5,4]decane (NPS4).

In a round bottom flask, 3.0 g (12.2 mmoles) of 4-hydroxy-6-azonia-spiro[5,4]decane was dissolved in 30 ml of anhydrous DMSO. The solution was gradually added to another round bottom flask containing 1.02 g (25.5 mmoles) of sodium hydride equipped with a magnetic stirrer. The reaction proceeded at room temperature for 1 h. Afterwards, 5.44 g (25.4 mmoles) of norbornenepropylbromide dispersed in 30 ml anhydrous DMSO was gradually added into the reaction mixture. The color of the mixture changes from white to light brown. The reaction was allowed to proceed for 20 h. Thereafter, the mixture was vacuum filtered to remove unreacted sodium hydride. The filtrate was a viscous clear brown liquid. The filtrate was then precipitated into diethyl ether to give a white solid. After filtration, the white solid was then washed with diethyl ether again and dried. The white solid was then dissolved in 200 ml of hot acetone to filter-off unreacted 4-hydroxy-6-azonia-spiro[5,4]decane and sodium bromide. The product was then recrystallized from acetone by cooling the solution to 4 ºC. After filtration, the crystals were then washed with diethyl ether and dried in vacuum to afford 3.5 g (77% yield) of the product.

Characterization of the product by ^{1}H NMR confirm the successful synthesis of norbornenpropoxy-6-azonia-spiro[5,4]decane. The protons of norbornenpropoxy-6-azonia-spiro[5,4]decane and their corresponding peaks on the ^{1}H NMR spectrum are shown in Figure 7.21.

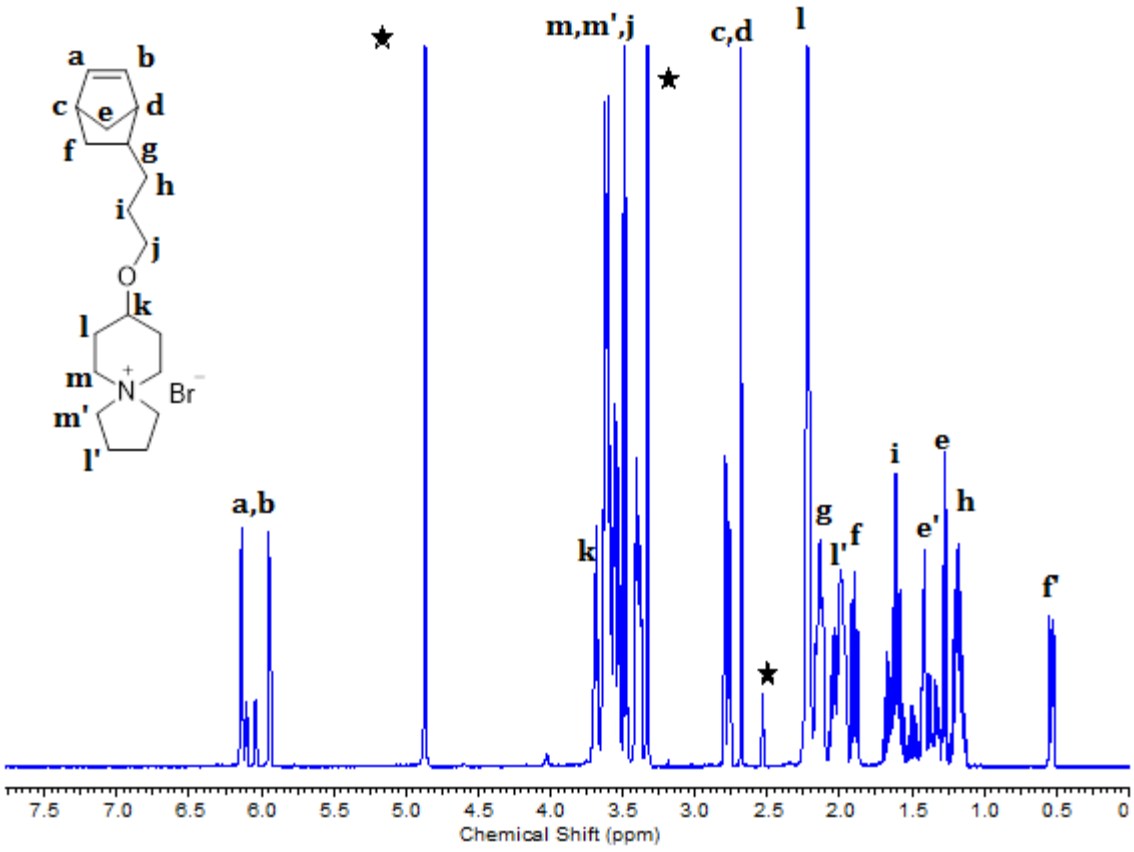

Figure 7.21. The ^{1}H NMR spectrum of norbornenepropoxy-6-azonia-spiro[5,4]decane.

The product, norbornenepropoxy-6-azonia-spiro[5,4]decane, was further characterized by TOF-mass spectrometer. From the chromatogram of norbornenepropoxy-6-azonia-spiro[5,4]decane, shown in Figure 7.22, a spectral line on the molecular weight to charge ratio of 290 g/mol.C corresponds to the molecular weight of norbornenepropoxy-6-azonia-spiro[5,4]decane without the bromide counterion. Two spectral lines on 659 and 661 g/mol.C resulting from the two isotopes of bromine (79 and 81 g/mol) are visible on the spectra at higher m/z ratios. These spectral lines corresponds to two norbornenepropoxy-6-azonia-spiro[5,4]decane and one bromide (with its two isotopes) counterion. These results confirm that norbornenepropoxy-6-azonia-spiro[5,4]decane was successfully synthesized.

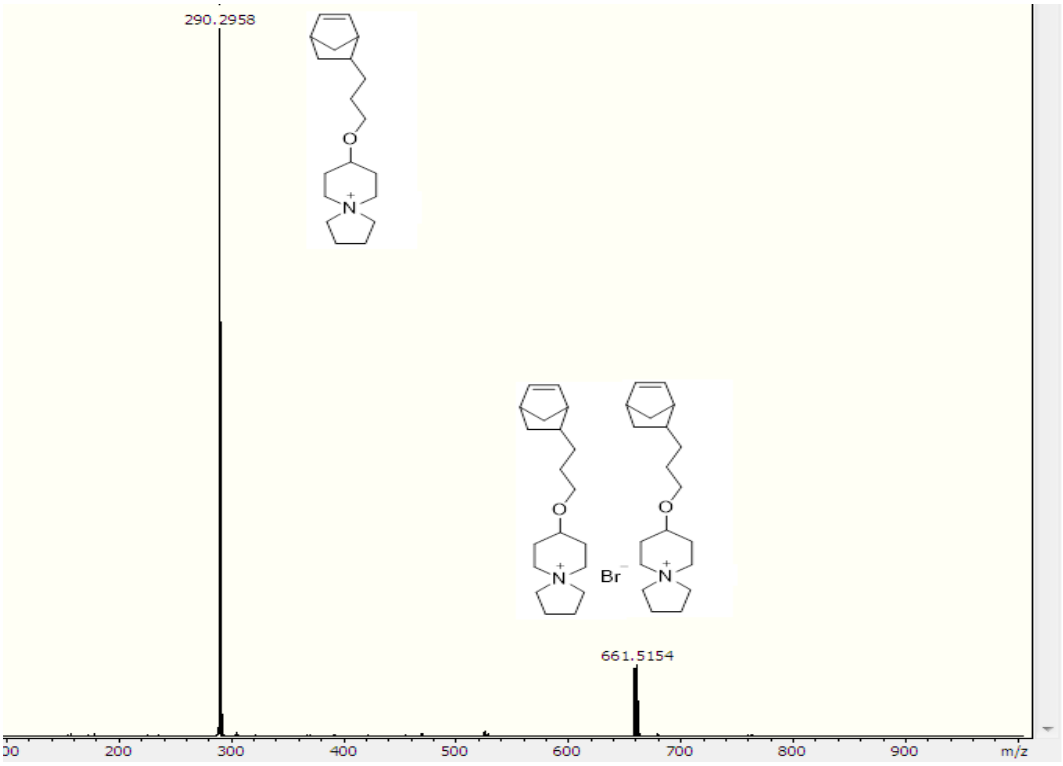

Figure 7.22. The TOF-mass spectrometer chromatogram of norbornenepropoxy-6-azonia-spiro[5,4]decane (NPS4).

7.2.26 Synthesis of Norbornenehexoxy-6-azonia-spiro[5,4]decane (NHS4)

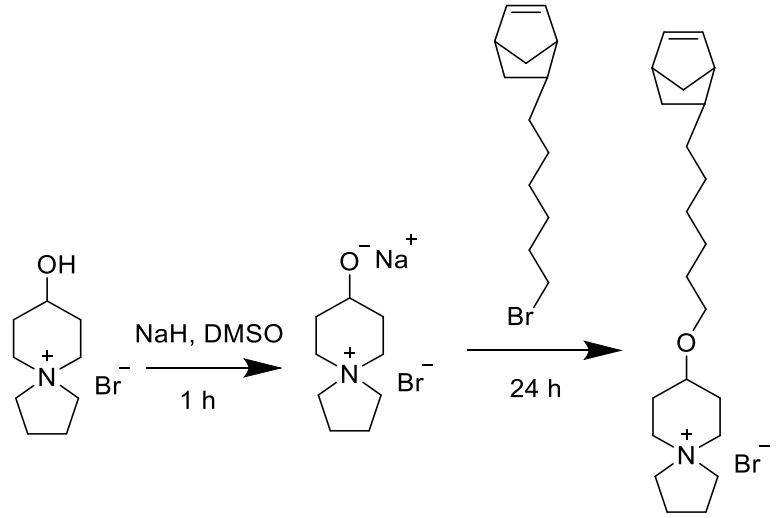

Scheme 7.16. Synthesis of norbornenehexoxy-6-azonia-spiro[5,4]decane (NHS4).

In a round bottom flask, 2.0 g (8.5 mmoles) of 4-hydroxy-6-azonia-spiro[5,4]decane was dissolved in 30 ml of anhydrous DMSO. The solution was gradually added to another round bottom flask containing 0.68 g (17.0 mmoles) of sodium hydride equipped with a magnetic stirrer. The reaction proceeded at room temperature for 1 h. Afterwards, 4.4 g (17.2 mmoles) of norbornenehexylbromide dispersed in 30 ml anhydrous DMSO was gradually added into the reaction mixture. The color of the mixture changes from white to light brown. The reaction was allowed to proceed for 20 h. Thereafter, the mixture was vacuum filtered to remove unreacted sodium hydride. The filtrate was a viscous clear brown liquid. The filtrate was then precipitated into diethyl ether to give a white solid. After filtration, the white solid was then washed with diethyl ether again and dried. The white solid was then dissolved in 200 ml of hot acetone to filter-off unreacted 4-hydroxy-6-azonia-spiro[5,4]decane and sodium bromide. The product was then recrystallized from acetone by cooling the solution to 4 ºC. After filtration, the crystals were then washed with diethyl ether and dried in vacuum to afford 2.1 g (60% yield) of desired product.

Characterization of the product by ^{1}H NMR confirm the successful synthesis of norbornenehexoxy-6-azonia-spiro[5,4]decane. The protons of norbornenehexoxy-6-azonia-spiro[5,4]decane and their corresponding peaks on the ^{1}H NMR spectrum are represented in Figure 7.23.

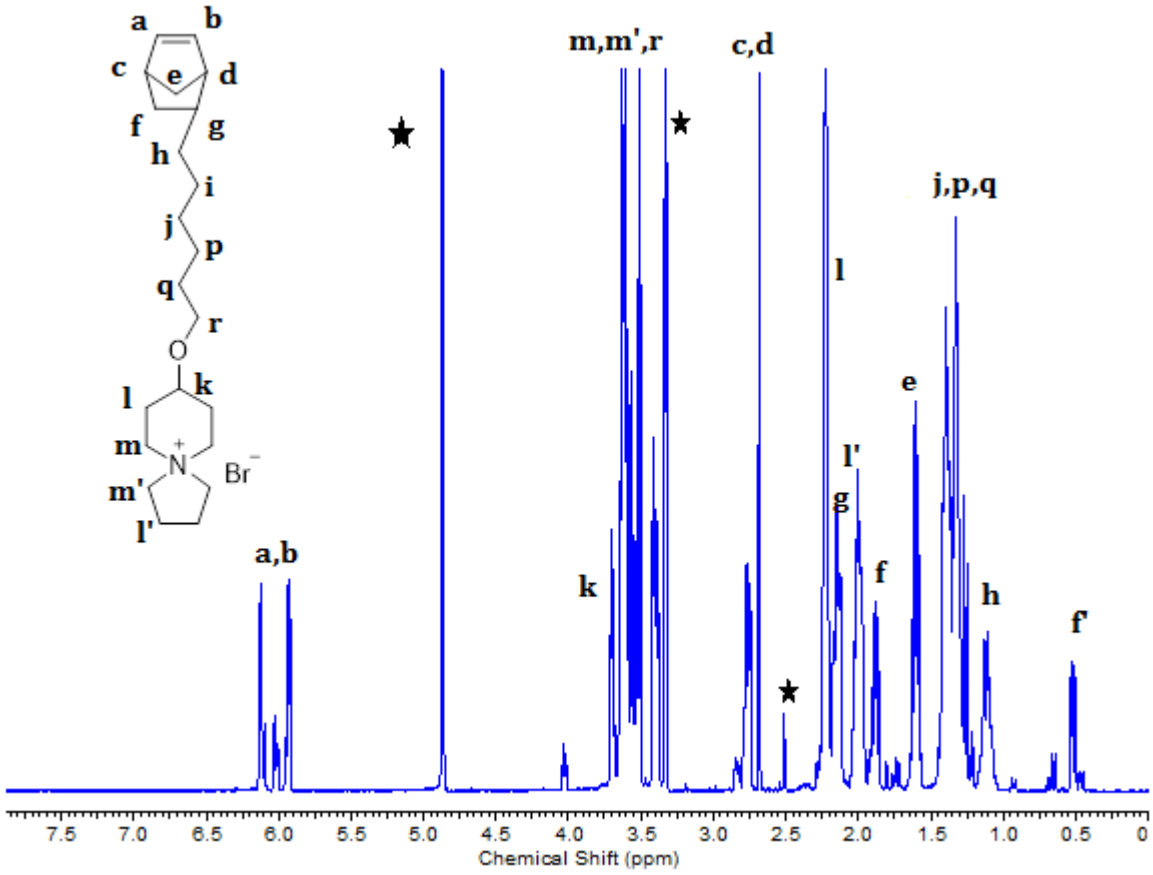

Figure 7.23. The ^{1}H NMR spectrum norbornenehexoxy-6-azonia-spiro[5,4]decane.

The product, norbornenehexoxy-6-azonia-spiro[5,4]decane, was further characterized by TOF-mass spectrometer. From the chromatogram of norbornenehexoxy-6-azonia-spiro[5,4]decane, shown in Figure 7.24, a spectral line on the molecular weight to charge ratio of 332 g/mol.C

corresponds to the molecular weight of norbornenehexoxy-6-azonia-spiro[5,4]decane without the bromide counterion. These results confirm that norbornenehexoxy-6-azonia-spiro[5,4]decane was successfully synthesized.

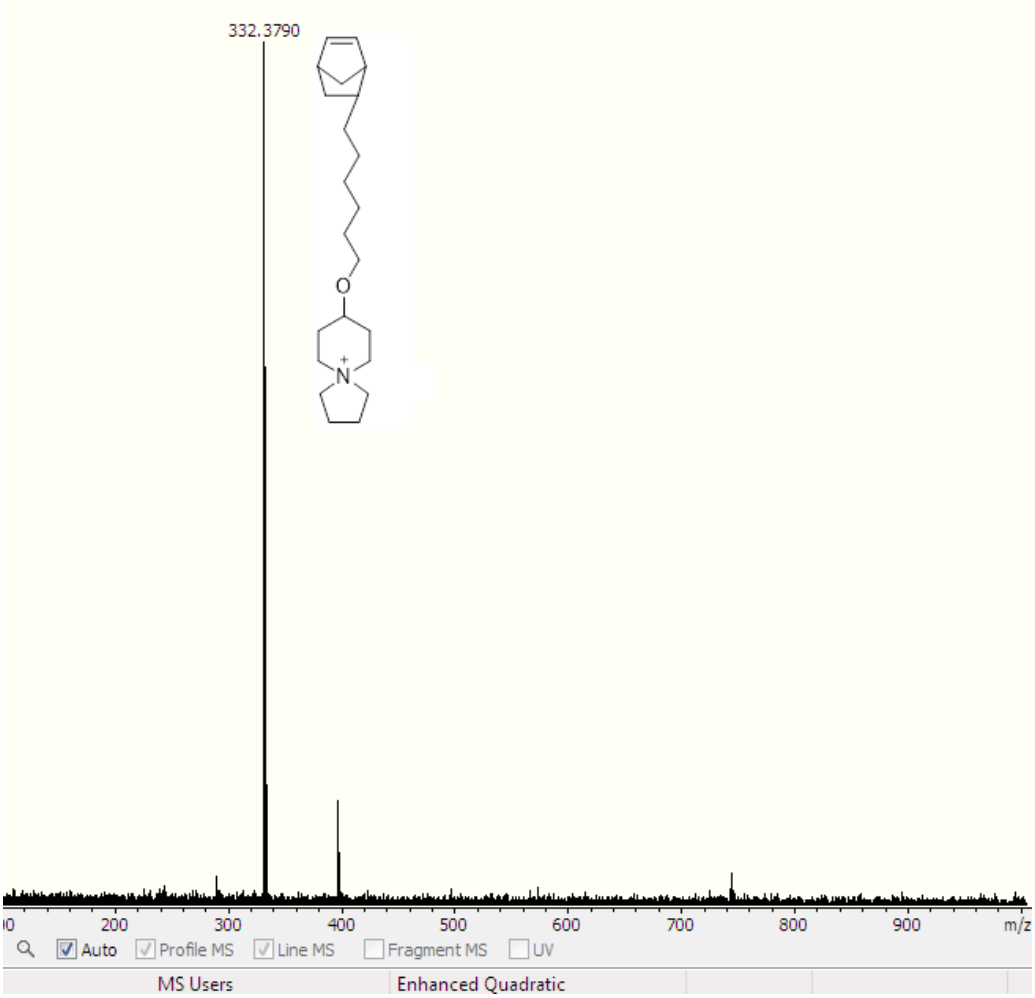

Figure 7.24. The TOF-mass spectrometer chromatogram of norbornenepropoxy-6-azonia-spiro[5,4]decane (NPS4).

7.2.27 Synthesis of 4-Hydroxy-6-azonia-spiro[5,6]dodecane

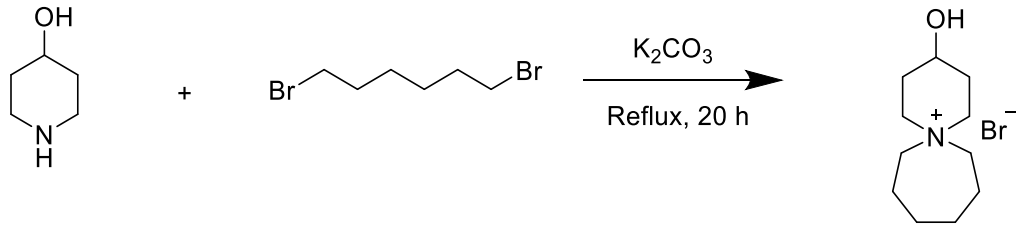

Scheme 7.17. Synthesis of 4-hydroxy-6-azonia-spiro[5,6]dodecane.

In a two-neck round bottom flask, 21 g (0.152 moles) of potassium carbonate was charged into a solution of 29.16 g (0.120 moles) of 1,6 dibromohexane in 300 ml of ethanol. The mixture was heated to reflux. After 10 minutes, a solution of 10.1 g (0.1 moles) of 4-hydroxypiperidine in 50 ml of ethanol was added to the mixture. The reaction proceeded for 20 h after which it was cooled to room temperature. Excess potassium carbonate was removed by filtration. The solution was then partially evaporated to obtain a concentrated solution that was precipitated into diethyl ether. Afterwards, the yellowish solid formed was filtered and washed in dichloromethane thrice. The solid was then dried in vacuo at room temperature to afford 19.6 g (74% yield) of an off-white solid.

Characterization of the product by ^{1}H NMR confirm the successful synthesis of 4-hydroxy-6-azonia-spiro[5,6]dodecane. The protons of and their corresponding peaks on the ^{1}H NMR spectrum are represented in Figure 7.25.

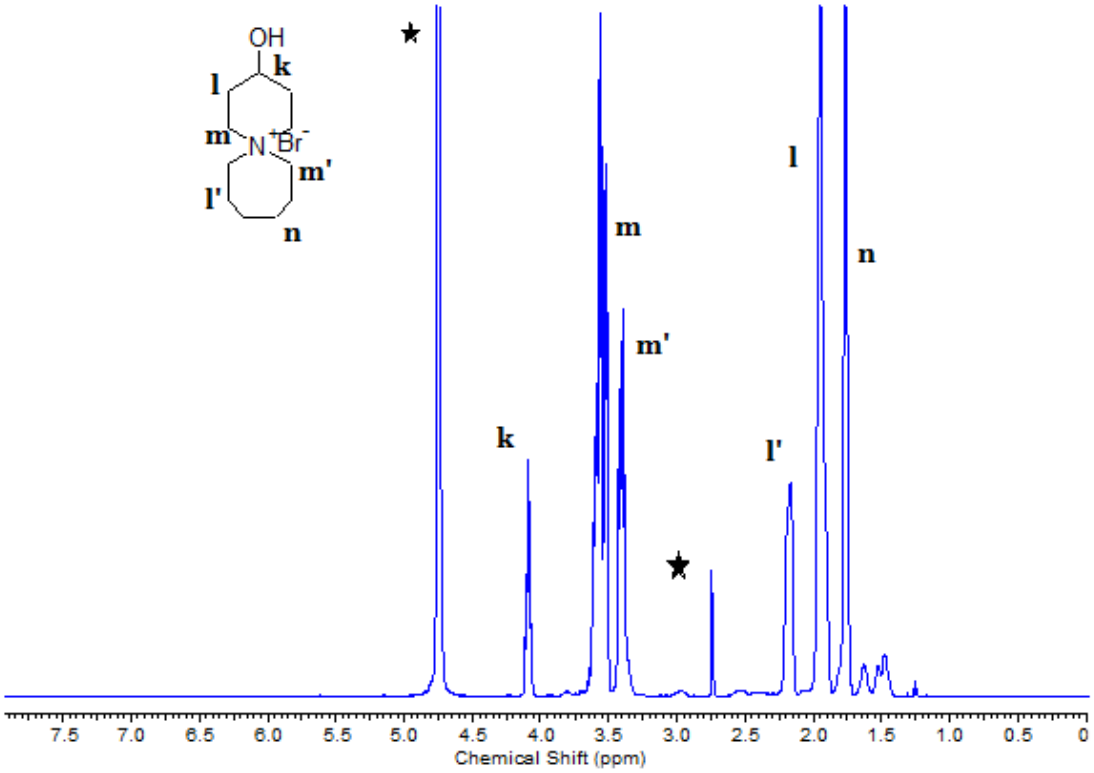

Figure 7.25. The ^{1}H NMR spectrum of 4-hydroxy-6-azonia-spiro[5,6]dodecane.

The product, 4-hydroxy-6-azonia-spiro[5,6]dodecane, was further characterized by TOF-mass spectrometer. From the chromatogram of 4-hydroxy-6-azonia-spiro[5,6]dodecane, shown in Figure 7.26, a spectral line on the molecular weight to charge ratio of 184 g/mol.C corresponds to the molecular weight of 4-hydroxy-6-azonia-spiro[5,6]dodecane without the bromide counterion. Two spectral lines on 447 and 449 g/mol.C resulting from the two isotopes of bromine (79 and 81 g/mol) are visible on the spectra at higher m/z ratios. These spectral lines corresponds to two 4-hydroxy-6-azonia-spiro[5,6]dodecane and one bromide (with its two isotopes) counterion. These results confirm that 4-hydroxy-6-azonia-spiro[5,6]dodecane was successfully synthesized.

Figure 7.26. The TOF-mass spectrometer chromatogram of 4-hydroxy-6-azonia-spiro[5,6]dodecane.

7.2.28 Synthesis of Norbornenepropoxy-6-azonia-spiro[5,6]dodecane (NPS6)

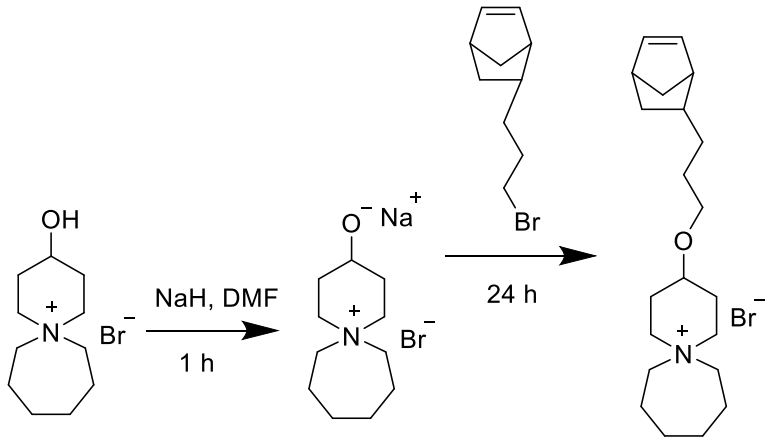

Scheme 7.18. Synthesis of norbornenepropoxy-6-azonia-spiro[5,6]dodecane (NPS6).

In a round bottom flask, 3.75 g (14.2 mmoles) of 4-hydroxy-6-azonia-spiro[5,6]dodecane was dissolved in 50 ml of anhydrous DMF. The solution was gradually added to 1.14 g (28.5 mmoles) of sodium hydride in another round bottom flask equipped with a magnetic stirrer. The reaction proceeded at room temperature for 1 h. Afterwards, 3.75 g (17.6 mmoles) of norbornenepropylbromide dispersed in 30 ml anhydrous DMF was gradually added into the reaction mixture. The color of the mixture changes from white to light brown. The reaction was allowed to proceed for 20 h. Thereafter, the mixture was vacuum filtered to remove unreacted sodium hydride. The filtrate was a viscous clear brown liquid. The filtrate was then precipitated into diethyl ether to give a white solid. After filtration, the white solid was then washed in diethyl ether again and dried. The white solid was then dissolved in 100 ml of hot acetone to filter-off unreacted 4-propoxy-6-azonia-spiro[5,6]dodecane and sodium bromide. The product was then recrystallized from acetone by cooling the solution to 4ºC. After filtration, the crystals were then washed in diethyl ether and dried in vacuum to afford 3.4 g (60% yield) of desired product.

Characterization of the product by ^{1}H NMR confirm the successful synthesis of norbornenepropoxy-6-azonia-spiro[5,6]dodecane. The protons of norbornenepropoxy-6-azonia-spiro[5,6]dodecane and their corresponding peaks on the ^{1}H NMR spectrum are represented in Figure 7.27.

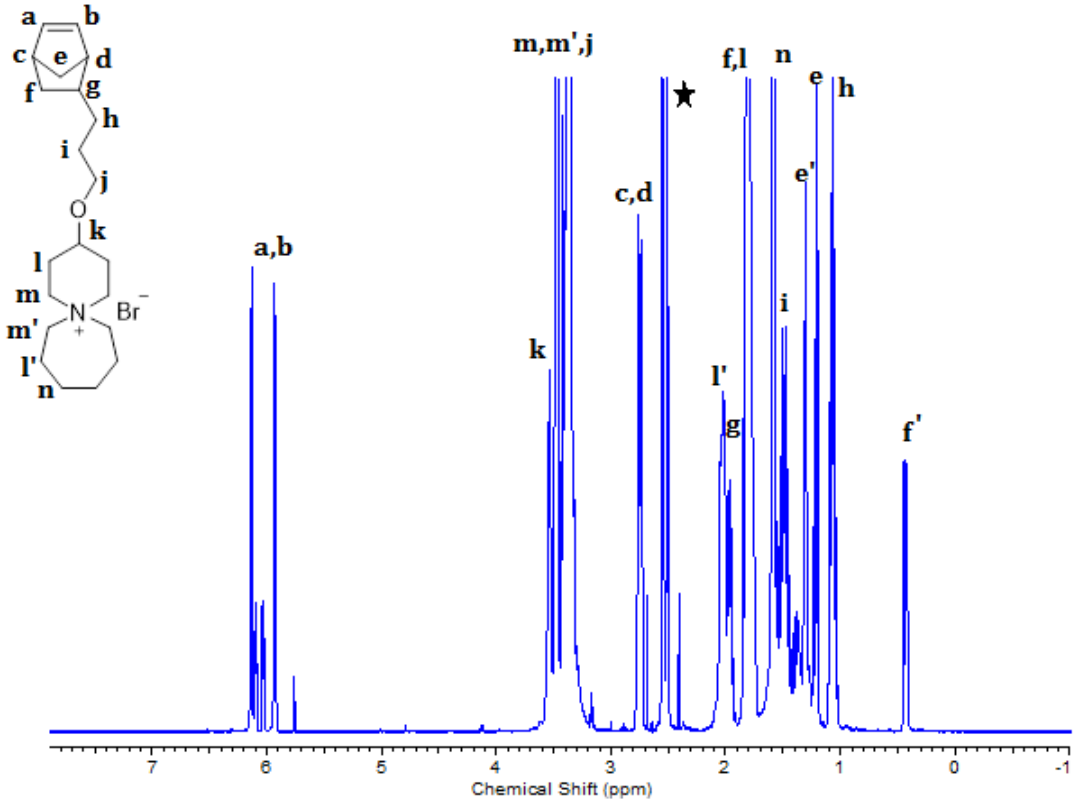

Figure 7.27. The ^{1}H NMR spectrum of norbornepropoxy-6-azonia-spiro[5,6]dodecane.

7.2.29 Synthesis of Norbornenehexoxy-6-azonia-spiro[5,6]dodecane (NHS6)

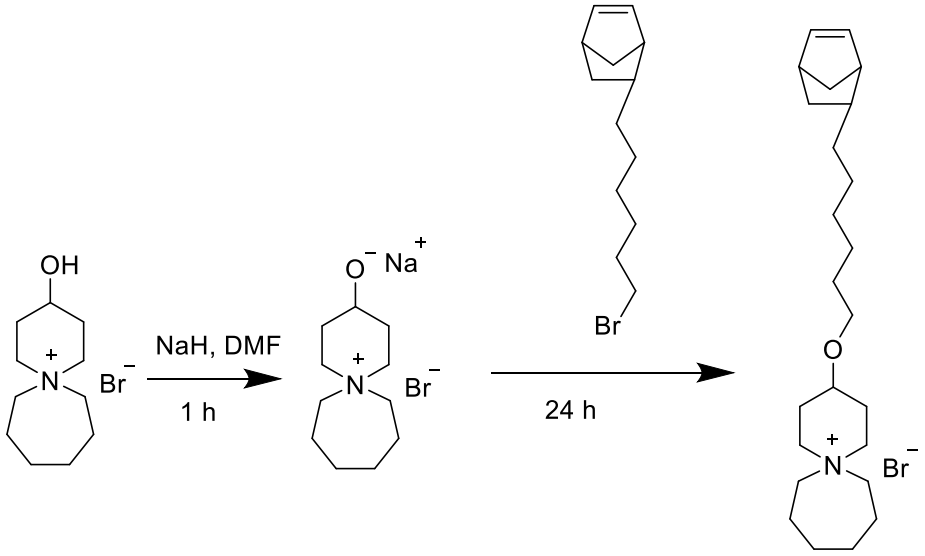

Scheme 7.19. Synthesis of norbornenehexoxy-6-azonia-spiro[5,6]dodecane (NHS6).

In a round bottom flask, 4.0 g (15.2 mmoles) of 4-hydroxy-6-azonia-spiro[5,6]dodecane was dissolved in 50 ml of anhydrous DMF. The solution was gradually added to 1.2 g (30 mmoles) of sodium hydride in another round bottom flask equipped with a magnetic stirrer. The reaction proceeded at room temperature for 1 h. Afterwards, 8 g (31.3 mmoles) of norbornenehexylbromide dispersed in 30 ml anhydrous DMF was gradually added into the reaction mixture. The color of the mixture changes from white to light brown. The reaction was allowed to proceed for 20 h. Thereafter, the mixture was vacuum filtered to remove unreacted sodium hydride. The filtrate was a viscous clear brown liquid. The filtrate was then precipitated into diethyl ether to give a white solid. After filtration, the white solid was then washed in diethyl ether again and dried. The white solid was then dissolved in 100 ml of hot acetone to filter-off unreacted 6-azonia-spiro[5,6]dodecane and sodium bromide. The product was then recrystallized from acetone by

cooling the solution to 4 ºC. After filtration, the crystals were then washed in diethyl ether and dried in vacuum to afford 5.7 g (86 % yield) of desired product.

Characterization of the product by ^{1}H NMR confirm the successful synthesis of norbornenehexoxy-6-azonia-spiro[5,6]dodecane. The protons of norbornenehexoxy-6-azonia-spiro[5,6]dodecane and their corresponding peaks on the ^{1}H NMR spectrum are represented in Figure 7.28.

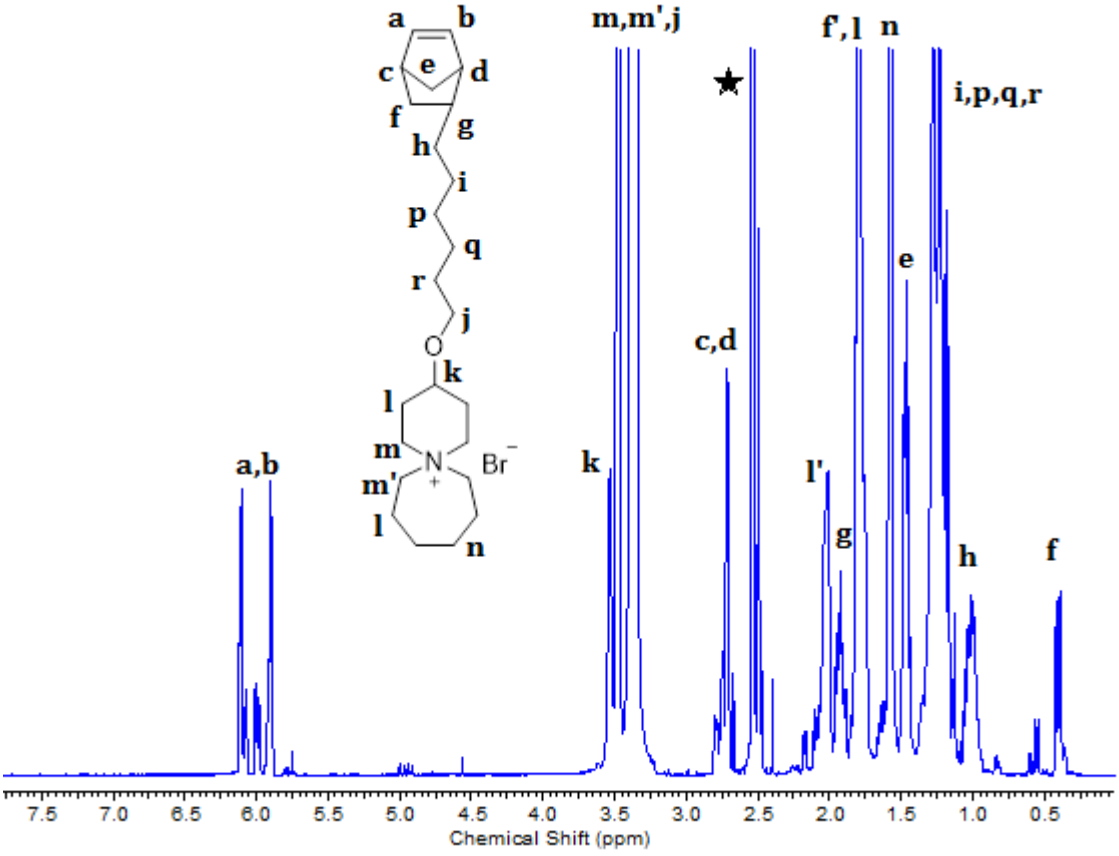

Figure 7.28. The ^{1}H NMR spectrum of norbornenehexoxy-6-azonia-spiro[5,6]dodecane.

Interestingly, the monomers NPS6 and NHS6 were insoluble in water and so were there polymers. The addition of one carbon atom to the base ring of the NPS5 and NHS5 structure increased its hydrophobicity.

7.3 Conclusion

The following ASU-type salts, 4-hydroxy-6-azonia-spiro[5,4]decane, 4-hydroxy-6-azonia-spiro[5,5]undecane, and 4-hydroxy-6-azonia-spiro[5,6]dodecane were successfully synthesized. The norbornene-based monomers, norbornepropoxy-6-azonia-spiro[5,4]decane (NPS4) and norbornehexoxy-6-azonia-spiro[5,4]decane (NHS4), were synthesized from 4-hydroxy-6-azonia-spiro[5,4]decane. The norbornene-based monomers, norbornepropoxy-6-azonia-spiro[5,5]undecane (NPS5) and norbornehexoxy-6-azonia-spiro[5,5]undecane (NHS5), were synthesized from 4-hydroxy-6-azonia-spiro[5,5]undecane. The norbornene-based monomers, norbornepropoxy-6-azonia-spiro[5,6]dodecane (NPS6) and norbornehexoxy-6-azonia-spiro[5,6]dodecane (NHS6), were synthesized from 4-hydroxy-6-azonia-spiro[5,6]dodecane. Preliminary degradation studies on NPS5 and NHS5 confirm the stability of the ether linkage in NPS5 and NHS5. The monomers, NPS5 and PNHS5, were successfully polymerized by ring-opening metathesis polymerization. The X-ray scattering profile of these homopolymers show a scattering peak indicative of backbone-backbone ordering. And as in the case of P4VP_CnBr, the spacing and intensity corresponding to these peaks increased with increasing number of carbons on the side-chain.

7.4 References

(1) Merle, G.; Wessling, M.; Nijmeijer, K. Anion Exchange Membranes for Alkaline Fuel Cells: A Review. *J. Memb. Sci.* **2011**, *377* (1–2), 1–35.

(2) Couture, G.; Alaaeddine, A.; Boschet, F.; Ameduri, B. Polymeric Materials as Anion-Exchange Membranes for Alkaline Fuel Cells. *Prog. Polym. Sci.* **2011**, *36* (11), 1521–1557.

(3) Arges, C. G.; Ramani, V.; Pintauro, P. N. Anion Exchange Membrane Fuel Cells. *Elctrochemical Soc. Interface* **2010**, 31–35.

(4) Marino, M. G.; Kreuer, K. D. Alkaline Stability of Quaternary Ammonium Cations for Alkaline Fuel Cell Membranes and Ionic Liquids. *ChemSusChem* **2015**, *8* (3), 513–523.

(5) Maeda, Y.; Sato, Y. Mechanism of the Stevens Rearrangement of Ammonium Ylides. *J. Chem. Soc. Perkin Trans. 1* **1997**, *4* (10), 1491–1494.

(6) Vanecko, J. A.; Wan, H.; West, F. G. Recent Advances in the Stevens Rearrangement of Ammonium Ylides. Application to the Synthesis of Alkaloid Natural Products. *Tetrahedron* **2006**, *62* (6), 1043–1062.

(7) Hauser, R. C.; Weinheimer, J. A. The Ortho Substitution Rearrangement Uersus P-Elimination of Certain Quaternary Ammonium Ions with Sodium Amide. Extension of the Method of Synthesis of Vicinal Alkyl Aromatic Derivatives. *J. Am. Chem. Soc.* **1953**, *76* (5), 1264–1267.

(8) Tsai, T. H.; Ertem, S. P.; Maes, A. M.; Seifert, S.; Herring, A. M.; Coughlin, E. B. Thermally Cross-Linked Anion Exchange Membranes from Solvent Processable Isoprene

Containing Ionomers. *Macromolecules* **2015**, *48* (3), 655–662.

(9) Zhang, W.; Liu, Y.; Jackson, A. C.; Savage, A. M.; Ertem, S. P.; Tsai, T. H.; Seifert, S.; Beyer, F. L.; Liberatore, M. W.; Herring, A. M.; et al. Achieving Continuous Anion Transport Domains Using Block Copolymers Containing Phosphonium Cations. *Macromolecules* **2016**, *49* (13), 4714–4722.

(10) Tsai, T. Ionic Copolymers for Alkaline Anion Exchange Membrane Fuel Cells (AAEMFCs), University of Massachusetts, 2014.

(11) Smith, M. B.; March, J. March's Advanced Organic Chemistry: Reactions, Mechanisms, and Structure, 5th Edition. *Molecules* **2001**, *6* (12), 1064–1065.

(12) Cospito, G.; Illuminati, G.; Lillocci, C.; Petride, H. Ring-Opening Reactions. 3. Mechanistic Path vs. Ring-Strain Control in Elimination and Substitution Reactions of 1,1-Dimethyl Cyclic Ammonium Ions and Their .alpha.,.alpha.'-dimethyl-Substituted Derivatives. *J. Org. Chem.* **1981**, *46* (14), 2944–2947.

(13) Yang, Y.; Xu, Y.; Ye, N.; Zhang, D.; Yang, J. Alkali Resistant Anion Exchange Membranes Based on Saturated Heterocyclic Quaternary Ammonium Cations Functionalized Poly (2 , 6-Dimethyl-1 , 4-Phenylene Oxide) S. *J. Electrochem. Soc.* **2018**, *165* (5), 350–356.

(14) Strasser, D. J.; Graziano, B. J.; Knauss, D. M. Base Stable Poly(diallylpiperidinium Hydroxide) Multiblock Copolymers for Anion Exchange Membranes. *J. Mater. Chem. A Mater. energy Sustain.* **2017**, *5*, 9627–9640.

(15) Pham, T. H.; Olsson, J. S.; Jannasch, P. N‐Spirocyclic Quaternary Ammonium Ionenes

for Anion-Exchange Membranes. *J. Am. Chem. Soc.* **2017**, 13–16.

(16) Pham, T. H.; Jannasch, P. Aromatic Polymers Incorporating Bis‐N‐Spirocyclic Quaternary Ammonium Moieties for Anion-Exchange Membranes. *ACS Macro Lett.* **2015**, 1370–1375.

(17) Olsson, J. S.; Pham, T. H.; Jannasch, P. Poly (N , N -Diallylazacycloalkane) S for Anion-Exchange Membranes Functionalized with N‐Spirocyclic Quaternary Ammonium Cations. *Macromolecules* **2017**.

(18) Olsson, J. S.; Pham, T. H.; Jannasch, P. Poly (Arylene Piperidinium) Hydroxide Ion Exchange Membranes : Synthesis , Alkaline Stability , and Conductivity. *Adv. Funct. Mater.* **2018**, *1702758*, 1–10.

(19) Gu, L.; Dong, H.; Sun, Z.; Li, Y.; Yan, F. RSC Advances Spirocyclic Quaternary Ammonium Cations for Alkaline Anion Exchange Membrane Applications : An Experimental and Theoretical Study †. *RSC Adv.* **2016**, *6*, 94387–94398.

(20) Dang, H.; Jannasch, P. Membranes Tethered with Di Ff Erent Hetero-. *J. Mater. Chem. A Mater. energy Sustain.* **2017**, *5*, 21965–21978.

(21) Chen, N.; Long, C.; Li, Y.; Lu, C.; Zhu, H. Ultrastable and High Ion-Conducting Polyelectrolyte Based on Six- Membered N‐Spirocyclic Ammonium for Hydroxide Exchange Membrane Fuel Cell Applications. *ACS Appl. Mater. Interfaces* **2018**, *10*, 15720–15732.

(22) Matson, J. B. Bottlebrush Polymer Synthesis by Ring-Opening Metathesis Polymerization: The Signi Fi Cance of the Anchor Group. *J. Am. Chem. Soc.* **2016**, *138*,

6998–7004.

(23) Nikovia, C.; Maroudas, A.; Goulis, P.; Tzimis, D.; Paraskevopoulou, P.; Pitsikalis, M. Statistical Ring Opening Metathesis Copolymerization of Norbornene and Cyclopentene by Grubbs'1st-Generation Catalyst. *Molecules* **2015**, *20*, 15597–15615.

(24) Steinbach, T.; Alexandrino, E. M.; Wurm, F. R. Unsaturated Poly(phosphoester)s via Ring-Opening Metathesis Polymerization. *Polym. Chem.* **2013**, *4*, 3800–3806.

(25) Bielawski, C. W.; Grubbs, R. H. Living Ring-Opening Metathesis Polymerization. *Prog. Polym. Sci.* **2007**, *32*, 1–29.

(26) Nomura, K.; Abdellatif, M. M. Precise Synthesis of Polymers Containing Functional End Groups by Living Ring-Opening Metathesis Polymerization (ROMP): Ef Fi Cient Tools for Synthesis of Block / Graft Copolymers. *Polymer (Guildf).* **2010**, *51*, 1861–1881.

(27) Leitgeb, A.; Wappel, J.; Slugovc, C. The ROMP Toolbox Upgraded. *Polymer (Guildf).* **2010**, *51* (14), 2927–2946.

(28) Nguyen, S. T.; Johnson, L. K.; Grubbs, R. H.; Beckman, M.; Joseph, W. Polymerization, Ring-Opening Metathesis. *J. Am. Ceram. Soc. Commun. to Ed.* **1992**, *114*, 3974–3975.

(29) Sutthasupa, S.; Shiotsuki, M.; Sanda, F. Recent Advances in Ring-Opening Metathesis Polymerization, and Application to Synthesis of Functional Materials. *Polym. J.* **2010**, *42* (12), 905–915.

(30) Nuyken, O.; Pask, S. D. Ring-Opening Polymerization-An Introductory Review. *Polymers (Basel).* **2013**, *5* (2), 361–403.

(31) Mortell, K.; Weatherman, R.; Kiessling, L. Recognition Specificity of Neoglycopolymers by Ring-Opening Metathesis Polymerization. *J. Am. Chem. Soc.* **1996**, *118* (14), 2297–2298.

(32) Manning P. Cooke, J. and J. L. C. Elimination Reactions. III. Hofmann Elimination in Cyclic Compounds. *J. Am. Chem. Soc.* **1968**, *3565* (1964), 5556–5561.

(33) Bielawski, C. W.; Grubbs, R. H. Highly Efficient Ring-Opening Metathesis Polymerization (ROMP) Using New Ruthenium Catalysts Containing N-Heterocyclic Carbene Ligands. *Angew. Chemie - Int. Ed.* **2000**, *39* (16), 2903–2906.

(34) Bielawski, C. W.; Grubbs, R. H. Living Ring-Opening Metathesis Polymerization. *Prog. Polym. Sci.* **2007**, *32* (1), 1–29.

(35) Platé, N. A.; Shibaev, V. P. Comb-like Polymers. Structure and Properties. *J. Polym. Sci. Macromol. Rev.* **1974**, *8* (1), 117–253.

CHAPTER 8

SYNTHESIS AND CHARACTERIZATION OF RANDOM COPOLYMERS OF NPS5 AND NHS5 WITH NOR AND BLOCK COPOLYMERS OF NPS5 AND NHS5 WITH NDMDC

8.1 Random Copolymer Synthesis and Characterization

8.1.1 Introduction

Although the syntheses of the homopolymers PNPS5 and PNHS5 (see Chapter 7) have been successful, they can be of little to no use if the homopolymers lack mechanical integrity in polar solvents. These homopolymers are soluble in water and methanol. Hydrophilic monomers and hydrophobic monomers have been copolymerized to improve the resistance of their corresponding hydrophilic polymers to polar solvents. This will improve the mechanical properties of these hydrophilic in a humidified environment.[1–10]

Random copolymers are also of interest to study because of their morphology. It is well documented in the literature that these copolymers form ionic clusters that are randomly distributed within a hydrophobic polymer matrix.[1-3] These clusters act as fillers in the matrix thereby providing improved mechanical properties otherwise absent in non-polyelectrolyte copolymers. Experimental and theoretical motivations also motivate the study of the competing parameters for ionomer formation since the theory of this polymer morphology, though abundantly discussed in the literature, remains a puzzle to polymer physicists.[1,3,11,12] From the previous chapters, especially Chapter 4 and Chapter 5, we have discussed the role backbone-backbone spacing and electrostatic interaction has on the formation of ionomer cluster morphology. Unlike the P4VP-*r*-PI_CnBr series, in which spacing between dipoles on adjacent backbones increase with increasing number

of carbons on the pendant side-chain, the spacing between dipoles on adjacent backbones in PNPS5 and PNHS5 did not change with increasing number of carbons on the pendant side-chain. It will be thus interesting to study how the spacing between the dipoles in PNPS5 and PNHS5 affect the formation of ionomer clusters when NPS5 and NHS5 are randomly copolymerized with a hydrophobic comonomer. Furthermore, ionomers are also reported to form water channels in their hydrated states for effective charge transport thus possibly having better ion conductivity than their homocopolymer counterpart.[13] This project would therefore explore the following questions:

- Can NPS5 and NHS5 be copolymerized with a hydrophobic monomer to give a random copolymer?
- Is there a change in the mechanical properties, namely solubility of the copolymer, in polar solvent?
- Do these random copolymers form ionomer clusters?
- Is there a transition from backbone-backbone spacing morphology to ionic clusters when probed by SAXS?

8.1.2 Materials and Methods

8.1.2.1 Random Copolymerization of NPS5 and Norbornene (NOR)

In a 20 ml scintillation vial equipped with a magnetic stirrer, 200 mg (0.52 mmoles) of NPS5 in 5 ml of DMF was mixed with a solution of 49 mg (0.52 mmoles) of norbornene (NOR) in 0.5 ml DCM. A solution of 3 mg (0.0035 mmoles) of Grubbs' II catalyst in 0.5 ml of DCM was charged into the monomer mixture. The reaction was allowed to proceed for 24 h. The reaction mixture was then precipitated in diethyl ether to afford 199 mg (80% yield) of polymer.

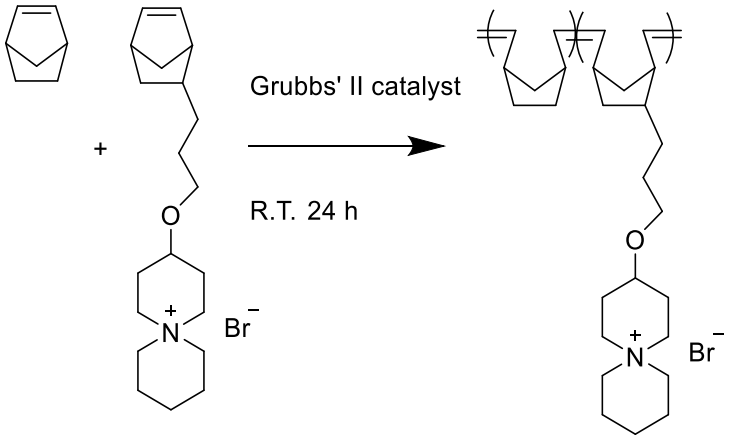

Scheme 8.1. Synthesis of PNOR-*r*-PNPS5.

8.1.2.2 Random Copolymerization of NHS5 and Norbornene (NOR)

In a 20 ml scintillation vial equipped with a magnetic stirrer, 100 mg (0.23 mmoles) of NHS5 in 5 ml of DMF was mixed with a solution of 135 mg (1.44 mmoles) of norbornene (NOR) in 2 ml DCM. A solution of 3 mg (0.0035 mmoles) of Grubbs' II catalyst in 0.5 ml of DCM was charged into the monomer mixture. The reaction was allowed to proceed for 24 h. The reaction mixture was then precipitated in diethyl ether to afford 180 mg (77% yield) of polymer.

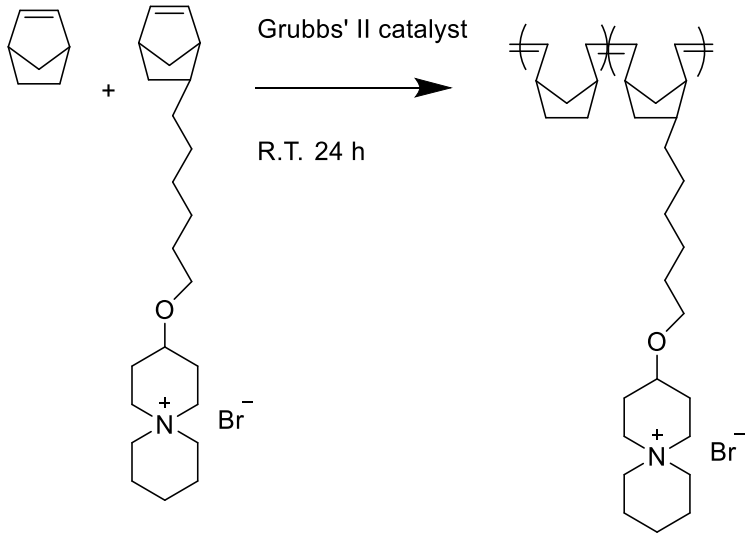

Scheme 8.2. Synthesis of PNOR-*r*-PNHS5.

8.1.2.3 Characterization of PNOR-*r*-PNPS5 and PNOR-*r*-PNHS5 by ^{1}H NMR

The chemical composition of PNOR-*r*-PNPS5 and PNOR-*r*-PNHS5 was determined using a Bruker 500 Fourier-transform nuclear magnetic resonance (FT-NMR).

8.1.2.4 Characterization of PNOR-*r*-PNPS5 and PNOR-*r*-PNHS5 by MAXS

Ganesha SAXS Measurement: medium-angle X-ray scattering (MAXS) measurements were performed in transmission geometry on Molmex Scientific Ganesha SAXS Lab. A double aperture for the Cu-Kα radiation (λ = 1.54 Å), which was the X-ray source, was used. Silver behenate was used as the standard for the momentum transfer calibration. Data collection was performed with a typical exposure time of two minutes. Depending on the signal-to-noise ratio, data collection could be longer. Azimuthal averaging of the obtained isotropic 2-D pattern was performed to obtain the intensity against wave vector plot.

8.1.2.5 Sample Preparation

In a 5 ml scintillation vial, 100 mg of PNOR-*r*-PNPS5 was dissolved in 1.5 ml of methanol and was solution cast on a Teflon® plate. After 24 h a thin film with a thickness of about 200 µm was obtained.

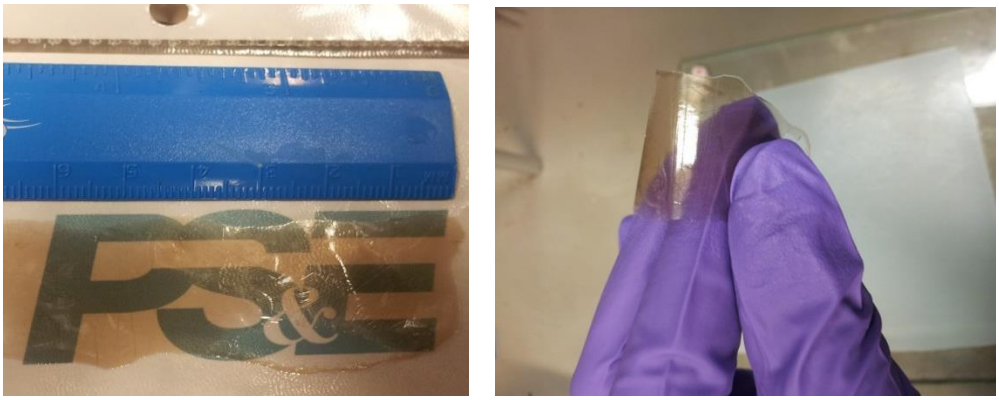

Figure 8.1. A picture of PNOR-*r*-PNPS5 random copolymer.

8.1.3 Results and Discussion

The ^{1}H NMR results confirm the successful random copolymerization of NPS5 and norbornene (NOR). Composition of NPS5 and NOR in PNOR-*r*-PNPS5 as calculated from NMR was different from the feed ratio composition of the monomers. The ^{1}H NMR results also confirm the successful random copolymerization of NHS5 and norbornene (NOR). The NMR composition for PNPS5 and PNOR were calculated from the vinyl peak for both PNOR and PNPS5 and the alpha proton on the secondary carbon in the ether linkage in PNPS5. See Figure 8.2.

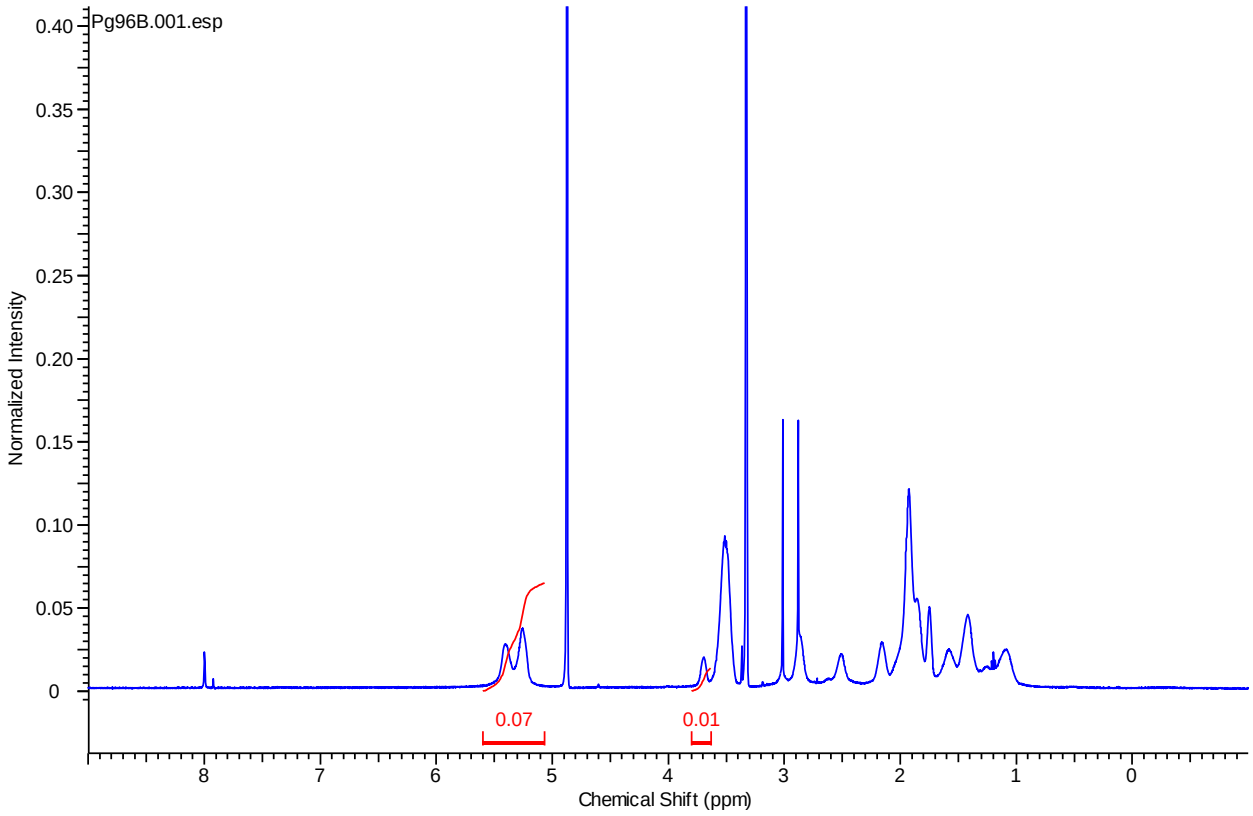

Figure 8.2. The ^{1}H NMR spectrum of PNOR-*r*-PNPS5(60:40)_1.91.

As regards the nomenclature of PNOR-*r*-PNPS5(60:40)_1.91, in the parenthesis is the mol% of PNPS5 and PNOR in the copolymer determined from the ^{1}H NMR, and 1.91 is the IEC calculated from the mol% determined from ^{1}H NMR. A better control of polymer composition relative to monomer feed ratio was observed for the PNHS5-*r*-PNOR series in comparison to the PNPS5-*r*-PNOR series.

The NMR composition for PNHS5 and PNOR were calculated from the vinyl peak for both PNOR and PNHS5 and the alpha proton on the secondary carbon in the ether linkage in PNPS5. See Figure 8.3.

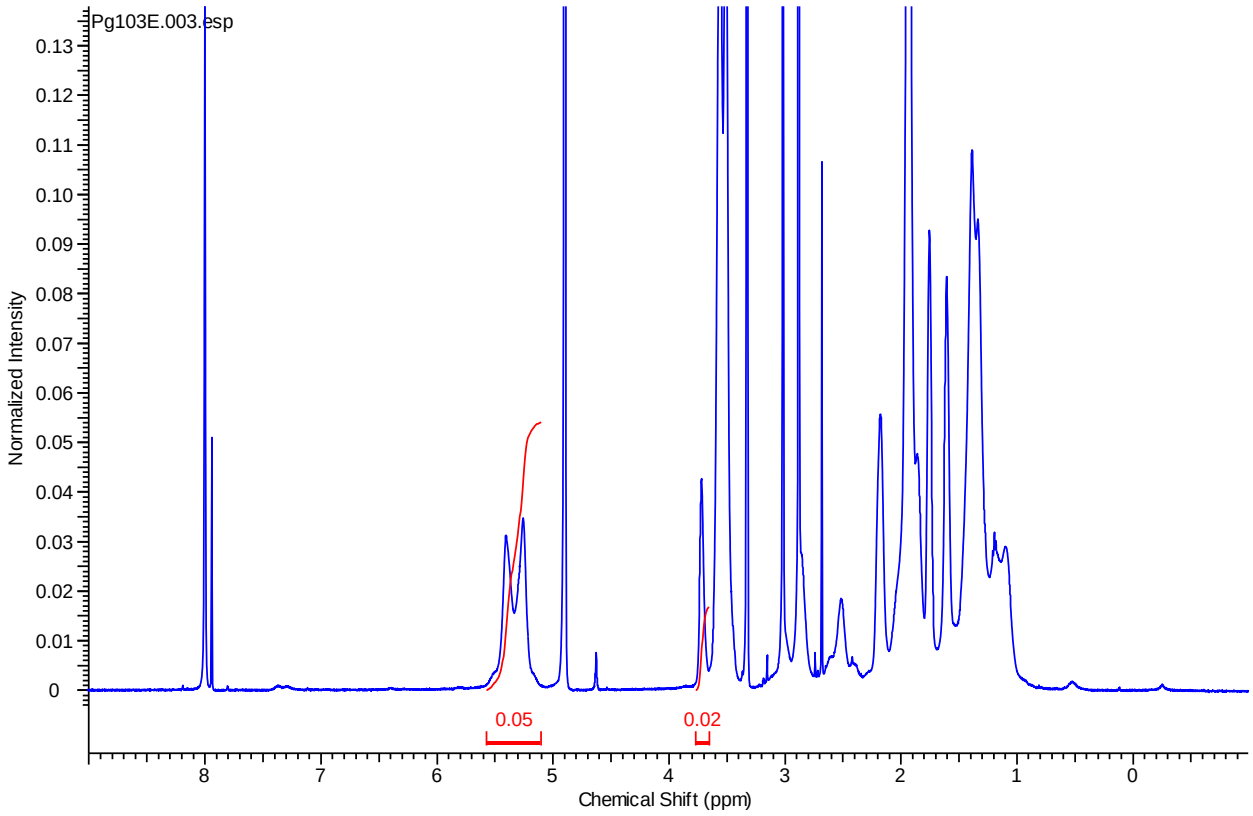

Figure 8.3. The ^{1}H NMR spectrum of PNOR-*r*-PNHS5(76:24)_1.38.

A tabular summary of the target composition, NMR composition, target IEC, NMR IEC, and the MAXS d-spacing for PNPS5-*r*-PNOR is presented in Table 8.1.

Table 8.1. Summary of NMR and SAXS characterization of PNOR-*r*-PNPS5 at varying compositions.

Sample	**Target Composition NOR:NPS5**	**NMR Nor:NPS5**	**IEC projected**	**IEC NMR(mmol/g)**	***d*- spacing (Å)**	**Solubility in Water**
PNOR-*r*-NPS5_1.04	**90:10**	**86:14**	**1.00**	**1.04**	**42**	**No**
PNOR-*r*-NPS5_1.91	**75:25**	**60:40**	**1.50**	**1.91**	**62**	**Partially**
PNOR-*r*-NPS5_2.56	**60:40**	**6:94**	**1.91**	**2.56**	**44**	**Yes**
***P*NPS5_2.60**	**0:100**	**0:100**	**2.60**	**2.60**	**27**	**Yes**

Random copolymerization of PNPS5 and PNHS5 with PNOR decreased the solubility of the resultant random copolymer. For the PNOR-*r*-PNPS5 series at about 40 mol % PNPS5 the polymer becomes insoluble in water. However, random copolymers with 40 mol% was soluble in methanol. At 80 mol% of the PNPS5 component, the random copolymer was insoluble in both methanol and water. In the PNOR-*r*-PNHS5 series, solubility also decreased with increasing hydrophobic content. At 76 mol% of PNHS5, the polymer is still partially insoluble in methanol.

A tabular summary of the target composition, NMR composition, target IEC, NMR IEC, and the MAXS d-spacing for PNPS5-*r*-PNOR is presented in Table 8.2.

Table 8.2. Summary of NMR and SAXS characterization of PNOR-*r*-PNHS5 at varying compositions.

Sample	**Target Composition (NOR:NHS5)**	**NMR composition (NOR:NHS5)**	**Target IEC (mmol/g)**	**NMR IEC (mmol/g)**	***d*-Spacing (Å)**
PNOR-*r*-PNHS5_1.25	**86:14**	**76:24**	**1.0**	**1.38**	**75**
PNOR-*r*-PNHS5_1.56	**72:28**	**68:32**	**1.50**	**1.61**	**59**
PNOR-*r*-PNHS5_1.90	**61:39**	**60:40**	**1.74**	**1.76**	**49**
PNOR-*r*-PNHS5_1.87	**44:56**	**40:60**	**2.0**	**2.04**	**41**
PNHS5_2.34	**0:100**	**35:65**	**2.34**	**2.34**	**34**

From the SAXS profile of both PNOR-*r*-PNPS5 and PNOR-*r*-PNHS5 (see Figure 8.4), there is a scattering peak whose corresponding dimension increases with increasing polynorbornene (non-ionic) concentration. This suggests that these random copolymers form ionomers. From the study of P4VP-*r*-PI_CnBr, at high concentration of the alkyl pyridinium unit (~ 40 mol%) and higher values of *n* (i.e *n > 3)*, SAXS spectra show backbone-backbone spacing (see Chapter 4). Samples of PNOR-*r*-PNPS5 and PNOR-*r*-PNHS5 have ionic content ranging from (30-100 mol%). The homopolymers, PNPS5 and PNHS5 have side-chain lengths of approximately 9 and approximately 12 carbons away from the backbone respectively; thus, random copolymers with high concentration of PNPS5 and PNHS5 should show backbone-backbone spacing. The scattering data

for PNOR-*r*-PNPS5(86:14)_1.04 and PNOR-*r*-PNHS5(76:24)_1.38 show a broad ionomer peak. For the PNOR-*r*-PNHS5 series, a peak whose appearance and shape is similar to the backbone-backbone peak in the homopolymer can be observed for PNOR-*r*-PNHS5(68:32)_1.61, PNOR-*r*-PNHS5(60:40)_1.76, and PNOR-*r*-PNHS5(40:60)_2.04. A clear indication that the scattering peak observed in PNOR-*r*-PNHS5(68:32)_1.61, PNOR-*r*-PNHS5(60:40)_1.76, and PNOR-*r*-PNHS5(40:60)_2.04 are not due to ionomer cluster morphology is that the spacing corresponding to these peaks decreases with increasing hydrophobic content. This behavior is not typical for ionomer cluster morphology in which the spacing increases with increasing concentration of the non-ionic component.[6,7] At about 32 mol% of PNHS5, the series has transitioned to a backbone-backbone dominant morphology.

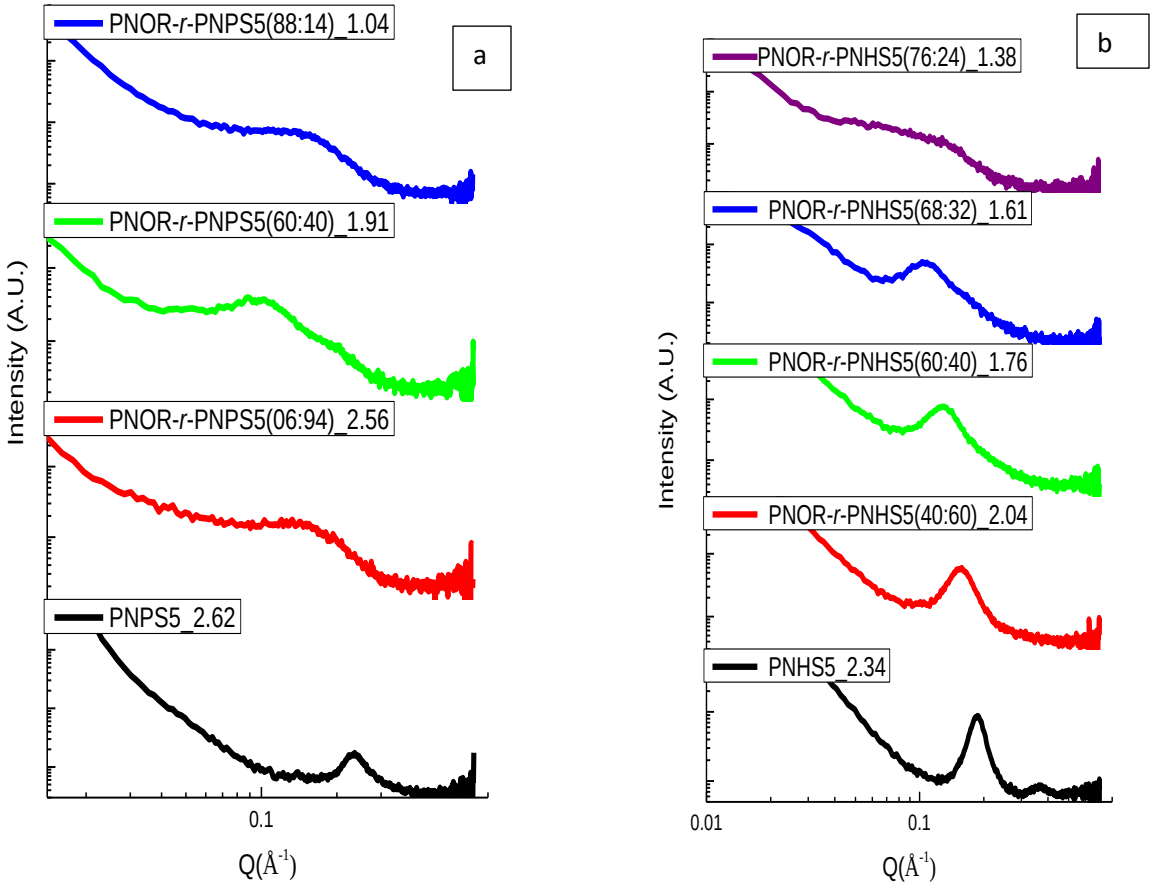

Figure 8.4. The SAXS profile of the a) PNOR-r-PNPS5 and b) PNOR-*r*-PNHS5 series.

The decrease in the backbone-backbone spacing for the PNOR-*r*-PNHS5 series with increasing ionic content may be due to the fixed distance between dipoles on adjacent polymer backbones. With increasing concentration of PNHS5, the concentration of charges per backbones increases consequently the dipole attraction between adjacent backbones becomes stronger. This will lead to decreasing backbone-backbone spacing with increasing concentration of the charged copolymer component in the random copolymer. This behavior is unlike the backbone-backbone spacing behavior evident during the quaternization of P4VP-*r*-P4VP_CnBr series. In these random copolymer systems, the spacing between backbones increased with increasing conversion of the 4-vinylpyridine unit to 4-vinyl pyridinium bromide unit for all the studied samples. In these systems, P4VP-*r*-P4VP_CnBr, the dipoles are situated near the backbone of the polymers, hence steric effects will dominate the interaction between tails of the pendant side-chains on adjacent backbones. As the concentration of pendant side-chains on the backbones increases, the steric repulsive effects between these pendant side-chains on the backbones also increases, consequently increasing the spacing between the backbones. In the PNOR-*r*-PNPS5 and PNOR-*r*-PNHS5 series however, the dipoles are situated away from the backbones towards the tail of the pendant side-group. Thus, with increasing concentration of PNPS5 and PNHS5, the dipolar attraction between dipoles on adjacent polymer backbones increases, decreasing the effective backbone-backbone spacing between adjacent polymers in these random copolymers.

In the studied P4VP-*r*-PI_CnBr series, P4VP-*r*-PI-*r*-PS_CnBr series, and P4VP-*r*-PS_CnBr series, the transition from ionomer cluster morphology to backbone-backbone morphology is dependent on the length of the pendant side-chain. The further the dipoles are separated from the backbones, the less likely is the randomly charged comb-like polymer to form ionomer cluster morphology. This is the pendant side-chain steric effect. However, in the PNOR-*r*-PNHS5 series, the transition

from ionomers cluster morphology to backbone-backbone morphology is dependent on the large concentration of the PNHS5 component. With decreasing concentration of the non-ionic copolymer, the random copolymer cannot form a hydrophobic matrix in which ionic clusters can be evenly distributed. This is effect, the matrix effect, is further analyzed in Chapter 9.

Backbone-backbone spacing exists in the PNPS5 and PNHS5 because of steric repulsion similar to that observed in P4VP_CnBr. In their random copolymer counterpart (PNOR-*r*-PNPS5(86:14)_1.04 and PNOR-*r*-PNHS5(76:24)_1.38), clustering of ions give rise to ionomer peaks. Thus, as in P4VP-*r*-PI_CnBr and P4VP-*r*-PI-*r*-PS_CnBr, there will be a competition between dipole forces and sterics in these copolymers. However, no coexistence peaks were observed for these copolymers. This suggests that clustering of ions and backbone-backbone spacing may be mutually exclusive.

8.1.4 Summary

Characterization of the synthesized random copolymers of PNOR-*r*-PNPS5 and PNOR-*r*-PNHS5 by ^{1}H NMR confirm that these homopolymers were successfully synthesized by ring-opening metathesis chemistry. All the random copolymers of PNOR-*r*-PNPS5 and PNOR-*r*-PNHS5 are were solvent processable. With decreasing concentration of PNPS5 in the PNOR-*r*-PNPS5 series, the corresponding polymer became less soluble in water and methanol. These random copolymers are solvent processable. The same solvent processable behavior was observed in the PNOR-*r*-PNHS5 series. X-ray scattering data for PNOR-*r*-PNHS5 show ionomer morphology at lower ionic concentration (PNOR-*r*-PNHS5(76:24)_1.38) and a transition to backbone-backbone spacing at higher ionic concentration (PNOR-*r*-PNHS5(32:68)_1.61). Unlike in P4VP-*r*-P4VP_CnBr, where the increase in the concentration of the ionic component increases the backbone-backbone spacing;

in the PNOR-*r*-PNHS5 series, backbone-backbone spacing decreased with increasing concentration of PNHS5. This may have resulted from the position of the dipoles in both polymers. In P4VP-*r*-P4VP_CnBr, the dipoles are situated near the backbone, while they are situated near the tail of the pendant side-chain in PNOR-*r*-PNHS5 series. Finally, the transition from ionomer cluster to backbone-backbone morphology in P4VP-*r*-PI_CnBr depended on the length of the side-chain, however, in PNOR-*r*-PNHS5 series, this morphological transition was dependent on the concentration of the PNHS5 in the random copolymer.

8.2 Block Copolymer Synthesis and Characterization

8.2.1 Introduction

Block copolymers have been well known to have interesting morphological features as a result of nanoscale phase separation of the different blocks. In the literature, block copolymers of polyelectrolytes have been shown to produce high conductivity.[8,14,15] A possible reason for this improved conductivity may arise from the ability of the ionic blocks, through electrostatic interactions, to skew the traditional block copolymer phase diagram. In some block copolymers, electrostatic interactions may lead to phase-inversion. Thus, the minor ionic block may become the major phase, and the major hydrophobic block the minor phase. A beneficial consequence of this phase-inversion may be unimpeded ionic conduction.[1,15]

Polyelectrolyte block copolymers also have superior mechanical properties than the homopolymer of the polyelectrolyte. Improved mechanical properties arise from a robust block, especially hydrophobic, which will provide the membrane with mechanical integrity. Furthermore, unlike

random copolymers, block copolymers of hydrophobic and hydrophilic sections are generally insoluble in polar solvents.[8,15–18]

The morphology of block copolymers is always an interesting aspect of polymer physics. In the literature, different length scale ordering can exist for different block copolymers, and this can have a profound impact on some properties of these polymers. These block copolymers can find use in bandgap switching, proton conduction, and for optical or electrical purposes.[19–24]

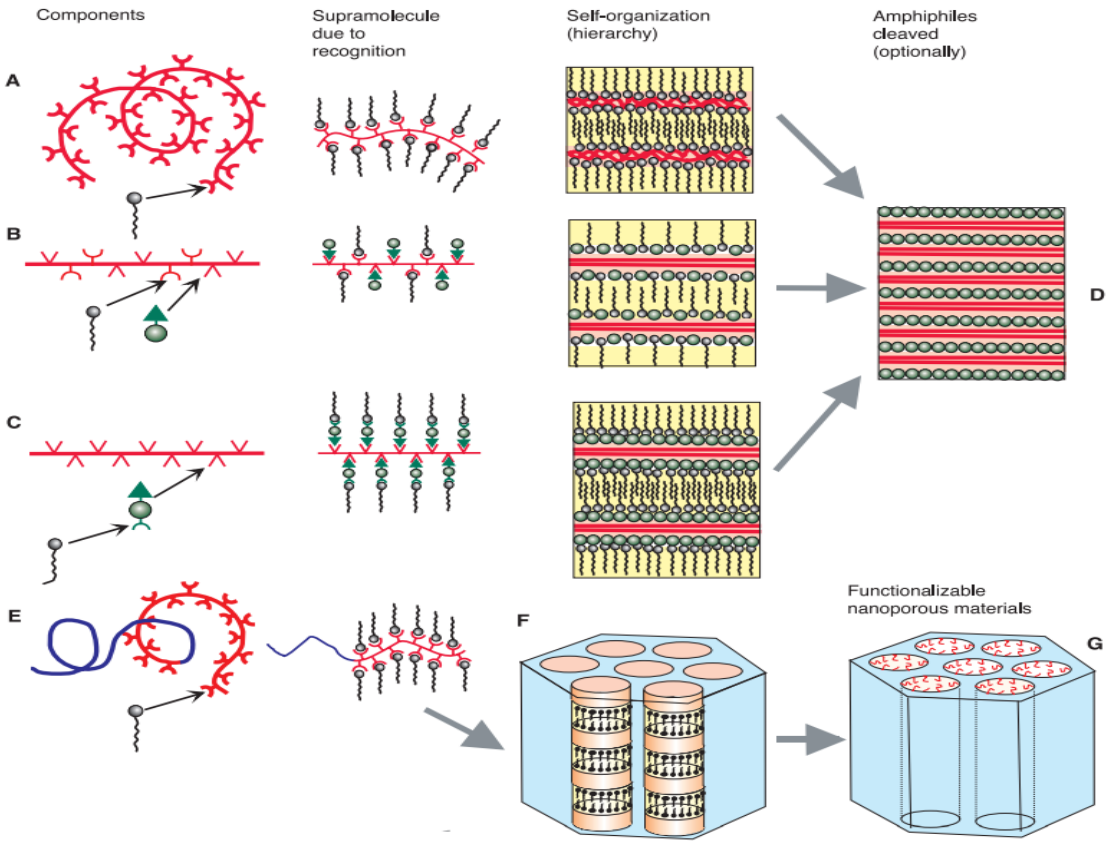

Figure 8.5. Depiction of structure-*within*-structure arrangement in block copolymers. [Image taken from Ref 25].[25]

Studying varying length-scales of order in block copolymers is rare in the literature even more rare in block polyelectrolytes. From the homopolymer morphology of PNPS5 and PNHS5, it is evident

that the backbones of these block copolymers have a periodic arrangement. Since it is possible to obtain different morphologies by a structure-*within*-structure arrangement, this can lead to optimization of structure-property relationships.[7,10,11] This is particularly useful for AEMs. With an array of morphological possibilities at different length scales, the effect of these morphologies on a particular property, e.g. conductivity, can be investigated.

Although norbornene can theoretically form a block copolymer with many norbornene based monomers, the reaction must be performed at very low temperatures. Furthermore, even at low temperatures, PNOR as the first block has a relatively broad dispersity. Grubbs and Choi suggested different monomers that should be good starting monomers for block copolymer synthesis using ring-opening metathesis chemistry.[26] Most monomers shown in that study have a certain degree of symmetry. However, norbornenedimethyl dichloride was conspicuously absent in that study.

Norbornenedimethyl dichloride is relatively easy to synthesize. The synthesis is based on Diels-Alder chemistry of dicyclopentadiene and cis1,4,dichlorobut-2-ene.[27] It is relatively cheaper in comparison to norbornene dimethanol which is a precursor to norbornenedibenzyldiether. It is also soluble in DMF as are NPS5 and NHS5. A common solvent for the first and second block is an important consideration for the synthesis of block copolymers. The choice for this monomer also has a curious note. This monomer has not been well utilized for ROMP and thus it presents an academic motivation. Finally, the monomer is relatively stable and does not undergo Fickelstein reactions most probably because of its exo form being favored in its synthesis.

This project will seek answers to the following questions:

- Can NPS5 and NHS5 be copolymerized with a norbornenedimethyldichloride (NDMDC) monomer to give a block copolymer?

- Do the resultant polymers from the block copolymerization form morphologies characteristics of block copolymers?
- What role does the chain spacing have on the block morphology? Can both order types coexist or are they mutually exclusive?

To perform block copolymer synthesis, Grubbs' generation III catalyst was synthesized from Grubbs' generation II catalyst. The synthetic procedure has been reported in the literature.[16]

8.2.2 Materials and Methods

8.2.2.1 Synthesis of Grubbs' III catalyst

In a 20 ml scintillation vial equipped with a magnetic stirrer, 500 mg (0.59 mmoles) of Grubbs' 2 was dissolved in 1 ml (10 mmoles) of 3-bromopyridine and stirred for 30 minutes in the glove box. The solution was precipitated in hexanes. Excess 3-bromopyridine in hexanes was cannulated out of the reaction mixture under nitrogen. The desired green Grubbs' III catalyst was dried in vacuum at room temperature to afford 363 mg (61% yield) of product.

8.2.2.1 Synthesis of Norbornenedimethyldichloride

In a round bottom flask, 7 g (0.037 moles) of dicyclopentadiene was dissolved in 20 g (0.11 moles) of cis1,4-dichlorobutene. The solution was charged into a Schlenk tube equipped with a magnetic stirrer and trace amount of hydroquinone, 50 mg (0.45 mmoles). The mixture was placed in an oil bath with a temperature of 185°C and allowed to proceed for 18 h. Fractional distillation was performed on the mixture to remove excess cis 1,4 dichlorobutene (40°C, 200 mTorr) and 5.46 g (54% yield) of desired product, norbornenediemethyl dichloride (70°C, 150 mTorr).

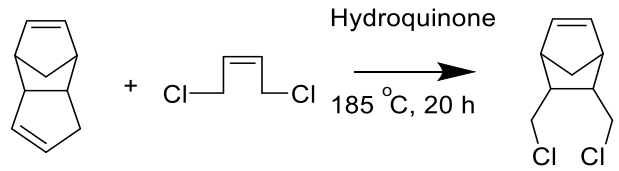

Scheme 8.3. Synthesis of Norbornenedimethyldichloride (NDMDC).

8.2.2.2 Synthesis of Block Copolymer

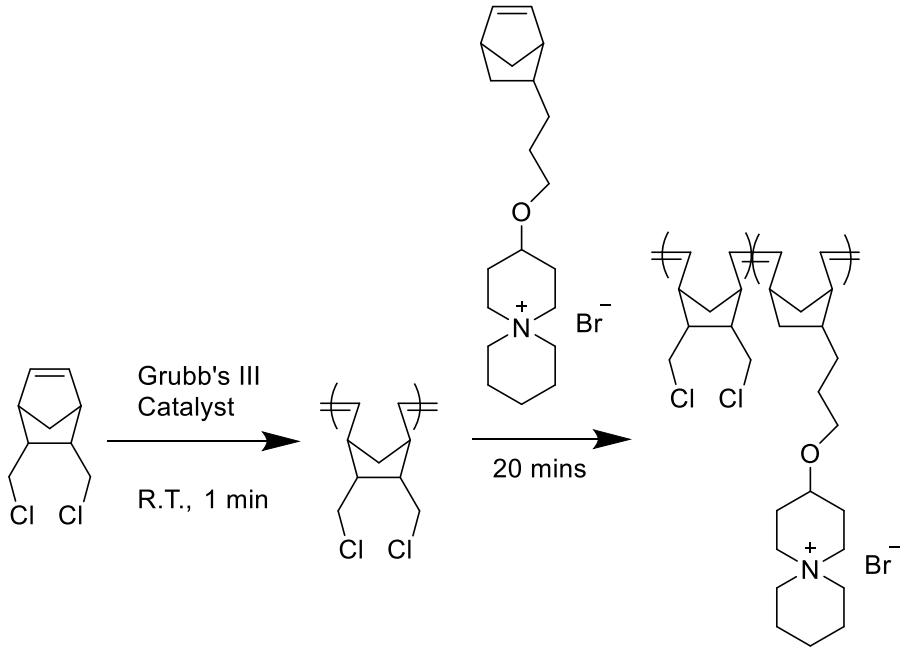

Scheme 8.4. Synthesis of PNDMDC-*b*-PNPS5.

In a 20 ml scintillation vial equipped with a magnetic stirrer, 75 mg (0.39 mmoles) of NDMDC in 0.5 ml of DCM was charged into a solution of 1 mg (0.001 mmoles) of Grubbs' III catalyst in 1 ml DCM. After 1 min, 100 mg (0.26 mmoles) of NPS5 in 5 ml of DMF was added to the reaction mixture. After 20 mins, the reaction is quenched by adding excess ethyl vinyl ether. The polymer was then precipitated in diethyl ether to afford 136 mg (77% yield) of polymer.

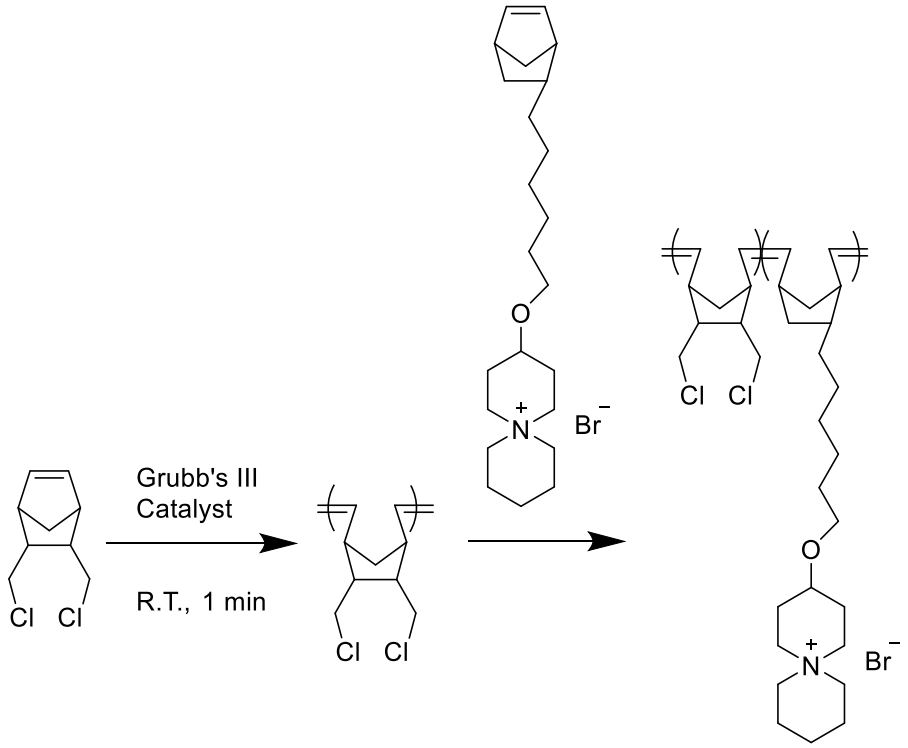

Scheme 8.5. Synthesis of PNDMDC-*b*-PNHS5.

In a 20 ml scintillation vial equipped with a magnetic stirrer, 85 mg (0.45 mmoles) of NDMDC in 0.5 ml of DCM was charged into a solution of 1 mg (0.001 mmoles) of Grubbs' III catalyst in 1 ml DCM. After 1 min, 150 mg (0.35 mmoles) of NHS5 in 5 ml of DMF was added to the reaction mixture. After 20 mins, the reaction is quenched by adding excess ethyl vinyl ether. The polymer was then precipitated in diethyl ether to afford 186 mg (79% yield) of polymer.

8.2.2.3 Characterization of PNDMDC-*b*-PNPS5 and PNDMDC-*b*-PNHS5 by ^{1}H NMR

The chemical composition of PNDMDC-*b*-PNPS5 and PNDMDC-*b*-PNHS5 was determined using a Bruker 500 Fourier-Transform Nuclear Magnetic Resonance (FT-NMR).

8.2.2.4 Characterization of PNDMDC-*b*-PNPS5 and PNDMDC-*b*-PNHS5 by MAXS

Ganesha SAXS Measurement: Medium-angle X-ray scattering (MAXS) measurements were performed in transmission geometry on Molmex Scientific Ganesha SAXS Lab. A double aperture for the Cu-Kα radiation (λ = 1.54 Å), which was the X-ray source, was used. Silver behenate was used as the standard for the momentum transfer calibration. Data collection was performed with a typical exposure time of two minutes. Depending on the signal-to-noise ratio, data collection could be longer. Azimuthal averaging of the obtained isotropic 2-D pattern was performed to obtain the intensity against wave vector plot.

8.2.2.5 Preparation of Polymer Samples:

Due to the nature of the monomers in the block copolymer, the polymers are solvent processable only from DMF, however the right balance of dichloromethane and methanol also presents a viable option to casting these films. Films were cast on Teflon® sheet.

Figure 8.6. A picture of a PNDMDC-*b*-PNPS5 film.

8.2.3 Results and Discussion

Characterization of the NDMDC monomer by ^{1}H NMR confirm the successful synthesis of norbornenedimethyldichloride. The protons of norbornenedimethyldichloride and their corresponding peaks on the ^{1}H NMR spectrum are represented in Figure 8.7.

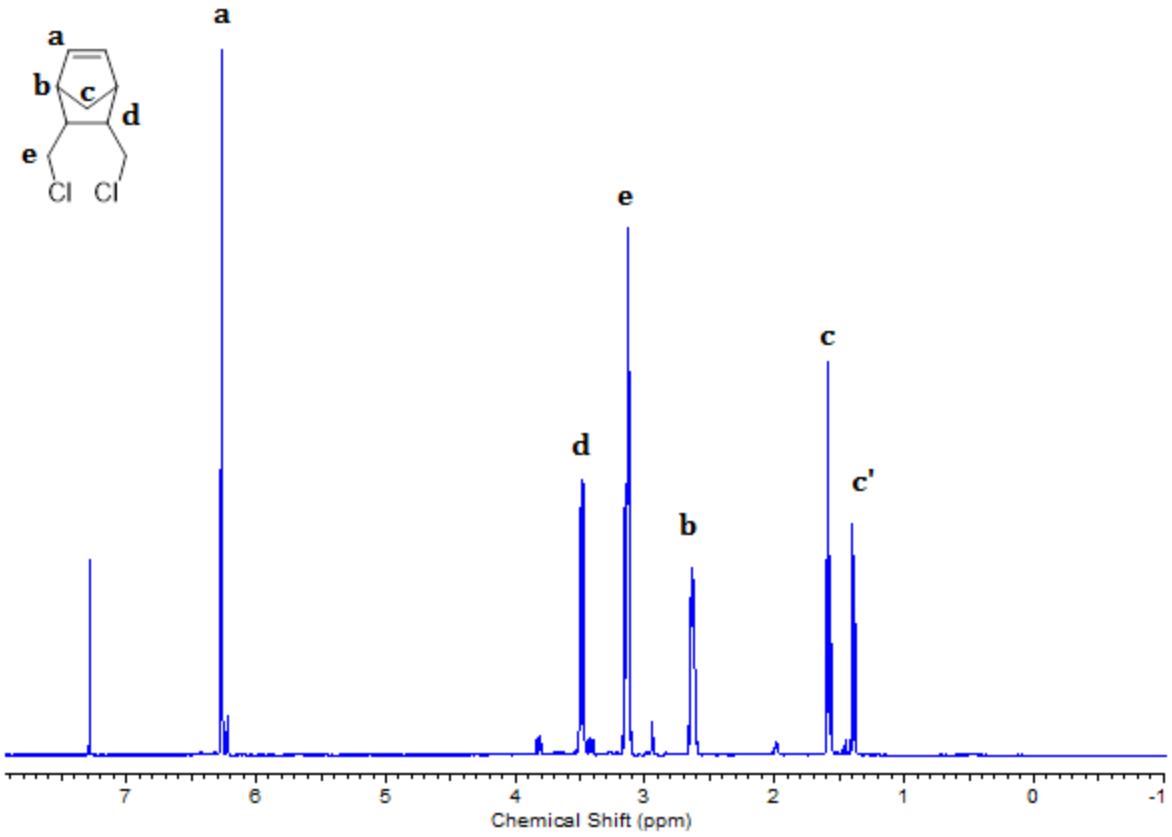

Figure 8.7. The ^{1}H NMR spectrum of norbornenedimethyldichloride.

The ^{1}H NMR characterization of the product of the homopolymerization of norbornenedimethyldichloride confirm the successful synthesis of poly(norbornenedimethyldichloride), PNDMDC. The protons of PNDMDC and their corresponding peaks on the ^{1}H NMR spectrum are represented in Figure 8.8.

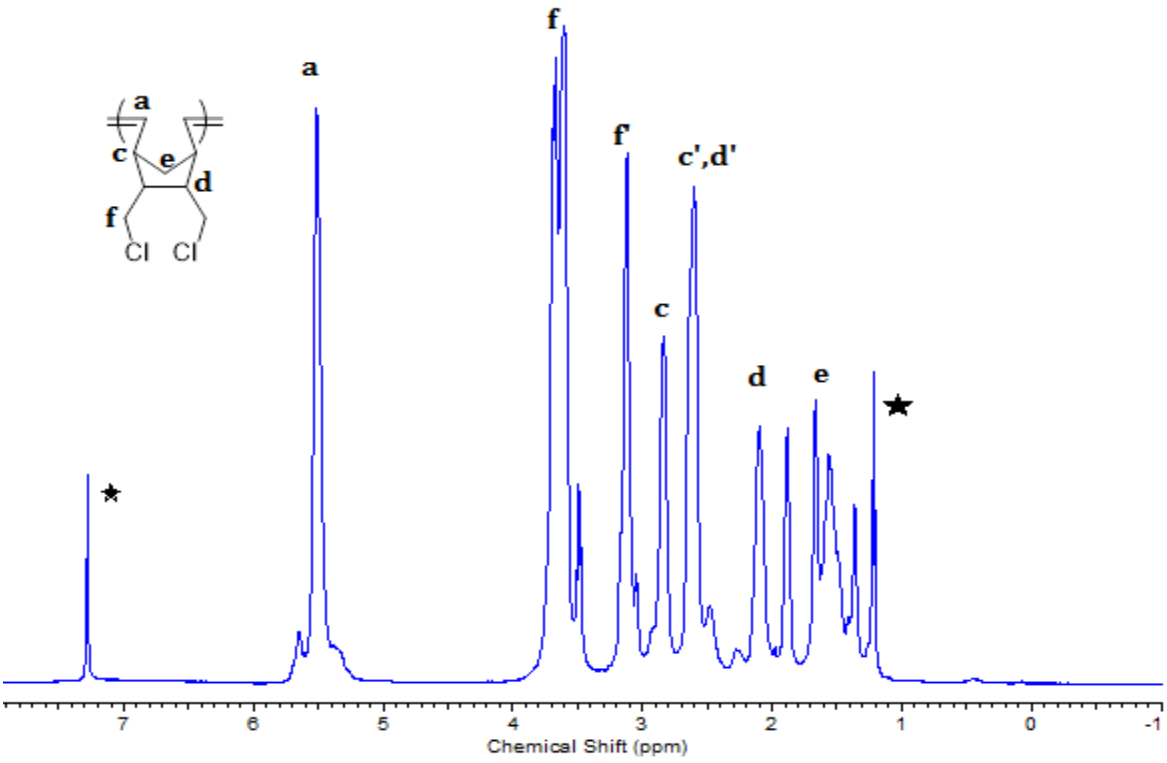

Figure 8.8. The ^{1}H NMR spectrum of poly(norbornenedimethyldichloride).

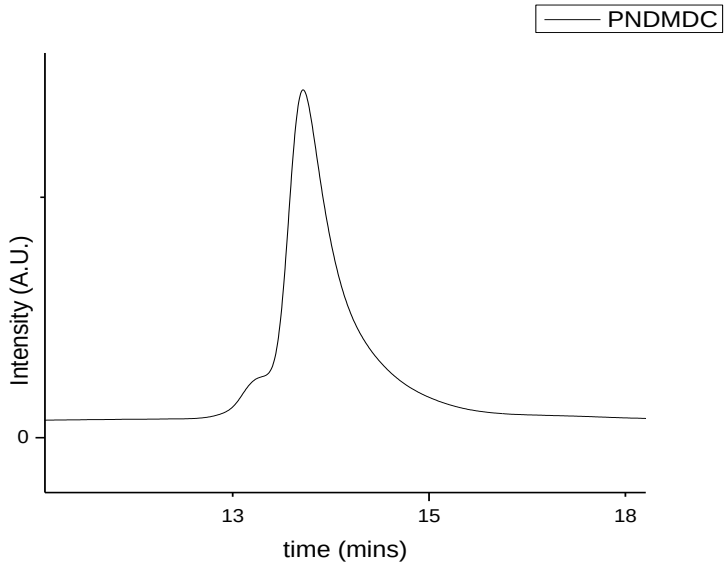

Figure 8.9. The GPC chromatogram of PNDMDC.

The GPC trace for the first block, PNDMDC, is shown in Figure 8.9. The shoulder peak is due to secondary metathesis. The analysis of this GPC chromatogram, by PMMA standards, show that PNDMDC has a number average molecular weight of 33 Kg/mol with a dispersity of 1.15. This relatively narrow dispersity of the first block is indicative of a potential to synthesize block copolymers using PNDMDC as the first block. Due to the composition of the block copolymer, (PNPS5-*b*-PNDMDC), could not be characterized by GPC after the addition of NPS5 or NHS5 blocks. Although both blocks are soluble in DMF, attempts to characterize even PNPS5 or PNHS5 homopolymers by DMF GPC were unsuccessful.

It is obvious from the ^{1}H NMR that block copolymers could be synthesized by ROMP using NDMDC as one block. Again, as in the random copolymer series, ^{1}H NMR data for the PNHS5 block copolymers showed better agreement between the target and the ^{1}H NMR composition in comparison to the PNPS5 block copolymers. Unlike in the PNOR-*r*-PNPS5 in which the distinctive tertiary ether peak from the copolymer could be used to obtain the composition of the respective polymers in the block copolymer, the alpha proton of the secondary carbon in the ether linkage is always non-distinct in the ^{1}H NMR spectrum of the block copolymers. Fortuitously, in the ^{1}H NMR spectra of PNDMDC-*r*-PNPS5, the vinyl peak of PNDMDC does not overlap with the vinyl peak of PNPS5 or PNHS5 unlike in the ^{1}H NMR spectra of PNOR-*r*-PNPS5. Thus, the composition of PNPS5 and PNDMDC in the copolymer can be computed from the integral of the vinyl peaks due to the respective blocks. See Figure 8.10.

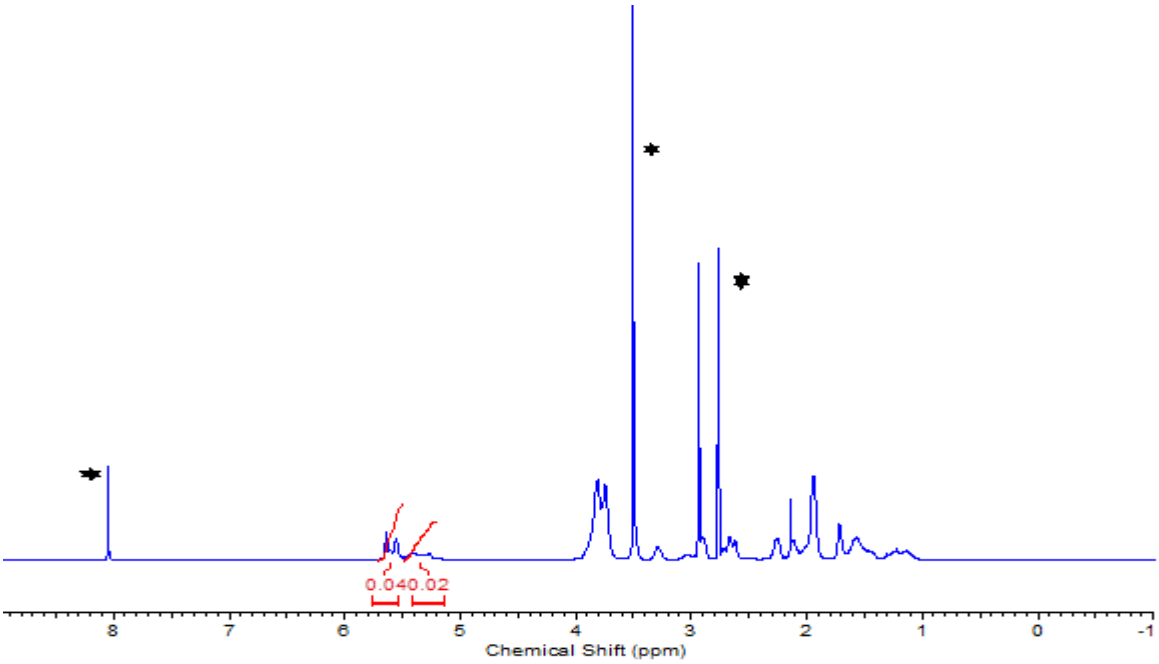

Figure 8.10. The ^{1}H NMR spectrum of PNDMDC-*b*-PNPS5(56:44)_1.60.

Table 8.3. Summary of NMR and SAXS characterization of PNDMDC-*b*-PNPS5 at varying compositions.

Sample	**Feed ratio (NDMDC:NPS5)**	**NMR ratio (NDMDC:NPS5)**	**IEC_{feed} (mmol/g)**	**IEC_{NMR} (mmol/g)**	***d*-spacing(nm)**
PNDMDC-*b*-PNPS5_0.9	**80:20**	**79:21**	**0.9**	**0.9**	**35**
PNDMDC-*b*-PNPS5_1.56	**60:40**	**57:43**	**1.50**	**1.56**	**31**
PNDMDC-*b*-PNPS5_1.60	**50:50**	**56:44**	**1.74**	**1.60**	**33**
PNDMDC-*b*-PNPS5_2.0	**40:60**	**38:62**	**1.96**	**2.0**	**31**
PNDMDC-*b*-PNPS5_2.50	**20:80**	**8:92**	**2.32**	**2.50**	**24**

Table 8.4. Summary of NMR and SAXS characterization of the PNDMDC-*b*-PNHS5 at varying compositions.

Sample	**Target Composition (NDMDC:NHS5)**	**NMR Composition (NDMDC:NHS5)**	**Target IEC (mmol/g)**	**NMR IEC (mmol/g)**	***d*-spacing** (Å)
PNDMDC-*b*-PNHS5 **_1.25**	**66:34**	**66:34**	**1.25**	**1.25**	**28**
PNDMDC-*b*-PNHS5 **_1.56**	**56:44**	**53:47**	**1.50**	**1.56**	**22**
PNDMDC-*b*-PNHS5 **_1.90**	**43:57**	**34:66**	**1.75**	**1.90**	**18**
PNDMDC-*b*-PNHS5 **_1.87**	**40:60**	**36:64**	**1.80**	**1.87**	**20**
PNDMDC-*b*-PNHS5 **_1.89**	**28:72**	**35:65**	**2.0**	**1.89**	**20**

The composition of PNHS5 and PNDMDC in the copolymer can be computed from the integral of the vinyl peaks due to the respective blocks. See Figure 8.11.

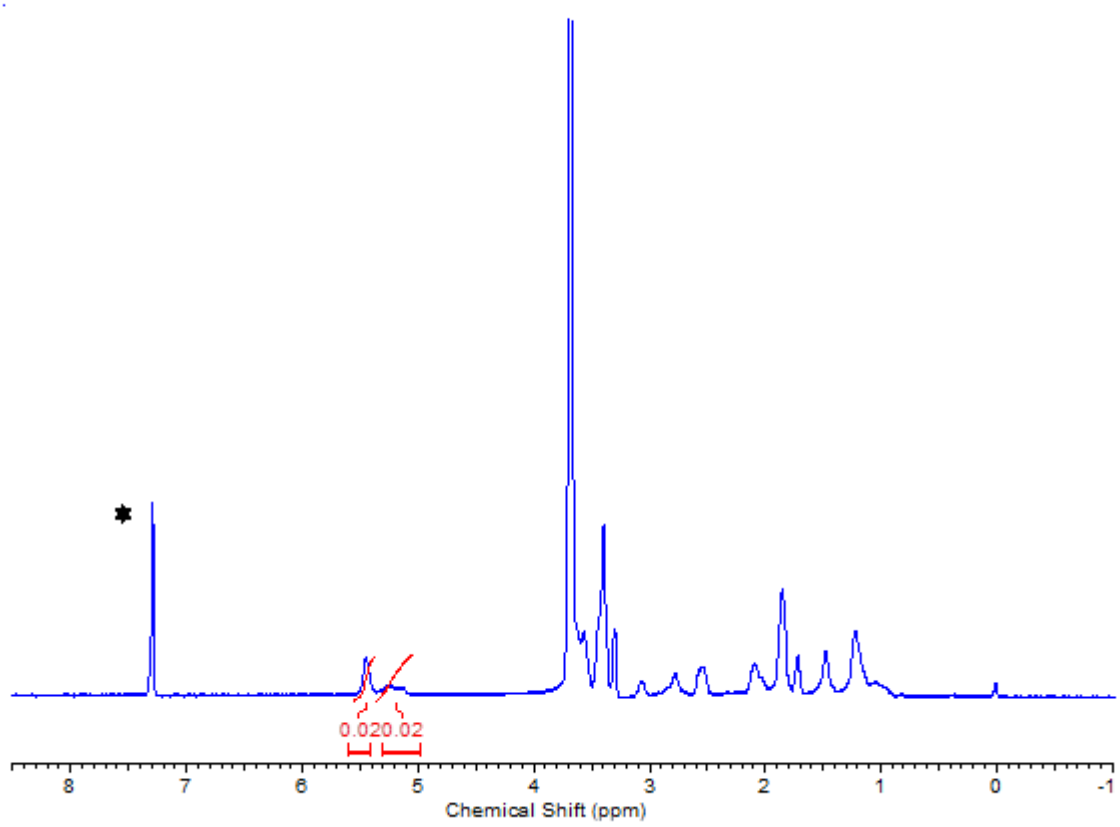

Figure 8.11. The ^{1}H NMR spectrum of PNDMDC-*b*-PNHS5(56:44)_1.56.

Corroborating evidences to the successful block copolymerization of NHS5 and NPS5 with NDMDC are the SAXS data for this block copolymers. The scattering spectra obtained from SAXS does not show very good phase separation between the ionic and non-ionic block in the PNDMDC-*b*-PNPS5 series. See Figure 8.12. However, scattering profiles of PNDMDC-*b*-PNHS5 series, see Figure 8.12, show distinctive peaks indicative of strong microphase separation between the ionic and non-ionic blocks. The SAXS data for the PNDMDC-*b*-PNPS5 series also show the arrangement of backbones as substructure *within* a microphase separated superstructure at higher values of *Q*. The morphology of the backbones, whether lamellar or cylindrical, within the ionic block could not be determined given that only one scattering peak could be observed in the

scattering data. The X-ray scattering peak indicative of a structure-*within*-structure for PNDMDC-*b*-PNHS5 also show a higher order peak closer to the primary peak. The ratio of this peak to the primary peak 2 as in the PNHS5 homopolymer. Thus, the structure-*within*-structure maintains a lamellar morphology within the parent morphology that is possibly cylindrical or lamellar.

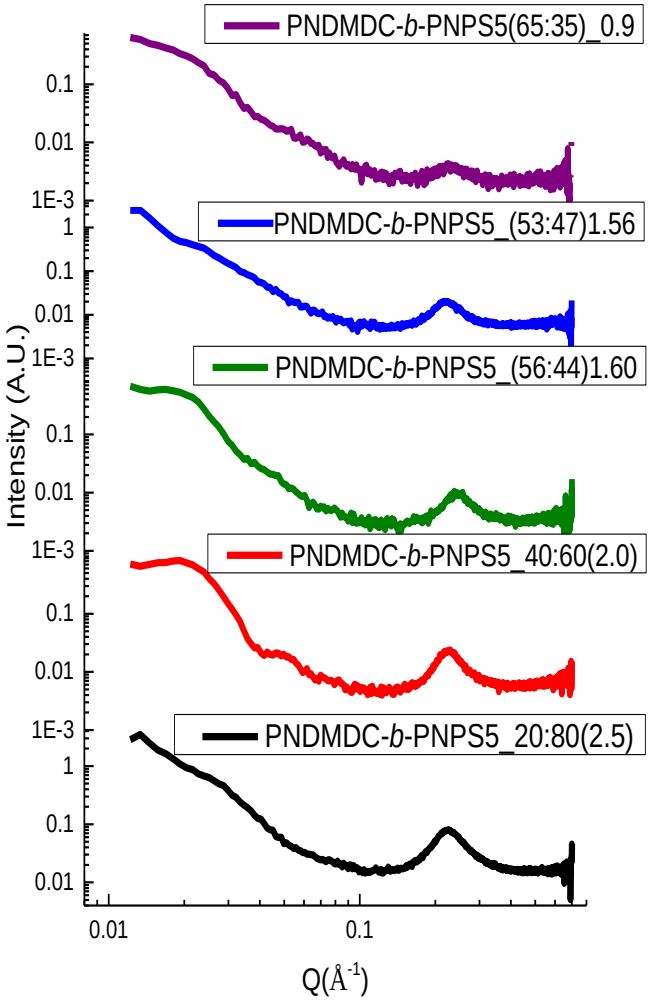

Figure 8.12. The SAXS profile for the PNDMDC-*b*-PNPS5 series .

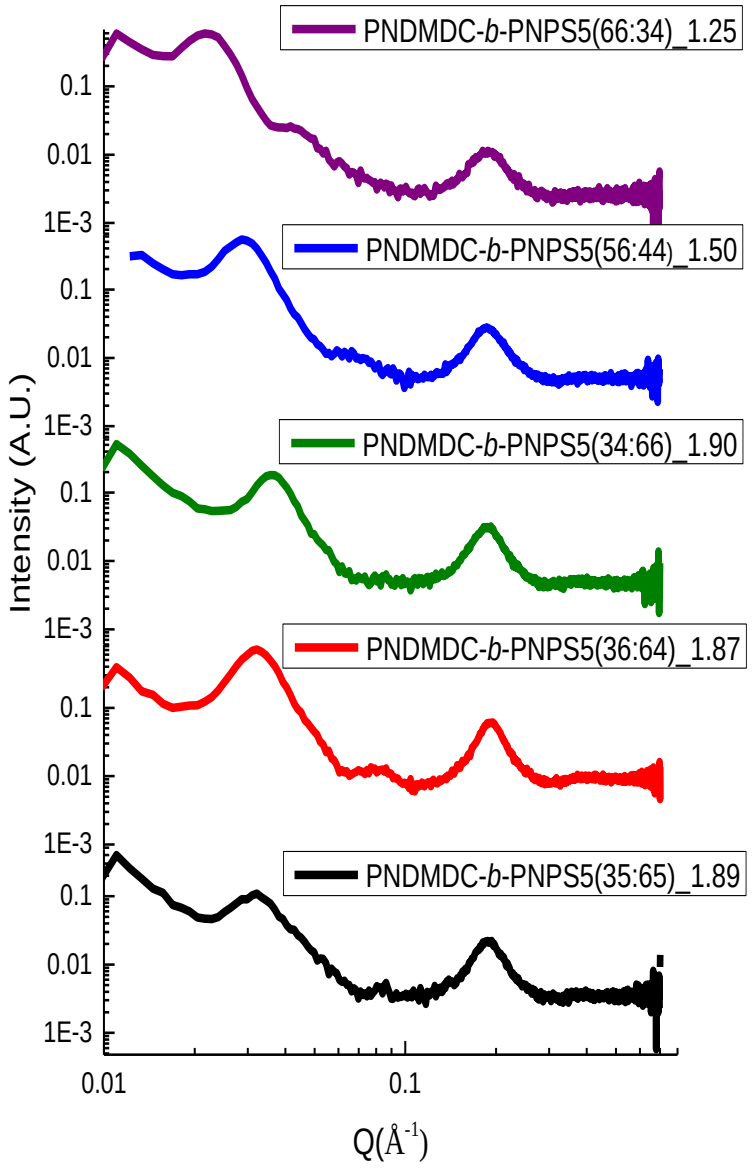

Figure 8.13. The SAXS profile for the PNDMDC-*b*-PNHS5 series.

It is also apparent from the SAXS data shown (see Figure 8.12 and Figure 8.13) that the domain size increased with increasing hydrophobic content for both PNDMDC-*b*-PNPS5 and PNDMDC-*b*-PNHS5. This appears counterintuitive because the hydrophilic domain has the side-chain and the bulky ASU group. It has been reported for PS-*b*-P4VP(PDP) system, that with increasing

P4VP(PDP) content, domain sizes of quaternized systems increases.[23] This phenomenon in which the domain spacing of the block copolymer decrease with increasing ionic content has been observed by Yuan.[28] It is possible that the domain size obtained from the scattering data is the size of the diameter of the cylinder and not the distance between cylinders in a hexagonal morphology. It thus makes sense that with decreasing hydrophobic content, the size of this cylinder will decrease.

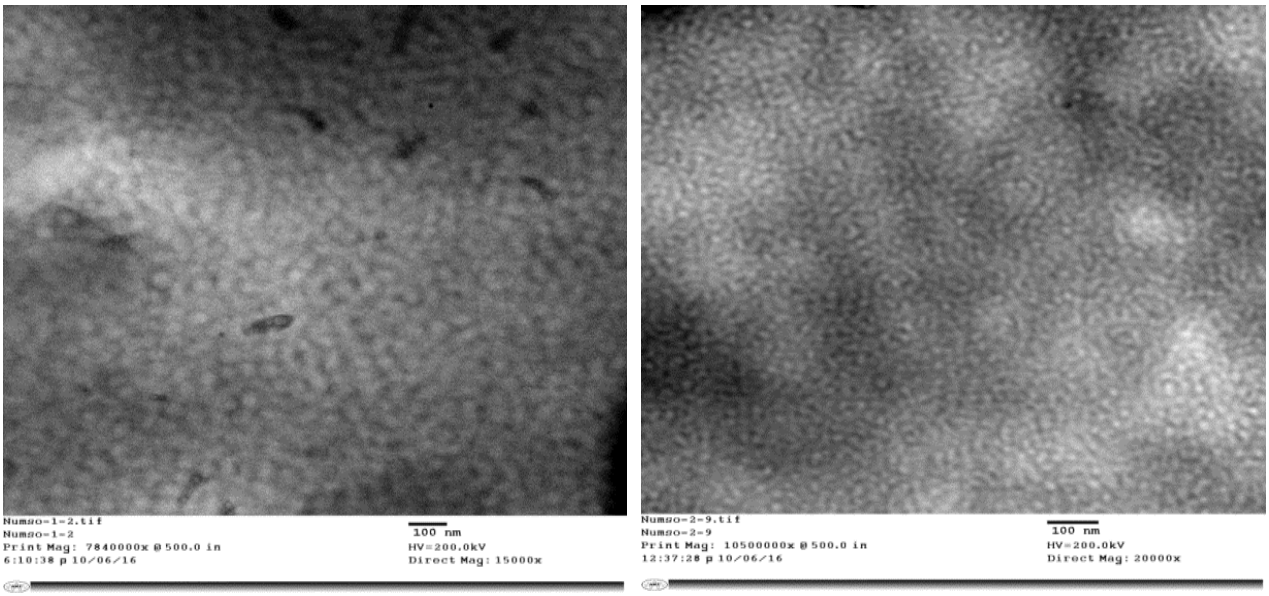

Figure 8.14. TEM micrographs showing the formation of cylindrical domains in a) PNDMDC-*b*-PNPS5(53:47)_1.60 and b) PNDMDC-*b*-PNPS5(40:60)_2.0.

From Figure 8.14, the TEM for PNDMDC-*b*-PNPS5 show ordered morphology brought about by a good phase separation. Although the χ parameter of this system is not known, the high electrostatic interactions between the NPS5 blocks may have helped to introduce stronger phase separation even though the SAXS data does not show intense scattering peaks. Furthermore, the TEM micrograph confirms that the primary chlorides of PNDMDC are not susceptible to halogen

exchange chemistry. If they are not inert, then there will be no contrast in the block copolymer resulting from the bromide counterion in this TEM micrographs.

Although this is a dark field image, the micrographs show that the PNDMDC block forms the minority phase in both block copolymers. This is the case even when it has the higher concentration in the block copolymer. This behavior has been predicted in ionic block copolymers by Olivera de la Cruz.[15]

Obtained block copolymers show better mechanical properties because all samples prepared are found to be insoluble in both water and methanol for the same IEC value in their random copolymer counterpart. However, due to the extremely fragile nature of the polymers, arising from the high T_g of PNDMDC (114 °C), further studies on these block copolymers were discontinued.

8.2.4 Summary

Block copolymers of PNDMDC-*b*-PNPS5 and PNDMDC-*b*-PNHS5 were successfully synthesized. The blocks do show microphase separation and also chain spacing within the parent domain as seen in PS-*b*-P4VP_CnBr. The size of the block domains do increase with increasing hydrophobic content which seem counterintuitive and would demand further inquiry. Also, TEM micrographs suggest that there was no halide exchange between the blocks of the copolymers.

8.3 References

(1) Eisenberg, A. Clustering of Ions in Organic Polymers. A Theoretical Approach. *Macromolecules* **1970**, *3* (2), 147–154.

(2) Eisenberg, A.; Cayrol, B. Viscoelastic Properties of Poly(phenylene Ethers). I. Unsubstituted and Methyl or Phenyl Substituted Polymers. *J. Polym. Sci. Part C Polym. Chem.* **1971**, *35*, 129–149.

(3) Kim, J. -S; Eisenberg, A. Effect of Sample Preparation Conditions and Degree of Neutralization on the Dynamic Mechanical Properties of Poly(styrene???co???sodium Methacrylate) Ionomers. *J. Polym. Sci. Part B Polym. Phys.* **1995**, *33* (2), 197–209.

(4) Moore, R. B.; Gauthier, M.; Williams, C. E.; Eisenberg, A. Heterogeneities in Random Ionomers - a Small-Angle X-Ray-Scattering Investigation of Alkylated Polystyrene-Based Materials. *Macromolecules* **1992**, *25* (21), 5769–5773.

(5) Wollmann, D.; Williams, C. E.; Eisenberg, a. Aggregate Modification via Plasticization of Ionomers-Dynamic Mechanical and Morphological Studies. *Macromolecules* **1992**, *25* (25), 6775–6783.

(6) Tsai, T. H.; Ertem, S. P.; Maes, A. M.; Seifert, S.; Herring, A. M.; Coughlin, E. B. Thermally Cross-Linked Anion Exchange Membranes from Solvent Processable Isoprene Containing Ionomers. *Macromolecules* **2015**, *48* (3), 655–662.

(7) Tsai, T. Ionic Copolymers for Alkaline Anion Exchange Membrane Fuel Cells (AAEMFCs), University of Massachusetts, 2014.

(8) Zhang, W.; Liu, Y.; Jackson, A. C.; Savage, A. M.; Ertem, S. P.; Tsai, T. H.; Seifert, S.;

Beyer, F. L.; Liberatore, M. W.; Herring, A. M.; et al. Achieving Continuous Anion Transport Domains Using Block Copolymers Containing Phosphonium Cations. *Macromolecules* **2016**, *49* (13), 4714–4722.

(9) Ding, J.; Chuy, C.; Holdcroft, S. A Self-Organized Network of Nanochannels Enhances Ion Conductivity through Polymer Films. *Chem. Mater.* **2001**, *13* (7), 2231–2233.

(10) Orfino, F. P.; Holdcroft, S. The Morphology of Nafion: Are Ion Clusters Bridged by Channels or Single Ionic Sites? *J. New Mater. Electrochem. Syst.* **2000**, *3* (4), 285–290.

(11) Grady, B. P. Review and Critical Analysis of the Morphology of Random Ionomers Across Many Length Scales. *Polym. Eng. Sci.* **2008**, 1029–1051.

(12) Eisenberg, A.; Hird, B.; Moore, R. B. A New Multiplet-Cluster Model for the Morphology of Random Ionomers. *Macromolecules* **1990**, *23* (18), 4098–4107.

(13) Beers, K. M.; Balsara, N. P. Design of Cluster-Free Polymer Electrolyte Membranes and Implications on Proton Conductivity. *ACS Macro Lett.* **2012**, *1* (10), 1155–1160.

(14) Soo, P. P.; Huang, B.; Jang, Y.-I.; Chiang, Y.-M.; Sadoway, D. R.; Mayes, A. M. Rubbery Block Copolymer Electrolytes for Solid-State Rechargeable Lithium Batteries. *J. Electrochem. Soc.* **1999**, *146* (1), 32.

(15) Sing, C.; Zwanikken, J.; Cruz, M. D. La. Electrostatic Control of Block Copolymer Morphology. *Nat. Mater.* **2014**, *13* (7), 694–698.

(16) Bouchet, R.; Maria, S.; Meziane, R.; Aboulaich, A.; Lienafa, L.; Bonnet, J.-P.; Phan, T. N. T.; Bertin, D.; Gigmes, D.; Devaux, D.; et al. Single-Ion BAB Triblock Copolymers as Highly Efficient Electrolytes for Lithium-Metal Batteries. *Nat. Mater.* **2013**, *12* (5), 452–

457.

(17) Borodin, O.; Smith, G. D. Mechanism of Ion Transport in Amorphous Poly(ethylene oxide)/LiTFSI from Molecular Dynamics Simulations. *Macromolecules* **2006**, *39* (4), 1620–1629.

(18) Singh, M.; Odusanya, O.; Wilmes, G. M.; Eitouni, H. B.; Gomez, E. D.; Patel, A. J.; Chen, V. L.; Park, M. J.; Fragouli, P.; Iatrou, H.; et al. Effect of Molecular Weight on the Mechanical and Electrical Properties of Block Copolymer Electrolytes. *Macromolecules* **2007**, *40* (13), 4578–4585.

(19) Bharatiya, B.; Schumers, J.-M.; Poggi, E.; Gohy, J.-F. Supramolecular Assemblies from Poly(styrene)-Block-poly(4-Vinylpyridine) Diblock Copolymers Mixed with 6-Hydroxy-2-Naphthoic Acid. *Polymers (Basel).* **2013**, *5*, 679–695.

(20) van Zoelen, W.; Asumaa, T.; Ruokolainen, J.; Ikkala, O.; ten Brinke, G. Phase Behavior of Solvent Vapor Annealed Thin Films of PS- B -P4VP(PDP) Supramolecules. *Macromolecules* **2008**, *41* (9), 3199–3208.

(21) Zoelen, W. Van. PS-B-P4VP (PDP) Comb-Shaped Supramolecules : Nanorods and Thin Films for Nanotemplating, University of Groningen, 2009.

(22) Chao, C. Y.; Li, X.; Ober, C. K.; Osuji, C.; Thomas, E. L. Orientational Switching of Mesogens and Microdomains in Hydrogen-Bonded Side-Chain Liquid-Crystalline Block Copolymers Using AC Electric Fields. *Adv. Funct. Mater.* **2004**, *14* (4), 364–370.

(23) Valkama, S.; Kosonen, H.; Ruokolainen, J.; Haatainen, T.; Torkkeli, M.; Serimaa, R.; ten Brinke, G.; Ikkala, O. Self-Assembled Polymeric Solid Films with Temperature-Induced

Large and Reversible Photonic-Bandgap Switching. *Nat. Mater.* **2004**, *3* (12), 872–876.

(24) Valkama, S.; Ruotsalainen, T.; Nykänen, A.; Laiho, A.; Kosonen, H.; Ten Brinke, G.; Ikkala, O.; Ruokolainen, J. Self-Assembled Structures in Diblock Copolymers with Hydrogen-Bonded Amphiphilic Plasticizing Compounds. *Macromolecules* **2006**, *39* (26), 9327–9336.

(25) Ikkala, O.; ten Brinke, G.; Pease, A. R.; Dodabalapur, A.; Batlogg, B.; Sirringhaus, H.; Schön, J. H.; Mena-Osteritz, E.; Bates, F. S.; Fredrickson, G. H.; et al. Functional Materials Based on Self-Assembly of Polymeric Supramolecules. *Science* **2002**, *295* (5564), 2407–2409.

(26) Choi, T.; Grubbs, R. H. Controlled Living Ring-Opening-Metathesis Polymerization by a Fast-Initiating Ruthenium Catalyst. *Angew. Chemie* **2003**, *115*, 1785–1788.

(27) Maslak, V.; Yan, Z.; Xia, S.; Gallucci, J.; Hadad, C. M.; Badjic, J. D. Design , Synthesis , and Conformational Dynamics of a Gated Molecular Basket. *J.* **2006**, 5887–5894.

(28) Yuan, H. SYNTHESIS AND STRUCTURE-PROPERTY RELATIONSHIPS OF POLYMERIC MEMBRANES FOR SMALL MOLECULE TRANSPORT, University of Massachusetts, Amherst, 2017.

CHAPTER 9

SYNTHESIS AND CHARACTERIZATION OF RANDOM AND BLOCK COPOLYMER OF NPS5 AND NHS5 WITH NMBzE

9.1 Introduction

One of the advantages of the use of solid electrolytes for anion exchange membranes is their robustness and flexibility in applications where the membranes may be subject to mechanical stress. The glass transition temperature, T_g, of these membranes should be high enough to impart mechanical fidelity in the membranes but also lower than the membrane operating temperature to avoid membranes fracture on mild contact.[1] Given that the operating temperatures of the membrane range from 30 – 90 °C, and these devices will most times be operated at room temperature, polymers with glass transition temperatures higher than room temperature may not suitable for application in anion exchange membranes. Poly(norbornenedimethyldichloride), PNDMDC, has a T_g of 114 °C. Membranes prepared from the copolymerization of NPS5/NHS5 and norbornenedimethyl dichloride (NDMDC) were found to be fragile and brittle. This made it difficult to perform conductivity tests on random and block copolymers of NPS5/NHS5 and NDMDC.

Some norbornene-based polymers with pendant ether linkages have glass transition temperatures that are lower than room temperature, and are suitable for preparing robust, flexible films. The polymer, poly(norbornenedimethyl dibenzylether), synthesized from the ring-opening metathesis polymerization of norbornenedimethyl dibenzylether, has a low T_g (-1 °C). Yuan and Coughlin reported that anion exchange membranes prepared from the copolymerization of norbornenedimethyldibenzylether and norbornene-based cobaltocenium chloride monomer were

robust and flexible.[2] However, norbornenedimethyldibenzylether is usually synthesized from norbornenedimethyl alcohol which is not readily available.

An alternative norbornene-based compound with pendant ether linkages, norbornenemethyl benzylether, can be readily synthesized from norbornenemethanol. Norbornenemethanol can be readily synthesized from the reduction of 5-norbornene-2-carboxyaldehyde which is commercially available. Furthermore, unlike norbornenedimethyldibenzyl ether, which has double pendant methylbenzylethers, norbornenemethylbenzylether, with a single methylbenzylether, should have a relatively lower T_g. Thus, membranes formed from the copolymerization of norbornenemethylbenzylether and NPS5 or NHS5 should be both robust and flexible, and consequently, their bromide ion conductivities could be measured.

In this chapter, random copolymers of NPS5 and NMBzE (PNPS5-*r*-PNMBzE) were synthesized by ROMP chemistry. Random copolymers of NHS5 and NMBzE (PNHS5-*r*-PNMBzE) were also synthesized ROMP chemistry. Random copolymers of ionic and non-ionic components provide a platform to study interesting morphologies of these charged and non-charged copolymers. In Chapter 4, Chapter 5, and Chapter 8, we have looked at the formation of ionomer cluster morphology and backbone-backbone morphology. Morphology-conductivity correlations have also been studied in Chapter 5. Results show that transition from an ionomer cluster morphology to a coexistence of both ionomer cluster and backbone-backbone morphology increased the conductivity of the material. This phenomenon warrants further investigations in random copolymers of PNPS5 and PNHS5 with a hydrophobic copolymer.

In this chapter, random copolymer series of PNPS5 and PNHS5 with PNMBzE were studied. The different morphologies (ionomer cluster, coexistence of ionomer cluster and backbone-backbone

morphology, and backbone-backbone morphology) for random copolymers of the PNPS5-*r*-PNMBzE and the PNHS5-*r*-PNMBzE series were evaluated by medium-angle X-ray scattering (MAXS). The morphologies were also evaluated by transmission electron microscopy (TEM). The bromide conductivities of the random copolymers were studied by electrochemical impedance spectroscopy (EIS). Relationships between morphologies and conductivities of these random copolymers were evaluated.

In the second part of this chapter, we synthesized random copolymers of NPS5 and NMBzE (PNPS5-*b*-PNMBzE) by ROMP chemistry. Random copolymers of NHS5 and NMBzE (PNHS5-*b*-PNMBzE) were also synthesized ROMP chemistry. The block copolymer morphologies were probed by extreme small-angle X-ray scattering (ESAXS). The substructure within a super structure were also probed by MAXS. The morphologies of the samples were also evaluated by TEM. Bromide conductivity of the block copolymers made from alkaline stable monomers were evaluated by EIS. Finally, the conductivities of these samples were interpreted in the light of their morphologies.

9.2 Materials and Methods

Sodium borohydride (98%), 5-norbornene-2-carboxyaldehyde (95%), cis 1,4 dichlorobutene (95%) was purchased from Alfa Aesar. Dicyclopentadiene (97%), dibromopentane (98%), benzylbromide (98%) were procured from TCI Chemicals. 4-hydroxypiperidine (98%), 3-bromopyridine (98%) were purchased from Matrix Scientific. Norbornene (99%), sodium hydride (60 wt% in mineral oil) and Grubbs' II catalysts were purchased from Sigma Aldrich.

9.2.1 Synthesis of Norborne Propoxy Spirocyclic Salt

9.2.1.1 Synthesis of Norbonenepropylbromide

In a round bottom flask, 20 g (0.134 moles) of 5-bromo-1-pentene was mixed with 5.9 g of dicyclopentadiene (0.045 moles). The solution was charged into a Schlenk tube equipped with a magnetic stirrer and containing 16 mg (0.15 mmoles) of hydroquinone. The tube was then placed in an oil bath at a temperature of 185 °C. After 20 h, the reaction was gradually cooled to room temperature. There was a change in color of the reaction mixture from a colorless solution to dark brown. Fractional vacuum distillation was performed at 27 – 40 °C, 300 mTorr to remove the excess reactant (5-bromo-1-pentene), and then at 58 – 60°C, 50 mTorr to obtain 11.5 g (60% yield) of norbornenepropylbromide colorless oil. See Chapter 7 for ^{1}H NMR spectrum of norbornenepropylbromide.

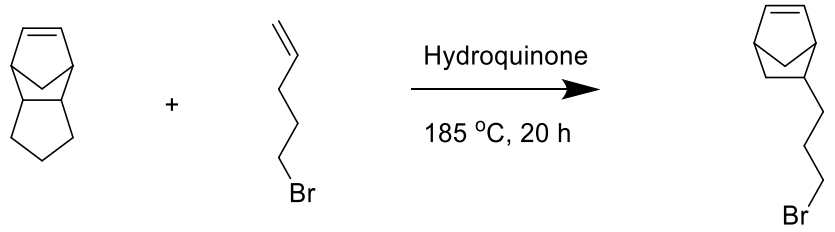

Scheme 9.1. Synthesis of norbornenepropylbromide.

92.1.2 Synthesis of Norbonenehexylbromide

In a round bottom flask, 10 g (0.052 moles) of 8-bromo-1-octene was mixed with 2.34 g of dicyclopentadiene (0.018 moles). The solution was charged into a Schlenk tube equipped with a stirrer and 21 mg (0.19 mmoles) of hydroquinone. The tube was then placed in an oil bath at a temperature of 185 °C. After 20 h, the reaction was gradually cooled to room temperature. There

was a change in color of the reaction mixture from a colorless solution to light brown. Vacuum distillation was performed at 60°C, 300 mTorr to remove the excess reactant. Flash chromatography of the residue was performed in hexanes to afford 5.3 g (58% yield) of a colorless oil of norbornenehexylbromide. See Chapter 7 for ^{1}H NMR spectrum of norbornenehexylbromide.

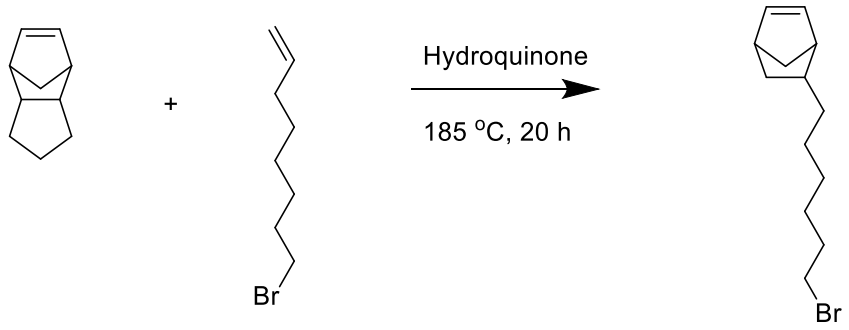

Scheme 9.2. Synthesis of Norbornenehexylbromide

9.2.1.3 Synthesis of 4-Hydroxy-6-azonia-spiro[5,5]undecane

In a round bottom flask, 21 g (0.152 moles) of potassium carbonate was charged into a solution of 27.6 g (0.124 moles) of 1,5 dibromopentane in 300 ml of acetonitrile in a round bottom flask at reflux. After 10 minutes, a solution of 10.1 g (0.1 moles) of 4-hydroxypiperidine in 50 ml of acetonitrile was added. After 20 h the reaction bath was gradually cooled to room temperature. The reaction mixture was then rotovapped to remove the solvent leaving a yellow like solid which was dissolved in 300 ml of ethanol and the excess potassium carbonate was removed by filtration. The solution was then partially evaporated to obtain a concentrated solution that was precipitated into diethyl ether. Afterwards, the yellowish solid was filtered and washed in dichloromethane thrice. The solid was then dried in vacuo at room temperature to afford 18.3 g (73% yield) of an

off-white solid. See Chapter 7 for ^{1}H NMR spectrum and ESI-TOFMass spectrometer chromatogram of 4-hydroxy-6-azonia-spiro[5,5]undecane.

9.2.1.4 Synthesis of Norbonenepropoxy-6-azonia-spiro[5,5]undecane (NPS5)

In a round bottom flask, 3.1 g (12.4 mmoles) of 4-hydroxy-6-azonia-spiro[5,5]undecane was dissolved in 50 ml of anhydrous DMSO. The solution was gradually added to a round bottom flask containing 1 g (25 mmoles) of sodium hydride equipped with a magnetic stirrer. After 1 h, 5.1 g (23.8 mmoles) of norbonenepropylbromide dispersed in 5 ml anhydrous DMSO was gradually added into the reaction mixture. The color of the mixture changes from white to light brown. The reaction was allowed to proceed for 20 h. Thereafter, the mixture was vacuum filtered to remove unreacted sodium hydride. The filtrate was a viscous clear brown liquid. The filtrate was then precipitated into diethyl ether to give a white solid. After filtration, the white solid was then washed with diethyl ether again and dried. The white solid was then dissolved in 200 ml of hot acetone to filter-off unreacted 4-hydroxy-6-azonia-spiro[5,5]undecane and sodium bromide. The product was then recrystallized from acetone by cooling the solution to 4 ºC. After filtration, the crystals were then washed with diethyl ether and dried in vacuum to afford 4.4 g (92% yield) of desired product. See Chapter 7 for ^{1}H NMR spectrum and ESI-TOF Mass spectrometer chromatogram of norbonenepropoxy-6-azonia-spiro[5,5]undecane (NPS5).

9.2.1.5 Synthesis of Norbonenehexoxy-6-azonia-spiro[5,5]undecane (NHS5)

In a round bottom flask, 1.15 g (4.6 mmoles) of 4-hydroxy-6-azonia-spiro[5,5]undecane was dissolved in 50 ml of anhydrous DMSO. The solution was gradually added to 0.35 g (9 mmoles) of sodium hydride equipped with a magnetic stirrer. After 1 hour, 1.96 g (7.7 mmoles) of norbonenehexylbromide dispersed in 5 ml anhydrous DMSO was gradually added into the reaction

mixture. The color of the mixture changes from white to light brown. The reaction was allowed to proceed for 20 h. Thereafter, the mixture was vacuum filtered to remove unreacted sodium hydride. The filtrate was a viscous clear brown liquid. The filtrate was then precipitated into diethyl ether to give a white solid. After filtration, the white solid was then washed in diethyl ether again and dried. The white solid was then dissolved in 100 ml of hot acetone to filter-off unreacted 4-hydroxy-6-azonia-spiro[5,5]undecane and sodium bromide. The product was then recrystallized from acetone by cooling the solution to 4ºC. After filtration, the crystals were then washed in diethyl ether and dried in vacuum to afford 1.86 g (95% yield) of desired product. See Chapter 7 for ^{1}H NMR spectrum and ESI-TOFMass spectrometer chromatogram of norbonenehexoxy-6-azonia-spiro[5,5]undecane (NPS5).

9.2.2 Synthesis of Norbornenemethanol

In a round bottom flask, 20 g (0.165 moles) 5-norbornene-2-carboxyaldehyde was dissolved in 80 ml of methanol. A suspension of 7 g of sodium borohydride (0.18 moles) in 25 ml aqueous solution of 4 M potassium hydroxide was added dropwise to the solution of 5-norbornene-2-carboxyaldehyde in methanol at 0 °C for 30 mins. Afterwards, 20 ml of H_2SO_4 (40 % by volume in water) was added dropwise to the reaction mixture. The mixture was then rotovapped to remove excess methanol. The organic layer formed on the aqueous layer was extracted by washing with 50 ml of diethylether three times. The organic extract was washed with 50 ml of saturated solution of $NaHCO_3$ three times. The organic (yellowish viscous liquid) was further dissolved in 50 ml of diethylether and then dried over anhydrous Na_2SO_4. The solution was filtered off and then concentrated by rotovapping. The viscous oil was finally passed through column using a mixture of hexane (95%) and ethylacetate (5%) as the eluent. The filtered solution was then concentrated in vacuum to afford 16.5 g (84 % yield) of organic oil.

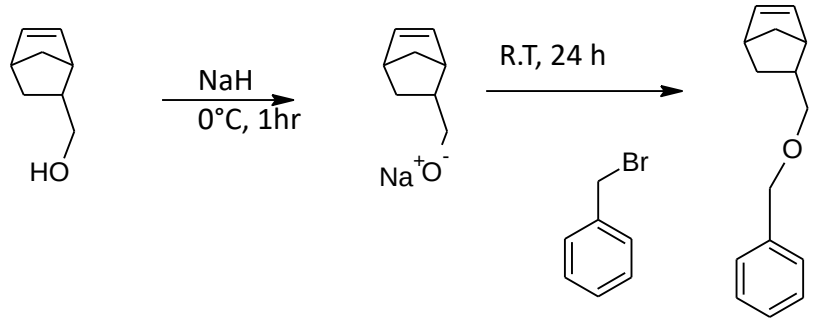

Scheme 9.3. Synthesis of Norbornenemethylbenzylether (NMBzE).

9.2.3 Synthesis of Norbornenemethylbenzylether

The procedure for the synthesis of norbornenemethylbenzylether was as follow: To 14 g (0.11 moles) of norbonenemethanol in 30 ml anhydrous acetonitrile was added 11 g (0.46 moles) of sodium hydride at 0 °C. The reaction mixture was stirred for 1 h. Afterwards, 13.8 g (0.08 moles) of benzylbromide was added to the mixture. The reaction was quenched after 1 hour with 50 ml of 0.5 M aqueous hydrochloric acid. The mixture was washed with 75 ml of diethylether thrice to extract the organic layer. The organic layer was vacuum distilled at 60 ˚C and 55 mTorr. The organic oil was further purified by flash chromatography using a 90:10 mixture of hexanes and ethylacetate. The product was rotavapped and concentrated in vacuo to afford 14.1 g (84% yield) of norbornenemethylbenzyl ether.

9.2.4 Synthesis of Polynorbornenemethylbenzylether

To 150 mg (0.7 mmoles) of the monomer, NMBzE, equipped with a stirrer 0.5 ml of DCM was added. A solution of 1 mg (0.001 mmoles) of Grubbs' III catalyst in 1 ml of DCM was charged into the monomer solution. After 1 min, the reaction was quenched by adding 1 ml of ethylvinyl

ether. The polymer was then precipitated in methanol to afford 130 mg (87% yield) of polynorbornenemethylbenzyl ether (PNMBzE).

9.2.5 Synthesis of PNPS5-*r*-PNMBzE

In a 20 ml scintillation vial equipped with a magnetic stirrer, 204 mg (0.95 mmoles) of NMBzE and 50 mg (0.13 mmoles) of NPS5 were dissolved in a mixture of 4 ml of DCM and 2.5 ml. A solution of 1 mg (0.001 mmoles) of Grubbs' III catalyst in 1 ml of DCM was charged into the monomer mixture solution. After 24 hours, the reaction was quenched by adding 2 ml of ethylvinylether. The polymer was then precipitated in diethyl ether to afford 193 mg (76% yield) of PNPS5-*r*-PNMBzE.

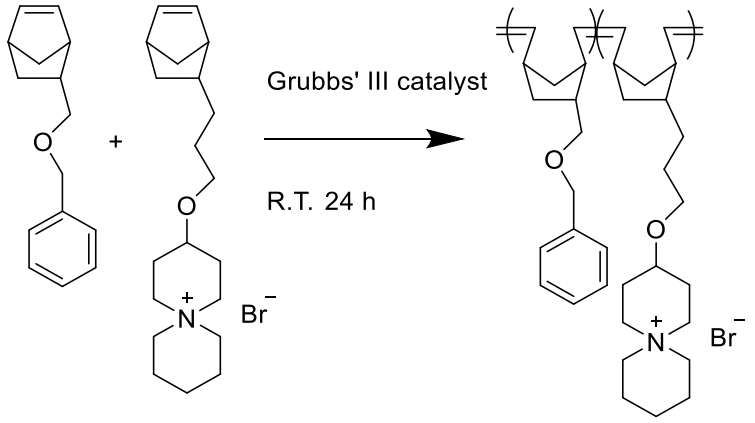

Scheme 9.4. Synthesis of PNPS5-*r*-PNMBzE.

9.2.6 Synthesis of PNHS5-*r*-PNMBzE

In a 20 ml scintillation vial equipped with a magnetic stirrer, 212 mg (0.99 mmoles) of NMBzE, and 50 mg (0.117 mmoles) of NPS5 were dissolved in a mixture of 4 ml of DCM and 1.5 ml of DMF. A solution of 1 mg (0.001 mmoles) of Grubb's III catalyst in 1 ml of DCM was charged into the monomer mixture solution. After 24 hours, the reaction was quenched by adding 2 ml of

ethylvinylether. The polymer was then precipitated in diethyl ether to afford 216 mg (82% yield) of PNHS5-*r*-PNMBzE.

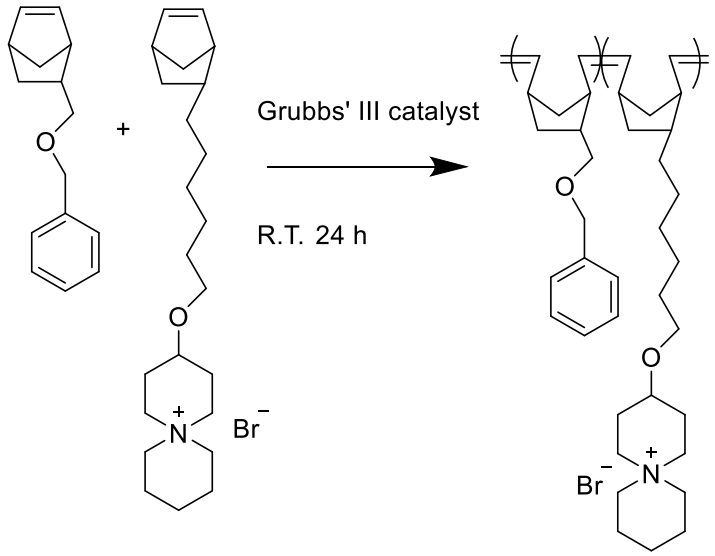

Scheme 9.5. Synthesis of PHPS5-*r*-PNMBzE

9.2.7 Synthesis of PNPS5-*b*-PNMBzE

In a 20 ml scintillation vial equipped with a magnetic stirrer, 235 mg (0.95) of the monomer, NMBzE, in 0.5 ml of DCM. (Approximately 15% more of NMBzE was used in the synthesis of the block copolymer in comparison to the random copolymer for the same target IEC because some fraction of PNMBzE undergo secondary metathesis resulting in dead chains). A solution of 1 mg (0.001 mmoles) of Grubbs' III catalyst in 1 ml of DCM was charged into the monomer solution. After 1 min, a solution of 50 mg (0.13 mmole) of NPS5 dissolved in 6 ml of a mixture of DCM and DMF (1:2) was added to the reaction. The reaction was quenched after 10 mins by

adding 1 ml of ethylvinyl ether. The polymer was then precipitated first in tetrahydrofuran and then methanol to afford 156 mg (55% yield) of PNPS5-*b*-PNMBzE.

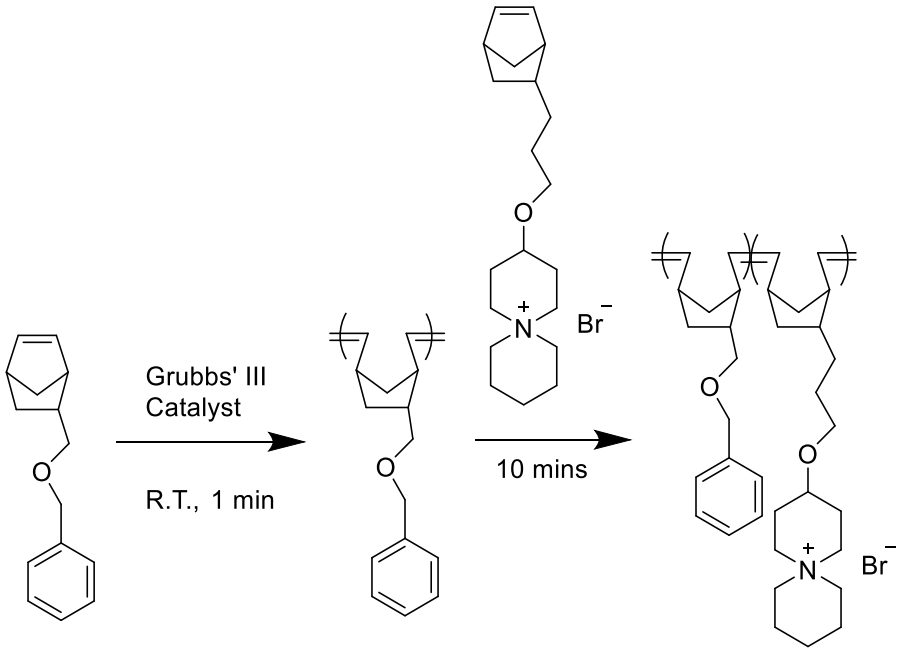

Scheme 9.6. Synthesis of PNPS5-*b*-PNMBzE.

9.2.8 Synthesis of PNHS5-*b*-PNMBzE

In a 20 ml scintillation vial equipped with a magnetic stirrer, 246 mg (0.99 mmole) of the monomer, NMBzE, in 0.5 ml of DCM. (Approximately 15% more of NMBzE was used in the synthesis of the block copolymer in comparison to the random copolymer for the same target IEC because some fraction of PNMBzE undergo secondary metathesis resulting in dead chains). A solution of 1 mg (0.001 mmoles) of Grubbs' III catalyst in 1 ml of DCM was charged into the monomer solution. After 1 min, a solution of 50 mg (0.117 mmoles) of NHS5 dissolved in 6 ml of a mixture of DCM and DMF (1:2) was added to the reaction. The reaction was quenched after 10 mins by adding 1 ml of ethylvinyl ether. The polymer was then precipitated first in tetrahydrofuran and then methanol to afford 171 mg (58% yield) of PNPS5-*b*-PNMBzE.

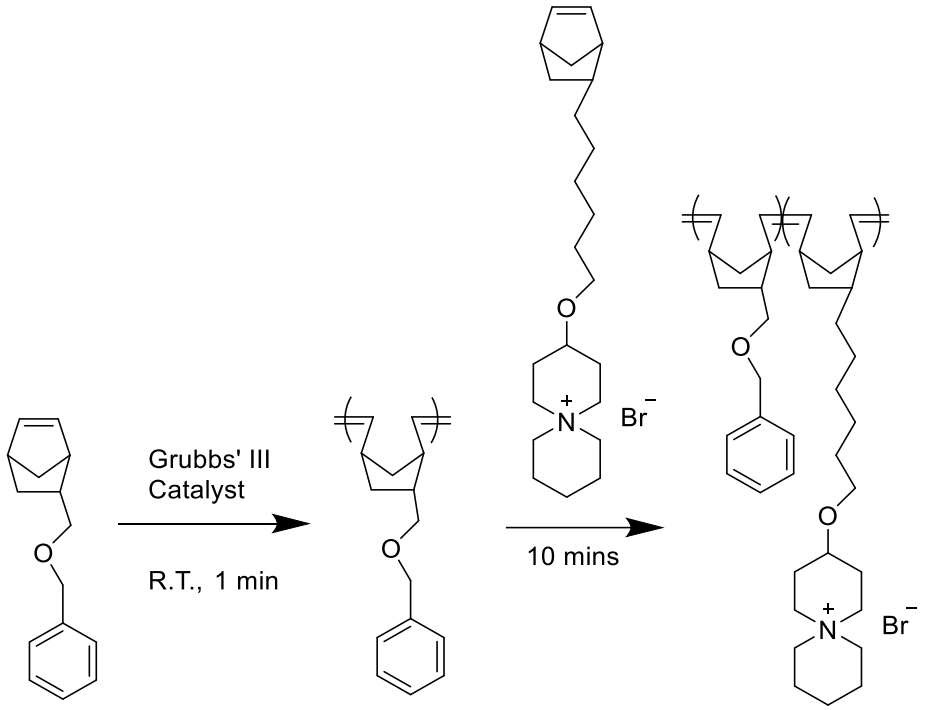

Scheme 9.7. Synthesis of PNHS5-*b*-PNMBzE.

9.2.9 Characterization of Random and Block Copolymers

Number average molecular weight, M_n, was determined using a gel permeation chromatography (GPC) in DMF at a flow rate of 1.0 mL/min using a refractive index detector on an Agilent Technologies 1260 Infinity system. The chemical composition P4VP-*r*-PI was determined using a Bruker 500 Fourier-transform nuclear magnetic resonance spectroscopy (FT-NMR). Quaternized samples, P4VP-*r*-PI_CnBr, were drop cast from methanol on Teflon® sheet. Characterization was performed on the resulting films. PerkinElmer Spectrum 100 FTIR with a universal ATR was used

to characterize the extent of quaternization. Film samples were mounted on the ATR crystal and secured by the sample holder. Impedance data was collected over the frequency range, 1Hz – 10 KHz by a four-electrode test cell connected to a BioLogic VMP3 multichannel potentiostat. The TestEquity chamber in which experiments were made ensured a proper control of temperature and relative humidity. Measurements were performed through a temperature range of 40 – 90 °C by 10 °C step and 95% RH. The membrane resistance was obtained from the frequency intercept of the Nyquist plot. Ionic conductivity was obtained by measuring the in-plane resistance of the sample. The resistance is then converted to conductivity using the equation

$$\sigma = \frac{d}{Rwt} \qquad (8.1)$$

Where *d* is the distance between the electrodes, *t* is the thickness of the sample and *w* is the width of the membrane defined by the four-electrodes of the test cell.[3,4]

Wide-angle X-ray scattering (WAXS), medium-angle X-ray scattering (MAXS), and extreme small-angle X-ray scattering (ESAXS) measurements were performed in transmission geometry on Molmex Scientific Ganesha SAXS Lab. A double aperture for the Cu-Kα radiation (λ = 1.54 Å), which was the X-ray source, was used. Silver behenate was used as the standard for the momentum transfer calibration. Data was collected for 180 seconds. Depending on the signal-to-noise ratio, data collection could be longer. Azimuthal averaging of the obtained isotropic 2-D pattern was performed to obtain the intensity against wave vector plot.

To obtain transmission electron microscopy micrographs, samples were first michrotomed over water using an RJ Ultra-Michrotome A. Samples were cut to 40 nm film thickness and collected on copper grids. There was no carbon film on the copper grid.

Transmission electron microscopy characterization was performed on the microtomed samples by the TEM JEOL 2000. The micrographs were taken in a dark field mode.

9.2.10 Determination of Membrane Density

The density of the polymer sample was determined as follows: 10 ml of methanol was added to 1 mg of PNMBzE film in a measuring cylinder. Water was then gradually added to the measuring cylinder until the PNMBzE film begins to travel upwards due to the increase in the density of the methanol-water mixture. When the film is positioned at the center of the filled cylinder, the density of the methanol-water mixture was determined from the volume and mass of the mixture. This is approximately the density of the PNMBzE film. For PNPS5 and PNHS5 homopolymers, a mixture of benzylbromide (specific gravity = 1.44) and tetrahydrofuran (specific gravity = 0.889) was used.

9.3 Results and Discussion for PNPS5-*r*-PNMBzE and PNHS5-*r*-PNMBzE

Characterization of the norbornenemethanol by ^{1}H NMR confirm the successful synthesis of the monomer. The protons norbornenemethanol and their corresponding exo peaks on the ^{1}H NMR spectrum are shown in Figure 9.1.

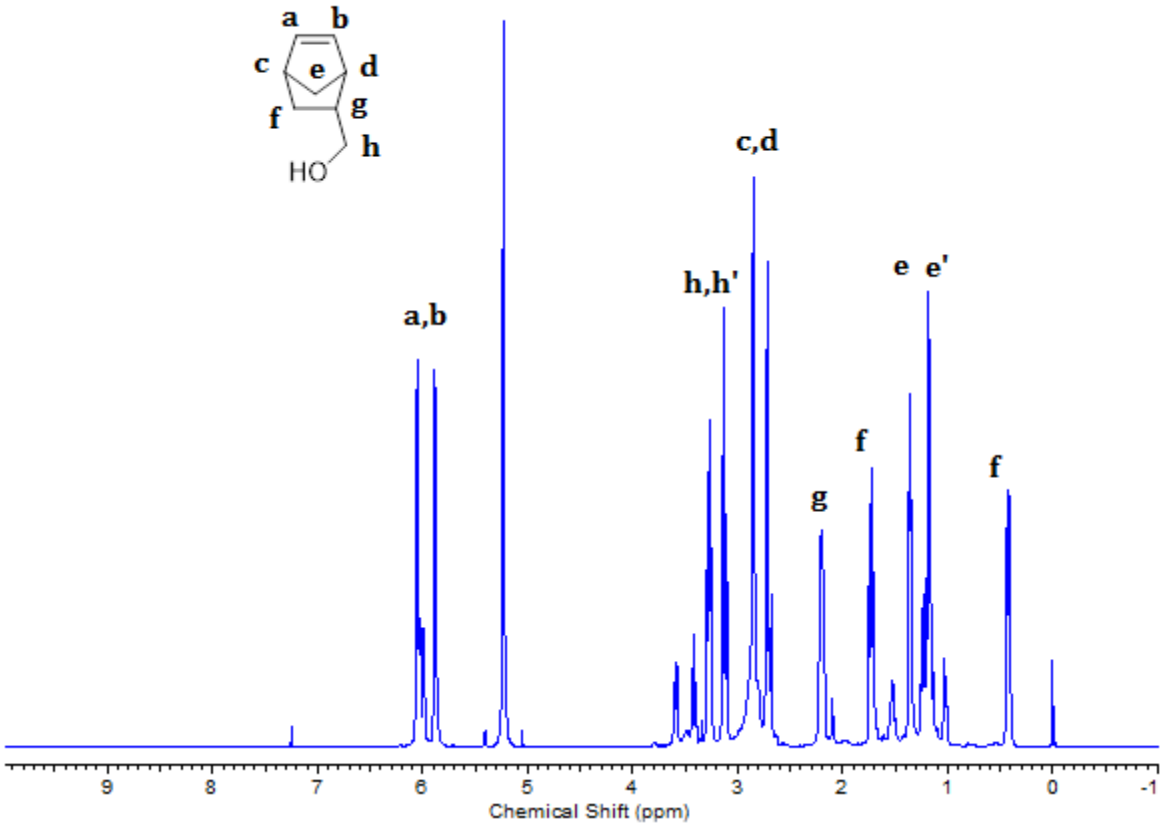

Figure 9.1. The ^{1}H NMR spectrum of norbornenemethanol.

Characterization of the norbornenemethylbenzyl ether by ^{1}H NMR confirm the successful synthesis of the monomer. The protons norbornenemethylbenzylether and their corresponding exo peaks on the ^{1}H NMR spectrum are shown in Figure 9.2.

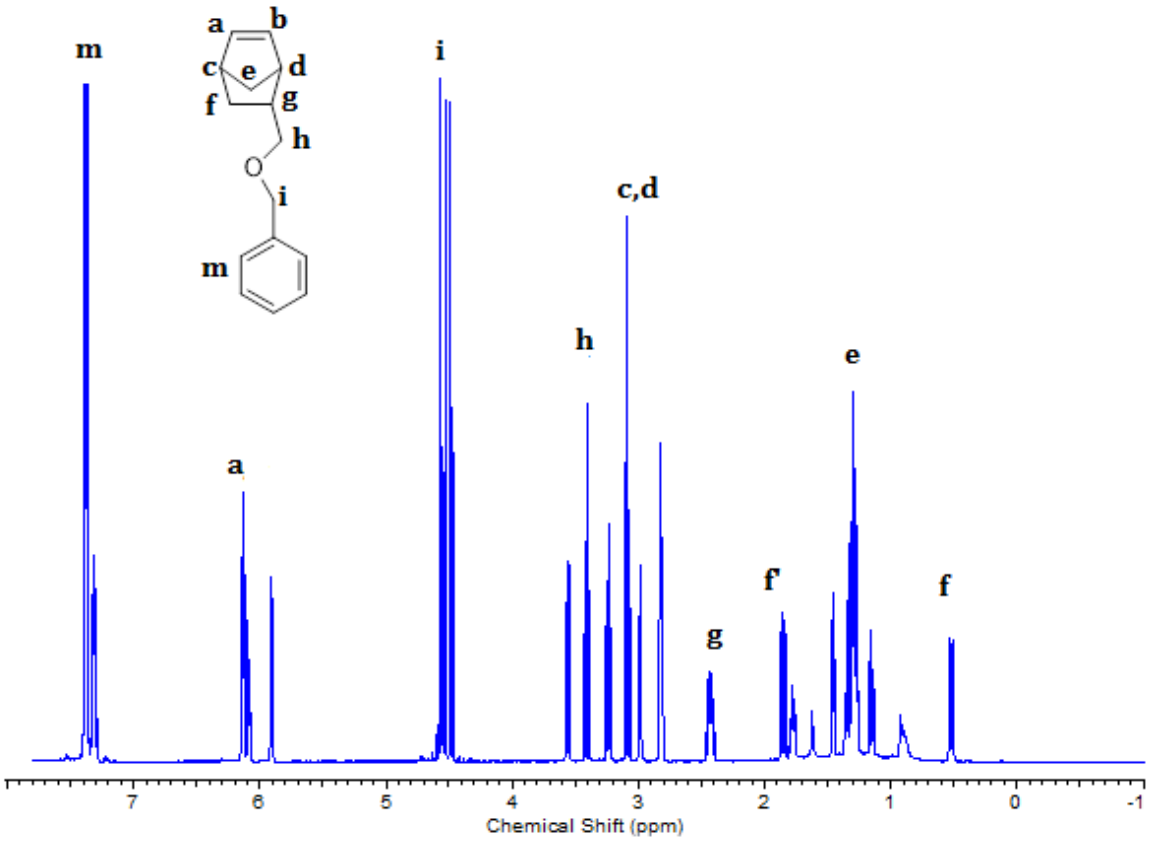

Figure 9.2. The ^{1}H NMR spectrum of norbornenemethylbenzylether.

The successful polymerization of NMBzE monomer to PNMBzE homopolymer, was confirmed by ^{1}H NMR. In the ^{1}H NMR spectrum (see Figure 9.3) only the exo peaks are labelled.

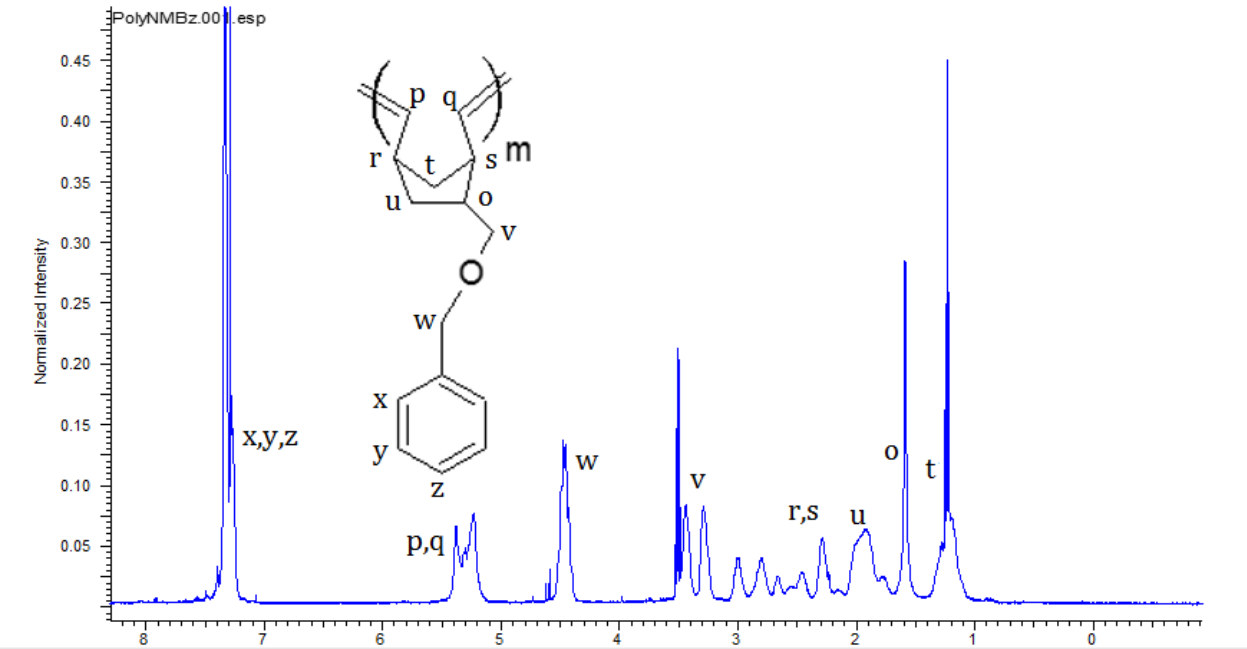

Figure 9.3. The ^{1}H NMR spectrum of PNMBzE.

The molecular weight of PNMBzE was characterized by THF GPC using PS standards. In Figure 9.4, the GPC chromatogram for PNMBzE shows a shoulder peak resulting from secondary metathesis during the ring-opening polymerization of NMBzE. A molecular weight of 280 Kg/mol and a dispersity of 1.11 were determined for PNMBzE from the GPC trace.

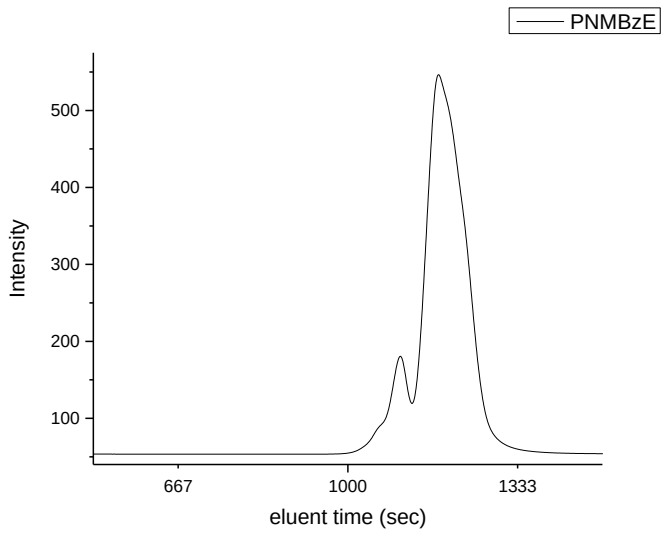

Figure 9.4. The GPC chromatogram of PNMBzE.

Characterization of PNMBzE by DSC shows that the homopolymer has a glass transition temperature of -7 °C. Since the T_g of PNMBzE is less than room temperature, films of the homopolymer prepared from DCM were robust and flexible. This suggests that PNMBzE should be a good copolymer substitute for the rigid PNDC. Thus, the anion exchange membranes prepared from the copolymerization of NPS5/NHS5 and NMBzE should be flexible, robust, and show good mechanical fidelity.

Random copolymers of NPS5 and NMBzE were successfully synthesized. Five different samples of PNPS5-*r*-PNMBzE with varying concentrations of NPS5 ranging from 15 – 52 mol% were prepared. The composition of the synthesized random copolymers was determined by ^{1}H NMR using the ratio of the combined vinyl protons of PNPS5 and PNMBzE, and the aromatic protons of PNMBzE. See Figure 9.5.

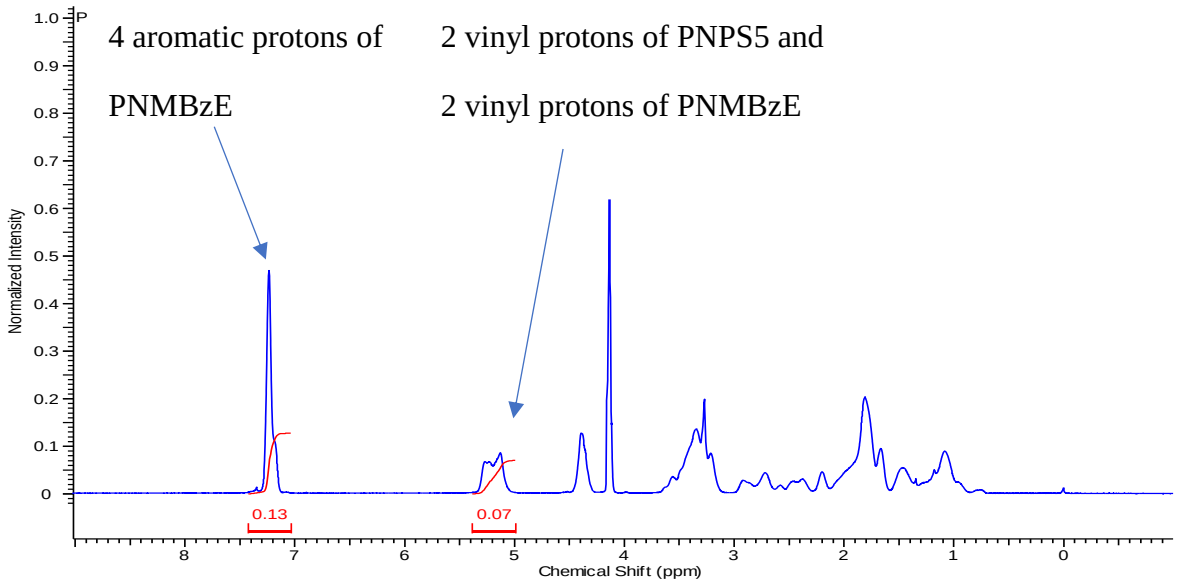

Figure 9.5. Determination of the composition of PNPS5-*r*-PNMBzE by ^{1}H NMR

A tabular summary of the feed composition, target IEC., sample composition determined by ^{1}H NMR, and sample IEC determined from ^{1}H NMR composition is presented in Table 9.1.

Table 9.1. Comparison of the feed composition and target IEC. and the ^{1}H NMR composition and ^{1}H NMR IEC. of the PNPS5-*r*-PNMBzE series.

Sample name	**Feed comp%**	**Target IEC.**	**NMR comp%**	**NMR IEC.**
PNPS5-*r*-PNMBzE_0.62	**12:88**	**0.50**	**15:85**	**0.62**
PNPS5-*r*-PNMBzE_1.07	**26:74**	**1.00**	**28:72**	**1.07**
PNPS5-*r*-PNMBzE_1.50	**43:57**	**1.50**	**43:57**	**1.50**
PNPS5-*r*-PNMBzE_1.72	**53:47**	**1.75**	**52:48**	**1.72**
PNPS5-*r*-PNMBzE_2.60	**100:0**	**2.60**	**100:0**	**2.60**

The composition of PNPS5 and PNMBzE in the random polymers determined by ^{1}H NMR is similar to the feed ratio of the monomers (NPS5 and NMBzE). This suggests that the samples have random character.

Random copolymers of NHS5 and NMBzE were successfully synthesized. Four different samples of PNHS5-*r*-PNMBzE with varying concentrations of NHS5 ranging from 12 – 57 mol% and the homopolymer, PNHS5, were prepared. The composition of the polymer was determined by ^{1}H NMR using the ratio of the combined vinyl protons of PNHS5 and PNMBzE, and the aromatic proton of PNMBzE. See Figure 9.6.

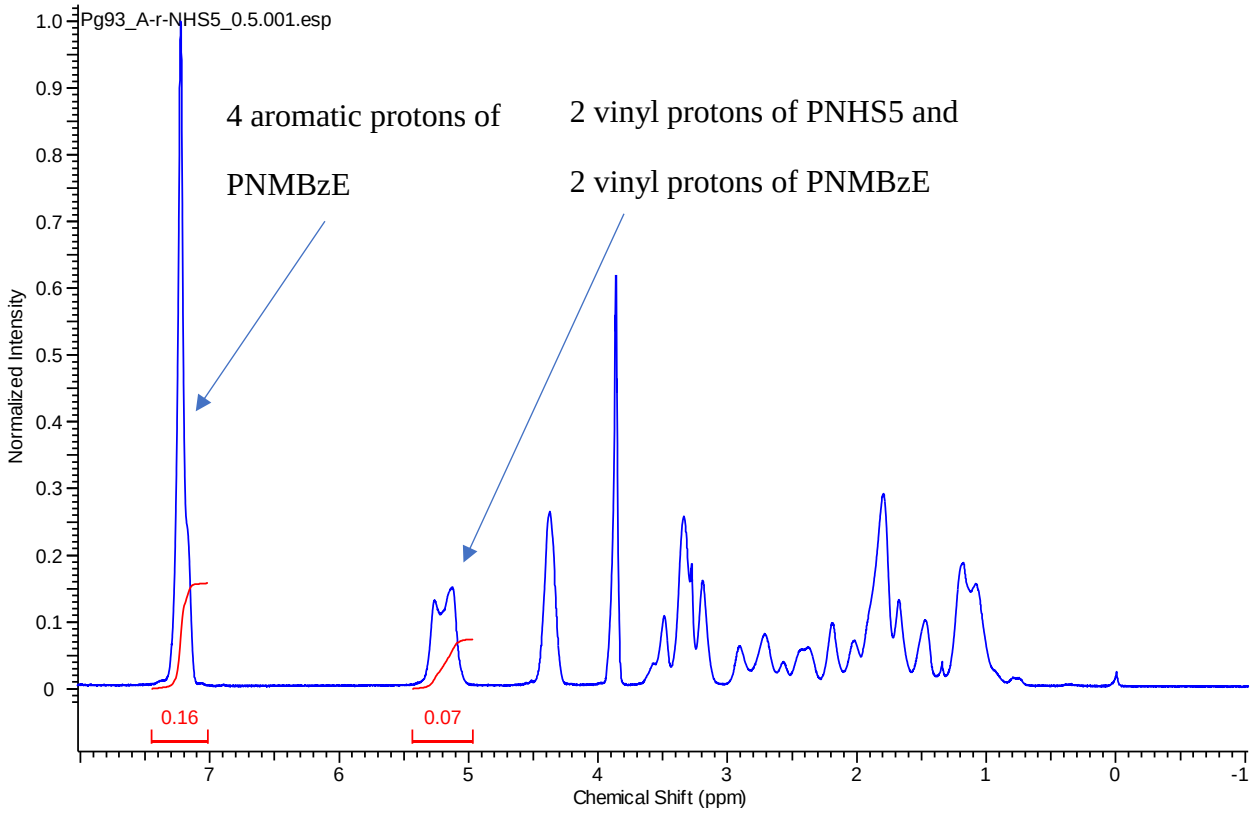

Figure 9.6. Determination of the composition of PNHS5-*r*-PNMBzE by ^{1}H NMR.

A tabular summary of the feed composition, target IEC, sample composition determined by ^{1}H NMR, and sample IEC determined from ^{1}H NMR composition is presented in Table 9.2.

Table 9.2. Comparison of the feed composition and target IEC. and the ^{1}H NMR composition and ^{1}H NMR IEC. of the PNHS5-*r*-PNMBzE series.

Sample name	**Feed comp (%)**	**Target IEC**	**NMR comp (%)**	**NMR IEC**
PNHS5-*r*-PNMBZE_0.50	**12:88**	**0.50**	**12:88**	**0.5**
PNHS5-*r*-PNMBZE_0.94	**27:73**	**1.00**	**25:75**	**0.94**
PNHS5-*r*-PNMBZE_1.48	**47:53**	**1.50**	**46:54**	**1.48**
PNHS5-*r*-PNMBZE_1.70	**60:40**	**1.75**	**57:43**	**1.70**
PNHS5-*r*-PNMBZE_2.34	**100:0**	**2.35**	**100:0**	**2.35**

The composition of PNHS5 and PNMBzE in the random polymers determined by ^{1}H NMR is similar to the feed ratio of the monomers (NHS5 and NMBzE). This suggests that PNHS5-*r*-PNMBzE samples have random character.

9.3.1 Morphology of Random Copolymers of NPS5, NPMBzE and NHS5, NPMBzE

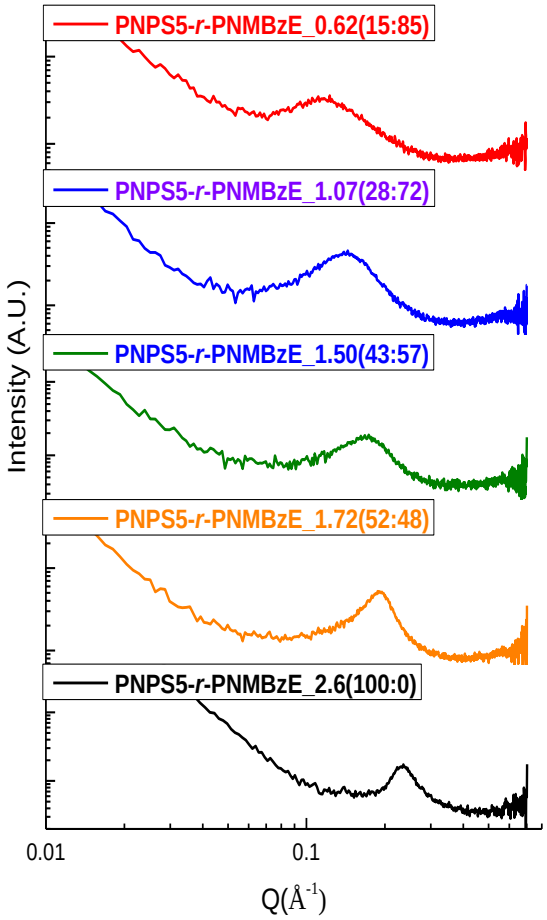

Figure 9.7. X-ray scattering data for PNPS5-*r*-PNMBzE.

Medium angle X-ray scattering of PNPS5-*r*-PNMBzE are presented in Figure 9.7. From the scattering data, the homopolymer of PNPS5 show a backbone-backbone spacing peak. This peak correlates to the periodic spacing between the backbones of the homopolymer. The backbone-backbone spacing results from the sterics of the pendant side-chains and increases with increasing length of the pendant side-chain (see Figure 9.8).

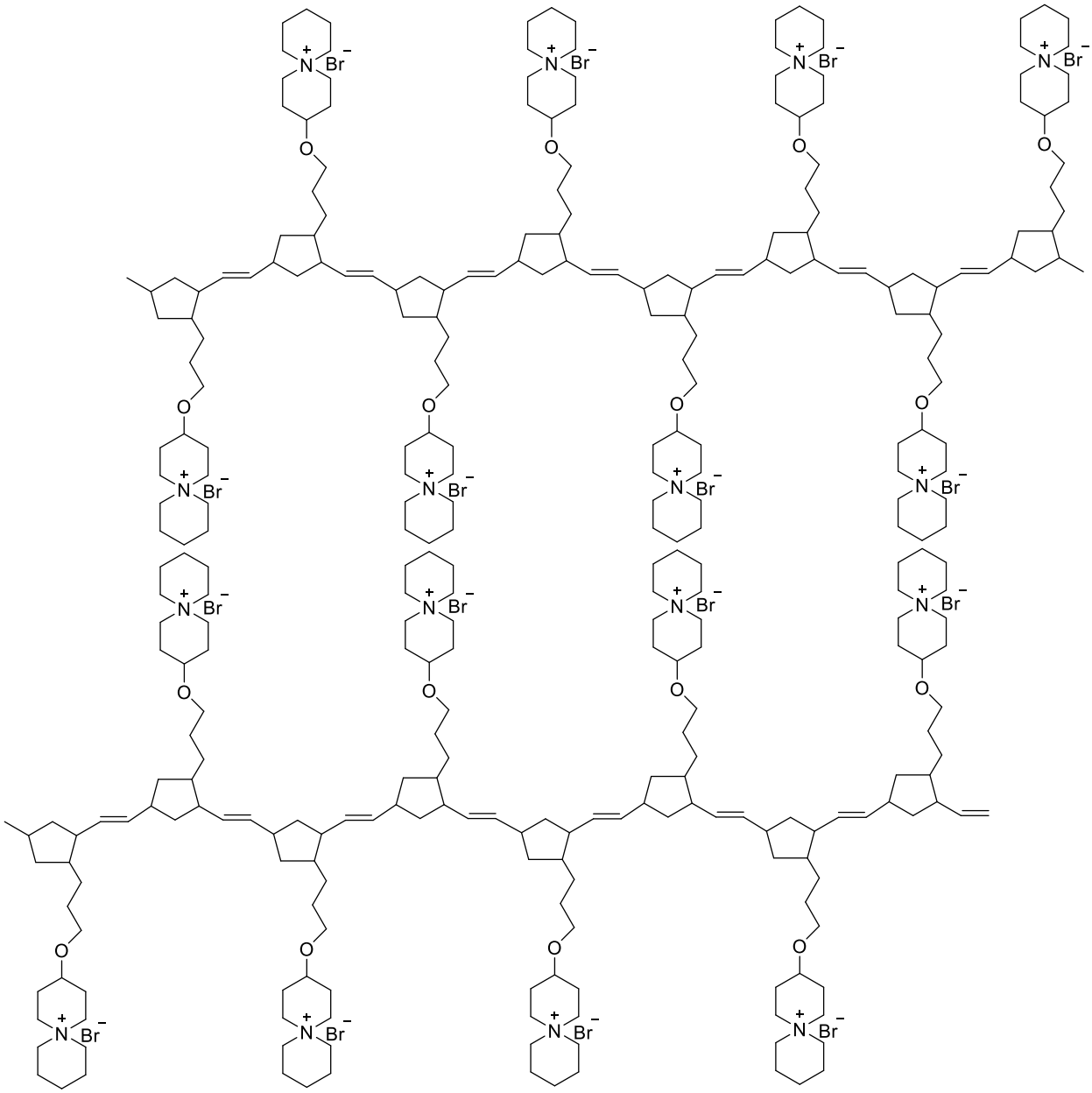

Figure 9.8. Depiction of backbone-backbone spacing in PNPS5.

However, for PNPS5-*r*-PNMBzE_0.62(15:85), the peak at lower *Q* values is the ionomer cluster peak that correlates to the cluster-cluster spacing between clustered dipoles in the hydrophobic matrix. The clustering of dipoles is due to dipole-dipole attraction between dipoles in the random copolymer.[5–7] Increasing the concentration of charges decreases the distance between these dipole

clusters. See Figure 9.9. This is consistent with the shift to higher *Q* values of the scattering peak in PNPS5-*r*-PNMBzE_1.07(28:72) in comparison to PNPS5-*r*-PNMBzE_0.62(15:85). Further decrease in the cluster-cluster spacing can be observed in PNPS5-*r*-PNMBzE_1.50(43:57) as the scattering peak shifts to higher *Q* values. However, the scattering peak observed for PNPS5-*r*-PNMBzE_1.72(52:48) is similar to the scattering peak observed in the PNPS5 spectrum which is the backbone-backbone peak.

a)

b)

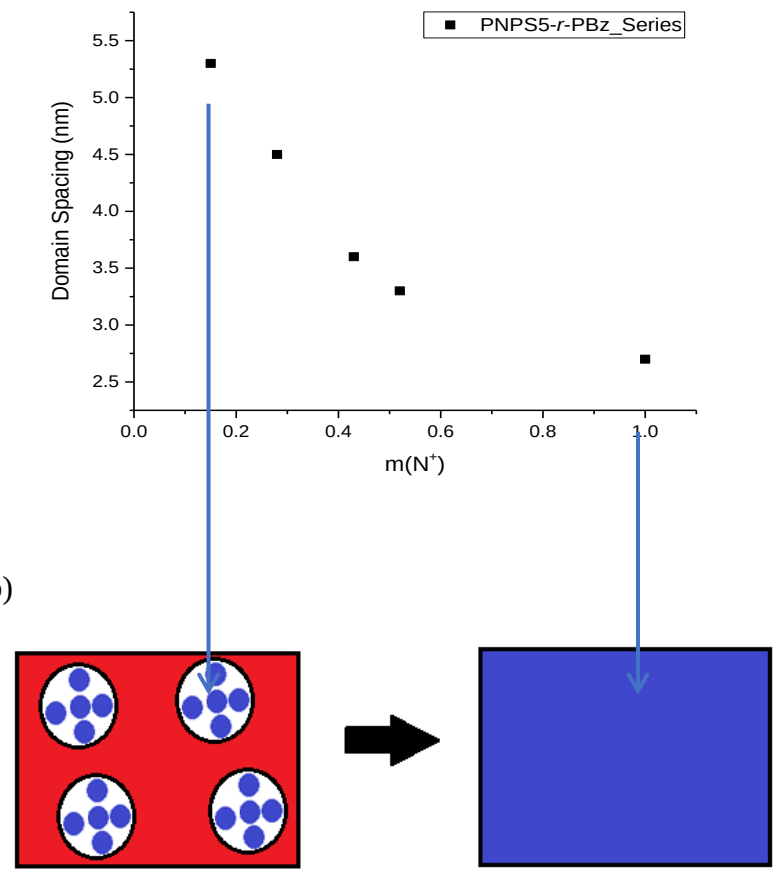

Figure 9.9. a) Variation of the characteristic spacing with mol% of NPS5, b) depiction of the transition from ionic cluster to ionic matrix/percolating structure.

The assignation of the scattering peak for PNPS5-*r*-PNMBzE_1.72(52:48) to correlate with backbone-backbone spacing rather than cluster-cluster spacing is due to the gaussian character of the peak. Ionomer clusters are usually poorly defined.[8–10] Theoretical evaluation of clusters show that clusters could range from a few dipoles to tens of dipoles.[11,12] Like in micellization in which a portion of the surfactant do not aggregate to form micelles; in charged random copolymers, a significant number of dipoles in charged random copolymers do not participate in the formation of dipole clusters. This contributes to a less defined cluster-cluster distance and consequently less defined ionomer cluster morphology. Thus, X-ray scattering peaks correlating to cluster-cluster spacing in ionomer morphology are usually broad. However, for backbone-backbone morphology the backbone-backbone spacing are well-defined. Backbone-backbone spacing is determined by the length of the pendant side-chain on the monomer. Thus, the X-ray scattering peaks correlating backbone-backbone spacing are usually sharp and narrow.[13–15] As a matter of fact, longer pendant side-chains have crystalline-like peaks and at times show higher order peaks. In the case of NPS5, all the monomers have the same length of pendant side-chains, thus resulting in a well-defined backbone-backbone spacing in the homopolymers. The scattering peak for PNPS5-*r*-PNMBzE_1.72(52:48) is narrower in comparison to the scattering peaks of PNPS5-*r*-PNMBzE_0.62(15:85), PNPS5-*r*-PNMBzE_1.07(28:72), and PNPS5-*r*-PNMBzE_1.50(43:57) and slightly broader than the scattering peak for PNPS5-*r*-PNMBzE_2.6(100:0). This peak shape suggests that the morphology of PNPS5-*r*-PNMBzE_1.72(52:48) would be dominated by backbone-backbone spacing with some degree of dipole clustering. Thus, PNPS5-*r*-PNMBzE_1.72(52:48) is thought to have a coexistence of both morphologies.

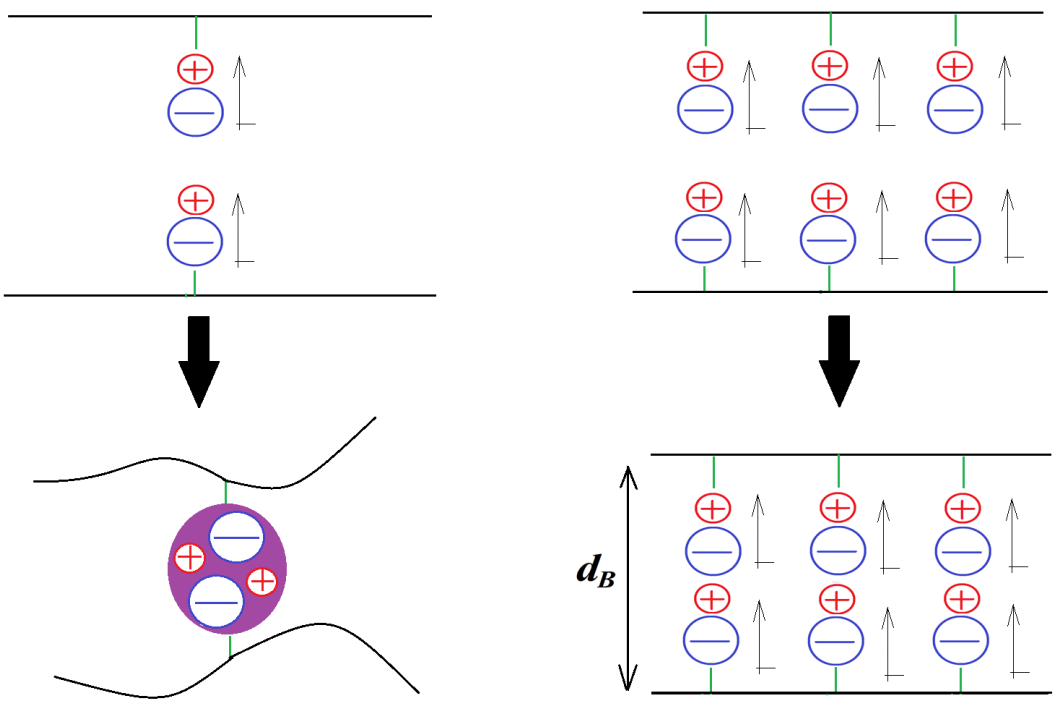

Figure 9.10. Schematic representation of the Matrix Effect.

Ionomer morphology is formed from the clustering of dipoles. On clustering of the dipoles, the hydrophobic copolymers form the matrix of the morphology with the dipole clusters randomly distributed in the hydrophobic matrix. With increasing concentration of the charged copolymer, the formation of ionomer cluster morphology becomes untenable because there are less hydrophobic copolymers to form the matrix. Furthermore, the driving force for cluster formation is the dipole-dipole interaction that depends on the effective dielectric constant of the medium. With increasing concentration of dipoles, the number of dipoles not participating in the formation of ionomer cluster increases. These unclustered dipoles will increase the dielectric constant of the medium, thus decreasing the strength of the dipole-dipole attraction. Consequently, the formation of dipole clusters will be unfeasible in materials with high concentration of dipoles. Ionomer cluster morphology is almost non-existent in homopolymer polyelectrolytes. By increasing the

concentration of ionic content, the dipoles transition from clusters to matrix (percolating phase). See Figure 9.9b. However, inverse ionomer cluster morphology may form. At high concentration of the ionic copolymer, hydrophobic copolymers, which are in small quantity, could interact by van der Waal's attraction and form hydrophobic clusters in a sea of ionic matrix. This will lead to an *inverse ionomer cluster morphology*. The formation of this morphology would be facilitated by the immiscibility of the ionic and non-ionic copolymers.

Ionomer cluster morphology has been observed in polyelectrolytes with about 50 mol% of charged comonomers.[6,16,17] The concentration at which the dipoles in a charged random copolymer morphology transitions from an ionomer cluster morphology to forming the matrix (a matrix of the dipoles morphology) will vary from charged monomer to charged monomer. Monomers with longer pendant side-chains in which sterics is dominant may disfavor the formation of dipole clusters. In this case, the transition from ionomer cluster morphology to a matrix of dipole morphology will occur at a relatively lower concentration of the charged monomer in comparison to monomers whose shorter pendant side-chain have minimal sterics.

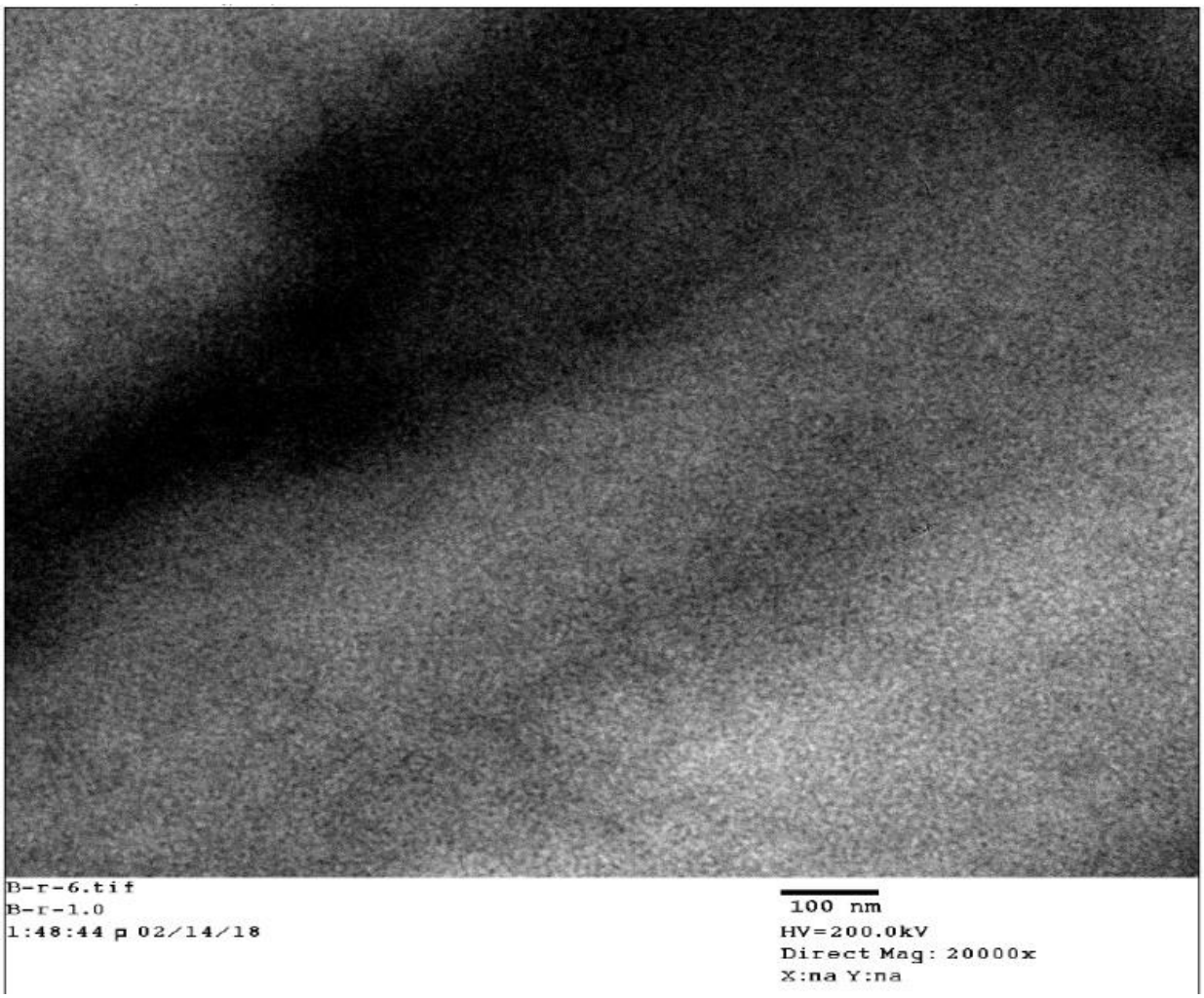

Figure 9.11. Transmission electron microscopy micrograph of PNPS5-*r*-PNMBzE_1.07(28:72).

The morphology of PNPS5-*r*-PNMBzE_1.07(28:72) and PNPS5-*r*-PNMBzE_1.72(52:48) were probed by transmission electron microscopy (TEM). The image was captured in darkfield mode. The contrast of the image results entirely from the bromide counterion. Black clusters and black matrices results from PNPS5 copolymer. White clusters and white matrices arising from PNMBzE copolymer. The obtained image for PNPS5-*r*-PNMBzE_1.07(28:72), presented in Figure 9.11, show PNPS5 (black) clusters in a PNMBzE (white) matrix and PNMBzE (white) clusters in a PNPS5 (black) matrix. The scattering data show the ionomer cluster morphology feature for

PNPS5-*r*-PNMBzE_1.07(28:72) which is consistent with the TEM image. A 5 nm cluster-cluster spacing can be determined from the TEM image which is also the approximate value of that observed in the scattering data. The TEM image for PNPS5-*r*-PNMBzE_1.07(28:72) also show the formation of tubular/vermicular structures of the PNMBzE copolymer in a PNPS5 matrix. Suggesting that even at concentrations as low as 28 mol% of NPS5, there is some degree of transition from ionomer cluster to a matrix of dipole morphology. The formation of a quasi-matrix by PNPS5 could also lead to some form of inverse ionomer cluster morphology. Although the transition from cluster to matrix is dependent on the mol% of NPS5 in the random copolymer, it is also dependent on the length of the pendant side-chain. Pendant side-chain sterics tend to stifle the formation of ionomer cluster morphology (see Chapter 4). For ionomer cluster morphology to form, polymer chains are sometimes stretched to accommodate the clustering of dipoles. The opposite is the case for the formation of backbone-backbone morphology in which backbones are parallel to one another. The presence of pendant side-chains in PNPS5 which facilitates the formation of backbone-backbone morphology may have disfavored the formation of ionomer cluster morphology in PNPS5-*r*-PNMBzE_1.07(28:72), thereby, facilitating the transition from ionomer cluster to a matrix of dipole morphology. Consequently, resulting in a coexistence of both clustering and inverse-matrix morphology of PNPS5 in PNPS5-*r*-PNMBzE_1.07(28:72). The presence of both ionomer cluster and inverse ionomer cluster morphology could improve ionic conductivity of PNPS5-*r*-PNMBzE_1.07(28:72). As already noted from the seminal work of Balsara and Beers, decreasing or eliminating dipole clusters in a random copolyelectrolyte will lead to an increase in conductivity.[16]

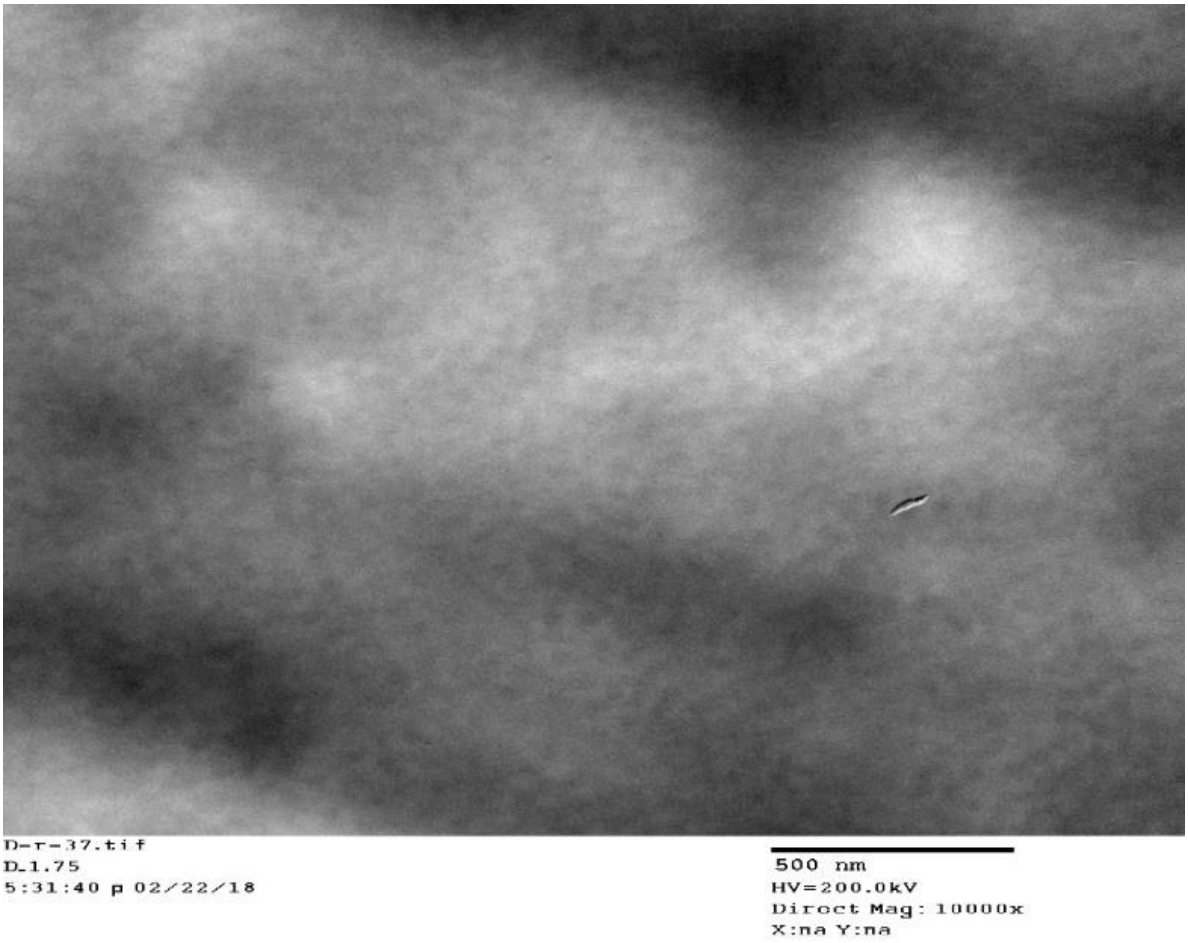

Figure 9.12. Transmission electron microscopy micrograph of PNPS5-*r*-PNMBzE_1.72(52:48).

The TEM image for PNPS5-*r*-PNMBzE_1.72(52:48), presented in Figure 9.12, shows larger aggregates of approximately 50 nm between aggregates-aggregate spacing. Domain spacing this large have also been reported for ionomers characterized by TEM. Interestingly though, both PNPS5 and PNMBzE form matrices and aggregates. However, in the X-ray scattering data, only backbone-backbone spacing was observed. Upon magnifying the TEM image for PNPS5-*r*-PNMBzE_1.72(52:48), it is evident that the interpenetration of PNMBZE matrix through PNPS5 matrix may have resulted from hierarchical structures. The PNMBzE (white) aggregates are comprised of a PNMBzE matrix (white background) with PNPS5 clusters (black dots) forming an

ionomer cluster morphology. The PNPS5 (black) aggregates are comprised of a PNPS5 matrix (black background) with PNMBzE cluster (white dots) forming an inverse ionomer cluster morphology. See Figure 9.13.

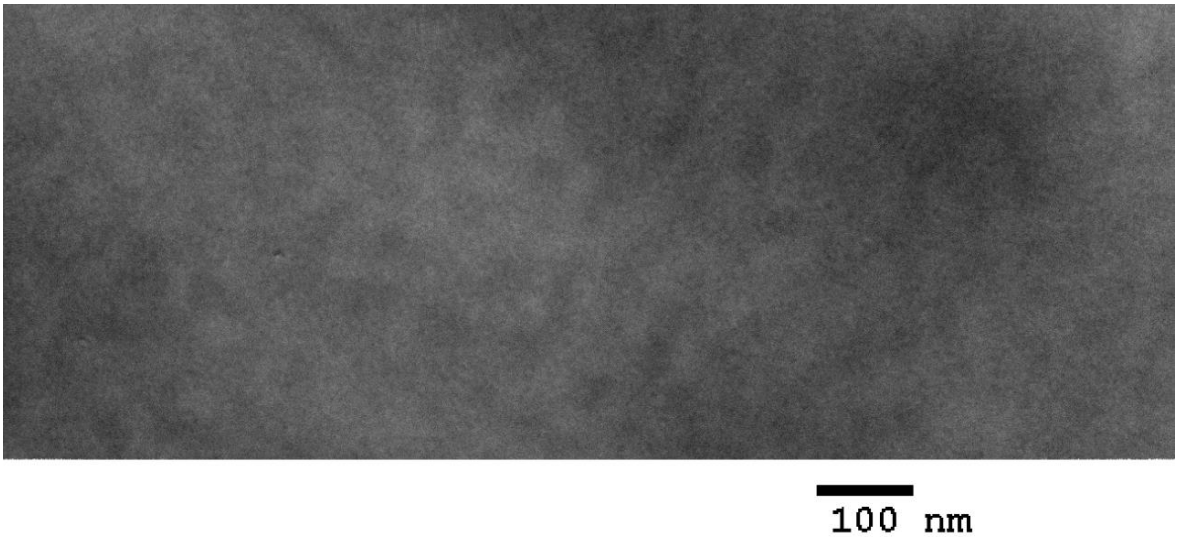

Figure 9.13. Magnified TEM micrograph of PNPS5-*r*-PNMBzE_1.72(52:48).

However, these structures within the aggregates may have also resulted from optical bias that may occur during magnification of the images. The average cluster-cluster spacing in both PNPS5 aggregates and PNMBzE aggregates, after magnifying the image, is approximately 3 nm.

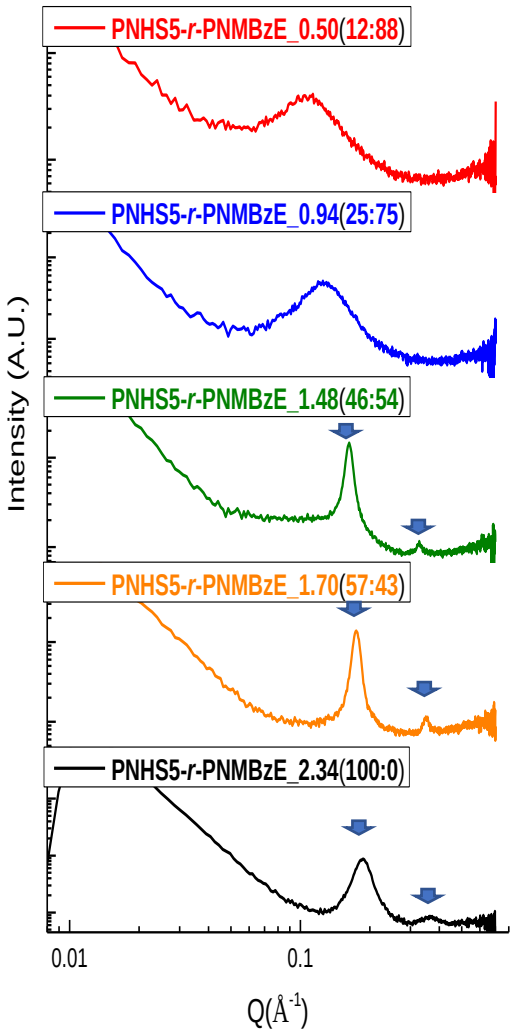

Figure 9.14. X-ray scattering data for the PNHS5-*r*-PNMBzE series.

The scattering results for the PNHS5-*r*-PNMBzE series presented in Figure 9.14 show similar trend to the results of the PNPS5-*r*-PNMBzE series. The scattering data for the PNHS5 homopolymer show a scattering peak at $Q = 0.1856\ Å^{-1}$ and a higher order peak at $Q = 0.3654\ Å^{-1}$. Arrows showing peak positions of the backbone-backbone spacing primary and secondary peaks. The primary peak correlates to the backbone-backbone spacing of polymer segments. The ratio of the primary peak to the second order peak is 1:2 and suggests that the backbones are arranged in a lamellar manner in the polymer. The presence of the second order peak in PNHS5

homopolymer, which is absent in the PNPS homopolymer, suggest that homopolymer has a large quantity of polymer backbones arranged in parallel bundles in comparison to the PNPS5 homopolymer. The backbone-backbone spacing for the PNHS5 homopolymer is 32 Å; while the backbone-backbone spacing for the PNPS5 homopolymer is 28 Å. This difference in backbone-backbone spacing results from the difference in the number of carbons on the pendant side-chains connecting the norbornene backbone to the azo-spirocyclic salt moiety. For NHS5, there are six carbons on the pendant side-chain, while for NPS5, there are three carbons on the pendant side-chain.

For PNHS5-*r*-PNMBzE_0.5(12:88), a scattering peak correlating to cluster-cluster spacing in ionomer cluster morphology can be observed at relatively higher *Q* in comparison to the PNHS5 homopolymer. By increasing the concentration of the NHS5 comonomer to 25 mol%, the scattering data for PNHS5-*r*-PNMBzE_0.94(25:75) show a decreased cluster-cluster spacing in comparison to PNHS5-*r*-PNMBzE_0.5(12:88). Increasing the concentration of the ionic component in random copolymers results in a decrease in the cluster-cluster spacing. The same trend was observed in PNPS5-*r*-PNMBzE series. However, for PNHS5-*r*-PNMBzE_1.48(46:54), the scattering data show two peaks similar to the peaks observed in the PNHS5 homopolymer. This suggest that at approximately 46 mol% of NHS5, the morphology of PNHS5-*r*-PNMBZE transitions from ionomer cluster morphology to backbone-backbone morphology (matrix of dipole morphology). For the PNPS5-*r*-PNMBZE series, X-ray scattering data show that the transition from ionomer cluster morphology to backbone-backbone morphology occurred at approximately 53 mol% NPS5. This suggest that the length of the pendant side-chain contributed to this transition as has been observed in P4VP-based copolymer series. For the samples, PNHS5-*r*-PNMBzE_1.48(46:54), PNHS5-*r*-PNMBzE_1.70(57:43), and the PNHS5 homopolymer, the

backbone-backbone spacing decreased with increasing mol% of NHS5 in the random copolymer. This is due to the increase in the dipole-dipole attraction between parallelly arranged dipoles on adjacent polymer backbones (see Figure 9.15).

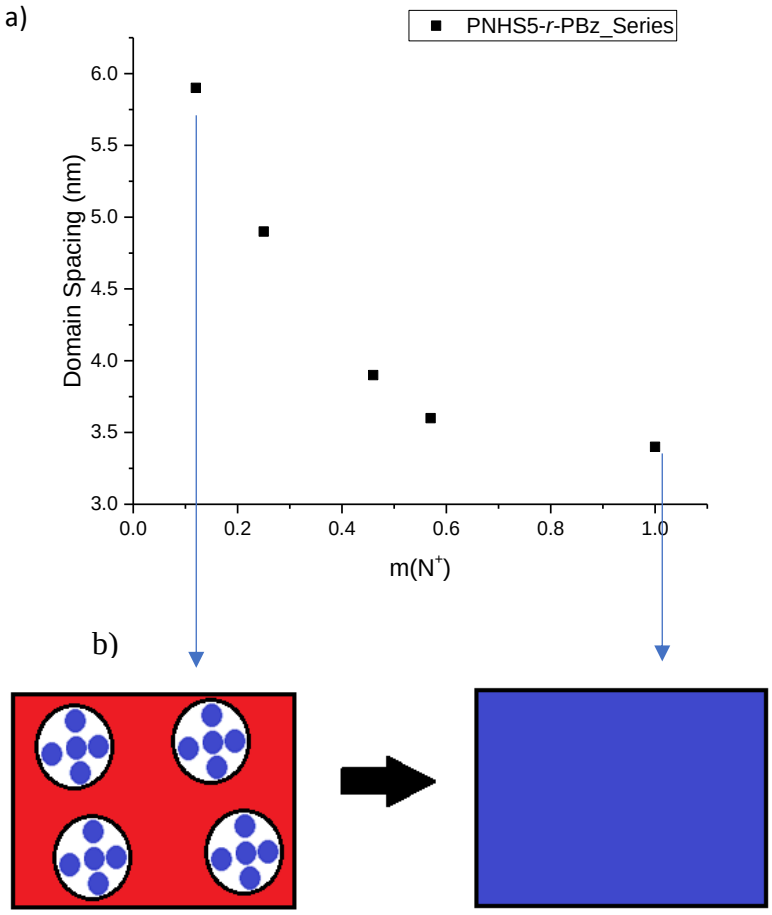

Figure 9.15. a) Variation of the characteristic spacing with mol% of NHS5, b) schematic representation of the transition from ionic cluster to ionic matrix/percolating structure.

The scattering spectra of PNHS5-*r*-PNMBzE_1.48(46:54) show a plateau (broad peak feature) to the left (lower *Q* values) of the backbone-backbone peak. This peak may have resulted from the presence of ionomer cluster morphology coexisting with the backbone-backbone morphologies.

X-ray scattering data for the PNPS5-*r*-PNMBzE samples suggest that coexistence of backbone-backbone and ionomer cluster morphologies occurs in PNPS5-*r*-PNMBzE_1.72(52:48). However, Figure 9.11 TEM micrograph show that a coexistence of both backbone-backbone and ionomer cluster morphology is present even in PNPS5-*r*-PNMBzE_1.07(28:72). Thus, the coexistence of both backbone-backbone and ionomer cluster morphologies in PNHS5-*r*-PNMBzE samples may have even been present in PNHS5-*r*-PNMBzE even at NHS5 concentrations < 46 mol%.

9.3.2 Conductivity of Random Copolymers of NPS5, NPMBzE and NHS5, NPMBzE

Conductivity measurements performed at 65% relative humidity (RH.) are presented in Figure 9.16. The conductivity results show that conductivity increased with increasing mol% of NPS5 (IEC.) for PNPS5-*r*-PNMBzE samples. The conductivity of PNHS5-*r*-PNMBzE also increased with increasing mol% of NHS5 and peak conductivities were observed at 80 ˚C for all samples followed by an unexpected decrease in the conductivity at 90 ˚C. This decrease may have arisen from the inelastic collision of bromide ions with each other at high temperature. At high temperature, counterions gain sufficient energy which increases their mobility. However, this also increases the probability of counterions colliding into one another. On collision, these counterions lose some of their kinetic energy, and thus, their mobility decreases. This conductivity behavior at elevated temperature has been observed in the conduction of electrons in metals. Thus, we can define two conducting regimes for these random copolymers. A first regime in which bromide counterions display ionic conducting behavior similar to the ionic conductivity of anion exchange membranes. A second regime at elevated temperature in which the conductivity of the bromide counterion is maximum so that any increase in temperature results in a drop in ionic conductivity similar to the electrical conductivity of electrons in metals.

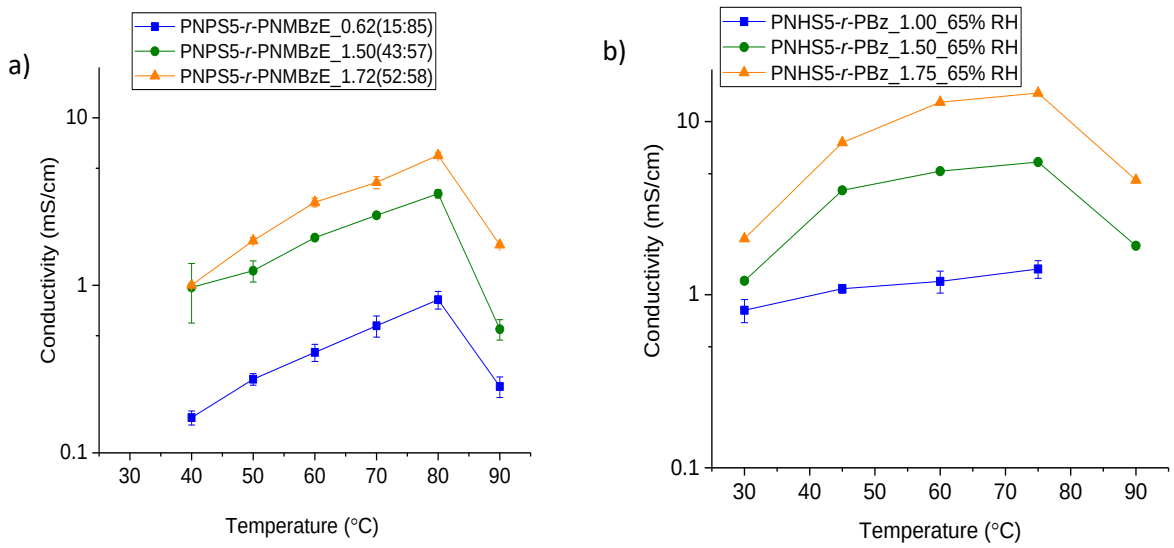

Figure 9.16. Conductivity of a) PNPS5-*r*-PNMBzE and b) PNHS5-*r*-PNMBzE samples. Conductivity measurements of both sample series were performed at 65% RH.

The conductivity values of PNHS5-*r*-PNMBzE samples outperformed PNPS5-*r*-PNMBzE samples. The conductivity values of PNHS5-*r*-PNMBzE was three times the conductivity of PNPS5-*r*-PNMBzE at similar IEC. values. This high ionic conductivity performance of PNHS5-*r*-PNMBzE may be due to their morphologies. The longer pendant side-chain of PNHS5 decreases the propensity for clustering in PNHS5-*r*-PNMBzE. Thus, the population of clusters in PNHS5-*r*-PNMBzE series will be less than that in PNPS5-*r*-PNMBzE series even at similar IEC. This decrease in the propensity to form ionomer cluster morphology is most visible in the scattering spectra of PNPS5-*r*-PNMBzE series and PNHS5-*r*-PNMBzE series. While backbone-backbone morphology was observed in 46 mol% of NHS5 in PNHS5-*r*-PNMBzE series, backbone-backbone morphology was observed in 52 mol% of NPS5 in the random copolymer. The tendency to disperse bromide counterions by forming a matrix of dipoles morphology/backbone-backbone morphology could explain the relatively high conductivity values measured for PNHS5-*r*-PNMBzE series at 65 % RH.

The conductivity data for PNPS5-*r*-PNMBzE_1.07(28:72) and PNHS5-*r*-PNMBzE_0.94(25:75) at 95% RH is shown in Figure 9.17. The data for PNHS5-*r*-PNMBzE_0.94(25:75) show an unexpected drop in conductivity at 90 °C, after a peak conductivity at 80 °C. The data for PNPS5-*r*-PNMBZE_1.07(28:72) show no such decrease but a steady increase in conductivity with increasing temperature.

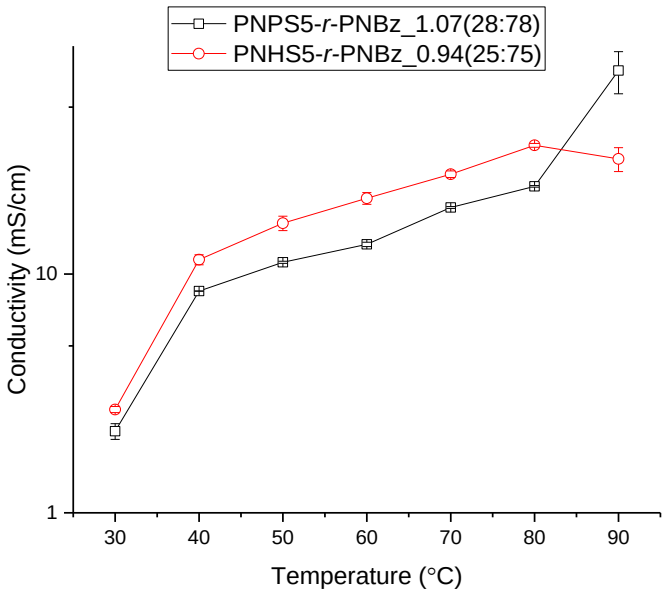

Figure 9.17. Conductivity of PNPS5-*r*-PNMBzE_1.07(28:72) and PNHS5-*r*-PNMBzE_0.94(25:75) at 95% RH.

At 95 % RH, the conductivity of the bromide counterion is facilitated by water molecules therefore the dependence on membrane morphology is decreased. Nevertheless, the conductivity values of PNHS5-*r*-PNMBzE_0.94(25:75) from 30 – 80 °C were higher than the conductivity values of PNPS5-*r*-PNMBzE_1.07(28:72) in the same temperature range. The same trend was observed in their conductivities at 65% RH. Conductivity values for PNPS5-*r*-PNMBzE_1.07(28:72) and PNHS5-*r*-PNMBzE_0.94(25:75) were exceptionally high given the low IEC. (approximately 1

mmol/g) of the samples. For both samples, three conductivity dependent temperature regimes can be defined. A first regime from 30 – 40 °C that show a steep rise in conductivity of both samples. A second regime from 40 – 80 °C that show a moderate increase in conductivity with increasing temperature for both samples. Finally, a third regime that show a steep increase in conductivity for PNPS5-*r*-PNMBzE_1.07(28:72) and a steep decrease in conductivity for PNHS5-*r*-PNMBzE_0.94(25:75). Peak bromide conductivities of 71 mS/cm at 90 °C and 36 mS/cm at 80 °C were recorded for PNPS5-*r*-PNMBzE_1.07(28:72) and PNHS5-*r*-PNMBzE_0.94(25:75) respectively. This may have resulted from the decreased dipole clustering in both samples due to the pendant side-chains that decreases tendency for dipole cluster formation. The higher conductivity of PNHS5-*r*-PNMBzE_0.94(25:75) in comparison to PNPS5-*r*-PNMBzE_1.07(28:72) may be due to the longer pendant-side chain in the PNHS5 copolymer.

9.4 Results and Discussion for PNPS5-*b*-PNMBzE and PNHS5-*b*-PNMBzE

Block copolymers of NPS5 and NMBzE were successfully synthesized. Four different samples of PNPS5-*b*-PNMBzE with varying concentrations of NPS5 ranging from 16 – 51 mol% and the PNPS5 homopolymer were prepared. The composition of the block copolymers was determined by ^{1}H NMR using the ratio of the combined vinyl protons of PNPS5 and PNMBzE, and the aromatic proton of PNMBzE. These protons have been used in the determination of the compositions of NPS5 and NPMBzE in the random copolymer (see Figure 9.5). The composition of NPS5 and NMBzE in PNPS5-*b*-PNMBzE determined by ^{1}H NMR are similar to their target compositions confirming the successful application of ring-opening metathesis polymerization chemistry in the synthesis of PNPS5-*b*-PNMBzE for anion exchange membranes.

A tabular summary of the feed composition, target IEC., sample composition determined by ^{1}H NMR, and sample IEC determined from ^{1}H NMR composition is presented in Table 9.3.

Table 9.3. Comparison of the feed composition and target IEC. and the ^{1}H NMR composition and ^{1}H NMR IEC. of the PNPS5-*b*-PNMBzE series.

Sample	**Feed comp%**	**Target IEC.**	**NMR comp%**	**NMR IEC**
PNPS5-*b*-PNMBzE_0.66	**12:88**	**0.50**	**16:84**	**0.66**
PNPS5-*b*-PNMBzE_1.10	**26:74**	**1.00**	**29:71**	**1.10**
PNPS5-*b*-PNMBzE_1.45	**43:57**	**1.50**	**41:59**	**1.45**
PNPS5-*b*-PNMBzE_1.70	**53:47**	**1.75**	**51:49**	**1.70**
PNPS5-*b*-PNMBzE_2.60	**100:0**	**2.60**	**100:0**	**2.60**

The density of the homopolymer, PNPS5, was determined experimentally to be 1.16 g/cm^{3}. The density was used to calculate the volume fractions of PNPS5 and PNMBzE in PNPS5-*b*-PNMBzE. To minimize confusion between volume fractions and mol% in PNPS5-*b*-PNMBzE and PNPS5-*r*-PNMBzE, the volume fractions are represented as bold fractions in the text while the mol% are expressed as plain percentages.

Block copolymers of NHS5 and NMBzE were successfully synthesized. Four different samples of PNHS5-*b*-PNMBzE with varying concentrations of NPS5 ranging from 13 – 47 mol% were prepared. The composition of the block copolymers was determined by ^{1}H NMR using the ratio of the combined vinyl protons of PNHS5 and PNMBzE, and the aromatic proton of PNMBzE. These protons have been used in the determination of the compositions of NPS5 and NPMBzE in

the random copolymer (see Figure 9.6). The composition of NHS5 and NMBzE in PNHS5-*b*-PNMBzE determined by ^{1}H NMR are similar to their target compositions confirming the successful application of ring-opening metathesis polymerization chemistry in the synthesis of PNPS5-*b*-PNMBzE for anion exchange membranes.

A tabular summary of the feed composition, target IEC., sample composition determined by ^{1}H NMR, and sample IEC determined from ^{1}H NMR composition is presented in Table 9.4.

Table 9.4. Comparison of the feed composition and target IEC. and the ^{1}H NMR composition and ^{1}H NMR IEC. of the PNHS5-*b*-PNMBzE series.

Sample	**Feed comp%**	**Target IEC**	**NMR comp%**	**NMR IEC**
PNHS5-*b*-PNMBzE_0.54	**12:88**	**0.50**	**13:87**	**0.54**
PNHS5-*b*-PNMBzE_1.02	**27:73**	**1.00**	**28:72**	**1.02**
PNHS5-*b*-PNMBzE_1.43	**47:53**	**1.50**	**44:56**	**1.43**
PNHS5-*b*-PNMBzE_1.50	**60:40**	**1.75**	**47:53**	**1.50**
PNHS5-*b*-PNMBzE_2.60	**100:0**	**2.35**	**100:0**	**2.35**

The density of the homopolymer, PNHS5, was determined experimentally to be 1.17 g/cm^{3}. The density was used to calculate the volume fractions of PNHS5 and PNMBzE in PNHS5-*b*-PNMBzE.

9.4.1 Morphology of Block Copolymers of NPS5, NPMBzE and NHS5, NPMBzE

Figure 9.18 show the X-ray scattering for PNPS5-*b*-PNMBzE block copolymers. All the samples show a hexagonal morphology with the domain spacing increasing with increasing volume fraction of the PNPS5 block. Arrows show the peak positions indicative of ordering resulting from the block copolymer microphase separation.

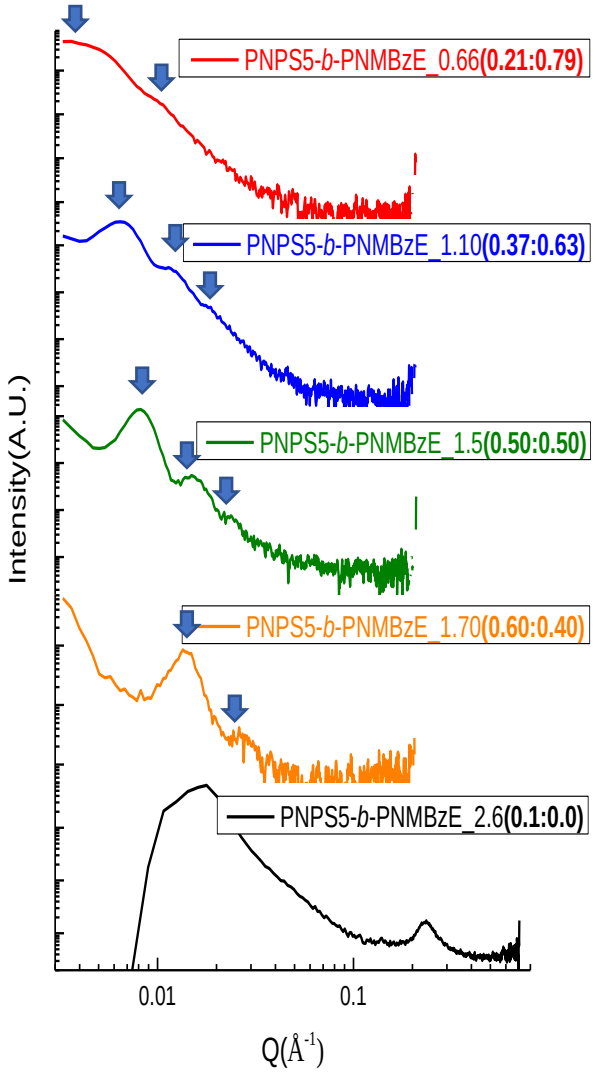

Figure 9.18. Extreme small-angle X-ray scattering data (ESAXS) for the PNPS5-*b*-PNMBzE series except PNPS5-*b*-PNMBzE_2.6(**0.1:0.0**) whose data was collected in the MAXS *Q* range.

Phase separation in block copolymers is governed by the product of Flory-Huggins interaction parameter,χ and the molecular weight of the block copolymers, N. In symmetric, non-charged, block copolymers, at a constant value of χN, the range of the volume fraction of PNPS5 (**0.21 – 0.60**) in PNPS5-*b*-PNMBzE should show a transition from hexagonal to lamellar to inverse hexagonal morphologies with a constant domain spacing. The block copolymers, PNPS5-*b*-PNMBzE_0.66(**0.21:0.79**), PNPS5-*b*-PNMBzE_1.10(**0.37:0.63**), PNPS5-*b*-PNMBzE_1.5(**0.5:0.5**), and PNPS5-*b*-PNMBzE_1.7(**0.60:0.40**) had similar values of N, and by extension similar values of χN. However, the morphologies observed in PNPS5-*b*-PNMBzE samples and the domain size variation across the series did not conform to the conventional morphologies and domain sizes of a symmetric, non-charged, block copolymer. The presence of charges on one of the blocks distorts the conventional block copolymer phase diagram. This distortion of the block copolymer phase diagram "traps" PNPS5-*b*-PNMBZE samples with varying volume fraction of PNPS5 in a hexagonal-type morphology. This phenomenon of block copolymers having an ionic block showing one morphology type across a range of volume fractions has been reported in by Yuan and Coughlin.[2] A decrease in the X-ray scattering domain spacing with increasing volume fraction of the non-ionic block has also been reported by the aforementioned researchers. A plot of the change in domain spacing with varying volume fraction is presented in Figure 9.19.

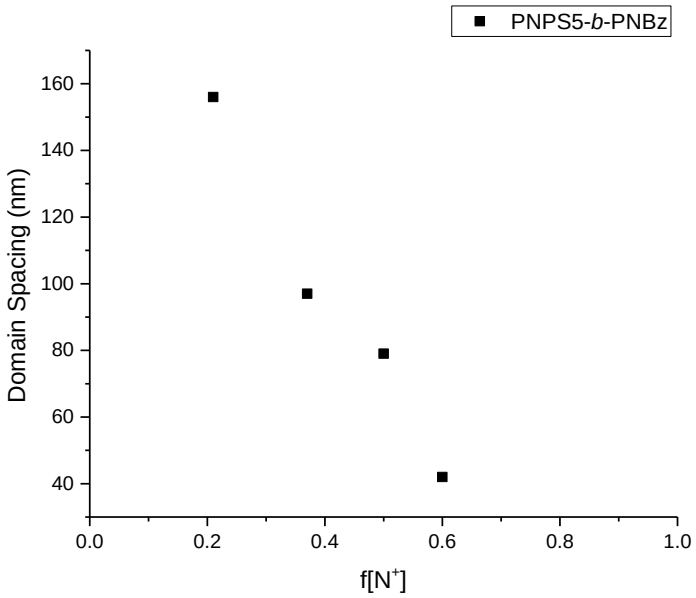

Figure 9.19. Variation of domain spacing with volume fraction in PNPS5-*b*-PNMBzE.

Medium-angle X-ray scattering (MAXS) for PNPS5-*b*-PNMBzE show a peak that corresponds to the backbone-backbone spacing between polymer chains of PNPS5. The same peak can be observed in PNPS5 homopolymer. See Figure 9.20.

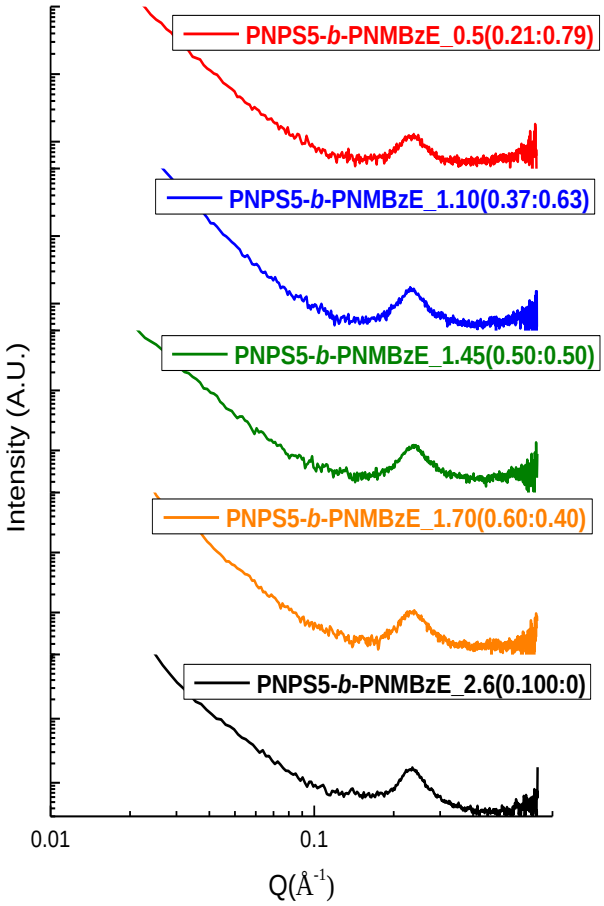

Figure 9.20. Medium-angle X-ray scattering, MAXS, for the PNPS5-*b*-PNMBzE series

This structure, due to backbone-backbone correlations in the ionic domain exists within the phase separated domains of PNPS5 and PNMBzE blocks (see Figure 9.21). The PNPS5 and PNMBzE blocks phase separates due to the differences in the Flory-Huggins interaction parameter,χ, however, within the PNPS5 block, there is short-range ordering arising from the correlation between polymer backbones. A structure-*within*-structure morphology.

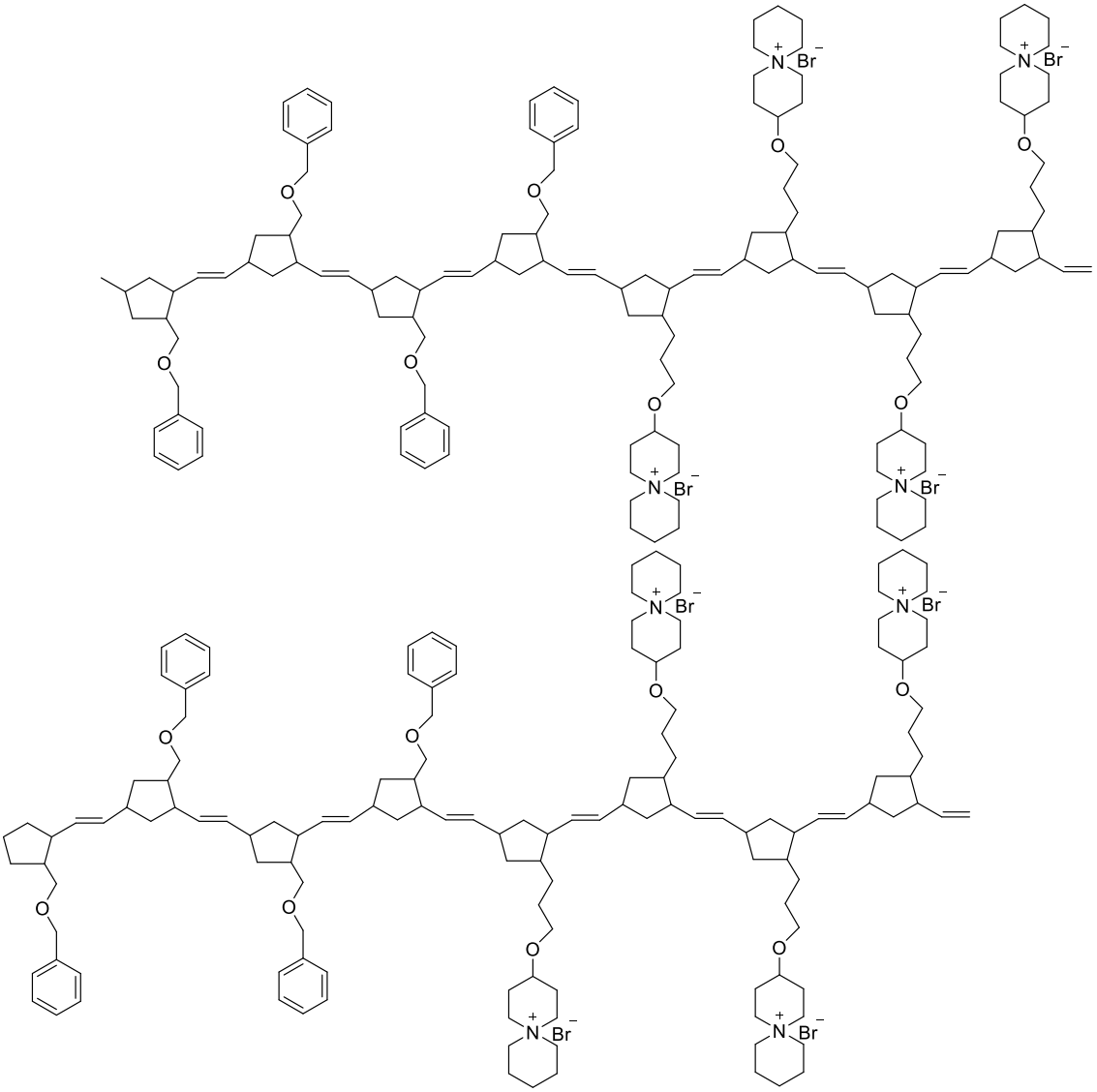

Figure 9.21. Depiction of polymer chain arrangement in PNPS5-*b*-PNMBzE.

Unlike in PNPS5-*r*-PNMBzE, in which the backbone-backbone spacing decreases with increasing mol% of NPS5, the backbone-backbone spacing was constant in the PNPS5-*b*-PNMBzE samples. This confirms that there was no variation in the concentration of NPS5 in the ionic block across the series. The parallel arrangement of counterions along the pendant side-chains of the parallelly arranged polymer backbones can facilitate the mobility of counterions through the percolating phase, thus, resulting in highly conducting membranes.

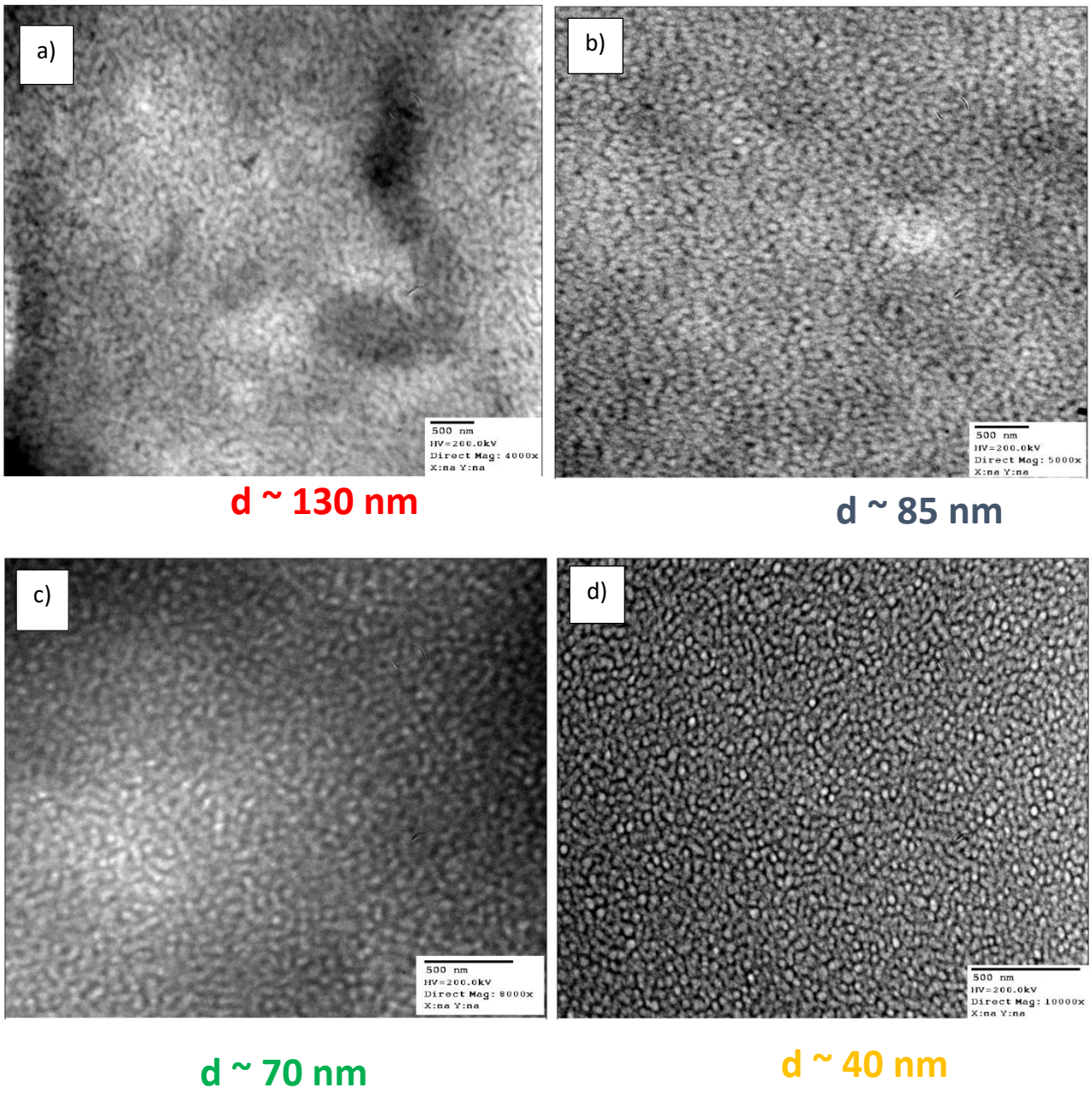

Figure 9.22. Transmission electron micrographs of micrographs of a) PNPS5-*b*-PNMBzE_0.66(**0.21:0.79**), b) PNPS5-*b*-PNMBzE_1.10(**0.37:0.63**), c)PNPS5-*b*-PNMBzE_1.5(**0.5:0.5**), and d)PNPS5-*b*-PNMBzE_1.7(**0.60:0.40**).

Characterization of PNPS5-*b*-PNMBzE samples by TEM (see Figure 9.22) confirm that all samples show a hexagonal type morphology, albeit, an inverse hexagonal morphology. The observed characteristic spacing arising from the primary peak of the X-ray scattering spectra correlates to the average diameter of the cylinder. The images collected in dark field mode show a dark matrix (PNPS5 block) with light hexagonally packed cylinders (PNMBzE block). The PNPS5 block forms the matrix even at low volume fraction, **0.21** for PNPS5-*b*-PNMBzE_0.66(**0.21:0.79**). This behavior is due to a combination of the strong electrostatic cohesion between charges and counterion entropy in the NPS5 block. Although electrostatic cohesion and counterion entropy appear to act counter to each other, however, a synergy of these thermodynamic parameters acts to distort the phase diagram and produce percolating/continuous phase from the ionic block with a lower volume fraction.[18] The electrostatic cohesion, defined as the degree to which Columbic interaction surpasses the thermal energy, K_BT, can skew the phase diagram. Increases in counterion entropy lowers the free energy of the system. For counterions to maximize their entropy, they must not be confined within a non-continuous phase, thus, ionic blocks usually endeavor to form a continuous domain. Consequently, ionic blocks with minority volume fraction forming a continuous phase is energetically favorable for the ionic block copolymer. On forming a percolating/continuous phase even at low volume fraction, the hydrophobic phase forms hexagonally packed cylinders. These cylinders formed from the high-volume fraction hydrophobic block will have large diameters. The diameter of this hydrophobic cylinder will decrease with decreasing volume fraction of the non-ionic block. The diameter of the hydrophobic cylinders obtained from TEM was similar to the domain spacing obtained from the scattering data for PNPS5-*b*-PNMBzE samples.

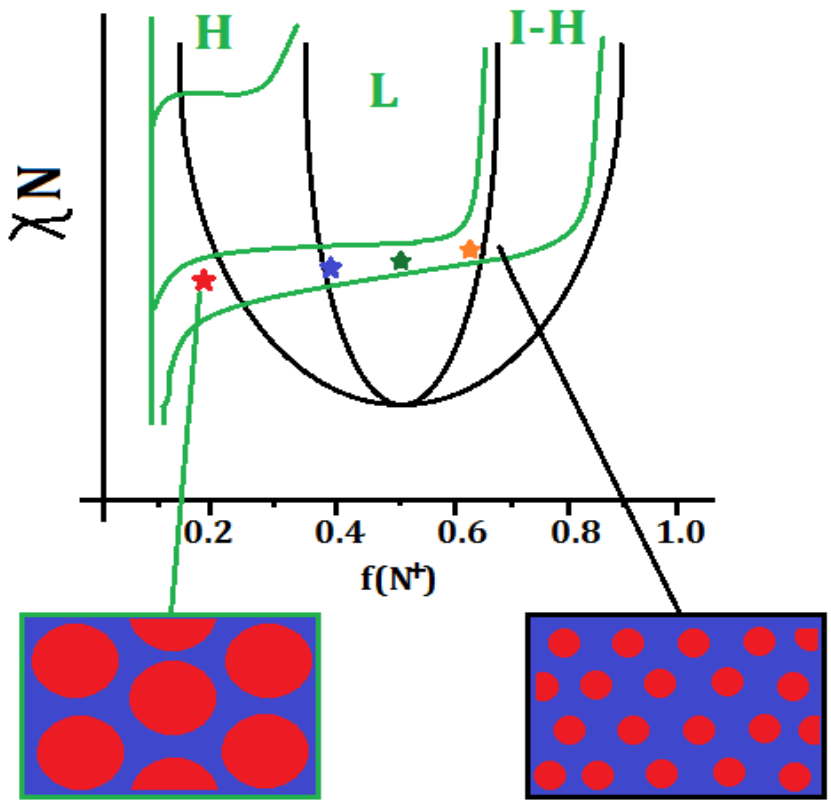

Figure 9.23. Depiction of the modified phase diagram for the PNPS5-*b*-PNMBzE series superimposed upon the phase diagram of a conventional, symmetric, non-charged block copolymer.

We can modify the block copolymer phase diagram to reflect the experimental findings from the characterization of PNPS5-*b*-PNMBzE. This modified phase diagram is presented in Figure 9.23. The strong electrostatic cohesion parameter, Γ, skews the phase diagram to favor the formation of a continuous phase at low volume fraction of the ionic component. In the modified phase diagram, PNPS5-*b*-PNMBzE with volume fraction of NPS5 ranging from **0.21** to **0.60** form inverse hexagonal morphologies at a constant χN. The χN value for PNPS5-*b*-PNMBzE_0.66(**0.21:0.79**), PNPS5-*b*-PNMBzE_1.10(**0.37:0.63**), PNPS5-*b*-PNMBzE_1.5(**0.5:0.5**), and PNPS5-*b*-

PNMBzE_1.7(**0.60:0.40**) is approximately constant. On the schematic representation of the modified phase diagram, the hexagonal, the lamellar, and the inverse hexagonal morphologies are represented by H, L, and I-H respectively. The "chimney" shape of the modified diagram has been predicted by Olivera de la Cruz in block copolyelectrolytes.[18]

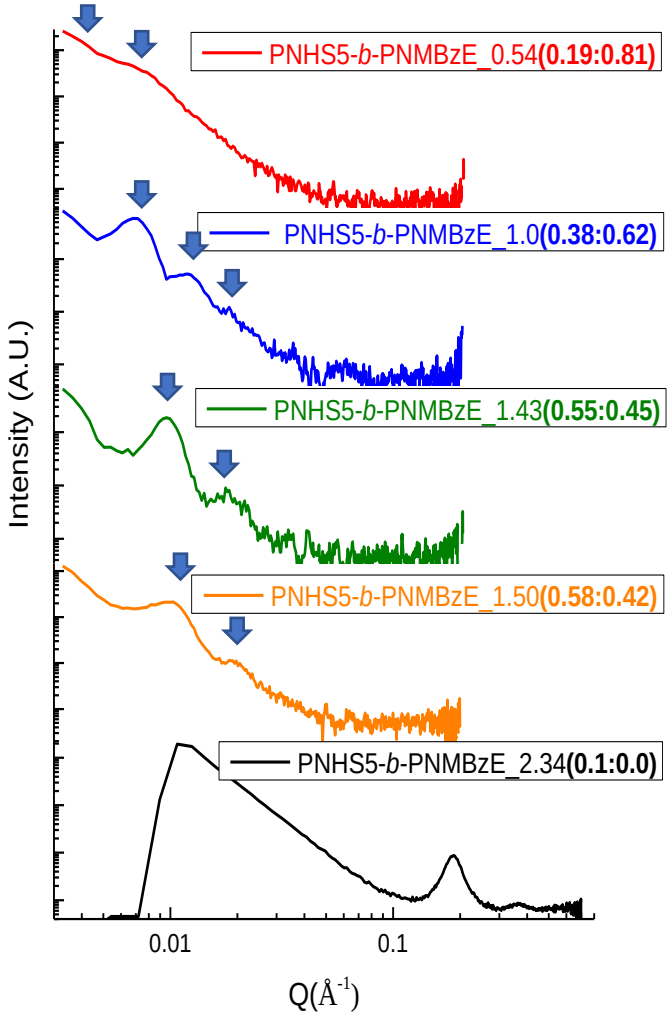

Figure 9.24. Extreme small-angle X-ray scattering data (ESAXS) for the PNHS5-*b*-PNMBzE series except PNHS5-*b*-PNMBzE_2.34(**0.1:0.0**) whose data was collected in the MAXS *Q* range

X-ray scattering data for the PNHS5-*b*-PNMBzE samples is shown in Figure 9.24. The scattering spectra for the PNHS5-*b*-PNMBzE samples with volume fraction of PNHS5 ranging from **0.19 – 0.58** also show hexagonal-type morphologies similar to those that have been observed in the PNPS5-*b*-PNMBzE samples. Like in the case of the PNPS5-*b*-PNMBzE samples, the domain spacing of the PNHS5-*b*-PNMBzE samples, obtained from the scattering data, also decreased with increasing volume fraction of the ionic block. This suggests that the PNHS5-*b*-PNMBzE samples, like the PNPS5-*b*-PNMBzE samples, form an inverse hexagonal morphology. This also suggests that the PNHS5 block forms the continuous phase even at low volume fraction while the PNMBzE block forms the cylinders which are packed in a hexagonal pattern. Upon decreasing volume fraction of the PNMBzE block, the domain spacing (which is equivalent to the diameter of the cylinders formed by the PNMBzE block) also decreases. This behavior is typical of inverse hexagonal morphologies of block polyelectrolytes like the PNPS5-*b*-PNMBzE samples. The dimensions of the domain spacing (the diameter of the hexagonally packed cylinders) obtained for the PNHS5-*b*-PNMBzE samples were equivalent to those measured for PNPS5-*b*-PNMBzE at approximately similar volume fractions (see Figure 9.25).

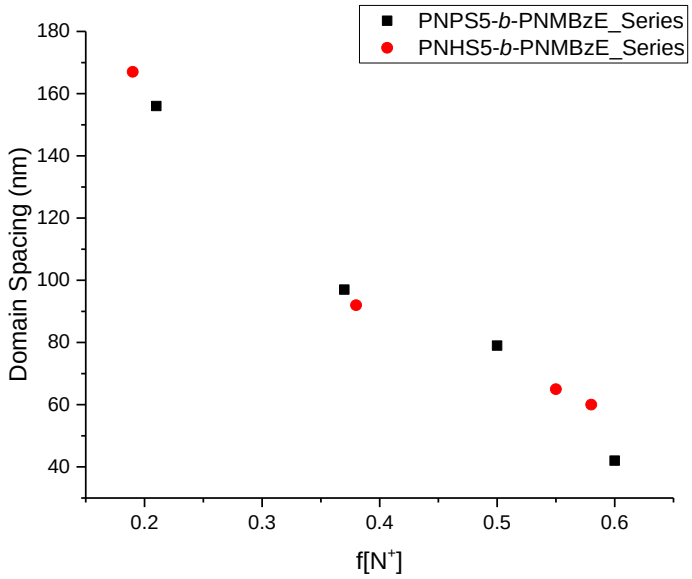

Figure 9.25. Variation of domain spacing with volume fraction in the PNPS5-*b*-PNMBzE and the PNHS5-*b*-PNMBzE series.

Furthermore, probing the PNHS5-*b*-PNMBzE samples by MAXS reveal similar structure-*within*-structure observed in PNHS5-*b*-PNMBzE. This further confirms the block character of the samples. This parallel arrangement of counterions could have beneficial consequence for ionic conductivity of these membranes.

9.4.2 Conductivity of Block Copolymers of NPS5, NPMBzE and NHS5, NPMBzE

The conductivity of PNPS5-*b*-PNMBzE_0.66(**0.21:0.79**) and PNPS5-*b*-PNMBzE_1.10(**0.37:0.63**) at 95 %RH are presented in Figure 9.26. The conductivities increased with increasing temperature. The conductivity of PNPS5-*b*-PNMBzE_1.10(**0.37:0.63**) was exceptionally high. In the morphology of PNPS5-*b*-PNMBzE_1.10(**0.37:0.63**), as seen from TEM micrographs, the ionic block forms a continuous phase with the non-ionic component forming the cylinders. This continuous phase facilitates the untrammeled mobility of bromide counterions

through the membrane. A comparison of the conductivity of PNPS5-*b*-PNMBzE_1.10(**0.37:0.63**) and PNPS5-*b*-PNMBzE_0.66(**0.21:0.79**), show that the sample with higher IEC. had higher conductivity. The high conductivity of PNPS5-*b*-PNMBzE_1.10(**0.37:0.63**) in comparison to PNPS5-*b*-PNMBzE_0.66(**0.21:0.79**) may have been further fostered by subtle differences in the morphologies of the membranes. The TEM micrographs of PNPS5-*b*-PNMBzE_0.66(**0.21:0.79**) and PNPS5-*b*-PNMBzE_1.10(**0.37:0.63**) show that the ionic phase is the continuous phase in both samples. However, the hydrophobic cylinders in PNPS5-*b*-PNMBzE_0.66(**0.21:0.79**) are larger compared to those in PNPS5-*b*-PNMBzE_1.10(**0.37:0.63**) and in some cases impinge on one another. This can result in blockades by the non-ionic block in the continuous ionic phase. Consequently, this could decrease the mobility of the counterion, and thus, the membrane conductivity. Higher conductivity can therefore be expected in PNPS5-*b*-PNMBzE_1.5(**0.5:0.5**), and PNPS5-*b*-PNMBzE_1.7(**0.60:0.40**) due to the small diameter of their hydrophobic cylinders; however, the formation of an ionic (hydrophilic) continuous phase which can excessively swell on humidification results in poor mechanical fidelity of the membranes. Consequently, we were unable to perform conductivity tests for PNPS5-*b*-PNMBzE_1.5(**0.5:0.5**), and PNPS5-*b*-PNMBzE_1.7(**0.60:0.40**) at 95% RH.

Comparing the conductivity of both the block and random copolymers of NPS5 and NMBzE show that the block copolymer had higher conductivity across the measured temperature range (30 – 80 °C). The higher conductivity of PNPS5-*b*-PNMBzE_1.10(**0.37:0.63**) may have resulted from the continuous phase of its ionic domain, whereas, PNPS5-*r*-PNMBzE_1.07(28:72) had a coexistence of continuous and clustered ionic phases.

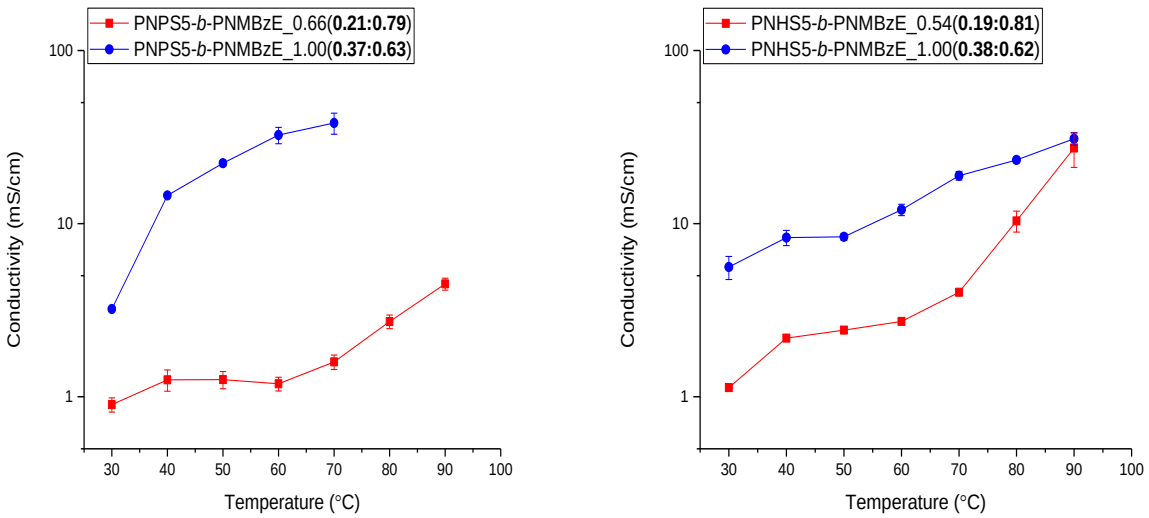

Figure 9.26. Conductivity at 95% RH of a) PNPS5-*b*-PNMBzE and b) PNHS5-*b*-PNMBzE series.

For NHS5 block copolymers, the conductivity of PNHS5-*b*-PNMBzE_0.54(**0.19:0.81**) and PNHS5-*b*-PNMBzE_1.0(**0.38:0.62**), increased with increasing temperature. The conductivity of PNHS5-*b*-PNMBzE_0.54(**0.19:0.81**) was exceptionally high, given its low IEC. The sample, PNHS5-*b*-PNMBzE_1.0(**0.38:0.62**), also showed high conductivity at lower temperatures and average conductivity values at high temperature. The effect of side-chain on the conductivity of block copolymers can be observed when PNHS5-*b*-PNMBzE_0.54(**0.19:0.81**) is compared to PNPS5-*b*-PNMBzE_0.66(**0.21:0.79**). The former had a higher conductivity. The longer the side-chain, the more the effect of sterics in facilitating backbones of polymer chains to arrange in parallel bundles. Thus, due to the longer length of the pendant side-chains of PNHS5-*b*-PNMBzE_0.54(**0.19:0.81**), in comparison to PNPS5-*b*-PNMBzE_0.66(**0.21:0.79**), the former will have a larger quantity of backbones arranged parallelly to one another. Parallel arrangement of ions can readily facilitate the transport of bromide counterions along the polymer chain of the ionic domain in PNHS5-*b*-PNMBzE_0.54(**0.19:0.81**). Resulting in increased ionic conductivity of PNHS5-*b*-PNMBzE_0.54(**0.19:0.81**) in comparison to PNPS5-*b*-PNMBzE_0.66(**0.21:0.79**).

However, in comparison to PNPS5-*b*-PNMBzE_1.10(**0.37:0.63**), PNHS5-*b*-PNMBzE_1.0(**0.38:0.62**) had low conductivity. This result, although unexpected may be due to the relatively low activation energy of PNHS5-*b*-PNMBzE_1.0(**0.38:0.62**) (26.5± 1.5 KJ/mol) in comparison to PNPS5-*b*-PNMBzE_1.10(**0.37:0.63**) (49.7± 4.3 KJ/mol). Lower activation energy suggests that the barrier to counterion mobility is too high that counterions cannot move or very low that there is no barrier to counterion mobility. In the case of the later, the mobility of counterions are maximum that little to no improvement in conductivity can be achieved in increasing the temperature of the system. However, in systems with higher activation energy, there will be a substantial increase in conductivity with temperature, which we see in PNPS5-*b*-PNMBzE_1.10(**0.37:0.63**). At 30 °C, PNHS5-*b*-PNMBzE_1.0(**0.38:0.62**) had a conductivity of 5.5±0.5 mS/cm which is about twice the conductivity of PNPS5-*b*-PNMBzE_1.10(**0.37:0.63**), 3.25±0.05 mS/cm. This is a very high bromide conductivity at that temperature for a sample with an IEC of about 1 g/mmol. No other studied sample had conductivity that high at that temperature (30 °C) at 95% RH. While PNHS5-*b*-PNMBzE_1.0(**0.38:0.62**) had little increase in conductivity from 30 – 40 °C, PNPS5-*b*-PNMBzE_1.10(**0.37:0.63**) showed a very steep rise in conductivity.

9.5 Conclusion

Flexible random copolymers of PNPS5-*r*-PNMBzE and PNHS5-*r*-PNMBzE were successfully synthesized by ring-opening metathesis polymerization. X-ray scattering performed on these samples show ionomer morphology at low concentration of the ionic component. However, at higher concentration of PNPS5 in the PNPS5-*r*-PNMBzE random copolymers, the morphology transitions from a random distribution of ionic clusters to a backbone-backbone morphology. Transmission electron microscopy micrographs of seem to corroborate the scattering data. Characterization of structure-property correlations in these polymers show that the structure of the

random copolymer significantly influences the conductivity of the random copolymer. Exceptionally high conductivity was obtained for both PNPS5-*r*-PNMBzE and PNHS5-*r*-PNMBzE at 65% relative humidity. The conductivity properties of PNHS5-*r*-PNMBzE was significantly higher than the conductivity of PNPS5-*r*-PNMBzE. This is may have resulted from the degree of ionomer clustering in both series. In PNHS5-*r*-PNMBzE, due to the longer pendant side-chain connecting the polymer backbone to the spirocyclic salt, the concentration of ionomer clusters in the polymer will be considerably less in comparison to the concentration of ionomer clusters PNPS5-*r*-PNMBzE samples. This morphology-conductivity relationship is also evident when comparing conductivity between PNPS5-*r*-PNMBzE and PNHS5-*r*-PNMBzE at 95% relative humidity.

Flexible block copolymers of PNPS5-*b*-PNMBzE and PNHS5-*b*-PNMBzE were also successfully synthesized by ring-opening metathesis polymerization. Characterization of the samples in both series by X-ray scattering show evidence of microphase separation in the block copolymers. The block copolymers show cylindrical morphology with large domain sizes. The domain sizes decrease with decreasing concentration of the hydrophobic block, PNMBzE. For both series, PNPS5-*b*-PNMBzE and PNHS5-*b*-PNMBzE, scattering data show a substructure of backbone-backbone spacing within a superstructure of phase-separated ionic and non-ionic block. Transmission electron microscopy micrograph confirm the cylindrical morphology, showing the ionic block forming the continuous phase at all volume fractions ranging from **0.2 – 0.6**. The block copolymers show excellent conductivity at relatively low IEC.

9.6 References

(1) Couture, G.; Alaaeddine, A.; Boschet, F.; Ameduri, B. Polymeric Materials as Anion-

Exchange Membranes for Alkaline Fuel Cells. *Prog. Polym. Sci.* **2011**, *36* (11), 1521–1557.

(2) Yuan, H. Synthesis and Structure-Property Relationships of Polymeric Membranes for Small Molecule Transport, University of Massachusetts, Amherst, 2017.

(3) Zhang, W.; Liu, Y.; Jackson, A. C.; Savage, A. M.; Ertem, S. P.; Tsai, T. H.; Seifert, S.; Beyer, F. L.; Liberatore, M. W.; Herring, A. M.; et al. Achieving Continuous Anion Transport Domains Using Block Copolymers Containing Phosphonium Cations. *Macromolecules* **2016**, *49* (13), 4714–4722.

(4) Tsai, T. H.; Ertem, S. P.; Maes, A. M.; Seifert, S.; Herring, A. M.; Coughlin, E. B. Thermally Cross-Linked Anion Exchange Membranes from Solvent Processable Isoprene Containing Ionomers. *Macromolecules* **2015**, *48* (3), 655–662.

(5) Kusoglu, A.; Weber, A. Z. New Insights into Per Fluorinated Sulfonic-Acid Ionomers. *Chem. Rev.* **2017**, *117*, 987–1104.

(6) Zhang, Z.; Liu, C.; Cao, X.; Wang, J.-H. H.; Chen, Q.; Colby, R. H. Morphological Evolution of Ionomer/Plasticizer Mixtures during a Transition from Ionomer to Polyelectrolyte. *Macromolecules* **2017**, *50* (3), 963–971.

(7) Chen, Q.; Bao, N.; Wang, J. H.; Tunic, T.; Liang, S.; Colby, R. H. Linear Viscoelasticity and Dielectric Spectroscopy of Ionomer / Plasticizer Mixtures : A Transition from Ionomer to Polyelectrolyte. *Macromolecules* **2015**, *48*, 8240–8252.

(8) Marino, M. G.; Melchior, J. P.; Wohlfarth, A.; Kreuer, K. D. Hydroxide, Halide and Water Transport in a Model Anion Exchange Membrane. *J. Memb. Sci.* **2014**, *464*, 61–71.

(9) Wohlfarth, A.; Smiatek, J.; Kreuer, K.; Takamuku, S.; Jannasch, P.; Maier, J. Proton Dissociation of Sulfonated Polysulfones: In Fl Uence of Molecular Structure and Conformation. *Macromolecules* **2015**, *48*, 1134–1143.

(10) Chen, D.; Hickner, M. A. Ion Clustering in Quaternary Ammonium Functionalized Benzylmethyl Containing Poly(arylene Ether Ketone)s. *Macromolecules* **2013**.

(11) Hsu, W. Y.; Gierke, T. D. Elastic Theory for Ionic Clustering in Perfluorinated Ionomers. *Macromolecules* **1982**, *15*, 101–105.

(12) Eisenberg, A. Clustering of Ions in Organic Polymers. A Theoretical Approach. *Macromolecules* **1970**, *3* (2), 147–154.

(13) Miller, R. L.; Boyer, R. F.; Heijboer, J. X-Ray Scattering from Amorphous Acrylate and Methacrylate Polymers: Evidence of Local Order. *J. Polym. Sci. Polym. Phys. Ed.* **1984**, *22* (12), 2021–2041.

(14) Platé, N. A.; Shibaev, V. P. Comb-like Polymers. Structure and Properties. *J. Polym. Sci. Macromol. Rev.* **1974**, *8* (1), 117–253.

(15) Salas-De La Cruz, D.; Green, M. D.; Ye, Y.; Elabd, Y. A.; Long, T. E.; Winey, K. I. Correlating Backbone-to-Backbone Distance to Ionic Conductivity in Amorphous Polymerized Ionic Liquids. *J. Polym. Sci. Part B Polym. Phys.* **2012**, *50* (5), 338–346.

(16) Beers, K. M.; Balsara, N. P. Design of Cluster-Free Polymer Electrolyte Membranes and Implications on Proton Conductivity. *ACS Macro Lett.* **2012**, *1* (10), 1155–1160.

(17) Kim, S. Y.; Park, M. J.; Jackson, A. Confinement Effects on Watery Domains in Hydrated Block Copolymer Electrolyte Membranes. *Macromolecules* **2010**, 8128–8135.

(18) Sing, C.; Zwanikken, J.; Cruz, M. D. La. Electrostatic Control of Block Copolymer Morphology. *Nat. Mater.* **2014**, *13* (7), 694–698.

CHAPTER 10

SUMMARY AND OUTLOOK

With the increasing global demand for energy, there are justifiable reasons for alternative energy to be pursued. Fuel cell technology, and more importantly, anion exchange membranes give reasons to be optimistic about finding solutions to the global energy challenge. Two major disadvantages hinder the commercialization of anion exchange membrane fuel cells (AEMFCs), one is the lack of membrane stability in alkaline environments, and the other is a poor understanding of structure-property relationships for the optimization of both mechanical properties and ion conductivity. Throughout this dissertation, we have made considerable progress in answering some of the basic questions on the morphology of alkaline exchange membrane (AEMs), and in synthesizing alkaline stable membranes.

It is a misconception that all small-angle scattering peaks present in randomly charged polycations corresponds to the presence of an ionomer cluster morphology. Caution must be taken when interpreting scattering data. X-ray scattering features arising from backbone-backbone morphology and ionomer cluster morphology can both be observed in a randomly charged, comb-shaped polycation, and possibly, in other random polyelectrolyte systems. In these random, charged, comb-shaped polycations, backbone-backbone morphology may exist, and even compete with, or, in some instances, exclude the formation of ionomer cluster morphology. The steric exclusion that leads to the backbone-backbone spacing feature in X-ray scattering is posited to arise from the exclusion of a pendant side-chain by another pendant side-chain on an adjacent polymer backbone from occupying the same space. Thus, with increasing number of carbons on the pendant side-chains, the backbone-backbone spacing will increase. This is due to the sterics of

the pendant side-chains on adjacent backbones excluding each other from occupying the same space. With increasing concentration of the pendant side-chain, there are more pendant side-chains between adjacent polymer backbones excluded by each other. Consequently, increasing the backbone-backbone spacing. Experimental evidence has been presented in this dissertation to suggest that there is a linear relationship between the backbone spacing of the polymer and the concentration of the pendant side-chains on the polymer backbone. The origin of this ordering is different from that of the ionomer cluster morphology that depends on the attraction between adjacent polymer dipoles. The In-Line Dipole Model was developed to relate the dipole-dipole interactions and pendant side-chain sterics at K_BT. By equating the dipole-dipole interaction that results in the lowest energy state of the dipoles to K_BT a limiting length, d_L, that defines the limit of the dipole-dipole interaction can be obtained.

To study the interplay between this exclusion of pendant side-chains that leads to backbone-backbone morphology and dipole-dipole attraction that facilitates the clustering of dipoles thereby resulting in an ionomer cluster morphology, a randomly charged comb-shaped model polymer was studied. The random copolymer, P4VP-*r*-PI, whose synthesis, to the best of our knowledge, has not been reported in the literature, was synthesized for this purpose. Characterization of the 1-alkylhalide quaternized P4VP-*r*-PI by X-ray scattering showed that samples with longer pendant side-chains, with their corresponding backbone-backbone spacing larger than d_L, were less likely to form ionomer cluster morphology. However, samples with shorter pendant side-chains, in which corresponding backbone-backbone spacing would be less than d_L were more likely to form the ionomer cluster morphology. The same trend was observed in the X-ray scattering characterization of P4VP-*r*-PS and P4VP-*r*-PI-*r*-PS after quaternization by various 1-alkylhalides. The iodide quaternized samples had smaller backbone-backbone spacing in comparison to the bromide

quaternized samples at the same number of carbons on the pendant side-chains. This may have resulted from the large dipole moment of the iodide quaternized samples since the iodide counterion is larger than the bromide.

Since longer pendant side-chains decrease the likelihood for ionomer cluster morphology and given that ionomer cluster morphology negatively affects counterion conductivity, we were able to optimize the conductivity of the quaternized and crosslinked P4VP-*r*-PI polymers. A peak bromide conductivity of 110 mS/cm at 95 % RH at 90 °C was measured for XP4VP-*r*-PI_C3Br. This is the highest bromide conductivity recorded for any anion exchange membrane, to the best of our knowledge. This finding has broader ramifications in the design of anion exchange membranes for fuel cell applications, and by extension, polyelectrolytes for battery applications.

The effect of the competition between electrostatics and sterics extends beyond short-range ordering in amorphous structures. Upon quaternization of P4VP by 1-alkylhalide with 1 or 2 carbons on the alkyl group, the resulting polymers, P4VP_C1I, P4VP_C2I, and P4VP_C2Br, showed evidence of semi-crystallinity when characterized by wide-angle X-ray scattering. Analysis of these polymers by DSC show reproducible melting endotherms and recrystallization exotherms which further confirms their semi-crystallinity. Further characterization of P4VP_C1I, P4VP_C2I, and P4VP_C2Br by OPM confirm the semi-crystalline structure of these samples. Characterization of P4VP_C2I, and P4VP_C2Br on cooling from the melt by POM show nucleation and then growth into a spherulite microstructure, while characterization of P4VP_C1I on cooling from the melt by POM show the so-called shish-kebab structure on nucleation and growth. The semi-crystallinity of P4VP_C1I, P4VP_C2I, and P4VP_C2Br is an exciting finding given that these quaternized P4VP homopolymers are atactic. Evidences of semi-crystallinity in quaternized P4VP samples disappear when the number of carbons on the pendant side chains, *n*,

is greater than 2. This semi-crystallinity of ethylbromide quaternized P4VP can also be found in a block copolymer of PS and P4VP_C2Br. These results present interesting future areas of research on the balance between electrostatically driven semi-crystallinity in quaternized P4VP and the opposing effects of sterics as the side-chains get longer. Characterization of the ionic conductivity of these membranes, especially at temperatures just below, and above, their melting points, will provide an avenue to compare the conductivity of these polymers in the solid and molten states. Large differences in conductivity before, and after, melting could be used to design materials for temperature sensing applications.

Synthesizing membranes that could be robust in alkaline environments is of keen interest to scientists and engineers developing anion exchange membranes. In this dissertation, we have designed, and synthesized stable monomers based on the ASU-type cations: Norbrononepropoxy-6-azonia-spiro(5,5)undecane (NPS5) and norbronenehexoxy-6-azonia-spiro(5,5)undecane (NHS5). Degradation studies conducted on these monomers as analyzed by ^{1}H NMR spectroscopy show that both NPS5 and NHS5 are very stable in alkaline medium. These monomers were readily polymerized by ring-opening metathesis polymerization into anion exchange membranes. Random copolymerization of the monomers, NPS5 and NHS5, with norbornene show that the formation of ionomer cluster morphology or backbone-backbone morphology depends on the concentration of the ionic component. Random copolymers of NHS5 and NPS5 with norbornenemethylbenzylether, NMBzE, also show concentration dependence on the transition from ionomer cluster morphology to backbone-backbone morphology. However, since PNHS5 has longer pendant side-chains in comparison to PNPS5, the transition from ionomer morphology to backbone-backbone morphology occurred at a relatively lower concentration of PNHS5 in PNHS5-*r*-PNMBzE in comparison to PNPS5 in PNPS5-*r*-PNMBzE. Thus, a combination of pendant side-chain (steric

effect) and concentration (matrix effect) facilitates this transition of between the two morphologies. Electrochemical Impedance Spectroscopy (EIS) measurements show high bromide conductivity in these samples at relatively low IEC. However, because of sterics effects on the formation of ionomer cluster morphology, the PNHS5-*r*-PNMBzE series had higher bromide conductivity in comparison to PNPS5-*r*-PNMBzE. The monomers, NPS5 and NHS5, were sequentially polymerized with NMBzE to synthesize block copolymers that were fabricated into robust anion exchange membranes. X-ray characterization of the block copolymer series of PNPS5-*b*-PNMBzE and PHPS5-*b*-PNMBzE show two morphology length scales. A larger length scale ordering corresponding to the microphase separation of the ionic and non-ionic blocks. At this length scale, all the characterized polymers showed a cylindrical morphology. A smaller length scale ordering corresponding to the backbone-backbone spacing within the ionic domain. The scattering spectra of PNPS5-*b*-PNMBzE and PNHS5-*b*-PNMBzE show that ionic and non-ionic blocks are phase separated into a cylindrical morphology. Transmission electron microscopy confirms the cylindrical morphology of the PNPS and PNMBZE block copolymers with the ionic block forming the continuous phase even at low volume fractions. Conductivity measurements show very high conductivity of both PNPS5-*b*-PNMBzE and PHPS5-*b*-PNMBzE series. The morphology-mechanical properties relationships of these membranes are important aspects of the PNPS5-*r*-PNMBzE series and the PHPS5-*r*-PNMBzE series that must be explored further. Morphology-mechanical properties relationships must also be explored for the PNPS5-*b*-PNMBzE series and the PHPS5-*b*-PNMBzE series.

Synthesis of stable anion exchange membranes is a great step forward in the search for alkaline exchange membranes with relative chemical stability that can mimic that of Nafion® while not compromising conductivity properties. An interesting component of the investigations presented

in this dissertation on the synthesis of stable AEMs is that the chemistry techniques used in these synthetic procedures are common, the materials are easily accessible, and the synthetic yields of these monomers and their polymers are good.

Over all, the findings in this dissertation can be divided into three parts: (i) addressing the morphology-conductivity challenges in AEMs (ii) addressing the challenges in synthesizing alkaline-stable AEMs, and finally (iii) utilizing the combined findings in (i) and (ii) to design highly stable and highly ion conducting AEMs. Initial results on the ionic conductivity of these ASU-type anion exchange membranes provide cause for cautious optimism for the future of anion exchange membranes and the discovery of solutions to the global energy problem in general. These findings also provide templates for future investigations into chemical stabilities and morphology-conductivity optimizations in other azonia spirocyclic undecane-type anion exchange membranes.

<The End>

APPENDIX A

FTIR CHARACTERIZATION SPECTRA

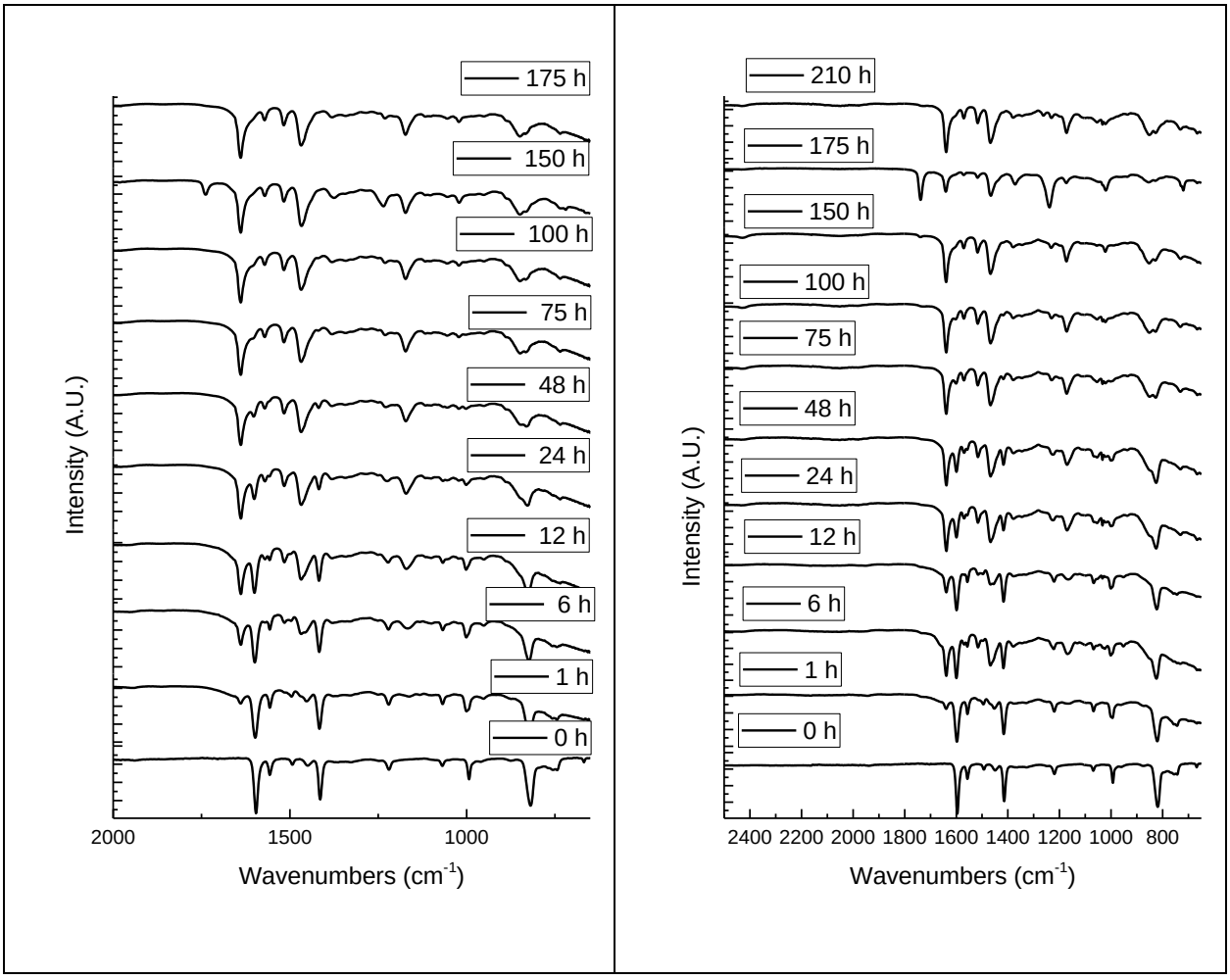

Figure 1. FTIR spectra of P4VP quternization with time by 1-butyllbromide (left) and 1-pentylbromide (right).

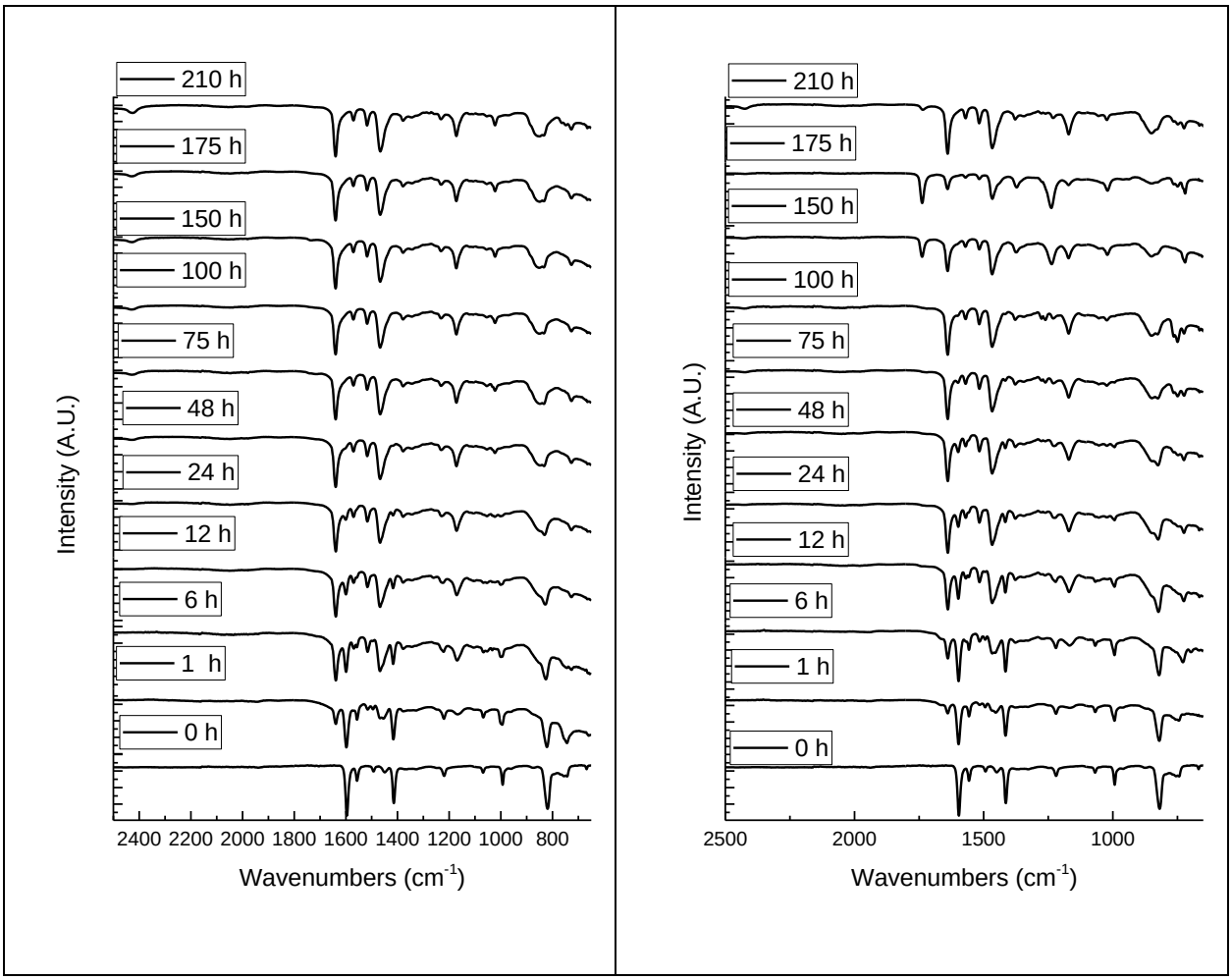

Figure 2. FTIR spectra of P4VP quternization with time by 1-hexylbromide (left) and 1-heptylbromide (right).

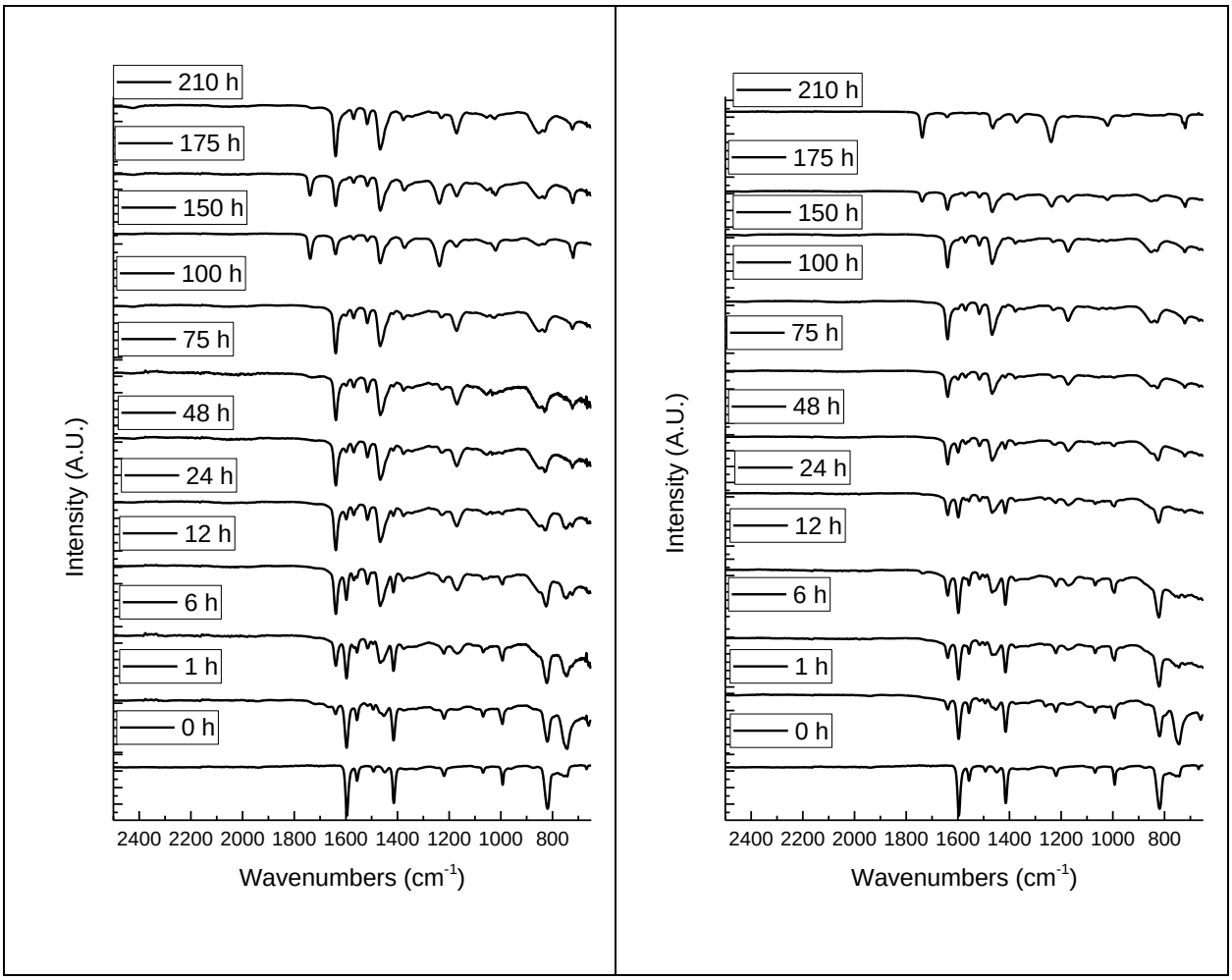

Figure 3. FTIR spectra of P4VP quternization with time by 1-octylbromide (left) and 1-decylbromide (right).

APPENDIX B

X-RAY SCATTERING SPECTRA

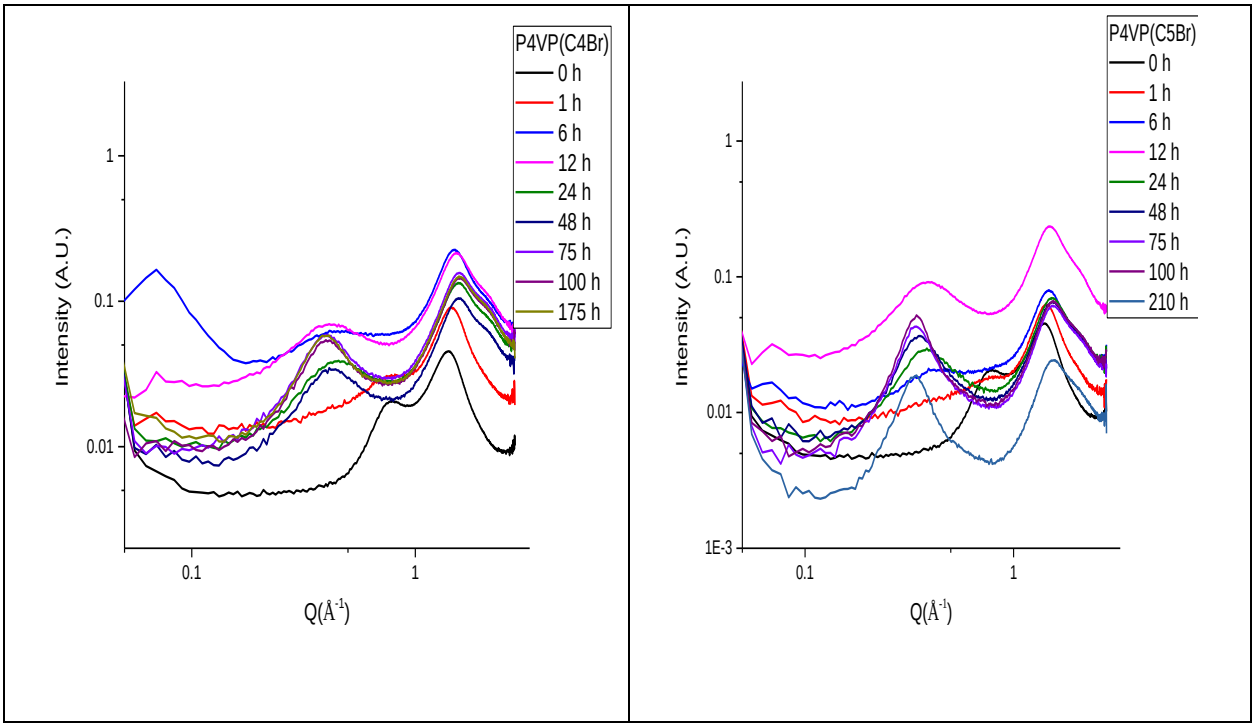

Figure 1. SAXS spectra of P4VP quternization with time by 1-butylbromide (left) and 1-pentylbromide (right).

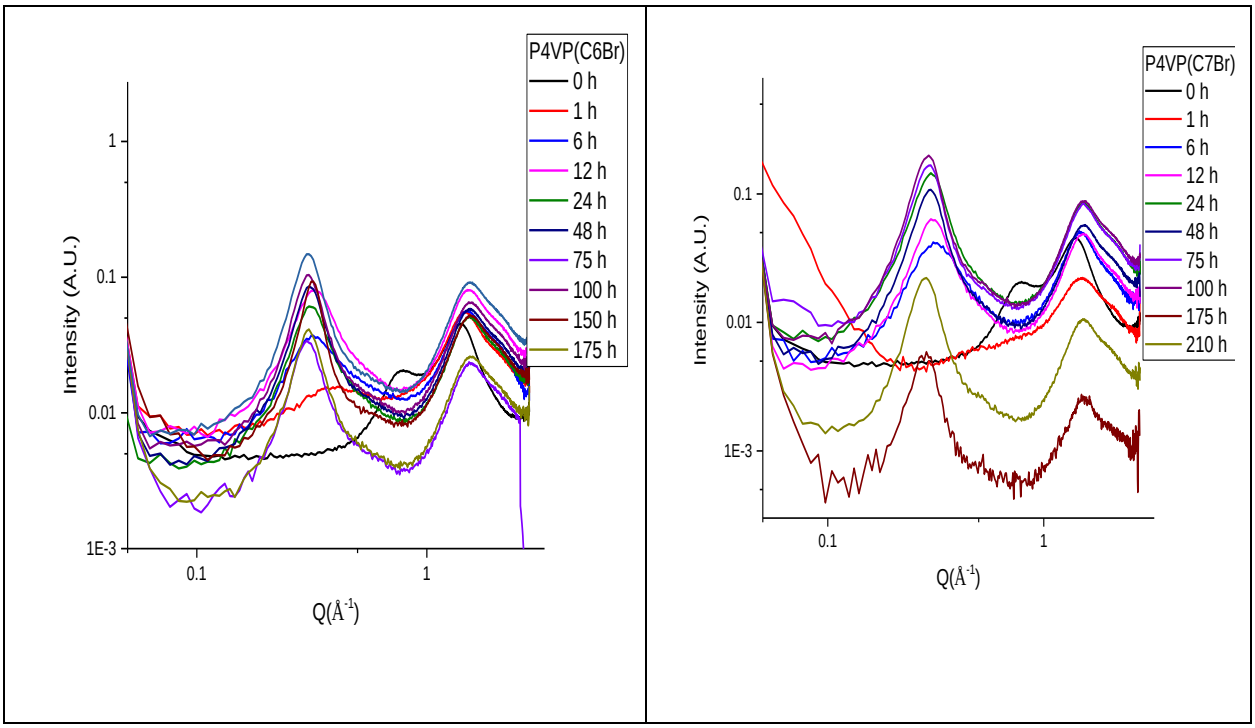

Figure 2. SAXS spectra of P4VP quternization with time by 1-hexylbromide (left) and 1-heptylbromide (right).

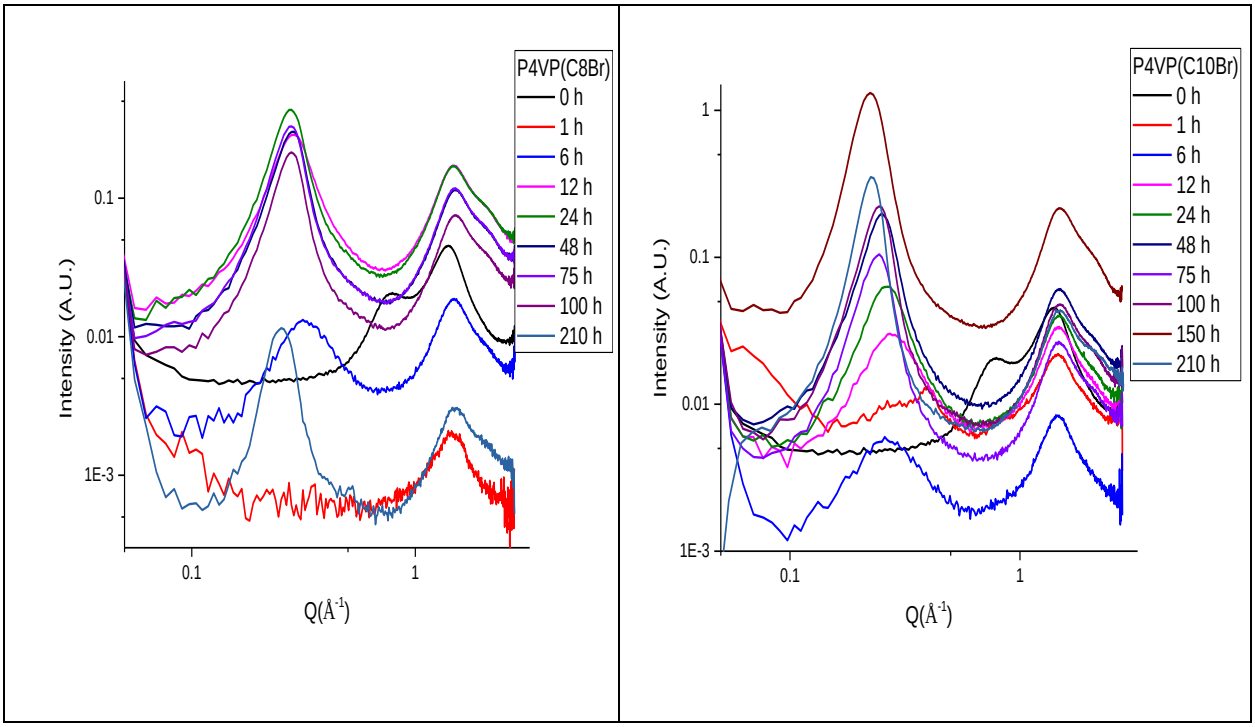

Figure 3. SAXS spectra of P4VP quternization with time by 1-octylbromide (left) and 1-dodecylbromide (right).

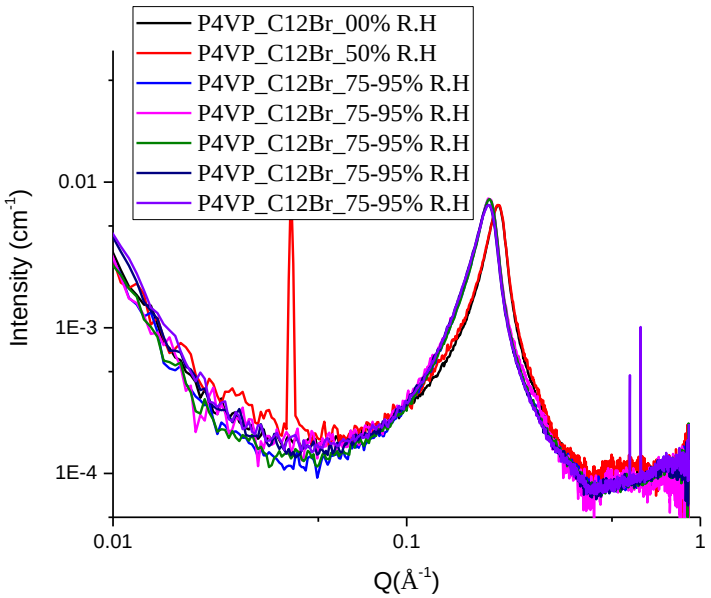

Figure 4. SAXS spectra of P4VP_C12Br in an environment with changing relative humidity (RH).

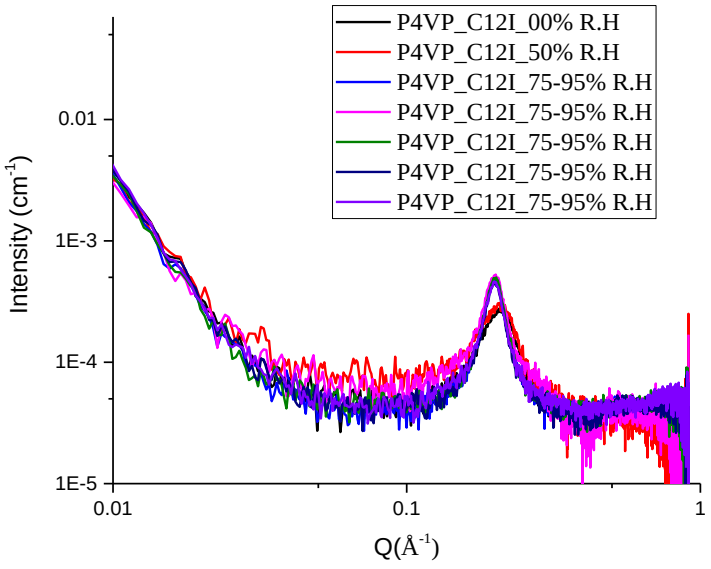

Figure 5. SAXS spectra of P4VP_C12I in an environment with changing relative humidity (RH).

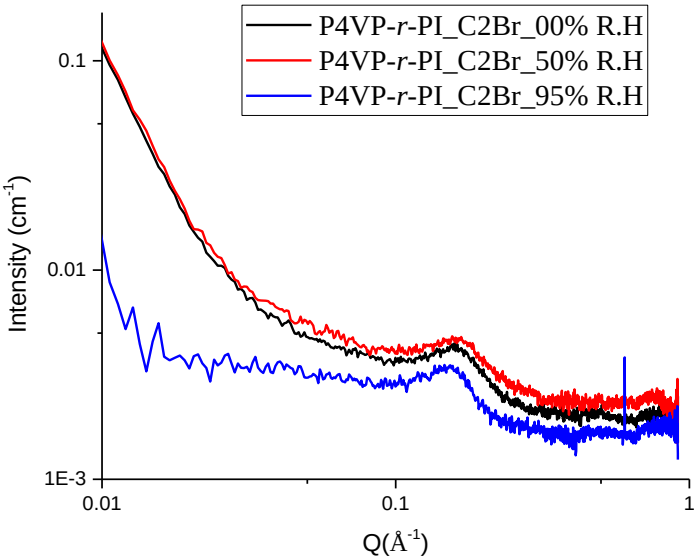

Figure 6. SAXS spectra of P4VP-*r*-PI_C2Br in an environment with changing relative humidity (RH).

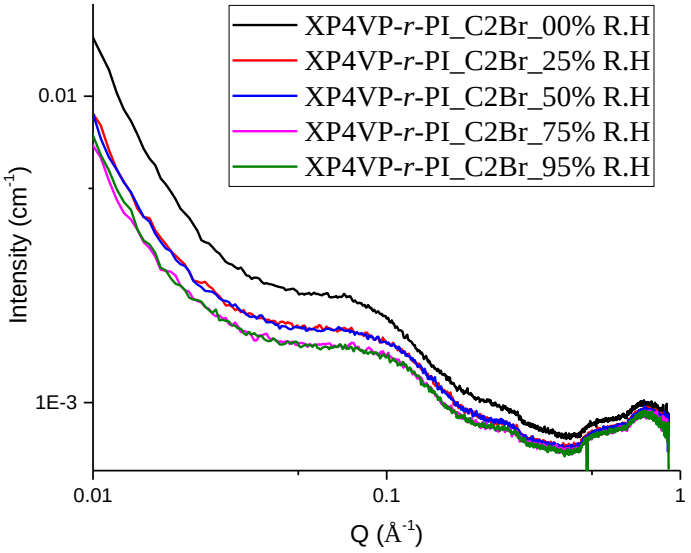

Figure 7. SAXS spectra of XP4VP-*r*-PI_C2Br in an environment with changing relative humidity (RH).

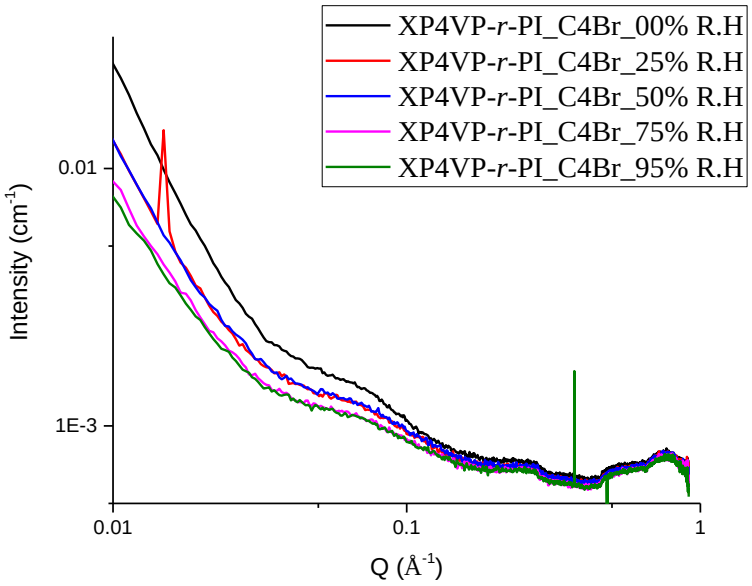

Figure 8. SAXS spectra of XP4VP-*r*-PI_C4Br in an environment with changing relative humidity (RH).

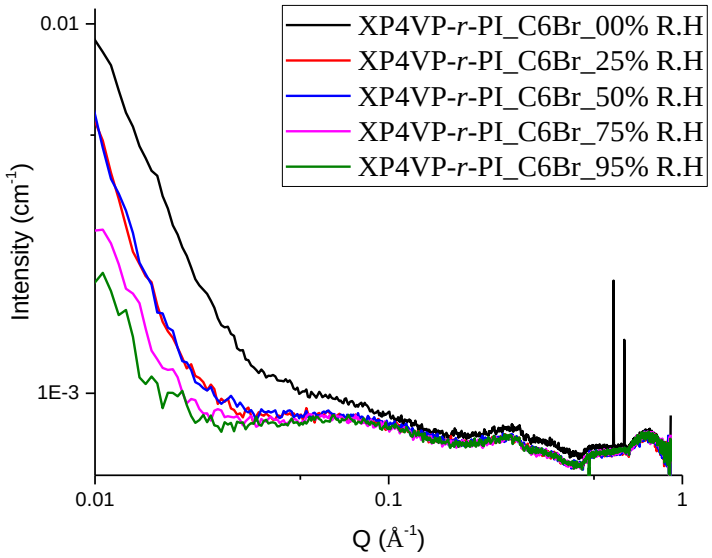

Figure 9. SAXS spectra of XP4VP-*r*-PI_C6Br in an environment with changing relative humidity (RH).

APPENDIX C

NMR CHARACTERIZATION SPECTRA

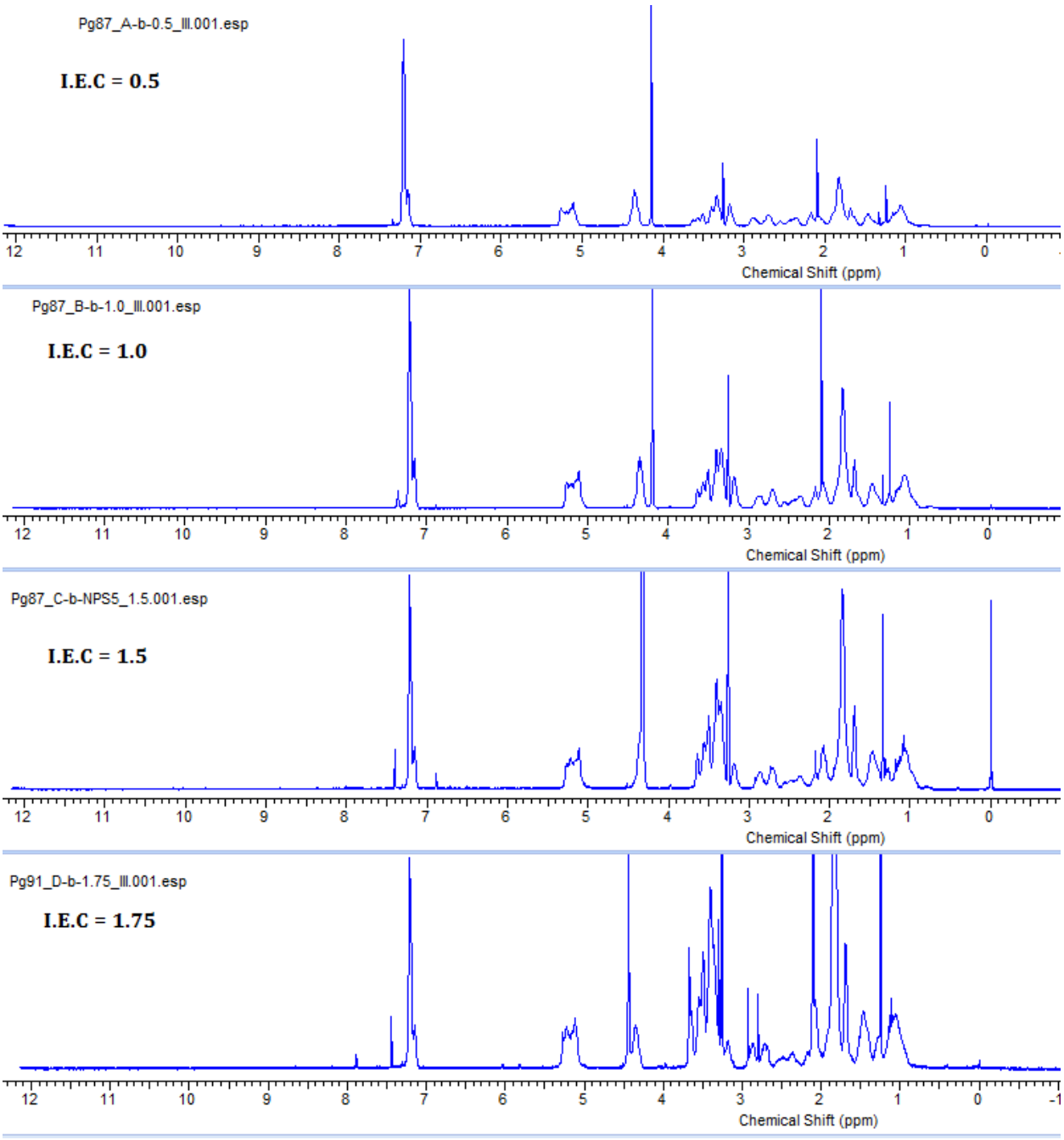

Figure 1. ^{1}H NMR spectra of the PNPS5-*b*-PNMBzE series.

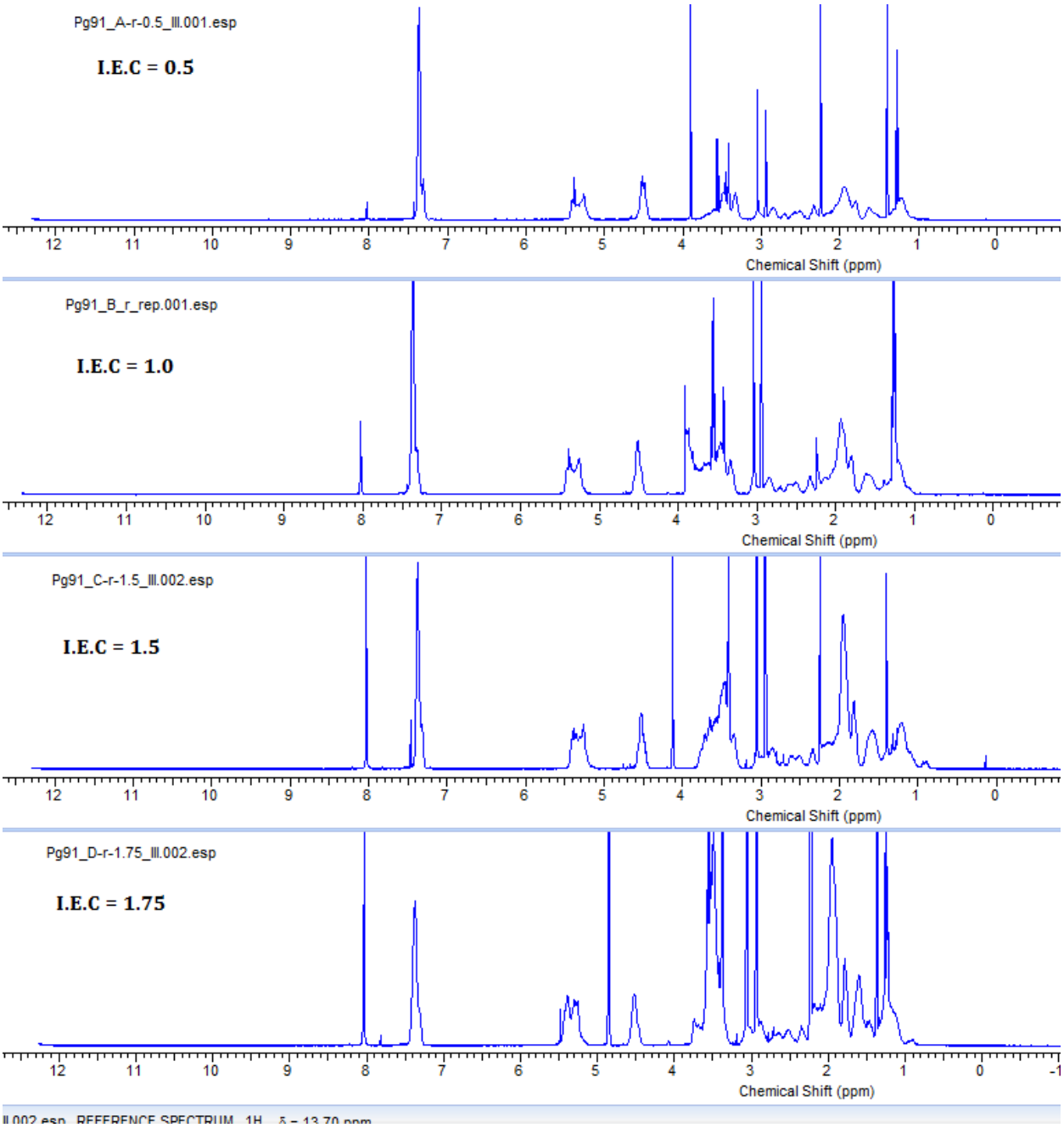

Figure 2. ^{1}H NMR spectra of the PNPS5-*r*-PNMBzE series.

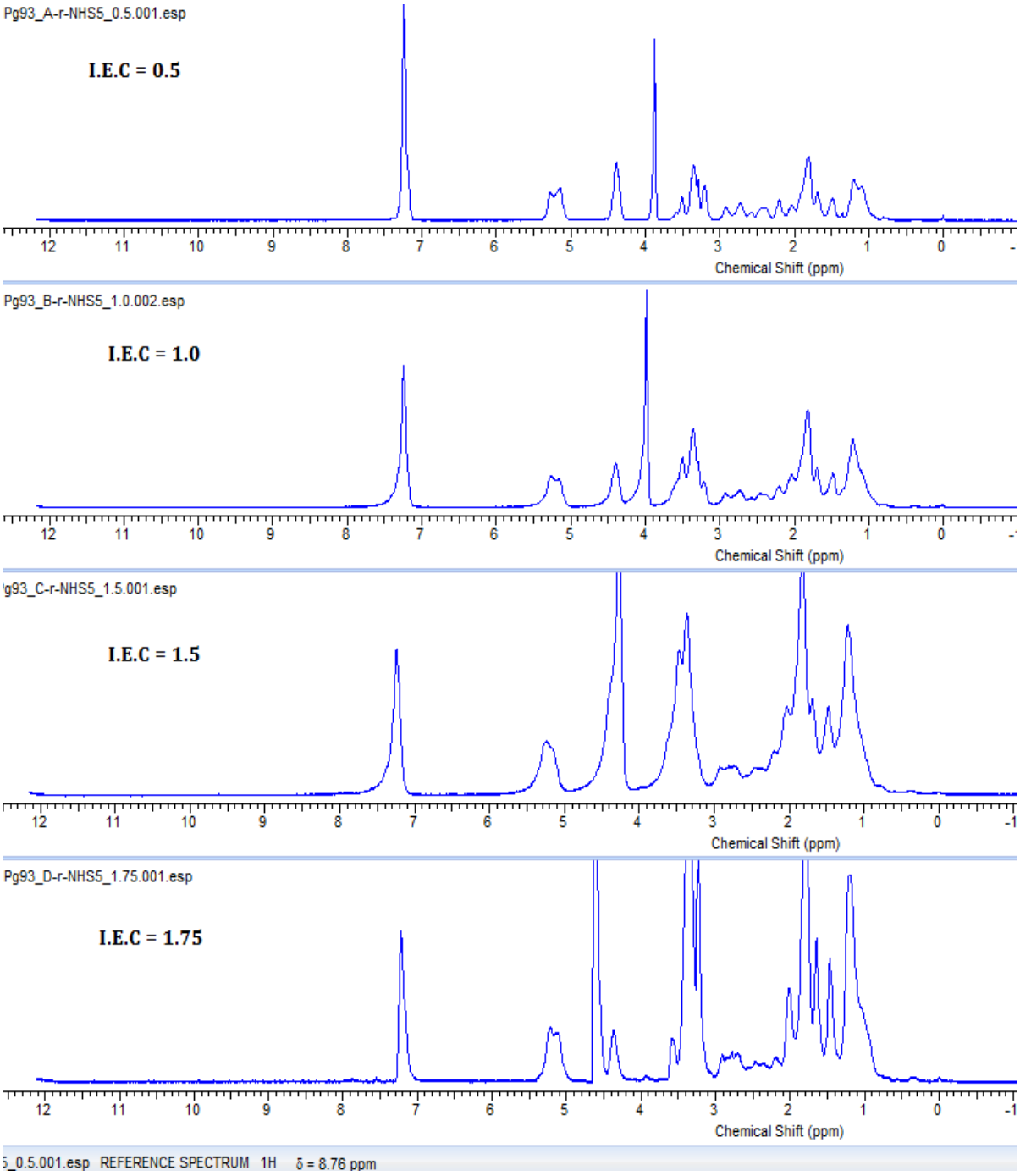

Figure 3. ^{1}H NMR spectra of the PNHS5-*r*-PNMBzE series.

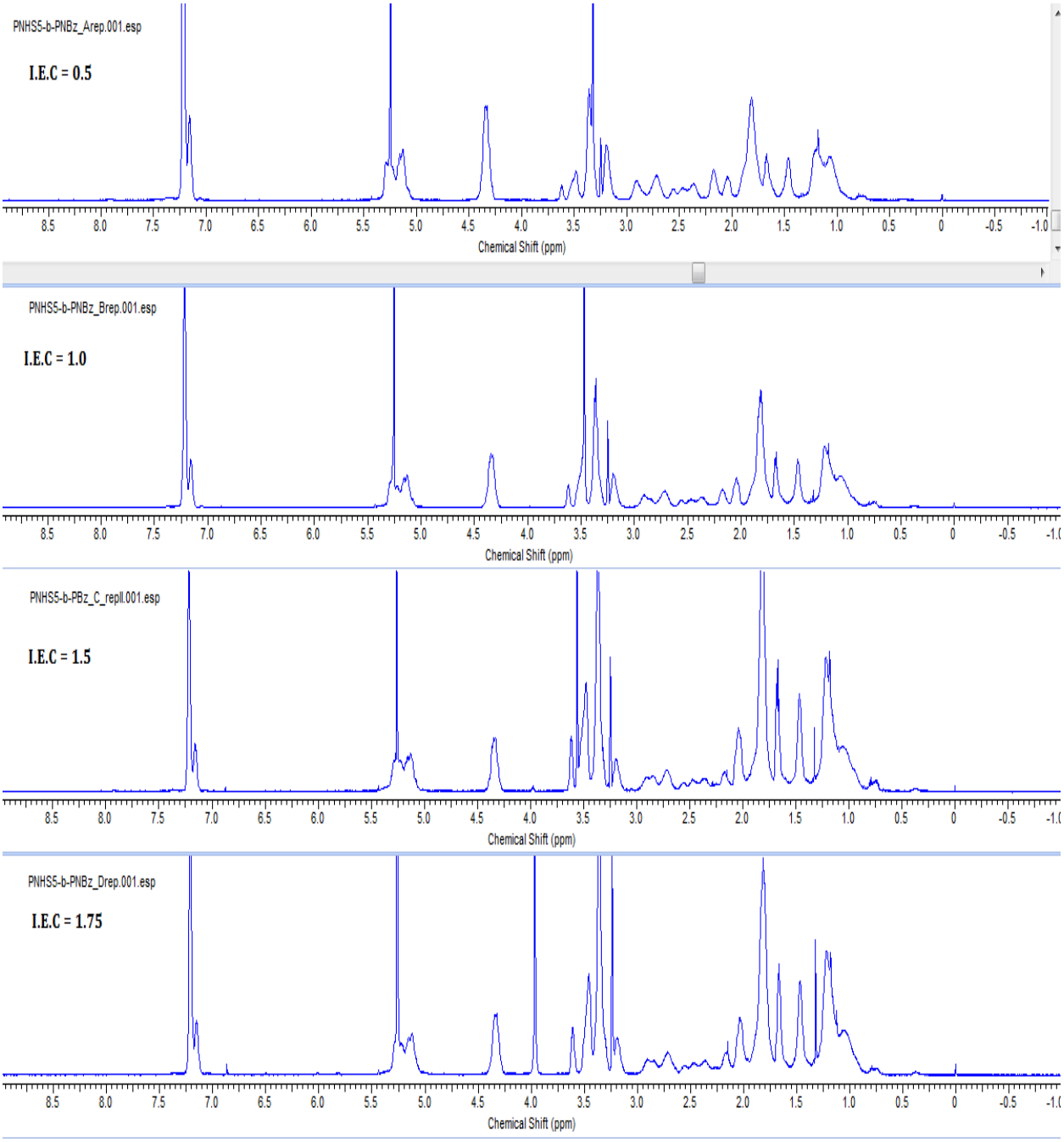

Figure 4. ^{1}H NMR spectra of the PNHS5-*b*-PNMBzE series.

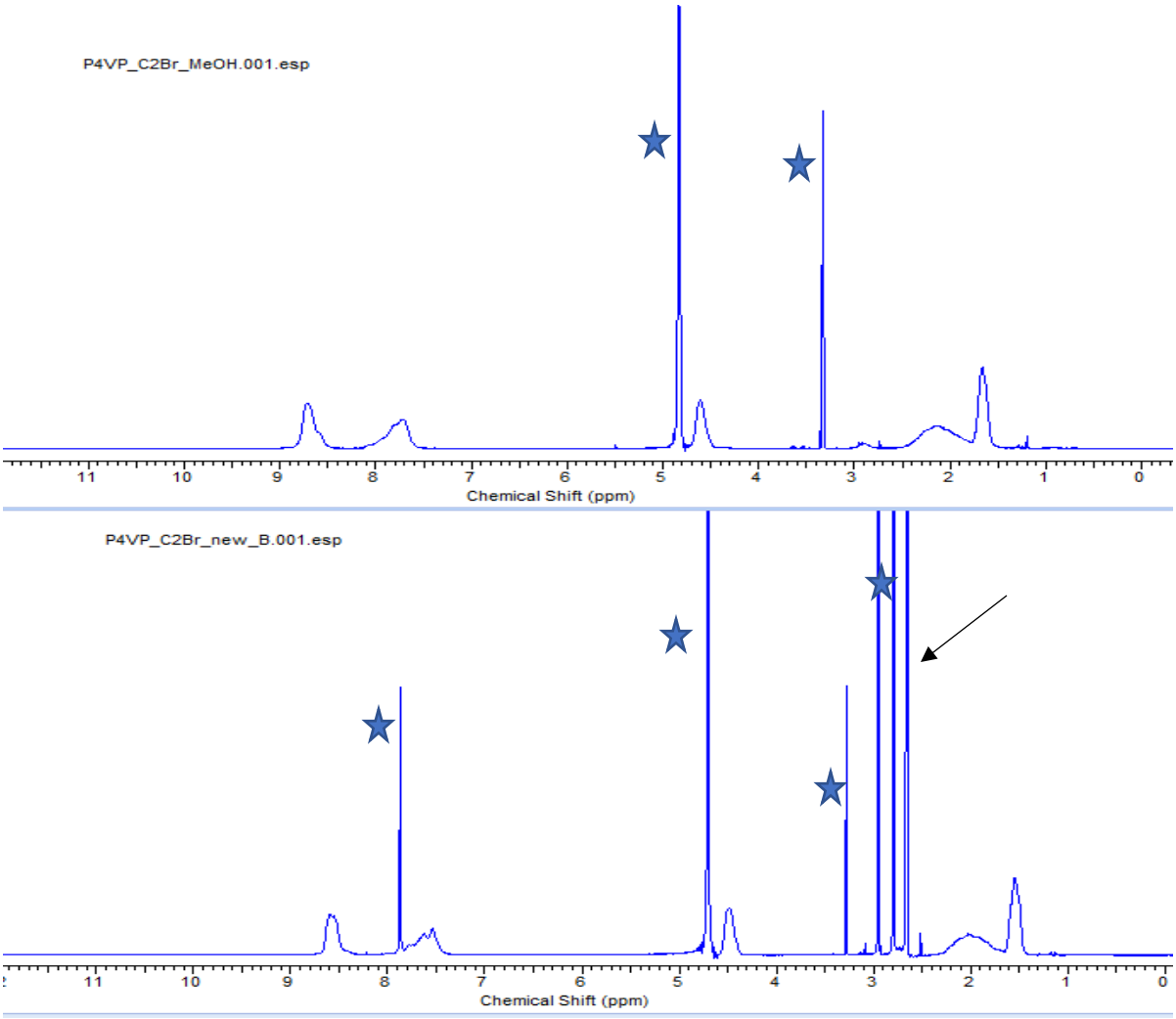

Figure 5. ^{1}H NMR spectrum of P4VP quaternized by 1-ethylbromide in methanol (top), and in DMF (bottom). Solvent peaks are marked by the star.

It is important to note that, P4VP quarternized by ethylhalide in methanol do not show evidence of crystallinity except when quarternized in DMF. The ^{1}H NMR spectra for P4VP quarternized by ethylbromide in methanol and DMF differ by a single peak (see arrow) which may be the reason for the visible crystalline peaks in the WAXS of P4VP_C2Br. This may be an impurity of sorts, and if so, suggests that alkylhalides can react with DMF in the presence of P4VP. More studies on the chemistry of this reaction is therefore warranted.

APPENDIX D

DSC CHARACTERIZATION SPECTRA

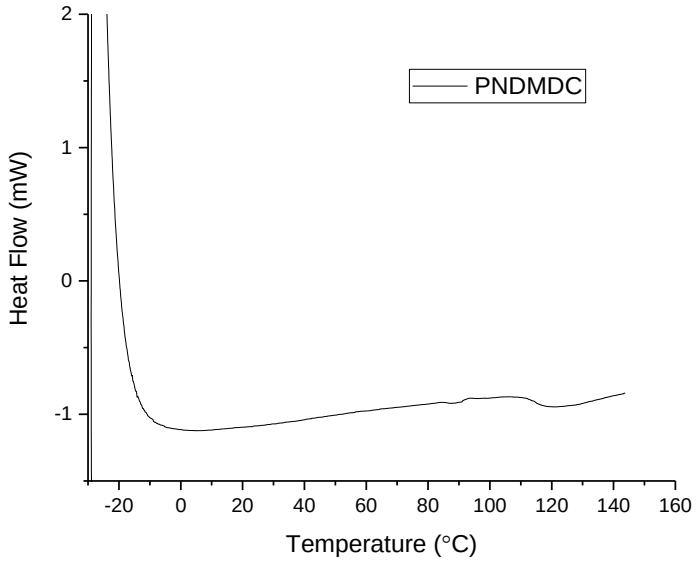

Figure 1. DSC spectrum of PNDMC.

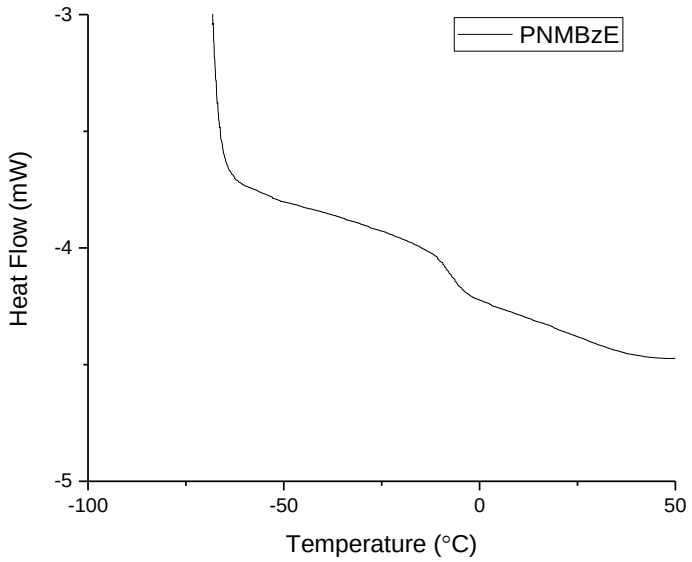

Figure 2. DSC spectrum of PNMBzE.

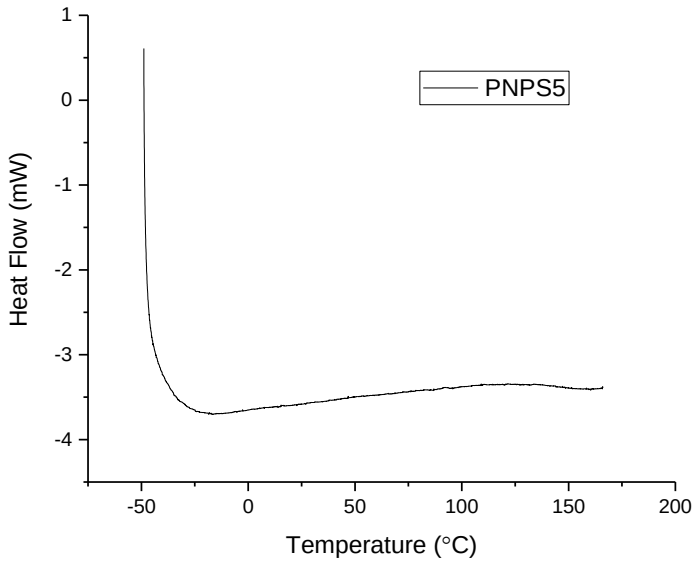

Figure 3. DSC spectrum of PNPS5.

BIBLIOGRAPHY

(1) Ahmad, Z. Polymer Dielectric Materials, Dielectric Material; Silaghi, M. A., Ed.; IntechOpen, 2012; pp 3–26.

(2) Akiba, I.; Takechi, A.; Sakou, M.; Handa, M.; Shinohara, Y.; Amemiya, Y.; Yagi, N.; Sakurai, K. Anomalous Small-Angle X ‐ Ray Scattering Study of Structure of Polymer Micelles Having Bromines in Hydrophobic Core. *Macromolecules* **2012**, No. 45, 6150–6157.

(3) Al-Ketan, O.; Al-Rub, R. K. A.; Rowshan, R. Mechanical Properties of a New Type of Architected Interpenetrating Phase Composite Materials. *Adv. Mater. Technol.* **2016**, 1600235.

(4) Allen, F. I.; Comolli, L. R.; Kusoglu, A.; Modestino, M. A.; Minor, A. M.; Weber, A. Z. Morphology of Hydrated as-Cast Nafion Revealed through Cryo Electron Tomography. *ACS Macro Lett.* **2015**, *4* (1), 1–5.

(5) Anderson, D. M.; Davis, H. T.; Scriven, L. E.; Nitsche, J. C. C. Periodic Surfaces of Prescribed Mean Curvature. *Adv. Chem. Phys.* **1990**, *77* (April), 337–396.

(6) Andruzzi, F.; Lupinacci, D.; Magagnini, P. L. Comb-like Polymers. 2. Poly(octadecylethy1ene Oxide). *Macromolecules* **1980**, *13* (1), 15–18.

(7) Arges, C. G.; Parrondo, J.; Johnson, G.; Nadhan, A.; Ramani, V. Assessing the Influence of Different Cation Chemistries on Ionic Conductivity and Alkaline Stability of Anion Exchange Membranes. *J. Mater. Chem.* **2012**, 3733–3744.

(8) Arges, C. G.; Ramani, V.; Pintauro, P. N. Anion Exchange Membrane Fuel Cells. *Elctrochemical Soc. Interface* **2010**, 31–35.

(9) Aricò, A. S. A. S.; Sebastian, D.; Schuster, M.; Bauer, B.; D'Urso, C.; Lufrano, F.; Baglio, V.; D'Urso, C.; Lufrano, F.; Baglio, V. Selectivity of Direct Methanol Fuel Cell Membranes. *Membranes (Basel).* **2015**, *5* (4), 793–809.

(10) Arunan, E.; Desiraju, G. R.; Klein, R. A.; Sadlej, J.; Scheiner, S.; Alkorta, I.; Clary, D. C.; Crabtree, R. H.; Dannenberg, J. J.; Hobza, P.; et al. Definition of the Hydrogen Bond (IUPAC Recommendations 2011)*. *Pure Appl. Chem.* **2011**, *83* (8), 1637–1641.

(11) Auriemma, F.; Rosa, C. De; Esposito, S.; Mitchell, G. R. Polymorphic Superelasticity in Semicrystalline Polymers. *Angew. Chemie, Semicrystalline Polym.* **2007**, *46*, 4325–4328.

(12) Bae, B.; Yoda, T.; Miyatake, K.; Uchida, H.; Watanabe, M. Proton-Conductive Aromatic Ionomers Containing Highly Sulfonated Blocks for High-Temperature-Operable Fuel Cells. *Angew. Chemie - Fuel Cell Membr.* **2010**, *49* (2), 317–320.

(13) Ballauff, M.; Jusufi, A. The Distribution of Sr 2 + Counterions around Polyacrylate Chains Analyzed by Anomalous Small- Angle X-Ray Scattering The Distribution of Sr 2 + Counterions around Small-Angle X -Ray Scattering. *Europhys. Lett.* **2004**, *66*, 331–337.

(14) Batten, S. R.; Champness, N. R.; Chen, X.-M.; Garcia-Martinez, J.; Kitagawa, S.; Öhrström, L.; O'Keeffe, M.; Suh, M. P.; Reedijk, J.; Rowsell, J. L. C.; et al. Coordination Polymers, Metal–organic Frameworks and the Need for Terminology Guidelines. *CrystEngComm* **2012**, *14* (9), 3001–3004.

(15) Bauer, J.; Schroer, A.; Schwaiger, R.; Kraft, O. Approaching Theoretical Strength in Glassy Carbon Nanolattices. *Nat. Mater.* **2016**, *15* (4), 438–443.

(16) Bauer, J.; Hengsbach, S.; Tesari, I.; Schwaiger, R.; Kraft, O. High-Strength Cellular Ceramic Composites with 3D Microarchitecture. *Proc. Natl. Acad. Sci. U. S. A.* **2014**, *111* (7), 2453–2458.

(17) Beers, K. M.; Balsara, N. P. Design of Cluster-Free Polymer Electrolyte Membranes and Implications on Proton Conductivity. *ACS Macro Lett.* **2012**, *1* (10), 1155–1160.

(18) Beiner, M.; Huth, H. Nanophase Separation and Hindered Glass Transition in Side-Chain Polymers. *Nat. Mater.* **2003**, *2*, 595–599.

(19) Benson, S. D. THE EFFECT OF NANOSCALE PARTICLES AND IONOMER ARCHITECTURE ON THE CRYSTALLIZATION BEHAVIOR OF SULFONATED SYNDIOTACTIC POLYSTYRENE, Virginia Polytechnic Institute and State University, 2010.

(20) Bernard, S.; Miele, P. Ordered Mesoporous Polymer-Derived Ceramics and Their Processing into Hierarchically Porous Boron Nitride and Silicoboron Carbonitride Monoliths. *New J. Chem.* **2014**, *38*, 1923.

(21) Bernard, S.; Miele, P. Polymer-Derived Boron Nitride: A Review on the Chemistry, Shaping and Ceramic Conversion of Borazine Derivatives. *Materials (Basel).* **2014**, *7* (11), 7436–7459.

(22) Bernardo, E.; Fiocco, L.; Parcianello, G.; Storti, E.; Colombo, P. Advanced Ceramics from Preceramic Polymers Modified at the Nano-Scale: A Review. *Materials (Basel).* **2014**, *7* (3), 1927–1956.

(23) Bharatiya, B.; Schumers, J.-M.; Poggi, E.; Gohy, J.-F. Supramolecular Assemblies from Poly(styrene)-Block-poly(4-Vinylpyridine) Diblock Copolymers Mixed with 6-Hydroxy-2-Naphthoic Acid. *Polymers (Basel).* **2013**, *5*, 679–695.

(24) Bielawski, C. W.; Grubbs, R. H. Living Ring-Opening Metathesis Polymerization. *Prog. Polym. Sci.* **2007**, *32* (1), 1–29.

(25) Bielawski, C. W.; Grubbs, R. H. Highly Efficient Ring-Opening Metathesis Polymerization (ROMP) Using New Ruthenium Catalysts Containing N-Heterocyclic Carbene Ligands. *Angew. Chemie - Int. Ed.* **2000**, *39* (16), 2903–2906.

(26) Bielawski, C. W.; Grubbs, R. H. Living Ring-Opening Metathesis Polymerization. *Prog. Polym. Sci.* **2007**, *32*, 1–29.

(27) Borodin, O.; Smith, G. D. Mechanism of Ion Transport in Amorphous Poly(ethylene oxide)/LiTFSI from Molecular Dynamics Simulations. *Macromolecules* **2006**, *39* (4), 1620–1629.

(28) Bouchet, R.; Maria, S.; Meziane, R.; Aboulaich, A.; Lienafa, L.; Bonnet, J.-P.; Phan, T. N. T.; Bertin, D.; Gigmes, D.; Devaux, D.; et al. Single-Ion BAB Triblock Copolymers as Highly Efficient Electrolytes for Lithium-Metal Batteries. *Nat. Mater.* **2013**, *12* (5), 452–457.

(29) Boukamp, B. A. Fuel Cells: The Amazing Perovskite Anode. *Nat. Mater.* **2003**, *2* (5), 294–296.

(30) Boutaous, M.; Bourgin, P.; Zinet, M. Journal of Non-Newtonian Fluid Mechanics Thermally and Flow Induced Crystallization of Polymers at Low Shear Rate. *J. Nonnewton. Fluid Mech.* **2010**, *165* (5–6), 227–237.

(31) Bunn, C. W. ©1948 Nature Publishing Group. *Nature* **1948**, *161*, 929–930.

(32) Caillier, L.; Taffin de Givenchy, E.; Levy, R.; Vandenberghe, Y.; Geribaldi, S.; Guittard, F. Polymerizable Semi-Fluorinated Gemini Surfactants Designed for Antimicrobial Materials. *J. Colloid Interface Sci.* **2009**, *332* (1), 201–207.

(33) Capek, I. Nature and Properties of Ionomer Assemblies. II. *Adv. Colloid Interface Sci.* **2005**, *118* (1–3), 73–112.

(34) Caruso, U.; De Maria, A.; Panunzi, B.; Roviello, A. Poly(4-Vinylpyridine) as the Host Ligand of Metal-Containing Chromophores for Second-Order Nonlinear Optical Active Materials. *J. Polym. Sci. Part A Polym. Chem.* **2002**, *40* (17), 2987–2993.

(35) Cellino, A.; Paolicchi, P.; Binzel, R. P. Molecular Basis of the Shish-Kebab Morphology in Polymer Crystallization. *Science (80-.).* **2007**, *316* (May), 1014–1017.

(36) Chao, C. Y.; Li, X.; Ober, C. K.; Osuji, C.; Thomas, E. L. Orientational Switching of Mesogens and Microdomains in Hydrogen-Bonded Side-Chain Liquid-Crystalline Block Copolymers Using AC Electric Fields. *Adv. Funct. Mater.* **2004**, *14* (4), 364–370.

(37) Chen, D.; Hickner, M. A. Ion Clustering in Quaternary Ammonium Functionalized Benzylmethyl Containing Poly(arylene Ether Ketone)s. *Macromolecules* **2013**.

(38) Chen, D.; Hickner, M. A. Degradation of Imidazolium- and Quaternary Ammonium-Functionalized Poly (Fl Uorenyl Ether Ketone Sulfone) Anion Exchange Membranes. *Appl. Mater. Interfaces* **2012**, *4* (11), 5776–5781.

(39) Chen, N.; Long, C.; Li, Y.; Lu, C.; Zhu, H. Ultrastable and High Ion-Conducting Polyelectrolyte Based on Six- Membered N ‑ Spirocyclic Ammonium for Hydroxide Exchange Membrane Fuel Cell Applications. *ACS Appl. Mater. Interfaces* **2018**, *10*, 15720–15732.

(40) Chen, Q.; Bao, N.; Wang, J. H.; Tunic, T.; Liang, S.; Colby, R. H. Linear Viscoelasticity and Dielectric Spectroscopy of Ionomer / Plasticizer Mixtures : A Transition from Ionomer to Polyelectrolyte. *Macromolecules* **2015**, *48*, 8240–8252.

(41) Chen, Y.; Fang, D.; Hsiao, B. S.; Li, Z. Insight into Unique Deformation Behavior of Oriented Isotactic Polypropylene with Branched Shish-Kebabs. *Polymer (Guildf).* **2015**, *60*, 274–283.

(42) Choi, T.; Grubbs, R. H. Controlled Living Ring-Opening-Metathesis Polymerization by a Fast-Initiating Ruthenium Catalyst. *Angew. Chemie* **2003**, *115*, 1785–1788.

(43) Clark, T. J.; Robertson, N. J.; Iv, H. A. K.; Lobkovsky, E. B.; Mutolo, P. F. A Ring-Opening Metathesis Polymerization Route to Alkaline Anion Exchange Membranes : Development of Hydroxide-Conducting Thin Films from an Ammonium-Functionalized Monomer. *J. Am. Chem. Soc.* **2009**, *131* (36), 12888–12889.

(44) Clausse, M.; Peyrelasse, J.; Heil, J.; Boned, C.; Lagourette, B. Bicontinuous Structure Zones in Microemulsions. *Nature*. 1981, pp 636–638.

(45) Colombo, P. Engineering Porosity in Polymer-Derived Ceramics. *J. Eur. Ceram. Soc.* **2008**, *28* (7), 1389–1395.

(46) Colombo, P.; Mera, G.; Riedel, R.; Sorar??, G. D. Polymer-Derived Ceramics: 40 Years of Research and Innovation in Advanced Ceramics. *J. Am. Ceram. Soc.* **2010**, *93* (7), 1805–1837.

(47) Cornet, N.; Diat, O.; Gebel, G.; Jousse, F.; Marsacq, D.; Mercier, R.; Pineri, M. Sulfonated Polyimide Membranes: A New Type of Ion-Conducting Membrane for Electrochemical Applications. *J. New Mater. Electrochem. Syst.* **2000**, *3* (1), 33–42.

(48) Cospito, G.; Illuminati, G.; Lillocci, C.; Petride, H. Ring-Opening Reactions. 3. Mechanistic Path vs. Ring-Strain Control in Elimination and Substitution Reactions of 1,1-Dimethyl Cyclic Ammonium Ions and Their .alpha.,.alpha.'-dimethyl-Substituted Derivatives. *J. Org. Chem.* **1981**, *46* (14), 2944–2947.

(49) Couture, G.; Alaaeddine, A.; Boschet, F.; Ameduri, B. Polymeric Materials as Anion-Exchange Membranes for Alkaline Fuel Cells. *Prog. Polym. Sci.* **2011**, *36* (11), 1521–1557.

(50) Crist, B.; Schultz, J. M. Progress in Polymer Science Polymer Spherulites : A Critical Review. *Prog. Polym. Sci.* **2016**, *56*, 1–63.

(51) Dang, H.-S.; Jannasch, P. Exploring Different Cationic Alkyl Side Chain Designs for Enhanced Alkaline Stability and Hydroxide Ion Conductivity of Anion-Exchange Membranes. *Macromolecules* **2015**, *48* (16), 5742–5751.

(52) Dang, H.; Jannasch, P. Membranes Tethered with Di Ff Erent Hetero-. *J. Mater. Chem. A Mater. energy Sustain.* **2017**, *5*, 21965–21978.

(53) de Robillard Q., Guo X., Dingenouts N., and Ballauff M., G. G. Application of Anomalous Small-Angle X-Ray Scattering to Spherical Polyelectrolyte Brushes. *Macromol. Symp.* **2001**, *164*, 81–90.

(54) Dekel, D. R. Review of Cell Performance in Anion Exchange Membrane Fuel Cells. *J. Power Sources* **2017**.

(55) Dekel, D. R. Review of Cell Performance in Anion Exchange Membrane Fuel Cells. *J. Power Sources* **2018**, *375*, 158–169.

(56) Diat, O.; Gebel, G. Fuel Cells: Proton Channels. *Nat. Mater.* **2008**, *7* (1), 13–14.

(57) Ding, J.; Chuy, C.; Holdcroft, S. A Self-Organized Network of Nanochannels Enhances Ion Conductivity through Polymer Films. *Chem. Mater.* **2001**, *13* (7), 2231–2233.

(58) Ding, J.; Chuy, C.; Holdcroft, S. Enhanced Conductivity in Morphologically Controlled Proton Exchange Membranes: Synthesis of Macromonomers by SFRP and Their Incorporation into Graft Polymers. *Macromolecules* **2002**, *35* (4), 1348–1355.

(59) Dobrynin, A. V.; Rubinstein, M. Theory of Polyelectrolytes in Solutions and at Surfaces. *Prog. Polym. Sci.* **2005**, *30* (11), 1049–1118.

(60) Dong, X.; Xue, B.; Qian, H.; Zheng, J.; Li, S. Novel Quaternary Ammonium Microblock Poly (P -Phenylene- Co -Aryl Ether Ketone) S as Anion Exchange Membranes for Alkaline Fuel Cells. *J. Power Sources* **2017**, *342*, 605–615.

(61) Dukovski, I.; Muthukumar, M. Langevin Dynamics Simulations of Early Stage Shish-Kebab Crystallization of Polymers in Extensional Flow Langevin Dynamics Simulations of Early Stage Shish-Kebab Crystallization of Polymers in Extensional Flow. *J. Chem. Phys.* **2003**, *6648* (14), 6648–6655.

(62) Dymitrowska, M.; Belloni, L. Integral Equation Theory of Flexible Polyelectrolytes. I. Debye-H??ckel Approach. *J. Chem. Phys.* **1998**, *109* (11), 4659–4669.

(63) Eckel, Z. C.; Zhou, C.; Martin, J. H.; Jacobsen, A. J.; Carter, W. B.; Schaedler, T. A. Additive Manufacturing of Polymer-Derived Ceramics. *Science* **2016**, *351* (6268), 58–62.

(64) Eisenberg, A. Clustering of Ions in Organic Polymers. A Theoretical Approach. *Macromolecules* **1970**, *3* (2), 147–154.

(65) Eisenberg, A.; Hird, B.; Moore, R. B. A New Multiplet-Cluster Model for the Morphology of Random Ionomers. *Macromolecules* **1990**, *23* (18), 4098–4107.

(66) Eisenberg, A.; Cayrol, B. Viscoelastic Properties of Poly(phenylene Ethers). I. Unsubstituted and Methyl or Phenyl Substituted Polymers. *J. Polym. Sci. Part C Polym. Chem.* **1971**, *35*, 129–149.

(67) Elabd, Y. A.; Hickner, M. A. Block Copolymers for Fuel Cells. *Macromolecules* **2011**, *44*, 1–11.

(68) Elbarbary, A. M.; Ghobashy, M. Thermal Behavior of Poly (2-Hydroxyethyl Thermal Behavior of Poly (2-Hydroxyethyl Methacrylate-Bis-[Trimethoxysilylpropyl] Amine) Networks. In *IOP Conference Series: Material Science and Engineering*; 2013; pp 1–5.

(69) Fan, L.; Degen, M.; Bendle, S.; Grupido, N.; Ilavsky, J. The Absolute Calibration of a Small-Angle Scattering Instrument with a Laboratory X-Ray Source. *J. Phys. Conf. Ser.* **2010**, *247* (1), 12005.

(70) Flores, O.; Schmalz, T.; Krenkel, W.; Heymann, L.; Motz, G. Selective Cross-Linking of Oligosilazanes to Tailored Meltable Polysilazanes for the Processing of Ceramic SiCN Fibres. *J. Mater. Chem. A* **2013**, *1* (48), 15406–15415.

(71) Fujimoto, C.; Kim, D.; Hibbs, M.; Wrobleski, D.; Seung, Y. Backbone Stability of Quaternized Polyaromatics for Alkaline Membrane Fuel Cells. *J. Memb. Sci.* **2012**, *423–424*, 438–449.

(72) Garcia, C. B. W.; Lovell, C.; Curry, C.; Faught, M.; Zhang, Y.; Wiesner, U. Synthesis and Characterization of Block Copolymer/ceramic Precursor Nanocomposites Based on a Polysilazane. *J. Polym. Sci. Part B Polym. Phys.* **2003**, *41* (24), 3346–3350.

(73) Ghigo, G.; Cagnina, S.; Maranzana, A.; Tonachini, G.; Generale, C.; Azeglio, C. M.; Torino, I.-. The Mechanism of the Stevens and Sommelet - Hauser Rearrangements . A Theoretical Study. *J. Org. Chem.* **2010**, *75* (11), 3608–3617.

(74) Gierke, T. D.; Munn, G. E.; Wilson, F. C. The Morphology in Nafion Perfluorinated Membrane Products, as Determined by Wide- and Small- Angle X-Ray Studies. *J. Polym. Sci. Polym. Phys. Ed.* **1981**, *19* (11), 1687–1704.

(75) Goerigk, G.; Huber, K.; Schweins, R. Probing the Extent of the Ion Condensation to Anionic Polyacrylate Coils : A Quantitative Anomalous Small-Angle X-Ray Scattering Study Probing the Extent of the Sr 2 + Ion Condensation to Anionic Polyacrylate Coils : A Quantitative Anomalous Small-Angle X. *J. Chem. Phys.* **2007**, *127* (154908), 1–8.

(76) Gottesfeld, S.; Dekel, D. R.; Page, M.; Bae, C.; Yan, Y.; Zelenay, P.; Seung, Y. Anion Exchange Membrane Fuel Cells : Current Status and Remaining Challenges. *J. Power Sources* **2018**, *375*, 170–184.

(77) Grady, B. P. Review and Critical Analysis of the Morphology of Random Ionomers Across Many Length Scales. *Polym. Eng. Sci.* **2008**, 1029–1051.

(78) Greenley. R. Z. Q. *Q and E Values for Free Radical Copolymerizations of Vinyl Monomers and Telogens*, In Polymer.; Brandrup, J., Imermergut, E. H., Grulke, E. A., Ed.; John Wiley & Sons, Inc.: New York, 1999.

(79) Gu, L.; Dong, H.; Sun, Z.; Li, Y.; Yan, F. RSC Advances Spirocyclic Quaternary Ammonium Cations for Alkaline Anion Exchange Membrane Applications : An Experimental and Theoretical Study †. *RSC Adv.* **2016**, *6*, 94387–94398.

(80) Guirguis, O. W.; Moselhey, M. T. H. Thermal and Structural Studies of Poly (Vinyl Alcohol) and Hydroxypropyl Cellulose Blends. *Nat. Sci.* **2012**, *4* (1), 57–67.

(81) Guisbiers, G. Size-Dependent Materials Properties toward a Universal Equation. *Nanoscale Res. Lett.* **2010**, *5* (7), 1132–1136.

(82) Günthner, M.; Kraus, T.; Dierdorf, A.; Decker, D.; Krenkel, W.; Motz, G. Advanced Coatings on the Basis of Si(C)N Precursors for Protection of Steel against Oxidation. *J. Eur. Ceram. Soc.* **2009**, *29* (10), 2061–2068.

(83) Günthner, M.; Wang, K.; Bordia, R. K.; Motz, G. Conversion Behaviour and Resulting Mechanical Properties of Polysilazane-Based Coatings. *J. Eur. Ceram. Soc.* **2012**, *32* (9), 1883–1892.

(84) Gupta, S.; Saxena, A. Negative Gaussian Curvature Distribution in Physical and Biophysical Systems-Curved Nanocarbons and Ion-Channel Membrane Proteins. *J. Appl. Phys.* **2012**, *112* (11).

(85) H., C. Y. F. and G. S. Miscibility of Some Hydroxyl-Containing Polymers with Poly(Acetonyl Methacry Late), Poly(Tetrahydropyranyl-2- Methacrylate), and Poly(Cyclohexyl Methacrylate). *J. Appl. Polym. Sci.* **1992**, *44*, 633–637.

(86) Haifeng Shi, Ying Zhao, Xia Dong, Y. Z. and D. W. Frustrated Crystallisation and Hierarchical Self-Assembly Behaviour of Comb-like Polymers. *Chem. Soc. Rev.* **2012**, *42*, 2075–2099.

(87) Hallinan, D. T.; Balsara, N. P. Polymer Electrolytes. *Annu. Rev. Mater Res* **2013**, *43*, 503–525.

(88) Hao, E.; Lian, T. Layer-by-Layer Assembly of CdSe Nanoparticles Based on Hydrogen Bonding. *Langmuir* **2000**, *16* (21), 7879–7881.

(89) Hauser, R. C.; Weinheimer, J. A. The Ortho Substitution Rearrangement Uersus P-Elimination of Certain Quaternary Ammonium Ions with Sodium Amide. Extension of the Method of Synthesis of Vicinal Alkyl Aromatic Derivatives. *J. Am. Chem. Soc.* **1953**, *76* (5), 1264–1267.

(90) Heard, G. L.; Yates, B. F. Competing Rearrangements of Ammonium Ylides: A Quantum Theoretical Study. *J. Org. Chem.* **1996**, *61* (21), 7276–7284.

(91) Hehmeyer, O. J.; Arya, G.; Panagiotopoulos, A. Z.; Szleifer, I. Monte Carlo Simulation and Molecular Theory of Tethered Polyelectrolytes. *J. Chem. Phys.* **2007**, *126* (24), 244902.

(92) Helfand, E.; Wasserman, Z. R. Block Copolymer Theory. 4. Narrow Interphase Approximation. *Macromolecules* **1976**, *9* (6), 879–888.

(93) Hill, R. K.; Chan, T.-H. Transfer of Assymetry from Nitrogen to Carbon in Stevens's Rearrangement. *J. Am. Chem. Soc. Commun. to Ed.* **1966**, *88* (4), 866–867.

(94) Hiller, S.; Pascui, O.; Budde, H.; Kabisch, O.; Reichert, D.; Beiner, M. Nanophase Separation in Side Chain Polymers: New Evidence from Structure and Dynamics. *New J. Phys.* **2004**, *6*.

(95) Hird, B. Structure-Morphology Property Relations in Random Styrene Ionomers by, McGill University, 1991.

(96) Hobbs, J. K.; Miles, M. J. Direct Observation of Polyethylene Shish-Kebab Crystallization Using in-Situ Atomic Force Microscopy. *Macromolecules* **2001**, *34* (3), 353–355.

(97) Hofmann, T.; Winkler, R. G.; Reineker, P. Self-Consistent Integral Equation Theory for Solutions of Finite Extensible Semiflexible Polyelectrolyte Chains. *J. Chem. Phys.* **2003**, *118* (14), 6624–6633.

(98) Holyst, R. Infi Nite Networks of Surfaces. *Nature* **2005**, *4* (July), 510–511.

(99) Hsiao, B. S.; Yang, L.; Somani, R. H.; Avila-orta, C. A.; Zhu, L. Unexpected Shish-Kebab Structure in a Sheared Polyethylene Melt. *Phys. Rev. Lett.* **2005**, *94* (March), 1–4.

(100) Hsu, W. Y.; Gierke, T. D. Elastic Theory for Ionic Clustering in Perfluorinated Ionomers. *Macromolecules* **1982**, *15*, 101–105.

(101) Hu, F. X.; Neoh, K. G.; Cen, L.; Kang, E. T. Antibacterial and Antifungal Efficacy of Surface Functionalized Polymeric Beads in Repeated Applications. *Biotechnol. Bioeng.* **2005**, *89* (4), 474–484.

(102) Huber, K.; Scheler, U. New Experiments for the Quanti Fi Cation of Counterion Condensation. *Curr. Opin. Colloid Interface Sci.* **2012**, *17*, 64–73.

(103) Hugar, K. M.; Kostalik, H. A.; Coates, W. Imidazolium Cations with Exceptional Alkaline Stability: A Systematic Study of Structure − Stability Relationships. *J. Am. Chem. Soc.* **2015**, *137* (27), 8730–8737.

(104) Huskens, J.; Jong, F. De; Timmerman, P.; Jong, F. De; Timmerman, P.; Reinhoudt, D. N.; Timmerman, P.; Reinhoudt, D. N.; Thede, R.; Heller, D.; et al. Functional Materials Based on Self-Assembly of Polymeric. *Science (80-.).* **2002**, *295* (March), 2407–2410.

(105) Ikkala, O.; ten Brinke, G. Hierarchical Self-Assembly in Polymeric Complexes: Towards Functional Materials. *Chem. Commun.* **2004**, No. 19, 2131–2137.

(106) Ikkala, O.; ten Brinke, G.; Pease, A. R.; Dodabalapur, A.; Batlogg, B.; Sirringhaus, H.; Schön, J. H.; Mena-Osteritz, E.; Bates, F. S.; Fredrickson, G. H.; et al. Functional Materials Based on Self-Assembly of Polymeric Supramolecules. *Science* **2002**, *295* (5564), 2407–2409.

(107) Iojoiu, C.; Genova-Dimitrova, P.; Maréchal, M.; Sanchez, J. Y. Chemical and Physicochemical Characterizations of Ionomers. *Electrochim. Acta* **2006**, *51* (23), 4789–4801.

(108) Ionescu, E.; Kleebe, H.-J.; Riedel, R. Silicon-Containing Polymer-Derived Ceramic Nanocomposites (PDC-NCs): Preparative Approaches and Properties. *Chem. Soc. Rev.* **2012**, *41* (15), 5032.

(109) Israelachvili, J. N. *Intermolecular and Surface Forces*; 2011; Vol. 53.

(110) It, M. Consideration on the Q-E Scheme. In *Eingegangen am 29. August 1961*; 1961; pp 70–79.

(111) J. Ruokolainen, R. Makinen, M. Torkkeli, T. Makela, R. Serimaa, G. ten Brinke, O. I. Switching Supramolecular Polymeric Materials with Multiple Length Scales. *Science (80-.).* **1998**, *280*, 557–560.

(112) Janakiraman, N.; Aldinger, F. Fabrication and Characterization of Fully Dense Si-C-N Ceramics from a Poly(ureamethylvinyl)silazane Precursor. *J. Eur. Ceram. Soc.* **2009**, *29* (1), 163–173.

(113) Jannasch, P.; Weiber, E. A. Configuring Anion-Exchange Membranes for High Conductivity and Alkaline Stability by Using Cationic Polymers with Tailored Side Chains. *Macromol. Chem. Phys.* **2016**, 1108–1118.

(114) Jean-Francois, B. J.-L. D. and J. Theory of Polyelectrolyte Solutions. *Adv. Chem. Phys.* **1995**, 1–79.

(115) Jiang, X.; Shen, M.; Tang, Y.; Li, C. Chemoselective Monobromination of Alkanes Promoted by Unactivated MnO 2. *Tetrahedron Lett.* **2005**, *46* (3), 487–489.

(116) Jin, H.; An, Q.; Zhao, Q.; Qian, J.; Zhu, M. Pervaporation Dehydration of Ethanol by Using Polyelectrolyte Complex Membranes Based on Poly (N-Ethyl-4-Vinylpyridinium Bromide) and Sodium Carboxymethyl Cellulose. *J. Memb. Sci.* **2010**, *347* (1–2), 183–192.

(117) Jose, J.; Shehzad, F.; Al-harthi, M. A. Preparation Method and Physical, Mechanical, Thermal Characterization of Poly(vinyl Alcohol)/poly(acrylic Acid) Blends. *Polym Bull. Bull.* **2014**, *71*, 2787–2802.

(118) Julia Ponce-Gonzalez, John R. Varcoe, and D. K. W. Commercial Monomer Availability Leading to Missed Opportunities? Anion-Exchange Membranes Made from Meta - Vinylbenzyl Chloride Exhibit an Alkali Stability Enhancement. *Appl. Energy Mater.* **2018**, *In print*.

(119) Kafkalidis, M. S.; Thouless, M. D. The Effects of Geometry and Material Properties on the Fracture of Single Lab-Shear Joints. *Int. J. Solids Stucts.* **2002**, *39* (April 2002), 4367–4383.

(120) Kamperman, M.; Fierke, M. A.; Garcia, C. B. W.; Wiesner, U. Morphology Control in Block Copolymer/polymer Derived Ceramic Precursor Nanocomposites. *Macromolecules* **2008**, *41* (22), 8745–8752.

(121) Kapfer, S. C.; Hyde, S. T.; Mecke, K.; Arns, C. H.; Schr??der-Turk, G. E. Minimal Surface Scaffold Designs for Tissue Engineering. *Biomaterials* **2011**, *32* (29), 6875–6882.

(122) Katsuhiro Inomata, Yoshiaki Sakamaki, T. N. & S. S. Solid-State Structure of Comb-Like Polymers Having N-Octadecyl Side Chains II. Cocrystallization of Side Chain with N-Octadecanoic Acid. *Polym. J.* **1996**, No. 28, 986–991.

(123) Keesom, W. H. The Second Viral Coefficient for Rigid Spherical Molecules, Whose Mutual Attraction Is Equivalent to that of a Quadruplet Placed at Their Centre. *KNAW Proc.* **1915**, *18I* (September), 636–646.

(124) Keller, A.; Chemical, I.; Division, D. The Spherulitic Structure of Crystalline Polymers. Part II. The Problem of Molecular Orientation in Polymer Spherulites. *J. Polym. Sci.* **1955**, *43* (19), 8128–8135.

(125) Kim, H.-S.; Kim, J.-S.; Shin, J.-W.; Lee, Y.-K. Cluster Formation in Plasticized Poly(phyenylene Oxide) Ionomers. *Polym. J.* **1999**, *31* (3), 306–308.

(126) Kim, J. S.; Yeon Hwa Nah; Jarng, S. S. Comparison of Clustering in Various Acrylate Ionomers. *Polymer (Guildf).* **2001**, *42* (13), 5567–5571.

(127) Kim, J. -S; Eisenberg, A. Effect of Sample Preparation Conditions and Degree of Neutralization on the Dynamic Mechanical Properties of Poly(styrene-co-sodium Methacrylate) Ionomers. *J. Polym. Sci. Part B Polym. Phys.* **1995**, *33* (2), 197–209.

(128) Kim, S. Y.; Park, M. J.; Jackson, A. Confinement Effects on Watery Domains in Hydrated Block Copolymer Electrolyte Membranes. *Macromolecules* **2010**, 8128–8135.

(129) Kimata, S.; Sakurai, T.; Nozue, Y.; Kasahara, T.; Karino, T.; Shibayama, M.; Kornfield, J. A. Molecular Basis of the Shish-Kebab Morphology in Polymer Crystallization. *Science (80-.).* **2018**, *316* (5827), 1014–1017.

(130) Kreuer, K. D.; Portale, G. A Critical Revision of the Nano-Morphology of Proton Conducting Ionomers and Polyelectrolytes for Fuel Cell Applications. *Adv. Funct. Mater.* **2013**, *23* (43), 5390–5397.

(131) Kroke, E.; Li, Y.; Konetschny, C.; Lecomte, E.; Fasel, C.; Riedel, R. Silazane Derived Ceramics and Related Materials. *Mater. Sci. Eng. R Reports* **2000**, *26* (4–6), 97–199.

(132) Kumaraswamy, G. Crystallization of Polymers from Stressed Melts Crystallization of Polymers from Stressed Melts. *J. Macromol. Sci. Part C Polym. Rev.* **2005**, *1797* (45), 375–397.

(133) Kuo, S. W.; Chang, F. C. Studies of Miscibility Behavior and Hydrogen Bonding in Blends of Poly (Vinylphenol) and Poly (Vinylpyrrolidone). *Macromolecules* **2001**, *34*, 5224–5228.

(134) Kusoglu, A.; Savagatrup, S.; Clark, K. T.; Weber, A. Z. Role of Mechanical Factors in Controlling the Structure − Function Relationship of PFSA Ionomers. *Macromolecules* **2012**, *45* (18), 7467–7476.

(135) Kusoglu, A.; Weber, A. Z. New Insights into Per Fluorinated Sulfonic-Acid Ionomers. *Chem. Rev.* **2017**, *117*, 987–1104.

(136) Laschewsky, A. Recent Trends in the Synthesis of Polyelectrolytes. *Curr. Opin. Colloid Interface Sci.* **2012**, *17* (2), 56–63.

(137) Lee, M.-S.; Kim, T.; Park, S.-H.; Kim, C.-S.; Choi, Y.-W. A Highly Durable Cross-Linked Hydroxide Ion Conducting Pore-Filling Membrane. *J. Mater. Chem.* **2012**, *22* (28), 13928–13931.

(138) Lee, W.; Kim, Y. S.; Bae, C. Robust Hydroxide Ion Conducting Poly(biphenyl Alkylene)s for Alkaline Fuel Cell Membranes. *ACS Macro Lett.* **2015**, *4*, 814–818.

(139) Lee, W.-H.; Kim, Y. S.; Bae, C. Robust Hydroxide Ion Conducting Poly(biphenyl Alkylene)s for Alkaline Fuel Cell Membranes. *ACS Macro Lett.* **2015**, *4* (8), 814–818.

(140) Lee, W.-H.; Mohanty, A. D.; Bae, C. Fluorene-Based Hydroxide Ion Conducting Polymers for Chemically Stable Anion Exchange Membrane Fuel Cells. *ACS Macro Lett.* **2015**, *4* (4), 453–457.

(141) Lee, W.; Mohanty, A. D.; Bae, C. Fluorene-Based Hydroxide Ion Conducting Polymers for Chemically Stable Anion Exchange Membrane Fuel Cells. *ACS Macro Lett.* **2015**, *4* (4), 453–457.

(142) Leitgeb, A.; Wappel, J.; Slugovc, C. The ROMP Toolbox Upgraded. *Polymer (Guildf).* **2010**, *51* (14), 2927–2946.

(143) Li, D. and J. B. DMTA and FTIR Investigation of the Phase Behavior of Poly (Methyl Methacrylate) - Poly (4-Vinylphenol) Blends. *Macromolecules* **1996**, *29*, 868–874.

(144) Li, D.; He, Q.; Cui, Y.; Li, J.; Potsdam, G. Fabrication of pH-Responsive Nanocomposites of Gold Nanoparticles / Poly (4-Vinylpyridine). *Chem. Mater.* **2007**, *19*, 412–417.

(145) Li, N.; Leng, Y.; Hickner, M. A.; Wang, C. Y. Highly Stable, Anion Conductive, Comb-Shaped Copolymers for Alkaline Fuel Cells. *J. Am. Chem. Soc.* **2013**, *135* (27), 10124–10133.

(146) Li, N.; Yan, T.; Li, Z.; Thurn-Albrecht, T.; Binder, W. H. Comb-Shaped Polymers to Enhance Hydroxide Transport in Anion Exchange Membranes. *Energy Environ. Sci.* **2012**, *5*, 7888–7892.

(147) Li, W.; Liang, C.; Qiu, J.; Zhou, W.; Han, H.; Wei, Z.; Sun, G.; Xin, Q. Carbon Nanotubes as Support for Cathode Catalyst of a Direct Methanol Fuel Cell. *Lett. to Ed.* **2002**, *40* (5), 787–803.

(148) Li, Y.; Yang, M. J.; She, Y. Humidity Sensitive Properties of Crosslinked and Quaternized Poly (4-Vinylpyridine-Co-Butyl Methacrylate). *Sensors Actuators B* **2005**, *107*, 252–257.

(149) *Handbook of Chemistry and Physics*, 84th ed.; Lide, D. R., Ed.; CRC Press, Florida, 2004.

(150) Lin, C. X.; Zhuo, Y. Z.; Lai, A. N.; Zhang, Q. G.; Zhu, A. M.; Ye, M. L.; Liu, Q. L. Side-Chain-Type Anion Exchange Membranes Bearing Pendent Imidazolium-Functionalized Poly(phenylene Oxide) for Fuel Cells. *J. Memb. Sci.* **2016**, *513*, 206–216.

(151) Liu, K.; Clendenning, S. B.; Riebe, L.; Chan, W. Y.; Zhu, X.; Freeman, M. R.; Yang, G. C.; Yip, C. M.; Grozea, D.; Lu, Z. H.; et al. Pyrolysis of Highly Metallized Polymers: Ceramic Thin Films Containing Magnetic CoFe Alloy Nanoparticles from a Polyferrocenylsilane with Pendant Cobalt Clusters. *Chem. Mater.* **2006**, *18* (10), 2591–2601.

(152) Long, H.; Pivovar, B. Hydroxide Degradation Pathways for Imidazolium Cations : A DFT Study. *J. Phys. Chem.* **2014**, *118* (19), 9880–9888.

(153) Lord, E. A.; Mackay, A. L. Periodic Minimal Surfaces of Cubic Symmetry. *Curr. Sci.* **2003**, *85* (3), 346–362.

(154) M. Ciulla, M.; Nicolini, P.; Benfenati, C.; Vecchiato, C.; Acquistapace, G.; L. Perrucci, G.; Magrini, F. Limited Hypotensive Effect of Sildenafil in a High-Risk Population: A Preliminary Report. *Curr. Drug Saf.* **2011**, *6* (4), 219–223.

(155) Maeda, Y.; Sato, Y. Mechanism of the Stevens Rearrangement of Ammonium Ylides. *J. Chem. Soc. Perkin Trans. 1* **1997**, *4* (10), 1491–1494.

(156) Manning P. Cooke, J. and J. L. C. Elimination Reactions. III. Hofmann Elimination in Cyclic Compounds. *J. Am. Chem. Soc.* **1968**, *3565* (1964), 5556–5561.

(157) Marino, M. G.; Kreuer, K. D. Alkaline Stability of Quaternary Ammonium Cations for Alkaline Fuel Cell Membranes and Ionic Liquids. *ChemSusChem* **2015**, *8* (3), 513–523.

(158) Marino, M. G.; Melchior, J. P.; Wohlfarth, A.; Kreuer, K. D. Hydroxide, Halide and Water Transport in a Model Anion Exchange Membrane. *J. Memb. Sci.* **2014**, *464*, 61–71.

(159) Maslak, V.; Yan, Z.; Xia, S.; Gallucci, J.; Hadad, C. M.; Badjic, J. D. Design , Synthesis , and Conformational Dynamics of a Gated Molecular Basket. *J.* **2006**, 5887–5894.

(160) Matson, J. B. Bottlebrush Polymer Synthesis by Ring-Opening Metathesis Polymerization: The Signi Fi Cance of the Anchor Group. *J. Am. Chem. Soc.* **2016**, *138*, 6998–7004.

(161) Mera, G.; Gallei, M.; Bernard, S.; Ionescu, E. Ceramic Nanocomposites from Tailor-Made Preceramic Polymers. *Nanomaterials* **2015**, *5* (2), 468–540.

(162) Merle, G.; Wessling, M.; Nijmeijer, K. Anion Exchange Membranes for Alkaline Fuel Cells: A Review. *J. Memb. Sci.* **2011**, *377* (1–2), 1–35.

(163) Michel, G.; Divoux, M.; Moore, R. B.; Baird, D. G.; Ellis, M. W.; Mcgrath, J. E.; Mauritz, K. A.; Michel, G.; Divoux, M. No Title, Virginia Polytechnic Institute and State, 2012.

(164) Michielsen, K.; Stavenga, D. . G. G.; Michielsen, K.; Stavenga, D. . G. G. Gyroid Cuticular Structures in Butterfly Wing Scales: Biological Photonic Crystals. *J. R. Soc. Interface* **2008**, *5* (18), 85–94.

(165) Mickel, W.; Schroder-Turk, G. E.; Mecke, K. Tensorial Minkowski Functionals of Triply Periodic Minimal Surfaces. *Interface Focus* **2012**, *2* (5), 623–633.

(166) Middleton, L. R.; Winey, K. I. Nanoscale Aggregation in Acid- and Ion-Containing Polymers. *Annu. Chem. Biomol. Eng* **2017**, *8*, 499–523.

(167) Miller, R. L.; Boyer, R. F.; Heijboer, J. X-Ray Scattering from Amorphous Acrylate and Methacrylate Polymers: Evidence of Local Order. *J. Polym. Sci. Polym. Phys. Ed.* **1984**, *22* (12), 2021–2041.

(168) Mohanty, A. D.; Bae, C. Mechanistic Analysis of Ammonium Cation Stability for Alkaline Exchange Membrane Fuel Cells. *J. Mater. Chem. A Mater. energy Sustain.* **2014**, *2* (41), 17314–17320.

(169) Moon, G. Y.; Rhim, J. W. Self-Assembly Modification of Perfluorosulfonic Acid Membranes for the Application to Direct Methanol Fuel Cells. *Macromol. Res.* **2008**, *16* (6), 524–531.

(170) Mooney, R. C. L. An X-Ray Study of the Structure of Polyvinyl Alcohol. In *American Physical Society, 1941*; Washington, 1941; Vol. 63, pp 2828–2832.

(171) Moore, R. B.; Gauthier, M.; Williams, C. E.; Eisenberg, A. Heterogeneities in Random Ionomers - a Small-Angle X-Ray-Scattering Investigation of Alkylated Polystyrene-Based Materials. *Macromolecules* **1992**, *25* (21), 5769–5773.

(172) Mortell, K.; Weatherman, R.; Kiessling, L. Recognition Specificity of Neoglycopolymers by Ring-Opening Metathesis Polymerization. *J. Am. Chem. Soc.* **1996**, *118* (14), 2297–2298.

(173) Nguyen, N.-T.; Chan, S. H. Micromachined Polymer Electrolyte Membrane and Direct Methanol Fuel Cells—a Review. *J. Micromechanics Microengineering* **2006**, *16* (4), R1–R12.

(174) Nguyen, S. T.; Johnson, L. K.; Grubbs, R. H.; Beckman, M.; Joseph, W. Polymerization, Ring-Opening Metathesis. *J. Am. Ceram. Soc. Commun. to Ed.* **1992**, *114*, 3974–3975.

(175) Nie, Y.; Zhao, Y.; Matsuba, G.; Hu, W. Shish-Kebab Crystallites Initiated by Shear Fracture in Bulk Polymers. *Macromolecules* **2018**, *51*, 480–487.

(176) Nikovia, C.; Maroudas, A.; Goulis, P.; Tzimis, D.; Paraskevopoulou, P.; Pitsikalis, M. Statistical Ring Opening Metathesis Copolymerization of Norbornene and Cyclopentene by Grubbs'1st-Generation Catalyst. *Molecules* **2015**, *20*, 15597–15615.

(177) Nishikawa, Y.; Jinnai, H.; Koga, T.; Hashimoto, T.; Hyde, S. T. Measurements of Interfacial Curvatures of Bicontinuous Structure from Three- Dimensional Digital Images. 1. A Parallel Surface Method. *Langmuir* **1998**, *14* (11), 1242–1249.

(178) Nomura, K.; Abdellatif, M. M. Precise Synthesis of Polymers Containing Functional End Groups by Living Ring-Opening Metathesis Polymerization (ROMP): Ef Fi Cient Tools for Synthesis of Block / Graft Copolymers. *Polymer (Guildf).* **2010**, *51*, 1861–1881.

(179) Nun, S. A.; Hickner, M. A. Quantitative 1 H NMR Analysis of Chemical Stabilities in Anion- Exchange Membranes. *ACS Macro Lett.* **2013**, *2* (1), 49–52.

(180) Nuyken, O.; Pask, S. D. Ring-Opening Polymerization-An Introductory Review. *Polymers (Basel).* **2013**, *5* (2), 361–403.

(181) Odijk, T. Possible Scaling Relations for Semidilute. *Macromolecules* **1979**, 688–693.

(182) Of, J.; Science, P. Organized Polymerization of Vinyl Pyridinium Salts. *J. Polym. Sci. Part C* **1968**, *23*, 357–363.

(183) Olgun, C. T. and G. The Effect of Filler Type on the Thermal Degradation of Inorganic Filled Poly (2-Hydroxyethyl Methacrylate) Composites. *Polym. Degredation Stab.* **1998**, *62*, 267–270.

(184) Olsson, J. S.; Pham, T. H.; Jannasch, P. Poly (Arylene Piperidinium) Hydroxide Ion Exchange Membranes : Synthesis , Alkaline Stability , and Conductivity. *Adv. Funct. Mater.* **2018**, *1702758*, 1–10.

(185) Olsson, J. S.; Pham, T. H.; Jannasch, P. Poly (N , N -Diallylazacycloalkane) S for Anion-Exchange Membranes Functionalized with N ‑ Spirocyclic Quaternary Ammonium Cations. *Macromolecules* **2017**.

(186) Orfino, F. P.; Holdcroft, S. The Morphology of Nafion: Are Ion Clusters Bridged by Channels or Single Ionic Sites? *J. New Mater. Electrochem. Syst.* **2000**, *3* (4), 285–290.

(187) Pabit, S. A.; Meisburger, S. P.; Li, L.; Blose, J. M.; Jones, C. D.; Pollack, L. Counting Ions around DNA with Anomalous Small-Angle X-Ray Scattering. *J. Chem. Soc.* **2010**, *132*, 16334–16336.

(188) Pan, J.; Chen, C.; Li, Y.; Wang, L.; Tan, L.; Li, G.; Tang, X.; Xiao, L.; Lu, J.; Zhuang, L. Constructing Ionic Highway in Alkaline Polymer Electrolytes. *Energy Environ. Sci.* **2014**, *7* (1), 354.

(189) Pan, J.; Lu, S.; Li, Y.; Huang, A.; Zhuang, L.; Lu, J. High-Performance Alkaline Polymer Electrolyte for Fuel Cell Applications. *Adv. Funct. Mater.* **2010**, *20* (2), 312–319.

(190) Pankaj, S.; Beiner, M. Long-Term Behavior and Side Chain Crystallization of poly(3-Alkyl Thiophenes). *Soft Matter* **2010**, *6* (15), 3506–3516.

(191) Pankaj, S.; Hempel, E.; Beiner, M. Side-Chain Dynamics and Crystallization in a Series of Regiorandom Poly (3-Alkylthiophenes). *Macromolecules* **2009**, *42*, 716–724.

(192) Patel, M.; Rosenfeldt, S.; Ballauff, M.; Dingenouts, N.; Pontoni, D.; Narayanan, T. Analysis of the Correlation of Counterions to Rod-like Macroions by Anomalous Small-Angle X-Ray Scattering. *Phys. Chem. Chem. Phys* **2004**, *6*, 2962–2967.

(193) Patel, M.; Patel, R.; Chi, W. S.; Kim, J. H.; Sung, J. S. Antibacterial Behaviour of Quaternized Poly(vinyl Chloride)-G-poly(4-Vinyl Pyridine) Graft Copolymers. *Chinese J. Polym. Sci. (English Ed.* **2015**, *33* (2), 265–274.

(194) Pham, T. H.; Jannasch, P. Aromatic Polymers Incorporating Bis ‑ N ‑ Spirocyclic Quaternary Ammonium Moieties for Anion-Exchange Membranes. *ACS Macro Lett.* **2015**, 1370–1375.

(195) Pham, T. H.; Olsson, J. S.; Jannasch, P. N ‐ Spirocyclic Quaternary Ammonium Ionenes for Anion-Exchange Membranes. *J. Am. Chem. Soc.* **2017**, 13–16.

(196) Pierin, G.; Grotta, C.; Colombo, P.; Mattevi, C. Direct Ink Writing of Micrometric SiOC Ceramic Structures Using a Preceramic Polymer. *J. Eur. Ceram. Soc.* **2015**, *36* (7), 1589–1594.

(197) Platé, N. A.; Shibaev, V. P. Comb-like Polymers. Structure and Properties. *J. Polym. Sci. Macromol. Rev.* **1974**, *8* (1), 117–253.

(198) Poly, S.; Russell, G. A.; K, P. A. H.; Donald, E.; C, A.; Andrade, J. D.; Al, R. E. T. Thermal and Dynamic Mechanical Relaxation. *J. Polym. Sci. Polym. Phys. Ed.* **1980**, *18*, 1271–1283.

(199) Polymerization, S. Polymerization of 4-Vinylpyridinium Salts. III. A Clarification of the Mechanism of Spontaneous Polymerization. *J. Polym. Sci. Part A-1* **1971**, *9*, 1493–1504.

(200) Price, S. C.; Williams, K. S.; Beyer, F. L. Relationships between Structure and Alkaline Stability of Imidazolium Cations for Fuel Cell Membrane Applications. *ACS Macro Lett.* **2014**, *3* (2), 160–165.

(201) Qin, J. Studies of Block Copolymer Melts by Field Theory and Molecular Simulation, University of Minnesota, 2009.

(202) Rajagopalan, S.; Robb, R. A. Schwarz Meets Schwann: Design and Fabrication of Biomorphic and Durataxic Tissue Engineering Scaffolds. *Med. Image Anal.* **2006**, *10* (5), 693–712.

(203) Rault, J.; Lucas, A.; Neffati, R.; Monleo, M. Thermal Transitions in Hydrogels of Poly (Ethyl Acrylate)/ Poly (Hydroxyethyl Acrylate) Interpenetrating Networks. *Macromolecules* **1997**, *30*, 7866–7873.

(204) Reshetenko, T.; Odgaard, M.; Schlueter, D.; Serov, A. Analysis of Alkaline Exchange Membrane Fuel Cells Performance at Di Ff Erent Operating Conditions Using DC and AC Methods. *J. Power Sources* **2018**, *375* (September 2017), 185–190.

(205) Ritz, H.; Dawson, P.; Marin, T. Analyzing the Orientation Dependence of Stresses in Polycrystals Using Vertices of the Single Crystal Yield Surface and Crystallographic Fibers of Orientation Space. *J. Mech. Phys. Solids* **2010**, *58* (1), 54–72.

(206) Roozemond, P. C.; Cui, K.; Li, L.; Peters, G. W. M. Multimorphological Crystallization of Shish-Kebab Structures in Isotactic Polypropylene: Quantitative Modeling of Parent − Daughter Crystallization Kinetics. *Macromolecules* **2014**, *47*, 5152–5162.

(207) Roy, R. K.; Gowd, E. B.; Ramakrishnan, S. Periodically Grafted Amphiphilic Copolymers: Nonionic Analogues of Ionenes. *Macromolecules* **2012**, *45* (7), 3063–3069.

(208) Rusa, C. C.; Wei, M.; Bullions, T. A.; Rusa, M.; Gomez, M. A.; Porbeni, F. E.; Wang, X.; Shin, I. D.; Balik, C. M.; White, J. L.; et al. Controlling the Polymorphic Behaviors of Semicrystalline Polymers with Cyclodextrins. *Cryst. Growth Des.* **2004**, *4* (6), 1431–1441.

(209) Russina, O.; Triolo, A.; Gontrani, L.; Caminiti, R.; Xiao, D.; Hines Jr, L. G.; Bartsch, R. A.; Quitevis, E. L.; Pleckhova, N.; Seddon, K. R. Morphology and Intermolecular Dynamics of 1-Alkyl-3-Methylimidazolium Bis{(trifluoromethane)sulfonyl}amide Ionic Liquids: Structural and Dynamic Evidence of Nanoscale Segregation. *J. Phys. Condens. Matter* **2009**, *21* (42), 424121.

(210) Saha, A.; Raj, R.; Williamson, D. L.; Kleebe, H. J. Characterization of Nanodomains in Polymer-Derived SiCN Ceramics Employing Multiple Techniques. *J. Am. Ceram. Soc.* **2005**, *88* (1), 232–234.

(211) Sahiner, N.; Yasar, A. O. Journal of Colloid and Interface Science The Generation of Desired Functional Groups on Poly (4-Vinyl Pyridine) Particles by Post-Modification Technique for Antimicrobial and Environmental Applications. *J. Colloid Interface Sci.* **2013**, *402*, 327–333.

(212) Salas-De La Cruz, D.; Green, M. D.; Ye, Y.; Elabd, Y. A.; Long, T. E.; Winey, K. I. Correlating Backbone-to-Backbone Distance to Ionic Conductivity in Amorphous Polymerized Ionic Liquids. *J. Polym. Sci. Part B Polym. Phys.* **2012**, *50* (5), 338–346.

(213) Sarkar, S.; Zou, J.; Liu, J.; Xu, C.; An, L.; Zhai, L. Polymer-Derived Ceramic Composite Fibers with Aligned Pristine Multiwalled Carbon Nanotubes. *ACS Appl. Mater. Interfaces* **2010**, *2* (4), 1150–1156.

(214) Sax, J.; Ottino, J. M. Modeling of Transport of Small Molecules in Polymer Blends: Application of Effective Medium Theory. *Polym. Eng. Sci.* **1983**, *23* (1 l), 165–176.

(215) Schee, H. Van Der; Lyklema, J. A Lattice Theory of Polyelectrolyte Adsorption. *J. Phys. Chem.* **1984**, *88* (26), 6661–6667.

(216) Schröder-Turk, G. E.; Wickham, S.; Averdunk, H.; Brink, F.; Fitz Gerald, J. D.; Poladian, L.; Large, M. C. J.; Hyde, S. T. The Chiral Structure of Porous Chitin within the Wing-Scales of Callophrys Rubi. *J. Struct. Biol.* **2011**, *174* (2), 290–295.

(217) Seguela, R. On the Strain - Induced Crystalline Phase Changes in Semi - Crystalline Polymers : Mechanisms and Incidence on the Mechanical Properties On the Strain-Induced Crystalline Phase Changes in Semi-Crystalline Polymers : Mechanisms and Incidence on the. *J. Macromol. Sci. Part C Polym. Rev.* **2005**, *45* (263–287).

(218) Seitz, H.; Rieder, W.; Irsen, S.; Leukers, B.; Tille, C. Three-Dimensional Printing of Porous Ceramic Scaffolds for Bone Tissue Engineering. *J. Biomed. Mater. Res. - Part B Appl. Biomater.* **2005**, *74* (2), 782–788.

(219) Shahid, S. *Polymer-Metal Organic Frameworks (MOFs) Mixed Matrix Membranes for Gas Separation Applications Salman Shahid*; 2015.

(220) Shaplov, A. S.; Ponkratov, D. O.; Vlasov, P. S.; Lozinskaya, E. I.; Malyshkina, I. A.; Vidal, F.; Aubert, P. H.; Armand, M.; Vygodskii, Y. S. Solid-State Electrolytes Based on Ionic Network Polymers. *Polym. Sci., Ser. B* **2014**, *56* (2), 164–177.

(221) Shaplov, A. S.; Vlasov, P. S.; Lozinskaya, E. I.; Shishkan, O. A.; Ponkratov, D. O.; Malyshkina, I. A.; Vidal, F.; Wandrey, C.; Godovikov, I. A.; Vygodskii, Y. S. Thiol-Ene Click Chemistry as a Tool for a Novel Family of Polymeric Ionic Liquids. *Macromol. Chem. Phys.* **2012**, *213* (13), 1359–1369.

(222) Shi, Y.; Wan, Y.; Zhai, Y.; Liu, R.; Meng, Y.; Tu, B.; Zhao, D. Ordered Mesoporous SiOC and SiCN Ceramics from Atmosphere-Assisted in Situ Transformation. *Chem. Mater.* **2007**, *19* (7), 1761–1771.

(223) Shim, H. K.; Paul, D. K.; Karan, K. Resolving the Contradiction between Anomalously High Water Uptake and Low Conductivity of Nanothin Nafion Films on SiO2Substrate. *Macromolecules* **2015**, *48* (22), 8394–8397.

(224) Shtukenberg, A. G.; Punin, Y. O.; Gunn, E.; Kahr, B. Spherulites. *Chem. Rev.* **2012**, *112*, 1805–1838.

(225) Si, Z.; Qiu, L.; Dong, H.; Gu, F.; Li, Y.; Yan, F. Effects of Substituents and Substitution Positions on Alkaline Stability of Imidazolium Cations and Their Corresponding Anion-Exchange Membranes. *Appl. Mater. Interfaces* **2014**, *6*, 4346−4355.

(226) Sing, C.; Zwanikken, J.; Cruz, M. D. La. Electrostatic Control of Block Copolymer Morphology. *Nat. Mater.* **2014**, *13* (7), 694–698.

(227) Singh, M.; Odusanya, O.; Wilmes, G. M.; Eitouni, H. B.; Gomez, E. D.; Patel, A. J.; Chen, V. L.; Park, M. J.; Fragouli, P.; Iatrou, H.; et al. Effect of Molecular Weight on the Mechanical and Electrical Properties of Block Copolymer Electrolytes. *Macromolecules* **2007**, *40* (13), 4578–4585.

(228) Smith, M. B.; March, J. March's Advanced Organic Chemistry: Reactions, Mechanisms, and Structure, 5th Edition. *Molecules* **2001**, *6* (12), 1064–1065.

(229) Smitha, B.; Sridhar, S.; Khan, A. A. Solid Polymer Electrolyte Membranes for Fuel Cell Applications - A Review. *J. Memb. Sci.* **2005**, *259* (1–2), 10–26.

(230) Soo, P. P.; Huang, B.; Jang, Y.-I.; Chiang, Y.-M.; Sadoway, D. R.; Mayes, A. M. Rubbery Block Copolymer Electrolytes for Solid-State Rechargeable Lithium Batteries. *J. Electrochem. Soc.* **1999**, *146* (1), 32.

(231) Steele, B. C.; Heinzel, A. Materials for Fuel-Cell Technologies. *Nature* **2001**, *414*, 345–352.

(232) Steinbach, T.; Alexandrino, E. M.; Wurm, F. R. Unsaturated Poly(phosphoester)s via Ring-Opening Metathesis Polymerization. *Polym. Chem.* **2013**, *4*, 3800–3806.

(233) Strasser, D. J.; Graziano, B. J.; Knauss, D. M. Base Stable Poly(diallylpiperidinium Hydroxide) Multiblock Copolymers for Anion Exchange Membranes. *J. Mater. Chem. A Mater. energy Sustain.* **2017**, *5*, 9627–9640.

(234) Studart, A. R.; Gonzenbach, U. T.; Tervoort, E.; Gauckler, L. J. Processing Routes to Macroporous Ceramics: A Review. *J. Am. Ceram. Soc.* **2006**, *89* (6), 1771–1789.

(235) Sturhmann, H. B. Resonance Scattering in Macromolecular Structure Research. *Adv. Polym. Sci.* **1885**, *67*, 123–163.

(236) Sung, I. K.; Christian; Mitchell, M.; Kim, D. P.; Kenis, P. J. A. Tailored Macroporous SiCN and SiC Structures for High-Temperature Fuel Reforming. *Adv. Funct. Mater.* **2005**, *15* (8), 1336–1342.

(237) Susca, E. M.; Beaucage, P. A.; Hanson, M. A.; Werner-Zwanziger, U.; Zwanziger, J. W.; Estroff, L. A.; Wiesner, U. Self-Assembled Gyroidal Mesoporous Polymer-Derived High Temperature Ceramic Monoliths. *Chem. Mater.* **2016**, *28* (7), 2131–2137.

(238) Sutthasupa, S.; Shiotsuki, M.; Sanda, F. Recent Advances in Ring-Opening Metathesis Polymerization, and Application to Synthesis of Functional Materials. *Polym. J.* **2010**, *42* (12), 905–915.

(239) Sztucki, M.; Cola, E. Di; Narayanan, T. Anomalous Small-Angle X-Ray Scattering from Charged Soft Matter. *Eur. Phys. J. Spec. Top.* **2012**, *208*, 319–331.

(240) Torquato, S.; Donev, A. Minimal Surfaces and Multifunctionality. *Proc. R. Soc. A Math. Phys. Eng. Sci.* **2004**, *460* (2047), 1849–1856.

(241) Transport, P. Book Overview. *Top. Appl. Phys.* **2009**, *113*, 349–363.

(242) Triolo, A.; Russina, O.; Fazio, B.; Triolo, R.; Di Cola, E. Morphology of 1-Alkyl-3-Methylimidazolium Hexafluorophosphate Room Temperature Ionic Liquids. *Chem. Phys. Lett.* **2008**, *457* (4–6), 362–365.

(243) Triolo, A.; Russina, O.; Hans-Jurgen Bleif, A.; Cola, E. Di. Nanoscale Segregation in Room Temperature Ionic Liquids†. *J. Phys. Chem. B* **2007**, No. 111, 4641–4644.

(244) Tsai, T. H.; Ertem, S. P.; Maes, A. M.; Seifert, S.; Herring, A. M.; Coughlin, E. B. Thermally Cross-Linked Anion Exchange Membranes from Solvent Processable Isoprene Containing Ionomers. *Macromolecules* **2015**, *48* (3), 655–662.

(245) Tsai, T. Ionic Copolymers for Alkaline Anion Exchange Membrane Fuel Cells (AAEMFCs), University of Massachusetts, 2014.

(246) Tsang, E. M.; Zhang, Z.; Shi, Z.; Soboleva, T.; Holdcroft, S. Considerations of Macromolecular Structure in the Design of Proton Conducting Polymer Membranes: Graft versus Diblock Polyelectrolytes. *J Am Chem Soc* **2007**, *129* (49), 15106–15107.

(247) Tuncer Caykara, Cengiz Ozyurek, Omer Kantoglu. Investigation of Thermal Behavior of Poly (2-Hydroxyethyl Methacrylate- Co -Itaconic Acid) Networks. *J. Appl. Polym. Sci* **2005**, *103*, 1602–1607.

(248) Tyler, A. I. I.; Barriga, H. M. G.; Parsons, E. S.; McCarthy, N. L. C.; Ces, O.; Law, R. V; Seddon, J. M.; Brooks, N. J. Electrostatic Swelling of Bicontinuous Cubic Lipid Phases. *Soft Matter* **2015**, *11*, 3279–3286.

(249) Umeyama, H.; Morokuma, K. The Origin of Hydrogen Bonding. An Energy Decomposition Study. *J. Am. Chem. Soc.* **1977**, *99* (5), 1316–1332.

(250) Valkama, S.; Kosonen, H.; Ruokolainen, J.; Haatainen, T.; Torkkeli, M.; Serimaa, R.; ten Brinke, G.; Ikkala, O. Self-Assembled Polymeric Solid Films with Temperature-Induced Large and Reversible Photonic-Bandgap Switching. *Nat. Mater.* **2004**, *3* (12), 872–876.

(251) Valkama, S.; Ruotsalainen, T.; Nykänen, A.; Laiho, A.; Kosonen, H.; Ten Brinke, G.; Ikkala, O.; Ruokolainen, J. Self-Assembled Structures in Diblock Copolymers with Hydrogen-Bonded Amphiphilic Plasticizing Compounds. *Macromolecules* **2006**, *39* (26), 9327–9336.

(252) van Zoelen, W.; Asumaa, T.; Ruokolainen, J.; Ikkala, O.; ten Brinke, G. Phase Behavior of Solvent Vapor Annealed Thin Films of PS- B -P4VP(PDP) Supramolecules. *Macromolecules* **2008**, *41* (9), 3199–3208.

(253) Van Zoelen, W.; Van Ekenstein, G. A.; Ikkala, O.; Ten Brinke, G. Incorporation of PPE in Lamellar Self-Assembled PS-B-P4VP(PDP) Supramolecules and PS-B-P4VP Diblock Copolymers. *Macromolecules* **2006**, *39* (19), 6574–6579.

(254) Vanecko, J. A.; Wan, H.; West, F. G. Recent Advances in the Stevens Rearrangement of Ammonium Ylides. Application to the Synthesis of Alkaloid Natural Products. *Tetrahedron* **2006**, *62* (6), 1043–1062.

(255) Verma, P. L.; Rao, S. S.; Gejji, S. P. Probing Molecular Interactions Underlying Imidazolium and Pyridinium Based Ionic Liquids. *J. Mol. Liq.* **2015**, *212*, 885–899.

(256) Volkov, V. V; Plat, N. A. Aggregation State and Mesophase Structure of Comb-Shaped Polymers with Fluorocarbon Side Groups. *Polymer (Guildf).* **1992**, *33* (6), 1316–1320.

(257) Wan, J.; Alizadeh, A.; Taylor, S. T.; Malenfant, P. R. L.; Manoharan, M.; Loureiro, S. M. Nanostructured Non-Oxide Ceramics Templated via Block Copolymer Self-Assembly. *Chem. Mater.* **2005**, *17* (23), 5613–5617.

(258) Wan, J.; Malenfant, P. R. L.; Taylor, S. T.; Loureiro, S. M.; Manoharan, M. Microstructure of Block Copolymer/precursor Assembly for Si-C-N Based Nano-Ordered Ceramics. *Mater. Sci. Eng. A* **2007**, *463* (1–2), 78–88.

(259) Wanakule, N. S.; Virgili, J. M.; Teran, A. A.; Wang, Z. G.; Balsara, N. P. Thermodynamic Properties of Block Copolymer Electrolytes Containing Imidazolium and Lithium Salts. *Macromolecules* **2010**, *43* (19), 8282–8289.

(260) Wang, K.; Chen, F.; Zhang, Q.; Fu, Q. Shish – Kebab of Polyolefin by "' Melt Manipulation '" Strategy in Injection-Molding : A Convenience Pathway from Fundament to Application. *Polymer (Guildf).* **2008**, *49* (22), 4745–4755.

(261) Weiber, E. A.; Jannasch, P. Ion Distribution in Quaternary-Ammonium-Functionalized Aromatic Polymers : Effects on the Ionic Clustering and Conductivity of Anion-Exchange Membranes. *ChemSusChem* **2014**, *7*, 2621–2630.

(262) Weill, G. Conformation and Order in Polyelectrolyte Solutions. *J. Phys.* **1988**, *49* (6), 1049–1054.

(263) Williams, M. C. Status and Promise of Fuel Cell Technology. *Fuel Cells* **2001**, *1* (2), 87–91.

(264) Wohlfarth, A.; Smiatek, J.; Kreuer, K.; Takamuku, S.; Jannasch, P.; Maier, J. Proton Dissociation of Sulfonated Polysulfones: In Fl Uence of Molecular Structure and Conformation. *Macromolecules* **2015**, *48*, 1134–1143.

(265) Wohlgemuth, M.; Yufa, N.; Hoffman, J.; Thomas, E. L. Triply Periodic Bicontinuous Cubic Microdomain Morphologies by Symmetries. *Macromolecules* **2001**, *34* (17), 6083–6089.

(266) Wollmann, D.; Williams, C. E.; Eisenberg, a. Aggregate Modification via Plasticization of Ionomers-Dynamic Mechanical and Morphological Studies. *Macromolecules* **1992**, *25* (25), 6775–6783.

(267) Xiao, D.; Rajian, J. R.; Cady, A.; Li, S.; Bartsch, R. a; Quitevis, E. L. Nanostructural Organization and Anion Effects on the Temperature Dependence of the Optical Kerr Effect Spectra of Ionic Liquids. *J. Phys. Chem. B* **2007**, *111* (18), 4669–4677.

(268) Xie, G.; Okada, T. Water Transport Behavior in Nation 117 Membranes. *J. Electrochem. Soc.* **1995**, *142* (9), 2–7.

(269) Xie, G.; Okada, T.; I, A. P. I. A. Characteristics of Water Transport in Relation to Microscopic Structure in Nafion Membranes. *J. Chem. Soc., Faraday Tans.*, **1996**, *92* (4), 663–669.

(270) Xing, P.; Dong, L.; An, Y.; Feng, Z. Miscibility and Crystallization of Poly (-Hydroxybutyrate) and Poly (P -Vinylphenol) Blends. *Macromolecules* **1997**, *30*, 2726–2733.

(271) Yakunin, A. N. A Bicontinuous Structure in Some Systems with Cubic Mesophases. *Cent. Eur. J. Phys.* **2004**, *2* (3), 535–555.

(272) Yang, M.; Zhang, Z.; Yuan, F.; Wang, W.; Hess, S.; Lienkamp, K.; Lieberwirth, I.; Wegner, G. Self-Assembled Structures in Organogels of Amphiphilic Diblock Codendrimers. *Chem. - A Eur. J.* **2008**, *14* (11), 3330–3337.

(273) Yang, Y.; Xu, Y.; Ye, N.; Zhang, D.; Yang, J. Alkali Resistant Anion Exchange Membranes Based on Saturated Heterocyclic Quaternary Ammonium Cations Functionalized Poly (2 , 6-Dimethyl-1 , 4-Phenylene Oxide) S. *J. Electrochem. Soc.* **2018**, *165* (5), 350–356.

(274) Yao, C.; Li, X.; Neoh, K. G.; Shi, Z.; Kang, E. T. Surface Modification and Antibacterial Activity of Electrospun Polyurethane Fibrous Membranes with Quaternary Ammonium Moieties. *J. Memb. Sci.* **2008**, *320* (1–2), 259–267.

(275) Yarusso, D. J.; Cooper, S. L. Microstructure of Ionomers : Interpretation of Small-Angle X-Ray Scattering Data. *Macromolecules* **1983**, *16* (12), 1871–1880.

(276) Ye, Y.; Elabd, Y. A. Relative Chemical Stability of Imidazolium-Based Alkaline Anion Exchange Polymerized Ionic Liquids. *Macromolecules* **2011**, *44* (21), 8494–8503.

(277) Yuan, H. Synthesis and Structure-Property Relationships of Polymeric Membranes for Small Molecule Transport, University of Massachusetts, Amherst, 2017.

(278) Zander, N. E.; Orlicki, J. A.; Rawlett, A. M. Thermal and FTIR Characterization of Poly (4-Vinylpyridine) Crosslinked with Metal Salts. *Mater. Res.* **2010**, No. March.

(279) Zhang, W.; Liu, Y.; Jackson, A. C.; Savage, A. M.; Ertem, S. P.; Tsai, T. H.; Seifert, S.; Beyer, F. L.; Liberatore, M. W.; Herring, A. M.; et al. Achieving Continuous Anion Transport Domains Using Block Copolymers Containing Phosphonium Cations. *Macromolecules* **2016**, *49* (13), 4714–4722.

(280) Zhang, X.; Chen, P.; Shi, Q.; Li, S.; Gong, F.; Chen, X.; An, Z. ScienceDirect Block Poly (Arylene Ether Sulfone) Copolymers Bearing Quaterinized Aromatic Pendants : Synthesis , Property and Stability. *Int. J. Hydrogen Energy* **2017**, *42* (42), 26320–26332.

(281) Zhang, Z.; Liu, C.; Cao, X.; Wang, J.-H. H.; Chen, Q.; Colby, R. H. Morphological Evolution of Ionomer/Plasticizer Mixtures during a Transition from Ionomer to Polyelectrolyte. *Macromolecules* **2017**, *50* (3), 963–971.

(282) Zhang, Z.; Yang, M.; Hu, C.; Liu, B.; Hu, M.; Zhang, X.; Wang, W.; Zhou, Y.; Wang, H. Correlation between Gel-Forming Ability, Supramolecular Aggregates and Main-Chain Conformation of Dendronized Polymer Gelators. *New J. Chem.* **2011**, *35* (1), 103.

(283) Zhang, Z.; Yang, M.; Zhang, X.; Zhang, L.; Liu, B.; Zheng, P.; Wang, W. Enhancing Gelation Ability of a Dendritic Gelator through Complexation with a Polyelectrolyte. *Chem. - A Eur. J.* **2009**, *15* (10), 2352–2361.

(284) Zhou, Q.; Liu, F.; Guo, C.; Fu, Q.; Shen, K.; Zhang, J. Shish E Kebab-like Cylindrulite Structures Resulted from Periodical Shear-Induced Crystallization of Isotactic Polypropylene. *Polymer (Guildf).* **2011**, *52* (13), 2970–2978.

(285) Zhu, T.; Xu, S.; Rahman, A.; Dogdibegovic, E.; Yang, P.; Pageni, P.; Kabir, M. P.; Zhou, X.; Tang, C. Cationic Metallo-Polyelectrolytes for Robust Alkaline Anion- Exchange Membranes. *Angew. Chemie Funct. Met.* **2018**, *57*, 1–6.

(286) Zoelen, W. Van. PS-B-P4VP (PDP) Comb-Shaped Supramolecules : Nanorods and Thin Films for Nanotemplating, University of Groningen, 2009.

(287) Zoelen, W. Van; Polushkin, E.; Brinke, G. Hierarchical Terrace Formation in PS-b-P4VP (PDP) Supramolecular Thin Films Hierarchical Terrace Formation in PS-b-P4VP (PDP) Supramolecular Thin Films. *Macromolecules* **2008**, 8807–8814.

(288) Zornoza, B.; Tellez, C.; Coronas, J.; Gascon, J.; Kapteijn, F. Metal Organic Framework Based Mixed Matrix Membranes: An Increasingly Important Field of Research with a Large Application Potential. *Microporous Mesoporous Mater.* **2013**, *166*, 67–78.

(289) Zuo, F.; Keum, J. K.; Yang, L.; Somani, R. H.; Hsiao, B. S. Thermal Stability of Shear-Induced Shish-Kebab Precursor Structure from High Molecular Weight Polyethylene Chains. *Macromolecules* **2006**, *39*, 2209–2218.